UNIVERSITY OF SOUTHAMPTON

FACULTY OF ENGINEERING AND THE ENVIRONMENT

Institute of Sound and Vibration Research

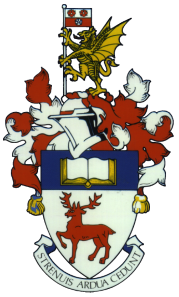

Boundary Integral Methods for Sound Propagation with Subsonic Potential Mean Flows

by

Simone Mancini

A thesis submitted in partial fulfillment
of the requirements for the degree of
Doctor of Philosophy

February 2017

UNIVERSITY OF SOUTHAMPTON

ABSTRACT

FACULTY OF ENGINEERING AND THE ENVIRONMENT
Institute of Sound and Vibration Research

Doctor of Philosophy

BOUNDARY INTEGRAL METHODS FOR SOUND PROPAGATION WITH SUBSONIC POTENTIAL MEAN FLOWS

by Simone Mancini

This work deals with including non-uniform mean flow effects into boundary integral solutions to acoustic wave propagation. A time harmonic boundary integral solution is proposed for low Mach number potential flows with small non-uniform mean flow velocities and a free-field Green's function is recovered to solve the corresponding kernel. The boundary integral formulation can be used as a means of solving both wave extrapolation and boundary element problems. For boundary element solutions to external sound propagation, the non-uniqueness issue is worked around by extending the conventional combined Helmholtz integral equation formulation and the Burton–Miller approach to non-uniform mean flows. Nonetheless, the proposed integral formulation is shown to be consistent with a combination of the physical models associated with the Taylor and Lorentz transforms. The combined Taylor–Lorentz transformation allows mean flow effects on acoustic wave propagation to be resolved by using a standard boundary integral formulation for the Helmholtz problem with quiescent media in a transformed space.

Numerical experiments are performed to benchmark the proposed integral formulations against finite element solutions based on the linearised potential equation. Numerical examples are also used to validate a weakly-coupled approach exploiting the proposed integral formulations in order to predict forward fan noise installation effects. Nonetheless, the integral formulations in a transformed space are used to simulate mean flow effects based on standard boundary element solvers for quiescent media. The results suggest that, for low Mach numbers, boundary element solutions to wave propagation with non-uniform mean flows represent a good approximation of finite element solutions based on the linearised potential equation. It is shown that the boundary element solutions including non-uniform mean flow effects improve on the corresponding approximations assuming a uniform flow in the whole computational domain. This is observed when sound propagation is predicted in the near field and in a region where the non-uniformity in the mean flow velocity is significant.

Contents

List of Figures

List of Tables

Declaration of Authorship

I, Simone Mancini, declare that the thesis entitled *Boundary Integral Methods for Sound Propagation with Subsonic Potential Mean Flows* and the work presented in the thesis are both my own, and have been generated by me as the result of my own original research. I confirm that:

- This work was done wholly or mainly while in candidature for a research degree at this University;
- Where any part of this thesis has previously been submitted for a degree or any other qualification at this University or any other institution, this has been clearly stated;
- Where I have consulted the published work of others, this is always clearly attributed;
- Where I have quoted from the work of others, the source is always given. With the exception of such quotations, this thesis is entirely my own work;
- I have acknowledged all main sources of help;
- Where the thesis is based on work done by myself jointly with others, I have made clear exactly what was done by others and what I have contributed myself;
- Either none of this work has been published before submission, or parts of this work have been published as: Refs. [1], [2], [3], [4], [5] and [6].

Signed:.....

Date:.....

Acknowledgements

This research is supported by the European Commission through the CRANE project, grant agreement 606844, and has been carried out, in part, at the Institute of Sound and Vibration Research, within the University of Southampton, and at Siemens Industry Software.

I would like to express my deepest gratitude to Prof. Jeremy Astley, Dr. Gwénaël Gabard and Dr. Michel Tournour, for their patience, guidance and support throughout this work. Nonetheless, I am grateful to Dr. Samuel Sinayoko for the insightful technical discussions and encouragement during most of this project. Above all, I appreciated their invaluable expertise and humanity.

My sincere thanks goes to all the people that shared this life experience with me. Despite the difficult moments, you made it a mindful and rewarding path. I have learnt something from all of you. Most importantly, my profound recognition goes to my mother and to my sister, for their unconditional understanding, courage and care.

To the memory of my father

Nomenclature

Symbol	Description	Units
a	reference radius	m
$\mathbf{a_{1,2,3}}$	orthonormal basis of vectors	-
$\mathbf{A}$	system matrix, acoustic velocity potential	-
$\mathbf{B}$	system matrix, acoustic velocity	-
$\mathcal{B}$	Taylor–Lorentz space-time operator	-
c	isentropic sound speed	m s^{-1}
$\mathbf{C}$	r.h.s. vector acoustic velocity potential	-
C_v	specific heat at constant volume	kg m^2 K^{-1} s^{-2}
C_p	specific heat at constant pressure	kg m^2 K^{-1} s^{-2}
d	normal particle displacement	m
D	geometrical length scale	m
$\mathbf{D}$	r.h.s. vector, acoustic velocity	-
dof_e	number of degrees of freedom per element	-
E	error term	-
E_{L^2}	Euclidean error	-
$\mathbf{E}$	system matrix, Neumann problem	-
f	frequency	s^{-1}
$\mathbf{f}_e$	volume forces	kg m^{-2} s^{-2}
$\mathbf{F}$	r.h.s. forcing vector	-
g	generic sound source term	-
G	Green's function	-
h_n	normal velocity to the boundary surface	m s^{-1}
$\mathbf{H}$	system matrix, indirect formulation	-
i	imaginary unit	-
$\mathbf{i}$	x-axis unit vector	-
$\mathbf{j}$	y-axis unit vector	-
J	norm of the Jacobian, Taylor–Lorentz transform	-
J_g	norm of the Jacobian, transformation to the reference element	-
k	wavenumber	m^{-1}
$\mathbf{k}$	z-axis unit vector	-
L_A	acoustic length scale	m

L_M	mean flow length scale	m
$\mathcal{L}_n$	generalized double-derivative operator	-
$\boldsymbol{L}$	generalized Taylor–Lorentz derivative operator	-
$\dot{m}$	mass source per unit of volume	kg m^{-3} s^{-1}
$\mathbf{M}$	Mach number vector	-
M	absolute value of the Mach number	-
$\mathbf{n}$	normal unit vector	-
N	shape function	-
N_i	number of iterations	-
N_{dof}	number of degrees of freedom	-
p	pressure	kg m^{-1} s^{-2}
$\mathcal{P}$	weakly non-uniform flow wave operator	-
$\mathbf{q}$	heat flux per unit mass	J kg m^{-2} s^{-1}
Q_h	generated heat per unit mass	J kg m^{-3} s^{-1}
$\mathbf{Q}$	r.h.s. indirect formulation	-
r_n	nacelle radius	m
r	radial distance	m
r_{fp}	2D radial distance, field points	m
R	radius	m
R_{fp}	3D radial distance, field points	m
R_M	amplitude radius	m
$\mathcal{R}$	specific gas costant	J kg^{-1} K^{-1}
t	time	s
T	transformed time	-
T_e	thermodynamic temperature	K
$\mathbf{u}$	velocity vector	m s^{-1}
$\mathbf{U}$	r.h.s. vector iterative solution	-
$\mathbf{V}_n$	vector of nodal velocity	-
w	weighting function	-
$\mathbf{x}$	physical space location vector	-
x	x-component Cartesian coordinate	m
$\mathbf{X}$	transformed space location vector	-
y	y-component Cartesian coordinate	m
z	z-component Cartesian coordinate	m
α	Burton–Miller coefficient	-
β_∞	characteristic parameter, Lorentz transform	-
γ	specific heat ratio	-
δ	Dirac delta function	-
δ_{lm}	Kronecker delta	-
ε	error weakly non-uniform flow wave operator	-
ϵ	tolerance value	-

ζ	local coordinate, reference element	m
$\boldsymbol{\eta}$	tangent unit vector	-
θ	polar angle	$^\circ$
Θ	polar angle mean flow potential	rad
λ	wavelength	m
λ_ν	second Lamé constant	kg m^{-1} s^{-2}
μ	normal derivative projection factor	-
μ_ν	first Lamé constant	kg m^{-1} s^{-2}
$\boldsymbol{\Pi}$	stress tensor	-
ρ	mass density	kg m^{-3}
ξ	local coordinate reference element	-
ξ'	double layer potential	-
σ	phase radius	-
σ'	single layer potential	-
$\boldsymbol{\tau}$	tangent unit vector	-
ϕ	acoustic velocity potential	m^2 s^{-1}
$[\phi]$	characteristic value acoustic velocity potential	m^2 s^{-1}
Φ	velocity potential	m^2 s^{-1}
ψ	test function	-
ω	angular frequency	rad s^{-1}
Ω	computational domain	-
$\partial\Omega$	boundary surface	-

Superscripts

Symbol	Description
$\hat{\bullet}$	time domain
$\bullet'$	acoustic field
$\tilde{\bullet}$	Taylor–Lorentz space
$\bar{\bullet}$	Taylor space
$\bullet^\dagger$	Lorentz space
$\bullet^*$	complex conjugate
$\bullet^l$	row, index
$\bullet^m$	column, index

Subscripts

Symbol	Description
$\bullet_0$	mean flow component

$\bullet_{2D}$	two-dimensional problem
$\bullet_{\alpha}$	Burton–Miller related quantities
$\bullet_{\infty}$	uniform flow component
$\bullet_{adj}$	adjoint operator
$\bullet_{ch}$	combined integral formulation
$\bullet_{fp}$	field point
$\bullet_{inc}$	incident field
$\bullet_{j}$	index
$\bullet_{l}$	l-th collocation point
$\bullet_{n}$	normal component
$\bullet_{p}$	collocation point
$\bullet_{q}$	q-th iterative step
$\bullet_{ref}$	reference value
$\bullet_{rms}$	root mean square value
$\bullet_{s}$	assigned values
$\bullet_{sc}$	scattered field
$\bullet_{T}$	Taylor–Helmholtz formulation
$\bullet_{x}$	x-axis component
$\bullet_{y}$	y-axis component
$\bullet_{z}$	z-axis component

Abbreviations

Symbol	Description
APE	Acoustic Perturbation Equations
BEM	Boundary Element Method
CAA	Computational Aero-Acoustics
CAEP	Committee on Aviation Environmental Protection
CFD	Computational Fluid-Dynamics
DGM	Discontinuous Galerkin Method
DNS	Direct Numerical Simulation
DRM	Dual Reciprocity Method
DRP	Dispersion-Relation-Preserving
EPNdB	Effective Perceived Noise level in dB
FAR	Federal Aviation Regulation
FD	Finite Difference
FEM	Finite Element Method
ICAO	International Civil Aviation Organisation
LEE	Linearised Euler Equations
LES	Large Eddy Simulation
LNSE	Linearized Navier–Stokes Equations
LPE	Linearized Potential Equation
PML	Perfectly Matched Layer
RANS	Reynolds Averaged Navier–Stokes
SPL	Sound Pressure Level

Chapter 1

Introduction

Contents

Aircraft noise is an important concern in the aviation sector because it significantly affects both communities near airports and passengers. From a commercial point of view, it has a negative impact on sales. Predicting aircraft noise is an essential component to aircraft design, since it can reduce environmental impact along with costs of testing and certification. In Sec. 1.1, a general overview of aircraft noise issues is given; regulations, main noise sources and future reduction technologies are discussed. Some examples of aircraft noise installation effects are also reviewed. The general context of this work is then presented and the main objectives are detailed in Sec. 1.2. Finally, the outline to the rest of the thesis is provided.

1.1 Aircraft noise

Aircraft noise is a clear environmental issue and represents a constraint to airport activities and expansion. Controlling aircraft noise levels and reducing community noise impact is of high importance to the aviation sector. Air traffic also contributes to air quality and a strong design trade-off is seen between noise, carbon emissions and fuel efficiency.

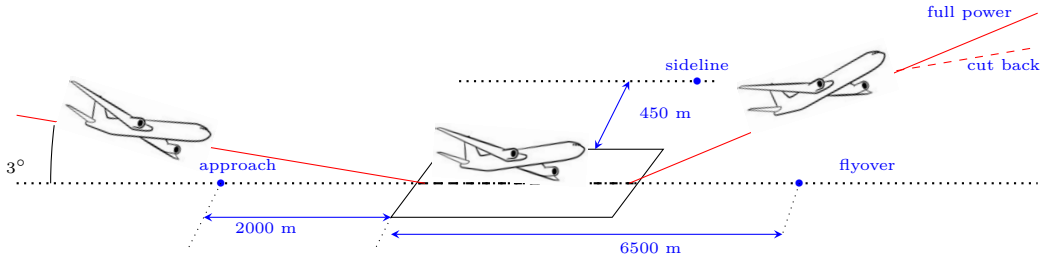

Figure 1.1: Sketch of aircraft certification points.

1.1.1 Regulation and future trends

Since the adoption of the jet engine by all large civil aircraft in the 1960s, aircraft noise has grown as an environmental issue. Currently, the evaluation of noise emission levels for aircraft is based on either a single aircraft operation or a longer term impact of noise on community. In the former case, noise is measured in Effective Perceived Noise Level (EPNL). In the latter, a number of metrics are used to measure community noise, taking into account aircraft age and airport location [7]. All the metrics generally consider absolute level of exposure, duration of a single noise occurrence and number of events occurring in a prescribed period of time. A number of regulations are also enforced by local authorities.

The Federal Aviation Regulation (FAR) Part 36 [8] and Annex 16 [9], issued by the International Civil Aviation Organization (ICAO), define the current regulations for aircraft noise certification. Certification levels at entry into service, measured in EPNdB, are assessed at three certification points along the flight path. The sideline measurement is taken 450 m from the runaway axis at take-off and full power conditions (see Fig. 1.1). The flyover, or cutback, point is positioned on the line of the runway below the aircraft and measured as the aircraft reduces power and rate of climb. The approach is measured along the flight path before landing, when the aircraft is approaching with a glide angle of 3 degrees. The maximum allowable EPNL for each operation condition depends on the Maximum Take-Off Mass (MTOM) and the age of the aircraft.

Since the introduction of noise regulations, aircraft noise, measured in EPNdB, has been reduced at a rate of about 0.3 dB per operation per year [7]. On the other hand, air traffic has globally grown by 20% in the first decade since 2000 (see Fig. 1.2) and is expected to grow at 4.8% per year in the upcoming 20 years [10].

Further reductions are expected both in the short and long term, namely between 2020 and 2030, according to an estimate by independent expert panels appointed by the ICAO's Committee on Aviation Environmental Protection (CAEP). The target in Europe is to reduce emissions by 50% by 2020 and then 65% by 2050 [11] (see Fig. 1.3). In 2013, CAEP lowered the cumulative noise certification levels for commercial aircraft with respect to the standard established by Chapter 4 of the ICAO regulation. Further improvement to noise technologies is needed in order to maintain at least the status quo. The main strategy for

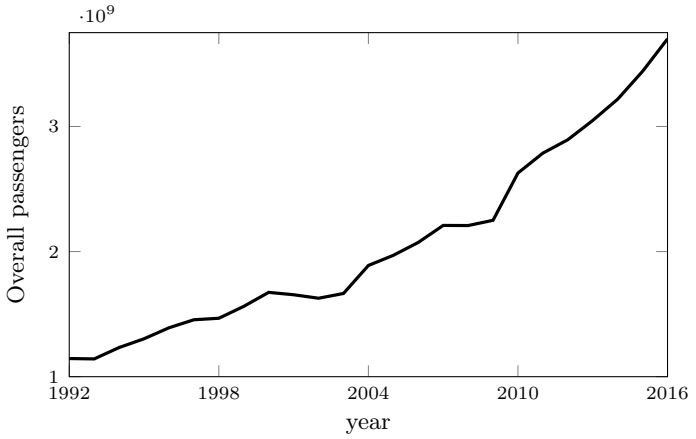

Figure 1.2: Passengers carried per year around the world (based on data from ICAO [12]; the values for 2016 are based on preliminary estimation of ICAO).

reducing noise emission will focus on optimising design and operations as well as investigating new technologies.

1.1.2 Noise sources

The noise signature of an aircraft results from a combination of propulsive and non-propulsive sound sources generated by the engine and airframe (see Fig. 1.4). During take-off and cruise, the noise sources from the engine are dominant (see Figs. 1.5 and 1.6).

Airframe noise sources are generated by unsteady flow mainly due to high-lift devices, landing gear [13] and cavities in the airframe. Noise generation is linked to the development of shear layers, flow separation and recirculation. For example, landing gear noise results from the interaction of unsteady turbulent flow generated by bluff structures and solid surfaces [14]. It is significant at approach and scales as M_∞^6 [10], where M_∞ is the Mach number. Flap noise [15] is a combination of sources developed along the flap side edge between the deployed and stowed part of the wing, whereas self noise is caused by the scattering of the boundary layer hydrodynamic field by the wing trailing edge. Furthermore, slat noise is caused by the high turbulent flow in both the gap between the slat and the leading edge of the wing and the slat cove, where a region of flow recirculation, shear and reattachment with strong anisotropy is generated. Both flap and slat noise make a significant contribution at approach. However, during cruise, all of these source mechanisms are strongly attenuated when the high-lift surfaces are retracted and the landing gear is stowed.

The engine is the other major noise contributor, both at take-off and approach, and is responsible for complex source generations. Exhaust noise is mainly characterized by a broadband signature. Jet mixing noise is due to fluctuating turbulent shear stress in the mixing region of the jet. Jet mixing noise scales with a high power of the Mach number, M_∞^α, where α varies between 6 and 8 [16], so it can be effectively tackled by decreasing jet velocity. This is achieved by increasing the bypass ratio. Supersonic jets introduce further

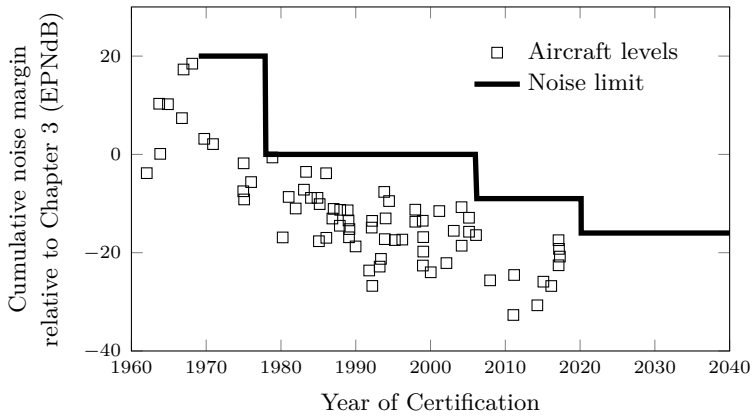

Figure 1.3: Historic and future trends in cumulative certified aircraft noise levels (extracted from Discussion Paper 05: Aviation Noise [17]).

noise generation mechanisms due to shock formation. Broadband shock noise is due to the interaction of shock cells with turbulence, whereas jet screech noise has a tonal signature. Screech is due to a feedback mechanism between sound radiated toward the nozzle lip and the development of shock cells.

Fan and compressor noise generate both tonal and broadband noise. Discrete tones are mainly generated by rotor-stator turbulence interaction, such as between fan blades and outlet guide vanes. Rotor-alone tones are also produced at supersonic operating conditions. The shocks generated at the supersonic blade tip produce sound which propagates to the far field (*buzz-saw noise*). The main causes of broadband noise are the scattering of the turbulent boundary layer at the trailing edge and the interaction of the turbulent scales in the rotor wake with the stator leading edge. These noise sources can propagate sound both in the forward and rear arcs. Turbine noise has a similar character to compressor noise but radiates mainly towards the rear arc of the engine.

Combustion noise is also characterized by a broadband signature. Direct noise is generated by the temperature fluctuations in the combustion chamber, while indirect noise is generated by turbulent flow structures at high temperatures moving downstream through the turbine.

Forward fan noise and fan exhaust noise are comparable at most of the certification points, whereas core and turbine noise generally have a lower impact. Fan noise is comparable to airframe noise at approach and is a dominant source at departure. Jet noise is only a significant contributor to the overall noise signature at take-off (see Figs. 1.5 and 1.6).

The important sources of aircraft noise during ground operations are those produced by Auxiliary Power Units (APUs) and air/hydraulic systems. Noise from the APUs is of concern for “ramp” noise and its signature is strongly affected by the presence of the ground. By “ramp” we mean the workforce operating around the aircraft in an airport. Sound radiated by air/hydraulic systems is also a major concern for cabin noise.

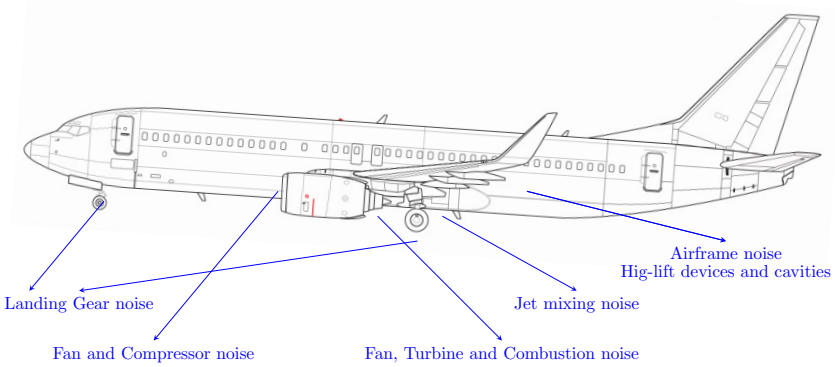

Figure 1.4: Sketch of an aircraft showing the location of the main sound sources.

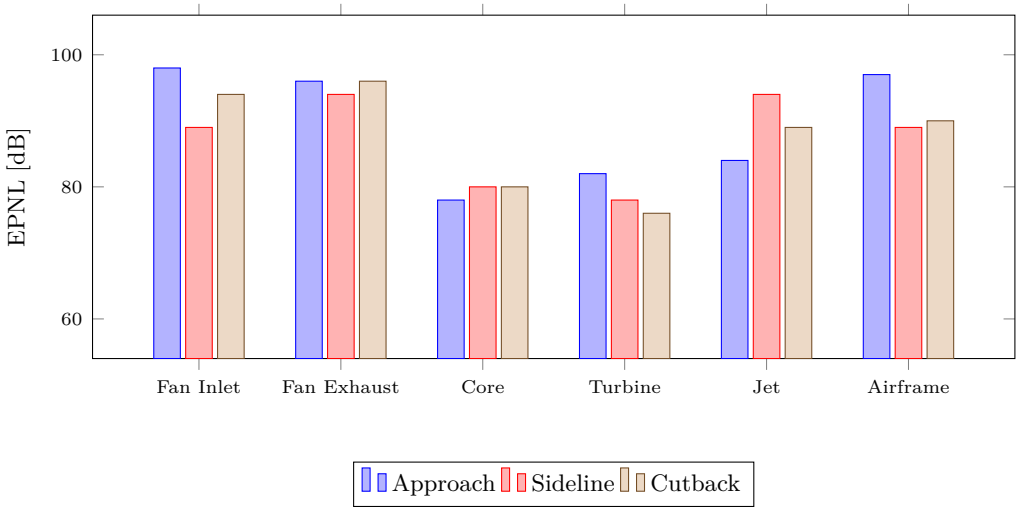

Figure 1.5: EPNL contributions of engine components and airframe sources for a four-engine 1990's aircraft [7].

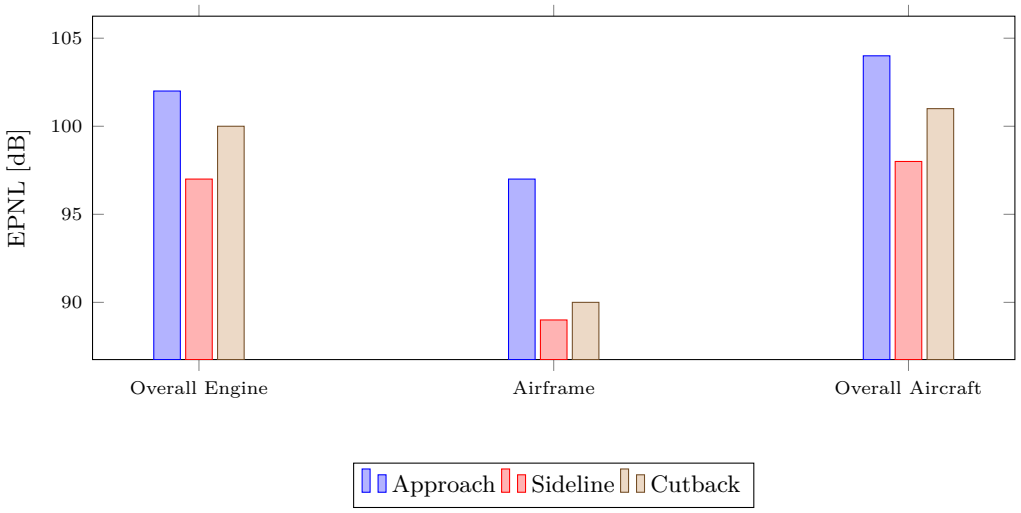

Figure 1.6: EPNL contribution of the overall engine sources compared to the airframe for a four-engine 1990's aircraft [7].

1.1.3 Installation effects

When a sound source is radiating in the presence of the airframe, changes in the radiation pattern occur due to both scattering effects and generation of secondary sources. These are the so-called *installation effects*. They generally consist of refraction and reflection effects due to the presence of a solid surface and can significantly affect the noise signature of the isolated source. However, acoustic installation effects depend both on the relative position of the sound source and the change in flow around the airframe. For example, a wing-mounted engine, in the configuration where the engine is below the wing, is likely to increase the noise signature at all certification points. In this case, the sound produced by the jet is scattered by the wing, but the interaction of the jet with the wing itself, such as with high-lift surfaces, can also produce additional sound sources [18]. Jet noise consists of two main mechanisms when the engine is installed. Jet-surface reflection is due to the presence of the wing and/or flap and modifies the high-frequency noise radiated from the jet. The second mechanism occurs at low frequency, where the jet near field pressure is scattered by the wing trailing edge.

Another well-known installation effect is produced by a fuselage-mounted engine. The presence of the fuselage increases the level of sound radiated laterally from the nacelle. This occurs for sound radiated by both the fan and the jet exhaust. The sound produced by the landing gear is also a major aircraft contributor. Sound is scattered by the wing and the fuselage, significantly affecting the overall signature.

Predicting acoustic installation effects is relevant to the aircraft industry because of the significant impact of the airframe on the directivity of the isolated sound sources. Assessing installation effects is challenging due to the complexity of the physics involved, such as the changes in the flow field. The large size of the problem domain compared to the characteristic wavelengths is also a constraint for numerical methods. In fact, large-scale short-wavelength noise propagation requires high computational resources.

1.1.4 Future noise reduction technologies

In order to achieve a significant reduction in aircraft noise, all the source contributions must be lowered concurrently. Since the early 1970s and particularly over the last three decades, aircraft engine noise reduction has been progressively achieved by the introduction of high bypass ratio engines. This reduction in engine noise has turned airframe noise into one of the main contributors to the overall noise signature, particularly at approach. Overall, current aircraft are 20-30 dB quieter than the aircraft produced at the early stage of turbofan propulsion.

Future engine design will see an increase in the bypass ratio, including larger and slower fans, which will further reduce the impact of fan and exhaust noise. An increase in engine

diameter, however, will cause a reduction in the length of the nacelle, limiting the space available for acoustic liners.

Currently, geared turbofans are entering into service to further reduce the rotational speed of the fan and the noise generated. In addition, to reduce the fan noise signature, shielding effects from the airframe may also be exploited in the future. Hybrid wing-body configurations may potentially provide a reduction in noise level on the community of about 45 EPNdB [10] cumulative compared to current aircraft design. The introduction of hybrid-electric propulsion may also be welcomed due to the positive effect on carbon and noise emissions. New technologies for core noise are also likely to be introduced, including quiet bleed valves and hot-stream liners. Airframe noise may also see the introduction of porous materials and serrations to reduce flap and slat noise. Landing gear fairings may also be introduced [10].

In order to achieve current noise reduction targets for 2020 and 2050 [11], the use of robust numerical techniques for the prediction of noise generation and propagation will be needed during the design cycle of future aircraft. Effective numerical methods are needed to reduce the time and cost of certification.

1.2 Project description

The general context of the work in this thesis is discussed in this section along with the general scope and the main contributions. This work has been carried out over a three-year period within an industrial framework and aims to clarify some concerns from the numerical simulation industry pertaining to the prediction of large-scale acoustic installation effects for aircraft.

1.2.1 Background and numerical challenges

At the moment, there is an increasing need to predict aircraft noise emissions at the design stage in order to meet noise targets for certification. Predictions of aircraft acoustic installation effects should be accurate and able to include detailed geometrical features and non-uniform mean flow effects on wave propagation. Although semi-analytical and empirical models represent valuable assets for quick estimations of installation effects, they are not flexible enough either to include geometrical details or to assess significant design modifications. Therefore we focus on numerical solutions.

Computational Fluid Dynamics (CFD) is used to predict unsteady aerodynamics in engines and airframe and, therefore, the noise sources. Reynolds Averaged Navier–Stokes (RANS) simulations operate at the limit of the capability to predict tonal turbomachinery sources. The prediction of broadband noise with compressible Large Eddy Simulation (LES)

or Detached Eddy Simulation (DES) is even more demanding. Direct Numerical Simulation (DNS) is still impracticable, except at low Reynolds numbers.

In aeroacoustics, conventional CFD methods can be used to predict noise generation but are computationally too demanding at the moment to solve noise propagation problems for industrial applications. This is the main reason why hybrid methods, generally referred to as Computational Aero-Acoustics (CAA) [19], are devised. In this case, noise generation is considered to be independent of noise propagation and scattering. This assumption allows linear methods to be used for noise propagation.

In the aeronautical industry, noise propagation in non-uniform flow is conventionally predicted using frequency domain Finite Element Methods (FEM) [20], and time domain Discontinuous Galerkin Methods (DGM) [21] and high order finite difference schemes [22]. These methods are referred to as volume-based methods and allow wave propagation in a non-uniform flow to be solved, accounting for complex physical models. Due to the high computational cost, they are more readily applied to potential formulations [23]. Despite the assumption of a potential flow and the relatively simplified physical model, these methods are only viable at relatively low frequency in the case of large-scale domains.

Only fast numerical algorithms applied to boundary element methods, such as the fast multipole method [24] and the H-matrix approach [25], are viable industrial solutions to deal with large-scale acoustic installation effects for aircraft [26, 27]. Alternative methods, such as volume-based methods, become too demanding in terms of memory requirement to solve these problems [23]. While methods based on ray theory are not memory intensive for standard formulations, they are not flexible enough to assess the design for these applications [28]. If the wavelength becomes comparable to the size of geometrical features or the frequency considered is not high enough to consider the ray theory, these methods can lead to inaccurate results.

On the other hand, a viable solution to include non-uniform flow effects in boundary element solutions has yet to be demonstrated. Currently, boundary element solutions to wave propagation with non-uniform flow are based on approximate physics by making an assumption about the medium, e.g. uniform flow [29, 30], low Mach number potential flow [31, 32, 33, 34] and mean flow with small velocity gradient [35, 36]. This is also the case for "wave extrapolation" methods. For wave extrapolation, we mean approaches based on an integral formulation defined for a closed surface on which the acoustic field is sampled from an inner domain to predict the solution in the far field. At the moment, these methods are limited to uniform mean flows [37, 38, 39].

Boundary Element Methods (BEM) can only exactly solve wave propagation problems with uniform mean flows [40, 41, 42]. Conventional methods to include mean flow effects on boundary element solutions are based on variable transformations involving both dependent and independent variables. They allow wave operators with mean flow to be reduced to the standard wave operator for which an integral solution is well-known [43]. The Lorentz

transform [29, 44] allows noise propagation within a uniform mean flow to be solved exactly. It is generally used in the aviation industry to assess large-scale installation effects, accepting the limitation of considering only uniform flow effects on wave propagation [41].

1.2.2 General scope

This work deals with computational methods for large-scale short-wavelength noise propagation and scattering with non-uniform flows. It targets the prediction of large-scale aircraft acoustic installation effects for real geometries and complex flows, considering forward fan noise radiation and scattering by the airframe as an important application. In particular, we are interested in dealing with certification requirements where aircraft speed does not exceed $M_\infty = 0.3$. For design cycles [27, 45], the boundary element method in combination with fast algorithms [24, 25] can be used to predict large-scale noise propagation and scattering around aircraft.

The scientific challenge of this work is to include non-uniform mean flow effects in boundary integral solutions to wave propagation and scattering problems. Since the scattering of tonal components of fan noise from the airframe is a relevant application, frequency domain formulations are proposed in this work. The development of boundary integral solutions in this thesis is not meant to be academic but it is seen as a possible enhancement to current industrial practices [27]. The conventional variable transformations used to include mean flow effects on boundary element solutions, such as Taylor [31] and Lorentz transforms [44], are the foundations to this work. We consider potential flows – it is unlikely that more complex mean flows (except for quasi-potential flows) can be included in conventional boundary element solutions to wave propagation [46, 47] although some attempts without a clear success have been made [26, 35].

This thesis develops three main threads. First, a boundary integral solution to wave propagation with non-uniform flow is developed in a physical space, namely without transformations. The proposed solution is based on a combination of the Taylor and Lorentz physical models which, in turn, is an approximation of the linearised potential wave equation [48]. A Green's function for non-uniform potential flows is recovered as a kernel to solve boundary integral problems. The proposed integral formulation is then used as a means to solve both wave extrapolation and boundary element problems.

Second, a solution in a transformed Taylor–Lorentz space-time is recovered to solve the same physical model as that proposed in the physical space. This formulation allows conventional boundary element solvers for the Helmholtz problem to be used to predict wave propagation in a non-uniform flow. Boundary element solutions are devised based on the transformed formulation. The limitations of this method are discussed compared to the corresponding physical space formulation.

Third, a weakly-coupled approach to solve scattering problems is proposed based on the developed surface integral formulations. This method is oriented to predict forward fan noise installation effects. We assume that the nacelle near field can be computed using volume-based methods applied to exact physical models [23]. The nacelle near field is sampled along an open radiating surface lying along the inlet. The integral formulation is used along the open surface to project the acoustic field along the fuselage and to solve a scattering problem by using a boundary element method. This solution is applicable to cabin noise predictions and design assessment for certification.

Numerical experiments are performed as proof-of-concept for the proposed formulations. Solutions based on the boundary integral formulations with non-uniform flow are compared to finite element solutions of the corresponding exact physical model, i.e. the linearised potential wave equation [49]. Comparisons with more conventional solutions based on a uniform flow in the entire domain [40] are also provided.

1.2.3 Key contributions

The original contributions of this thesis are:

1. A framework to solve wave propagation on a non-uniform potential flow based on a boundary integral formulation in a physical space, i.e. without transformations. This formulation generalises the results of Wu and Lee [40] based on a uniform mean flow (see Chapter 4).

2. The development of an equivalent boundary integral solution in a transformed Taylor-Lorentz space-time (see Chapter 2) to exploit standard boundary element solutions to the Helmholtz problem with quiescent media and to simulate non-uniform flow effects. The boundary conditions in the transformed space are derived for practical applications (see Chapters 4 and 8).

3. A boundary element model for wave propagation in a non-uniform flow based on the integral solution in the physical space. A combined boundary integral formulation [50] and a generalised Burton–Miller [51] approach are devised to work around the non-uniqueness issue [52] in the presence of non-uniform mean flow (see Chapter 5).

4. A review of boundary element kernels in a transformed Taylor–Lorentz space. In the case of velocity boundary conditions, an iterative approach is proposed to use existing boundary element solvers for the Helmholtz problem with quiescent media to solve wave propagation with a non-uniform flow (see Chapter 5).

5. A weakly-coupled formulation based on a high-fidelity near-field solution and a boundary element formulation to solve external scattering on a larger domain with non-uniform mean flow (see Chapter 4). An open radiating surface approach is developed and benchmarked to solve forward fan noise installation effects (see Chapter 7).

6. Benchmark of the proposed integral formulations with non-uniform mean flow against solutions for the linearised potential wave equation (see Chapters 6-8). An error analysis is performed to understand the limitations of the integral solutions (see Chapter 6). A comparison with more conventional boundary element formulations assuming a uniform mean flow is also provided.

1.3 Thesis outline

The thesis is organised as follows. In Chapter 2, the physical models are derived and the variable transformations relevant to this work are presented. In Chapter 3, current numerical methods for wave propagation with mean flow are outlined. In Chapter 4, boundary integral solutions to wave propagation with non-uniform mean flow are presented. Boundary element formulations corresponding to these solutions are then presented in Chapter 5. Chapter 6 provides numerical examples to validate and benchmark the proposed integral formulations. In Chapter 7, an application to a proof-of-concept test case representing forward fan noise installation effects is presented. In Chapter 8, the application of boundary element formulations with mean flow to three-dimensional problems is discussed. Conclusions to the present work and a roadmap to possible future developments are given in Chapter 9.

Chapter 2

Wave Propagation with Mean Flow

Contents

The key point of this chapter is the derivation of a simplified potential formulation, which is obtained as a subset of the linearised potential wave equation [48]. The governing equations for a continuum are reviewed in Sec. 2.1. The physical models available for sound generation and propagation are then discussed in Sec. 2.2, while in Sec. 2.3 the equations of state are introduced to complement the governing equations and obtain a well-posed problem. In Sec. 2.4, the mean flow is separated from the corresponding perturbations and the equations are linerised assuming an inviscid fluid. In Sec. 2.5, the linearised formulation is simplified accepting the assumption of potential flows. The linearised potential wave equation is then used to derive a simplified potential formulation in a non-uniform flow assuming small Mach numbers and small non-uniform velocity components of the mean flow, i.e. the weakly

non-uniform flow wave equation. This equation can be further simplified to derive the uniform flow and the Taylor wave equations. The acoustic boundary conditions for potential formulations are also summarised. In Sec. 2.6, we introduce a set of variable transformations as a tool to reduce the simplified potential wave equations to the standard wave operator with quiescent media. Conclusions are finally provided.

2.1 Governing equations

In continuum-mechanics, fluid motion can be described by the conservation of mass, momentum and energy [53]. The conservation of mass can be written as

$$\frac{\partial \rho}{\partial t} + \boldsymbol{\nabla} \cdot (\rho \mathbf{u}) = \dot{m}, \tag{2.1}$$

where ρ is the mass density, $\mathbf{u}$ is the flow velocity and $\dot{m}$ the generic source of mass per unit of volume. The above equation indicates that the time variation of mass in a control volume balances the production of mass within the volume and the mass flux through the boundary surface.

The momentum equation is a representation of Newton's second law for a fluid control volume:

$$\frac{\partial \rho \mathbf{u}}{\partial t} + \boldsymbol{\nabla} \cdot (\rho \mathbf{u} \otimes \mathbf{u}) = \boldsymbol{\nabla} \cdot \boldsymbol{\Pi} + \mathbf{f}_e + \dot{m}\mathbf{u}, \tag{2.2}$$

where $\boldsymbol{\Pi}$ is the Cauchy viscous-stress tensor and $\mathbf{f}_e$ is the vector of the external volume forces. The convective flux tensor of the momentum is denoted by $\rho \mathbf{u} \otimes \mathbf{u}$.

The Cauchy tensor contains the contribution of the fluid pressure, p, and the viscous stress, τ_{ij}, namely

$$\Pi_{ij} = -p\delta_{ij} + \tau_{ij}, \tag{2.3}$$

where δ_{ij} is the Kronecker delta. A constitutive equation is needed to characterize the stress tensor. For Newtonian fluids, $\tau_{ij} = \mu_\nu(\frac{\partial u_i}{\partial x_j} + \frac{\partial u_j}{\partial x_i}) + \lambda_\nu \frac{\partial u_k}{\partial x_k}\delta_{ij}$, where the Lamé constants, μ_ν and λ_ν, are determined by considering that the deviatoric part of the stress tensor has zero trace, namely $2\mu_\nu + 3\lambda_\nu = 0$ and $\tau_{ij} = \tau_{ji}$.

The conservation of energy states the condition by which the sum of potential and kinetic energies is stationary. It can be written as

$$\frac{\partial \rho(e + u^2/2)}{\partial t} + \boldsymbol{\nabla} \cdot (\rho(e + u^2/2)\mathbf{u}) = \boldsymbol{\nabla} \cdot (\boldsymbol{\Pi} \cdot \mathbf{u}) + \mathbf{f}_e \cdot \mathbf{u} - \boldsymbol{\nabla} \cdot \mathbf{q} + Q_h + \dot{m}(e + u^2/2), \tag{2.4}$$

where e is the specific potential energy per unit mass and u is the norm of the vector $\mathbf{u}$. On the right-hand side, $\mathbf{q}$ is the heat flux and Q_h the heat generated per unit volume.

2.2 Physical models

The mechanisms involved in noise generation and propagation can be represented by the Navier–Stokes equations. There are few analytical solutions to the Navier–Stokes equations so numerical solutions have to be devised for engineering applications.

The Lattice-Boltzmann model [54] can also be used for noise generation problems with complex geometries. The method is based on the kinetic theory of gases. It is based on the fundamental idea that the flow can be considered to be made of particles. It models the exchange of momentum among particles by representing their collision and streaming. Unlike the Navier–Stokes equations, the Lattice-Boltzmann model can be used even when flow continuity does not hold. It has been shown, however, that these models are consistent if the assumption of continuity holds [55].

If viscous effects are neglected, the Navier–Stokes equations reduce to the Euler equations. Euler equations model non-linear sound propagation. They can be used to solve mean flow and acoustic perturbations at the same time as well as including their interactions. Non-linear effects are relevant for high amplitude sound propagation problems. However, an issue with solving Euler equations is that they support the Kelvin–Helmholtz instability [56, 57] which can overwhelm the acoustic solution. In fact, due to the lack of viscous effects in the Euler equations, a convective instability can develop downstream from an initial discontinuity of the velocity field.

Linear models can also be used if perturbations on fluid density, pressure and velocity fluctuations are small compared to the respective mean flow quantities [58]. The linearisation is based on the assumption that the time scale associated with the mean flow variations is larger than that associated with the propagation of the corresponding perturbation. If a steady background flow is considered and viscous effects on perturbations are modelled, the Linearised Navier–Stokes Equations (LNSE) can be solved [59]. These equations are suitable to solve sound propagation in boundary layers [60].

Further, if the viscous effects are negligible, a linearised form of the Euler equations can be derived [61]. Linearised Euler Equations (LEE) model acoustic, vorticity and entropy waves in a rotational mean flow. LEE also support the development of instability waves, such as the Kelvin–Helmholtz instability. The mean flow gradient terms can be removed from LEE to avoid the instability developing [62]. Alternatively, the Acoustic Perturbation Equations (APE) can also be used [63] to work around the same problem. APE are developed by filtering acoustic and vorticity perturbations so that the system of equations does not support vortical modes. They are applicable to flow fields which vary slowly in space compared to the wavelength reason, which is why they can be inaccurate at low frequencies.

If a parallel shear flow can be assumed, the Pridmore-Brown [64] equation can be derived from LEE. This hypothesis reduces the five-equation LEE model to a third order single

equation model in pressure. This formulation supports hydrodynamic modes and instability waves. Alternatively, the Möhring equation [65] can be used for rotational mean flows. This single equation model is based on the definition of the stagnation enthalpy and the rotational mean flow effects are included as equivalent sources. In other words, rotational mean flow effects are not fully accounted for in the acoustic propagator, which supports only non-rotational waves.

On the other hand, if a potential flow is assumed both for the mean and the perturbation components, the linearised Euler equations reduce to the Linearised Potential wave Equation (LPE) [48]. This is a reasonable assumption outside turbulent flow regions and boundary layers. This one-equation model is applicable to irrotational flows, but it can be reasonably applied to rotational flows for long wavelength problems [48]. However, even for potential formulations, non-linearity and unsteady time averaged flows have to be modelled in some instances, such as high-amplitude sound propagation. These features can be introduced by using more complex formulations [66].

2.3 Additional equations

Equations (2.1), (2.2) and (2.4) depend on p, $\mathbf{u}$, ρ and e. It is a set of five equations with six unknowns. Therefore, further relationships are needed to reach a well-posed problem. Thermodynamic laws are used to describe the relations between the mechanical quantities.

Introduce the entropy, s. According to the first law of thermodynamics, one has

$$T_e \mathrm{d}s = \mathrm{d}e - \frac{p}{\rho^2}\mathrm{d}\rho, \tag{2.5}$$

where T_e is the thermodynamic temperature. The above equation, in combination with Eq. (2.4), gives [61]

$$\rho\frac{Ds}{Dt} = \frac{1}{T_e}\left(\boldsymbol{\Pi} : \boldsymbol{\nabla u} - \boldsymbol{\nabla}\cdot\mathbf{q} + Q_h - \frac{p}{\rho}\dot{m}\right) \tag{2.6}$$

where $D/Dt = \partial/\partial t + \mathbf{u}\cdot\boldsymbol{\nabla}$ denotes the material derivative.

From these definitions, a dependence between the thermodynamic quantities can be expressed as $e = e(p, s)$ and $\rho = \rho(p, s)$. The total variation of density, $d\rho$, can be written based on the second law of thermodynamics as

$$\mathrm{d}\rho = \left(\frac{\partial\rho}{\partial p}\right)_s \mathrm{d}p + \left(\frac{\partial\rho}{\partial s}\right)_p \mathrm{d}s. \tag{2.7}$$

If an isentropic flow is considered, the term $\mathrm{d}s = 0$ and Eq. (2.7) reduces to

$$\mathrm{d}p = c^2\mathrm{d}\rho, \tag{2.8}$$

where $c(\rho, T_e)$ is referred to as the speed of sound.

Assume an ideal gas, so that an equation of state can be introduced to relate pressure and density, i.e. $p = \rho \mathcal{R} T_e$, where $\mathcal{R} = 286.73$ J·(kg·K)$^{-1}$ is the specific gas constant for air. It is equal to the difference in the specific heat capacities, $\mathcal{R} = C_p - C_v$. For a perfect gas, the potential energy and thermodynamic temperature are related by $\mathrm{d}e = C_v \mathrm{d}T_e$ and for an isentropic process, the first law of thermodynamics gives

$$C_v \mathrm{d}T_e = \frac{p}{\rho^2} \mathrm{d}\rho. \tag{2.9}$$

Hence, differentiating the equation of state for an ideal gas and using the definition of $\mathcal{R}$ as a function of the specific heat capacities yields

$$\frac{\mathrm{d}p}{p} = \frac{\mathrm{d}T_e}{T_e} + \frac{\mathrm{d}\rho}{\rho} = \gamma \frac{\mathrm{d}\rho}{\rho}, \tag{2.10}$$

where $\gamma = C_p/C_v$. These considerations allow the variable, c, in Eq. (2.8) to be defined as $c = \sqrt{\gamma p/\rho} = \sqrt{\gamma \mathcal{R} T_e}$.

Equation (2.4) can then be rewritten for an isentropic flow, namely inviscid and non-conductive, based on Eqs. (2.6)-(2.10) as [61]

$$\frac{1}{c^2} \frac{Dp}{Dt} + \rho \nabla \cdot \mathbf{u} = \frac{1}{C_p T_e} Q_h + \left(1 - \frac{p}{C_p \rho T_e}\right) \dot{m}. \tag{2.11}$$

This equation is commonly known as the pressure equation and can be used in lieu of Eq. (2.4). Note that, in the absence of heat and mass sources, the right-hand side of the above equation vanishes. The set of equations Eqs. (2.1), (2.2) and (2.11) define a closed problem, based on the assumption of an ideal gas and an isentropic flow. These are reasonable assumptions for many physical phenomena, such as wave propagation for low pressure and density media and at moderate temperatures.

2.4 Linearised Euler equations

We consider the Navier–Stokes equations but the viscous terms in Eqs. (2.2) and (2.4) are ignored. A flow can be considered inviscid when viscous effects are negligible compared to inertia. This assumption is normally acceptable for sound propagation [67]. For convenience, we neglect any source of mass, momentum and energy. In addition, we neglect heat transfer and include Eq. (2.11) to give the Euler equations:

$$\frac{\partial \rho}{\partial t} + \boldsymbol{\nabla} \cdot (\rho \mathbf{u}) = 0, \tag{2.12}$$

$$\frac{\partial \rho \mathbf{u}}{\partial t} + \boldsymbol{\nabla} \cdot (\rho \mathbf{u} \otimes \mathbf{u}) = \mathbf{0}, \tag{2.13}$$

and

$$\frac{1}{c^2}\frac{Dp}{Dt} + \rho\boldsymbol{\nabla}\cdot\mathbf{u} = 0. \tag{2.14}$$

The main purpose of this analysis is to separate the contribution of the mean flow quantities from the corresponding perturbations. This allows the evolution of the perturbations on the mean flow to be modelled explicitly. This assumption is applicable as long as the perturbations are small compared to the mean flow quantities. An asymptotic expansion of density, velocity, pressure and speed of sound is introduced as

$$\begin{aligned}
\rho(\mathbf{x},t) &= \rho_0(\mathbf{x}) + \rho'(\mathbf{x},t),\\
\mathbf{u}(\mathbf{x},t) &= \mathbf{u}_0(\mathbf{x}) + \mathbf{u}'(\mathbf{x},t),\\
p(\mathbf{x},t) &= p_0(\mathbf{x}) + p'(\mathbf{x},t),\\
c^2(\mathbf{x},t) &= c_0^2(\mathbf{x}) + (c^2(\mathbf{x},t))',
\end{aligned} \tag{2.15}$$

where the subscript " $_0$ " denotes the mean flow quantities and the superscript " $'$ " the acoustic perturbations. A steady mean flow is then considered, namely

$$\boldsymbol{\nabla}\cdot(\rho_0\mathbf{u}_0) = 0, \tag{2.16}$$

$$\rho_0\mathbf{u}_0\cdot\boldsymbol{\nabla}\mathbf{u}_0 + \boldsymbol{\nabla}p_0 = \mathbf{0}, \tag{2.17}$$

$$\frac{1}{c_0^2}\mathbf{u}_0\cdot\boldsymbol{\nabla}p_0 + \rho_0\boldsymbol{\nabla}\cdot\mathbf{u}_0 = 0. \tag{2.18}$$

Let us substitute the above relations into Eqs. (2.12), (2.13) and (2.14), and introduce the linearised equation of state

$$\frac{(c^2)'}{c_0^2} = \frac{p'}{p_0} - \frac{\rho'}{\rho_0}. \tag{2.19}$$

Finally, neglecting high-order terms in the acoustic perturbation gives [67]

$$\frac{D_0\rho'}{Dt} + \rho_0\boldsymbol{\nabla}\cdot\mathbf{u}' + \mathbf{u}'\cdot\boldsymbol{\nabla}\rho_0 + \rho'\boldsymbol{\nabla}\cdot\mathbf{u}_0 = 0, \tag{2.20}$$

$$\rho_0\frac{D_0\mathbf{u}'}{Dt} + \boldsymbol{\nabla}p' + \rho_0(\mathbf{u}'\cdot\boldsymbol{\nabla})\mathbf{u}_0 + \rho'(\mathbf{u}_0\cdot\boldsymbol{\nabla})\mathbf{u}_0 = \mathbf{0}, \tag{2.21}$$

and

$$\frac{D_0p'}{Dt} + \rho_0c_0^2\boldsymbol{\nabla}\cdot\mathbf{u}' + \mathbf{u}'\cdot\boldsymbol{\nabla}p_0 + \rho'c_0^2\boldsymbol{\nabla}\cdot\mathbf{u}_0 - \mathbf{u}_0\cdot\boldsymbol{\nabla}p_0\left(\frac{p'}{p_0} - \frac{\rho'}{\rho_0}\right) = 0, \tag{2.22}$$

where $D_0/Dt = \partial/\partial t + \mathbf{u}_0\cdot\boldsymbol{\nabla}$ denotes the material derivative.

The Linearised Euler Equations, Eqs. (2.20), (2.21) and (2.22) are a closed set of equations that can be used to predict wave propagation. These equations support entropy and vorticity waves, in addition to the acoustic perturbations, and describe their interactions. An analytical solution to LEE is not generally available and the solution can be obtained adopting numerical schemes.

2.5 Wave propagation with potential flows

First, the linearised potential wave equation is reviewed in this section. It is then used as a means of deriving a simplified formulation assuming small non-uniform velocity components of the mean flow. The convected wave equation with uniform flow is also derived while the formulation, referred to as the Taylor wave equation, is reviewed. Conventional formulations for boundary conditions with mean flow are then discussed.

2.5.1 Linearised potential wave equation

Solving numerically, LEE can be computationally expensive for large-scale short-wavelength problems due to the large number of degrees of freedom obtained when the five unknown set of equations are discretized. If the mean flow is irrotational, LEE is reduced to a single second-order differential equation for the acoustic velocity potential, namely the full potential linearised wave equation [49]. It is also referred to as linearised potential equation (LPE). Although, in this case, the interaction of acoustic waves with entropy and hydrodynamic perturbations is neglected, the linearised potential wave equation is still a reasonable model for wave propagation in many practical flows. The exception, here, is for boundary and mixing layer regions [46].

For an isentropic potential flow, the velocity potential, Φ, is defined as

$$\boldsymbol{\nabla}\Phi(\mathbf{x},t) = \mathbf{u}(\mathbf{x},t), \tag{2.23}$$

where $\mathbf{u}$ is the total flow field velocity vector.

Based on an asymptotic expansion of the velocity potential in terms of mean flow $\Phi_0(\mathbf{x})$ and the acoustic perturbation, $\hat{\phi}(\mathbf{x},t)$, $\Phi(\mathbf{x},t)$ can be written

$$\Phi(\mathbf{x},t) = \Phi_0(\mathbf{x}) + \hat{\phi}(\mathbf{x},t), \tag{2.24}$$

where the mean flow satisfies $\boldsymbol{\nabla}\Phi_0(\mathbf{x}) = \mathbf{u}_0(\mathbf{x})$.

Consider the Bernoulli equation for an unsteady flow,

$$\frac{\partial\Phi}{\partial t} + \frac{1}{2}\mathbf{u}\cdot\mathbf{u} + \frac{c^2}{\gamma-1} = const, \tag{2.25}$$

where $\int \frac{dp}{\rho} = \frac{c^2}{\gamma-1}$ has been used. The isentropic equation of state $(\rho/\rho_0) = (c^2/c_0^2)^{1/(\gamma-1)}$ can be linearised to give

$$\frac{\rho_0}{\rho'} = (\gamma-1)\frac{c_0^2}{(c^2)'}. \tag{2.26}$$

In the above equation, the density perturbation ρ' can be expressed in terms of acoustic velocity potential, $\hat{\phi}$, linearising Eq. (2.25) to give

$$\rho' = -\frac{\rho_0}{c_0^2}\left(\frac{\partial\hat{\phi}}{\partial t} + \mathbf{u}_0 \cdot \boldsymbol{\nabla}\hat{\phi}\right). \tag{2.27}$$

The linearised momentum equation, Eq. (2.21), and the pressure equation, Eq. (2.22), can then be replaced by Eq. (2.27). In combination with Eq. (2.20), it gives

$$\frac{D_0}{Dt}\left(\frac{\rho_0}{c_0^2}\frac{D_0\hat{\phi}}{Dt}\right) + \frac{\rho_0}{c_0^2}\frac{D_0\hat{\phi}}{Dt}\boldsymbol{\nabla}\cdot\mathbf{u}_0 - \boldsymbol{\nabla}\cdot(\rho_0\nabla\hat{\phi}) = 0. \tag{2.28}$$

Equation (2.28) is conventionally referred to as the linearised potential wave equation. It is the most general potential formulation for a linearised wave equation with mean flow [68]. Alternatively, the above equation can be rewritten as [68]

$$\frac{\partial}{\partial t}\left(-\frac{\rho_0}{c_0^2}\frac{D_0\hat{\phi}}{Dt}\right) + \boldsymbol{\nabla}\cdot\left(\rho_0\boldsymbol{\nabla}\hat{\phi} - \frac{\rho_0}{c_0^2}\frac{D_0\hat{\phi}}{Dt}\mathbf{u}_0\right) = 0 \tag{2.29}$$

or [19, 48, 66]

$$\frac{D_0}{Dt}\left(\frac{\rho_0}{c_0^2}\frac{D_0\hat{\phi}}{Dt}\right) - \boldsymbol{\nabla}\cdot\left(\rho_0\boldsymbol{\nabla}\hat{\phi}\right) = 0. \tag{2.30}$$

In summary, the linearised potential wave equation describes convection and refraction of acoustic waves in a non-uniform potential mean flow, neglecting any interaction with vorticity and entropy waves. In all that follows, this work will focus on potential formulations and the linearised potential wave equation will represent the reference physical model.

2.5.2 Weakly non-uniform flow potential wave equation

In this section, an approximate formulation of the linearised potential wave equation is presented based on the dimensional analysis of the dependence of Eq. (2.30) on the mean flow Mach number, M_∞, the characteristic length scale of the base flow, L_M, and the acoustic characteristic length scale, L_A, which can be seen as the acoustic wavelength [32, 34]. The ratio between the non-uniform and uniform components of the mean flow Mach number, i.e. M_0'/M_∞, is another quantity relevant to the present approximation.

These parameters are interdependent; the Mach number, M_∞, is representative of wave convention. The characteristic length scale of the mean flow, L_M, is associated with the geometric length scale of the scattering body, while M_0' pertains to the gradients of the mean flow generated by the presence of the body. The non-uniform component of the mean flow, M_0', is significant for wave refraction.

For the sake of notation, the characteristic value of the potential field will be denoted as $[\hat{\phi}]$. We consider a potential isentropic mean flow. The local sound speed can be rewritten

based on the Bernoulli equation for a steady flow [34]

$$c_0^2 = c_\infty^2 - \frac{\gamma - 1}{2}(u_0^2 - u_\infty^2), \tag{2.31}$$

and the equation of state gives

$$\frac{\mathrm{d}\rho_0}{\rho_0} = \frac{\gamma - 1}{2}\frac{\mathrm{d}c_0^2}{c_0^2}, \tag{2.32}$$

where u_∞ and u_0 are the absolute values of the uniform and non-uniform mean flow velocity vectors respectively, and c_∞ is the speed of sound for the undisturbed flow. The above equations allow Eq. (2.29) to be rewritten as

$$\begin{aligned}&\frac{\partial^2\hat{\phi}}{\partial t^2} + 2\mathbf{u}_0 \cdot \boldsymbol{\nabla}\frac{\partial\hat{\phi}}{\partial t} - c_\infty^2\boldsymbol{\nabla}^2\hat{\phi} + \mathbf{u}_0 \cdot \boldsymbol{\nabla}(\mathbf{u}_0 \cdot \boldsymbol{\nabla}\hat{\phi}) \\ &+ \frac{1}{2}\boldsymbol{\nabla}\hat{\phi} \cdot \boldsymbol{\nabla}(\mathbf{u}_0 \cdot \mathbf{u}_0) + (\gamma - 1)\frac{D_0\hat{\phi}}{Dt}\boldsymbol{\nabla} \cdot \mathbf{u}_0 + \frac{\gamma - 1}{2}(u_0^2 - u_\infty^2)\boldsymbol{\nabla}^2\hat{\phi} = 0.\end{aligned} \tag{2.33}$$

The mean flow is now decomposed as a sum of a uniform flow component, $\mathbf{u}_\infty$, and a non-uniform component, $\mathbf{u}_0'$, such that $\mathbf{u}_0(\mathbf{x}) = \mathbf{u}_\infty + \mathbf{u}_0'(\mathbf{x})$. We assume that $M_\infty \ll 1$ and $L_A \ll L_M$. These assumptions will allow us to neglect compressibility effects on the mean flow and the effects of wake generation on wave propagation [36, 69]. Clancy [69] and Heffernon *at al.* [70] have shown that at low Mach numbers, such as at take-off and landing, the scattering of acoustic energy into vorticity, such as for wakes shed by slender bodies, is small compared to the refraction effects by a potential non-uniform flow.

With the assumption that $L_A \ll L_M$, we consider wave convection more significant compared to refraction due to mean flow velocity gradients. $L_A \ll L_M$ is generally true for large-scale short-wavelength noise propagation. Nonetheless, for slender bodies, L_M increases with the ratio of the length of the scattering body in the direction of the mean flow to its thickness. Note that in the limit of a uniform flow $L_M \to \infty$. However, since we are interested to model wave scattering, we inherently consider L_A to be much smaller than the geometrical length scale of the body, a condition that is more clearly satisfied for slender bodies.

Following the dimensional analysis of Eq. (2.33) in Astley and Bain [32] and considering low Mach numbers, we retain only terms of order $[\hat{\phi}]/L_A^2$, $M_0[\hat{\phi}]/L_A^2$, $M_0^2[\hat{\phi}]/L_A^2$ to give

$$\frac{\partial^2\hat{\phi}}{\partial t^2} + 2\mathbf{u}_0 \cdot \boldsymbol{\nabla}\frac{\partial\hat{\phi}}{\partial t} - c_\infty^2\boldsymbol{\nabla}^2\hat{\phi} + \mathbf{u}_0 \cdot \boldsymbol{\nabla}(\mathbf{u}_0 \cdot \boldsymbol{\nabla}\hat{\phi}) + \frac{\gamma - 1}{2}(u_0^2 - u_\infty^2)\boldsymbol{\nabla}^2\hat{\phi} = 0. \tag{2.34}$$

Then, we assume that $M_0' \ll M_\infty$, meaning $M_0'M_\infty \ll M_\infty^2$ and $M_0'^2 \ll M_\infty^2$, where $M_0' = u_0'/c_\infty$ and $M_\infty' = u_\infty/c_\infty$. In other words, we consider a small non-uniform component of the mean flow compared to M_∞. When scattering occurs from an impermeable surface, the ansatz $M_0' \ll M_\infty$ is pushed to the limit since these quantities are comparable at the stagnation point. However, the condition $M_0' \ll M_\infty$ is rapidly recovered as the observer

moves away from the boundary surface. This assumption allows us to neglect high order terms in the mean flow non-uniformity to give

$$\frac{\partial^2\hat{\phi}}{\partial t^2} + 2\mathbf{u}_0 \cdot \boldsymbol{\nabla}\frac{\partial\hat{\phi}}{\partial t} - c_\infty^2\boldsymbol{\nabla}^2\hat{\phi} + (\mathbf{u}_\infty \cdot \boldsymbol{\nabla})(\mathbf{u}_\infty \cdot \boldsymbol{\nabla}\hat{\phi}) = 0. \tag{2.35}$$

In all that follows, Eq. (2.35) will be referred to as the *weakly non-uniform potential flow wave equation*. Equation (2.35) is a first order approximation of Eq. (2.29), with respect to the non-uniform mean flow component $\mathbf{u}_0'$, that models wave refraction from a potential mean flow. It differs from a uniform flow formulation in that $\mathbf{u}_0(\mathbf{x})$, depends on the local mean flow, but it reduces to the convected wave equation as soon as a uniform mean flow region is reached. In other words, it is exact within a uniform mean flow region.

Note that Eq. (2.35) differs from the Taylor formulation of Astley and Bain [32]; Eq. (2.35) is based on the assumption that $M_\infty \ll 1$ and $M_0' \ll M_\infty$, whereas the Taylor formulation assumes $M_0 \ll 1$. Equation (2.35) was also considered in the work of Clancy [36] based on a variable transformation including non-uniform flow effects, which is further discussed in Sec. 2.6.

2.5.3 Uniform flow convected wave equation

If the background flow is uniform, Eqs. (2.29) and (2.35) reduce to the well-known convected wave equation,

$$\frac{D_\infty^2\hat{\phi}}{Dt^2} - c_\infty^2\boldsymbol{\nabla}^2\hat{\phi} = 0. \tag{2.36}$$

where $D_\infty/Dt = \partial/\partial t + \mathbf{u}_\infty \cdot \boldsymbol{\nabla}$. The above equation can also be written as

$$\frac{\partial^2\hat{\phi}}{\partial t^2} + 2\mathbf{u}_\infty \cdot \boldsymbol{\nabla}\frac{\partial\hat{\phi}}{\partial t} - c_\infty^2\boldsymbol{\nabla}^2\hat{\phi} + (\mathbf{u}_\infty \cdot \boldsymbol{\nabla})(\mathbf{u}_\infty \cdot \boldsymbol{\nabla}\hat{\phi}) = 0. \tag{2.37}$$

Alternatively, Eq. (2.36) can be written in terms of either acoustic pressure, p', or density, ρ'.

2.5.4 Taylor wave equation

Equation (2.35) currently includes terms of order M_0 and M_∞^2. It can be simplified, by neglecting terms of order M_∞^2, to give [32]

$$\frac{\partial^2\hat{\phi}}{\partial t^2} + 2\mathbf{u}_0 \cdot \boldsymbol{\nabla}\frac{\partial\hat{\phi}}{\partial t} - c_\infty^2\boldsymbol{\nabla}^2\hat{\phi} = 0, \tag{2.38}$$

Equation (2.38) is referred to as the *Taylor wave equation* [32, 31]. Note that Eq. (2.38) is also an approximation of the uniform flow convected wave equation, Eq. (2.37). In other words, it is not exact when wave propagation occurs in a uniform flow. It reduces to the standard wave equation for $\mathbf{u}_0 \to \mathbf{0}$.

2.5.5 Boundary conditions

The boundary conditions that can be assigned to close the problem described by Eq. (2.35), (2.36) and (2.38) are reviewed in this section. The boundary conditions for inviscid media must include mean flow effects, since the mean flow velocity does not generally vanish on the boundary surface. The radiation conditions for unbounded domains are first reviewed.

In an unbounded domain, incoming sound waves cannot propagate from infinity. This statement can be expressed by the Sommerfeld radiation condition with mean flow [22]. It imposes a vanishing acoustic perturbation at infinity using an asymptotic relation that models the propagation of only outgoing acoustic waves. It can be expressed in terms of either pressure, p',

$$\lim_{r\to\infty} r^b \left[(\mathbf{u}_\infty \cdot \mathbf{n} + c_\infty)\frac{\partial}{\partial r} + \frac{\partial}{\partial t}\right] p' = 0, \tag{2.39}$$

or acoustic velocity potential, $\hat{\phi}$,

$$\lim_{r\to\infty} r^b \left[(\mathbf{u}_\infty \cdot \mathbf{n} + c_\infty)\frac{\partial}{\partial r} + \frac{\partial}{\partial t}\right] \hat{\phi} = 0, \tag{2.40}$$

where $\mathbf{u}_\infty$ is the mean flow velocity in the uniform region, $\mathbf{n}$ is the normal unit vector to the wave front, $r = \|\mathbf{x}\|$ and $b = 1$ or 0.5 for either three-dimensional or two-dimensional problems.

A Dirichlet boundary condition would prescribe the acoustic potential, i.e. $\hat{\phi} = \hat{\phi}_s$, however it is not generally of practical interest. A condition on the acoustic pressure is more common. It can be retrieved from the linearised Bernoulli equation (see Eq. (2.27)) to give

$$-\rho_0 \left(\frac{\partial \hat{\phi}}{\partial t} + \mathbf{u}_0 \cdot \boldsymbol{\nabla}\hat{\phi}\right) = p'_s, \tag{2.41}$$

where p'_s is a known acoustic pressure distribution on the boundary.

A Neumann boundary condition is also relevant to many applications. In this case, normal particle velocity to the boundary surface is prescribed. It can be written as $\mathbf{u}' \cdot \mathbf{n} = u_{n,s}$, while $u_{n,s} = 0$ if the boundary surface is rigid. Note that for a potential formulation, $\mathbf{u}' = \boldsymbol{\nabla}\hat{\phi}$.

Robin boundary conditions are also of practical interest. At the boundary surface, the continuity of surface and particle displacements must be imposed [71]. For an inviscid mean flow, Myers [71] provided a condition by linearising the continuity of pressure and normal particle displacements:

$$\mathbf{u}' \cdot \mathbf{n} = \left(\frac{\partial}{\partial t} + \mathbf{u}_0 \cdot \boldsymbol{\nabla} - \mathbf{n} \cdot \frac{\partial \mathbf{u}_0}{\partial n}\right) d, \tag{2.42}$$

where d is the particle displacement normal to the boundary surface. This formulation was presented following the model previously derived by Ingard [72] for a flat plate. The effect of the curvature of a vibrating surface in the presence of a non-uniform flow is modelled.

Myers' condition is imposed on the edge of the boundary layer, which is considered to be infinitely thin. Although Myers' condition is conventionally used for many applications, recently Gabard [73] has shown that it can lead to significant errors when compared to finite-thickness boundary layers. For harmonic problems, $\mathrm{e}^{\mathrm{i}\omega t}$, if the thickness of the boundary layer is small, the standard impedance boundary condition can be used along the boundary surface to give [71, 74]

$$\mathbf{u}'(\omega)\cdot\mathbf{n} = \Big(\mathrm{i}\omega + \mathbf{u}_0\cdot\boldsymbol{\nabla} - \mathbf{n}\cdot\frac{\partial\mathbf{u}_0}{\partial n}\Big)\frac{A(\omega)p'(\omega)}{\mathrm{i}\omega}, \tag{2.43}$$

where ω denotes the angular frequency, $\mathrm{i}=\sqrt{-1}$ is the imaginary unit and the dependence on $\mathbf{x}$ is implied. In the above equation, the admittance $A(\omega)$ of the surface is generally prescribed and p' can be expressed in terms of the acoustic velocity potential (see Eq. (2.41)). In the absence of a mean flow, Eq. (2.43) reduces to the condition for the standard wave equation with quiescent media.

2.6 Variable transformations

A set of variable transformations is presented as a mathematical tool to reduce wave operators in the presence of a mean flow to the standard wave operator with quiescent media. In the transformed space, a standard wave propagation problem with modified boundary conditions and sound sources can then be solved. A combination of the Taylor [31] and Lorentz [44] transformations is presented as a generalized transform from which either a Taylor or Lorentz transform can be derived based on different assumptions, respectively a low Mach number or a uniform flow. The combined transformation will be extensively used in this work as a systematic tool to deal with Eq. (2.35). In fact, the weakly non-uniform flow formulation will be shown to be nothing but the physical model associated with a combination of Taylor and Lorentz transforms. First, we review the Lorentz and the Taylor transforms. Second, their combination is discussed.

2.6.1 Lorentz transform

The Lorentz transform [44, 75] has been conventionally used in acoustics to reduce the convected wave equation with uniform flow, Eq. (2.36), to the standard Helmholtz equation with quiescent media.

We denote the variables in the Lorentz space with "†". For a uniform flow aligned with the x-axis, the Lorentz transform can be written as

$$X^\dagger = \frac{x}{\beta_\infty},\quad Y^\dagger = y,\quad Z^\dagger = z,\quad T^\dagger = \beta_\infty t + \frac{M_\infty x}{c_\infty\beta_\infty}, \tag{2.44}$$

where $(\mathbf{X}^\dagger, T^\dagger)$ and $(\mathbf{x}, t)$ denote the Lorentz and the physical space-time coordinates. We have also introduced $\beta_\infty = \sqrt{1 - M_\infty^2}$. Using the chain rule and Eq. (2.44), the derivative operators reduce to

$$\begin{aligned} \boldsymbol{\nabla}_{X^\dagger} = \left(\beta_\infty \frac{\partial}{\partial x} - \frac{1}{c_\infty}\frac{M_\infty}{\beta_\infty}\frac{\partial}{\partial t}, \quad \frac{\partial}{\partial y}, \quad \frac{\partial}{\partial z}\right), \\ \frac{\partial}{\partial T^\dagger} = \frac{1}{\beta_\infty}\frac{\partial}{\partial t}, \end{aligned} \tag{2.45}$$

where $\boldsymbol{\nabla}_{X^\dagger}$ is the gradient in the Lorentz space.

Considering that we will focus on boundary integral solutions, the normal derivatives of the acoustic variables to a prescribed boundary surface, $\partial\Omega^\dagger$ (see Fig. 2.1), are relevant to this work. A generalized formulation for the normal derivative in the Lorentz space is obtained below. We consider Eq. (2.56) and define the normal unit vector $\mathbf{n} = n_x\mathbf{i} + n_y\mathbf{j} + n_z\mathbf{k}$ to the boundary surface $\partial\Omega$. The normal vector in the transformed space $\mathbf{n}^\dagger = n_{X^\dagger}\mathbf{i}^\dagger + n_{Y^\dagger}\mathbf{j}^\dagger + n_{Z^\dagger}\mathbf{k}^\dagger$ can then be written as

$$\mathbf{n}^\dagger = \frac{1}{\sqrt{1 - M_\infty^2 n_x^2}}(\beta_\infty n_x\mathbf{i} + n_y\mathbf{j} + n_z\mathbf{k}), \tag{2.46}$$

where $\mathbf{n}^\dagger$ is referred to as the generalized normal vector. In the above equation, the basis of vectors in the transformed space, $(\mathbf{i}^\dagger, \mathbf{j}^\dagger, \mathbf{k}^\dagger)$, is written by transforming each component of the physical basis, $(\mathbf{i}, \mathbf{j}, \mathbf{k})$, according to Eq. (2.44) and normalising the resulting vector.

A generalized normal derivative in the Lorentz space is recovered by projecting the gradient in Eq. (2.45) onto the normal vector in Eq. (2.46) to give

$$\frac{\partial}{\partial n^\dagger} = \frac{1}{\sqrt{1 - M_\infty^2 n_x^2}}\left(\frac{\partial}{\partial n} - n_x M_\infty^2\frac{\partial}{\partial x} - \frac{M_\infty n_x}{c_\infty}\frac{\partial}{\partial t}\right), \tag{2.47}$$

where n_x is the x-component of the normal vector to the boundary surface.

An important geometrical feature of the Lorentz transformation is the norm of the Jacobian, J, to transform surface elements from the physical to the transformed space, i.e. $dS = JdS^\dagger$. This has been derived by Balin *et al.* [27]. Let us consider the following orthonormal basis of vectors (see Fig. 2.3)

$$\mathbf{a}_1 = \mathbf{i}, \qquad \mathbf{a}_2 = \frac{\mathbf{n} - (\mathbf{n}\cdot\mathbf{a}_1)\mathbf{a}_1}{\sqrt{n_y^2 + n_z^2}}, \qquad \mathbf{a}_3 = \mathbf{a}_1 \times \mathbf{a}_2. \tag{2.48}$$

The normal vector to the boundary can then be written as

$$\mathbf{n} = (\mathbf{n}\cdot\mathbf{a}_1)\mathbf{a}_1 + \sqrt{1 - n_x^2}\mathbf{a}_2, \tag{2.49}$$

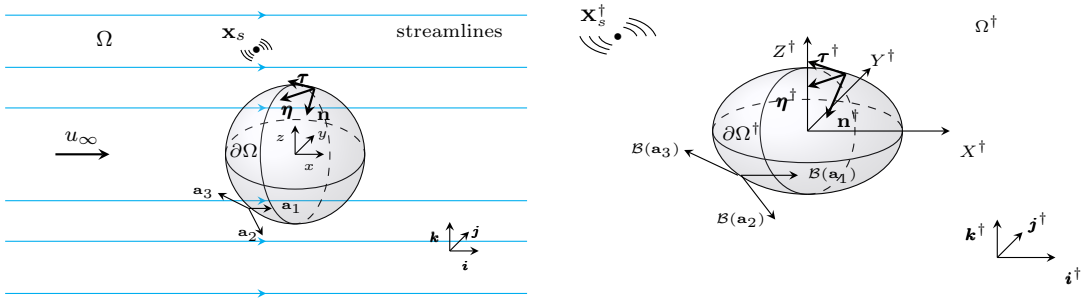

(a) Physical domain (b) Lorentz domain

Figure 2.1: Geometrical features for the scattering of a sound field in a non-uniform potential flow. Description of the same problem either in a physical or in a transformed Lorentz space-time.

whereas the tangent vectors are

$$\boldsymbol{\tau}_1 = -\sqrt{1-n_x^2}\mathbf{a}_1 + (\mathbf{n}\cdot\mathbf{a}_1)\mathbf{a}_2, \qquad \boldsymbol{\tau}_2 = \mathbf{a}_3. \tag{2.50}$$

Note that $\boldsymbol{\tau}_1\cdot\mathbf{n} = \boldsymbol{\tau}_2\cdot\mathbf{n} = 0$. As such, $(\boldsymbol{\tau}_1, \boldsymbol{\tau}_2)$ is an orthonormal basis of vectors. Hence, the norm of the Jacobian of the transformation can be defined as $J = 1/\|\det(\mathcal{B}(\boldsymbol{\tau}_1), \mathcal{B}(\boldsymbol{\tau}_2))\|$, where $\mathcal{B} = (1/\beta_\infty, 1, 1)$ denotes the Lorentz operator. It gives

$$\mathcal{B}(\boldsymbol{\tau}_1) = -\frac{\sqrt{1-n_x^2}}{\beta_\infty}\mathbf{a}_1 + (\mathbf{n}\cdot\mathbf{a}_1)\mathbf{a}_2, \qquad \mathcal{B}(\boldsymbol{\tau}_2) = \mathbf{a}_3. \tag{2.51}$$

Therefore, the norm of the Jacobian of this transformation can be written as

$$J = \frac{1}{\|\mathcal{B}(\boldsymbol{\tau}_1)\|\|\mathcal{B}(\boldsymbol{\tau}_2)\|} = \frac{\beta_\infty}{\sqrt{1-M_\infty^2 n_x^2}}. \tag{2.52}$$

2.6.2 Taylor transform

The Taylor transform has been introduced to reduce Eq. (2.38) to the standard wave equation with quiescent media. The Taylor transform [31, 32] can be written as

$$X = x, \quad Y = y, \quad Z = z, \quad T = t + \frac{\Phi_0(\mathbf{x})}{c_\infty^2}, \tag{2.53}$$

where $(\mathbf{X}, T)$ denotes the Taylor space-time coordinates. Using the chain rule based on Eq. (2.44), the derivative operators can then be rewritten as

$$\begin{gathered}\boldsymbol{\nabla}_X = \left(\frac{\partial}{\partial x} - \frac{M_{0,x}}{c_\infty}\frac{\partial}{\partial t}, \quad \frac{\partial}{\partial y} - \frac{M_{0,y}}{c_\infty}\frac{\partial}{\partial t}, \quad \frac{\partial}{\partial z} - \frac{M_{0,z}}{c_\infty}\frac{\partial}{\partial t}\right), \\ \frac{\partial}{\partial T} = \frac{\partial}{\partial t},\end{gathered} \tag{2.54}$$

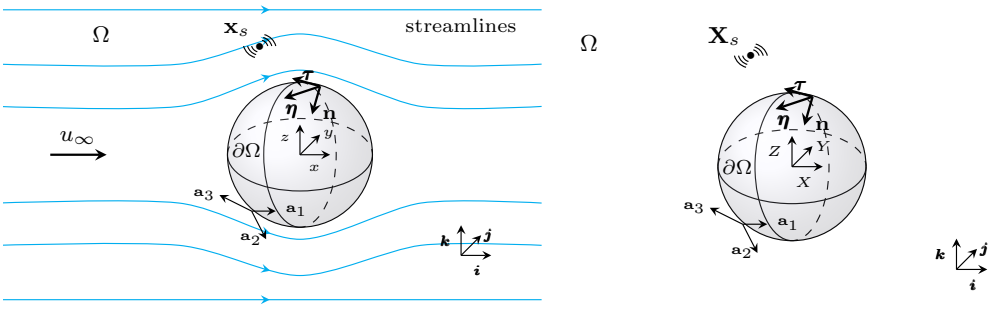

(a) Physical domain (b) Taylor domain

Figure 2.2: Geometrical features for the scattering of a sound field in a non-uniform potential flow. Description of the same problem either in a physical or in a transformed Taylor space-time.

where $\mathbf{M}_0 = (M_{0,x}, M_{0,y}, M_{0,z})$. In the Taylor space, the length scales are the same as those in the physical space (see Fig. 2.2). Therefore, the normal vector is the same as that in the physical space and the normal derivative to the boundary surface, $\partial\Omega$, is given by

$$\mathbf{n} \cdot \boldsymbol{\nabla}_X = \left[\frac{\partial}{\partial n} - \frac{\mathbf{M}_0 \cdot \mathbf{n}}{c_\infty} \frac{\partial}{\partial t} \right]. \tag{2.55}$$

Note that for impermeable stationary surfaces $\mathbf{M}_0 \cdot \mathbf{n} = 0$. As shown by Astley and Bain [32], Eq. (2.38) can be reduced to the standard wave equation by using the Taylor transform. Gregory *et al.* [47] showed that there are not frequency restrictions to the validity of the Taylor transform. However, unlike the Lorentz transform, which reduces the convected wave equation to the standard wave equation with quiescent media without approximation, the Taylor transform relies on a number of approximations listed in Secs. 2.5.2 and 2.5.4.

2.6.3 Taylor–Lorentz transform

The main features of a Taylor–Lorentz space-time transformation are presented in this section. It is obtained by combining the Lorentz transform for a uniform flow with the Taylor transform operating on the non-uniform velocity component of the mean flow. The focus is on the transformation of the independent variables and derivative operators.

The orthonormal bases in the physical and in the transformed space are defined as $(\mathbf{i}, \mathbf{j}, \mathbf{k})$ and $(\tilde{\mathbf{i}}, \tilde{\mathbf{j}}, \tilde{\mathbf{k}})$ (see Fig. 2.3). Assume a uniform mean flow aligned at large distances from the origin with the x-axis. This assumption of alignment with the x-axis is not a limitation for the present work, but it is convenient because it clearly simplifies the notation. Note that a reference frame can be arbitrarily defined in any instance such that the mean flow is aligned with one of the axes. This formal simplification is adopted in all that follows.

The combination of Taylor [31, 32] and Lorentz [44, 75] transformations gives

$$\tilde{X} = \frac{x}{\beta_\infty}, \quad \tilde{Y} = y, \quad \tilde{Z} = z, \quad \tilde{T} = \beta_\infty \left(t + \frac{\Phi_0'(\mathbf{x})}{c_\infty^2} \right) + \frac{M_\infty x}{c_\infty \beta_\infty}, \tag{2.56}$$

where $(\tilde{\mathbf{X}}, \tilde{T})$ denote the transformed space-time coordinates, and $\Phi_0'(\mathbf{x}) = \Phi_0(\mathbf{x}) - M_\infty x$ is the velocity potential associated with the non-uniform component of the mean flow. Using the chain rule based on Eq. (2.56) (see also Appendix. C.6), the derivative operators can be specified as follows

$$\begin{gathered} \boldsymbol{\nabla}_{\tilde{X}} = \left(\beta_\infty \frac{\partial}{\partial x} - \frac{1}{c_\infty} \left[\frac{M_\infty}{\beta_\infty} + \beta_\infty M_{0,x}' \right] \frac{\partial}{\partial t}, \quad \frac{\partial}{\partial y} - \frac{M_{0,y}'}{c_\infty} \frac{\partial}{\partial t}, \quad \frac{\partial}{\partial z} - \frac{M_{0,z}'}{c_\infty} \frac{\partial}{\partial t} \right), \\ \frac{\partial}{\partial \tilde{T}} = \frac{1}{\beta_\infty} \frac{\partial}{\partial t}, \end{gathered} \tag{2.57}$$

where the Mach number $\mathbf{M}_0(\mathbf{x}) = \mathbf{u_0}(\mathbf{x})/c_\infty = \mathbf{M}_\infty + \mathbf{M}_0'(\mathbf{x})$, $\mathbf{M}_\infty = (M_\infty, 0, 0)$ and $\mathbf{M}_0'(\mathbf{x}) = (M_{0,x}', M_{0,y}', M_{0,z}')$. The term $\boldsymbol{\nabla}_{\tilde{X}} = (\partial/\partial\tilde{X}, \partial/\partial\tilde{Y}, \partial/\partial\tilde{Z})$ denotes the gradient in the transformed space.

The space transformation operated on $\mathbf{x}$ by Eq. (2.56) is the same as for the Lorentz transform. Therefore, the normal vector in the Taylor–Lorentz space, $\tilde{\mathbf{n}}$, and the norm of the Jacobian (to transform surface elements) are the same as for Eqs. (2.46) and (2.52). Nonetheless, the orthogonal bases of unit vectors are coincident, namely $(\mathbf{i}^\dagger, \mathbf{j}^\dagger, \mathbf{k}^\dagger) = (\tilde{\mathbf{i}}, \tilde{\mathbf{j}}, \tilde{\mathbf{k}})$ (see Fig. 2.3).

Note that, lengths are invariant to a Taylor–Lorentz transform since they are invariant to either Taylor [31] or Lorentz [44] transforms being applied separately. Hence, the normal derivative to the boundary surface can be recovered by combining Eqs. (2.46) and (2.57):

$$\frac{\partial}{\partial \tilde{n}} = \frac{1}{\sqrt{1 - M_\infty^2 n_x^2}} \left[\frac{\partial}{\partial n} - n_x M_\infty^2 \frac{\partial}{\partial x} - \frac{(\mathbf{M}_0 \cdot \mathbf{n} - M_{0,x}' M_\infty^2)}{c_\infty} \frac{\partial}{\partial t} \right], \tag{2.58}$$

where $\partial/\partial\tilde{n} = \boldsymbol{\nabla}_{\tilde{X}} \cdot \tilde{\mathbf{n}}$. It is consistent with the approximations used to derive Eq. (2.35), namely $M_0' \ll M_\infty$, that the terms of order $M_\infty^2 M_{0,x}'$ in the above equation can be neglected to give

$$\frac{\partial}{\partial \tilde{n}} \simeq \frac{1}{\sqrt{1 - M_\infty^2 n_x^2}} \left(\frac{\partial}{\partial n} - n_x M_\infty^2 \frac{\partial}{\partial x} - \frac{\mathbf{M}_0 \cdot \mathbf{n}}{c_\infty} \frac{\partial}{\partial t} \right). \tag{2.59}$$

The transformation proposed in this section differs from the work of Clancy [36] in that the Taylor transform of the non-uniform flow component of the mean flow is applied following a Lorentz transform of the uniform flow part. On the contrary, Clancy [36] considered a local Lorentz transform where the non-uniform mean flow velocity component was included into the Lorentz transform. In that case, the uniform flow component M_∞ modifies the corresponding non-uniform flow part, M_0', with a factor $\sqrt{1 - M_\infty^2}$, which is independent of the specific geometry and the mean flow around it. This dependence has yet to be

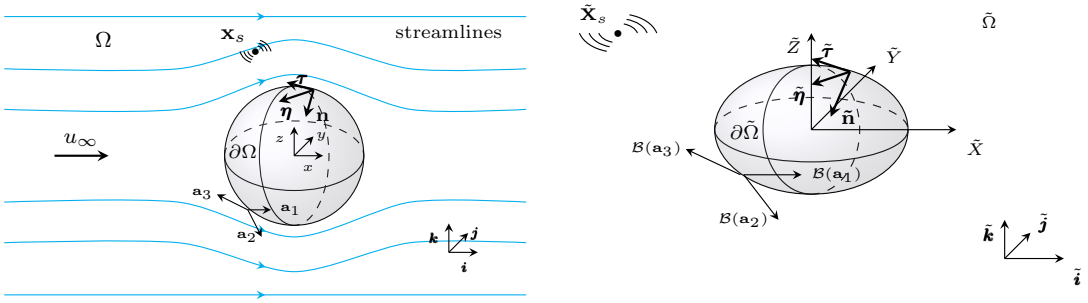

(a) Physical domain

(b) Taylor–Lorentz domain

Figure 2.3: Geometrical features for the scattering of a sound field in a non-uniform potential flow. Description of the same problem either in a physical or in a transformed Taylor–Lorentz space-time.

demonstrated and, therefore, we do not imply it in this work. In fact, we propose a more general transformation, i.e. Eq. (2.56).

2.7 Concluding remarks

We want to solve sound propagation and scattering on a non-uniform potential flow. Generally, we aim to predict sound scattering in an unbounded domain around slender bodies. Starting from the Navier–Stokes equation, the linearised potential wave equation (LPE) has been derived assuming potential flows and small acoustic perturbations. Previous works [36, 70] showed that a potential flow is a reasonable approximation for wave propagation with low Mach number mean flows around slender bodies with small angles of attack.

Based on the assumption that $M_\infty \ll 1$ and considering small non-uniform mean flow components, i.e. $M_0' \ll M_\infty$, an approximate formulation of the linearised potential equation (LPE), referred to as the *weakly non-uniform flow potential wave equation*, was obtained. In general, we are interested in low Mach number mean flows, such as would be the case for an aircraft at take-off or landing. Nonetheless, we target the prediction of noise propagation and scattering around slender bodies. Although the $M_0' \ll M_\infty$ ansatz is violated at the stagnation point for impermeable surfaces, this condition is rapidly recovered for slender bodies as an observer moves away from the boundary [69, 70]. We rely on these assumptions for the development of this work and its applications, such as forward fan noise large-scale installation effects.

We also discussed how the convected wave equation with uniform flow and the Taylor wave equation can be derived as different subsets of the weakly non-uniform formulation by either assuming a uniform flow or neglecting terms of order M_∞^2. The Lorentz and the Taylor transforms have been reviewed since they are consistent respectively with the uniform flow convected and the Taylor wave equation. Nonetheless, a combined Taylor–Lorentz transform

and its geometrical and algebraic features were discussed. The combined transformation was devised as a fundamental tool for the development of this work. It will be shown to be consistent with the weakly non-uniform formulation and will be extensively used in the following chapters.

Chapter 3

Numerical Methods for Sound Propagation with Moving Media

Contents

This chapter aims to review the state-of-the-art of numerical methods applied to sound propagation and scattering for aircraft noise prediction. However, it is not meant to be a comprehensive review of the numerical methods available in the literature, rather a framework for the boundary integral methods developed and presented in the following chapters. It provides the main motivations for using boundary integral solutions for noise propagation and scattering around aircraft rather than other methods that are currently available. In Sec. 3.1, the context of the present work is provided. In Sec. 3.2, boundary element methods are reviewed. In Sec. 3.3, alternative volume-based methods, acoustic analogies and high-frequency formulations are briefly discussed. In Sec. 3.4, the most recent numerical methods applied for large-scale aircraft acoustic installation effect problems are reviewed. Concluding remarks are given in Sec. 3.5.

3.1 General context

Predicting noise propagation and scattering of complex sources is important to automotive, energy and aeronautical industries. Noise radiation and scattering from nacelles in flight and Auxiliary Power Units (APUs) on the ground are problems concerning the aviation sector and aircraft certification. Numerical methods can support faster design cycles of such devices and reduce the cost of certification. A number of numerical methods have been developed to potentially assess sound propagation and scattering around these devices in the presence of the airframe. For these applications, wave propagation and scattering with mean flow must be modelled. We refer to numerical methods based on the discretisation of a geometrical volume as *volume-based methods*, such as FEM, DGM and FD. Methods based on the discretisation of the boundary surfaces are referred to as *boundary element methods*.

Conventional CFD methods, such as Reynolds Averaged Navier–Stokes (RANS), compressible Large Eddy Simulations (LES) and Direct Numerical Simulations (DNS), can be used to predict aerodynamic sound generation by solving the acoustic and the hydrodynamic field concurrently [76, 77, 78]. The major drawback of these methods is the very high cost for realistic computations where a high level of mesh refinement is required to achieve good accuracy. In fact, high order methods and high mesh refinement are needed to avoid numerical attenuation and dispersion of acoustic waves travelling over long distances. At the current state of development, practical applications of these methods are limited. The lattice Boltzmann method appear to be promising in terms of working around these constraints [79] but it is not yet fully validated or developed for acoustics.

CFD solutions to sound generation are conventionally coupled with numerical methods relying on linear models for wave propagation. These methods can be based either on time or frequency domain formulations. Time domain formulations are suitable for transient analyses and, therefore, can be used to predict the propagation of broadband noise sources. Time domain formulations are convenient when a large frequency spectrum for the solution must be evaluated. However, they also allow time harmonic solutions from steady harmonic sources to be computed.

In the presence of non-uniform flow, volume-based methods are conventionally used. However, time-domain volume-based methods can provide solutions that are unstable when impedance boundary conditions are considered with a mean flow [80, 81]. Instability waves, such as the Kelvin–Helmholtz instability [56, 57], are also supported by non-potential formulations, such as Linearised Euler Equations, leading to inaccurate numerical solutions. Filtering the equations, such as is done by APE [63], allows the development of instability waves to be worked around but at the cost of solving a different set of equations. Alternatively, the terms triggering these instabilities can be removed from the physical model to achieve the same result [82]. Potential formulations also do not support instability waves

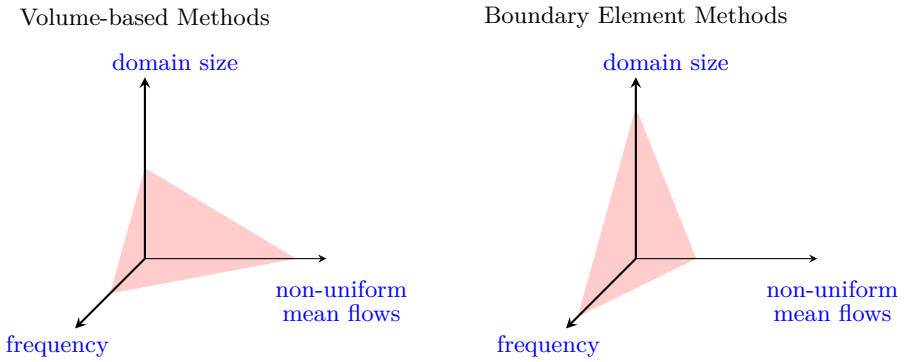

Figure 3.1: Features of frequency-based numerical methods for wave propagation, comparing boundary element to volume-based methods.

and are limited to acoustic wave propagation. On the other hand, time domain boundary element methods are limited to uniform mean flows and do not suffer from instability issues [41].

Direct frequency domain solutions can also be applied to work around the instability issue for volume-based methods, such as is done by direct solvers based on LEE [83]. They are conventionally used for tonal noise propagation and scattering but can be applied to broadband sources by using assumptions such as equal modal power [84]. Frequency-domain formulations can be solved using either volume-based or boundary element methods. In the former case, there are not strong limitations on the characteristics of the non-uniform flow but the dimension of the sparse discrete system of equations is large and computationally demanding at high frequencies when direct solvers are used, such as for elliptic equations. In the latter case, the complexity of the medium is clearly reduced, as we will discuss in the following section, and conventional boundary element methods are also characterized by dense matrices of coefficients; despite the fact that the discrete system of equations is small compared to corresponding volume-based models, boundary element models are computationally demanding at high frequency when conventional formulations are used (see Fig. 3.1). However, boundary element methods can rely on fast algorithms [24, 25] to work around this limitation and efficiently solve large-scale short-wavelength problems.

Another fundamental modelling issue is related to sound propagation in unbounded domains. For volume-based methods, the computational domain must be truncated and non-reflecting boundary conditions must be applied. The truncation of the domain often requires the acoustic waves to be damped in a non-physical absorbing zone to simulate the radiation condition at the outer boundary of the domain. This is accomplished using absorbing boundary conditions [85], infinite elements [86, 87] and the Perfectly Matched Layer (PML) [88, 89]. On the contrary, boundary element methods [43, 90, 91, 92] are generally devised with kernels that inherently satisfy the radiation condition.

Another important distinction among numerical methods is the use of either structured or unstructured grids [93]. Methods based on unstructured grids have the advantage of being

more flexible in terms of meshing. In other words, it is easier to fit an unstructured mesh to a geometry than it is for a structured grid. These methods are suitable for automatic mesh generation. On the contrary, structured grids perform better than unstructured grids in terms of limiting numerical dissipation and dispersion, but they require more effort than unstructured grids to be created when dealing with complex geometries.

3.2 Boundary element methods

The boundary element method [43, 91] is a numerical approach based on boundary integral solutions which relates the solution on the boundary of a domain to the corresponding field variables. Unlike volume-based methods, the boundary element method requires only the discretisation of the boundary surface and a priori knowledge of the Green's function of the related governing equation [94]. This method is suitable to solve sound radiation in an unbounded domain since a Green's function can be recovered to inherently satisfy the Sommerfeld radiation condition.

The boundary element method was initially developed in acoustics to solve wave propagation in quiescent media [43, 52, 90, 92]. It is based on the boundary integral solution to the wave operator and has been devised to solve both transient problems by using time domain formulations [95] and harmonic problems based on frequency domain formulations [96]. In this thesis, we will develop frequency domain solutions since the target application is forward fan noise installation effects. Therefore, we will focus on reviewing frequency-based solutions.

In the frequency domain, the discretisation of boundary surfaces leads to linear systems of equations of small dimensions compared to volume-based methods. However, the matrix of the coefficients is fully populated. Although a direct solver can be applied, the use of iterative algorithms can reduce the computational cost of solving the discrete system. Conjugate gradient [97], bi-conjugate gradient solvers and the generalized minimal residual algorithms [98] have been developed. For iterative algorithms, a pre-conditioner is conventionally used in most of the cases [99] and the use of iterative solvers is suggested to solve large systems of equations.

Advanced solutions based on non-polynomial shape functions have also been developed. They are conventionally based on enriching functions that are solutions of the governing differential equations. Wave-based boundary element solutions [100, 101, 102] have been presented by enriching the polynomial basis functions with plane waves. The introduction of enrichment functions based on the physics of the problem allows the discretisation to be reduced down to 2-3 points per wavelength [101, 103, 102]. However, the main drawback of introducing enriching functions is the rapid increase of the condition number of the coefficient matrix which leads to ill-conditioned systems [100].

CFD methods have also been coupled with boundary element methods to solve noise generation, propagation and scattering problems [104, 105]. For example, boundary element solutions have been developed based on Lighthill's acoustic analogy [105, 106, 107, 108]. The sound sources have been characterized using either LES or RANS and sound propagation has then been solved by BEM [105, 109]. The use of boundary element methods, however, has been based on either quiescent media [107, 110, 108] or low Mach number mean flows based on the Taylor transformation [105]. Alternatively, uniform mean flows have been considered with moderate success [29].

3.2.1 Computational cost

In its standard formulation [43], BEM is not suitable for large-scale short-wavelength problems. The most demanding operation in BEM is the computation of the matrices. For a discrete problem with N degrees of freedom, N^2 evaluations of the Green's function and its derivatives are required [111]. Nonetheless, the computational cost of the matrix-vector product scales as $O(N^2)$ while the cost of factorisation is generally proportional to $O(N^3)$ for direct solvers. The computational cost associated with the solution of the corresponding linear system scales as $O(N^2)$ for a direct solver and $O(N^2 N_{iter})$ for an iterative solver, where N_{iter} denotes the number of iterations. Therefore, since the number of degrees of freedom scales almost linearly with frequency, the application of conventional BE algorithms is constrained to low frequencies.

However, BEM can be extended to medium-high frequency problems using more advanced techniques for matrix compression and storage. Both the fast multipole method [24] or the hierarchical matrix approach (H-matrix) [25, 112] (see Fig. 3.1) have been successfully applied to solve wave propagation problems [45]. The fast multipole method [24, 113, 114, 115] is based on the idea that wave interactions can be computed between clusters of points instead of point by point. The method is based on the analytical expansion of Boundary Element (BE) kernels and reduces the cost of the matrix-vector product to $O(Nlog^2(N))$ or less [45, 115]. Fast algorithms based on plane wave expansions have also been developed [116]. These approaches perform better than conventional fast multipole methods for far-field interactions. However, they are less accurate for near-field interactions.

On the other hand, the hierarchical matrix approach [25] can be used for the same purpose without expanding the kernel. The BE domain is divided into clusters. Interaction between admissible clusters, i.e. clusters that are far from each other, are represented with low-rank approximations of the block matrices. Second, the compression is accomplished by storing two low-rank matrices instead of the entire block. This approach allows the matrix-vector product to be lowered to $O(Nlog(N))$ [117]. Note that this cost can be further reduced to $O(N)$ [117, 118] for H^2-matrix approaches, where clustered columns and rows are nested based on a uniform H-matrix [117].

The H-matrix is generally used with direct solvers while the fast multipole method is more conventionally applied to iterative solvers [45]. Direct solvers have a computational advantage over iterative solvers if a high number of right-hand sides must be evaluated.

3.2.2 Mean flow effects

The boundary element method allows scattering problems from complex geometries to be solved. Fast algorithms also allow large-scale short-wavelength noise radiation and scattering problems to be tackled. However, boundary element solutions to wave propagation are exact only for uniform mean flows for which an analytical kernel exists [44]. For a uniform medium, a boundary integral solution to the convected wave equation can be recovered along with an exact Green's function [40]. Current industrial practices are based on a uniform mean flow [45].

On the other hand, only approximate physical models accounting for non-uniform mean flow can be solved by BEM [32, 36]. Although some exceptions exist for small mean flow velocity gradients [35] which do not seem to provide accurate results [26], boundary element solutions are conventionally limited to potential flows, with some extensions to quasi-potential flows which have been not fully developed and validated [36, 46]. These solutions are based on approximate formulations of the linearised potential equation. A potential solution both for the mean flow and the acoustic perturbation can be computed based on an integral solution over the boundary [46]. On the other hand, local effects in the domain pertaining to non-potential flows, such as viscous effects, cannot generally be considered with an integral over the boundary of the domain [46]. Nonetheless, it is unlikely that mean flow compressibility effects can also be included [47].

Conventionally in aeroacoustics, uniform mean flow effects on boundary integral solutions are developed in a reference frame connected with the undisturbed air. In other words, the reference frame is stationary compared to the observer. However, for specific applications, such as helicopter noise, the problem has been formulated in a reference frame in arbitrary motion [46, 119]. Note that these approaches are equivalent if the sound sources are modelled consistently with the reference frame adopted [120].

3.2.2.1 Uniform flow

Current boundary element models for scattering in low Mach number flows use the Lorentz transformation [44, 75] (see Sec. 2.6.1) to solve wave propagation in a uniform mean flow. This variable transformation allows the uniform flow convected wave equation to be reduced to the standard wave problem without approximations. By means of a Lorentz transformation, BE solvers for the standard Helmholtz equation can be used for wave propagation in uniform flow [42]. Therefore, all the fast algorithms developed for BE solutions in quiescent

media can be applied to solve wave propagation in uniform flow. However, source definitions and boundary conditions must be consistent with the transformed space.

Due to the Lorentz transformation, the physical space is deformed in the direction of the mean flow. The deformation of the domain complicates both the formulation of the boundary conditions and the implementation of the transmission conditions [121, 122] for coupled formulations [27, 42]. This drawback can be overcome using an integral formulation in the physical space, such as that proposed by Wu and Lee [40] in the frequency domain and that of Hu [41, 123] in the time domain.

The Lorentz transformation applied to BE solutions has been tested for aeronautical applications. Balin *et al.* [27] have modelled radiation and scattering by an aeroengine. Papamoschou and Mayoral [29] have used the same approach to investigate jet noise shielding effects. Heffernon *et al.* [70] applied the method to assess landing gear installation effects. Fast multipole schemes were also applied to boundary element solutions with uniform flow based on Lorentz transformation [27].

On the other hand, Hu [41] has developed a time BE solution with uniform mean flow in the physical space. Barbarino and Bianco [124] have also solved the convected wave equation with uniform flow based on a physical-space boundary element formulation in the frequency domain. In their work, a fast multipole algorithm was also implemented.

3.2.2.2 Non-uniform flow

From the literature, only approximate formulations are available to solve wave propagation in non-uniform mean flows based on boundary element methods. At the moment, these solutions are generally provided in the frequency domain. Conventionally, a BE solution is sought in a transformed space-time, where wave propagation in non-uniform flow is reduced to the standard wave propagation problem. Astley and Bain [32] provided a boundary element solution for wave propagation on low Mach number potential mean flows based on the Taylor transformation [31, 33]. In the same work, Astley and Bain [32] have reported an error analysis for the Taylor wave equation showing that the accuracy of the physical model depends on the uniform mean flow Mach number, the characteristic length scale of the mean flow and the wavelength. This approach has been used by a number of researchers in aeroacoustics [26, 33, 34, 70]. The fast multipole method has also been applied to boundary element solutions based on the Taylor transform [26].

Alternatively, Tinetti and Dunn [35] derived a generalized local Lorentz transformation to represent the effect of non-uniform mean flows on wave propagation. The term "generalized" means that it is applicable to any flow but in the limit of small mean flow velocity gradients. It is "local" because it considers the local Mach number of the mean flow in the Lorentz transform in lieu of the Mach number at infinity. Solutions based on fast algorithms and

the local Lorentz transform have also been presented [125]. However, this formulation does not seem to be more accurate than solutions based on the Taylor transform [26].

A similar method based on a variable transformation but limited to potential mean flows was used by Clancy [36] to predict shielding effects from wings in flight. In this case, a Prandtl-Glauert transform including non-uniform flow effects was considered. The formulation was extended to quasi-potential flows pushing the assumption behind using the underlying variable transformation for potential flows to the limit. Nonetheless, the assumption that the uniform flow velocity component modifies the effect of the corresponding non-uniform flow part was not clearly justified and the formulation has yet to be validated for complex geometries.

The terms including non-uniform flow effects in the linearised full potential wave equation can also be moved to the right-hand side and treated as sources. The Dual Reciprocity Method (DRM) [30, 126, 127] was then used to convert the volume integrals into boundary integrals. The dependence of the accuracy of the method on the interpolating functions used for the volume terms and the computational cost of DRM restrict the applicability of this approach [128, 129, 130]. Therefore, solving wave propagation problems in non-uniform flow using BE is still an open problem.

3.2.3 Non-uniqueness issue

Boundary element solutions to external noise propagation suffer from a non-uniqueness issue [91]. Consider that every boundary element solution to external sound propagation has a complementary solution in the corresponding interior domain. The problem in the interior domain is conventionally characterized by resonances which occur at well-defined frequencies. These frequencies are referred to as irregular frequencies since the coefficient matrix of the BE system of equations associated with the exterior problem becomes rank deficient. At these frequencies, BE solutions fail to give a unique solution since the matrix of the coefficient is singular. The matrix of the coefficient is ill-conditioned over a range of frequencies with a bandwidth that depends on the discretisation of the problem [131]. This occurs both for Dirichlet and Neumann boundary conditions [132, 133]. The Combined Helmholtz Integral Equation (CHIEF) [50] and the Burton–Miller formulation [51] are conventionally adopted to overcome this issue in quiescent media, producing a well-posed problem.

The CHIEF method provides a number of constraint equations to the conventional BE formulation based on the integral solution at the overdetermination points, namely the points lying in the inner domain to a boundary surface. A number of overdetermination points equal to the rank deficiency of the coefficient matrix is needed, assuming that the overdetermination points do not lie on either a nodal surface or at the intersection of two nodal surfaces [131]. If an overdetermination point lies on a nodal surface, the corresponding

constraint equation is not linearly independent and, therefore, it is not effective in restoring the rank of the coefficient matrix [131].

In practice, there is not a robust indication of how to select the location of the overdetermination points to ensure that the method is always effective [134]. Numerical experiments have shown that a minimum number of overdetermination points equal to 3% of the total number of nodal points is necessary as a rule of thumb for industrial applications [135]. This drawback can be mitigated using a CHIEF-block method as proposed by Wu and Syebert [136] who considered a variational formulation of the constraint equations integrated over an internal solid element. This approach was further enhanced by Lee and Wu [133] combining the integral formulation and its normal derivative at the boundary surface.

Nevertheless, an excessive number of collocation points also generates an ill-conditioned matrix of coefficients [135]. An increase in frequency implies an increase in the rank deficiency of this matrix [131] and, therefore, an increase in the number of overdetermination points. Hence, this method is not suitable for high-frequency short-wavelength problems [137]. At the overdetermination points, the combination of the boundary integral solution and its normal derivative to the boundary has been proposed by Cunefare *et al.* [138] to extend the frequency range of applicability of CHIEF. In this case, the equations have been combined for points external to the computational domain avoiding the complication of integrating the hyper-singular terms developed by the acoustic particle velocity equation. Alternatively, a practical approach is to prescribe internal impedance to create a discontinuity in the conditions along the boundary surface [135]. This method is suitable for indirect BE formulations [139].

An alternative approach to the issue of irregular frequencies is the Burton–Miller formulation. It is a more robust approach to work around the non-uniqueness issue for any frequencies but at the cost of a more complex formulation. It is based on a weighted summation of the boundary integral solution and its normal derivative to the boundary based on a complex coefficient. The combination of the integral equations provides a large imaginary part to the eigenfrequencies associated with the boundary element problem, moving them away from the real axis [140]. A well-judged choice of the coupling parameter is required in order to have accurate results at all frequencies [141]. The coupling parameter, α, must be purely imaginary [51]. For the convention $\mathrm{e}^{-\mathrm{i}\omega t}$, the value $-\mathrm{i}/k$ is required. Based on conventional boundary element problems with quiescent media, Amini [142] has shown that the value $1/k$ minimizes the condition number for a sphere at high frequencies. This value of the coupling parameter was also seen by Terai [143]. The parameter α is relevant to the coercivity of the BE matrix of coefficients, in that it determines the sign-defined nature of the matrix itself. This property depends on the sign of α. The linear system of equations for a Dirichlet problem is coercive for $\alpha = \mathrm{i}/k$ if the convention $\mathrm{e}^{\mathrm{i}\omega t}$ is used [141, 144].

The Burton–Miller formulation has also been tested with wave-based approaches [89]. It is also needed for time domain BE solutions [95, 41] because all of the frequencies in the

spectrum are excited. However, to implement the Burton–Miller formulation, a dedicated treatment of hyper-singular integrals developed by the boundary element kernel must be preformed. The most practical approach is the reduction of the singularity proposed by Hamdi [145], where the hyper-singular integrals are replaced by an equivalent integral formulation based only on weakly singular integrals [146], but at the cost of using a variational formulation of the integral solution.

For wave propagation in a mean flow, the non-uniqueness issue still affects BE solutions. Solutions to sound propagation in a mean flow are usually performed in the transformed domain [26, 29, 147], using either the Taylor [31, 32] or Lorentz [44, 75] transformation. Therefore, the non-uniqueness issue is worked around in the transformed domain in the same way as for the standard Helmholtz equation. On the other hand, Wu and Lee [40] have proposed an integral solution in the physical space for wave propagation in a uniform background flow, extending the CHIEF method to this formulation. Zhang and Wu [148] have presented a Burton–Miller approach based on the same integral equation, solving the non-uniqueness issue independently of Mach number.

3.3 Alternative methods

In this section, volume-based methods are first reviewed. Acoustic analogies and high-frequency formulations are then briefly discussed.

3.3.1 Volume-based methods

For linear wave propagation in non-uniform flows, high-order volume-based methods, such as Finite Element Methods (FEM) [20], Discontinuous Galerkin Methods (DGM) [149, 150] and Finite Difference (FD) schemes [22], are generally used. These methods are conventionally applied to solve Linearised Navier-Stokes Equations [60], Linearised Euler Equations [20, 62, 151], Acoustic Perturbation Equations [63] and the Linearised Potential Equation [23]. However, they suffer from dispersion error and pollution effects [152], limiting their application to relatively small domains where predictions for high-frequency sound propagation are required [83, 153, 154].

Linear models can be solved by using structured methods. For finite differences, a Dispersion-Relation-Preserving scheme (DRP) was proposed by Tam [22] to solve LEE. This formulation was applied in a number of works [82, 155] and a low-dispersion method to enhance its performance was also developed by Ashcroft and Zhang [156].

Unstructured methods, such as FEM and DGM, have also been developed. Frequency domain FEM [157] can generally be used to solve low frequency problems. At large frequency

the computational cost of this method is prohibitive when a direct solver is used. Enhanced schemes have been developed for this reason. The discontinuous Galerkin method is generally applied to time domain formulations [158], even though frequency domain formulations have also been developed [150, 159]. The main advantage of this method compared to standard FE schemes is flexibility in terms of the interpolation order. DGM solutions can use high-order interpolation which allows the problem of numerical dispersion to be controlled [160]. However, DGM suffers from low accuracy when curved geometries are considered [161].

Alternatively, high-order finite element methods, such as *p-FEM* [151, 162] are used for Helmholtz-type problems. *p-FEM* introduces high-order polynomial shape functions to reduce the dispersion error in the numerical solution [163, 23]. Adaptive schemes, i.e. when the order of interpolation is adjusted locally, have also been developed to extend the frequency of applicability of these methods [164]. Their convergence can be further enhanced by increasing spatial refinement. The so-called *hp-FEM* [165] significantly improves the convergence rate compared to standard *p-FEM* for Helmholtz-type problems.

Numerical methods, such as FEM and DGM, are conventionally developed using polynomial interpolating functions. However, physics-based interpolation, i.e. non-polynomial bases, has been proposed to reduce the numerical dispersion. This approach allows the grid refinement to be relaxed compared to polynomial-based methods, reducing the computational cost. The Partition of Unity Method (PUM) [166, 167] is based on using enrichment functions to match the physics of the problem while imposing inter-element continuity based on partition of unity functions. It has been applied to potential formulations [168] with mixed results. A wave-based DGM has also been applied to rotational flows [150], including plane wave expansions, to solve time-harmonic problems. Physics-based interpolation schemes, however, result in poor conditioning of the matrices of the coefficients compared to conventional methods based on polynomial interpolation [160]. Other advanced methods, such as the Ultra Weak Variational Formulation (UWVF) [169] and the Discontinuous Enrichment Method (DEM) [170], which have better conditioning, have also been proposed.

Although volume-based methods can solve complex physical models for wave propagation with mean flow, they remain computationally expensive when used to solve large-scale short-wavelength noise propagation problems, such as large-scale aircraft installation effects. A general rule of thumb tells us that a grid spacing with 5-10 nodes or grid points per wavelength is needed, corresponding to about 3000-27000 grid points per cubic metre for frequencies of 1 kHz.

3.3.2 Acoustic analogies

If the problem of noise propagation is separated from the area where sound is generated and where free-field wave propagation occurs, methods based on acoustic analogies can also

be used. Acoustic analogies are based on rearranging the Navier–Stokes equation in order to isolate a linear wave operator on the left-hand side, leaving the actual noise sources on the right-hand side. Noise sources can be predicted based on CFD approaches and an integral formulation can be used to propagate the sound to the far field. The Lighthill analogy [171] isolates a linear wave operator on the left-hand side and the effects of noise generation, convection and refraction are accounted for in the right-hand side term. Ffowcs Williams and Hawkings [37] extended the Lighthill analogy to account for solid surfaces in a mean flow [37] and Lilley's analogy [172] introduced the effect of a shear flow as a wave propagation effect [173]. A number of alternative analogies have been also developed but are left to more specific works. Alternatively, surface integral formulations, such as the Kirchhoff wave extrapolation [38], can also be used in free field to extrapolate the acoustic field but are limited to the linear flow region.

Acoustic analogies have been used to study trailing edge noise [174, 175] and to predict aeroengine jet noise [176, 177]. Reynolds Averaged Navier–Stokes (RANS) calculations for the characterisation of the noise sources have also been coupled with acoustic analogies [178, 179]. Although acoustic analogies allow the prediction of free-field noise propagation, it is not trivial to model scattering from complex geometries [119].

3.3.3 High-frequency methods

At high frequency, volume based methods become too expensive for large-scale noise propagation, while boundary element methods remain feasible, provided fast algorithms are applied. Ray theory can also be used to devise efficient solvers. A main ansatz for ray theory is that the acoustic wavelengths are much smaller than the characteristic scales of the propagating medium. Nonetheless, the theory assumes that the acoustic field propagates locally as a plane wave. The direction of propagation depends on the normal vector to the wavefront and the local mean flow velocity. This assumption allows an asymptotic expansion of the wave equation. The solutions based on ray theory depend on a product of plane waves and an infinite series of decreasing powers of the characteristic wavenumber [180]. The phase of the acoustic field is governed by the Eikonal equation while the asymptotic series expansion couples the phase and the amplitude. This method deals with inhomogeneous flows although the calculation of ray paths is greatly simplified for the homogeneous case.

For acoustic solutions at high frequency, the use of ray theory is a viable computational approach and numerical solutions can be obtained. However, some limitations exist. Wave diffraction in shadow zones is not directly represented. The Geometrical Theory of Diffraction (GTD) was proposed by Keller [181] to model diffraction by the addition of secondary sources or by the use of canonical schemes.

To deal with mean flows, Agarwal and Dowling [33] have used a Taylor transform to include low Mach number potential flow effects. For low Mach number mean flows, the use of

GTD allows scattering from complex geometry to be predicted, although solutions at low frequency are generally inaccurate. For high Mach numbers and non-potential flows the technique is not practical [182] because an ordinary differential equation must be solved with a significant increase of the computational cost. Even with these limitations, ray theory has been applied in aeroacoustics for free field [183] and boundary problems [184].

3.4 Prediction of aircraft acoustic installation effects

Aircraft installation effects can modify sound propagation around an aircraft and its far-field acoustic signatures. Noise shielding provided by the airframe may be used in future aircraft to meet the required reduction of community noise exposure levels. Robust, computationally efficient and accurate methods are needed to support the design process.

Predicting aircraft large-scale acoustic installation effects is still an open problem, which can only be partially addressed by current numerical techniques. The complexity of the problem is characterized by complex geometrical features and short-wavelength disturbances compared to the characteristic length scales of the domain. CAA methods are most likely to provide accurate solutions of these problems in the near future since they computationally outperform more conventional CFD methods. Sound scattering by a full-scale whole aircraft, however, poses a numerical challenge for current numerical techniques. A number of methods have been proposed for these applications. In this section, the numerical solutions for local acoustic scattering are reviewed and some examples of full aircraft installation effect predictions are referenced.

3.4.1 Assessment of local systems

If the size of the domain is not much larger than the characteristic acoustic wavelength, volume-based methods can be used to predict acoustic installation effects. A number of studies have been conducted based on different numerical techniques.

Stanescu *et al.* [149] solved the problem of forward fan noise scattering from a simplified system including the fuselage, the nacelle and the wing (see Fig. 3.2). DGM has been used to solve the non-linear Euler equations for a Helmholtz number, compared to the radius of the nacelle, equal to 8. It has been shown that the presence of the fuselage increases the Sound Pressure Level (SPL) on a horizontal plane symmetrically cutting the nacelle. Conversely, the wing reflects the sound creating a noise shadow below it. However, flow effects were not included in this study.

Redonnet *et al.* [185] investigated wing acoustic installation effects for nacelle exhaust noise. A hybrid method based on the solution of the Euler equations was used in the near field. A time harmonic boundary element method combined with a fast multipole approach was

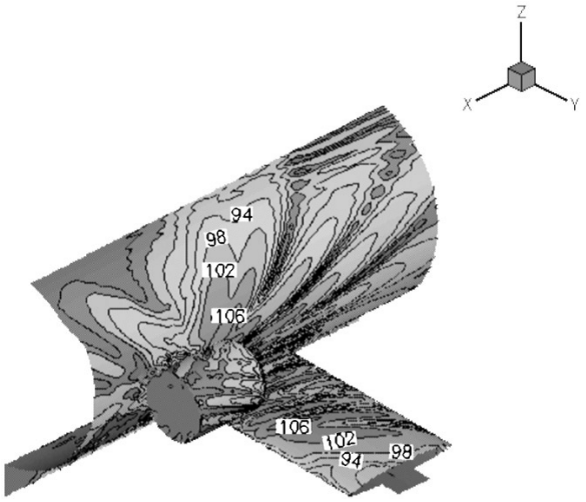

Figure 3.2: Prediction of aircraft acoustic installation effects showing contours of the sound pressure level around the nacelle and on the fuselage (extracted from Stanescu *et al.* [149]).

then used to solve the scattering by the wing. Wave extrapolation from the nacelle near field was performed using the Kirchhoff integral formulation. However, the boundary element problem was limited to a uniform flow.

A boundary element formulation for the prediction of the sound scattered by a finite wing in a low Mach number non-uniform flow was presented by Clancy and Rice [69]. A potential and homentropic flow was considered except for the wake shed at the trailing edge. Continuity of pressure and normal velocity across the vortex sheet, based on Myers's linearised acoustic boundary conditions, was imposed along the line of the wake. The wake was considered to be infinitesimally thin and the wavelength larger than the thickness of the wake. This assumption restricted the application of this method to low angle of attacks, low Mach numbers and large wavelengths. The scattering of a monopole point source on a planar wing was investigated and flow effects were included by introducing the Taylor transformation. The boundary element model for the acoustic problem also included an infinitely thin vortex sheet. Weak shielding effects due to the wake were predicted. A small increase in SPL was shown at the sideline angle because of refraction by the wake. Nevertheless, a robust validation of the proposed method was not provided.

In a later work, Clancy [36] improved his prediction by using a Prandtl-Glauert transformation including non-uniform flow effects. The effects of lift generation on wave propagation for an isolated wing were recovered. The main conclusion of this work was that, for low Mach numbers, potential non-uniform mean flow effects are dominant over both wake refraction effects and scattering of vorticity at the trailing edge. Although the method was benchmarked against more complex physical models, such as LEE, the results were provided comparing a flat plate to a NACA 0009 aerofoil and using an incident field generated by a monopole point source. However, the method was not benchmarked for more complex geometries and more general mean flow conditions.

Redonnet *et al.* [104] predicted acoustic shielding effects by an airfoil for a rear-mounted fuselage nacelle (RFN) configuration. They considered aft fan noise emitted by a coaxial engine. The mean flow was computed by using RANS. A methodology based on solving the full Euler equation was developed and an efficient grid relaxation approach to compute radiation and scattering was devised. The shear layer developed in the exhaust region was shown to deflect sound waves and to increase the shielding effect provided by the aerofoil. The results were also presented for the near field but at relatively low frequencies, i.e. $kR = 12$, where R is the outer radius of the secondary exhaust.

Papamoschou [186] investigated jet shielding effects for a under-wing installed engine. Jet noise sources were represented using superposition of wavepackets and monopole sources to model the noise generated by large and fine-scale turbulent structures respectively. It was found that large-scale structures mainly contribute to the far-field pressure signature at small angles from the engine axis, whereas the fine scales are less directional. Shielding effects due to the wing were predicted by using a boundary element approach based on a fast multipole method. Good agreement with experimental results was shown, however, the scattering from the wing did not include mean flow effects.

Mosson *et al.* [187] used a discontinuous Galerkin formulation applied to the LEE to solve the acoustic radiation in the near field of rear fan noise. A Ffowcs-Williams and Hawkings surface [37] was used to extrapolate the solution to the far field. The results were shown for a number of frequencies and compared to the experimental measurement obtained in the TURNEX project [83]. It was found that the mixing layer from the nacelle trailing edge can increase the shielding from the wing by up to 2 dB. The shear layer generated wave refraction and the hot jet blockage effect did not provide additional shielding. However, scattering effects from the fuselage were not included.

Heffernon *et al.* [70] have benchmarked boundary element solutions including mean flow effects using either Taylor or Lorentz transforms. Boundary element solutions based on either transformation were benchmarked against a LEE solution for the scattering by an airfoil from a point source. In the far field, Lorentz transformation provided better results compared to the Taylor transform, even though the Lorentz transform assumes a uniform flow in the entire domain. It was also confirmed that the effects of lift generation on noise propagation are small for angles of attack up to 8 degrees and frequencies of order 300 Hz, for low Mach numbers. Despite the insight given, a detailed analysis of the accuracy of the variable transformations at higher frequencies was not provided. Conclusions to this work were limited to slender bodies and simple geometries, such as an airfoil.

Recently, Croaker *at al.* [110] coupled a RANS method with a conventional BE solution to predict flow induced noise by a wall-mounted airfoil. A conventional BE solution based on Lighthill's formulation [171] was provided, where the source description was obtained from a statistical model of turbulence. The results were limited to an airfoil and did not include mean flow effects on wave propagation.

3.4.2 Whole aircraft solutions

The prediction of large-scale acoustic installation effects is computationally too expensive for volume-based methods. Boundary element approaches are preferred for this application. Solutions based on ray theory have also been proposed, showing less accuracy compared to boundary element solutions.

Agarwal and Dowling [33] have worked on the assessment of the shielding effect for the Silent Aircraft Concept design. In their work, a low Mach number mean flow was considered and the Taylor transformation [31] was applied to solve a boundary element problem. For frequencies consistent with fan noise emissions, the results indicated a reduction of 5 dB under the airframe, compared to a free-field situation, when the engine is mounted above the airframe. In a different work, Agarwal *et al.* [28] also used ray theory to solve the same problem. A Taylor transform was also used in this instance. A geometrical theory of diffraction was applied and the results compared to experimental data. A difference of up to 10 dB was shown, though the directivity pattern was well captured. To sum up, for the boundary element solutions, the results were not benchmarked and the results based on ray theory were clearly shown to be inaccurate.

Papamoschou and Mayoral [29] investigated jet noise shielding from a wing with uniform mean flow effects. In this case, a boundary element solution based on the Lorentz transform was used. Shielding effects due to the installation of the wing were shown to increase when a uniform mean flow was considered. On the other hand, using a Taylor transformation [32], Mayoral and Papamoschou [34] investigated the same problem including non-uniform mean flow effects. Although the effects of the mean flow on wave propagation and scattering were modelled, the accuracy of the proposed solution was not assessed and a critical comparison between the results was not provided.

Wolf and Lele [125] used a fast multipole approach applied to a boundary element method to investigate aircraft installation effects (see Fig. 3.3). They studied acoustic scattering from a under-wing mounted nacelle including mean flow effects. The solution was based on the Fast Scattering Code developed by Tinetti and Dunn [35], where a local Lorentz transform is implemented. More recently, the same authors solved sound scattering of a point monopole source by a full body aircraft [26]. In this case, low Mach number mean flow effects were included using either the Taylor [31] or the local Lorentz transform [35]. Despite the insight for simple geometries, where the Taylor transform outperformed the solution based on the local Lorentz transform [35], the results based on aircraft installation effects were not benchmarked.

Recently, Hu and co-authors [41, 188] developed a time domain boundary element approach to model wave propagation in a uniform flow. The formulation was presented in the physical space, i.e. without transformation. A Burton–Miller formulation, associated with a time domain propagation and a distribution algorithm, was used. The method was applied to

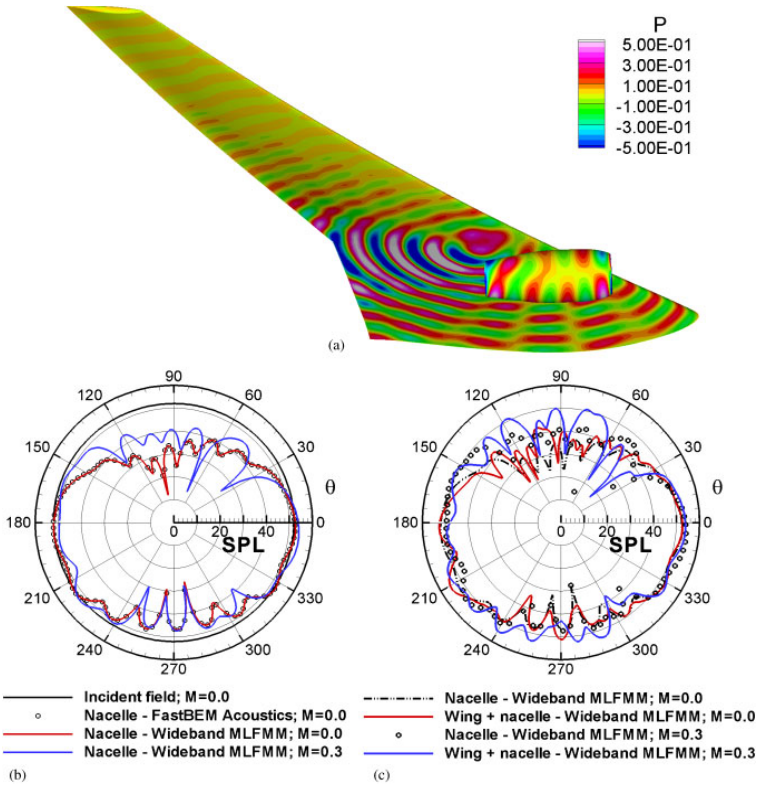

Figure 3.3: Prediction of aircraft acoustic installation effects showing contours of the pressure field on a wing and the far field directivity (extracted from Wolf and Lele [125]).

the scattering of a monopole point source from a full body aircraft (see Fig. 3.4). In a later work, Hu [123] improved the accuracy and efficiency of the method, which was benchmarked against experimental results for the scattering of a monopole source by a flat plate in a quiescent medium. The method was also applied to predict open rotor noise [188], however, non-uniform flow effects were not considered.

Casalino and Hazir [189] used the Lattice–Boltzmann Method (LBM) to predict installation effects for a conventional under-wing-mounted engine configuration using a full scale aircraft geometry. To predict far-field noise radiation, the Lattice-Boltzmann method was coupled with the Ffowcs Williams–Hawkings [37] analogy. The analogy was used to extract acoustic perturbation information from solid surfaces, such as the landing gear, and from permeable surfaces embedded within the engine. A breakdown of the individual isolated sources and the corresponding installation effects was provided, showing that installation effects significantly affect an individual aircraft noise source signature by up to 10 dB. However, the results for the full aircraft configuration were not benchmarked.

3.5 Discussion

The boundary element method is a viable numerical technique to solve large-scale short-wavelength noise propagation and scattering problems. A number of studies have shown

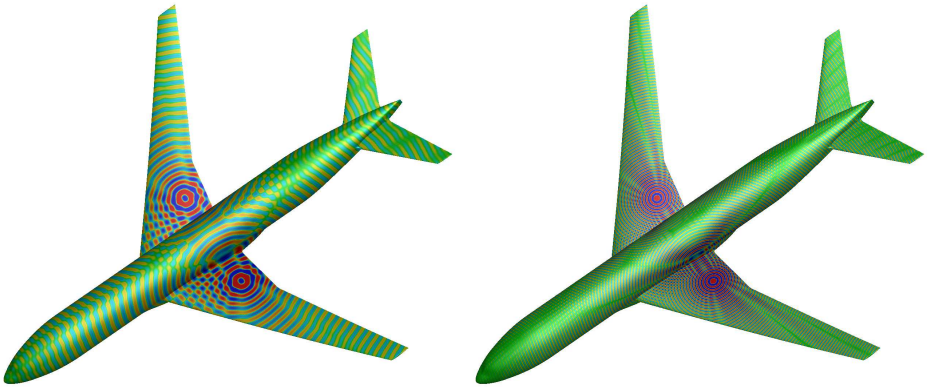

(a) kL =339.12 (b) kL =1017.36

Figure 3.4: Prediction of aircraft noise installation effects showing contours of the real part of the pressure field for a non-dimensional frequency kL (extracted from Hu [41]).

that it can be used for the prediction of aircraft installation effects when a uniform flow is assumed [27, 45]. Alternative methods, such as those based on ray theory, seem not to be sufficiently accurate [28, 36] and volume-based methods are computationally too expensive for these applications [23].

Although non-uniform flow effects on sound propagation are relevant to aircraft noise, there is no satisfactory procedure to include these effects in boundary element solutions in order to solve complex problems such as aircraft acoustic installation effects. Despite numerical examples were provided, a detailed analysis of the capability of BEM to represent non-uniform flow effects on wave propagation for these applications is not available in the literature. Nonetheless, current variable transformations, such as Taylor and Lorentz transforms, used for boundary element solutions have yet to be completely benchmarked.

From the literature, boundary element solutions based on the Lorentz transform achieve better accuracy compared to methods based on the Taylor transform, for simple geometries [70]. Nonetheless, solutions based on the local Lorentz transform [35] performed less well than those based on the Taylor transform [26] and, therefore, will not be considered further in this work. On the other hand, including non-uniform potential flow effects over a uniform moving media has been shown to be promising [36]. Therefore, in this work, we will focus on the combination of the physical models associated with the Taylor and Lorentz transforms in order to develop novel integral solutions to wave propagation in low Mach number potential mean flows.

Chapter 4

Integral Solutions

Contents

Currently, boundary integral solutions to wave propagation in a non-uniform mean flow are based on variable transformations that reduce complex Helmholtz-type equations with mean flow to the standard Helmholtz formulation with quiescent media [32, 35, 36]. This is achieved at the cost of introducing approximations to the dependence on the mean flow.

Nonetheless, the use of variable transforms generally requires the deformation of the physical space. The deformation of the computational domain complicates the formulation of boundary conditions and the implementation of transmission conditions for coupled problems [27, 42].

For uniform flows, the Lorentz transform is exact, in that it allows the uniform flow convected Helmholtz equation to be reduced to the standard Helmholtz formulation without approximation [29, 41]. Current industrial applications of BEM are based on the Lorentz transform to predict aircraft large-scale installation effects [45]. However, an integral formulation in the physical space that is consistent with the solution based on the Lorentz transform has been proposed by Wu and Lee [40] in the frequency domain, and by Hu [41] in the time domain. In these formulations, the geometry is not modified in order to solve the sound propagation problem.

In this chapter, boundary integral solutions to wave propagation in a non-uniform mean flow are proposed based on the weakly non-uniform flow formulation that was presented in Sec. 2.5.2. The solutions are devised for time harmonic problems. Contrary to previous approaches, in Sec. 4.3, an integral solution is presented in the physical space, i.e. without transformations. The formulation is provided to enhance the results based on the physical model associated with the Taylor wave equation. In Sec. 4.4, a free field Green's function is determined for a subsonic weakly non-uniform flow as a kernel for the integral solution in the physical space. It is based on a combination of the physical models associated with the Taylor and Lorentz transformations [32, 44]. In Sec. 4.5, an error analysis of the corresponding physical model is presented and the dependence of the error on mean flow Mach number and frequency is discussed. In Sec. 4.6, an approximation consistent with the Taylor wave equation [32] is presented as a subset of the results obtained for the weakly non-uniform formulation. While conventionally it has been provided in the transformed space, an integral solution to the Taylor equation is also presented in the physical space.

In Sec. 4.7, an alternative integral solution to the weakly non-uniform flow equation is presented in a transformed Taylor–Lorentz space. In the transformed space, the weakly non-uniform formulation is reduced to the Helmholtz problem with quiescent media for which a boundary integral formulation is derived.

In Sec. 4.8, a wave extrapolation approach to solve scattering problems with mean flow is presented either in the physical or in the transformed space. The solution allows a high fidelity source model to be represented by a radiating control surface containing the sound sources. The sound field can then be projected from any control surface along any other boundary to solve a scattering problem. This approach aims to devise boundary element solutions based on more complex sound sources.

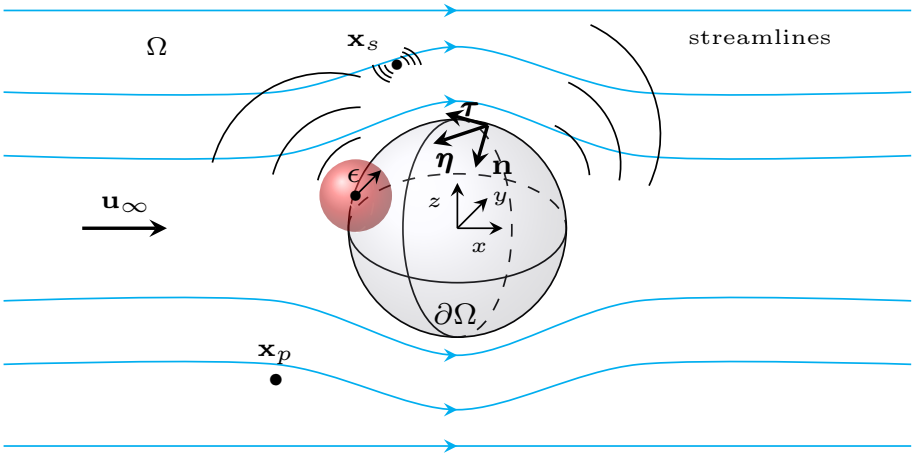

Figure 4.1: Sketch of the scattering of a sound source, $\mathbf{x}_s$, by a body in a non-uniform flow, showing the streamlines in the domain.

.

4.1 Physical model

External noise radiation and scattering of a sound source distribution is the problem to be solved in a three-dimensional domain, Ω, with a non-uniform mean flow (see Fig. 4.1). Consider the weakly non-uniform potential flow wave equation, Eq. (2.35), and a generic source distribution $\hat{q}(\mathbf{x}, t)$:

$$\frac{1}{c_\infty^2}\frac{\partial^2\hat{\phi}}{\partial t^2} + \frac{2}{c_\infty^2}\mathbf{u}_0 \cdot \boldsymbol{\nabla}\frac{\partial\hat{\phi}}{\partial t} - \boldsymbol{\nabla}^2\hat{\phi} + \frac{u_\infty^2}{c_\infty^2}\frac{\partial^2\hat{\phi}}{\partial x^2} = \hat{q}, \tag{4.1}$$

where the uniform mean flow $\mathbf{u}_\infty$ is assumed in the direction of the x-axis. Since the problem is solved in an unbounded domain, the Sommerfeld radiation condition with mean flow has to be satisfied for $\|\mathbf{x}\| \to \infty$ (see Eq. (2.40)). On other boundary surfaces, $\partial\Omega$, the condition can be assigned appropriately with the problem to solve.

We consider a harmonic solution to Eq. (4.1) using the convention $\mathrm{e}^{\mathrm{i}\omega t}$, where ω is the angular frequency and $\hat{q}(\mathbf{x}, t) = q(\mathbf{x})\mathrm{e}^{\mathrm{i}\omega t}$. Hence, Eq. (4.1) can be rewritten as

$$k^2\phi - 2\mathrm{i}k(\mathbf{M}_0 \cdot \boldsymbol{\nabla}\phi) + \boldsymbol{\nabla}^2\phi - M_\infty^2\frac{\partial^2\phi}{\partial x^2} = g, \tag{4.2}$$

where $\phi(\mathbf{x})$ and $g(\mathbf{x}) = -q(\mathbf{x})$ are complex amplitudes, $k = \omega/c_\infty$, $\mathbf{M}_\infty = (M_\infty, 0, 0)$ and $\mathbf{M}_0 = \mathbf{u}_0/c_\infty = (M_{0,x}, M_{0,y}, M_{0,z})$. In all that follows, Eq. (4.2) is referred to as the *weakly non-uniform potential flow Helmholtz equation* or simply *weakly non-uniform flow equation*. In Eq. (4.1), we have assumed that $M_\infty \ll 1$ and $M_0' \ll M_\infty$, where $\mathbf{M}_0'(\mathbf{x}) = \mathbf{u}_0'(\mathbf{x})/c_\infty$ and $M_0' = \|\mathbf{M}_0'\|$.

While the formulation has been provided so far in terms of acoustic velocity potential, ϕ, the acoustic pressure, p', can be recovered from ϕ via the linearised momentum equation as

$$p'(\omega) = -\rho_0(\mathrm{i}\omega\phi + \mathbf{u}_0 \cdot \boldsymbol{\nabla}\phi), \tag{4.3}$$

where the dependence on $\mathbf{x}$ has been omitted to simplify the notation. The dependence on the angular frequency, ω, is retained to denote the time harmonic solution.

The weakly non-uniform potential flow Helmholtz equation will be solved in either the physical or transformed Taylor–Lorentz space. A Green's function for these solutions will be also recovered. In the following section, we derive the adjoint operator to the weakly non-uniform flow equation.

4.2 Adjoint operator

The adjoint operator to Eq. (4.2) is presented in this section. First, let us define the differential operator associated with Eq. (4.2) as $\mathcal{P}$. The adjoint operator, $\mathcal{P}_{adj}$, can be expressed as

$$\langle \phi, \mathcal{P}_{adj}\psi \rangle = \langle \mathcal{P}\phi, \psi \rangle, \tag{4.4}$$

where ψ is a complex amplitude, $\langle \cdot, \cdot \rangle$ denotes the inner product between complex functions, i.e.

$$\langle \mathcal{P}\phi, \psi \rangle = \int_\Omega \mathcal{P}(\phi)\psi^* dV, \tag{4.5}$$

Ω is the physical domain (see Fig. 4.1) and "*" denotes the complex conjugate.

The right-hand side of Eq. (4.4) can be rewritten:

$$\langle \mathcal{P}\phi, \psi \rangle = \int_\Omega \psi^* \left(k^2\phi - 2\mathrm{i}k\mathbf{M}_0 \cdot \boldsymbol{\nabla}\phi + \boldsymbol{\nabla}^2\phi - M_\infty^2 \frac{\partial^2 \phi}{\partial x^2} \right) dV. \tag{4.6}$$

Integrating the right-hand side of Eq. (4.6) twice by parts gives

$$\begin{aligned} \langle \mathcal{P}\phi, \psi \rangle = &\int_\Omega \phi \left(k^2\psi^* + 2\mathrm{i}k\boldsymbol{\nabla} \cdot (\mathbf{M}_0\psi^*) + \boldsymbol{\nabla}^2\psi^* - M_\infty^2 \frac{\partial \psi^*}{\partial x^2} \right) dV \\ &+ \int_{\partial\Omega} \left(\frac{\partial \phi}{\partial n}\psi^* - \frac{\partial \psi^*}{\partial n}\phi - 2\mathrm{i}k\psi^*\phi\mathbf{M}_0 \cdot \mathbf{n} - M_\infty^2 n_x \left[\frac{\partial \phi}{\partial x}\psi^* - \frac{\partial \psi^*}{\partial x}\phi \right] \right) dS, \end{aligned} \tag{4.7}$$

where $\mathbf{n}$ is the normal unit vector to $\partial\Omega$ directed away from the domain Ω (see Fig. 4.1).

The integrand on the boundary, $\partial\Omega$, has to satisfy the boundary conditions. In other words, it vanishes if ϕ and ψ satisfy these conditions. This is verified for homogeneous boundary conditions, either for Dirichlet or Neumann problems, in the case of an impermeable stationary surface, where the generalized normal derivative in Eq. (2.59) vanishes. Nonetheless,

as will be shown in Sec. 4.6, the integral on the boundary can be reduced to the standard Helmholtz integral operator with quiescent media in a Taylor–Lorentz space. This guarantees that the above boundary integral vanishes for $\|\mathbf{x}\| \to \infty$, if ϕ and ψ satisfy the Sommerfeld radiation condition in the transformed space. Hence, Eq. (4.7) can be reduced to

$$\langle \mathcal{P}\phi, \psi \rangle = \int_\Omega \phi \left(k^2\psi^* + 2\mathrm{i}k\boldsymbol{\nabla} \cdot (\mathbf{M}_0\psi^*) + \boldsymbol{\nabla}^2\psi^* - M_\infty^2 \frac{\partial^2 \psi^*}{\partial x^2} \right) dV. \tag{4.8}$$

The above equation is then simplified based on the dependence on the mean flow Mach number. Following Astley and Bain [32], note that

$$\boldsymbol{\nabla} \cdot \mathbf{M}_0 = \frac{\frac{1}{2}\mathbf{M}_0 \cdot \boldsymbol{\nabla}(\mathbf{M}_0 \cdot \mathbf{M}_0)}{1 - \frac{\gamma-1}{2}(M_0^2 - M_\infty^2)}, \tag{4.9}$$

where $\boldsymbol{\nabla} \cdot \mathbf{M}_0$ is of the same order as $M_0'^3$. Higher order terms than M_∞^2 have already been neglected in the weakly non-uniform Helmholtz equation based on the assumption that $M_\infty \ll 1$ and $M_0' \ll M_\infty$. Therefore, we neglect the term $\boldsymbol{\nabla} \cdot \mathbf{M}_0$ in Eq. (4.8) to give

$$\langle \mathcal{P}\phi, \psi \rangle = \int_\Omega \phi \left(k^2\psi^* + 2\mathrm{i}k\mathbf{M}_0 \cdot \boldsymbol{\nabla}\psi^* + \boldsymbol{\nabla}^2\psi^* - M_\infty^2 \frac{\partial^2 \psi^*}{\partial x^2} \right) dV. \tag{4.10}$$

The right-hand side in Eq. (4.10) is nothing but $\langle \phi, \mathcal{P}_{adj}\psi \rangle$. The adjoint operator $\mathcal{P}_{adj}$ is consistent with $\mathcal{P}$ if the mean flow is reversed. In other words, $\mathcal{P}$ is invariant to time reversal if the direction of the mean flow is reversed at the same time [65]. We then infer that the principle of reciprocity can be applied to the Green's function for Eq. (4.2), which is derived in Sec. 4.4.

4.3 Boundary integral formulation

In this section, an integral solution to the weakly non-uniform potential flow Helmholtz equation is derived. The formulation is developed for the homogeneous Eq. (4.2) in a reference frame connected to the undisturbed air. Following the approach proposed by Wu and Lee [40] for a uniform flow, we use the Green's function of the reverse flow operator, i.e.

$$k^2 G + 2\mathrm{i}k\mathbf{M}_0 \cdot \boldsymbol{\nabla} G + \boldsymbol{\nabla}^2 G - M_\infty^2 \frac{\partial^2 G}{\partial x^2} = -\delta(\mathbf{x}_p - \mathbf{x}), \tag{4.11}$$

where $\mathbf{x}$ and $\mathbf{x}_p$ are respectively the source and the observer position and $\delta(\mathbf{x}_p - \mathbf{x})$ denotes the Dirac delta function. It is referred to as the reverse flow operator because we consider $-\mathbf{M}_0$ in lieu of $\mathbf{M}_0$. The solution $G = G(\mathbf{x}_p, \mathbf{x})$ represents the effect of a point source of unit magnitude within a non-uniform mean flow. The Green's function, G, is derived in Sec. 4.4 and is presented for a free-field problem satisfying the Sommerfeld radiation condition.

4.3.1 Integral operator

First, a boundary integral solution to the weakly non-uniform flow Helmholtz equation is presented for an observer $\mathbf{x}_p$ in the domain Ω. We multiply Eq. (4.11) for ϕ and the homogeneous Eq. (4.2) for G. Then we subtract these equations and integrate their difference over the domain Ω (see Fig. 4.1) to give

$$\begin{aligned}&\int_\Omega \phi\left(k^2G + 2\mathrm{i}k\mathbf{M}_0\cdot\boldsymbol{\nabla}G + \boldsymbol{\nabla}^2G - M_\infty^2\frac{\partial^2 G}{\partial x^2}\right)dV(\mathbf{x})\\ &-\int_\Omega G\left(k^2\phi - 2\mathrm{i}k\mathbf{M}_0\cdot\boldsymbol{\nabla}\phi + \boldsymbol{\nabla}^2\phi - M_\infty^2\frac{\partial^2 \phi}{\partial x^2}\right)dV(\mathbf{x}) = -\int_\Omega \phi\delta(\mathbf{x}_p-\mathbf{x})dV(\mathbf{x}).\end{aligned} \tag{4.12}$$

The divergence theorem is applied to the left-hand side of the above equation to recover an integral over the boundary surface $\partial\Omega$. Consistent with the hypotheses made to derive Eq. (4.2), higher order terms than M_0' will be neglected. Consider the term depending on $\mathbf{M}_0$ in the above equation,

$$\int_\Omega \left(2\mathrm{i}k\phi\mathbf{M}_0\cdot\boldsymbol{\nabla}G + 2\mathrm{i}kG\mathbf{M}_0\cdot\boldsymbol{\nabla}\phi\right)dV(\mathbf{x}) = \int_\Omega 2\mathrm{i}k\left[\boldsymbol{\nabla}\cdot(\mathbf{M}_0G\phi) - G\phi(\boldsymbol{\nabla}\cdot\mathbf{M}_0)\right]dV(\mathbf{x}). \tag{4.13}$$

Based on Eq. (4.9), $\boldsymbol{\nabla}\cdot\mathbf{M}_0$ is a term of order $M_0'^3$. Therefore, it can be neglected to give

$$\int_\Omega 2\mathrm{i}k\left[\boldsymbol{\nabla}\cdot(\mathbf{M}_0G\phi) - G\phi(\boldsymbol{\nabla}\cdot\mathbf{M}_0)\right]dV(\mathbf{x}) \simeq \int_{\partial\Omega} 2\mathrm{i}k\mathbf{M}_0\cdot\mathbf{n}G\phi dS(\mathbf{x}), \tag{4.14}$$

where $\mathbf{n}$ is, again, the normal unit vector to $\partial\Omega$. Note that if the flow is incompressible, i.e. $\boldsymbol{\nabla}\cdot\mathbf{M}_0 = 0$, the above equation is exact.

Hence, Eq. (4.12) is rewritten as

$$\phi(\mathbf{x}_p) = \int_{\partial\Omega}\left[G\frac{\partial\phi}{\partial n} - \phi\frac{\partial G}{\partial n} - 2\mathrm{i}k\mathbf{M}_0\cdot\mathbf{n}G\phi - M_\infty^2\left(G\frac{\partial\phi}{\partial x} - \phi\frac{\partial G}{\partial x}\right)n_x\right]dS(\mathbf{x}), \tag{4.15}$$

where n_x is the component of the normal vector in the direction of the mean flow and $\phi = \phi(\mathbf{x})$, unless otherwise stated. As shown by Wu and Lee [40] for a uniform flow, the contribution of the above boundary integral at infinity is zero. In other words, the above equation satisfies the Sommerfeld radiation condition, if ϕ and G separately satisfy the same condition. Note that, for a uniform flow, namely $\mathbf{M}_0 = \mathbf{M}_\infty$, Eq. (4.15) reduces to the formulation derived by Wu and Lee [40]. This differs from the solution of Wu and Lee [40] for a uniform flow in which $\mathbf{M}_0$ is constant in that Eq. (4.15) holds for a non-uniform Mach number $\mathbf{M}_0(\mathbf{x})$, provided that the terms of order $M_0'^2$ and $M_0'M_\infty$ can be ignored. It models refraction effects of sound waves travelling in a non-uniform potential flow.

However, Eq. (4.15) is valid for any point $\mathbf{x}_p$ within the domain Ω, while it is singular if the observer lies on the boundary surface $\partial\Omega$. In the following section, we find a solution for $\mathbf{x}_p \in \partial\Omega$.

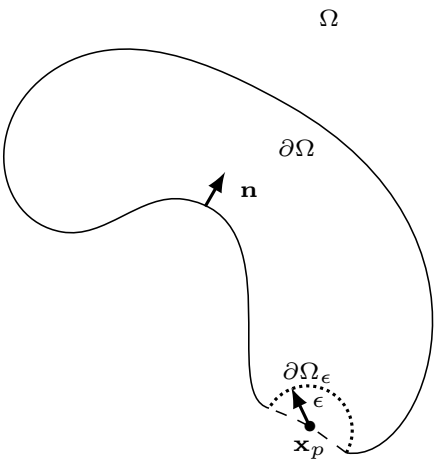

Figure 4.2: Sketch of the problem of singularity on the boundary surface, showing the hemisphere of radius ϵ subtracted from the solution using the Cauchy principal value integral.

.

4.3.2 Singularity on the boundary

Although Eq. (4.15) is singular for $\mathbf{x}_p \in \partial\Omega$, it is solvable using the Cauchy principal value integral. An extension of Eq. (4.15) to the boundary surface can be recovered based on a limit approach [40, 43]. For an exterior wave propagation problem, the domain Ω is modified by subtracting a hemisphere of radius ϵ from the complementary domain (see Figs. 4.1 and 4.2), namely the region outside Ω:

$$\phi(\mathbf{x}_p) = \int_{\partial\Omega+\partial\Omega_\epsilon} \left[G\frac{\partial\phi}{\partial n} - \phi\frac{\partial G}{\partial n} - 2\mathrm{i}k\mathbf{M}_0\cdot\mathbf{n}G\phi - M_\infty^2\left(G\frac{\partial\phi}{\partial x} - \phi\frac{\partial G}{\partial x}\right)n_x \right] dS(\mathbf{x}). \quad (4.16)$$

In the limit $\epsilon \to 0$, the surface of the hemisphere tends to zero as ϵ^2. Since G will be shown to vary as $1/\epsilon$, the contribution of the terms including G to the integral over the infinitesimal surface is zero. Hence, Eq. (4.16) gives

$$\begin{aligned}\phi(\mathbf{x}_p) = &\int_{\partial\Omega} \left[G\frac{\partial\phi}{\partial n} - \phi\frac{\partial G}{\partial n} - 2\mathrm{i}k\mathbf{M}_0\cdot\mathbf{n}G\phi - M_\infty^2\left(G\frac{\partial\phi}{\partial x} - \phi\frac{\partial G}{\partial x}\right)n_x \right] dS(\mathbf{x}) \\ &- \phi(\mathbf{x}_p)\int_{\partial\Omega_\epsilon}\left(\frac{\partial G}{\partial n} - M_\infty^2\frac{\partial G}{\partial x}n_x\right)dS(\mathbf{x}).\end{aligned} \quad (4.17)$$

Let us consider the limit of the weakly non-uniform flow equation for an infinitesimal hemisphere. For $\epsilon \to 0$, the Green's function for the reverse flow operator, Eq. (4.11), tends to the Green's function for the static operator $G_0(\mathbf{x}_p, \mathbf{x})$, which satisfies

$$\boldsymbol{\nabla}^2 G_0 - M_\infty^2\frac{\partial^2 G_0}{\partial x^2} = -\delta(\mathbf{x}_p - \mathbf{x}). \quad (4.18)$$

The operator in the above equation is self-adjoint. The solution to Eq. (4.18) for a free-field problem is $G_0 = 1/(4\pi R_M)$ where $R_M = \sqrt{(x_p - x)^2 + \beta_\infty^2[(y_p - y)^2 + (z_p - z)^2]}$, namely the actual distance of the observer, depends on the mean flow, $\beta_\infty = \sqrt{1 - M_\infty^2}$. The integral solution to the above equation for points outside the domain Ω is [40]

$$\int_{\partial\Omega+\partial\Omega_\epsilon} \left[G_0 \frac{\partial \phi}{\partial n} - \phi \frac{\partial G_0}{\partial n} - M_\infty^2 \left(G_0 \frac{\partial \phi}{\partial x} - \phi \frac{\partial G_0}{\partial x} \right) n_x \right] dS(\mathbf{x}) = 0. \tag{4.19}$$

The integral on the hemisphere of radius ϵ can then be rewritten on the boundary surface, $\partial\Omega$, as

$$\int_{\partial\Omega_\epsilon} \left(\frac{\partial G_0}{\partial n} - M_\infty^2 \frac{\partial G_0}{\partial x} n_x \right) dS(\mathbf{x}) = - \int_{\partial\Omega} \left(\frac{\partial G_0}{\partial n} - M_\infty^2 \frac{\partial G_0}{\partial x} n_x \right) dS(\mathbf{x}). \tag{4.20}$$

Therefore, applying Eq. (4.20) to Eq. (4.17) gives

$$\hat{C}(\mathbf{x}_p)\phi(\mathbf{x}_p) = \int_{\partial\Omega} \left[G \frac{\partial \phi}{\partial n} - \phi \frac{\partial G}{\partial n} - 2ik\mathbf{M}_0 \cdot \mathbf{n} G\phi - M_\infty^2 \left(G \frac{\partial \phi}{\partial x} - \phi \frac{\partial G}{\partial x} \right) n_x \right] dS(\mathbf{x}), \tag{4.21}$$

where

$$\hat{C}(\mathbf{x}_p) = \begin{cases} 1 & \mathbf{x}_p \in \Omega \\ 0 & \mathbf{x}_p \notin \Omega \cup \partial\Omega \\ 1 - \int_{\partial\Omega} \left(\frac{\partial G_0}{\partial n} - M_\infty^2 \frac{\partial G_0}{\partial x} n_x \right) dS(\mathbf{x}) & \mathbf{x}_p \in \partial\Omega \end{cases}, \tag{4.22}$$

where the value $\hat{C}(\mathbf{x}_p) = 0$ for $\mathbf{x}_p \notin \Omega \cup \partial\Omega$ can be derived based on the Taylor–Lorentz transform. This derivation is performed in Sec. 5.2.5.1 as part of a different problem. Nonetheless, the integral in the definition of $\hat{C}(\mathbf{x}_p)$, for $\mathbf{x}_p \in \partial\Omega$, is non-singular and, therefore, integrable in a conventional sense [40].

While Eq. (4.21) has been provided for the homogeneous weakly non-uniform flow equation, the incident field generated by a distribution of sound sources in Ω can be recovered by convolving the Green's function, G, with the source model. Including a sound source, such as in the right-hand side of Equation (4.2), gives an incident field

$$\phi_{inc}(\mathbf{x}_p) = \int_\Omega G(\mathbf{x}_p, \mathbf{x}) g(\mathbf{x}) dV(\mathbf{x}), \tag{4.23}$$

such that

$$\hat{C}(\mathbf{x}_p)\phi(\mathbf{x}_p) = \int_{\partial\Omega} \left[G \frac{\partial \phi}{\partial n} - \phi \frac{\partial G}{\partial n} - 2ik\mathbf{M}_0 \cdot \mathbf{n} G\phi - M_\infty^2 \left(G \frac{\partial \phi}{\partial x} - \phi \frac{\partial G}{\partial x} \right) n_x \right] dS(\mathbf{x}) + \phi_{inc}(\mathbf{x}_p). \tag{4.24}$$

In summary, Eq. (4.24) provides a boundary integral formulation for wave propagation in a weakly non-uniform potential mean flow. It accounts for first order non-uniform mean flow effects on wave propagation based on the assumption that $M_\infty \ll 1$ and $M_0' \ll M_\infty$, meaning that $M_0'^2 \ll M_\infty^2$ and $M_0' M_\infty \ll M_\infty^2$. The accuracy of the formulation depends on the ratio between the non-uniform component of the mean flow M_0' and the uniform flow component M_∞. Nonetheless, it is exact for wave propagation in a uniform flow and the

integral solution to the Helmholtz problem with quiescent media is retrieved for $M_0 \to 0$. However, the Green's function, G, has to be derived to solve Eq. (4.24). It is presented in the following section based on a Taylor–Lorentz transform.

4.4 Green's function for weakly non-uniform mean flows

The Green's function for the operator in Eq. (4.11) is derived in this section using a variable transformation. To determine G, a Lorentz transformation [75] is applied following a Taylor transformation [31] of the fundamental reverse flow problem, i.e.

$$\frac{\partial^2 \hat{G}}{\partial t^2} - 2\mathbf{u}_0 \cdot \boldsymbol{\nabla} \frac{\partial \hat{G}}{\partial t} - c_\infty^2 \boldsymbol{\nabla}^2 \hat{G} + u_\infty^2 \frac{\partial^2 \hat{G}}{\partial x^2} = c_\infty^2 \delta(\mathbf{x}, t), \tag{4.25}$$

where we assume that $\hat{G}(\mathbf{x}, t) = G(\mathbf{x})\mathrm{e}^{\mathrm{i}\omega t}$. In the Taylor–Lorentz space, Eq. (4.25) can be reduced to the standard Helmholtz problem. Since the fundamental solution to the Helmholtz operator is well-known [43], the Green's function in the physical space, G, can be finally recovered by applying the inverse Taylor–Lorentz transformation (see Eq. (2.56)) to the Green's function in the transformed domain.

4.4.1 Transformation of the wave operator

First, a Taylor transformation is applied including the non-uniform flow component, $\mathbf{u}_0'$, to Eq. (4.25). The independent variables are transformed as

$$X = x, \quad Y = y, \quad Z = z, \quad T = t - \frac{\Phi_0'(\mathbf{x})}{c_\infty^2}, \tag{4.26}$$

where $\Phi_0'(\mathbf{x})$ is the mean flow velocity potential corresponding to the non-uniform flow part $\mathbf{u}_0'$, $\mathbf{X} = (X, Y, Z)$ and T denote the Taylor space-time, while (x, y, z) and t denote the physical space-time. The differential operators in the Taylor space are

$$\frac{\partial}{\partial t} = \frac{\partial}{\partial T}, \quad \boldsymbol{\nabla} = \boldsymbol{\nabla}_X - \frac{\mathbf{M}_0'}{c_\infty} \frac{\partial}{\partial T}, \tag{4.27}$$

where $\mathbf{M}_0' = \mathbf{u}_0'/c_\infty$. Based on the above equation, Eq. (4.25) can be rewritten in the Taylor space:

$$\begin{aligned} &\frac{\partial^2 \bar{G}}{\partial T^2} - c_\infty^2 \left[\boldsymbol{\nabla}_X^2 \bar{G} - \left(\boldsymbol{\nabla}_X \cdot \frac{\mathbf{M}_0'}{c_\infty} \right) \frac{\partial \bar{G}}{\partial T} - \frac{\|\mathbf{M}_0'\|^2}{c_\infty^2} \frac{\partial^2 \bar{G}}{\partial T^2} \right] - 2c_\infty \mathbf{M}_\infty \cdot \frac{\partial}{\partial T} \left[\boldsymbol{\nabla}_X \bar{G} - \frac{\mathbf{M}_0'}{c_\infty} \frac{\partial \bar{G}}{\partial T} \right] \\ &+ c_\infty^2 M_\infty^2 \left(\frac{\partial^2 \bar{G}}{\partial X^2} - 2 \frac{M_{0,x}'}{c_\infty} \frac{\partial^2 \bar{G}}{\partial X \partial T} + \frac{M_{0,x}'^2}{c_\infty^2} \frac{\partial^2 \bar{G}}{\partial T^2} - \frac{1}{c_\infty} \frac{\partial M_{0,x}'}{\partial X} \frac{\partial \bar{G}}{\partial T} \right) = c_\infty^2 \delta(\mathbf{X}, T), \end{aligned} \tag{4.28}$$

where the superscript "$^-$" denotes the dependent variables in the transformed Taylor space. As seen in the above equation, the Taylor transform builds the effect of the linear terms in $\mathbf{M}_0' = (M_{0,x}', M_{0,y}', M_{0,z}')$ into the standard wave operator and introduces additional terms depending on the mean flow non-uniformity $\mathbf{M}_0'$.

In the above equation, consider that $M_\infty M_0' \ll M_\infty^2$ and $\nabla_X \cdot \mathbf{M}_0'$ is of order $M_0'^3$ (see Eq. (4.9)). Hence, we neglect higher order terms than M_0', consistently with Eq. (4.1), to give

$$\frac{\partial^2 \bar{G}}{\partial T^2} - 2c_\infty \mathbf{M}_\infty \cdot \boldsymbol{\nabla}_X \frac{\partial \bar{G}}{\partial T} - c_\infty^2 \boldsymbol{\nabla}_X^2 \bar{G} + c_\infty^2 M_\infty^2 \frac{\partial^2 \bar{G}}{\partial X^2} = c_\infty^2 \delta(\mathbf{X}, T). \tag{4.29}$$

Equation (4.29) is nothing but the convected wave equation in the Taylor space for uniform flow with M_∞.

Now, we assume a uniform mean flow aligned with the x-axis but opposite to the actual direction of the mean flow $\mathbf{M}_\infty$ and apply a Lorentz transformation [44, 75] to the above equation. The independent variables are transformed as

$$\tilde{X} = \frac{X}{\beta_\infty}, \quad \tilde{Y} = Y, \quad \tilde{Z} = Z, \quad \tilde{T} = \beta_\infty T - \frac{M_\infty X}{c_\infty \beta_\infty} \tag{4.30}$$

where $\tilde{\mathbf{X}} = (\tilde{X}, \tilde{Y}, \tilde{Z})$ and $\tilde{T}$ denote the Taylor–Lorentz space-time and $\beta_\infty = \sqrt{1 - M_\infty^2}$. The differential operators in the Lorenz space are

$$\frac{\partial}{\partial X} = \frac{1}{\beta_\infty}\frac{\partial}{\partial \tilde{X}} - \frac{M_\infty}{\beta_\infty c_\infty}\frac{\partial}{\partial \tilde{T}}, \qquad \frac{\partial}{\partial Y} = \frac{\partial}{\partial \tilde{Y}}, \qquad \frac{\partial}{\partial Z} = \frac{\partial}{\partial \tilde{Z}}, \qquad \frac{\partial}{\partial T} = \beta_\infty \frac{\partial}{\partial \tilde{T}}. \tag{4.31}$$

Hence, we use Eq. (4.31) in Eq. (4.29) to give

$$\frac{\partial^2 \hat{\tilde{G}}}{\partial \tilde{T}^2} - c_\infty^2 \boldsymbol{\nabla}_{\tilde{X}}^2 \hat{\tilde{G}} = c_\infty^2 \delta(\tilde{\mathbf{X}}, \tilde{T}), \tag{4.32}$$

where $\hat{\tilde{G}}$ is the Green's function in the Taylor–Lorentz space for the standard wave equation with quiescent media [91] and $\boldsymbol{\nabla}_{\tilde{X}}^2$ is the Laplacian in the transformed space. The left-hand side of the above equation is independent of the mean flow. In Sec. 4.4.2, we rewrite the above equation for a time harmonic problem and recover the value of the Green's function in the physical space by applying the inverse Taylor–Lorentz transform.

4.4.2 Recovering the physical space formulation

In this section, we recover the value of the Green's function in the physical space. Since a steady state problem is considered, Eq. (4.32) is rewritten in the frequency domain. The Lorentz transformation introduces a time contraction depending on the factor β_∞ and a delay which varies with M_∞. A time contraction represents a frequency dilation in the Fourier domain while a time delay corresponds to a phase shift. In particular, the angular frequency in the Taylor–Lorentz space is $\tilde{\omega} = \omega/\beta_\infty$. On the other hand, the Taylor

transformation introduces only a phase shift. Equation (4.32) can then be rewritten in the frequency domain as

$$\tilde{k}^2\tilde{G} + \boldsymbol{\nabla}^2_{\tilde{X}}\tilde{G} = -\delta(\tilde{\mathbf{X}}), \tag{4.33}$$

where $\hat{\tilde{G}}(\tilde{\mathbf{X}}, T) = \tilde{G}(\tilde{\mathbf{X}})\mathrm{e}^{\mathrm{i}\tilde{\omega}\tilde{T}}$, $\tilde{k} = \tilde{\omega}/c_\infty$ and $\delta(\tilde{\mathbf{X}}, \tilde{T}) = \delta(\tilde{\mathbf{X}})\mathrm{e}^{\mathrm{i}\tilde{\omega}\tilde{T}}$. For free-field boundary conditions, the solution of Eq. (4.33), given by the monopole source solution [43], is

$$\tilde{G}(\tilde{\mathbf{X}}) = \frac{\mathrm{e}^{-\mathrm{i}\tilde{k}\tilde{R}}}{4\pi\tilde{R}}, \tag{4.34}$$

where $\tilde{R} = \sqrt{\tilde{X}^2 + \tilde{Y}^2 + \tilde{Z}^2}$.

Following Morino [46], Eq. (4.34) is reformulated in the physical space where a harmonic solution $\hat{G}(\mathbf{x}, t) = G(\mathbf{x})\mathrm{e}^{\mathrm{i}\omega t}$ is sought. An equivalent harmonic solution in the Taylor–Lorentz space is given by $\hat{\tilde{G}}(\tilde{\mathbf{X}}, T) = \tilde{G}(\tilde{\mathbf{X}})\mathrm{e}^{\mathrm{i}\tilde{\omega}\tilde{T}}$. If we apply the inverse Taylor–Lorentz transformation to the independent variables in $\hat{\tilde{G}}(\tilde{\mathbf{X}}, \tilde{T})$ and consider that $d\tilde{T} = \beta_\infty dT$ (See Appendix B), we yield

$$\tilde{G}(\tilde{\mathbf{X}})\mathrm{e}^{\mathrm{i}\tilde{\omega}\tilde{T}} = \frac{\tilde{G}(\mathbf{x})}{\beta_\infty}\exp\left[\mathrm{i}\frac{\omega}{\beta_\infty}\left(\beta_\infty t - \frac{M_\infty x}{c_\infty\beta_\infty} - \beta_\infty\frac{\Phi_0'(\mathbf{x})}{c_\infty^2}\right)\right] = G(\mathbf{x})\mathrm{e}^{\mathrm{i}\omega t}, \tag{4.35}$$

where

$$G(\mathbf{x}) = \frac{\tilde{G}(\mathbf{x})}{\beta_\infty}\mathrm{e}^{-\mathrm{i}\omega\left(\frac{M_\infty x}{c_\infty\beta_\infty^2} + \frac{\Phi_0'(\mathbf{x})}{c_\infty^2}\right)}. \tag{4.36}$$

In the above equation, $\tilde{G}(\mathbf{x})$ is obtained by replacing the independent variables in Eq. (4.34) using Eqs. (4.26) and (4.30). Therefore, Eqs. (4.35) and (4.36) allow an explicit expression for the Green's function to be recovered,

$$G(\mathbf{x}) = \frac{\exp\left[-\mathrm{i}k\left(\frac{\sqrt{x^2+\beta_\infty^2(y^2+z^2)}}{\beta_\infty^2} + \frac{M_\infty x}{\beta_\infty^2} + \frac{\Phi_0'(\mathbf{x})}{c_\infty}\right)\right]}{4\pi\sqrt{x^2+\beta_\infty^2(y^2+z^2)}}. \tag{4.37}$$

The above equation can be extended to a generic source position (x_s, y_s, z_s). Consider $\delta(\mathbf{x}, \mathbf{x}_s; t)$ in Eq. (4.25) and use for the time transformation $T = t - [\Phi_0'(\mathbf{x}) - \Phi_0'(\mathbf{x}_s)]/c_\infty^2$ and $\tilde{T} = \beta_\infty T - M_\infty(X - X_s)/(c_\infty\beta_\infty)$ in lieu of the definitions provided in Eqs. (4.26) and (4.30), to give

$$G(\mathbf{x}, \mathbf{x}_s) = \frac{\mathrm{e}^{-\mathrm{i}k\sigma_M}}{4\pi R_M}, \tag{4.38}$$

where $\sigma_M = [R_M + M_\infty(x - x_s)]/\beta_\infty^2 + [\Phi_0'(\mathbf{x}) - \Phi_0'(\mathbf{x}_s)]/c_\infty$ extends the definition given by Garrick and Watkins [190] for a uniform flow, and the amplitude radius is $R_M = \sqrt{(x - x_s)^2 + \beta_\infty^2[(y - y_s)^2 + (z - z_s)^2]}$. A Green's function for two-dimensional problems consistent with the present formulation is given in Appendix B. In the case of a uniform flow, Eq. (4.38) is equivalent to the solution provided by Wu and Lee [40].

Nonetheless, note that based on the definition of the adjoint operator of the weakly non-uniform flow formulation (see Sec. 4.2), reciprocity is applicable to G [65] by reversing the

mean flow, i.e.

$$\hat{G}(\mathbf{x}, t, \mathbf{x}_s, t_s, \mathbf{u}_0) = \hat{G}(\mathbf{x}_s, -t_s, \mathbf{x}, -t, -\mathbf{u}_0), \tag{4.39}$$

where t_s denotes the retarded time. In other words, the source and the observer can be interchanged by reversing the time and the mean flow simultaneously.

4.5 Error estimate

The weakly non-uniform potential flow wave equation, Eq. (2.35), is an approximation of the linearised potential wave equation, Eq. (2.29), accurate to the first order with respect to M_0'. The main assumptions are that $M_\infty \ll 1$ and $M_0' \ll M_\infty$, meaning that $M_0' M_\infty \ll M_\infty^2$ and $M_0'^2 \ll M_\infty^2$. It is an exact formulation only for wave propagation in a uniform mean flow. This section presents a dimensional error analysis of the weakly non-uniform potential flow wave equation compared to the linearised potential wave equation.

4.5.1 Dimensional analysis

In this section, we provide a dimensional analysis of the terms either included or ignored in the weakly non-uniform flow formulation compared to the linearised potential wave equation. The analysis is based on the mean flow Mach number and the characteristic length scales associated with the acoustic field and the mean flow field, i.e. L_A and L_M. The linearised potential wave equation, Eq. (2.29), can be written in the frequency domain as

$$\omega^2\phi - 2\mathrm{i}\omega\mathbf{u}_0 \cdot \boldsymbol{\nabla}\phi + c_\infty^2 \boldsymbol{\nabla}^2\phi - u_\infty^2 \frac{\partial^2 \phi}{\partial x^2} = E(\phi), \tag{4.40}$$

where

$$\begin{aligned} E =& \mathbf{u}_0' \cdot \boldsymbol{\nabla}(\mathbf{u}_0 \cdot \boldsymbol{\nabla}\phi) + \mathbf{u}_\infty \cdot \boldsymbol{\nabla}(\mathbf{u}_0' \cdot \boldsymbol{\nabla}\phi) + \frac{1}{2}\boldsymbol{\nabla}\phi \cdot \boldsymbol{\nabla}(\mathbf{u}_0 \cdot \mathbf{u}_0) \\ &+ (\gamma - 1)(\mathrm{i}\omega\phi + \mathbf{u}_0 \cdot \boldsymbol{\nabla}\phi)\boldsymbol{\nabla} \cdot \mathbf{u}_0 + \frac{\gamma - 1}{2}(u_0^2 - u_\infty^2)\boldsymbol{\nabla}^2\phi. \end{aligned} \tag{4.41}$$

In the time harmonic formulation of Eq. (2.35), the terms on the left-hand side of Eq. (4.40) are retained while the terms included in the function E are dropped by assuming $M_0' \ll M_\infty$ and $M_\infty \ll 1$.

Let us divide Eq. (4.40) by c_∞^2. The right-hand side terms equating E scales with M_0', M_∞, L_A and L_M as:

$$\begin{aligned}
&\frac{1}{c_\infty^2}\mathbf{u}_0'\cdot\boldsymbol{\nabla}(\mathbf{u}_0'\cdot\boldsymbol{\nabla}\phi)\sim M_0'^2\frac{[\phi]}{L_AL_M}, && \frac{1}{c_\infty^2}\mathbf{u}_0'\cdot\boldsymbol{\nabla}(\mathbf{u}_\infty\cdot\boldsymbol{\nabla}\phi)\sim M_0'M_\infty\frac{[\phi]}{L_AL_M},\\
&\frac{1}{c_\infty^2}\mathbf{u}_\infty\cdot\boldsymbol{\nabla}(\mathbf{u}_0'\cdot\boldsymbol{\nabla}\phi)\sim M_0'M_\infty\frac{[\phi]}{L_AL_M}, && \frac{1}{2c_\infty^2}\boldsymbol{\nabla}\phi\cdot\boldsymbol{\nabla}(\mathbf{u}_0\cdot\mathbf{u}_0)\sim M_0'M_\infty\frac{[\phi]}{L_AL_M},\\
&\frac{1}{c_\infty^2}(\gamma-1)\boldsymbol{\nabla}\cdot\mathbf{u}_0\mathrm{i}\omega\phi\sim M_0'^3\frac{[\phi]}{L_AL_M}, && \frac{(\gamma-1)}{c_\infty^2}(\boldsymbol{\nabla}\cdot\mathbf{u}_0)\mathbf{u}_0\cdot\boldsymbol{\nabla}\phi\sim M_0'^3M_\infty\frac{[\phi]}{L_AL_M},\\
&\frac{1}{c_\infty^2}\frac{\gamma-1}{2}(\mathbf{u}_0\cdot\mathbf{u}_0-\mathbf{u}_\infty\cdot\mathbf{u}_\infty)\boldsymbol{\nabla}^2\phi\sim M_0'M_\infty\frac{[\phi]}{L_A^2},
\end{aligned} \tag{4.42}$$

where $[\phi]$ is the characteristic magnitude of ϕ, $\omega/c_\infty\sim 1/L_A$ and M_0' is the characteristic scale for $\mathbf{M}_0'$. Nonetheless, the terms on the left-hand side of Eq. (4.40) can be rewritten as

$$\begin{aligned}
&\frac{1}{c_\infty^2}\omega^2\phi\sim\frac{[\phi]}{L_A^2}, && \frac{1}{c_\infty^2}2\mathrm{i}\omega\mathbf{u}_0\cdot\boldsymbol{\nabla}\phi\sim M_\infty\frac{[\phi]}{L_A^2},\\
&\boldsymbol{\nabla}^2\phi\sim\frac{[\phi]}{L_A^2}, && \frac{1}{c_\infty^2}u_\infty^2\frac{\partial^2\phi}{\partial x^2}\sim M_\infty^2\frac{[\phi]}{L_A^2}.
\end{aligned} \tag{4.43}$$

Note that, unlike the terms in Eq. (4.42), all the terms in the above equation do not vanish in a uniform flow since they are not proportional to M_0'.

A combined Taylor–Lorentz transformation is applied to Eq. (4.40) to obtain a left-hand side to which an exact solution is known. In fact, in the transformed space, $\tilde{\phi}$ and $\tilde{G}$ are exact for the Helmholtz problem with quiescent media. Following the procedure described in Sec. 4.4 to obtain Eq. (4.32), Eq. (4.40) can be reduced to

$$\tilde{\omega}^2\tilde{\phi}+c_\infty^2\boldsymbol{\nabla}_{\tilde{X}}^2\tilde{\phi}=\tilde{E}, \tag{4.44}$$

where

$$\begin{aligned}
\tilde{E}=E(\tilde{\mathbf{X}},\tilde{\omega})&-\mathrm{i}\tilde{\omega}\left[\beta_\infty\boldsymbol{\nabla}_{\tilde{X}}\cdot\mathbf{u}_0'+\beta_\infty(\beta_\infty-1)\frac{\partial u_{0,x}'}{\partial\tilde{X}}\right]\tilde{\phi}\\
&-\tilde{\omega}^2\left[-\beta_\infty^2\mathbf{M}_0'\cdot\mathbf{M}_0'+2M_\infty M_{0,x}'+\beta_\infty^2M_{0,x}'^2M_\infty^2\right]\tilde{\phi}+2M_\infty^2u_{0,x}'\mathrm{i}\tilde{\omega}\frac{\partial\tilde{\phi}}{\partial\tilde{X}}
\end{aligned} \tag{4.45}$$

and $E(\tilde{\mathbf{X}},\tilde{\omega})$ is the same term as that given in Eq. (4.41) but written in a Taylor–Lorentz space. Therefore, for $M_\infty\ll 1$, the additional error terms in Eq. (4.45) scale as:

$$\begin{aligned}
&\frac{1}{c_\infty^2}\mathrm{i}\tilde{\omega}\beta_\infty\left(\boldsymbol{\nabla}_{\tilde{X}}\cdot\mathbf{u}_0'+(\beta_\infty-1)\frac{\partial u_{0,x}'}{\partial\tilde{X}}\right)\tilde{\phi}\sim M_0'^3\frac{[\phi]}{L_AL_M}, && \frac{\tilde{\omega}^2}{c_\infty^4}\beta_\infty^2\mathbf{u}_0'\cdot\mathbf{u}_0'\tilde{\phi}\sim M_0'^2\frac{[\phi]}{L_A^2},\\
&\frac{2\tilde{\omega}^2}{c_\infty^4}u_\infty u_{0,x}'\tilde{\phi}\sim M_0'M_\infty\frac{[\phi]}{L_A^2}, && \frac{\tilde{\omega}^2}{c_\infty^4}\beta_\infty^2u_\infty'^2u_{0,x}'^2\tilde{\phi}\sim M_0'^2M_\infty^2\frac{[\phi]}{L_A^2},\\
&\frac{2\mathrm{i}\tilde{\omega}}{c_\infty^3}u_\infty^2u_{0,x}'\frac{\partial\tilde{\phi}}{\partial\tilde{X}}\sim M_0'M_\infty^2\frac{[\phi]}{L_A^2}, &&
\end{aligned} \tag{4.46}$$

Based on Eqs. (4.42) and (4.46), the sources of error associated with the weakly non-uniform potential flow wave equation can then be approximated as

$$\begin{aligned}\tilde{E} \sim\, & C_1\frac{M_0^{'}M_\infty[\phi]}{L_AL_M} + C_2\frac{M_0^{'2}[\phi]}{L_AL_M} + C_3\frac{M_0^{'}M_\infty[\phi]}{L_A^2} + C_4\frac{M_0^{'2}[\phi]}{L_A^2} + C_5\frac{M_0^{'3}[\phi]}{L_AL_M} \\ & + C_6\frac{M_0^{'}M_\infty^2[\phi]}{L_A^2} + C_7\frac{M_0^{'3}M_\infty[\phi]}{L_AL_M} + C_8\frac{M_0^{'2}M_\infty^2[\phi]}{L_A^2},\end{aligned} \tag{4.47}$$

where $C_1, C_2, .., C_8$ are constants of order 1. In Sec. 4.5.2, the sources of error are convoluted with the Green's function to derive the order of magnitude for the error introduced in the above equation.

4.5.2 Characterisation of the error

According to Eq. (4.47), the term $\tilde{E}$ in Eq. (4.47) scales with $1/L_A = f/c_\infty$ where f is the frequency. In terms of mean flow length scale, the error varies with $1/L_M$. Therefore $\tilde{E}$ decreases as the mean flow becomes more uniform and it vanishes in a uniform flow ($M_0' = 0$). In other words, the accuracy of the formulation deteriorates only for sound propagation within a non-uniform mean flow region.

The error ε on the solution ϕ to Eq. (4.44) can be obtained by convolving the error source $\tilde{E}$ with the Green's function, $\tilde{G}$, to give

$$\varepsilon(\tilde{\mathbf{X}}_p) = \int_{\tilde{\Omega}} \tilde{G}(\tilde{\mathbf{X}}_p, \tilde{\mathbf{X}})\tilde{E}(\tilde{\mathbf{X}})\; dV(\tilde{\mathbf{X}}), \tag{4.48}$$

where $\tilde{\Omega}$ represents the transformed domain. Consider that $\tilde{G}$ varies with $1/R_M$, where R_M is the amplitude radius of Eq. (4.38). Introducing the geometrical length scale, D, associated with the domain, $\tilde{\Omega}$, the above equation can be rewritten by using Eqs. (4.42) and (4.46). The error contribution to Eq. (4.48) provided by the second and third terms in Eq. (4.42) scales as

$$\varepsilon_1 \sim [\phi]M_0^{'}M_\infty\frac{D}{L_M}\frac{D^2}{L_AR_M}. \tag{4.49}$$

Therefore, the error ε_1 scales as $1/L_A$. However, if L_AR_M is constant, namely if the amplitude radius is inversely proportional to the wavelength, the error becomes independent of frequency.

This also applies to all of the remaining terms in Eqs. (4.42) and (4.46), except for the error terms of order $1/L_A^2$. In this case, the last term of Eq. (4.42) produces an error ε_2 in Eq. (4.40) that is

$$\varepsilon_2 \sim [\phi]M_0^{'}M_\infty D\frac{D^2}{L_A^2R_M}. \tag{4.50}$$

Note that, since $f = c_\infty/L_A$, the above equation scales quadratically with frequency. Therefore, the contribution of this term is more significant at high frequency.

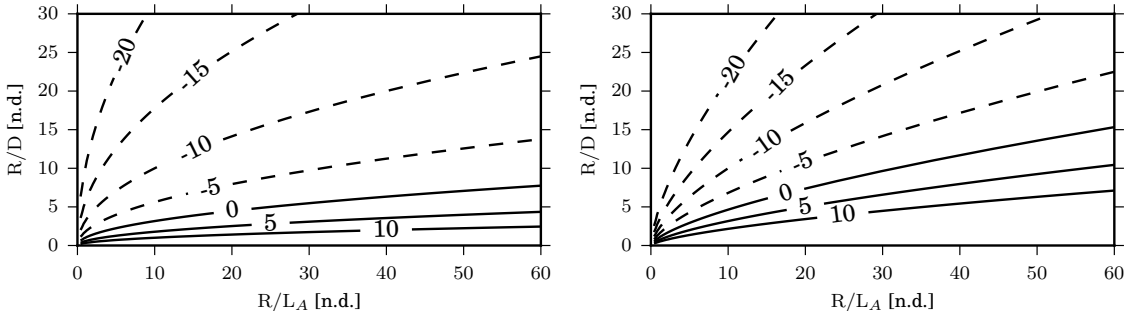

(a) ε_1 (dB) (b) ε_1 (dB)

Figure 4.3: Contour of the error estimates, ε_1 and ε_2, for solutions based on the weakly non-uniform potential flow equation, Eq. (2.35), against solutions to the linearised potential wave equation, Eq. (2.29), for $D/L_M = 1$; $\varepsilon_{i,dB} = 10\log_{10}(\varepsilon_i)$.

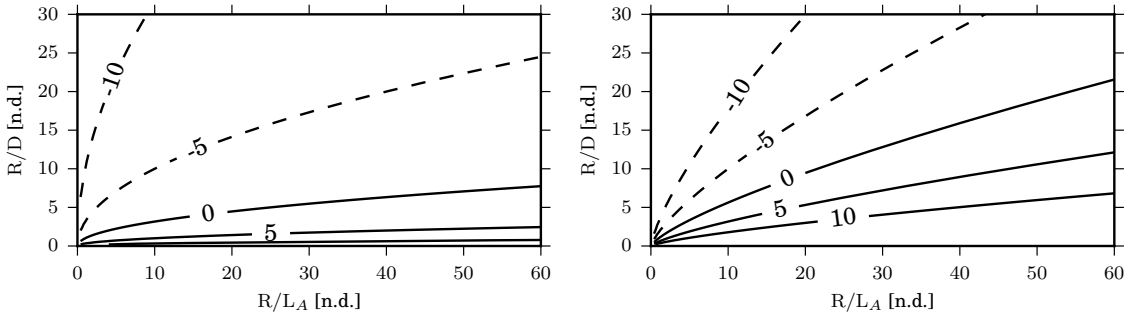

(a) $\varepsilon_{1,2D}$ (dB) (b) $\varepsilon_{2,2D}$ (dB)

Figure 4.4: Contour of the error estimates, $\varepsilon_{1,2D}$ and $\varepsilon_{2,2D}$, for solutions based on the weakly non-uniform potential flow equation, Eq. (2.35), against solutions to the linearised potential wave equation, Eq. (2.29), for $D/L_M = 1$; $\varepsilon_{i,2D,dB} = 10\log_{10}(\varepsilon_{i,2D})$.

Equations (4.49) and (4.50) can be rewritten by introducing the geometrical and acoustic relative distances of the observer, i.e. R_M/D and R_M/L_A, to give

$$\varepsilon_1 \sim [\phi] M_0' M_\infty \frac{D}{L_M}\left(\frac{D}{R_M}\right)^2 \frac{R_M}{L_A}, \qquad \varepsilon_2 \sim [\phi] M_0' M_\infty \left(\frac{D}{R_M}\right)^3 \left(\frac{R_M}{L_A}\right)^2. \tag{4.51}$$

Small values of R_M/D denote the geometrical near field whereas large values of R_M/D are associated with the geometrical far field. Similar definitions can be given for the acoustic field on the basis of R_M/L_A. The above equations show that, when sound propagates in a non-uniform flow, the error decreases in the geometrical far field but increases in the acoustic far field. Contours of ε_1 and ε_2 in dB are shown in Fig. 4.3 for $D/L_M = 1$. For clarity, the values reported in dB are computed as $\varepsilon_{i,dB} = 10\log_{10}(\varepsilon_i)$.

The present error analysis can be extended to 2D problems, where $\tilde{G}$ scales with $1/\sqrt{kR_M}$.

The error estimates are derived again based on the 2D Green's function provided in Appendix B. The term corresponding to ε_1 is

$$\varepsilon_{1,2D} \sim [\phi] M_0^{'} M_\infty \frac{D}{L_M} \frac{D}{\sqrt{L_A R_M}} = [\phi] M_0^{'} M_\infty \frac{D}{L_M} \frac{D}{R_M} \sqrt{\frac{R_M}{L_A}}, \tag{4.52}$$

whereas that associated to ε_2 is

$$\varepsilon_{2,2D} \sim [\phi] M_0^{'} M_\infty D \frac{D}{L_A \sqrt{L_A R_M}} = [\phi] M_0^{'} M_\infty \left(\frac{D}{R_M}\right)^2 \sqrt{\left(\frac{R_M}{L_A}\right)^3}. \tag{4.53}$$

Contours of $\varepsilon_{1,2D}$ and $\varepsilon_{2,2D}$ on a dB scale are shown in Fig. 4.4 for $D/L_M = 1$. They are computed as indicated for $\varepsilon_{1,2}$ in Fig. 4.3. As expected, the error in a two-dimensional problem is consistent with the error for a three-dimensional problem. However, they differ in terms of magnitude (see Figs. 4.3 and 4.4).

4.6 Taylor–Helmholtz equation

In this section, we present a first order approximation in the mean flow Mach number to the weakly non-uniform flow integral solution. The formulation consistent with the Taylor equation [32] (see Eq. (2.38)) is presented in the physical space. An additional set of assumptions is made, compared to the weakly non-uniform flow wave equation, in that terms of order M_∞^2 are ignored.

Under the Taylor ansatz, the Taylor–Helmholtz formulation can be derived from Eq. (2.30) [32]. Using the approximations detailed in Sec. 2.5.2 and 2.5.4, yields

$$k^2\phi - 2\mathrm{i}k\mathbf{M}_0 \cdot \boldsymbol{\nabla}\phi + \boldsymbol{\nabla}^2\phi = 0. \tag{4.54}$$

An integral solution to the above equation in the frequency domain is sought. The Green's function for the reverse flow operator, G_T, associated with the above equation satisfies

$$k^2 G_T + 2\mathrm{i}k\mathbf{M}_0 \cdot \boldsymbol{\nabla} G_T + \boldsymbol{\nabla}^2 G_T = -\delta(\mathbf{x}_p - \mathbf{x}). \tag{4.55}$$

G_T differs from G and is derived in Appendix A. For a 3D problem and a generic point source, the Green's function can be written as

$$G_T(\mathbf{x}_p, \mathbf{x}) = \frac{\mathrm{e}^{-ik\sigma_T}}{4\pi R}. \tag{4.56}$$

where $\sigma_T = R + [\Phi_0(\mathbf{x}_p) - \Phi_0(\mathbf{x})]/c_\infty$, $R = \sqrt{(x_p - x)^2 + (y_p - y)^2 + (z_p - z)^2}$ and $\Phi_0(\mathbf{x})$ denotes the total mean flow velocity potential.

External noise propagation and scattering (see Fig. 4.1) can be determined based on this formulation, i.e. a boundary integral solution to Eq. (4.54) can be derived from Eq. (4.15)

by neglecting the terms of order M_∞^2, i.e.

$$\phi(\mathbf{x}_p) = \int_{\partial\Omega} \left(G_T \frac{\partial \phi}{\partial n} - \phi \frac{\partial G_T}{\partial n} - 2ik\mathbf{M}_0 \cdot \mathbf{n} G_T \phi \right) dS(\mathbf{x}). \tag{4.57}$$

Equation (4.57) is written for a generic point, $\mathbf{x}_p$, within the domain Ω. However, the right-hand side of Eq. (4.57) is singular on the boundary surface $\partial\Omega$. On $\partial\Omega$, the singularity is solvable using the Cauchy principal value.

Following the procedure showed in Sec. 4.3, a limit approach to the boundary surface is performed. In this case, the static operator associated with Eq. (4.55) is the Laplacian, $\nabla^2 G_0 = -\delta(\mathbf{x}_p - \mathbf{x})$. The static operator is the same as for the standard Helmholtz problem. Therefore, the Cauchy principal value integral obtained in this case is the same as for the standard Helmholtz equation with quiescent media [43], i.e.

$$C(\mathbf{x}_p) = \begin{cases} 1 & \mathbf{x}_p \in \Omega \\ 0 & \mathbf{x}_p \notin \Omega \cup \partial\Omega \\ 1 - \int_{\partial\Omega} \frac{\partial G_0}{\partial n} dS(\mathbf{x}) & \mathbf{x}_p \in \partial\Omega \end{cases}, \tag{4.58}$$

where $G_0 = 1/(4\pi R)$ and R is the distance between the source and the observer. The integral solution based on Eq. (4.57) reduces to

$$C(\mathbf{x}_p)\phi(\mathbf{x}_p) = \int_{\partial\Omega} \left(G_T \frac{\partial \phi}{\partial n} - \phi \frac{\partial G_T}{\partial n} - 2ik\mathbf{M}_0 \cdot \mathbf{n} G_T \phi \right) dS(\mathbf{x}). \tag{4.59}$$

An alternative derivation of the above equation is given in Appendix A.

4.7 Taylor–Lorentz space-time

While the integral solution provided in Sec. 4.3 has been derived in the physical space, an equivalent solution in the transformed space is presented in this section. A Taylor–Lorentz transformation is used to provide a boundary integral solution to Eq. (2.35) in a transformed space-time. The Taylor–Lorentz transform is used to reduce the weakly non-uniform flow wave equation to the standard wave operator with quiescent media. This differs from the transformation applied by Clancy [36] in that the Taylor transformation of the non-uniform mean flow part is applied following the Lorentz transform rather than including non-uniform flow effects in the Lorentz transform.

In the transformed space, the free-field Green's function can be written as that for the standard Helmholtz problem with quiescent media. This is achieved at the cost of rewriting sound sources and boundary conditions in the transformed space. Unlike the physical space formulation, the transformed space allows the use of conventional numerical methods for the standard Helmholtz problem to solve sound propagation in a non-uniform flow.

4.7.1 Governing equation

In this section, Eq. (4.1) is reduced to the standard Helmholtz equation with quiescent media in a Taylor–Lorentz space. A Lorentz transformation [75] is applied following a Taylor transformation [31] of Eq. (4.1). As shown in Sec. 4.4, the weakly non-uniform flow wave equation, Eq. (4.1), can be reduced to

$$\frac{1}{c_\infty^2}\frac{\partial^2\hat{\tilde{\phi}}}{\partial\tilde{T}^2} - \boldsymbol{\nabla}^2_{\tilde{X}}\hat{\tilde{\phi}} = \tilde{q}(\tilde{\mathbf{X}},\tilde{T}), \tag{4.60}$$

where $\hat{\tilde{\phi}}$ is the acoustic potential in the transformed space and $\tilde{q}$ denotes the source distribution in the Taylor–Lorentz space. The left-hand side of the above equation is independent of the mean flow.

A steady state problem, namely $\hat{\tilde{\phi}}(\tilde{\mathbf{X}},\tilde{T}) = \tilde{\phi}(\tilde{\mathbf{X}})\mathrm{e}^{\mathrm{i}\tilde{\omega}\tilde{T}}$, is considered such that Eq. (4.32) can be rewritten in the frequency domain as

$$\tilde{k}^2\tilde{\phi} + \boldsymbol{\nabla}^2_{\tilde{X}}\tilde{\phi} = \tilde{g}(\tilde{\mathbf{X}}), \tag{4.61}$$

where $\tilde{k} = \tilde{\omega}/c_\infty$, the harmonic sound source is $\tilde{q}(\tilde{\mathbf{X}},\tilde{T}) = -\tilde{g}(\tilde{\mathbf{X}})\mathrm{e}^{\mathrm{i}\tilde{\omega}\tilde{T}}$ and the superscript "$\tilde{}$" denotes all the quantities in the transformed Taylor–Lorentz space. In the transformed space, the Sommerfeld radiation condition reduces to the same condition as for quiescent media, that is

$$\lim_{\tilde{r}\to\infty} \tilde{r}^b\left[c_\infty\frac{\partial}{\partial\tilde{r}} + \frac{\partial}{\partial\tilde{T}}\right]\hat{\tilde{\phi}} = 0, \tag{4.62}$$

where $\tilde{r} = \|\tilde{\mathbf{X}}\|$ and the parameter b is the same as that in Eq. (2.40).

In the physical space, a time harmonic solution $\hat{\phi}(\mathbf{x},t) = \phi(\mathbf{x})\mathrm{e}^{\mathrm{i}\omega t}$ due a harmonic source $\hat{g}(\mathbf{x},t) = g(\mathbf{x})\mathrm{e}^{\mathrm{i}\omega t}$ is sought, with ϕ and g complex numbers. In the transformed space, we also seek the harmonic solution, $\tilde{\phi}$, given a harmonic source $\tilde{g}(\tilde{\mathbf{X}})\mathrm{e}^{\mathrm{i}\tilde{\omega}\tilde{T}}$. Hence, we use Eq. (2.56) to give

$$\tilde{\phi}(\tilde{\mathbf{X}}) = \phi(\mathbf{x})\mathrm{e}^{-\mathrm{i}\omega\left(\frac{M_\infty x}{c_\infty \beta_\infty^2} + \frac{\Phi_0'(\mathbf{x})}{c_\infty^2}\right)}, \tag{4.63}$$

$$\tilde{g}(\tilde{\mathbf{X}}) = g(\mathbf{x})\mathrm{e}^{-\mathrm{i}\omega\left(\frac{M_\infty x}{c_\infty \beta_\infty^2} + \frac{\Phi_0'(\mathbf{x})}{c_\infty^2}\right)}. \tag{4.64}$$

Note that, neglecting terms of order M_∞^2, Eq. (2.38) has been recovered in lieu of Eq. (4.1). The same set of assumptions can be used to derive an analogous formulation in the Taylor space, as extensively discussed in the work of Astley and Bain [32]. A boundary integral solution to Eq. (4.61) is presented in the following section.

4.7.2 Boundary integral solution

The boundary integral solution to the non-homogeneous Helmholtz equation, Eq. (4.61), is well-known [43]:

$$C(\tilde{\mathbf{X}}_p)\tilde{\phi}(\tilde{\mathbf{X}}_p) = \int_{\partial\tilde{\Omega}} \left[\tilde{G}\frac{\partial\tilde{\phi}}{\partial\tilde{n}} - \tilde{\phi}\frac{\partial\tilde{G}}{\partial\tilde{n}}\right] d\tilde{S}(\tilde{\mathbf{X}}) + \int_{\tilde{\Omega}} \tilde{G}\tilde{g}\; d\tilde{V}(\tilde{\mathbf{X}}), \tag{4.65}$$

with

$$C(\tilde{\mathbf{X}}_p) = \begin{cases} 1 & \tilde{\mathbf{X}}_p \in \tilde{\Omega} \\ 0 & \tilde{\mathbf{X}}_p \notin \partial\tilde{\Omega} \cup \tilde{\Omega} \\ 1 - \int_{\partial\tilde{\Omega}} \frac{\partial\tilde{G}_0}{\partial\tilde{n}} d\tilde{S}(\tilde{\mathbf{X}}) & \tilde{\mathbf{X}}_p \in \partial\tilde{\Omega} \end{cases}, \tag{4.66}$$

where $\tilde{\Omega}$ and $\partial\tilde{\Omega}$ denote the transformed space and its boundary. Note that applying an inverse Taylor–Lorentz transform to Eq. (4.65) written for $\tilde{\mathbf{X}}_p \notin \partial\tilde{\Omega} \cup \tilde{\Omega}$ allows the value $\hat{C}$ in Eq. (4.22) to be recovered. The details of this derivation will be presented in Sec. 5.2.5.1.

In Eq. (4.65), $\tilde{G}(\tilde{\mathbf{X}}_p, \tilde{\mathbf{X}})$ denotes the free-field Green's function associated with the Helmholtz problem with quiescent media:

$$\tilde{G}(\tilde{\mathbf{X}}_p, \tilde{\mathbf{X}}) = \frac{\mathrm{e}^{-\mathrm{i}\tilde{k}\tilde{R}}}{4\pi\tilde{R}}, \tag{4.67}$$

where $\tilde{R} = \sqrt{(\tilde{X}_p - \tilde{X})^2 + (\tilde{Y}_p - \tilde{Y})^2 + (\tilde{Z}_p - \tilde{Z})^2}$, with $\tilde{\mathbf{X}}_p$ and $\tilde{\mathbf{X}}$ respectively the position of the observer and the source point. On the other hand, $\tilde{G}_0$ is the Green's function associated with the Laplace operator, $\nabla^2_{\tilde{X}}\tilde{G}_0 = -\delta(\tilde{\mathbf{X}}_p - \tilde{\mathbf{X}})$, written in the transformed space, namely $\tilde{G}_0(\tilde{\mathbf{X}}_p, \tilde{\mathbf{X}}) = 1/(4\pi\tilde{R})$. The Green's function for a 2D problem is also well-known [43],

$$\tilde{G}(\tilde{\mathbf{X}}_p, \tilde{\mathbf{X}}) = -\frac{\mathrm{i}}{4}H_0^{(2)}\left(\tilde{k}\tilde{R}_{2D}\right), \tag{4.68}$$

where $\tilde{R}_{2D} = \sqrt{(\tilde{X}_p - \tilde{X})^2 + (\tilde{Y}_p - \tilde{Y})^2}$ and $H_0^{(2)}$ is the Hankel function of the second type and order zero.

After solving Eq. (4.65) along $\partial\tilde{\Omega}$ and computing $\tilde{\phi}$ in the transformed domain $\tilde{\Omega}$, the solution ϕ in the physical domain can be retrieved based on Eq. (4.63). Once the problem is solved in terms of velocity potential, ϕ, the pressure in the physical space can be recovered from the linearised momentum equation based on Eqs. (2.56), (2.57) and (4.3). Let us deal with the convective term $\mathbf{u}_0 \cdot \boldsymbol{\nabla}\phi$. Considering that

$$\boldsymbol{\nabla}\left(\phi \mathrm{e}^{\mathrm{i}\omega t}\right) = \boldsymbol{\nabla}\left(\phi \mathrm{e}^{\mathrm{i}\tilde{\omega}\tilde{T}} \mathrm{e}^{-\mathrm{i}\tilde{\omega}\left(\frac{M_\infty x}{c_\infty \beta_\infty} + \beta_\infty \frac{\Phi_0'(\mathbf{x})}{c_\infty^2}\right)}\right) = \boldsymbol{\nabla}\left(\tilde{\phi}\mathrm{e}^{\mathrm{i}\tilde{\omega}\tilde{T}}\right) \tag{4.69}$$

and the gradient $\boldsymbol{\nabla} = (\partial/\partial x, \partial/\partial y, \partial/\partial z)$ can be written as

$$\boldsymbol{\nabla} = \left(\frac{1}{\beta_\infty}\frac{\partial}{\partial\tilde{X}} + \frac{1}{c_\infty}\left[\frac{M_\infty}{\beta_\infty} + \beta_\infty M_{0,x}'\right]\frac{\partial}{\partial\tilde{T}}, \quad \frac{\partial}{\partial\tilde{Y}} + \beta_\infty \frac{M_{0,y}'}{c_\infty}\frac{\partial}{\partial\tilde{T}}, \quad \frac{\partial}{\partial\tilde{Z}} + \beta_\infty \frac{M_{0,z}'}{c_\infty}\frac{\partial}{\partial\tilde{T}}\right), \tag{4.70}$$

the term $\mathbf{u}_0 \cdot \boldsymbol{\nabla}\phi$ can be calculated based on the solution in the transformed space, considering that for a harmonic problem $\partial/\partial\tilde{T} = \mathrm{i}\tilde{\omega}$. Therefore, the acoustic pressure in the physical space can be evaluated using the above equation to give

$$p'(\omega) = -\rho_0\left(\mathrm{i}\beta_\infty\tilde{\omega}\tilde{\phi} + \mathbf{u}_0 \cdot \boldsymbol{\nabla}\tilde{\phi}\right)\mathrm{e}^{\mathrm{i}\tilde{k}\left(\frac{M_\infty x}{\beta_\infty} + \beta_\infty \frac{\Phi_0'(\mathbf{x})}{c_\infty}\right)}. \tag{4.71}$$

In summary, the boundary integral solution to Eq. (4.61) has been devised based on the well-known solution to the Helmholtz problem with quiescent media. As will be shown in Sec. 4.7.3, this is achieved at the cost of more complex boundary conditions than in the case of the corresponding physical space formulation.

4.7.3 Boundary conditions

The boundary conditions relevant for sound propagation in a transformed Taylor–Lorentz space (see Eq. (4.61)) are discussed in this section. In particular, we present how to recover the boundary conditions in the transformed space if the corresponding values in the physical space are assigned. This is done for velocity and pressure boundary conditions while their combination can be used to define impedance boundary conditions. Note that a Dirichlet problem, namely a condition on the velocity potential, ϕ, is not of practical interest because ϕ is not usually measured.

4.7.3.1 Normal velocity

Velocity boundary conditions in the physical space can be written as

$$\frac{\partial\phi(\mathbf{x})}{\partial n} = h_n(\mathbf{x}) \quad \text{for} \quad \mathbf{x} \in \partial\Omega, \tag{4.72}$$

where $\mathbf{n}$ is the normal vector to the boundary surface (see Figs. 4.5), $\partial\Omega$, and h_n is an assigned complex value. The acoustic particle velocity normal to the boundary surface, $\partial\phi(\mathbf{x})/\partial n$, can be written in the Taylor–Lorentz space using Eq. (4.63) to give

$$\frac{\partial\phi(\mathbf{x})}{\partial n} = \left[\frac{\partial\tilde{\phi}(\tilde{\mathbf{X}})}{\partial n} + \mathrm{i}\frac{k}{\beta_\infty^2}\left(M_\infty n_x + M'_{0,n}\beta_\infty^2\right)\tilde{\phi}\right]\mathrm{e}^{\mathrm{i}k\left(\frac{M_\infty x}{\beta_\infty^2}+\frac{\Phi'_0(\mathbf{x})}{c_\infty}\right)}. \tag{4.73}$$

We now consider the second term on the right-hand side of the above equation. Since it is assumed that $M'_0 \ll M_\infty \ll 1$,

$$M_\infty n_x + M'_{0,n}\beta_\infty^2 = M_\infty n_x + M'_{0,n}(1 - M_\infty^2) \simeq M_\infty n_x + M'_{0,n} = M_{0,n}. \tag{4.74}$$

For an impermeable stationary surface, such as $\partial\Omega$ (see Fig. 4.5), the normal component of the mean flow to the boundary surface $\partial\Omega$ is zero, i.e. $M_{0,n} = 0$. It applies both to rigid and vibrating surfaces. In fact, the condition that $M_{0,n} = 0$ is imposed on the mean flow rather than on the acoustic field and, therefore, is independent of the acoustic boundary conditions. Combining Eqs. (4.73) and (4.74) yields

$$\frac{\partial\tilde{\phi}(\tilde{\mathbf{X}})}{\partial n} = h_n(\mathbf{x})\mathrm{e}^{-\mathrm{i}k\left(\frac{M_\infty x}{\beta_\infty^2}+\frac{\Phi'_0(\mathbf{x})}{c_\infty}\right)}. \tag{4.75}$$

Note that the normal vector $\mathbf{n}$ to the boundary surface, $\partial\Omega$, is not normal to the boundary surface in the transformed domain, $\partial\tilde{\Omega}$ (see Fig. 4.5). We deal with this term by defining the tangent vector to the transformed boundary surface $\tilde{\boldsymbol{\tau}}$ such that, given the normal vector $\tilde{\mathbf{n}}$ to the same surface, an orthonormal triplet can be assigned as $\tilde{\mathbf{n}} = \tilde{\boldsymbol{\eta}} \times \tilde{\boldsymbol{\tau}}$ (see Fig. 4.5). The definition of $\tilde{\mathbf{n}}$, $\tilde{\boldsymbol{\tau}}$ and $\tilde{\boldsymbol{\eta}}$ allows $\partial\tilde{\phi}(\tilde{\mathbf{X}})/\partial n$ to be rewritten as

$$\frac{\partial\tilde{\phi}(\tilde{\mathbf{X}})}{\partial n} = \frac{\partial\tilde{\phi}(\tilde{\mathbf{X}})}{\partial\tilde{n}}\frac{\partial\tilde{n}}{\partial n} + \frac{\partial\tilde{\phi}(\tilde{\mathbf{X}})}{\partial\tilde{\tau}}\frac{\partial\tilde{\tau}}{\partial n} + \frac{\partial\tilde{\phi}(\tilde{\mathbf{X}})}{\partial\tilde{\eta}}\frac{\partial\tilde{\eta}}{\partial n}, \tag{4.76}$$

giving

$$\frac{\partial\tilde{\phi}(\tilde{\mathbf{X}})}{\partial\tilde{n}} = \frac{\left[\frac{\partial\tilde{\phi}(\tilde{\mathbf{X}})}{\partial n} - \frac{\partial\tilde{\phi}(\tilde{\mathbf{X}})}{\partial\tilde{\tau}}\frac{\partial\tilde{\tau}}{\partial n} - \frac{\partial\tilde{\phi}(\tilde{\mathbf{X}})}{\partial\tilde{\eta}}\frac{\partial\tilde{\eta}}{\partial n}\right]}{\frac{\partial\tilde{n}}{\partial n}}. \tag{4.77}$$

Let us define

$$\mu(\tilde{\mathbf{X}}) = \left(\frac{\partial\tilde{n}(\tilde{\mathbf{X}})}{\partial n}\right)^{-1}, \tag{4.78}$$

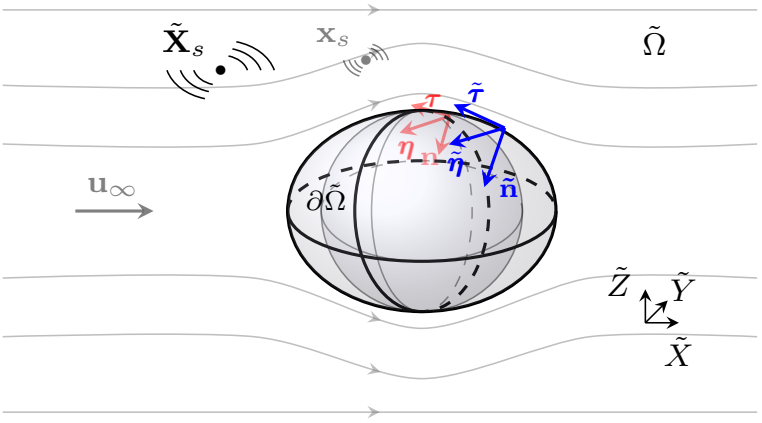

Figure 4.5: Geometrical features for the scattering of a sound field in a non-uniform potential flow. Superposition of the physical and transformed Taylor–Lorentz space showing the corresponding normal and tangent vectors to the boundary surface.

where μ represents the projection of the normal vector in the deformed space along the corresponding vector in the physical space (see Fig. 4.5). All the surfaces that are not aligned with the uniform mean flow at infinity undergo a change of orientation when the transformation is applied. This transformation therefore affects the normal vector. We can introduce the above geometrical relations in the formulation of the boundary conditions. Using Eq. (4.75) in Eq. (4.77) yields

$$\frac{\partial\tilde{\phi}(\tilde{\mathbf{X}})}{\partial\tilde{n}} = \mu(\tilde{\mathbf{X}})\left[h_n(\mathbf{x})\mathrm{e}^{-\mathrm{i}k\left(\frac{M_\infty x}{\beta_\infty^2}+\frac{\Phi_0'(\mathbf{x})}{c_\infty}\right)} - \frac{\partial\tilde{\phi}(\tilde{\mathbf{X}})}{\partial\tilde{\tau}}\frac{\partial\tilde{\tau}}{\partial n} - \frac{\partial\tilde{\phi}(\tilde{\mathbf{X}})}{\partial\tilde{\eta}}\frac{\partial\tilde{\eta}}{\partial n}\right]. \tag{4.79}$$

Consistent with Eq. (4.63), the above equation can be rewritten by defining

$$\frac{\tilde{h}_n(\tilde{\mathbf{X}})}{\mu(\tilde{\mathbf{X}})} = h_n(\mathbf{x})\mathrm{e}^{-\mathrm{i}k\left(\frac{M_\infty x}{\beta_\infty^2}+\frac{\Phi_0'(\mathbf{x})}{c_\infty}\right)}, \tag{4.80}$$

to give

$$\frac{\partial\tilde{\phi}(\mathbf{X})}{\partial\tilde{n}} = \tilde{h}_n(\tilde{\mathbf{X}}) - \mu(\tilde{\mathbf{X}})\left[\frac{\partial\tilde{\phi}(\tilde{\mathbf{X}})}{\partial\tilde{\tau}}\frac{\partial\tilde{\tau}}{\partial n} + \frac{\partial\tilde{\phi}(\tilde{\mathbf{X}})}{\partial\tilde{\eta}}\frac{\partial\tilde{\eta}}{\partial n}\right]. \tag{4.81}$$

Note that the tangent derivatives of ϕ are not conventionally assigned for wave propagation since we consider an inviscid flow and, therefore, the acoustic particles are free to slip in the direction tangential to the boundary. However, they can be computed numerically as will be shown in Chapter 5. For rigid body scattering, i.e. $\partial\phi/\partial n = 0$, the above equation can be simplified to

$$\frac{\partial\tilde{\phi}(\tilde{\mathbf{X}})}{\partial\tilde{n}} = -\mu(\tilde{\mathbf{X}})\left[\frac{\partial\tilde{\phi}(\tilde{\mathbf{X}})}{\partial\tilde{\tau}}\frac{\partial\tilde{\tau}}{\partial n} + \frac{\partial\tilde{\phi}(\tilde{\mathbf{X}})}{\partial\tilde{\eta}}\frac{\partial\tilde{\eta}}{\partial n}\right]. \tag{4.82}$$

4.7.3.2 Prescribed pressure

In problems of practical interest, boundary conditions are generally specified in terms of acoustic pressure rather than velocity potential. A condition for the acoustic pressure, consistent with the transformed space formulation, is derived in this section.

The acoustic pressure in the physical space is recovered from the linearised momentum equation. If $p'_s(\omega)$ is a known pressure distribution assigned on the boundary surface, Eq. (4.71) can be used to derive a relation between the acoustic velocity potential on the boundary of the transformed space and the acoustic pressure. The formulation in terms of $\tilde{\phi}$ and $\partial\tilde{\phi}/\partial\tilde{n}$, consistent with Eq. (4.65), can be derived based on

$$\begin{aligned}
\frac{\partial\tilde{\phi}(\tilde{\mathbf{X}})}{\partial x} &= \frac{\partial\tilde{\phi}(\tilde{\mathbf{X}})}{\partial\tilde{n}}\tilde{n}_x + \frac{\partial\tilde{\phi}(\tilde{\mathbf{X}})}{\partial\tilde{\tau}}\tilde{\tau}_x + \frac{\partial\tilde{\phi}(\tilde{\mathbf{X}})}{\partial\tilde{\eta}}\tilde{\eta}_x,\\
\frac{\partial\tilde{\phi}(\tilde{\mathbf{X}})}{\partial y} &= \frac{\partial\tilde{\phi}(\tilde{\mathbf{X}})}{\partial\tilde{n}}\tilde{n}_y + \frac{\partial\tilde{\phi}(\tilde{\mathbf{X}})}{\partial\tilde{\tau}}\tilde{\tau}_y + \frac{\partial\tilde{\phi}(\tilde{\mathbf{X}})}{\partial\tilde{\eta}}\tilde{\eta}_y,\\
\frac{\partial\tilde{\phi}(\tilde{\mathbf{X}})}{\partial z} &= \frac{\partial\tilde{\phi}(\tilde{\mathbf{X}})}{\partial\tilde{n}}\tilde{n}_z + \frac{\partial\tilde{\phi}(\tilde{\mathbf{X}})}{\partial\tilde{\tau}}\tilde{\tau}_z + \frac{\partial\tilde{\phi}(\tilde{\mathbf{X}})}{\partial\tilde{\eta}}\tilde{\eta}_z.
\end{aligned} \tag{4.83}$$

The components of the normal and tangent vectors, $\tilde{\boldsymbol{n}}$, $\tilde{\boldsymbol{\tau}}$ and $\tilde{\boldsymbol{\eta}}$, defined in the transformed space, to the boundary surface in the physical space, such as $\tilde{n}_x = \partial\tilde{n}/\partial x$, can be computed; they can be evaluated provided the geometry of the boundary surface, $\partial\Omega$, and M_∞ (see Sec. 2.6.3).

Let us consider the non-dimensional mean flow velocity vector $\mathbf{M}_0 = (M_\infty + M'_{0,x}, M'_{0,y}, M'_{0,z})$. Including the above relations in Eq. (4.71) gives

$$\begin{aligned}
\tilde{\phi} = &-\frac{p'_s(\omega)\mathrm{e}^{-\mathrm{i}k\left(\frac{M_\infty x}{\beta_\infty^2} + \frac{\Phi'_0(\mathbf{x})}{c_\infty}\right)}}{\rho_0 \mathrm{i}\tilde{\omega}\beta_\infty}\\
&- \frac{(M_\infty + M'_{0,x})}{\mathrm{i}\tilde{k}\beta_\infty}\left(\frac{\partial\tilde{\phi}(\tilde{\mathbf{X}})}{\partial\tilde{n}}\tilde{n}_x + \frac{\partial\tilde{\phi}(\tilde{\mathbf{X}})}{\partial\tilde{\tau}}\tilde{\tau}_x + \frac{\partial\tilde{\phi}(\tilde{\mathbf{X}})}{\partial\tilde{\eta}}\tilde{\eta}_x\right)\\
&- \frac{M'_{0,y}}{\mathrm{i}\tilde{k}\beta_\infty}\left(\frac{\partial\tilde{\phi}(\tilde{\mathbf{X}})}{\partial\tilde{n}}\tilde{n}_y + \frac{\partial\tilde{\phi}(\tilde{\mathbf{X}})}{\partial\tilde{\tau}}\tilde{\tau}_y + \frac{\partial\tilde{\phi}(\tilde{\mathbf{X}})}{\partial\tilde{\eta}}\tilde{\eta}_y\right)\\
&- \frac{M'_{0,z}}{\mathrm{i}\tilde{k}\beta_\infty}\left(\frac{\partial\tilde{\phi}(\tilde{\mathbf{X}})}{\partial\tilde{n}}\tilde{n}_z + \frac{\partial\tilde{\phi}(\tilde{\mathbf{X}})}{\partial\tilde{\tau}}\tilde{\tau}_z + \frac{\partial\tilde{\phi}(\tilde{\mathbf{X}})}{\partial\tilde{\eta}}\tilde{\eta}_z\right).
\end{aligned} \tag{4.84}$$

Equation (4.84) can be used in Eq. (4.65) to solve the boundary integral problem for a prescribed pressure distribution. As seen for velocity boundary conditions, the terms including the tangential derivatives are not conventionally assigned and can be included in the kernel of the integral formulation.

4.8 Weak coupling for scattering problems

In order to solve the scattering of a sound field from either an accurate sound source model or a high-fidelity acoustic near-field prediction, a weakly-coupled approach [185] is proposed in this section in the presence of a non-uniform mean flow. The integral formulations presented in Secs. 4.3 and 4.7 are used to deal with wave extrapolation and scattering problems. An incident field defined in an "inner" domain $\Omega_{in,m}$ is extrapolated to a scattering surface $\partial\Omega$ based on an integral formulation written along an interface $\partial\Omega_m$ that encloses Ω_{in} (see Fig. 4.6). The subscript m denotes the m-th inner domain. Then, wave propagation in the domain Ω can be solved by using the boundary integral formulation written on $\partial\Omega$ in either the physical or the Taylor–Lorentz space.

Therefore, by "weakly" we mean that the backscattered field towards $\Omega_{in,m}$ is negligible. In other words, the problem in $\Omega_{in,m}$ can be solved independently of the solution in Ω. This is generally the case if the wavelength is larger than the size of the inner domain $\Omega_{in,m}$. We also assume that the surface $\partial\Omega_m$ lies in a region where the mean flow is weakly non-uniform and can be considered potential. First, the solution in the physical space is presented. Second, we describe how to recover a potential field in a transformed space where an analogous solution is proposed.

4.8.1 Physical space-time

A weakly-coupled approach is proposed based on Eq. (4.15). First, the potential field is recovered from a solution of the acoustic field within an "inner" domain in terms of acoustic pressure and velocity. Second, the integral formulation is used to project the acoustic field on a solid surface and solve a scattering problem.

We then assume a potential flow along an interface, $\partial\Omega_m$, between two acoustic domains (see Fig. 4.6). A distribution of acoustic pressure p' and velocity $\mathbf{u}'$ is assumed to be known based either on an accurate source model or a near-field high-fidelity solution in an "inner" domain $\Omega_{in,m}$ (see Fig. 4.6). The acoustic pressure and velocity can be written, at the interface, as

$$\begin{aligned} p'(\omega) &= -\rho_0(\mathrm{i}\omega\phi + \mathbf{u}_0 \cdot \boldsymbol{\nabla}\phi), \\ \mathbf{u}'(\omega) &= \boldsymbol{\nabla}\phi. \end{aligned} \tag{4.85}$$

Inverting the above equation gives

$$\begin{aligned} \phi &= \frac{\mathrm{i}}{\omega}\left(\frac{p'_s(\omega)}{\rho_0} + \mathbf{u}_0 \cdot \mathbf{u}'_s(\omega)\right) = \phi_s, \\ \boldsymbol{\nabla}\phi &= \mathbf{u}'(\omega) = \mathbf{u}'_s(\omega). \end{aligned} \tag{4.86}$$

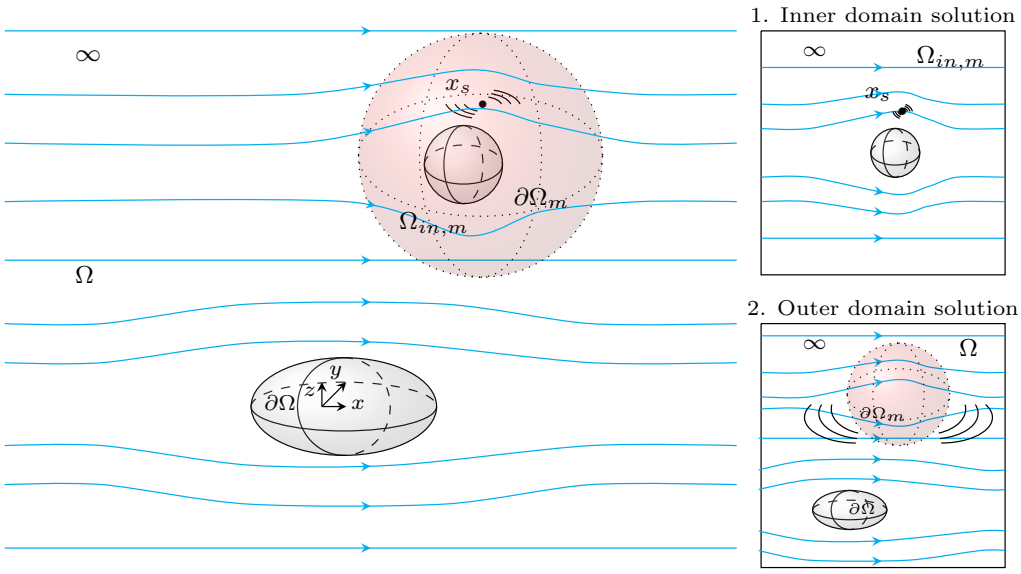

Figure 4.6: Schematic representation of the weakly-coupled approach; scattering of a sound field projected from a control surface, based on a near-field prediction along $\partial\Omega_{in,m}$, onto a boundary $\partial\Omega$ in a non-uniform potential mean flow.

where p_s and $\mathbf{u}'_s$ are known complex amplitudes of a known time harmonic solution. The above equations allow the acoustic potential and its derivatives to be sampled at any point of the envelope $\partial\Omega_m$ (see Fig. 4.6).

We solve the problem defined in Fig. 4.6 considering that the sound field in the domain $\Omega_{in,m}$ can be predicted independently of the sound propagation occurring in Ω. This approach can also be referred to as *one-way coupling*. The number of inner domains, such as $\Omega_{in,m}$, is not a limitation, provided that it is possible to define a region where the flow can be considered potential and the backscattered field towards $\Omega_{in,m}$ is negligible at any instance. Assume that the acoustic field in $\Omega_{in,m}$ is known. The solution in $\Omega_{in,m}$ can then be interpolated over $\partial\Omega_m$ and projected along $\partial\Omega$ using Eq. (4.15). The scattering problem in the domain Ω is then solved by means of Eq. (4.21).

Hence, we rewrite Eq. (4.21) for the problem in Fig. 4.6 to give

$$\begin{aligned}\hat{C}(\mathbf{x}_p)\phi(\mathbf{x}_p) = &\int_{\partial\Omega}\left[G\left(\frac{\partial\phi}{\partial n}-\frac{\partial\phi}{\partial x}n_x M_\infty^2\right)-\phi\left(\frac{\partial G}{\partial n}-\frac{\partial G}{\partial x}n_x M_\infty^2\right)-2\mathrm{i}k\mathbf{M}_0\cdot\mathbf{n}\phi G\right]dS(\mathbf{x})\\ &+\int_{\partial\Omega_m}\left[G\left(\frac{\partial\phi}{\partial n}-\frac{\partial\phi}{\partial x}n_x M_\infty^2\right)-\phi\left(\frac{\partial G}{\partial n}-\frac{\partial G}{\partial x}n_x M_\infty^2\right)-2\mathrm{i}k\mathbf{M}_0\cdot\mathbf{n}\phi G\right]dS(\mathbf{x}),\end{aligned} \tag{4.87}$$

where $G = G(\mathbf{x}_p, \mathbf{x})$ and $\phi = \phi(\mathbf{x})$. Note that $\mathbf{x}_p$ is a point external to $\partial\Omega_m$. We also assume that the solution along the surface $\partial\Omega_m$ is known and extend the problem to M

inner domains. The above equation can be rewritten by using Eq. (4.86) as

$$\hat{C}(\mathbf{x}_p)\phi(\mathbf{x}_p) = \int_{\partial\Omega}\left[G\left(\frac{\partial\phi}{\partial n} - \frac{\partial\phi}{\partial x}n_x M_\infty^2\right) - \phi\left(\frac{\partial G}{\partial n} - \frac{\partial G}{\partial x}n_x M_\infty^2\right) - 2\mathrm{i}k\mathbf{M}_0\cdot\mathbf{n}\phi G\right]dS(\mathbf{x}) + \sum_{m=1}^{\mathrm{M}}\int_{\partial\Omega_m}\left[G\left(\mathbf{u}_s'\cdot\mathbf{n} - u_{s,x}' n_x M_\infty^2\right) - \phi_s\left(\frac{\partial G}{\partial n} - \frac{\partial G}{\partial x}n_x M_\infty^2\right) - 2\mathrm{i}k\mathbf{M}_0\cdot\mathbf{n}\phi_s G\right]dS(\mathbf{x}), \tag{4.88}$$

where $\mathbf{u}_s' = (u_{s,x}', u_{s,y}', u_{s,z}')$ and ϕ_s are known values. Based on the above equation, an incident field can be derived at any point $\mathbf{x}_p \in \Omega \cup \partial\Omega$,

$$\begin{aligned}\phi_{inc}(\mathbf{x}_p) = &\sum_{m=1}^{\mathrm{M}}\int_{\partial\Omega_m} G\left(\mathbf{u}_s'\cdot\mathbf{n} - u_{s,x}' n_x M_\infty^2\right)dS(\mathbf{x}) \\ &- \sum_{m=1}^{\mathrm{M}}\int_{\partial\Omega_m}\left[\phi_s\left(\frac{\partial G}{\partial n} - \frac{\partial G}{\partial x}n_x M_\infty^2\right) + 2\mathrm{i}k\mathbf{M}_0\cdot\mathbf{n}\phi_s G\right]dS(\mathbf{x}),\end{aligned} \tag{4.89}$$

such that

$$\begin{aligned}\hat{C}(\mathbf{x}_p)\phi(\mathbf{x}_p) = &\int_{\partial\Omega}\left[G\left(\frac{\partial\phi}{\partial n} - \frac{\partial\phi}{\partial x}n_x M_\infty^2\right) - \phi\left(\frac{\partial G}{\partial n} - \frac{\partial G}{\partial x}n_x M_\infty^2\right) - 2\mathrm{i}k\mathbf{M}_0\cdot\mathbf{n}\phi G\right]dS(\mathbf{x}) \\ &+ \phi_{inc}(\mathbf{x}_p).\end{aligned} \tag{4.90}$$

4.8.2 Transformed space-time

A weakly-coupled approach can also be formulated in a Taylor–Lorentz space. Again, the main idea is to replace a generic sound source distribution with an equivalent radiating surface containing the sources, based on a Kirchhoff integral approach and Eq. (4.65). In this section, the formulation presented in Sec. 4.8.1 is rewritten in a transformed space.

4.8.2.1 Equivalent potential field

The definition of an equivalent potential field in a Taylor–Lorentz space is given in this section. Acoustic pressure and particle velocity have been rewritten as a function of ϕ and $\boldsymbol{\nabla}\phi$ in Eq. (4.86) for the physical space. Using Eqs. (4.63) and (4.70), the acoustic velocity potential and its derivatives can be written in the transformed Taylor–Lorentz space.

Consider the acoustic velocity potential ϕ as

$$\phi(\mathbf{x}) = \phi_s(\mathbf{x}), \tag{4.91}$$

where $\phi_s(\mathbf{x})$ is a known function of complex value defined on $\partial\tilde{\Omega}_m$, that is nothing but the interface between Ω_m and Ω in the transformed space. Apply a Taylor–Lorentz transform to give

$$\phi_s(\mathbf{x}) = \tilde{\phi}_s(\tilde{\mathbf{X}})\mathrm{e}^{\mathrm{i}k\left(\frac{M_\infty x}{\beta_\infty^2}+\frac{\Phi_0'(\mathbf{x})}{c_\infty}\right)} \tag{4.92}$$

or

$$\tilde{\phi}_s(\tilde{\mathbf{X}}) = \phi_s(\mathbf{x})\mathrm{e}^{-\mathrm{i}k\left(\frac{M_\infty x}{\beta_\infty^2}+\frac{\Phi_0'(\mathbf{x})}{c_\infty}\right)}. \tag{4.93}$$

Let us consider the gradient of the acoustic potential, $\boldsymbol{\nabla}\phi_s$, given by

$$\boldsymbol{\nabla}\phi = \mathbf{u}_s'(\mathbf{x}). \tag{4.94}$$

We also assume that a harmonic solution $\tilde{\phi}_s(\tilde{\mathbf{X}})\mathrm{e}^{\mathrm{i}\tilde{\omega}T}$ in the transformed space, corresponding to a physical space solution $\phi_s(\mathbf{x})\mathrm{e}^{\mathrm{i}\omega t}$, is provided. Apply the chain rule based on a Taylor–Lorentz transform (see Sec. 2.6.3) to give

$$\frac{\partial\tilde{\phi}_s}{\partial\tilde{X}}\mathrm{e}^{\mathrm{i}\tilde{\omega}T} = \left[\beta_\infty\frac{\partial\phi_s}{\partial x} - \mathrm{i}k\phi_s\left(\frac{M_\infty}{\beta_\infty}+\beta_\infty M_{0,x}'\right)\right]\mathrm{e}^{\mathrm{i}\omega t}, \tag{4.95}$$

$$\frac{\partial\tilde{\phi}_s}{\partial\tilde{Y}}\mathrm{e}^{\mathrm{i}\tilde{\omega}T} = \left[\frac{\partial\phi_s}{\partial y} - \mathrm{i}k\phi_s M_{0,y}'\right]\mathrm{e}^{\mathrm{i}\omega t}, \tag{4.96}$$

$$\frac{\partial\tilde{\phi}_s}{\partial\tilde{Z}}\mathrm{e}^{\mathrm{i}\tilde{\omega}T} = \left[\frac{\partial\phi_s}{\partial z} - \mathrm{i}k\phi_s M_{0,z}'\right]\mathrm{e}^{\mathrm{i}\omega t}. \tag{4.97}$$

Note that $\tilde{T} = \beta_\infty[t + \Phi_0'(\mathbf{x})/c_\infty^2] + M_\infty x/(c_\infty\beta_\infty)$. Since ϕ_s and $\mathbf{u}_s'$ are known values, the above equation can be rewritten:

$$\frac{\partial\tilde{\phi}_s}{\partial\tilde{X}} = \left[\beta_\infty u_{x,s}' - \mathrm{i}k\phi_s\left(\frac{M_\infty}{\beta_\infty}+\beta_\infty M_{0,x}'\right)\right]\mathrm{e}^{-\mathrm{i}k\left(\frac{M_\infty x}{\beta_\infty^2}+\frac{\Phi_0'(\mathbf{x})}{c_\infty}\right)}, \tag{4.98}$$

$$\frac{\partial\tilde{\phi}_s}{\partial\tilde{Y}} = \left[u_{y,s}' - \mathrm{i}k\phi_s M_{0,y}'\right]\mathrm{e}^{-\mathrm{i}k\left(\frac{M_\infty x}{\beta_\infty^2}+\frac{\Phi_0'(\mathbf{x})}{c_\infty}\right)}, \tag{4.99}$$

$$\frac{\partial\tilde{\phi}_s}{\partial\tilde{Z}} = \left[u_{z,s}' - \mathrm{i}k\phi_s M_{0,z}'\right]\mathrm{e}^{-\mathrm{i}k\left(\frac{M_\infty x}{\beta_\infty^2}+\frac{\Phi_0'(\mathbf{x})}{c_\infty}\right)}. \tag{4.100}$$

To derive the acoustic velocity normal to the boundary surface, $\partial\tilde{\phi}_s/\partial\tilde{n}$, the term $\boldsymbol{\nabla}_{\tilde{X}}\tilde{\phi}_s$, namely the gradient of $\tilde{\phi}_s$ in the transformed domain, is projected along the normal vector in the transformed space, $\tilde{\mathbf{n}}$. The vector $\tilde{\mathbf{n}}$ (see Sec. 2.6.3) is

$$\tilde{\mathbf{n}} = \frac{1}{\sqrt{1-M_\infty^2 n_x^2}}(\beta_\infty n_x, n_y, n_z), \tag{4.101}$$

where $\mathbf{n}$ is the normal vector to the boundary surface in the physical space. In the transformed space, $\boldsymbol{\nabla}_{\tilde{X}}\tilde{\phi}_s = (\partial\tilde{\phi}_s/\partial\tilde{X}, \partial\tilde{\phi}_s/\partial\tilde{Y}, \partial\tilde{\phi}_s/\partial\tilde{Z})$ is the gradient of the acoustic velocity

potential. Projecting $\boldsymbol{\nabla}_{\tilde{X}}\tilde{\phi}_s$ along the normal vector $\tilde{\mathbf{n}}$ gives

$$\boldsymbol{\nabla}_{\tilde{X}}\tilde{\phi}_s \cdot \tilde{\mathbf{n}} = \frac{1}{\sqrt{1-M_\infty^2 n_x^2}} \left\{ \left[\beta_\infty u'_{x,s} - \mathrm{i}k\phi_s \left(\frac{M_\infty}{\beta_\infty} + \beta_\infty M'_{0,x} \right) \right] \beta_\infty n_x \right\} \mathrm{e}^{-\mathrm{i}k\left(\frac{M_\infty x}{\beta_\infty^2} + \frac{\Phi'_0(\mathbf{x})}{c_\infty} \right)} + \frac{1}{\sqrt{1-M_\infty^2 n_x^2}} \left\{ \left[u'_{y,s} - \mathrm{i}k\phi_s M'_{0,y} \right] n_y + \left[u'_{z,s} - \mathrm{i}k\phi_s M'_{0,z} \right] n_z \right\} \mathrm{e}^{-\mathrm{i}k\left(\frac{M_\infty x}{\beta_\infty^2} + \frac{\Phi'_0(\mathbf{x})}{c_\infty} \right)}. \tag{4.102}$$

The right-hand side of Eq. (4.102) can then be simplified considering the weakly non-uniform flow ansatz and an impermeable stationary surface:

$$\boldsymbol{\nabla}_{\tilde{X}}\tilde{\phi}_s \cdot \tilde{\mathbf{n}} = \frac{1}{\sqrt{1-M_\infty^2 n_x^2}} \left[u'_{n,s} - M_\infty^2 u'_{x,s} n_x - \mathrm{i}k M_{0,n} \phi_s \right] \mathrm{e}^{-\mathrm{i}k\left(\frac{M_\infty x}{\beta_\infty^2} + \frac{\Phi'_0(\mathbf{x})}{c_\infty} \right)}, \tag{4.103}$$

where $u'_{n,s} = \mathbf{u}'_s \cdot \mathbf{n}$ and $M_{0,n} = 0$. Equations (4.93) and (4.103) describe the acoustic potential and the acoustic particle velocity in the transformed space, having been provided with the corresponding quantities in the physical space, ϕ_s and $\mathbf{u}'_s$.

4.8.2.2 Kirchhoff surface integral

In Sec. 4.4, we showed that the weakly non-uniform potential flow Helmholtz equation can be reduced to the standard Helmholtz problem in a Taylor–Lorentz space. An integral solution to this problem is well-known [43] (see Eq. (4.65)). In this section, we obtain a formulation consistent with Eq. (4.90). Extending Eq. (4.65) to M control surfaces gives

$$C(\tilde{\mathbf{X}}_p)\tilde{\phi}(\tilde{\mathbf{X}}_p) = \int_{\partial\tilde{\Omega}} \left[\tilde{G}\frac{\partial\tilde{\phi}}{\partial\tilde{n}} - \tilde{\phi}\frac{\partial\tilde{G}}{\partial\tilde{n}} \right] d\tilde{S}(\tilde{\mathbf{X}}) + \sum_{m=1}^{\mathrm{M}} \int_{\partial\tilde{\Omega}_m} \left[G\frac{\partial\tilde{\phi}}{\partial\tilde{n}} - \tilde{\phi}\frac{\partial\tilde{G}}{\partial\tilde{n}} \right] d\tilde{S}(\tilde{\mathbf{X}}), \tag{4.104}$$

where $\tilde{\phi}$ and $\partial\tilde{\phi}/\partial\tilde{n}$ along $\partial\tilde{\Omega}_m$ are given in Eqs. (4.93) and (4.102), and $\tilde{G} = \tilde{G}(\tilde{\mathbf{X}}_p, \tilde{\mathbf{X}})$.

Consistent with the above equation, the incident field generated by M radiating surfaces can be written as

$$\tilde{\phi}_{inc}(\tilde{\mathbf{X}}_p) = \sum_{m=1}^{\mathrm{M}} \int_{\partial\tilde{\Omega}_m} \left[\tilde{G}\frac{\partial\tilde{\phi}}{\partial\tilde{n}} - \tilde{\phi}\frac{\partial\tilde{G}}{\partial\tilde{n}} \right] d\tilde{S}(\tilde{\mathbf{X}}). \tag{4.105}$$

The above equation can be reformulated based on Eqs. (4.93) and (4.102), as

$$\begin{aligned}\tilde{\phi}_{inc}(\tilde{\mathbf{X}}_p) = &\sum_{m=1}^{\mathrm{M}} \int_{\partial\tilde{\Omega}_m} \frac{\tilde{G}\mathrm{e}^{-\mathrm{i}k\left(\frac{M_{\infty}x}{\beta_{\infty}^2}+\frac{\Phi_0'(\mathbf{x})}{c_{\infty}}\right)}}{\sqrt{1-M_{\infty}^2 n_x^2}} \left\{\left[\beta_{\infty}u_{x,s}' - \mathrm{i}k\phi_s\left(\frac{M_{\infty}}{\beta_{\infty}} + \beta_{\infty}M_{0,x}'\right)\right]\beta_{\infty}n_x\right\} d\tilde{S}(\tilde{\mathbf{X}}) \\ &+ \sum_{m=1}^{\mathrm{M}} \int_{\partial\tilde{\Omega}_m} \frac{\tilde{G}\mathrm{e}^{-\mathrm{i}k\left(\frac{M_{\infty}x}{\beta_{\infty}^2}+\frac{\Phi_0'(\mathbf{x})}{c_{\infty}}\right)}}{\sqrt{1-M_{\infty}^2 n_x^2}} \left\{\left[u_{y,s}' - \mathrm{i}k\phi_s M_{0,y}'\right]n_y + \left[u_{z,s}' - \mathrm{i}k\phi_s M_{0,z}'\right]n_z\right\} d\tilde{S}(\tilde{\mathbf{X}}) \\ &- \sum_{m=1}^{\mathrm{M}} \int_{\partial\tilde{\Omega}_m} \phi_s \mathrm{e}^{-\mathrm{i}k\left(\frac{M_{\infty}x}{\beta_{\infty}^2}+\frac{\Phi_0'(\mathbf{x})}{c_{\infty}}\right)} \frac{\partial\tilde{G}}{\partial\tilde{n}} d\tilde{S}(\tilde{\mathbf{X}})\end{aligned} \tag{4.106}$$

and simplified using Eq. (4.103) to give

$$\begin{aligned}\tilde{\phi}_{inc}(\tilde{\mathbf{X}}_p) = &\sum_{m=1}^{\mathrm{M}} \int_{\partial\tilde{\Omega}_m} \frac{\tilde{G}}{\sqrt{1-M_{\infty}^2 n_x^2}} \left[u_{n,s}' - M_{\infty}^2 u_{x,s}' n_x - \mathrm{i}kM_{0,n}\phi_s\right] \mathrm{e}^{-\mathrm{i}k\left(\frac{M_{\infty}x}{\beta_{\infty}^2}+\frac{\Phi_0'(\mathbf{x})}{c_{\infty}}\right)} d\tilde{S}(\tilde{\mathbf{X}}) \\ &- \sum_{m=1}^{\mathrm{M}} \int_{\partial\tilde{\Omega}_m} \phi_s \mathrm{e}^{-\mathrm{i}k\left(\frac{M_{\infty}x}{\beta_{\infty}^2}+\frac{\Phi_0'(\mathbf{x})}{c_{\infty}}\right)} \frac{\partial\tilde{G}}{\partial\tilde{n}} d\tilde{S}(\tilde{\mathbf{X}}),\end{aligned} \tag{4.107}$$

such that

$$C(\tilde{\mathbf{X}}_p)\tilde{\phi}(\tilde{\mathbf{X}}_p) = \int_{\partial\tilde{\Omega}} \left[\tilde{G}\frac{\partial\tilde{\phi}}{\partial\tilde{n}} - \tilde{\phi}\frac{\partial\tilde{G}}{\partial\tilde{n}}\right] d\tilde{S}(\tilde{\mathbf{X}}) + \tilde{\phi}_{inc}(\tilde{\mathbf{X}}_p). \tag{4.108}$$

Equation (4.107) equates a left-hand side in the transformed space to a right-hand side where the integral is performed along the deformed surface. However, the corresponding integrand is defined in the physical space, where ϕ_s and $\mathbf{u}_s'$ are provided. The dependence between the physical and transformed space coordinates, given in Eq. (2.56), can be used to relate every point $\tilde{\mathbf{X}}$ to $\mathbf{x}$ and, therefore, recover the value of the corresponding dependent variables. In conclusion, Eqs. (4.104) and (4.107) can be used to solve a weakly-coupled problem in the transformed space to predict sound propagation.

4.9 Summary

Boundary integral solutions to the weakly non-uniform flow wave equation have been presented. Time harmonic solutions have been provided both in a physical and in a transformed Taylor–Lorentz space-time, based on the assumption that $M_{\infty} \ll 1$ and $M_0' \ll M_{\infty}$. It has been shown that the weakly non-uniform flow Helmholtz equation is consistent with a combination of the physical models associated with Taylor and Lorentz transformations and it reduces to the standard Helmholtz equation with quiescent media when the combined transform is applied.

The Taylor–Lorentz transform has been used either to derive a free-field Green's function for the integral solution in the physical space or to reduce the weakly non-uniform flow formulation to the standard Helmholtz equation with quiescent media. Note that the formulations provided in either the physical or the transformed space are consistent with the weakly non-uniform flow ansatz. In other words, differences of order $M_\infty M_0'$ and $M_0'^2$ may arise between the corresponding solutions. An error analysis of the weakly non-uniform wave equation against the reference physical model, i.e. the linearised potential wave equation, has been presented. It is expected that the accuracy of the approximate formulation increases in the acoustic near field and in the geometric far field. Nonetheless, the error is constant once the uniform mean flow domain is reached. These conclusions will be further validated using numerical examples in Chapters 6-8.

Based on further assumptions, namely neglecting terms of order M_∞^2, a solution to the Taylor wave equation was also presented in the physical space, complementing the work of Astley and Bain [32] where the formulation was developed in a transformed space. Unlike the formulation consistent with the Taylor–Lorentz physical model, that based on the Taylor wave equation is not exact for wave propagation in a uniform flow.

A weakly-coupled formulation to predict noise radiation and scattering has been presented based on the integral solutions to the weakly non-uniform wave equation. Solutions in either the physical or the transformed space have been proposed. They allow a high-fidelity near-field solution or sound source model to be sampled on a control surface. The surface is then used to radiate the acoustic field and solve a scattering problem. The two main assumptions are that the control surface lies on a potential flow and that the backscattered field towards the radiating surface is weak compared to the incident field. This is always the case if the source domain is acoustically compact.

The integral solutions developed in this chapter will be used to solve either boundary element or wave extrapolation problems. In the following chapter, a boundary element approach is proposed to solve the integral solutions either in the physical or in the transformed space.

Chapter 5

Boundary Element Model

Contents

In this chapter, we propose discrete solutions to the formulations developed in Chapter 4 to solve sound radiation and scattering in a non-uniform flow. In Sec. 5.1, the background to the modelling practices adopted in the rest of this chapter is presented. In Sec. 5.2, we derive discrete linear models to solve the integral formulation in the physical space associated with the weakly non-uniform wave equation. A combined integral formulation and a generalized Burton–Miller approach are proposed to work around the non-uniqueness issue. In Sec. 5.3, a boundary element model is presented in a transformed Taylor–Lorentz space. Concluding remarks are then provided.

5.1 Overview

The boundary element method [90] is based on integral formulations relating the physical variables in the domain to their distribution on the boundary of the domain. First, the

solution is computed on the boundary. Second, the boundary integral is used to evaluate the solution at any point of the domain. The boundary integral solutions presented in Secs. 4.3 and 4.7 are suitable for this method.

For wave propagation with quiescent media, the solution on the boundary can be evaluated based on either a collocation [43] or a variational formulation [89, 139]. The variational formulation requires a double integration over the boundary surface. This leads to a higher computational cost compared to a collocation formulation in which a single integration over the boundary is performed. However, for quiescent media a variational formulation facilitates the implementation of the Burton–Miller approach [51]. The double integration over the boundary surface simplifies the regularisation of the hyper-singular integrals [191] developed by this approach [145, 192]. The Burton–Miller formulation provides robust solutions to large-scale short-wavelength external sound propagation problems because it gets around the non-uniqueness issue that inevitably affects the accuracy of conventional boundary element solutions at resonant frequencies of an associated interior problem.

Another substantial distinction is made between direct and indirect boundary element formulations. A direct formulation is generally provided in terms of primary physical variables, such as acoustic pressure and acoustic velocity potential, and can be used to solve either external or internal noise propagation. However, it is not able to provide solutions in the presence of open surfaces or coupled internal-external sound propagation problems. On the other hand, an indirect formulation [193] can also cope with these problems and is generally provided in terms of double layer and single layer potential, namely the difference in acoustic pressure and particle velocity across the boundary surface.

In this work, we are interested in solving external sound propagation in unbounded domains. Nonetheless, for the applications of interest to this thesis, such as the prediction of large-scale aircraft acoustic installation effects, closed surfaces are usually modelled [26, 45]. Therefore, we have chosen a direct formulation to solve Eq. (4.21). A variational statement is preferred to a more conventional collocation method in order to simplify the implementation of a generalized Burton–Miller formulation with mean flow. In fact, it will allow the hyper-singular integrals developed by this formulation to be regularised. However, a collocation formulation is reported in Appendix C.

The solutions based on the physical-space formulation, presented in Chapter 4, can be more easily coupled with other numerical methods than those based on the corresponding transformed space-time; the former formulation do not require geometry and boundary conditions to be modified. On the other hand, boundary element solutions in a Taylor–Lorentz space can exploit the numerical techniques developed for wave propagation with quiescent media [43]; the transformed-space formulation can rely on the methods developed to work around the non-uniqueness issue [50, 51] and fast algorithms for high-frequency problems [24, 194]. However, the resulting BE kernel in the transformed space will not generally be consistent with that for wave propagation with quiescent media [43, 91] because

of modified boundary conditions. To work around this drawback, an iterative approach is proposed in this chapter for velocity boundary conditions.

5.2 Physical space-time

A boundary element formulation is devised to solve Eq. (4.21) in the physical space. First, a convenient form of the integral solution to the weakly non-uniform flow is derived. Second, the formulation is discretised based on a variable expansion. Then, an equivalent solution to the Taylor formulation is presented. Finally, we propose solutions to work around the non-uniqueness issue.

5.2.1 Reference formulation

Consider the weakly non-uniform potential flow Helmholtz equation, Eq. (4.2),

$$k^2\phi - 2\mathrm{i}k\mathbf{M}_0\cdot\boldsymbol{\nabla}\phi + \boldsymbol{\nabla}^2\phi - M_\infty^2\frac{\partial^2\phi}{\partial x^2} = g(\mathbf{x}). \tag{5.1}$$

Following the procedure shown in Sec. 4.3, Eq. (4.11) is multiplied by ϕ and Eq. (5.1) by G. The difference between these equations integrated over the domain Ω is rewritten using the divergence theorem to give

$$\begin{aligned}\hat{C}(\mathbf{x}_p)\phi(\mathbf{x}_p) = &\int_\Omega Gg\ dV(\mathbf{x}) + \int_{\partial\Omega}\left[G\frac{\partial\phi}{\partial n} - \phi\frac{\partial G}{\partial n} - 2\mathrm{i}k\mathbf{M}_0\cdot\mathbf{n}G\phi\right]dS(\mathbf{x})\\ &- \int_{\partial\Omega}\left[M_\infty^2\left(G\frac{\partial\phi}{\partial x} - \phi\frac{\partial G}{\partial x}\right)n_x\right]dS(\mathbf{x}),\end{aligned} \tag{5.2}$$

where $G = G(\mathbf{x}_p, \mathbf{x})$, $\phi = \phi(\mathbf{x})$ and $\mathbf{x}\in\partial\Omega$, unless otherwise stated. We denote with $\mathbf{x}_p$ an arbitrary point either in Ω or on $\partial\Omega$. In the above equation, $\mathbf{M}_0(\mathbf{x})$ and $\mathbf{n}(\mathbf{x})$ are provided along the surface $\partial\Omega$ (see Fig. 4.1) assuming a steady potential flow solution.

Equation (5.2) can be rewritten replacing the derivative along the direction of the uniform mean flow at infinity as [40]

$$\frac{\partial\phi}{\partial x} = \frac{\partial\phi}{\partial n}\frac{\partial n}{\partial x} + \frac{\partial\phi}{\partial\tau}\frac{\partial\tau}{\partial x} + \frac{\partial\phi}{\partial\eta}\frac{\partial\eta}{\partial x} = \frac{\partial\phi}{\partial n}n_x + \frac{\partial\phi}{\partial\tau}\tau_x + \frac{\partial\phi}{\partial\eta}\eta_x, \tag{5.3}$$

where τ and η denote the coordinates along the unit tangent vectors $\boldsymbol{\tau}$ and $\boldsymbol{\eta}$ on $\partial\Omega$, such that the normal vector to the boundary is given by $\mathbf{n} = \boldsymbol{\tau}\times\boldsymbol{\eta}$ (see Fig. 5.1). The x-component of the tangent vectors to the boundary surface are denoted as τ_x and η_x. Using

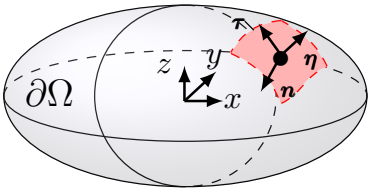

Figure 5.1: Boundary surface with tangent and normal vectors to an element patch.

Eq. (5.3) in Eq. (5.2) yields

$$\begin{aligned}\hat{C}(\mathbf{x}_p)\phi(\mathbf{x}_p) = &\int_{\partial\Omega}\left[G\frac{\partial\phi}{\partial n} - \phi\frac{\partial G}{\partial n} - 2ik\mathbf{M}_0\cdot\mathbf{n}G\phi\right]dS(\mathbf{x})\\ &- \int_{\partial\Omega} M_\infty^2\left[G\left(\frac{\partial\phi}{\partial n}n_x + \frac{\partial\phi}{\partial\tau}\tau_x + \frac{\partial\phi}{\partial\eta}\eta_x\right) - \phi\frac{\partial G}{\partial x}\right]n_x dS(\mathbf{x}) + \phi_{inc}(\mathbf{x}_p),\end{aligned} \tag{5.4}$$

where the incident field is

$$\phi_{inc}(\mathbf{x}_p) = \int_\Omega G(\mathbf{x}_p,\mathbf{x})g(\mathbf{x})dV(\mathbf{x}). \tag{5.5}$$

Equation (5.4) is convenient from a computational point of view because the tangential derivatives can be discretised as a sum of derivatives of the interpolating functions multiplied by the nodal values of ϕ [40]. This approach is discussed in Sec. 5.2.2.

5.2.2 Variable expansion

The field variables in Eq. (5.4) can be interpolated based on the discretisation of the computational domain. A polynomial interpolation is proposed. Let us consider a discrete system with N_{dof} degrees of freedom. As conventionally used for boundary element solutions with quiescent media [43], we can approximate ϕ and $\partial\phi/\partial n$ in Eq. (5.4) as

$$\phi(\mathbf{x}) \simeq \sum_{j=1}^{\mathrm{N_{dof}}} N_j(\mathbf{x})\phi_j, \tag{5.6}$$

$$\frac{\partial\phi(\mathbf{x})}{\partial n} \simeq \sum_{j=1}^{\mathrm{N_{dof}}} N_j(\mathbf{x})\frac{\partial\phi_j}{\partial n}, \tag{5.7}$$

where $N_j(\mathbf{x})$ is the j-th shape function and ϕ_j and $\partial\phi_j/\partial n$ denote the nodal degrees of freedom. Lagrange polynomials and an isoparametric formulation are adopted in this work (see Fig. 5.2 and 5.3).

The derivatives of ϕ in the tangential directions (see Eq. (5.4)) are discretised by deriving the known shape functions along $\boldsymbol{\tau}$ and $\boldsymbol{\eta}$ rather than retaining the corresponding derivatives of the acoustic potential as degrees of freedom. The approach proposed by Wu and Lee [40]

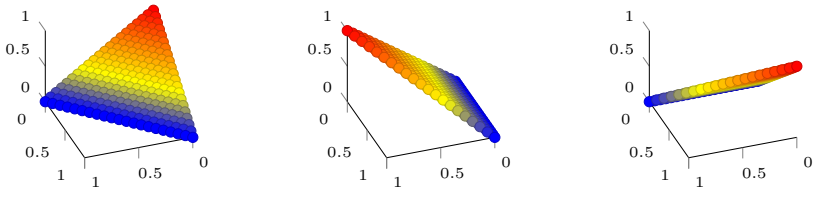

(a) linear

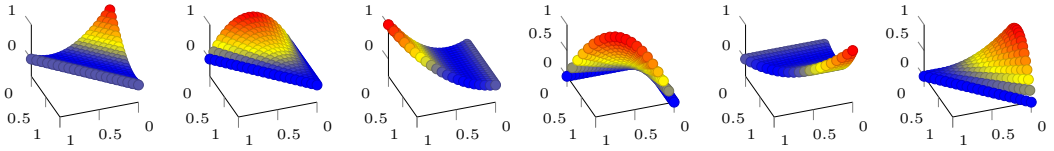

(b) quadratic

Figure 5.2: Example of linear and quadratic Lagrange triangular shape functions.

for a uniform mean flow is used in this instance:

$$\frac{\partial \phi(\mathbf{x})}{\partial \tau} \simeq \sum_{j=1}^{\mathrm{N_{dof}}} \frac{\partial N_j(\mathbf{x})}{\partial \tau} \phi_j \tag{5.8}$$

and

$$\frac{\partial \phi(\mathbf{x})}{\partial \eta} \simeq \sum_{j=1}^{\mathrm{N_{dof}}} \frac{\partial N_j(\mathbf{x})}{\partial \eta} \phi_j. \tag{5.9}$$

Consider that the polynomial interpolating function $N(\mathbf{x})$ must be at least linear to allow the above terms to be computed. If $N(\mathbf{x})$ is linear, a piecewise discontinuous approximation of the tangential derivatives is performed. The variable discretisation proposed in this section is used to formulate a linear system of equations based on Eq. (5.4).

5.2.3 Discrete model

A boundary integral solution to the weakly non-uniform flow equation has been given in Eq. (5.4) and a suitable variable expansion has been presented in Eqs. (5.6)–(5.9). A variational formulation of Eq. (5.4) is here presented. For this formulation, we derive a linear system of equations and describe the numerical approach used to compute the coefficients of its matrices.

5.2.3.1 Variational formulation

First, we use a Galerkin method and impose the condition that the residuals in Eq. (5.4) are orthogonal to a test function ϕ^*. In the presence of the generic source term, g, the

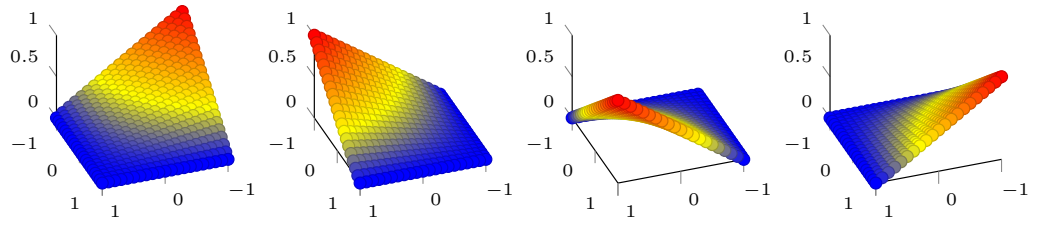

(a) linear

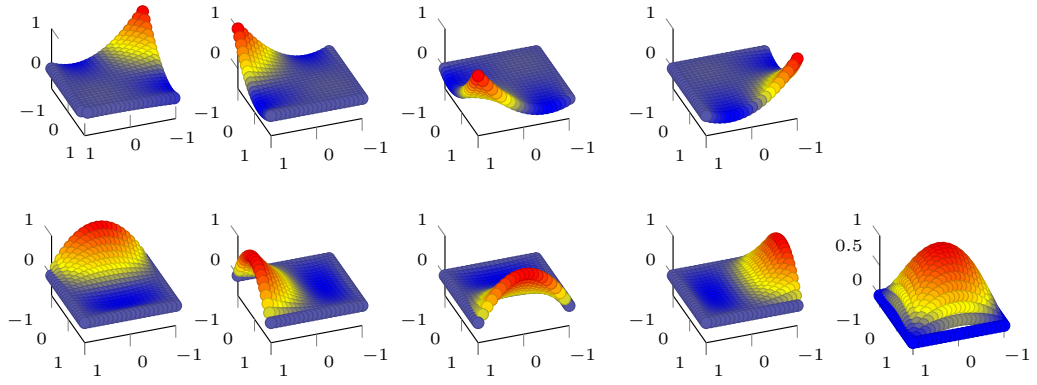

(b) quadratic

Figure 5.3: Example of linear and quadratic Lagrange quadrangular shape functions.

projection of the residuals of Eq. (5.4) on ϕ^* gives

$$\begin{aligned}
&\int_{\partial\Omega} \phi^*(\mathbf{x}_p)\hat{C}(\mathbf{x}_p)\phi(\mathbf{x}_p)dS(\mathbf{x}_p) = \int_{\partial\Omega}\int_{\Omega} \phi^*(\mathbf{x}_p)Gg(\mathbf{x})dV(\mathbf{x})dS(\mathbf{x}_p) \\
&+ \int_{\partial\Omega}\int_{\partial\Omega} \phi^*(\mathbf{x}_p)\left(G\frac{\partial\phi}{\partial n} - \phi\frac{\partial G}{\partial n} - 2\mathrm{i}k\mathbf{M}_0\cdot\mathbf{n}G\phi\right)dS(\mathbf{x})dS(\mathbf{x}_p) \\
&- \int_{\partial\Omega}\int_{\partial\Omega} \phi^*(\mathbf{x}_p)M_\infty^2\left[G\left(\frac{\partial\phi}{\partial n}n_x + \frac{\partial\phi}{\partial\tau}\tau_x + \frac{\partial\phi}{\partial\eta}\eta_x\right) - \phi\frac{\partial G}{\partial x}\right]n_x dS(\mathbf{x})dS(\mathbf{x}_p),
\end{aligned} \tag{5.10}$$

where "*" denotes the complex conjugate and $G = G(\mathbf{x}_p, \mathbf{x})$. Note that ϕ^* is bounded and uniquely defined on the boundary of the domain $\partial\Omega$.

5.2.3.2 Linear system

A discrete form of Eq. (5.10) is presented in this section. The dependent variables ϕ and $\partial\phi/\partial n$ are discretised as in Sec. 5.2.2. The same interpolating functions as those used for ϕ are used to approximate $\phi^*(\mathbf{x})$ to give

$$\boldsymbol{A\phi} + \boldsymbol{B}\frac{\partial\boldsymbol{\phi}}{\partial n} = \boldsymbol{F} \tag{5.11}$$

where the coefficients

$$\begin{aligned} A^{(lm)} = & \int_{\partial\Omega} N_l(\mathbf{x}_p)\delta_{lm}\hat{C}(\mathbf{x}_p)dS(\mathbf{x}_p) \\ & + \int_{\partial\Omega}\int_{\partial\Omega} N_l(\mathbf{x}_p)\left(\frac{\partial G}{\partial n} - M_\infty^2\frac{\partial G}{\partial x}n_x\right)N_m(\mathbf{x})dS(\mathbf{x})dS(\mathbf{x}_p) \\ & + \int_{\partial\Omega}\int_{\partial\Omega} N_l(\mathbf{x}_p)\left[M_\infty^2 G\left(\frac{\partial N_m(\mathbf{x})}{\partial\tau}\tau_x + \frac{\partial N_m(\mathbf{x})}{\partial\eta}\eta_x\right)n_x\right]dS(\mathbf{x})dS(\mathbf{x}_p), \end{aligned} \tag{5.12}$$

$$B^{(lm)} = -\int_{\partial\Omega}\int_{\partial\Omega} N_l(\mathbf{x}_p)G\left[1 - M_\infty^2 n_x^2\right]N_m(\mathbf{x})dS(\mathbf{x})dS(\mathbf{x}_p) \tag{5.13}$$

and the forcing term gives

$$F^{(l)} = \int_{\partial\Omega}\int_{\Omega} N_l(\mathbf{x}_p)Gg(\mathbf{x})dV(\mathbf{x})dS(\mathbf{x}_p), \tag{5.14}$$

with $G = G(\mathbf{x}_p, \mathbf{x})$, and $l = 1, 2, ..., N_{dof}$ and $m = 1, 2, ..., N_{dof}$ are the l-th row and m-th column of the corresponding matrix/vector. The Kronecker delta is denoted by δ_{lm}. In Eq. (5.12), $\mathbf{M}_0 \cdot \mathbf{n} = 0$ has been imposed. This is always applicable to impermeable stationary surfaces because this condition is imposed on the mean flow rather than on the acoustic field.

For a variational formulation, the integration over the boundary surface, $\partial\Omega$, is performed twice. The singularity of the Green's function complicates the convergence of the integrals performed over adjacent or overlapped elements. To improve the accuracy of the numerical integration, either a singularity subtraction [195] or a singularity cancellation method [196] can be performed. Note that the order of singularity of the Green's function defined in Eq. (4.38) is the same as that for the Green's function of the standard Helmholtz operator with quiescent media [43], i.e. $1/R_M$ for 3D problems and $\log(R_M)$ for 2D problems. Therefore, conventional approaches used to integrate across the singularity can be extended to the present formulation. In this work, for 2D problems, the singularity issue is solved in the same way as in the work of Bonnet and Guiggiani [197] where a singularity subtraction is performed followed by a transformation of the domain of integration, while the integration over the singularity is performed using a log-weighted Gauss quadrature [89]. On the other hand, for 3D problems, the solution proposed by Sauter and Schwab [198] can be applied to map the space of integration over triangles where the integrand becomes smooth and, therefore, to allow the use of a conventional Gauss quadrature in order to evaluate the integral.

In Eq. (5.11), either ϕ or $\partial\phi/\partial n$ is assigned on the boundary surface. Alternatively, a linear relation between ϕ and $\partial\phi/\partial n$, such as for impedance boundary conditions, can be prescribed to solve the boundary element problem. After solving the system of equations in Eq. (5.11), the solution at any point of the domain, Ω, can be evaluated, based on Eq. (5.4), as

$$\phi(\mathbf{x}_p) = \boldsymbol{C}\boldsymbol{\phi} + \boldsymbol{D}\frac{\partial\boldsymbol{\phi}}{\partial n} + F_p, \tag{5.15}$$

where $\mathbf{x}_p$ is a generic collocation point in the domain,

$$C^{(m)} = -\int_{\partial\Omega} N_m(\mathbf{x}) \left(\frac{\partial G}{\partial n} + 2\mathrm{i}k\mathbf{M_0}\cdot\mathbf{n}G - M_\infty^2 \frac{\partial G}{\partial x} n_x \right) dS(\mathbf{x}) + \int_{\partial\Omega} \left[M_\infty^2 G \left(\frac{\partial N_m(\mathbf{x})}{\partial \tau}\tau_x + \frac{\partial N_m(\mathbf{x})}{\partial \eta}\eta_x \right) n_x \right] dS(\mathbf{x}), \tag{5.16}$$

$$D^{(m)} = \int_{\partial\Omega} N_m(\mathbf{x}) G \left[1 - M_\infty^2 n_x^2 \right] dS(\mathbf{x}) \tag{5.17}$$

and

$$F_p = \int_\Omega G g dV(\mathbf{x}). \tag{5.18}$$

Note that if $\boldsymbol{\phi}$ and $\partial\boldsymbol{\phi}/\partial n$ are $N_{dof} \times 1$ nodal value vectors, $\boldsymbol{C}$ and $\boldsymbol{D}$ are $1 \times N_{dof}$ vectors. The coefficients of the matrices in Eqs. (5.11) and (5.15) must be evaluated numerically.

Equation (5.15) is also applicable to a permeable surface. It can be used for wave extrapolation if ϕ and $\partial\phi/\partial n$ are prescribed along $\partial\Omega$. For impermeable surfaces, the condition $\mathbf{M}_0 \cdot \mathbf{n} = 0$ applies, while for permeable surfaces, the normal component of the Mach number to the surface does not generally vanish.

5.2.3.3 Numerical integration

The approach used in this work to compute the integrals in Eq. (5.12)-(5.14) and (5.16)-(5.18) is reviewed in this section [43]. The discretisation of the boundary, $\partial\Omega$, allows the boundary integral formulation in Eq. (5.4) to be written as a summation of integrals performed along the discrete boundary surface, namely $\int_{\partial\Omega} = \sum_{m=1}^{\mathrm{N_e}} \int_{\partial\Omega_m}$ where N_e is the number of elements. Therefore, local shape functions $N_p^{(m)}(\xi,\zeta)$ can be defined on a reference element in lieu of global shape functions. Every element, m, is mapped on that reference where the integration is then performed (see Fig. 5.4):

$$\begin{aligned} x(\xi,\zeta) &= \sum_{p=1}^{\mathrm{dof_e}} N_p^{(m)}(\xi,\zeta) x_p, \\ y(\xi,\zeta) &= \sum_{p=1}^{\mathrm{dof_e}} N_p^{(m)}(\xi,\zeta) y_p, \\ z(\xi,\zeta) &= \sum_{p=1}^{\mathrm{dof_e}} N_p^{(m)}(\xi,\zeta) z_p, \end{aligned} \tag{5.19}$$

where dof_e is the number of degrees of freedom per element. The normal vector, $\boldsymbol{v}$, to a generic element of the boundary can be written as [43]

$$\boldsymbol{v}(\xi,\zeta) = \begin{bmatrix} \boldsymbol{i} & \boldsymbol{j} & \boldsymbol{k} \\ \frac{\partial x}{\partial \xi} & \frac{\partial y}{\partial \xi} & \frac{\partial z}{\partial \xi} \\ \frac{\partial x}{\partial \zeta} & \frac{\partial y}{\partial \zeta} & \frac{\partial z}{\partial \zeta} \end{bmatrix} = v_x\boldsymbol{i} + v_y\boldsymbol{j} + v_z\boldsymbol{k}. \tag{5.20}$$

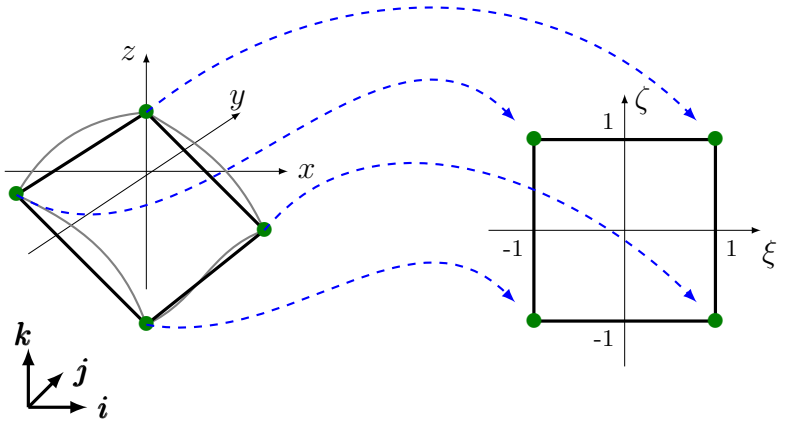

Figure 5.4: Mapping of a quadrangular linear element from the physical space to the reference domain.

Hence, the unit normal vector can be recovered as $\mathbf{n} = \boldsymbol{\upsilon}/J_g$, where J_g is the determinant of the Jacobian associated to the transformation from the physical to the reference element. It represents the ratio between the actual surface of the element and that of reference, namely $dS = J_g d\xi d\zeta$. The determinant of the Jacobian is

$$J_g = \sqrt{\upsilon_x^2 + \upsilon_y^2 + \upsilon_z^2}. \tag{5.21}$$

Gauss quadrature is then used to evaluate the integrals along every element. For a generic function, $h(x, y, z)$, and a rectangular element (see Fig. 5.4) one has

$$\int_{\partial\Omega_m} h(x,y,z)dS \simeq \int_{-1}^{1}\int_{-1}^{1} N_p(\xi,\zeta)h_p J_g d\xi d\zeta \simeq \sum_{l=1}^{\mathrm{N_g}}\sum_{m=1}^{\mathrm{N_g}} w_l w_m N_p(\xi_l,\zeta_m)h_p J_g \tag{5.22}$$

where w_l denotes the l-th Gauss weight, (ξ_l, ζ_m) are the corresponding Gauss points, N_g is the number of integration points and h_p the nodal value of h. Note that this approach is applicable also to triangular elements and two-dimensional problems.

5.2.4 Taylor–Helmholtz model

A discrete formulation is here presented for the Taylor–Helmholtz formulation (see Eq. (4.59)). With a source term, g, in the domain, the integral solution to the Taylor-Helmholtz problem is:

$$C(\mathbf{x}_p)\phi(\mathbf{x}_p) = \int_{\partial\Omega}\left[G_T\frac{\partial\phi}{\partial n} - \phi\frac{\partial G_T}{\partial n} - 2ik\mathbf{M}_0\cdot\mathbf{n}G_T\phi\right]dS(\mathbf{x}) + \int_\Omega G_T g dV(\mathbf{x}), \tag{5.23}$$

where $G_T = G_T(\mathbf{x}_p, \mathbf{x})$ and the subscript " $_T$" denotes the Taylor–Helmholtz formulation. The Mach number and the normal vector to the boundary surface are denoted by $\mathbf{M}_0(\mathbf{x})$ and $\mathbf{n}(\mathbf{x})$.

A variational statement of the above equation can be obtained by projecting the residuals along a test function ϕ^*. Then, we use the variable expansion provided in Sec. 5.2.2 to rewrite Eq. (5.23) as

$$\boldsymbol{A}_T\boldsymbol{\phi} + \boldsymbol{B}_T\frac{\partial\boldsymbol{\phi}}{\partial n} = \boldsymbol{F}_T, \tag{5.24}$$

where

$$A_T^{(lm)} = \int_{\partial\Omega} N_l(\mathbf{x}_p)\delta_{lm}C(\mathbf{x}_p)dS(\mathbf{x}_p) + \int_{\partial\Omega}\int_{\partial\Omega} N_l(\mathbf{x}_p)\frac{\partial G_T}{\partial n}N_m(\mathbf{x})dS(\mathbf{x})dS(\mathbf{x}_p), \tag{5.25}$$

$$B_T^{(lm)} = -\int_{\partial\Omega}\int_{\partial\Omega} N_l(\mathbf{x}_p)G_T N_m(\mathbf{x})dS(\mathbf{x})dS(\mathbf{x}_p), \tag{5.26}$$

and

$$F_T^{(l)} = \int_{\partial\Omega}\int_{\Omega} N_l(\mathbf{x}_p)G_T g(\mathbf{x})dV(\mathbf{x})dS(\mathbf{x}_p). \tag{5.27}$$

In Eq. (5.24), since the problem is solved for an impermeable stationary boundary surface, we have imposed that $\mathbf{M}_0 \cdot \mathbf{n} = 0$.

Once the problem on the boundary in Eq. (5.24) is solved, the solution at any point of the domain can be computed from the distribution of ϕ and $\partial\phi/\partial n$ along $\partial\Omega$, based on Eq. (5.23):

$$\phi(\mathbf{x}_p) = \boldsymbol{C}_T\boldsymbol{\phi} + \boldsymbol{D}_T\frac{\partial\boldsymbol{\phi}}{\partial n} + F_{T,p}, \tag{5.28}$$

where $\mathbf{x}_p$ is a generic point in the domain Ω,

$$C_T^{(m)} = -\int_{\partial\Omega}\left[N_m(\mathbf{x})\left(\frac{\partial G_T}{\partial n} + 2\mathrm{i}k\mathbf{M}_0\cdot\mathbf{n}G_T\right)\right]dS(\mathbf{x}), \tag{5.29}$$

$$D_T^{(m)} = \int_{\partial\Omega} N_m(\mathbf{x})G_T dS(\mathbf{x}) \tag{5.30}$$

and

$$F_{T,p} = \int_{\Omega} G_T g dV(\mathbf{x}). \tag{5.31}$$

Note that, Eq. (5.24) has been written for a generic surface either permeable or impermeable, meaning that it can also be applied for wave extrapolation. Equations (5.24) and (5.28) are nothing but a subset of Eqs. (5.11) and (5.15) obtained by neglecting terms of order M_∞^2.

5.2.5 Non-uniqueness issue

Boundary element (BE) solutions to external noise propagation suffer from the non-uniqueness issue [91]. This also pertains to boundary element solutions based on the weakly non-uniform flow integral formulation, Eq. (5.2). For wave propagation with quiescent media, the Combined Helmholtz Integral Equation Formulation (CHIEF) [50] and the Burton–Miller formulation [51] are the conventional methods used to work around this issue. In this section, we extend these methods to boundary element solutions to the weakly non-uniform flow wave equation.

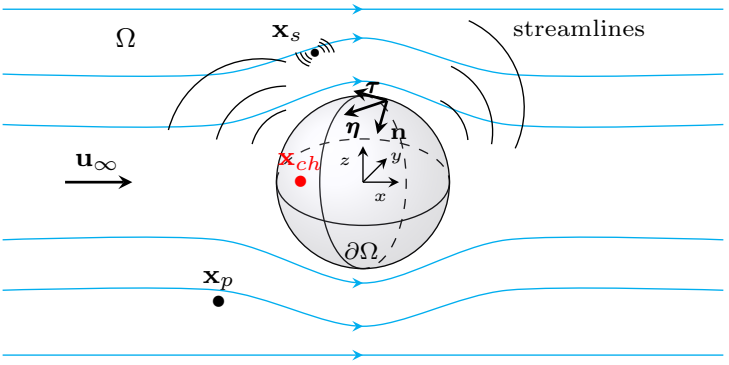

Figure 5.5: Geometry and main features of the reference problem showing an overdetermination point, $\mathbf{x}_{ch}$, for scattering of a sound field by a body in a non-uniform potential mean flow.

5.2.5.1 Generalised combined integral formulation

A combined integral equation formulation based on Eq. (5.2) is presented as a generalisation of the Combined Helmholtz Integral Equation Formulation (CHIEF) [50] including non-uniform mean flow effects. Note that, an integral solution to Eq. (4.2) for a point $\mathbf{x}_p$ either in Ω or on the boundary surface $\partial\Omega$ was given in Eq. (5.4). However, we have yet to derive the solution for a point $\mathbf{x}_p \notin \Omega \cup \partial\Omega$. First, the integral solution at the overdetermination points, namely $\mathbf{x}_p \notin \Omega \cup \partial\Omega$ or $\mathbf{x}_{ch}$ (see Fig. 5.5), is derived. Second, a linear overdetermined system of equations is set to solve the weakly non-uniform flow formulation.

Integral solution at the overdetermination points

An integral formulation at the overdetermination points, namely $\mathbf{x}_p \notin \Omega \cup \partial\Omega$, can be derived by reducing Eq. (4.2) to the standard Helmholtz equation using a Taylor–Lorentz transform (see Sec. 4.7.1). The integral equation at every overdetermination point is well-known for the standard Helmholtz equation [91] and the corresponding formulation in the physical space, therefore, can be recovered using an inverse Taylor–Lorentz transformation (see Sec. 2.6.3). The independent variables in the transformed domain $\tilde{\Omega}$ are denoted again by $(\tilde{\mathbf{X}}, \tilde{T})$ and the dependent variables by the superscript "~".

Consider the homogeneous equation associated with Eq. (4.2) and apply a Taylor–Lorentz transformation to give

$$\tilde{k}^2 \tilde{\phi} + \boldsymbol{\nabla}^2_{\tilde{X}} \tilde{\phi} = 0, \tag{5.32}$$

where $\tilde{k} = k/\beta_\infty$, $\tilde{\phi}(\tilde{\mathbf{X}})$ is the acoustic velocity potential in the Taylor–Lorentz space and $\nabla^2_{\tilde{X}}$ denotes the Laplace operator in the transformed domain. The Green's function associated with the standard Helmholtz operator in the transformed space, $\tilde{G}(\tilde{\mathbf{X}}_p, \tilde{\mathbf{X}})$, and the normal vector, $\tilde{\mathbf{n}}$, to the transformed boundary surface $\partial\tilde{\Omega}$ are both known (see Eqs. (4.67) and (4.101)).

The boundary integral solution to the standard Helmholtz equation, Eq. (5.32), is [43]

$$C(\tilde{\mathbf{X}}_p)\tilde{\phi}(\tilde{\mathbf{X}}_p) = \int_{\partial\tilde{\Omega}} \left[\tilde{G}\frac{\partial\tilde{\phi}}{\partial\tilde{n}} - \tilde{\phi}\frac{\partial\tilde{G}}{\partial\tilde{n}} \right] d\tilde{S}(\tilde{\mathbf{X}}), \tag{5.33}$$

where

$$C(\tilde{\mathbf{X}}_p) = \begin{cases} 1 & \tilde{\mathbf{X}} \in \tilde{\Omega} \\ 1 - \int_{\partial\tilde{\Omega}} \frac{\partial\tilde{G}_0}{\partial\tilde{n}} d\tilde{S}(\tilde{\mathbf{X}}) & \tilde{\mathbf{X}} \in \partial\tilde{\Omega} \end{cases} \tag{5.34}$$

and $\tilde{G}_0(\tilde{\mathbf{X}}_p, \tilde{\mathbf{X}})$ is the Green's function which solves $\boldsymbol{\nabla}^2_{\tilde{X}}\tilde{G}_0 = -\delta(\tilde{\mathbf{X}}_p - \tilde{\mathbf{X}})$. In the Taylor–Lorentz space, $C(\tilde{\mathbf{X}}_p)$ represents the portion of solid angle covered in $\tilde{\Omega}$ by an observer located at $\tilde{\mathbf{X}}_p$. As such, $C(\tilde{\mathbf{X}}_{ch}) = 0$ at every overdetermination point, i.e. $\tilde{\mathbf{X}}_{ch} \notin \tilde{\Omega} \cup \partial\tilde{\Omega}$. Hence, Eq. (5.33) can be reduced to [50]

$$0 = \int_{\partial\tilde{\Omega}} \left[\tilde{G}\frac{\partial\tilde{\phi}}{\partial\tilde{n}} - \tilde{\phi}\frac{\partial\tilde{G}}{\partial\tilde{n}} \right] d\tilde{S}(\tilde{\mathbf{X}}). \tag{5.35}$$

The above integral solution can be rewritten in the physical space introducing an inverse Taylor–Lorentz transform based on Eqs. (2.52), (2.57) and (4.101) to give

$$0 = \int_{\partial\Omega} \left[G\frac{\partial\phi}{\partial n} - \phi\frac{\partial G}{\partial n} - 2ik\mathbf{M}_0 \cdot \mathbf{n}G\phi - M_\infty^2 \left(G\frac{\partial\phi}{\partial x} - \phi\frac{\partial G}{\partial x} \right) n_x \right] dS(\mathbf{x}), \tag{5.36}$$

where $G(\mathbf{x}_{ch}, \mathbf{x})$ is given in Eq. (4.38) and $\mathbf{x}_{ch}$ denotes an overdetermination point (see Fig. 5.5). Again, in the case of an impermeable stationary surface, $\mathbf{M}_0 \cdot \mathbf{n} = 0$.

Note that a potential mean flow can be specified at any overdetermination point, although $\Phi_0'(\mathbf{x}_{ch})$ can be singular in some instances. However, recovering the mean flow potential at the overdetermination points is non-trivial except for simple geometries, e.g. flow around a cylinder or a sphere. For non-lifting subsonic flows, the integral solution at the overdetermination points can be rewritten [199] as

$$0 = \int_{\partial\Omega} \left[G_0(\mathbf{x}_{ch}, \mathbf{x})\frac{\partial\Phi_0(\mathbf{x})}{\partial n} - \Phi_0(\mathbf{x})\frac{\partial G_0(\mathbf{x}_{ch}, \mathbf{x})}{\partial n} \right] dS(\mathbf{x}), \tag{5.37}$$

with $G_0(\mathbf{x}_{ch}, \mathbf{x}) = 1/(4\pi R)$ for three-dimensional problems. Imposing the impermeability condition and separating the uniform flow contribution from the non-uniform component gives

$$\int_{\partial\Omega} \Phi_0'(\mathbf{x})\frac{\partial G_0(\mathbf{x}_{ch}, \mathbf{x})}{\partial n} dS(\mathbf{x}) = -u_\infty \int_{\partial\Omega} x\frac{\partial G_0(\mathbf{x}_{ch}, \mathbf{x})}{\partial n} dS(\mathbf{x}). \tag{5.38}$$

Although the above equation can be solved on $\partial\Omega$, a solution for $\Phi_0'(\mathbf{x}_{ch})$ cannot readily be provided.

To avoid dealing with singularities in the mean flow solution and the complication of recovering the mean flow potential at the overdeterminations points, we can simplify Eq. (5.36) based on the definition of the Green's function at the overdetermination points. First, we

rewrite the Green's function in Eq. (4.38) as

$$G(\mathbf{x}_{ch},\mathbf{x}) = G_{ch}(\mathbf{x}_{ch},\mathbf{x})\mathrm{e}^{-\mathrm{i}k\Phi_0'(\mathbf{x}_{ch})/c_\infty}, \tag{5.39}$$

where

$$G_{ch}(\mathbf{x}_{ch},\mathbf{x}) = \frac{\exp\left\{-\mathrm{i}k\left([R_M + M_\infty(x_{ch}-x)]/\beta_\infty^2 - \Phi_0'(\mathbf{x})/c_\infty\right)\right\}}{4\pi R_M}. \tag{5.40}$$

Second, we use the above equation in Eq. (5.41) and simplify the dependence on the exponential to give

$$\begin{aligned} 0 = &\int_{\partial\Omega}\left[G_{ch}(\mathbf{x}_{ch},\mathbf{x})\frac{\partial\phi}{\partial n} - \phi\frac{\partial G_{ch}(\mathbf{x}_{ch},\mathbf{x})}{\partial n}\right]dS(\mathbf{x}) \\ &- \int_{\partial\Omega}\left[2\mathrm{i}k\mathbf{M}_0\cdot\mathbf{n}G_{ch}(\mathbf{x}_{ch},\mathbf{x})\phi + M_\infty^2\left(G_{ch}(\mathbf{x}_{ch},\mathbf{x})\frac{\partial\phi}{\partial x} - \phi\frac{\partial G_{ch}(\mathbf{x}_{ch},\mathbf{x})}{\partial x}\right)n_x\right]dS(\mathbf{x}). \end{aligned} \tag{5.41}$$

In Eq. (5.41), we consider nothing but a uniform mean flow at the overdetermination points.

However, Eq. (5.41) can be further modified by dropping the dependence of $G_{ch}(\mathbf{x}_{ch},\mathbf{x})$ on the uniform mean flow component at the overdetermination points. In practice, the term $\exp[-\mathrm{i}kM_\infty x_{ch}/\beta_\infty^2]$ can be simplified as already performed with the term depending on the non-uniform mean flow component. This is simply considering a quiescent media at the overdetermination points. Nevertheless, Eq. (5.41) is just as valid as that obtained by simplifying the term $\exp[-\mathrm{i}kM_\infty x_{ch}/\beta_\infty^2]$. Numerical comparisons between these solutions are performed in Sec. 6.6. Note that, the considerations developed in this section for three-dimensional problems can be applied to two-dimensional problems based on the Green's function presented in Eq. (B.3).

Overdetermined system of equations

Equation (5.41) can be used to constrain the BE system of equations based on Eq. (5.11). Therefore, a discrete form of Eq. (5.41) is written for a number M of overdetermination points, $\mathbf{x}_{ch}$, and included in the BE system of equations, Eq. (5.11). A discrete formulation is presented.

Consider an impermeable stationary surface and an incident field, ϕ_{inc}. Rewriting the term $\partial\phi/\partial x$ in Eq. (5.41) as a combination of tangential and normal derivatives to the boundary surface $\partial\Omega$ (see Eq. (5.3)) yields

$$\begin{aligned} 0 = &\int_{\partial\Omega}\left\{G_{ch}\frac{\partial\phi}{\partial n} - \phi\frac{\partial G_{ch}}{\partial n} - M_\infty^2\left[G_{ch}\left(\frac{\partial\phi}{\partial n}n_x + \frac{\partial\phi}{\partial\tau}\tau_x + \frac{\partial\phi}{\partial\eta}\eta_x\right) - \phi\frac{\partial G_{ch}}{\partial x}\right]n_x\right\}dS(\mathbf{x}) \\ &+ \phi_{inc}(\mathbf{x}_{ch}), \end{aligned} \tag{5.42}$$

where n_x, τ_x η_x denote, again, the x-component of the associated vectors and

$$\phi_{inc}(\mathbf{x}_{ch}) = \int_{\partial\Omega} G_{ch}(\mathbf{x}_{ch}, \mathbf{x}) g(\mathbf{x}) dV(\mathbf{x}). \tag{5.43}$$

Equation (5.42) can then be discretised by using a polynomial expansion of the acoustic velocity potential and its derivatives, as in Eqs. (5.6)-(5.9):

$$\mathbf{A}_{ch}\boldsymbol{\phi} + \mathbf{B}_{ch}\frac{\partial \boldsymbol{\phi}}{\partial n} = \boldsymbol{F}_{ch}, \tag{5.44}$$

where

$$\begin{aligned} A_{ch}^{(rm)} = &\int_{\partial\Omega} \left[\frac{\partial G_{ch}(\mathbf{x}_{ch,r}, \mathbf{x})}{\partial n} - M_\infty^2 \frac{\partial G_{ch}(\mathbf{x}_{ch,r}, \mathbf{x})}{\partial x} n_x \right] N_m(\mathbf{x}) dS(\mathbf{x}) \\ &+ \int_{\partial\Omega} M_\infty^2 G_{ch}(\mathbf{x}_{ch,r}, \mathbf{x}) \left[\frac{\partial N_m(\mathbf{x})}{\partial \tau}\tau_x + \frac{\partial N_m(\mathbf{x})}{\partial \eta}\eta_x \right] n_x dS(\mathbf{x}), \end{aligned} \tag{5.45}$$

$$B_{ch}^{(rm)} = -\int_{\partial\Omega} G_{ch}(\mathbf{x}_{ch,r}, \mathbf{x})[1 - M_\infty^2 n_x^2] N_m(\mathbf{x}) dS(\mathbf{x}), \qquad F_{ch}^{(r)} = \phi_{inc}(\mathbf{x}_{ch,r}), \tag{5.46}$$

with $\mathbf{x}_{ch,r}$ the r-th overdetermination point and where $G_{ch}(\mathbf{x}_{ch,r}, \mathbf{x})$ is given in Eq. (5.40). Equation (5.44) represents a linear system of $M \times N_{dof}$ equations.

A discrete formulation to solve the weakly non-uniform flow integral formulation has been given in Eq. (5.11). A $(N_{dof} + M) \times N_{dof}$ system of equations can be recovered from the combination of Eqs. (5.11) and (5.44):

$$\begin{bmatrix} \mathbf{A} & \mathbf{B} \\ \mathbf{A}_{ch} & \mathbf{B}_{ch} \end{bmatrix} \begin{pmatrix} \boldsymbol{\phi} \\ \frac{\partial \boldsymbol{\phi}}{\partial n} \end{pmatrix} = \begin{pmatrix} \boldsymbol{F} \\ \boldsymbol{F}_{ch} \end{pmatrix}. \tag{5.47}$$

The above non-square linear system of equations can be solved using the method of least squares. While this is performed in this thesis, a Single Value Decomposition [131] can also be used to generate an equivalent square matrix obtained by reducing the collocation points by one for every additional overdetermination point [102]. After solving Eq. (5.47), the solution at any point $\mathbf{x}_p$ of the domain Ω can be computed as in Eq. (5.15).

Note that the discrete formulation in Eq. (5.47) can be rewritten based on a collocation formulation. In that case, the integral equation at the overdetermination points can be used to constrain the system of equations in Appendix C.1.

5.2.5.2 Generalised Burton–Miller formulation

In this section, we extend the Burton–Miller formulation [51] to the integral solution based on the weakly non-uniform flow formulation. A method to reduce the hyper-singularity of the integrals developed by the generalized Burton–Miller formulation is proposed. A discrete system of equations is finally devised to solve the resulting integral formulation.

Normal derivative boundary integral equation

First, the normal derivative boundary integral equation is presented. It is obtained by deriving Eq. (5.4) in the generalized normal direction $\tilde{\mathbf{n}}$ (see Sec. 2.6.3). Unlike the solution with quiescent media, mean flow effects must be included where the boundary integral solution to the weakly non-uniform flow formulation is considered. The integral formulation written in terms of particle velocity, $\partial\phi/\partial n$, cannot be recovered only by using the normal derivative to the boundary surface but it requires a generalised normal derivative. It is "generalised" in that it includes mean flow convected terms. It is simply the derivative obtained by applying an inverse Taylor–Lorentz transform to the actual normal derivative to the boundary surface in the transformed space with quiescent media.

Projecting the spacial derivative in Eq. (2.57) along $\tilde{\mathbf{n}}$ yields Eq. (2.59). For an impermeable stationary surface ($\mathbf{M}_0 \cdot \mathbf{n} = 0$), Eq. (2.59) can be simplified to

$$\frac{\partial}{\partial \tilde{n}} = \frac{1}{\sqrt{1 - M_\infty^2 n_x^2}} \left(\frac{\partial}{\partial n} - n_x M_\infty^2 \frac{\partial}{\partial x} \right). \tag{5.48}$$

The above operator is consistent with the results of Zhang and Wu [148] and Hu [41] for a uniform flow.

If we derive Eq. (5.2) in the generalized normal direction to the boundary surface $\partial\Omega$ (see Fig. 5.5) by using Eq. (5.48) and apply the impermeability condition, $\mathbf{M}_0 \cdot \mathbf{n} = 0$, along $\partial\Omega$, we get

$$\begin{aligned}
\hat{C}(\mathbf{x}_p) &\left[\frac{\partial \phi(\mathbf{x}_p)}{\partial n_p} - \frac{\partial \phi(\mathbf{x}_p)}{\partial x_p} n_{x_p} M_\infty^2 \right] + \phi(\mathbf{x}_p) \left[\frac{\partial \hat{C}(\mathbf{x}_p)}{\partial n_p} - \frac{\partial \hat{C}(\mathbf{x}_p)}{\partial x_p} n_{x_p} M_\infty^2 \right] = \\
&+ \int_{\partial\Omega} \left[\left(\frac{\partial \phi}{\partial n} - \frac{\partial \phi}{\partial x} n_x M_\infty^2 \right) \left(\frac{\partial G}{\partial n_p} - \frac{\partial G}{\partial x_p} n_{x_p} M_\infty^2 \right) \right] dS(\mathbf{x}) \\
&- \int_{\partial\Omega} \phi \left(\frac{\partial^2 G}{\partial n \partial n_p} - n_{x_p} M_\infty^2 \frac{\partial^2 G}{\partial n \partial x_p} - n_x M_\infty^2 \frac{\partial^2 G}{\partial x \partial n_p} + n_x n_{x_p} M_\infty^4 \frac{\partial^2 G}{\partial x \partial x_p} \right) dS(\mathbf{x}) \\
&+ \frac{\partial \phi_{inc}(\mathbf{x}_p)}{\partial n_p} - \frac{\partial \phi_{inc}(\mathbf{x}_p)}{\partial x_p} n_{x_p} M_\infty^2,
\end{aligned} \tag{5.49}$$

where $\mathbf{n}_p = \mathbf{n}(\mathbf{x}_p) = (n_{x_p}, n_{y_p}, n_{z_p})$ and $G = G(\mathbf{x}_p, \mathbf{x})$. The above equation is referred to as the normal derivative boundary integral equation. In combination with Eq. (5.2), Eq. (5.49) will be used to obtain the generalized Burton–Miller formulation.

In Eq. (5.49), the integral including the double derivatives of the Green's function is hyper-singular [145]. In order to solve Eq. (5.49) using a boundary element method, the hyper-singular terms need to be regularised [146]. In this instance, a reduction of the singularity will be performed. For the sake of notation, the generalized hyper-singular term is denoted as

$$\mathcal{L}_n(G) = \frac{\partial^2 G}{\partial n \partial n_p} - n_{x_p} M_\infty^2 \frac{\partial^2 G}{\partial n \partial x_p} - n_x M_\infty^2 \frac{\partial^2 G}{\partial x \partial n_p} + n_x n_{x_p} M_\infty^4 \frac{\partial^2 G}{\partial x \partial x_p}. \tag{5.50}$$

Regularisation of the hyper-singular integral

To obtain a BE solution to Eq. (5.49), the hyper-singular integral has to be evaluated. A regularisation approach is proposed for this purpose. For quiescent media, Maue [200] and Mitzner [192] have provided a regularised formulation of hyper-singular integrals of the same form as that developed whenever the Helmholtz problem with quiescent media is solved by using the Burton–Miller formulation. This formulation was used in Burton and Miller [51] and applied by Hamdi [145] to a variational statement of the conventional Burton–Miller formulation. We extend this approach to the present formulation. The variational formulation of Eq. (5.49) allows the evaluation of the Hadamard finite part to be explicitly performed.

Equation (4.2) can be reduced to the standard Helmholtz operator in a Taylor–Lorentz space. In other words, the properties associated with the integral solution to the standard Helmholtz problem can be applied to Eq. (5.49) by performing an inverse Taylor–Lorentz transform. Therefore, the hyper-singular integral in Eq. (5.49) is regularised by applying an inverse Taylor–Lorentz transform (see Sec. 2.6.3) to the formulation given by Hamdi [145] for the Helmholtz operator with quiescent media. In the transformed space, the regularised integral can be written as [145]

$$\begin{aligned} &\int_{\partial\tilde{\Omega}} \int_{\partial\tilde{\Omega}} \tilde{\phi}_p^* \frac{\partial^2 \tilde{G}}{\partial \tilde{n} \partial \tilde{n}_p} \tilde{\phi} d\tilde{S}(\mathbf{X}) d\tilde{S}(\mathbf{X}_p) \\ &= \int_{\partial\tilde{\Omega}} \int_{\partial\tilde{\Omega}} \tilde{G} \left[\tilde{k}^2 \tilde{\mathbf{n}} \cdot \tilde{\mathbf{n}}_p \tilde{\phi} \tilde{\phi}_p^* - \left(\tilde{\mathbf{n}}_p \times \boldsymbol{\nabla}_X \tilde{\phi}_p^* \right) \cdot \left(\tilde{\mathbf{n}} \times \boldsymbol{\nabla}_X \tilde{\phi} \right) \right] d\tilde{S}(\mathbf{X}) d\tilde{S}(\mathbf{X}_p). \end{aligned} \tag{5.51}$$

In the above equation, $\tilde{G} = \tilde{G}(\tilde{\mathbf{X}}_p, \tilde{\mathbf{X}})$ is the Green's function associated with the standard Helmholtz problem with quiescent media [91], $\tilde{\phi} = \tilde{\phi}(\tilde{\mathbf{X}})$ and $\tilde{\phi}_p^* = \tilde{\phi}^*(\tilde{\mathbf{X}}_p)$ are respectively the acoustic velocity potential and its complex conjugate. In the transformed space, the circular frequency is given by $\tilde{\omega} = \omega/\beta_\infty$ and the wavenumber is given by $\tilde{k} = k/\beta_\infty$.

First, the acoustic velocity potential $\tilde{\phi}(\tilde{\mathbf{X}})$ and the Green's function $\tilde{G}(\tilde{\mathbf{X}}_p, \tilde{\mathbf{X}})$ in Eq. (5.51) can be rewritten in the physical space based on Eqs. (4.35) and (4.63) as

$$\tilde{\phi}(\tilde{\mathbf{X}}) = \phi(\mathbf{x}) \mathrm{e}^{-\mathrm{i}k\left(\frac{M_\infty x}{\beta_\infty^2} + \frac{\Phi_0'(\mathbf{x})}{c_\infty}\right)} \tag{5.52}$$

and

$$\tilde{G}(\tilde{\mathbf{X}}_p, \tilde{\mathbf{X}}) = G(\mathbf{x}_p, \mathbf{x}) \mathrm{e}^{-\mathrm{i}k\left(\frac{M_\infty (x_p - x)}{\beta_\infty^2} + \frac{\Phi_0'(\mathbf{x}_p) - \Phi_0'(\mathbf{x})}{c_\infty}\right)}. \tag{5.53}$$

In Eq. (5.53), we consider a generic observer $\mathbf{x}_p$ and a point source at $\mathbf{x}$. Hence, Eq. (5.52) and (5.53) allow the dependent variables in the transformed Taylor–Lorentz space to be written as a function of their values in the physical space.

Nonetheless, the derivatives of the acoustic potential and the Green's function can be transformed according to Eqs. (5.52) and (5.53). First, we combine Eqs. (2.57) and (5.52), and use Eq. (2.56) to give

$$\boldsymbol{\nabla}_{\tilde{X}} \tilde{\phi} = \left\{ \begin{array}{c} \beta_\infty \frac{\partial \phi}{\partial x} - \mathrm{i}k\phi \left(\frac{M_\infty}{\beta_\infty} + \beta_\infty M_{0,x}'\right) \\ \frac{\partial \phi}{\partial y} - \mathrm{i}k\phi M_{0,y}' \\ \frac{\partial \phi}{\partial z} - \mathrm{i}k\phi M_{0,z}' \end{array} \right\} \mathrm{e}^{-\mathrm{i}k\left(\frac{M_\infty x}{\beta_\infty^2} + \frac{\Phi_0'(\mathbf{x})}{c_\infty}\right)} = \boldsymbol{L}(\phi) \mathrm{e}^{-\mathrm{i}k\left(\frac{M_\infty x}{\beta_\infty^2} + \frac{\Phi_0'(\mathbf{x})}{c_\infty}\right)}. \tag{5.54}$$

Note that $\boldsymbol{\nabla}_{\tilde{X}} \tilde{\phi}_p^*$ in Eq. (5.51) is the complex conjugate of the above vector evaluated at $\mathbf{x}_p$. Second, the double derivative of the Green's function on the left-hand side of Eq. (5.51) can be rewritten in the physical space using Eqs. (5.48) and (5.53). Considering an impermeable stationary boundary surface and neglecting the terms of order $M_\infty^2 M_0'$ gives (see Appendix B)

$$\frac{\partial^2 \tilde{G}}{\partial \tilde{n} \partial \tilde{n}_p} \mathrm{e}^{\mathrm{i}\tilde{\omega}T} = \frac{\mathrm{e}^{\mathrm{i}\omega t}}{\|\hat{\mathbf{n}}\| \|\hat{\mathbf{n}}_p\|} \left[\frac{\partial^2 G}{\partial n \partial n_p} - n_{x_p} M_\infty^2 \frac{\partial^2 G}{\partial n \partial x_p} - n_x M_\infty^2 \frac{\partial^2 G}{\partial x \partial n_p} + n_x n_{x_p} M_\infty^4 \frac{\partial^2 G}{\partial x \partial x_p} \right], \tag{5.55}$$

where $\hat{\mathbf{n}}(\mathbf{x}) = (\beta_\infty n_x, n_y, n_z)$ and $\hat{\mathbf{n}}_p = \hat{\mathbf{n}}(\mathbf{x}_p)$. We can write the transformed time, $\tilde{T}$, in terms of the corresponding physical value, t (see Eq. (2.56)). Based on Eq. (5.50), Eq. (5.51) yields

$$\frac{\partial^2 \tilde{G}}{\partial \tilde{n} \partial \tilde{n}_p} = \frac{\exp\left[-\mathrm{i}k\left(\frac{M_\infty (x_p - x)}{\beta_\infty^2} + \frac{\Phi_0'(\mathbf{x}_p) - \Phi_0'(\mathbf{x})}{c_\infty}\right)\right]}{\|\hat{\mathbf{n}}\| \|\hat{\mathbf{n}}_p\|} \mathcal{L}_n(G). \tag{5.56}$$

Hence, Eq. (5.51) can be formulated in the physical space using Eqs. (2.56), (4.101), (5.52)-(5.54) and (5.56) as

$$\begin{aligned} &\int_{\partial\Omega} \int_{\partial\Omega} \phi_p^* \mathcal{L}_n(G) \phi \, dS(\mathbf{x}) dS(\mathbf{x}_p) = \\ &\int_{\partial\Omega} \int_{\partial\Omega} G \left\{ \frac{k^2}{\beta_\infty^2} \hat{\mathbf{n}} \cdot \hat{\mathbf{n}}_p \phi \phi_p^* - \left[\hat{\mathbf{n}}_p \times \boldsymbol{L}(\phi_p^*)\right] \cdot \left[\hat{\mathbf{n}} \times \boldsymbol{L}(\phi)\right] \right\} dS(\mathbf{x}) dS(\mathbf{x}_p), \end{aligned} \tag{5.57}$$

where $\boldsymbol{L}(\phi)$ has been defined in Eq. (5.54) and $\boldsymbol{L}(\phi_p^*)$ is the associated complex conjugate, computed at $\tilde{\mathbf{X}}_p$. Furthermore, the terms of order $M_\infty^2 M_{0,x}'$ on the right-hand side of Eq. (5.54) can be neglected as for the weakly non-uniform ansatz. Note that the determinant of the Jacobian associated with the Taylor–Lorentz transform (see Eq. (2.52)) has been used to derive Eq. (5.57).

Boundary element formulation

Due to the so-called non-uniqueness issue [91, 140], BE solutions based on Eq. (5.4) can fail to give a unique solution to external noise propagation problems. They fail at the eigenfrequencies associated with the corresponding interior problems. This applies also to the solutions based on Eq. (5.49). For a quiescent medium, Burton and Miller [51] have shown that the combination of the Helmholtz integral equation and the corresponding normal derivative yields a unique BE solution. However, Zheng *et al.* [140] gave a numerical proof that the unique solution is obtained only for certain values of the coupling coefficient, conveniently weighting the integral equation and the associated normal derivative.

The Burton–Miller formulation for a non-uniform potential mean flow is obtained combining Eqs. (5.2) and (5.49) by means of a coupling coefficient $\alpha = \mathrm{i}\beta_\infty/k$. The coupling coefficient is recovered by applying the Taylor–Lorentz transform to the definition of α conventionally used for the standard Helmholtz problem [51, 141]. The combination of Eqs. (5.4) and (5.49) gives

$$
\begin{aligned}
&\hat{C}(\mathbf{x}_p)\phi(\mathbf{x}_p) + \alpha\left\{\hat{C}(\mathbf{x}_p)\left[\frac{\partial\phi(\mathbf{x}_p)}{\partial n_p} - \frac{\partial\phi(\mathbf{x}_p)}{\partial x_p}n_{x_p}M_\infty^2\right] + \phi(\mathbf{x}_p)\left[\frac{\partial\hat{C}(\mathbf{x}_p)}{\partial n_p} - \frac{\partial\hat{C}(\mathbf{x}_p)}{\partial x_p}n_{x_p}M_\infty^2\right]\right\} = \\
&+ \int_{\partial\Omega}\left[G\left(\frac{\partial\phi}{\partial n} - \frac{\partial\phi}{\partial x}n_x M_\infty^2\right) - \phi\left(\frac{\partial G}{\partial n} - \frac{\partial G}{\partial x}n_x M_\infty^2\right)\right] dS(\mathbf{x}) \\
&+ \alpha\int_{\partial\Omega}\left[\left(\frac{\partial\phi}{\partial n} - \frac{\partial\phi}{\partial x}n_x M_\infty^2\right)\left(\frac{\partial G}{\partial n_p} - \frac{\partial G}{\partial x_p}n_{x_p}M_\infty^2\right)\right] dS(\mathbf{x}) \\
&- \alpha\int_{\partial\Omega}\phi\left(\frac{\partial^2 G}{\partial n\partial n_p} - n_{x_p}M_\infty^2\frac{\partial^2 G}{\partial n\partial x_p} - n_x M_\infty^2\frac{\partial^2 G}{\partial x\partial n_p} + n_x n_{x_p}M_\infty^4\frac{\partial^2 G}{\partial x\partial x_p}\right) dS(\mathbf{x}) \\
&+ \phi_{inc}(\mathbf{x}_p) + \alpha\left\{\frac{\partial\phi_{inc}(\mathbf{x}_p)}{\partial n_p} - \frac{\partial\phi_{inc}(\mathbf{x}_p)}{\partial x_p}n_{x_p}M_\infty^2\right\}.
\end{aligned}
\tag{5.58}
$$

A discrete variational formulation of Eq. (5.58) is derived below. First, we rewrite the derivative $\partial\phi/\partial x$ in Eq. (5.58) based on Eq. (5.3) [40]. We then exploit Eq. (5.57) and derive a statement from Eq. (5.49) including only weakly singular integrals. Using the variable expansion in Eqs. (5.6)-(5.9) gives

$$
(\boldsymbol{A} + \alpha\boldsymbol{A}_\alpha)\boldsymbol{\phi} + (\boldsymbol{B} + \alpha\boldsymbol{B}_\alpha)\frac{\partial\boldsymbol{\phi}}{\partial n} = \boldsymbol{F} + \alpha\boldsymbol{F}_\alpha, \tag{5.59}
$$

where $\boldsymbol{A}$, $\boldsymbol{B}$ and $\boldsymbol{F}$ are the same as those in Eqs. (5.12), (5.13) and (5.14), and

$$\begin{aligned} A_{\alpha}^{(lm)} = & \int_{\partial\Omega} N_l(\mathbf{x}_p)\delta_{lm}\frac{\partial \hat{C}_m(\mathbf{x}_p)}{\partial \hat{n}_p}N_m(\mathbf{x}_p)dS(\mathbf{x}_p) \\ & - \int_{\partial\Omega} N_l(\mathbf{x}_p)\hat{C}_m(\mathbf{x}_p)\delta_{lm}M_{\infty}^2 n_{x_p}\left(\frac{\partial N_m(\mathbf{x}_p)}{\partial \tau_p}\tau_{x_p} + \frac{\partial N_m(\mathbf{x}_p)}{\partial \eta_p}\eta_{x_p}\right)dS(\mathbf{x}_p) \\ & + \int_{\partial\Omega}\int_{\partial\Omega} N_l(\mathbf{x}_p)\mathcal{L}_n(G)N_m(\mathbf{x})dS(\mathbf{x})dS(\mathbf{x}_p) \\ & + \int_{\partial\Omega}\int_{\partial\Omega}\left\{N_l(\mathbf{x}_p)\frac{\partial G}{\partial \hat{n}_p}M_{\infty}^2 n_x\left[\frac{\partial N_m(\mathbf{x})}{\partial \tau}\tau_x + \frac{\partial N_m(\mathbf{x})}{\partial \eta}\eta_x\right]\right\}dS(\mathbf{x})dS(\mathbf{x}_p), \end{aligned} \tag{5.60}$$

$$\begin{aligned} B_{\alpha}^{(lm)} = & \int_{\partial\Omega}\delta_{lm}\left[N_l(\mathbf{x}_p)C_m(\mathbf{x}_p)(1-n_{x_p}^2M_{\infty}^2)N_m(\mathbf{x}_p)\right]dS(\mathbf{x}_p) \\ & - \int_{\partial\Omega}\int_{\partial\Omega}\left[N_l(\mathbf{x}_p)\frac{\partial G}{\partial \hat{n}_p}(1-n_x^2M_{\infty}^2)N_m(\mathbf{x})\right]dS(\mathbf{x})dS(\mathbf{x}_p), \end{aligned} \tag{5.61}$$

$$F_{\alpha}^{(l)} = \int_{\partial\Omega} N_l(\mathbf{x}_p)\frac{\partial \phi_{inc}(\mathbf{x}_p)}{\partial \hat{n}_p}dS(\mathbf{x}_p), \tag{5.62}$$

where $\partial/\partial\hat{n} = (\partial/\partial n - n_x M_{\infty}^2\partial/\partial x)$, the subscript "$_p$" denotes the point $\mathbf{x}_p$ and δ_{lm} denotes the Kronecker delta function. For any geometry, the terms $\hat{C}_m(\mathbf{x}_p)$ and $\partial\hat{C}_m(\mathbf{x}_p)/\partial\hat{n}_p$ can be computed numerically based on Eq. (4.22).

The hyper-singular integral in $A_{\alpha}^{(lm)}$ can be regularised based on Eq. (5.57). Therefore, the kernel in Eq. (5.59) can be rewritten as a combination of non-singular and weakly singular integrals. For weakly singular integrals, a conventional singularity subtraction approach can be used and Gauss quadrature allows the resulting kernel to be evaluated. After solving the problem on the boundary surface $\partial\Omega$, based on Eq. (5.59), the solution in the domain Ω can be computed using Eq. (5.15). Note that for $\mathbf{M}_0 \to 0$, Eq. (5.59) reduces to the standard Burton–Miller formulation [51].

5.3 Transformed space-time

In this section, a boundary element solution to the weakly non-uniform flow formulation is presented in a transformed Taylor–Lorentz space-time (see Eq. (4.65)). The solution in the transformed space allows conventional boundary element methods, for the Helmholtz equation with quiescent media, to solve wave propagation problems with weakly non-uniform potential flow. This is achieved by transforming sources and boundary conditions consistently with the deformed space-time.

A boundary element model based on a variational formulation is presented although a collocation formulation can also be used (see Appendix C). We exploit the existing Burton–Miller formulation [51] for quiescent media to devise a solution in the transformed space. This method is used to get around the non-uniqueness issue [43]. A discrete system of equations is presented. Practical issues of using standard BE kernels for the Helmholtz problem with quiescent media to solve the transformed space formulation are discussed. An iterative approach is proposed to use conventional boundary element kernels for quiescent media to solve problems with velocity boundary conditions and to simulate mean flow effects.

5.3.1 Variational formulation

A Burton–Miller formulation based on Eq. (4.65) is proposed. The standard Burton–Miller formulation for quiescent media was initially written in terms of acoustic pressure and particle velocity [51]. However, it can be formulated equivalently for the acoustic potential, $\tilde{\phi}$. In this case, the Burton–Miller formulation will combine the boundary integral solution to the acoustic potential and its normal derivative to the boundary surface [100].

In Eq. (4.65), we define an incident field in the transformed space, $\tilde{\phi}_{inc}$, due to a volume source distribution, $\tilde{g}$, as

$$\tilde{\phi}_{inc}(\tilde{\mathbf{X}}_p) = \int_{\tilde{\Omega}} \tilde{G}(\tilde{\mathbf{X}}_p, \tilde{\mathbf{X}}) \tilde{g}(\tilde{\mathbf{X}}) d\tilde{V}(\tilde{\mathbf{X}}). \tag{5.63}$$

The Burton–Miller formulation [51] for the integral equation in the transformed space, Eq. (4.65), can be written as

$$\begin{aligned} &C(\tilde{\mathbf{X}}_p)\left[\tilde{\phi}(\tilde{\mathbf{X}}_p) + \alpha \frac{\partial \tilde{\phi}(\tilde{\mathbf{X}}_p)}{\partial \tilde{n}_p}\right] + \alpha \frac{\partial C(\tilde{\mathbf{X}}_p)}{\partial \tilde{n}_p} \tilde{\phi}(\tilde{\mathbf{X}}_p) = \\ &+ \int_{\partial\tilde{\Omega}} \left[\tilde{G}\frac{\partial \tilde{\phi}}{\partial \tilde{n}} - \tilde{\phi}\frac{\partial \tilde{G}}{\partial \tilde{n}} + \alpha\left(\frac{\partial \tilde{G}}{\partial \tilde{n}_p}\frac{\partial \tilde{\phi}}{\partial \tilde{n}} - \tilde{\phi}\frac{\partial^2 \tilde{G}}{\partial \tilde{n}\partial \tilde{n}_p}\right)\right] d\tilde{S}(\tilde{\mathbf{X}}) + \tilde{\phi}_{inc}(\tilde{\mathbf{X}}_p) + \alpha \frac{\partial \tilde{\phi}_{inc}(\tilde{\mathbf{X}}_p)}{\partial \tilde{n}_p}, \end{aligned} \tag{5.64}$$

where $\tilde{\mathbf{n}}_p$ is the normal vector to the boundary surface $\partial\tilde{\Omega}$ at a collocation point $\tilde{\mathbf{X}}_p$ (see Fig. 2.3) and $\tilde{G} = \tilde{G}(\tilde{\mathbf{X}}_p, \tilde{\mathbf{X}})$. The coupling parameter is denoted by α and is prescribed

based on the work of Burton and Miller [51] as $\alpha = \mathrm{i}/\tilde{k}$, where $\tilde{k} = k/\sqrt{1-M_\infty^2}$. For smooth surfaces, the coefficient $C_m(\tilde{\mathbf{X}}_p)$ is equal to 0.5 [91].

A variational formulation of Eq. (5.64) can be written introducing a test function $\tilde{\phi}^*$ to give

$$\begin{aligned}
&\int_{\partial\tilde{\Omega}} \tilde{\phi}^*(\tilde{\mathbf{X}}_p) \left\{ C(\tilde{\mathbf{X}}_p) \left[\tilde{\phi}(\tilde{\mathbf{X}}_p) + \alpha \frac{\partial \tilde{\phi}(\tilde{\mathbf{X}}_p)}{\partial \tilde{n}_p} \right] + \alpha \frac{\partial C(\tilde{\mathbf{X}}_p)}{\partial \tilde{n}_p} \tilde{\phi}(\tilde{\mathbf{X}}_p) \right\} d\tilde{S}(\tilde{\mathbf{X}}_p) = \\
&+ \int_{\partial\tilde{\Omega}} \tilde{\phi}^*(\tilde{\mathbf{X}}_p) \left\{ \int_{\partial\tilde{\Omega}} \left[\tilde{G} \frac{\partial \tilde{\phi}}{\partial \tilde{n}} - \tilde{\phi} \frac{\partial \tilde{G}}{\partial \tilde{n}} \right] dS(\tilde{\mathbf{X}}) + \tilde{\phi}_{inc}(\tilde{\mathbf{X}}_p) \right\} d\tilde{S}(\tilde{\mathbf{X}}_p) \\
&+ \alpha \int_{\partial\tilde{\Omega}} \tilde{\phi}^*(\tilde{\mathbf{X}}_p) \left\{ \int_{\partial\tilde{\Omega}} \left[\frac{\partial \tilde{G}}{\partial \tilde{n}_p} \frac{\partial \tilde{\phi}}{\partial \tilde{n}} - \tilde{\phi} \frac{\partial^2 \tilde{G}}{\partial \tilde{n} \partial \tilde{n}_p} \right] dS(\tilde{\mathbf{X}}) + \frac{\partial \tilde{\phi}_{inc}(\tilde{\mathbf{X}}_p)}{\partial \tilde{n}_p} \right\} d\tilde{S}(\tilde{\mathbf{X}}_p),
\end{aligned} \tag{5.65}$$

where $\tilde{\phi}^*$ is the complex conjugate of $\tilde{\phi}$. The above equation will be discretised in the following section where we derive a linear system of equations.

5.3.2 Discrete system

A discrete formulation of Eq. (5.65) is presented in this section. The dependent variables in Eq. (5.65) are approximated using a variable expansion based on Eqs. (5.6) and (5.7) but performed in the transformed space.

The variable expansion allows Eq. (5.65) to be rewritten as

$$(\tilde{\boldsymbol{A}} + \alpha \tilde{\boldsymbol{A}}_\alpha)\tilde{\boldsymbol{\phi}} + (\tilde{\boldsymbol{B}} + \alpha \tilde{\boldsymbol{B}}_\alpha) \frac{\partial \tilde{\boldsymbol{\phi}}}{\partial \tilde{n}} = \tilde{\boldsymbol{F}} + \alpha \tilde{\boldsymbol{F}}_\alpha, \tag{5.66}$$

where

$$\tilde{A}^{(lm)} = \int_{\partial\tilde{\Omega}} \delta_{lm} N_l(\tilde{\mathbf{X}}_p) C_m(\tilde{\mathbf{X}}_p) N_m(\tilde{\mathbf{X}}_p) d\tilde{S}(\tilde{\mathbf{X}}_p) + \int_{\partial\tilde{\Omega}} \int_{\partial\tilde{\Omega}} N_l(\tilde{\mathbf{X}}_p) \frac{\partial \tilde{G}}{\partial \tilde{n}} N_m(\tilde{\mathbf{X}}) d\tilde{S}(\tilde{\mathbf{X}}) d\tilde{S}(\tilde{\mathbf{X}}_p), \tag{5.67}$$

$$\begin{aligned}
\tilde{A}_\alpha^{(lm)} = &\int_{\partial\tilde{\Omega}} \delta_{lm} N_l(\tilde{\mathbf{X}}_p) \frac{\partial C_m(\tilde{\mathbf{X}}_p)}{\partial \tilde{n}_p} N_m(\tilde{\mathbf{X}}_p) d\tilde{S}(\tilde{\mathbf{X}}_p) \\
&+ \int_{\partial\tilde{\Omega}} \int_{\partial\tilde{\Omega}} N_l(\tilde{\mathbf{X}}_p) \frac{\partial^2 \tilde{G}}{\partial \tilde{n} \partial \tilde{n}_p} N_m(\tilde{\mathbf{X}}) d\tilde{S}(\tilde{\mathbf{X}}) d\tilde{S}(\tilde{\mathbf{X}}_p),
\end{aligned} \tag{5.68}$$

$$\tilde{B}^{(lm)} = -\int_{\partial\tilde{\Omega}} \int_{\partial\tilde{\Omega}} N_l(\tilde{\mathbf{X}}_p) \tilde{G} N_m(\tilde{\mathbf{X}}) d\tilde{S}(\mathbf{X}) d\tilde{S}(\mathbf{X}_p), \tag{5.69}$$

$$\tilde{B}_\alpha^{(lm)} = \int_{\partial\tilde{\Omega}} \delta_{lm} N_l(\tilde{\mathbf{X}}_p) C_m(\tilde{\mathbf{X}}_p) N_m(\tilde{\mathbf{X}}_p) d\tilde{S}(\mathbf{X}_p) - \int_{\partial\tilde{\Omega}} \int_{\partial\tilde{\Omega}} N_l(\tilde{\mathbf{X}}_p) \frac{\partial \tilde{G}}{\partial \tilde{n}_p} N_m(\tilde{\mathbf{X}}) d\tilde{S}(\mathbf{X}) d\tilde{S}(\mathbf{X}_p) \tag{5.70}$$

and

$$\tilde{F}^{(l)} = \int_{\partial\tilde{\Omega}} N_l(\tilde{\mathbf{X}}_p) \tilde{\phi}_{inc} d\tilde{S}(\mathbf{X}_p), \qquad \tilde{F}_\alpha^{(l)} = \int_{\partial\tilde{\Omega}} N_l(\tilde{\mathbf{X}}_p) \frac{\partial \tilde{\phi}_{inc}}{\partial \tilde{n}_p} d\tilde{S}(\mathbf{X}_p), \tag{5.71}$$

with $l = 1, 2, ..., N_{dof}$ and $m = 1, 2, ..., N_{dof}$ the l-th row and m-th column of the corresponding matrix.

The hyper-singular term in $\tilde{A}_\alpha^{(lm)}$, involving the double derivative of the Green's function, can be regularised using the formulation proposed by Mitzner [192], extended by Hamdi to a variational formulation [145]. In the transformed space, the regularised integral is the same as that in Eq. (5.51). Therefore, Eq. (5.51) allows Eq. (5.65) to be rewritten as an integral equation depending only on non-singular and weakly singular integrals. The weakly singular integrals can then be evaluated using either a singularity subtraction [195, 197] or a singularity cancellation [196] approach. In this case, the former approach is used.

Note that the boundary conditions are conventionally prescribed in the physical space and, therefore, in order to use Eq. (5.66), they must be rewritten in the transformed space. For Dirichlet boundary conditions, a conventional boundary element method for the Helmholtz problem with quiescent media can be exploited to simulate mean flow effects. In fact, the matrices $\tilde{\boldsymbol{B}}$ and $\tilde{\boldsymbol{B}}_\alpha$ are consistent with a standard boundary element formulation without mean flow [43]. However, this is not the case for velocity, pressure and Robin-type boundary conditions, such as impedance boundary conditions.

For practical boundary value problems, either the normal acoustic particle velocity, $\partial\phi/\partial n$, or acoustic pressure, p', is assigned. The corresponding values in the transformed space can be recovered from Eqs. (4.81) and (4.84). Alternatively, their combination can also be prescribed, such as for impedance boundary conditions. This allows Eq. (5.66) to be solved based on a modified kernel. After solving the problem on the boundary $\partial\tilde{\Omega}$, Eq. (4.65) can be used to compute the solution in the domain $\tilde{\Omega}$:

$$\tilde{\phi}(\tilde{\mathbf{X}}_p) = \tilde{\mathbf{C}}\tilde{\boldsymbol{\phi}} + \tilde{\mathbf{D}}\frac{\partial\tilde{\boldsymbol{\phi}}}{\partial\tilde{n}} + \tilde{F}_p, \tag{5.72}$$

where

$$\tilde{C}^{(m)} = -\int_{\partial\tilde{\Omega}} N_m(\tilde{\mathbf{X}})\frac{\partial\tilde{G}}{\partial\tilde{n}}d\tilde{S}(\tilde{\mathbf{X}}), \tag{5.73}$$

$$\tilde{D}^{(m)} = \int_{\partial\tilde{\Omega}} N_m(\tilde{\mathbf{X}})\tilde{G}d\tilde{S}(\tilde{\mathbf{X}}), \qquad \tilde{F}_p = \int_{\tilde{\Omega}} \tilde{G}\tilde{g}d\tilde{V}(\tilde{\mathbf{X}}). \tag{5.74}$$

The solution in the physical space can finally be recovered using an inverse Taylor–Lorentz transform (see Eq. (5.52)).

5.3.3 Boundary conditions and standard kernels

As indicated in the previous section, boundary element problems in the transformed space based on either velocity or pressure boundary conditions are not compatible with a standard BE kernel for the Helmholtz problem with quiescent media. For prescribed pressure (see Sec. 4.7.3) and more in general for impedance boundary conditions, we cannot see how the

standard kernel can be recovered because of the terms depending on the local mean flow non-uniformities. On the other hand, for acoustic velocity boundary conditions, an iterative approach is proposed in this section.

5.3.3.1 Formulation for velocity boundary conditions

The integral problem for velocity boundary conditions corresponding to Eq. (5.66) is presented in the transformed Taylor–Lorentz space based on Eq. (4.81). Using Eq. (4.81) in Eq. (4.65) and performing a variable expansion of the acoustic potential and its normal derivative to the boundary surface, based on Eqs. (5.6) and (5.7), yields

$$(\tilde{\boldsymbol{E}} + \alpha\tilde{\boldsymbol{E}}_\alpha)\tilde{\boldsymbol{\phi}} + (\tilde{\boldsymbol{B}} + \alpha\tilde{\boldsymbol{B}}_\alpha)\tilde{\boldsymbol{h}}_n = \tilde{\boldsymbol{F}} + \alpha\tilde{\boldsymbol{F}}_\alpha, \tag{5.75}$$

where

$$\begin{aligned}\tilde{E}^{(lm)} = &\int_{\partial\tilde{\Omega}} \delta_{lm} N_l(\tilde{\mathbf{X}}_p) C_m(\tilde{\mathbf{X}}_p) N_m(\tilde{\mathbf{X}}_p) d\tilde{S}(\tilde{\mathbf{X}}_p) + \int_{\partial\tilde{\Omega}}\int_{\partial\tilde{\Omega}} N_l(\tilde{\mathbf{X}}_p)\frac{\partial\tilde{G}}{\partial\tilde{n}} N_m(\tilde{\mathbf{X}}) d\tilde{S}(\tilde{\mathbf{X}}) d\tilde{S}(\tilde{\mathbf{X}}_p) \\ &+ \int_{\partial\tilde{\Omega}}\int_{\partial\tilde{\Omega}} \mu_m(\tilde{\mathbf{X}}) N_l(\tilde{\mathbf{X}}_p)\tilde{G}\left[\frac{\partial N_m(\tilde{\mathbf{X}})}{\partial\tilde{\tau}}\frac{\partial\tilde{\tau}}{\partial n} + \frac{\partial N_m(\tilde{\mathbf{X}})}{\partial\tilde{\eta}}\frac{\partial\tilde{\eta}}{\partial n}\right] d\tilde{S}(\tilde{\mathbf{X}}) d\tilde{S}(\tilde{\mathbf{X}}_p),\end{aligned} \tag{5.76}$$

$$\begin{aligned}\tilde{E}_\alpha^{(lm)} = &\int_{\partial\tilde{\Omega}} \delta_{lm} N_l(\tilde{\mathbf{X}}_p)\frac{\partial C_m(\tilde{\mathbf{X}}_p)}{\partial n_p} N_m(\tilde{\mathbf{X}}_p) d\tilde{S}(\tilde{\mathbf{X}}_p) \\ &- \int_{\partial\tilde{\Omega}} \mu_m(\tilde{\mathbf{X}}_p)\delta_{lm} N_l(\tilde{\mathbf{X}}_p) C_m(\tilde{\mathbf{X}}_p)\left[\frac{\partial N_m(\tilde{\mathbf{X}}_p)}{\partial\tilde{\tau}}\frac{\partial\tilde{\tau}}{\partial n} + \frac{\partial N_m(\tilde{\mathbf{X}}_p)}{\partial\tilde{\eta}}\frac{\partial\tilde{\eta}}{\partial n}\right] d\tilde{S}(\tilde{\mathbf{X}}_p) \\ &+ \int_{\partial\tilde{\Omega}}\int_{\partial\tilde{\Omega}} N_l(\tilde{\mathbf{X}}_p)\frac{\partial^2\tilde{G}}{\partial\tilde{n}\partial\tilde{n}_p} N_m(\tilde{\mathbf{X}}) d\tilde{S}(\tilde{\mathbf{X}}) d\tilde{S}(\tilde{\mathbf{X}}_p) \\ &+ \int_{\partial\tilde{\Omega}}\int_{\partial\tilde{\Omega}} \mu_m(\tilde{\mathbf{X}}) N_l(\tilde{\mathbf{X}}_p)\frac{\partial\tilde{G}}{\partial\tilde{n}_p}\left[\frac{\partial N_m(\tilde{\mathbf{X}})}{\partial\tilde{\tau}}\frac{\partial\tilde{\tau}}{\partial n} + \frac{\partial N_m(\tilde{\mathbf{X}})}{\partial\tilde{\eta}}\frac{\partial\tilde{\eta}}{\partial n}\right] d\tilde{S}(\tilde{\mathbf{X}}) d\tilde{S}(\tilde{\mathbf{X}}_p),\end{aligned} \tag{5.77}$$

and the vector $\tilde{\boldsymbol{h}}_n$ is assigned from the boundary conditions in the physical space (see Eq. (4.80)). In practice, $\tilde{\boldsymbol{h}}_n$ is a known vector of nodal values. The coefficients of the matrices $\tilde{\boldsymbol{B}}$ and $\tilde{\boldsymbol{B}}_\alpha$ are the same as those in Eq. (5.66), while $\tilde{\boldsymbol{F}}$ and $\tilde{\boldsymbol{F}}_\alpha$ are given in Eq. (5.71).

It is clear that the matrices $\tilde{\boldsymbol{E}}$ and $\tilde{\boldsymbol{E}}_\alpha$ are not consistent with a standard kernel for the Helmholtz problem with quiescent media [91]. In the following section, a strategy to recover a standard kernel is presented.

5.3.3.2 Iterative solution

Unlike the matrices $\tilde{\boldsymbol{A}}$ and $\tilde{\boldsymbol{A}}_\alpha$ in Eq. (5.66), we have shown that the matrices $\tilde{\boldsymbol{E}}$ and $\tilde{\boldsymbol{E}}_\alpha$ in Eq. (5.75) are not consistent with a standard BE kernel for the Helmholtz problem with

quiescent media. The terms including the derivatives of $\tilde{\phi}$ along the vectors $\tilde{\boldsymbol{\tau}}$ and $\tilde{\boldsymbol{\eta}}$ are peculiarities of the solution with mean flow.

To solve Eq. (5.75) using a standard BE kernel, an iterative approach is proposed. A standard kernel for the Helmholtz problem allows efficient BE algorithms, such as the fast multipole BEM [24], to be applicable to wave propagation in a non-uniform mean flow, provided that geometry, boundary conditions and sound source distributions are written in a Taylor–Lorentz space. Therefore, to exploit existing efficient BE solvers, the kernel in Eq. (5.75) must be modified.

The main idea is to represent the terms including the tangential derivatives of $\tilde{\phi}$ as equivalent sources along the boundary surface. To do so, the tangential derivatives in Eq. (5.75) are moved to the right-hand side as equivalent sources. Therefore, the source terms along the boundary will depend on $\tilde{\phi}$. These terms can be computed iteratively along the boundary $\partial\tilde{\Omega}$ based on the solution $\tilde{\phi}$ at a previous iterative step (see Fig. 5.6). First, the solution is computed neglecting the tangential derivatives. Then, the sources on the boundary are updated at every iteration.

Formally, Eq. (5.75) is rewritten as

$$(\tilde{\boldsymbol{A}} + \alpha\tilde{\boldsymbol{A}}_\alpha)\tilde{\boldsymbol{\phi}}_{q+1} + (\tilde{\boldsymbol{B}} + \alpha\tilde{\boldsymbol{B}}_\alpha)\tilde{\boldsymbol{h}}_n = \tilde{\boldsymbol{U}}_q + \alpha\tilde{\boldsymbol{U}}_{\alpha,q}, \tag{5.78}$$

where $\tilde{\boldsymbol{A}}$, $\tilde{\boldsymbol{A}}_\alpha$, $\boldsymbol{B}$ and $\tilde{\boldsymbol{B}}_\alpha$ have been defined in Sec. 5.3.2, while

$$\begin{aligned}\tilde{U}_q^{(l)} = &\int_{\partial\tilde{\Omega}} N_l(\tilde{\mathbf{X}}_p)\tilde{\phi}_{inc} d\tilde{S}(\tilde{\mathbf{X}}_p) \\ &- \phi_{m,q}\int_{\partial\tilde{\Omega}}\int_{\partial\tilde{\Omega}} \mu_m(\tilde{\mathbf{X}}) N_l(\tilde{\mathbf{X}}_p)\tilde{G}\left[\frac{\partial N_m(\tilde{\mathbf{X}})}{\partial\tilde{\tau}}\frac{\partial\tilde{\tau}}{\partial n} + \frac{\partial N_m(\tilde{\mathbf{X}})}{\partial\tilde{\eta}}\frac{\partial\tilde{\eta}}{\partial n}\right] d\tilde{S}(\tilde{\mathbf{X}}) d\tilde{S}(\tilde{\mathbf{X}}_p)\end{aligned} \tag{5.79}$$

$$\begin{aligned}\tilde{U}_{\alpha,q}^{(l)} = &\int_{\partial\tilde{\Omega}} N_l(\tilde{\mathbf{X}}_p)\frac{\partial\tilde{\phi}_{inc}}{\partial\tilde{n}_p} d\tilde{S}(\tilde{\mathbf{X}}_p) \\ &- \phi_{m,q}\int_{\partial\tilde{\Omega}}\int_{\partial\tilde{\Omega}} \mu_m(\tilde{\mathbf{X}}) N_l(\tilde{\mathbf{X}}_p)\frac{\partial\tilde{G}}{\partial\tilde{n}_p}\left[\frac{\partial N_m(\tilde{\mathbf{X}})}{\partial\tilde{\tau}}\frac{\partial\tilde{\tau}}{\partial n} + \frac{\partial N_m(\tilde{\mathbf{X}})}{\partial\tilde{\eta}}\frac{\partial\tilde{\eta}}{\partial n}\right] d\tilde{S}(\tilde{\mathbf{X}}) d\tilde{S}(\tilde{\mathbf{X}}_p) \\ &+ \phi_{m,q}\int_{\partial\tilde{\Omega}} \mu_m(\tilde{\mathbf{X}}_p)\delta_{lm} N_l(\tilde{\mathbf{X}}_p) C_m(\tilde{\mathbf{X}}_p)\left[\frac{\partial N_m(\tilde{\mathbf{X}}_p)}{\partial\tilde{\tau}}\frac{\partial\tilde{\tau}}{\partial n} + \frac{\partial N_m(\tilde{\mathbf{X}}_p)}{\partial\tilde{\eta}}\frac{\partial\tilde{\eta}}{\partial n}\right] d\tilde{S}(\tilde{\mathbf{X}}_p),\end{aligned} \tag{5.80}$$

where q denotes the marching index and $\tilde{\phi}_{m,q}$ denotes the m-th nodal value of $\tilde{\phi}$ at the q-th iteration. The projection of the normal vector in the transformed space to the corresponding normal vector in the physical space is denoted as μ (see Sec. 4.7.3.1).

A tolerance, ϵ, can be defined to determine a convergence criterium for the iterative algorithm, that is

$$\frac{\|\tilde{\boldsymbol{\phi}}_{q+1} - \tilde{\boldsymbol{\phi}}_q\|}{\|\tilde{\boldsymbol{\phi}}_q\|} < \epsilon. \tag{5.81}$$

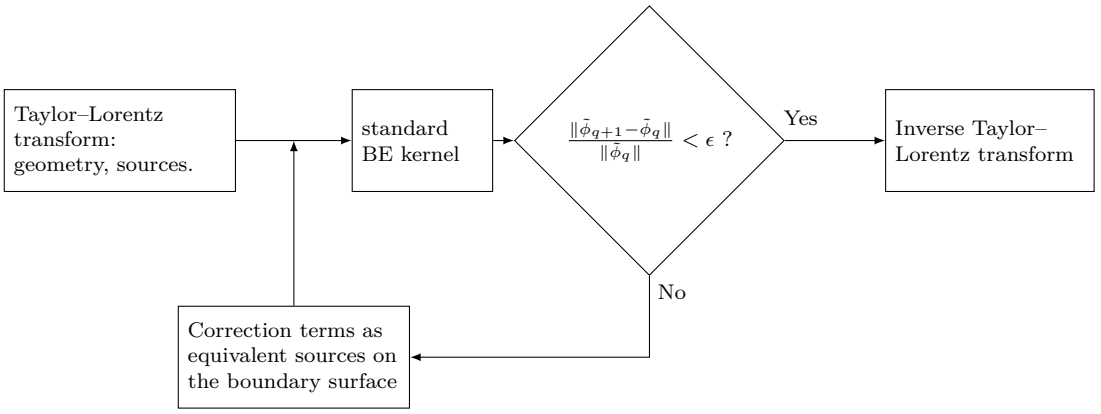

Figure 5.6: Block diagram describing the iterative solution proposed to exploit a standard BE kernel for the Helmholtz problem with quiescent media to solve the integral problem with mean flow in a transformed Taylor–Lorentz space.

On the other hand, as an initial solution, namely $q = 0$, the system of equations, Eq. (5.78), can be solved neglecting the tangential derivatives:

$$\tilde{U}_0^{(l)} = \int_{\partial\tilde{\Omega}} N_l(\tilde{\mathbf{X}}_p)\tilde{\phi}_{inc} d\tilde{S}(\tilde{\mathbf{X}}_p) \tag{5.82}$$

and

$$\tilde{U}_{\alpha,0}^{(l)} = \int_{\partial\tilde{\Omega}} N_l(\tilde{\mathbf{X}}_p)\frac{\partial\tilde{\phi}_{inc}}{\partial\tilde{n}_p} d\tilde{S}(\tilde{\mathbf{X}}_p). \tag{5.83}$$

To sum up, an iterative solution to exploit standard boundary element kernels with quiescent media has been devised for velocity boundary conditions to recover solutions with mean flow in a transformed Taylor–Lorentz space. It is based on an iterative approach in that the terms depending on the tangential derivatives of the field variables are considered as equivalent sound sources and they are updated based on the solution on the boundary at every iteration.

5.4 Concluding remarks

Boundary element models have been devised to solve the weakly non-uniform flow formulation in either the physical or transformed Taylor–Lorentz space. In the transformed space conventional methods to work around the non-uniqueness issue can be used. This is not the case for the physical space formulation. Extensions of the combined Helmholtz integral equation and Burton–Miller formulations have been proposed to get around this issue.

For the transformed space formulation, it was seen that boundary conditions on either acoustic velocity or pressure are not compatible with standard BE kernels for the Helmholtz problem with quiescent media. In the case of velocity boundary conditions, however, this limitation has been worked around proposing an iterative solution.

The models presented in this section will be benchmarked in the following chapters. First, numerical experiments will be performed to validate and assess the proposed discrete boundary integral solutions. Second, applications to more complex problems will be performed to assess these methods for forward fan noise installation effects and more general three-dimensional applications.

Chapter 6

Validation and Comparison

Contents

In this chapter, we benchmark the boundary integral solutions to wave propagation in a non-uniform potential flow presented in Chapters 4 and 5. The integral formulations are used either to solve a "wave extrapolation" problem, where an "inner" solution is obtained on an arbitrary closed surface in the flow and extrapolated to the far field, or to perform boundary element solutions where the sound field is solved in the entire domain up to the boundary surface. Solutions based on the weakly non-uniform formulation are compared to finite element solutions of the linearised potential wave equation and assessed against more

conventional boundary element solutions based on either the uniform flow convected wave equation or the Taylor–Helmholtz formulation in the physical space.

In Secs. 6.1 and 6.2, we describe the numerical set-up and the criteria used for the assessment of the integral solutions. In Sec. 6.3, the implementation of the boundary element formulation is verified. In Sec. 6.4, we present numerical results for wave extrapolation in a non-uniform flow and boundary element problems are solved in Sec. 6.5. First, the Taylor–Helmholtz formulation is assessed. Second, the weakly non-uniform flow formulation is benchmarked. In Sec. 6.6, numerical results pertaining to the non-uniqueness issue are presented. The limitations of a combined integral equation formulation are discussed. Numerical examples based on the generalized Burton–Miller formulation are then provided. Conclusions are finally given.

6.1 Numerical set-up

The scattering of the acoustic field from a volume point source in a non-uniform mean flow by a rigid cylinder is used as a test case (see Fig. 6.1). A time harmonic two-dimensional problem is solved. Solutions to external noise scattering are provided in an unbounded domain for far-field Mach numbers in the range $0 \rightarrow 0.3$. The limitation $M_\infty \leq 0.3$ is consistent with the assumption underlying the weakly non-uniform flow formulation that $M_\infty \ll 1$. This is further supported by the verification results of Sec. 6.3, where we showed that for two-dimensional problems and $M_\infty > 0.3$ the solutions to the weakly non-uniform formulation either in the physical or in the transformed space may not agree.

For $M_\infty \leq 0.3$, it is also reasonable to assume an incompressible mean flow. Therefore, the analytical solution of a potential incompressible flow around a cylinder without circulation (see Fig. 6.2), Φ_0, is used to define the background flow:

$$\Phi_0(r, \Theta) = u_\infty \left(r + \frac{a^2}{r} \right) \cos \Theta, \tag{6.1}$$

where r and a are respectively the distance from the origin and the radius of the cylinder, and Θ is the angle measured counterclockwise from the x-axis.

The boundary integral solution to the weakly non-uniform flow formulation (see Sec. 4.3) is used as a means of solving either a wave extrapolation or a boundary element problem. For any application where scattering occurs from an impermeable surface within the domain, the assumption behind the weakly non-uniform flow wave equation, i.e. $M_0' \ll M_\infty$, will necessarily be pushed to the limit since, at the stagnation point on the surface, the two quantities will be comparable. On the other hand, for a permeable surface, such as is used to extrapolate an inner solution obtained by a high-fidelity computation into a weakly non-uniform external flow, the assumption $M_0' \ll M_\infty$ will often be more clearly satisfied.

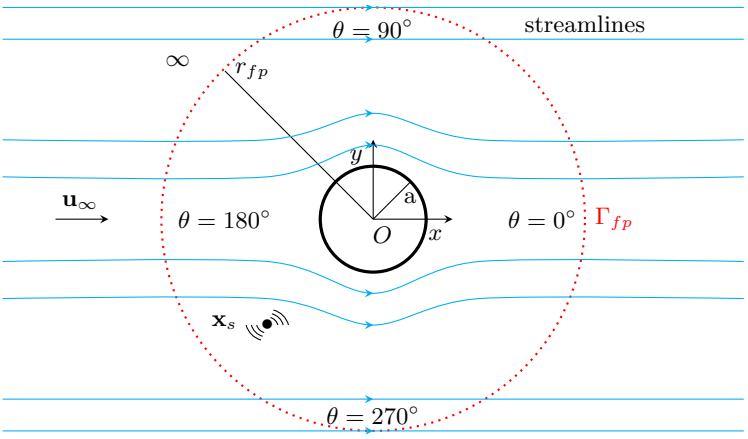

Figure 6.1: Main geometrical features of the reference domain for the problem of scattering of a monopole point source by a rigid cylinder in a non-uniform flow, depicting non uniform streamlines in the domain. The dotted surface Γ_{fp} denotes the arc of field points, while $\mathbf{x}_s$ is the point source location.

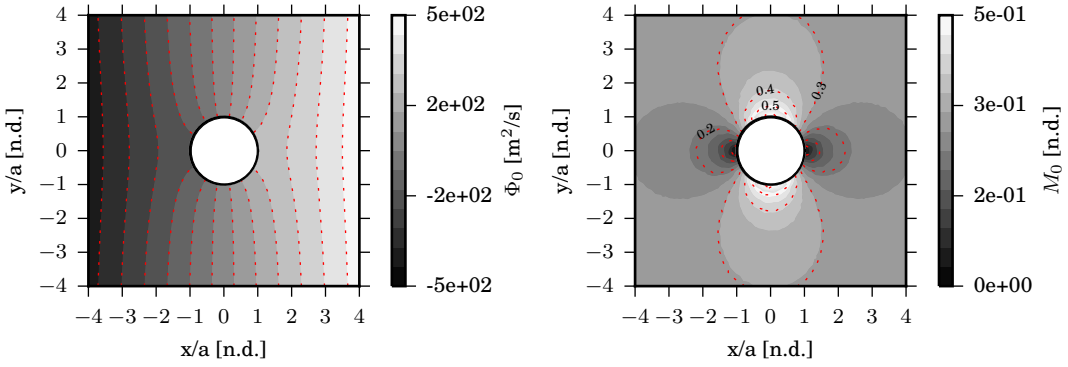

(a) Velocity potential

(b) Mach number, absolute component

Figure 6.2: Contours of an incompressible potential mean flow around a cylinder for $M_\infty = 0.3$, showing isolines of the velocity potential and Mach number.

Solutions based on wave extrapolation and boundary element models are provided based on cubic polynomial interpolation and ten degrees of freedom per wavelength. A direct boundary element method has been implemented to solve a variational formulation of the equations developed in both the physical, Eq. (4.21), and the transformed space, Eq. (4.65). The solver is based on an isoparametric Lagrangian formulation.

In the case of problems based on wave extrapolation, the solution is known on the boundary surface. Hence, the problem is not solved up to the boundary surface and, therefore, the non-uniqueness issue is not triggered. On the other hand, boundary element solutions are obtained by avoiding the spurious frequency issue in the first instance. The formulation based on the combined integral equation formulation and the generalized Burton–Miller formulation are then introduced in Sec. 6.6. For clarity, the physical space formulation is generally used to compute the results that follow, unless stated otherwise.

Finite element models based on twenty degrees of freedom per wavelength and an isoparametric cubic interpolation are also implemented to solve the linearised potential wave equation (LPE), Eq. (2.30). This serves as a reference physical model in the following analyses. Finite elements are used to solve a variational formulation of Eq. (2.30) with a harmonic source, g [201]:

$$\int_\Omega \left[\rho_0 \boldsymbol{\nabla}\phi^* \cdot \boldsymbol{\nabla}\phi - \frac{\rho_0}{c_0^2}\frac{D_0^*\phi}{Dt}\frac{D_0\phi}{Dt}\right] dV = \int_{\partial\Omega} \rho_0 \phi^* \left[\boldsymbol{\nabla}\phi \cdot \mathbf{n} - \frac{\mathbf{u}_0 \cdot \mathbf{n}}{c_0^2}\frac{D_0\phi}{Dt}\right] dS + \int_\Omega \phi^* g(\mathbf{x},\omega) dV, \tag{6.2}$$

where $\frac{D_0}{Dt} = \mathrm{i}\omega + \mathbf{u}_0 \cdot \boldsymbol{\nabla}$ is the material derivative on the mean flow. The FE domain is truncated and a perfectly matched layer (PML) based on a logarithmic stretching function [83, 88] is applied to satisfy the radiation condition at the outer surface. The PML is characterized by a wavelength thickness ratio of 0.125 and is extruded, for five wavelengths, from a closed circular surface of radius $r = 10a$.

A harmonic volume point source, or more precisely a line source in the context of 2D problems, is defined as

$$g(\mathbf{x}, t) = \delta(\mathbf{x} - \mathbf{x}_0)\mathrm{e}^{\mathrm{i}\omega t} \tag{6.3}$$

where $\delta(\mathbf{x})$ is the Dirac delta function and $\mathbf{x}_0$ is the location of the source. In the boundary element model, the sound source model is convoluted with the Green's function to obtain the incident field. On the other hand, in the finite element solution, a nodal point is defined at the source location and the mesh is refined in its vicinity so that twenty elements with cubic interpolation contribute to the nodal source point. Due to the approximation of the source model and the radiation condition, an error in the order of 0.05% at the outer surface of the computational domain affects the finite element solution with quiescent media.

The mean flow density, $\rho_\infty = 1.22$ kg·m^{-3}, and the speed of sound, $c_\infty = 340$ m·s^{-1}, are constant. The reference pressure for the calculation of the Sound Pressure Level, SPL $= 20\log_{10}(p'_{rms}/p'_{ref})$, is $p'_{ref} = 2 \cdot 10^{-5}$ Pa and $p'_{rms} = \|p'\|/\sqrt{2}$.

To solve the proposed models, we have developed a finite element and a boundary element solver based on Matlab [202] routines. The solvers have been devised under a collaborative framework between the Institute of Sound and Vibration Research, at the University of Southampton, and Siemens Industry Software. In this work, we implemented the boundary element formulations based on either the physical or the Taylor–Lorentz space-time. On the other hand, we developed a finite element solver of the linearised potential wave equation based on an existing solver of the Helmholtz problem with quiescent media. The direct Matlab solver [202] was used to solve the discrete system of equations.

6.2 Assessment criteria

The evaluation of the accuracy of a numerical solution can be based on a number of parameters, such as, the physical model, representation of the geometry, mean flow interpolation, interpolation error and source representation. In this instance, the focus is on the physical model. The results based on the integral solutions to the weakly non-uniform flow equation and the Taylor–Helmholtz formulation, Eq. (2.35) or Eq. (2.38), are benchmarked against a highly-refined finite element solution of the linearised potential wave equation, Eq. (2.30).

The solutions are compared both in terms of acoustic potential, ϕ, and pressure, p'. The acoustic potential is the field variable used to describe the model, while the acoustic pressure, p', can be recovered from the linearised momentum equation:

$$p'(\omega) = -\rho_0(\mathrm{i}\omega\phi + \mathbf{u}_0 \cdot \boldsymbol{\nabla}\phi). \tag{6.4}$$

Note that an analytical derivation of the Green's function is performed to recover the gradient of the potential, $\boldsymbol{\nabla}\phi$, in the boundary element solution, whereas the derivation is performed numerically for the reference finite element solution. In other words, in the finite element solution the pressure is one order of interpolation lower in accuracy than the acoustic potential. This drawback is mitigated by using a highly refined discretisation.

Error analyses are performed based on the Euclidean norm:

$$E_{L^2} = \sqrt{\frac{\int_{\Gamma_{fp}} \|\chi - \chi_{ref}\|^2 dS}{\int_{\Gamma_{fp}} \|\chi_{ref}\|^2 dS}}, \tag{6.5}$$

where χ is the numerical solution, χ_{ref} the reference value and Γ_{fp} is the surface along which the values are sampled. The L^2-error is used to measure the accuracy of the physical model.

However, other sources of error will inevitably be present in the solution. The truncation of the physical domain in the FE solution and the application of a PML create spurious reflections. Moreover the exact and the discrete wavenumbers differ. This results in the dispersion error which propagates and accumulates in the discrete FE domain, causing a so-called pollution effect [163, 152]. By using a highly-refined mesh, cubic element interpolation and truncating the domain in the acoustic and geometrical far field, these errors are reasonably controlled.

Nonetheless, solutions based on wave extrapolation will be affected by interpolation error. The finite element solutions in the inner domain are sampled on a control surface where the acoustic potential and its derivatives are recovered based on the discrete solution. Although the nodal points of the discrete control surface and finite element grid are chosen to coincide, $\boldsymbol{\nabla}\phi$ must be recovered numerically from the finite element solution in the inner domain.

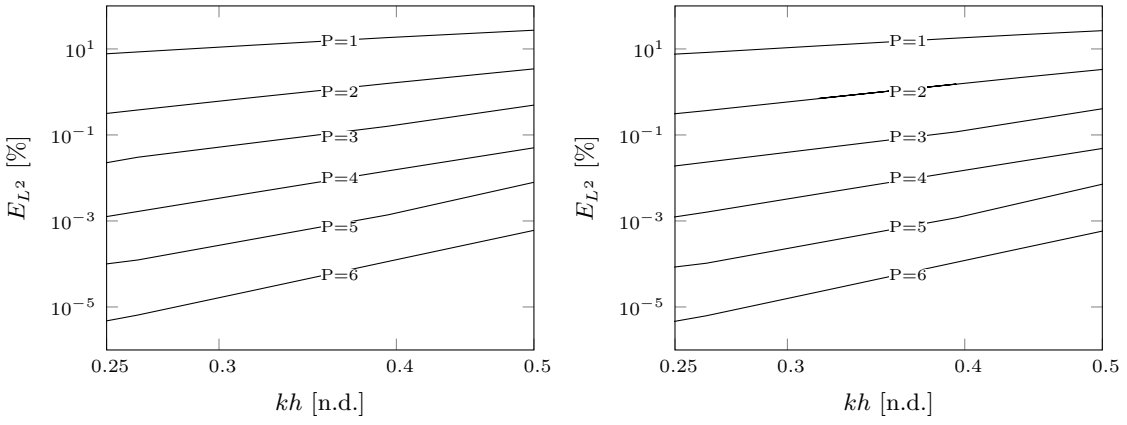

(a) $ka = 15$ (b) $ka = 30$

Figure 6.3: L^2-error for ϕ along a circular arc of field points with radius $r_{fp} = a$ for orders of interpolation of the solution $P = 1, 2, ..6$, the problem shown in Fig. 6.7 and $M_\infty = 0$. The non-dimensional element length is denoted by kh. The BE solution is benchmarked against the analytical solution of Morris and Brien [203].

6.3 Verification results

In this section, the implementation of the boundary element solver is verified. It is not meant to be a rigorous analysis of the numerical accuracy of the proposed methods, but an engineering reference for the results provided later in the chapter. First, we solve a scattering problem with a quiescent medium and then with a uniform flow. The proposed boundary element model for the weakly non-uniform flow formulation solves for the corresponding uniform flow formulation whenever $M_0 = M_\infty$ is considered in the entire domain. In practice, for a uniform flow, we solve the same formulation as Wu and Lee [40], while for $M_\infty = 0$, the standard Helmholtz equation is recovered. Second, a comparison between the results based on either the physical or the transformed space integral solution to the weakly non-uniform formulation is provided. The results are based on cubic interpolation and eight degrees of freedom per wavelength, unless otherwise stated.

6.3.1 Quiescent media

First, the problem in Fig 6.1 is solved with a quiescent medium, i.e. $M_\infty = 0$. The analytical solution to this problem is provided by Morris and Brien [203] and is used in this instance as a reference solution for the computation of the error. In Fig. 6.3, the L^2-error measured along the boundary surface, i.e. $r = a$, is shown for non-dimensional frequencies $ka = 15$ and 30 against the non-dimensional element length, kh. To solve these frequencies avoiding the non-uniqueness issue, a BE solution based on a conventional Burton–Miller formulation [51, 100] is used. As expected, the results show a convergence rate of order $P + 1$ [91], where P is the order of interpolation.

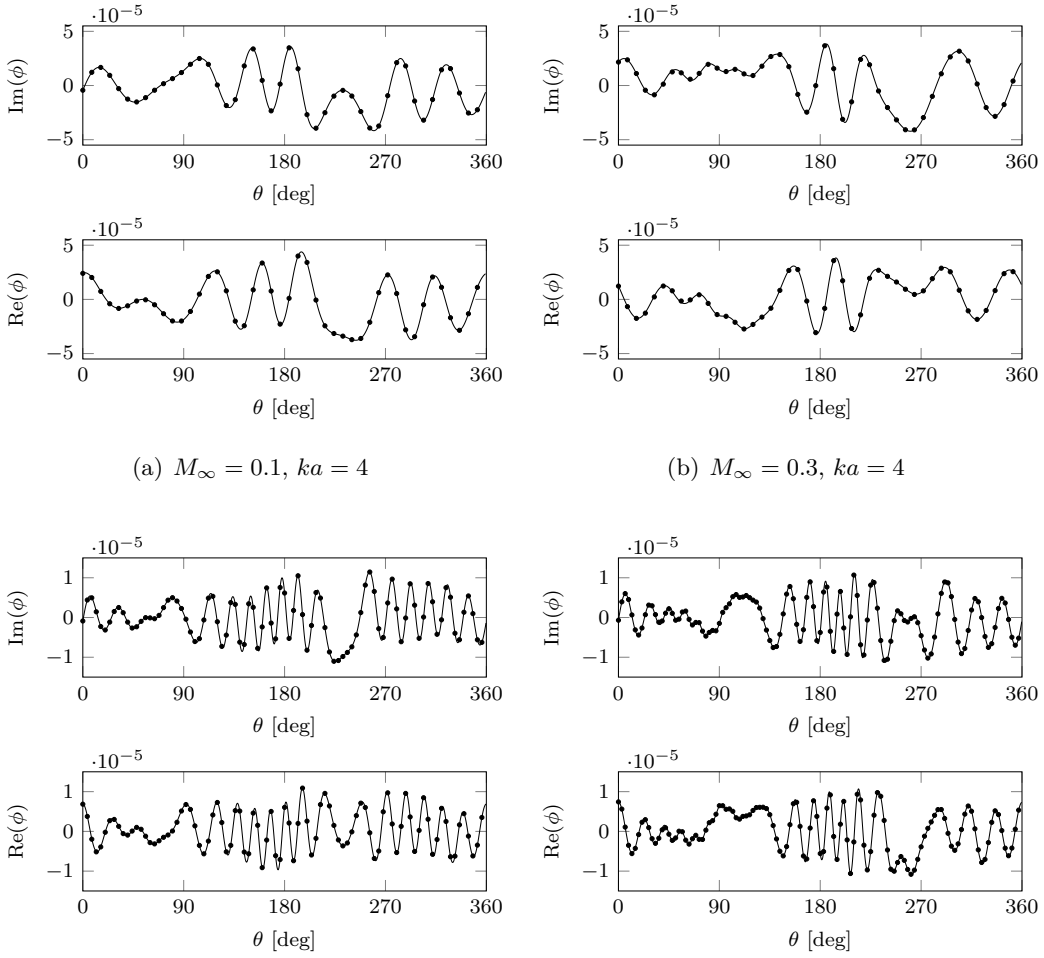

(a) $M_\infty = 0.1$, $ka = 4$

(b) $M_\infty = 0.3$, $ka = 4$

(c) $M_\infty = 0.1$, $ka = 10$

(d) $M_\infty = 0.3$, $ka = 10$

Figure 6.4: Real and imaginary parts of the acoustic velocity potential ϕ along an arc of field points with radius $r_{fp} = 7a$ for $ka = 4$, 10 and $M_\infty = 0.1$, 0.3. The problem in Fig. 6.1 is solved for a uniform flow, namely $\mathbf{u}_0 = \mathbf{u}_\infty$. The FE solution is based on Eq. (6.2) while the BE solution is based on Eq. (4.16). Solid line: FE solution. Symbols: BE solution.

6.3.2 Uniform mean flow

Results based on the convected wave equation with a uniform flow are used to validate the implementation of the boundary element solver in the presence of mean flow. Note that an exact boundary integral solution to wave propagation in a uniform flow is available in the literature [40]. It can be obtained assuming $\mathbf{u}_0 = \mathbf{u}_\infty$ in Eq. (4.21). The boundary element results are compared to the solutions based on finite elements applied to the weighted residual formulation corresponding to Eq. (6.2) for $\mathbf{u}_0 = \mathbf{u}_\infty$. Cubic interpolation is used both in the boundary element and finite element solutions. In this instance, the monopole point source for the problem in Fig. 6.1 lies at $\mathbf{x}_s = (-2a, -2a)$.

Figure 6.4 illustrates real and imaginary parts of the acoustic potential ϕ along an arc of field points centered at the origin of the reference frame and with radius $r_{fp} = 7a$. The solutions

are depicted for non-dimensional frequencies $ka = 4$ and 10 with $M_\infty = 0.1$ and 0.3. The results are reported using lines and symbols to discern clearly the different solutions. As expected, the solutions are in good agreement.

6.3.3 Non-uniform mean flow

We now consider a non-uniform mean flow, comparing boundary element solutions to the weakly non-uniform equation based on either the physical or the Taylor–Lorentz transformed formulation. The aim is to show the consistency between these formulations, since they solve the same physical model. Although the same physical model is solved, the approximations based on the mean flow Mach number and performed on the full potential linearised wave equation affect different quantities. In the physical space, we approximate the Green's function. In the case of the transformed space, the physical model, boundary conditions and sound sources are all approximated. In either case, the approximations are of order $M_\infty M_0'$, $M_0'^2$ or higher.

The problem in Fig. 6.1 is solved for a monopole point source at $\mathbf{x}_s = (-2a, -2a)$ and a non-uniform potential flow (see Eq. (6.1)). In Fig. 6.5, the real and imaginary parts of ϕ are shown on an arc of field points with radius $r_{fp} = 7a$, centered at the origin of the reference frame. The results are provided for $M_\infty = 0.1$ and 0.3, and non-dimensional frequencies $ka = 4$ and 10. It is clear that the results are in good agreement. This confirms that the two formulations are consistent, but says nothing at this stage about their accuracy compared to an exact reference solution.

Figure 6.6 illustrates the real part of ϕ on an arc of field points with radius $r_{fp} = 7a$ for $M_\infty = 0.4$ and 0.6. As M_∞ increases, the condition underlying the weakly non-uniform flow formulation, i.e. $M_\infty \ll 1$, is less clearly satisfied and the results based either on the physical or the transformed space formulation do not perfectly agree. As expected, the mismatch increases with Mach number. While for $M_\infty = 0.4$ the solutions are almost consistent, a more clear mismatch is shown for $M_\infty = 0.6$.

In summary, the results of this section confirm the considerations made in Sec. 4.9 that differences of order $M_0' M_\infty$ and M_∞^2 can appear due to the approximations performed; the Green's function was approximated in the physical space formulation, while in the transformed space we approximated both the integral solution and the boundary conditions. Therefore, for 2D problems, we consider $M_\infty \leq 0.3$ as a threshold for the proposed solutions. Under this hypothesis, an incompressible mean flow can be considered. However, note that the non-uniformity in the mean flow for 2D problems is more significant than for the corresponding 3D problems [204]. For an equivalent Mach number at infinity and consistent geometries, such as is the case for a cylinder and a sphere, the highest Mach number and the extension of region where the flow is non-uniform are larger for two-dimensional than

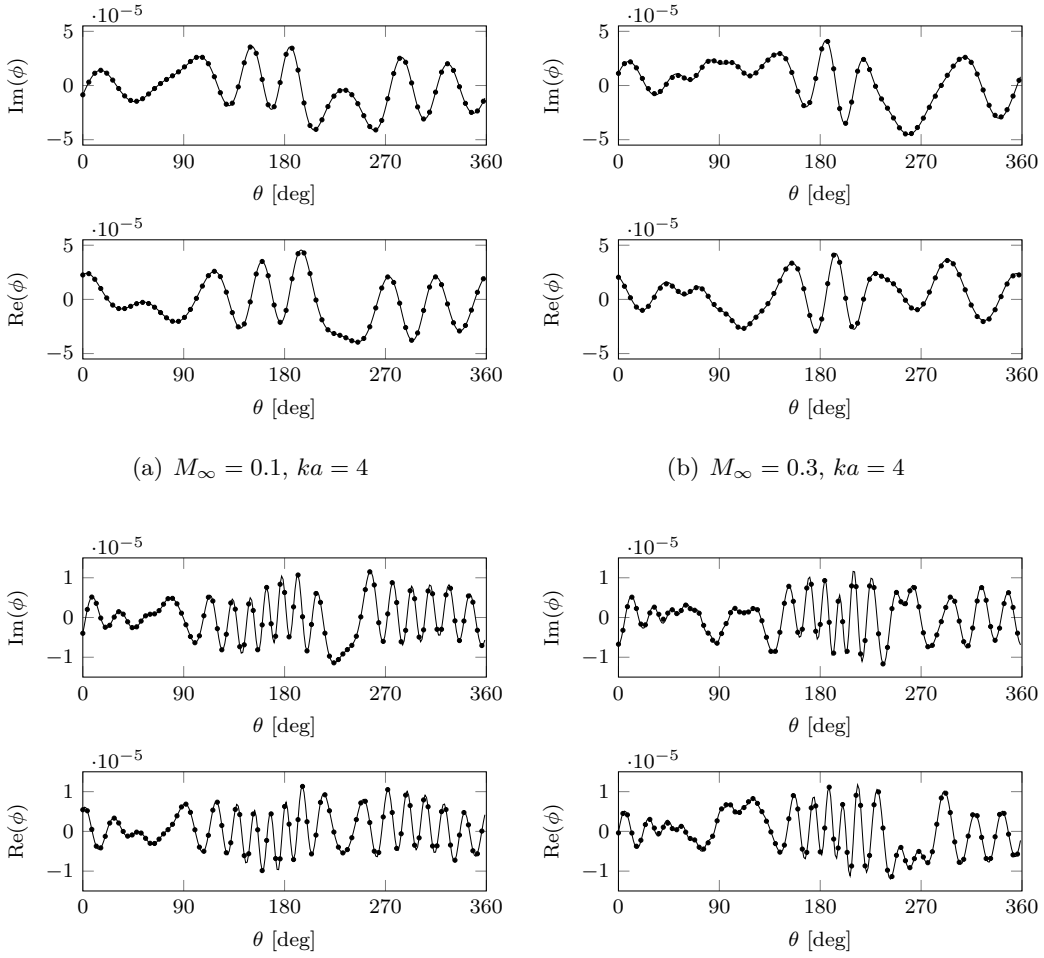

(a) $M_\infty = 0.1$, $ka = 4$

(b) $M_\infty = 0.3$, $ka = 4$

(c) $M_\infty = 0.1$, $ka = 10$

(d) $M_\infty = 0.3$, $ka = 10$

Figure 6.5: Real and imaginary parts of the acoustic velocity potential ϕ along an arc of field points with radius $r_{fp} = 7a$ for $ka = 4$ and 10, and $M_\infty = 0.1$ and 0.3. The problem in Fig. 6.1 is solved for a non-uniform potential flow without circulation. The BE solution in the transformed Taylor–Lorentz space based on Eq. (5.65) for $\alpha = 0$, and the BE solution in the physical space based on Eq. (5.10) are shown. Solid line: BE solution Taylor–Lorentz space. Symbols: BE solution physical space.

for three-dimensional problems. Therefore, for 3D problems, we will relax this limit to $M_\infty \leq 0.4$.

6.4 Wave extrapolation on non-uniform flow

In this section, a wave extrapolation approach based on the weakly non-uniform flow formulation is benchmarked against the reference solution (see Fig. 6.7 and 6.8). The integral formulation in Eq. (4.21) is used to solve a wave extrapolation problem where an "inner" solution is sampled on an arbitrary closed surface in the flow and extrapolated to the far field. The FE solution based on the linearised potential Helmholtz equation, Eq. (6.2), is

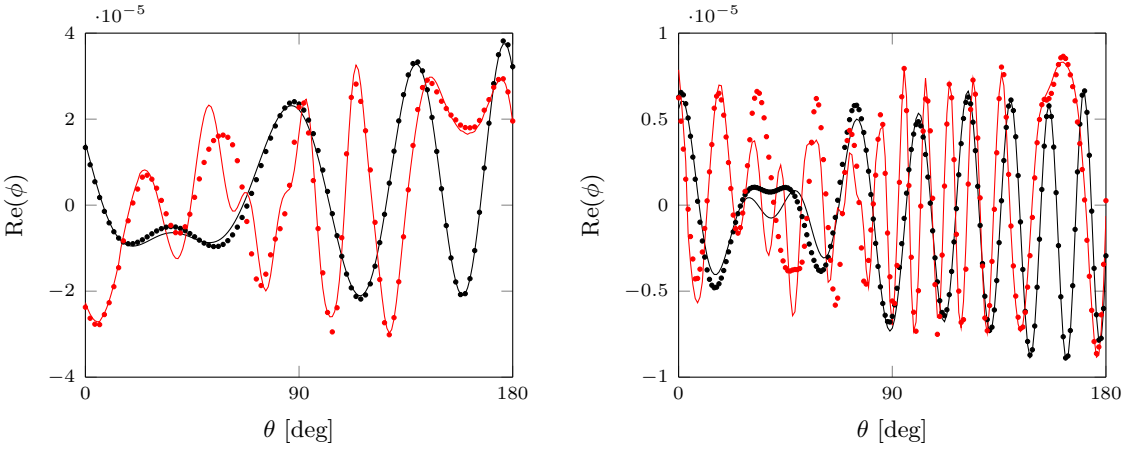

(a) $ka = 4$ (b) $ka = 10$

Figure 6.6: Real part of the acoustic velocity potential ϕ along an arc of field points with radius $r_{fp} = 7a$ for $M_\infty = 0.4$ and 0.6. The problem in Fig. 6.1 is solved for a non-uniform potential flow without circulation. The BE solution in the transformed Taylor–Lorentz space based on Eq. (5.65) for $\alpha = 0$, and the BE solution in the physical space based on Eq. (5.10) are shown. Solid line: BE solution Taylor–Lorentz space. Symbols: BE solution physical space. Black: $M_\infty = 0.4$. Red: $M_\infty = 0.6$.

computed to recover sound radiation and scattering around the cylinder in the inner domain Ω_{in}. Second, the reference solution is sampled on a closed control surface in a non-uniform flow, $\partial\Omega_{in}$, containing the cylinder and the source. Sound is radiated to the far field, Ω_{out}, by means of an integral formulation. Note that, while in previous works wave extrapolation has been performed on a uniform mean flow [23, 38], Eq. (4.16) allows the acoustic field to be extrapolated from a region where the flow is non-uniform.

The problem in Fig. 6.1 is solved for a monopole point source of unit magnitude located at $\mathbf{x}_s = (0, -1.5a)$ (see Fig. 6.7) in an unbounded domain and with uniform flow Mach numbers at infinity in the range $0 \to 0.3$. A circular permeable control surface, $\partial\Omega_{in}$, is centred at $\mathbf{x} = (0, 0)$ with radius $r_{cs} = 2a$. The maximum value of M_0' on $\partial\Omega_{in}$ is $M_\infty/4$. The order of interpolation of the integral solution on Ω_{in} is consistent with the finite element model. The FE solution is also used as a reference in the far field.

The accuracy of wave extrapolation based on the weakly non-uniform potential flow Helmholtz equation is assessed and a comparison with integral solutions based on the uniform flow convected Helmholtz [136] and the Taylor–Helmholtz (see Sec. 4.6) equations is presented. First, we show an error analysis where frequency and Mach number are the main parameters. Then, we discuss the results.

6.4.1 Error dependence on Mach number and frequency

Let us benchmark the integral solution to the weakly non-uniform potential flow Helmholtz equation against the reference FE solution. The L^2-error for the acoustic velocity potential,

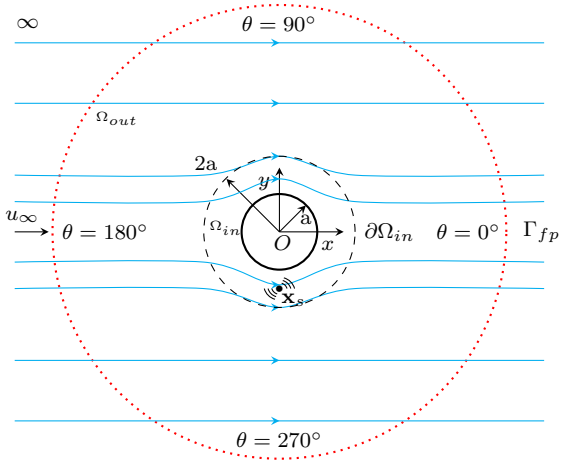

Figure 6.7: Geometry of reference for the wave extrapolation test case. Scattering by a cylinder from a monopole point source in a potential mean flow. The sound field in the outer domain Ω_{out} is extrapolated based on the acoustic field along the inner surface $\partial\Omega_{in}$.

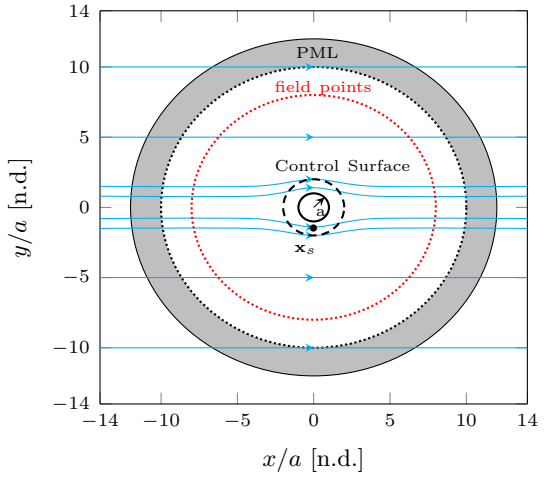

Figure 6.8: Main features of the FE model used to compute the reference solution for the wave extrapolation test case in Fig. 6.7. Scattering by a rigid cylinder from a monopole source in a potential mean flow.

ϕ, is shown in Fig. 6.9(a) plotted against the Helmholtz number, ka, on a circular arc of field points with radius $r_{fp} = 8a$. Note that the error is computed considering the physical distance of the observer R in lieu of R_M, where R_M has been defined in Sec. 4.4. As shown in Sec. 4.5, the accuracy of the solution based on the weakly non-uniform flow formulation depends on the relative distance of the observer, R_M, in terms of wavelengths. This distance, R_M, varies with M_∞ and represents the observer distance in the Taylor–Lorentz space. However, since $M_\infty \leq 0.3$, the maximum difference between R and R_M is about 5% of R and, therefore, we rely on the physical distance, R, to measure the error independently of Mach number.

The variation of the L^2-error against M_∞ is shown in Fig. 6.9(b), whereas the sensitivity of

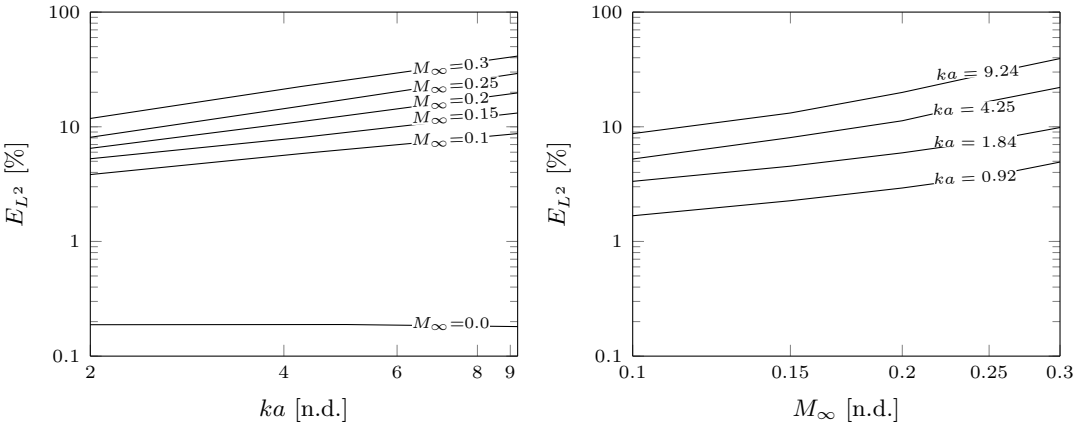

(a) Dependence on ka (b) Dependence on M_∞

Figure 6.9: L^2-error for ϕ along a circular arc of field points with radius $r_{fp} = 8a$ as a function of the non-dimensional frequency ka for the wave extrapolation test case of Fig. 6.7. The solution is based on the integral formulation for the weakly non-uniform potential flow Helmholtz equation, Eq. (4.21), and the error is measured against a finite element solution of the full potential linearised wave equation.

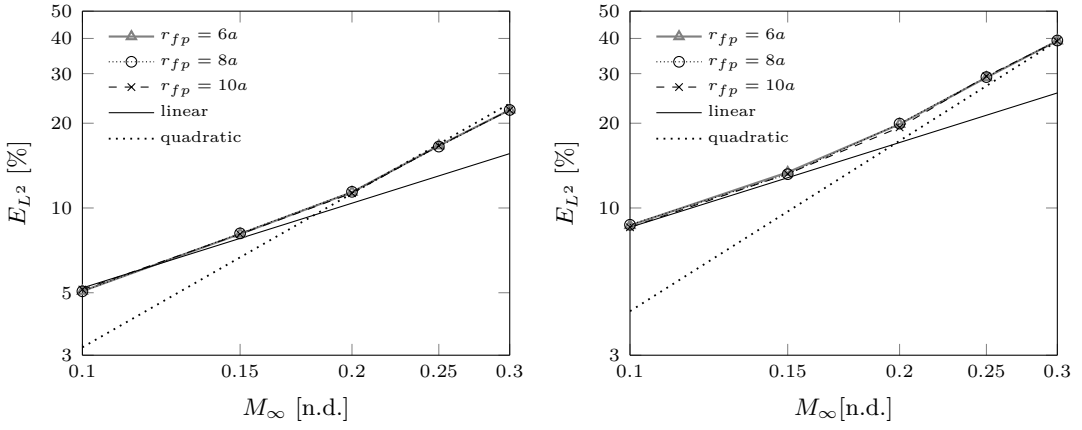

(a) $ka = 4.25$ (b) $ka = 9.24$

Figure 6.10: L^2-error for ϕ along circular arcs of field points with radii $r_{fp} = 6a$, $8a$ and $10a$ as a function of the mean flow Mach number M_∞ for the wave extrapolation test case of Fig. 6.7. The solution is based on the integral formulation for the weakly non-uniform flow Helmholtz equation, Eq. (4.21), and the error is measured against a finite element solution of the full potential linearised wave equation.

the L^2-error for ϕ to the distance to the observer is shown in Fig. 6.10. In the latter figure, the error is computed on circular arcs of field points with radii r_{fp} equal to $6a$, $8a$ and $10a$, and for non-dimensional frequencies $ka = 4.25$ and 9.24. Note that the mean flow is almost uniform at these distances from the cylinder. In this figure, we denote two reference lines with "linear" and "quadratic" indicating respectively the linear and the quadratic dependence on M_∞.

6.4.2 Comparison with alternative formulations

We want to compare the solutions based on the weakly non-uniform flow formulation to the solutions of Wu and Lee [40] based on a uniform flow and the Taylor–Helmholtz equation, Eq. (4.57). Contours of the real part of ϕ are shown in Fig. 6.11 for a non-dimensional frequency $ka = 9.24$ and Mach number $M_\infty = 0.3$. The acoustic field extrapolated by using the weakly non-uniform flow formulation, Eq. (4.21), the uniform flow Helmholtz equation [40] and the Taylor-Helmholtz integral equation, Eq. (4.59), is compared to the results based on the FE reference solution. In Fig. 6.12, the results from the different integral solutions are also benchmarked against the reference solution. The L^2-error for ϕ against M_∞ is given along an arc of field points with radius $r_{fp} = 8a$ and is plotted for different values of the non-dimensional frequency ka.

The results are now compared in terms of acoustic pressure, p'. Figure 6.13 illustrates the SPL along an arc of field points with radius $r_{fp} = 8a$ for $ka = 9.24$ and $M_\infty = 0.1$ and 0.3. The SPL is plotted against the angle θ, where $\theta = 0$ corresponds to the x-axis and θ is measured counterclockwise. The solution based on the Taylor–Helmholtz equation introduces local errors against the FE reference solution of up to 10 dB. On the other hand, the error on the weakly non-uniform potential flow Helmholtz solution and the corresponding uniform flow approximation [136] do not exceed 5 dB. As one might expect, the weakly non-uniform solution improves on the uniform flow Helmholtz equation in the shielded area [$\theta = 60 \rightarrow 120$ degrees], where the mean flow is not aligned with the uniform stream at infinity.

6.4.3 Discussion

The L^2-error based on the integral formulation with a weakly non-uniform flow, Eq. (4.21), increased almost linearly with frequency (see Fig. 6.9(a)). It scaled linearly with M_∞ for $M_\infty \leq 0.2$ and with M_∞^2 for $0.2 < M_\infty \leq 0.3$ (see Fig. 6.9(b)). Nevertheless, it was almost constant when wave propagation occurred in a uniform mean flow (see Fig. 6.10), since the integral formulation associated with the weakly non-uniform potential flow Helmholtz equation is exact for a uniform base flow.

These numerical results are supported by the dimensional error analysis in Sec. 4.5 where we have shown that the error terms scale either linearly or quadratically with frequency. The error analysis in Sec. 4.5 also indicated that, whenever the condition $M_0' \ll M_\infty$ is satisfied, terms of order $M_0' M_\infty$ should provide the most significant contribution to the error. Nonetheless, we have shown that all the sources of error vanish in a uniform flow.

On the contrary, the L^2-error for the Taylor–Helmholtz formulation scaled with M_∞^2 while the error based on the uniform flow formulation was linear with Mach number (see Fig. 6.12). Both formulations scaled almost linearly with frequency. Although the solutions based on

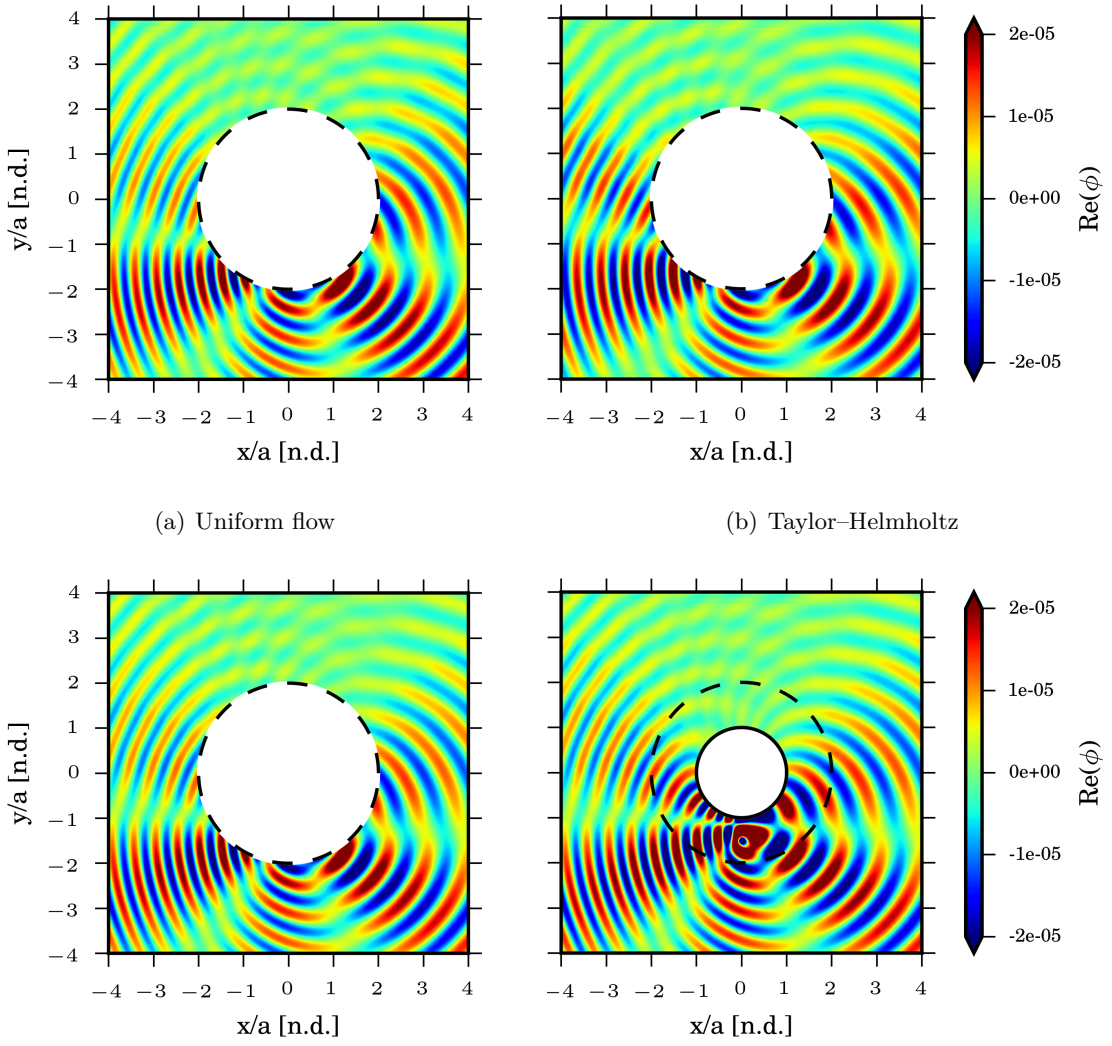

(a) Uniform flow

(b) Taylor–Helmholtz

(c) Weakly non-uniform flow

(d) FE LPE

Figure 6.11: Real part of ϕ for a non-dimensional frequency $ka = 9.24$, $M_\infty = 0.3$ and the wave extrapolation problem described in Fig. 6.7. (a) Uniform flow convected Helmholtz integral equation [40]. (b) Taylor–Helmholtz formulation, Eq. (4.59). (c) Weakly non-uniform formulation, Eq. (4.21). (d) FE reference solution, Eq. (6.2).

the uniform flow Helmholtz equation [40] did not model wave refraction, they outperformed those based on the Taylor–Helmholtz equation. The problem with the Taylor–Helmholtz formulation is that the error also grows in the uniform flow region whereas the uniform and the weakly non-uniform flow models are exact as this domain is reached. Nonetheless, it was seen that the integral formulation based on the weakly non-uniform potential flow Helmholtz equation provided better results than the integral solutions based on either a uniform flow or the Taylor–Helmholtz formulation (see Fig. 6.12). This might be expected since the weakly non-uniform formulation is a combination of these latter formulations.

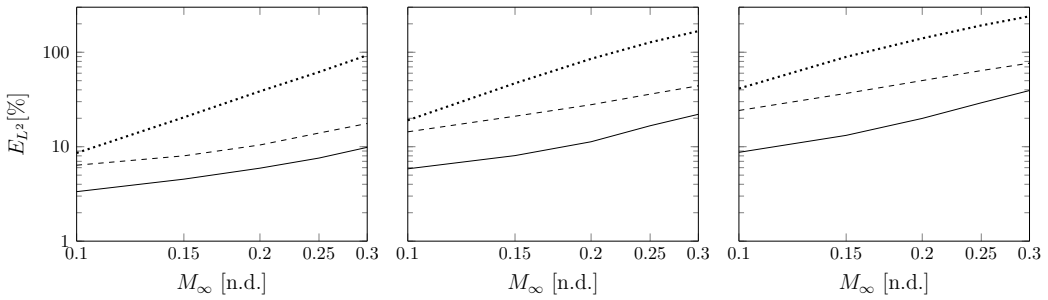

(a) $ka = 1.84$ (b) $ka = 4.25$ (c) $ka = 9.24$

Figure 6.12: L^2-error for ϕ along a circular arc of field points with radius $r_{fp} = 8a$ against the mean flow Mach number M_∞ for the wave extrapolation test case of Fig. 6.7, with $ka = 1.84$, 4.25 and 9.24. The error is computed against a FE solution of the reference physical model (see Eq. (6.2)). Solid: integral solution with non-uniform flow, Eq. (4.21). Dashed: uniform flow Helmholtz integral formulation [40]. Dotted: Taylor–Helmholtz integral formulation, Eq. (4.59).

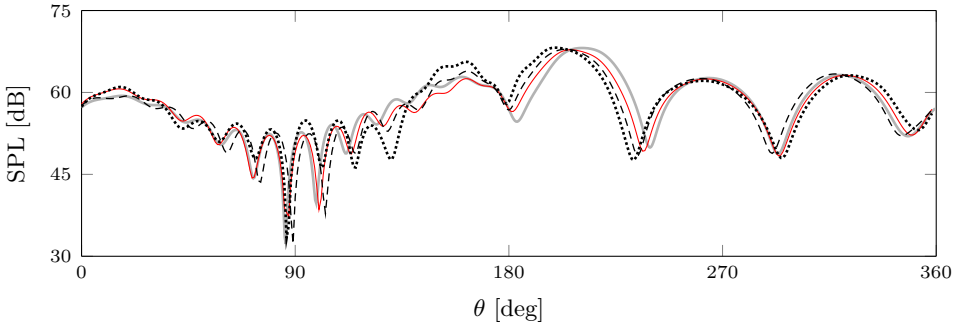

(a) $M_\infty = 0.1$

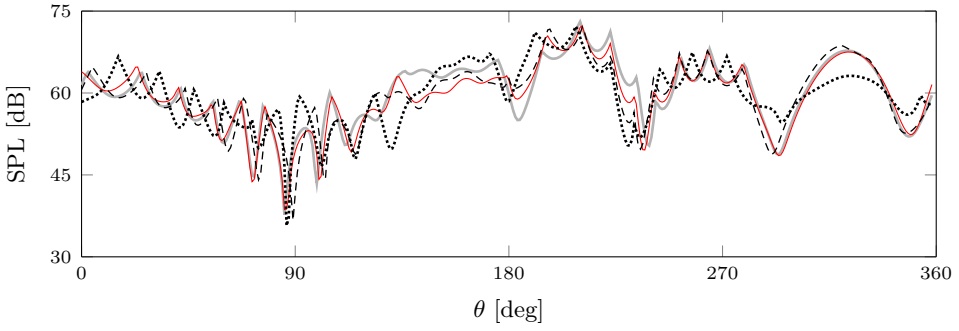

(b) $M_\infty = 0.3$

Figure 6.13: SPL along a circular arc of field points with radius $r_{fp} = 8a$ for $ka = 9.24$. The wave extrapolated solution (see Fig. 6.7) is based on Eq. (4.21) (weakly non-uniform), Wu and Lee [40] (uniform flow) and Eq. (4.59) (Taylor–Helmholtz). Solid, grey: FE linearised potential. Solid, red: weakly non-uniform flow. Dashed: uniform flow. Dotted: Taylor–Helmholtz.

6.5 Boundary element solutions

Boundary element solutions based on Eqs. (5.11) and (5.24) are now assessed. First, the Taylor–Helmholtz formulation, Eq. (5.24), is considered. Second, the weakly non-uniform flow formulation, Eq. (5.11), is benchmarked. A FE solution of the linearised potential wave equation (see Eq. (6.2)) is used again as a reference solution.

6.5.1 Limitations of the Taylor–Helmholtz formulation

In this section, we solve the problem in Fig. 6.1 for a monopole point source located at $\mathbf{x}_s = (-2a, -2a)$, unless otherwise stated. An error analysis is performed to assess the dependence of the accuracy of the physical model in Eq. (4.54) on Mach number, M_∞, and non-dimensional frequency, ka. The accuracy of the Taylor–Helmholtz formulation and its dependence on the distance to the observer and the location of the sound source are assessed.

6.5.1.1 Error dependence on mean flow Mach number

The L^2-error for ϕ against M_∞ is shown on logarithmic axes in Fig. 6.14 along a circular arc of field points with radius $r_{fp} = 4a$ (see Fig. 6.1) for non-dimensional frequencies $ka = 1.84$, 4.25, 8.50 and 12.66. The absolute value and phase of ϕ are shown in Figs. 6.15 and 6.16 for $M_\infty = 0.1$ and $M_\infty = 0.3$ along a circular arc of field points with radius $r_{fp} = 4a$ and a non-dimensional frequency $ka = 4.25$. BE solutions based on the Taylor–Helmholtz integral equation are compared to the FE reference solution. The likely explanation for such a large level of error reported for $M_\infty > 0.2$ (see Fig. 6.14) is that the Taylor formulation neglects terms of order M_∞^2 which are of the same order as the linear term with respect to the non-uniform Mach number, M_0.

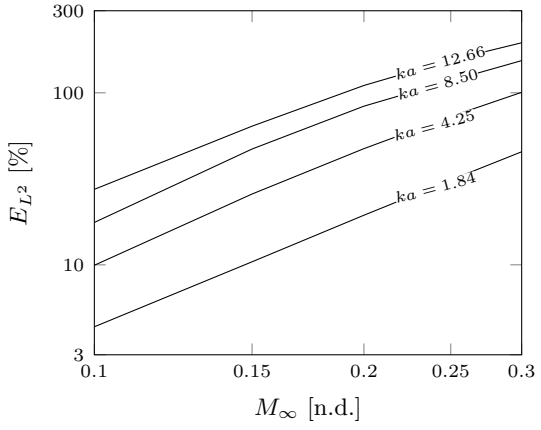

Figure 6.14: L^2-error for ϕ along a circular arc of field points with radius $r_{fp} = 4a$ against the mean flow Mach number M_∞ for the problem described in Fig. 6.1. The error for the solution based on Eq. (5.24) against the FE solution of Eq. (6.2) is reported.

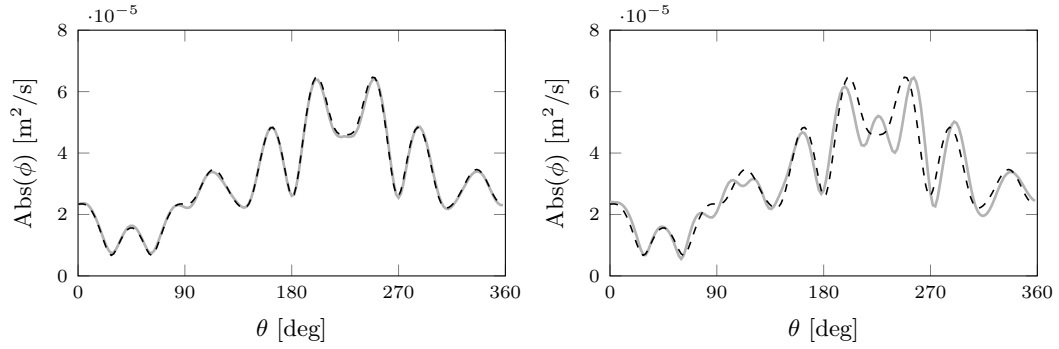

(a) $M_\infty = 0.1$ (b) $M_\infty = 0.3$

Figure 6.15: Absolute value of the acoustic velocity potential ϕ along an arc of field points with radius $r_{fp} = 4a$ for a non-dimensional frequency $ka = 4.25$ and the problem in Fig. 6.1. The FE reference solution is based on Eq. (6.2) while the BE Taylor–Helmholtz solution is based on Eq. (5.24). Solid line: FE reference. Dashed line: BE Taylor–Helmholtz.

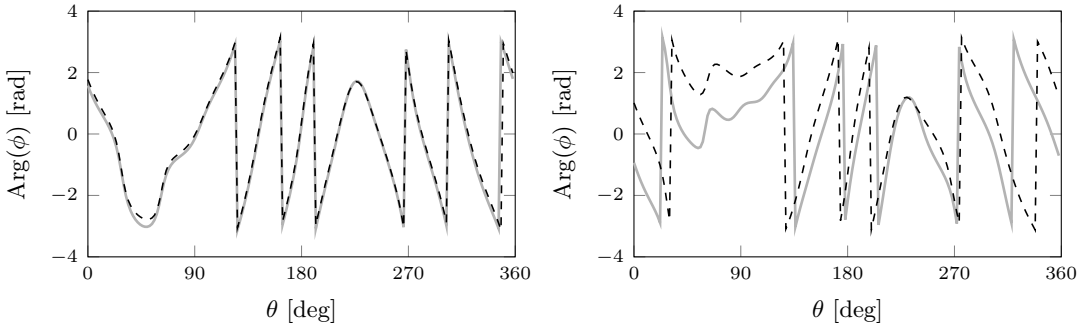

(a) $M_\infty = 0.1$ (b) $M_\infty = 0.3$

Figure 6.16: Phase of the acoustic velocity potential ϕ along an arc of field points with radius $r_{fp} = 4a$ for a non-dimensional frequency $ka = 4.25$ and the problem in Fig. 6.1. The FE reference solution is based on Eq. (6.2) while the BE Taylor–Helmholtz solution is based on Eq. (5.24). Solid line: FE reference. Dashed line: BE Taylor–Helmholtz.

In Figs. 6.17 and 6.18, contours of the real part of the acoustic velocity potential for $M_\infty = 0.1$ and 0.3 are presented for a non-dimensional frequency $ka = 8.50$. The Sound Pressure Level (SPL) computed along an arc of field points with radius $r_{fp} = 4a$ is plotted in Fig. 6.19 for a non-dimensional frequency $ka = 10$ at $M_\infty = 0.1$ and 0.3.

For $M_\infty = 0.1$, the results show that the Taylor–Helmholtz formulation favourably agrees with the finite element solution of the linearised potential wave equation, whereas for $M_\infty = 0.3$ the error on the phase of the potential field clearly increases (see Figs. 6.15 and 6.16). Note that the error on the phase of the acoustic potential is larger than the error on the absolute value. Let us compare the results in terms of SPL. For $M_\infty = 0.1$, the difference between the Taylor–Helmholtz and reference solutions is about 5 dB, while it increases to 13 dB for $M_\infty = 0.3$ (see Fig. 6.19).

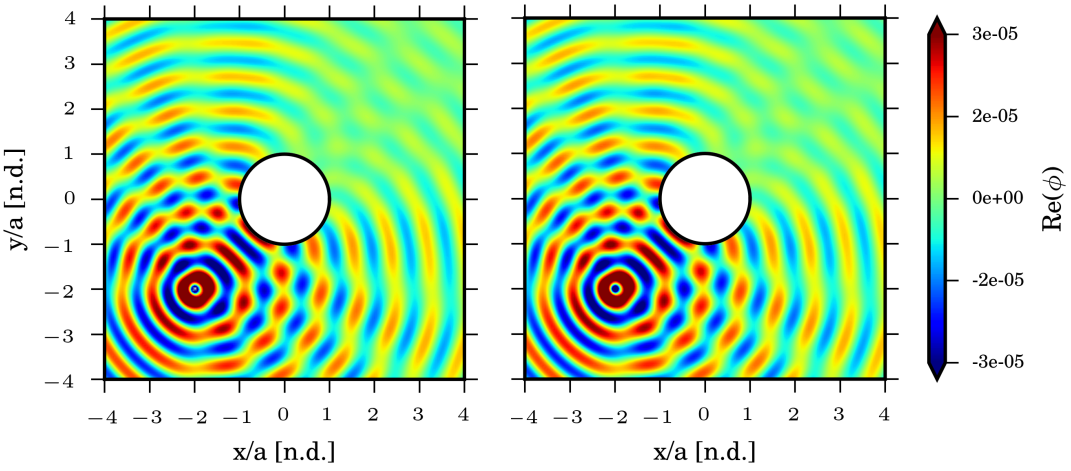

(a) BE Taylor–Helmholtz (b) FE LPE

Figure 6.17: Real part of the acoustic velocity potential, ϕ, for a non-dimensional frequency $ka = 8.50$, $M_\infty = 0.1$ and the problem described in Fig 6.1. The FE solution is based on Eq. (6.2) while the BE solution on Eq. (5.24).

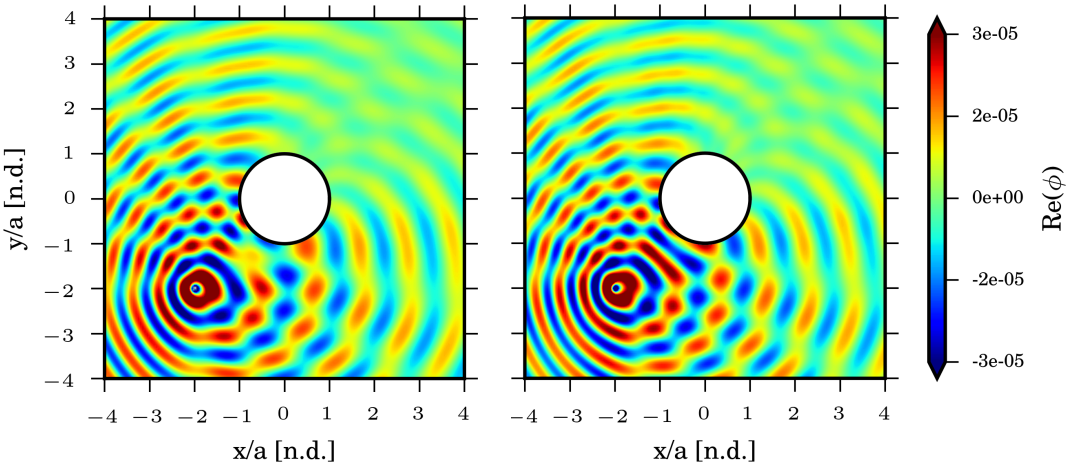

(a) BE Taylor–Helmholtz (b) FE LPE

Figure 6.18: Real part of the acoustic velocity potential, ϕ, for a non-dimensional frequency $ka = 8.50$, $M_\infty = 0.3$ and the problem described in Fig 6.1. The FE solution is based on Eq. (6.2) while the BE solution on Eq. (5.24).

6.5.1.2 Error dependence on frequency and observer location

In Fig. 6.20, the L^2-error for ϕ along a circular arc of field points with radius $r_{fp} = 4a$ is presented on logarithmic axes against the non-dimensional frequency ka for $M_\infty = 0.1$, 0.2 and 0.3. The L^2-error for ϕ is then computed keeping the ratio between the radius of the arc of field points and the wavelength constant at $kr_{fp} = 34$. The error is depicted in Fig. 6.21 against M_∞ for non-dimensional frequencies $ka = 1.84$, 4.25, 8.50 and 12.66. It shows that the error collapses onto a single curve independent of frequency.

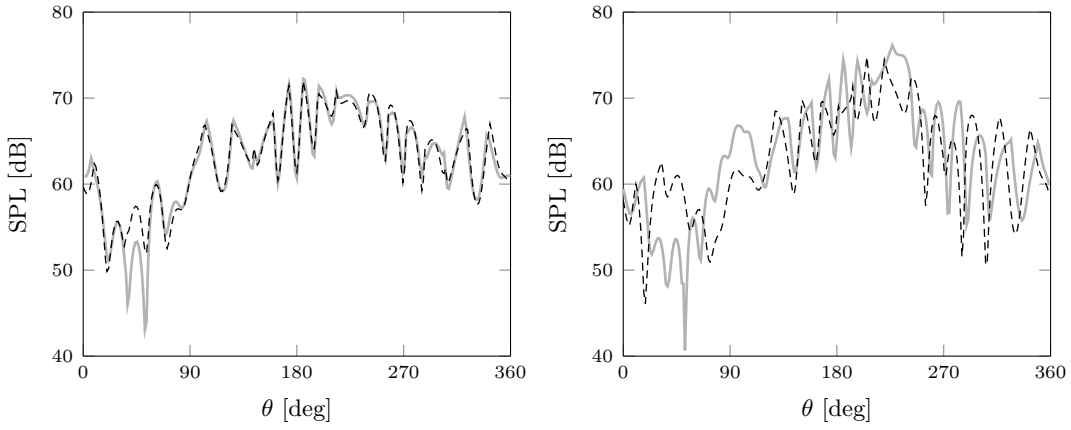

(a) $M_\infty = 0.1$ (b) $M_\infty = 0.3$

Figure 6.19: SPL along an arc of field points with radius $r_{fp} = 4a$ for a non-dimensional frequency $ka = 10$ and the test case in Fig. 6.1. The reference FE solution is based on Eq. (6.2) and the BE solution on Eq. (5.24). Solid line: FE reference. Dashed line: BE Taylor–Helmholtz.

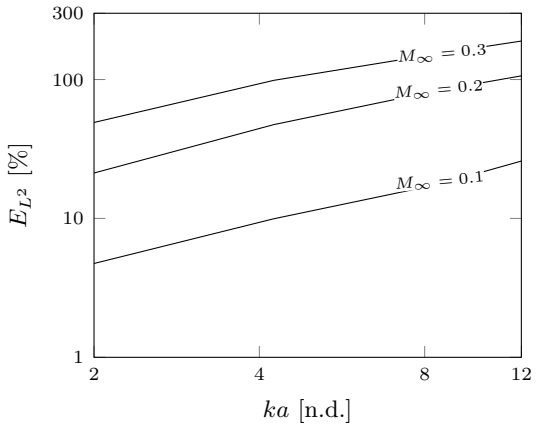

Figure 6.20: L^2-error for ϕ along a circular arc of field points with radius $r_{fp} = 4a$ against the non-dimensional frequency ka for the problem described in Fig. 6.1. The BE solution of Eq. (5.24) is assessed against a FE solution of Eq. (6.2).

The error relative to the observer location is now computed for different positions of the sound point source and the problem in Fig. 6.1. The monopole point source is moved in a number of positions: $\mathbf{x}_s = (-2a, 0)$, $(-2a, -2a)$ and $(-2a, -8a)$. An arc of field points with radius $r_{fp} = 4a$ is fixed at the origin of the reference frame. The L^2-error for ϕ, along this arc of field points, versus M_∞ is illustrated in Fig. 6.22 for non-dimensional frequencies $ka = 1.84$, 4.25 and 8.50. A clear increase in the error is shown if the source is moved away from the observer.

6.5.1.3 Analysis of the results

The results of this section have shown that the error of the boundary element solutions based on the Taylor–Helmholtz formulation compared with solutions based on the linearised

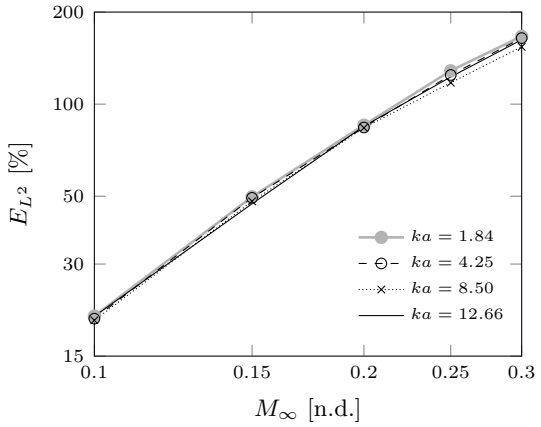

Figure 6.21: L^2-error for ϕ, along a circular arc of field points, against M_∞ for non-dimensional frequencies $ka = 1.84, 4.25, 8.50, 12.66$, a non-dimensional distance of the observer $kr_{fp} = 34$ and the problem in Fig. 6.1. The distance of the observer is scaled with the wavelength. The BE solution based on Eq. (5.24) is assessed against a FE solution based on Eq. (6.2).

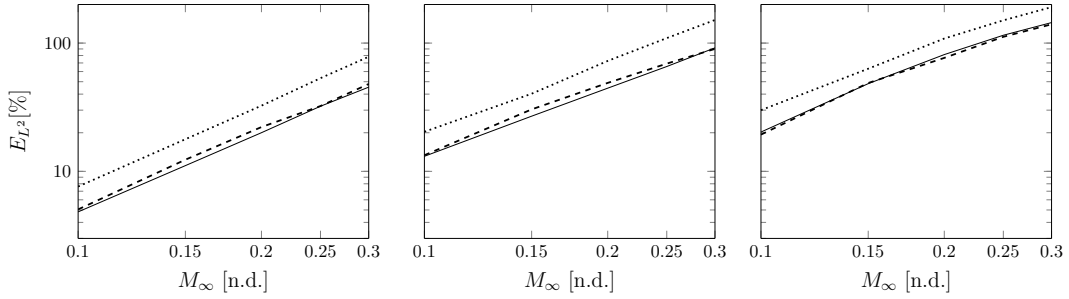

(a) $ka = 1.84$ (b) $ka = 4.25$ (c) $ka = 8.50$

Figure 6.22: L^2-error for ϕ along an arc of field points with radius $r_{fp} = 4a$ against M_∞ for a number of positions of the sound point source and the problem described in Fig. 6.1. The BE solution is based on the Taylor-Helmholtz integral equation Eq. (5.24). Solid: $\mathbf{x_s} = (-2a, 0)$. Dashed: $\mathbf{x_s} = (-2a, -2a)$. Dotted: $\mathbf{x_s} = (-2a, -8a)$.

potential wave equation, scales with M_∞^2 (see Fig. 6.14) and increases almost linearly with frequency (see Fig. 6.20). However, if the distance to the observer, R, is scaled with the wavelength, the error remains almost constant (see Fig. 6.21).

Nonetheless, since the Taylor–Helmholtz formulation is not exact for a uniform flow, the error increases even in regions where waves are propagated in a uniform flow (see Fig. 6.22). It was clearly seen that the error can be remarkably large for $M_\infty \geq 0.2$ (see Figs. 6.20 and 6.21). In the first instance, we infer that this is likely to be due to the lack of terms of order M_∞^2 in the formulation (see Sec. 2.5.4). The terms of order M_∞^2, dropped by the Taylor–Helmholtz formulation, become comparable to the terms of order M_0 for an increasing Mach number at infinity, significantly reducing the accuracy of the solution. The results confirm the error analysis reported in Appendix A and suggest that the Taylor–Helmholtz formulation is only applicable in the acoustic near field. Therefore, the Taylor–Helmholtz formulation is clearly not suited for problems of wave propagation in a non-uniform flow

generated by a uniform flow region at infinity. This is the case for the applications targeted by this work, such as aircraft large-scale acoustic installation effects.

6.5.2 Benchmark of the weakly non-uniform flow formulation

In this section, numerical examples are provided to assess the accuracy of boundary element solutions based on the weakly non-uniform flow Helmholtz equation (see Eq. (5.11)) against the FE solution of the linearised potential wave equation for a time harmonic problem, Eq. (6.2). A comparison with boundary element solutions based on the uniform flow convected Helmholtz equation [136] and the Taylor–Helmholtz equation, Eq. (5.24), is also presented. Again, the accuracy of boundary element solutions are assessed against the mean flow Mach number, M_∞, and the non-dimensional frequency, ka.

6.5.2.1 Sound source in an almost uniform flow

The BE solution based on Eq. (5.4) for the problem in Fig. 6.1 is provided. In the first instance, let us consider a monopole point source at $\mathbf{x}_s = (-2a, -2a)$ (see Fig. 6.1). The L^2-error for ϕ against the non-dimensional frequency, ka, along a circular arc of field points with radius $r_{fp} = 4a$ is illustrated in Fig. 6.23. Note that the error is computed again considering the physical distance of the observer, denoted as R, in lieu of R_M, since for $M_\infty \leq 0.3$ the maximum difference between R and R_M is about 5% of R (see Eq. (4.38)). The analysis is provided for M_∞ in the range $0 \rightarrow 0.3$. Figure 6.24 shows the sensitivity of the L^2-error for ϕ to the distance of the observer for a non-dimensional frequency $ka = 5$. In this case, the error is computed by sampling the results on circular arcs where the flow is almost uniform, namely $r_{fp} = 6a$, $8a$ and $10a$ (see Fig. 6.1).

In Fig. 6.25, a comparison of the L^2-error for ϕ is provided based on the different integral solutions. The L^2-error is computed along an arc of field points with radius $r_{fp} = 4a$ (see Fig. 6.1). The solutions based on the weakly non-uniform potential flow Helmholtz equation, Eq. (5.4), are compared to the corresponding solutions based on the uniform flow Helmholtz equation [40] and the Taylor–Helmholtz equation, Eq. (5.23). Figure 6.26 shows the real and the imaginary parts of the acoustic velocity potential ϕ depicted along the boundary surface, i.e. $r_{fp} = a$, for a non-dimensional frequency $ka = 5$ and $M_\infty = 0.1$ and 0.3. The FE solution of the linearised potential wave equation is presented again as a reference.

Contours of the real part of the acoustic velocity potential, ϕ, are shown in Figs. 6.27 and 6.28. BE solutions to either the uniform or weakly non-uniform flow Helmholtz equation are compared to the FE reference solution of the linearised potential wave equation for a non-dimensional frequency $ka = 10$, $M_\infty = 0.1$ and 0.3. The solution based on the Taylor–Helmholtz equation is also provided. A good agreement is shown for $M_\infty = 0.1$. On the contrary, for $M_\infty = 0.3$ only the integral formulation based on the weakly non-uniform flow ansatz is consistent with the FE reference solution.

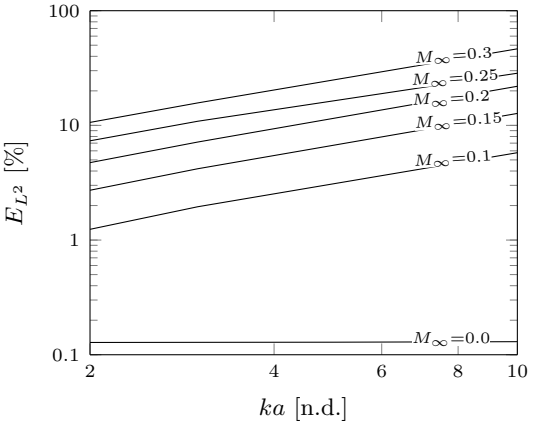

Figure 6.23: L^2-error for ϕ along a circular arc of field points with radius $r_{fp} = 4a$, for the problem in Fig. 6.1, against the non-dimensional frequency ka. The error of the BE solution based on Eq. (5.10) is computed against a FE solution of Eq. (6.2).

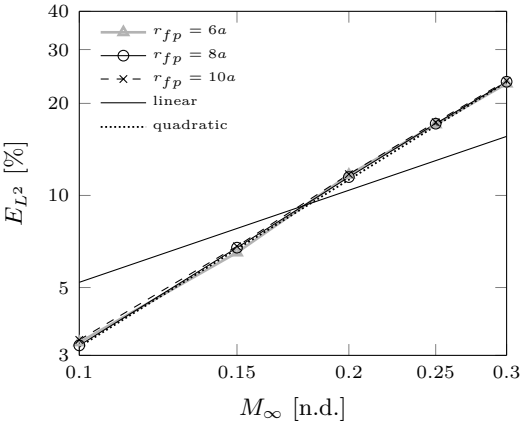

Figure 6.24: L^2-error for ϕ along arcs of field points with radii $r_{fp} = 6a, 8a$, $10a$ and a non-dimensional frequency $ka = 5$ for the problem in Fig. 6.1. The BE solution is based on Eq. (5.10) and the error is computed against a FE solution of Eq. (6.2).

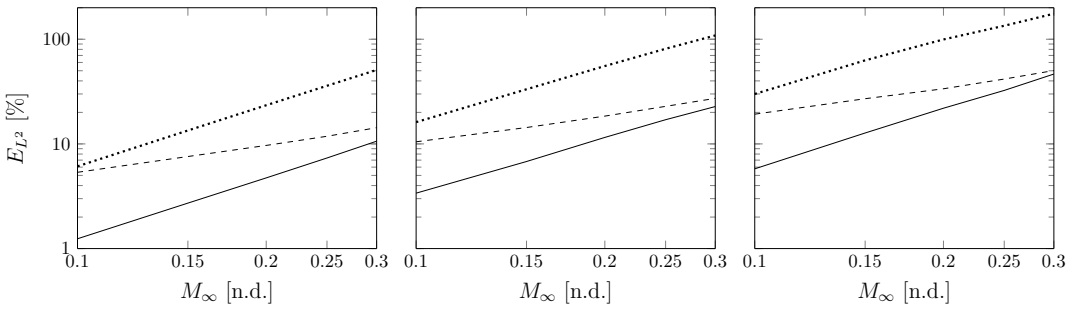

(a) $ka = 2$ (b) $ka = 5$ (c) $ka = 10$

Figure 6.25: L^2-error for ϕ along a circular arc of field points with radius $r_{fp} = 4a$ against M_∞, non-dimensional frequencies $ka = 2$, $ka = 5$ and $ka = 10$, and the problem in Fig. 6.1. Solid: BE weakly non-uniform potential flow Helmholtz equation Eq. (5.10). Dashed: BE uniform flow Helmholtz equation [40]. Dotted: Taylor-Helmholtz equation Eq. (5.25).

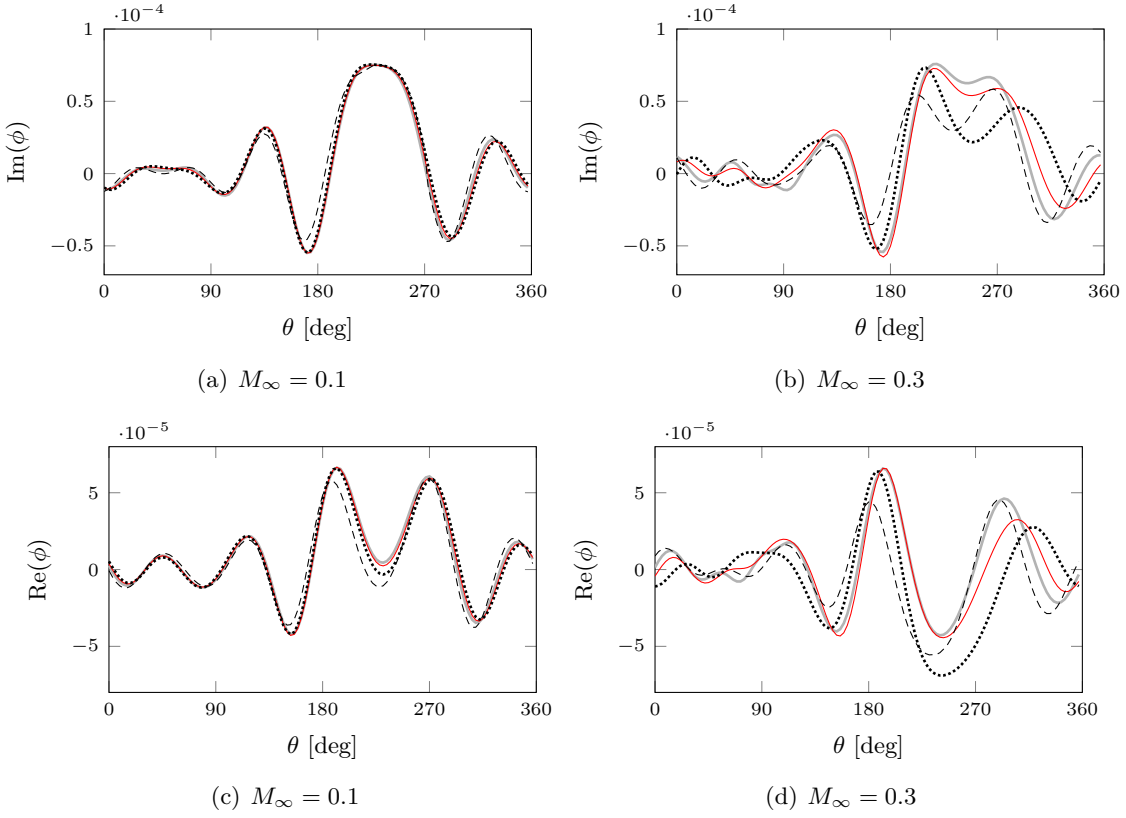

(a) $M_\infty = 0.1$ (b) $M_\infty = 0.3$

(c) $M_\infty = 0.1$ (d) $M_\infty = 0.3$

Figure 6.26: Real and imaginary parts of the acoustic velocity potential along a circular arc of field points with radius $r_{fp} = a$, a non-dimensional frequency $ka = 5$ and the problem in Fig. 6.1. The BE solutions based on Eq. (5.10) (BE non-uniform), Wu and Lee [40] (BE uniform) and the Taylor–Helmholtz formulation Eq. (5.25) are compared to an FE solution of the linearised potential wave equation. Solid, grey: FE LPE. Solid, red: BE weakly non-uniform flow. Dashed: BE uniform flow. Dotted: BE Taylor–Helmholtz.

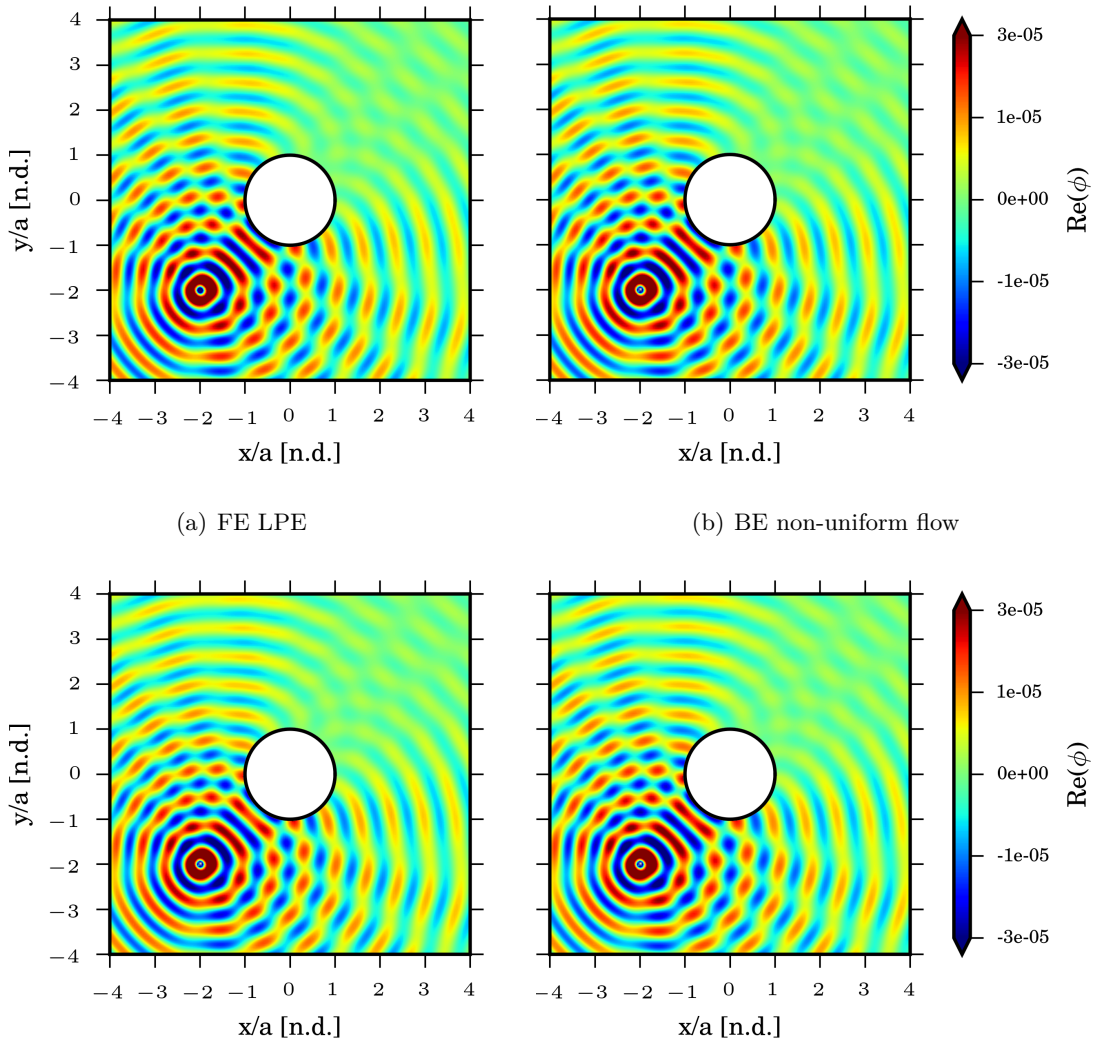

(a) FE LPE

(b) BE non-uniform flow

(c) BE uniform flow

(d) BE Taylor–Helmholtz

Figure 6.27: Real part of the acoustic velocity potential, ϕ, for a non-dimensional frequency $ka = 10$, $M_\infty = 0.1$ and the problem described in Fig. 6.1. The solutions are based on the weakly non-uniform potential flow Helmholtz equation Eq. (5.10), the uniform flow Helmholtz equation [40] and the Taylor–Helmholtz equation Eq. (5.25). A highly refined FE solution of the reference physical model, Eq. (6.2), is provided.

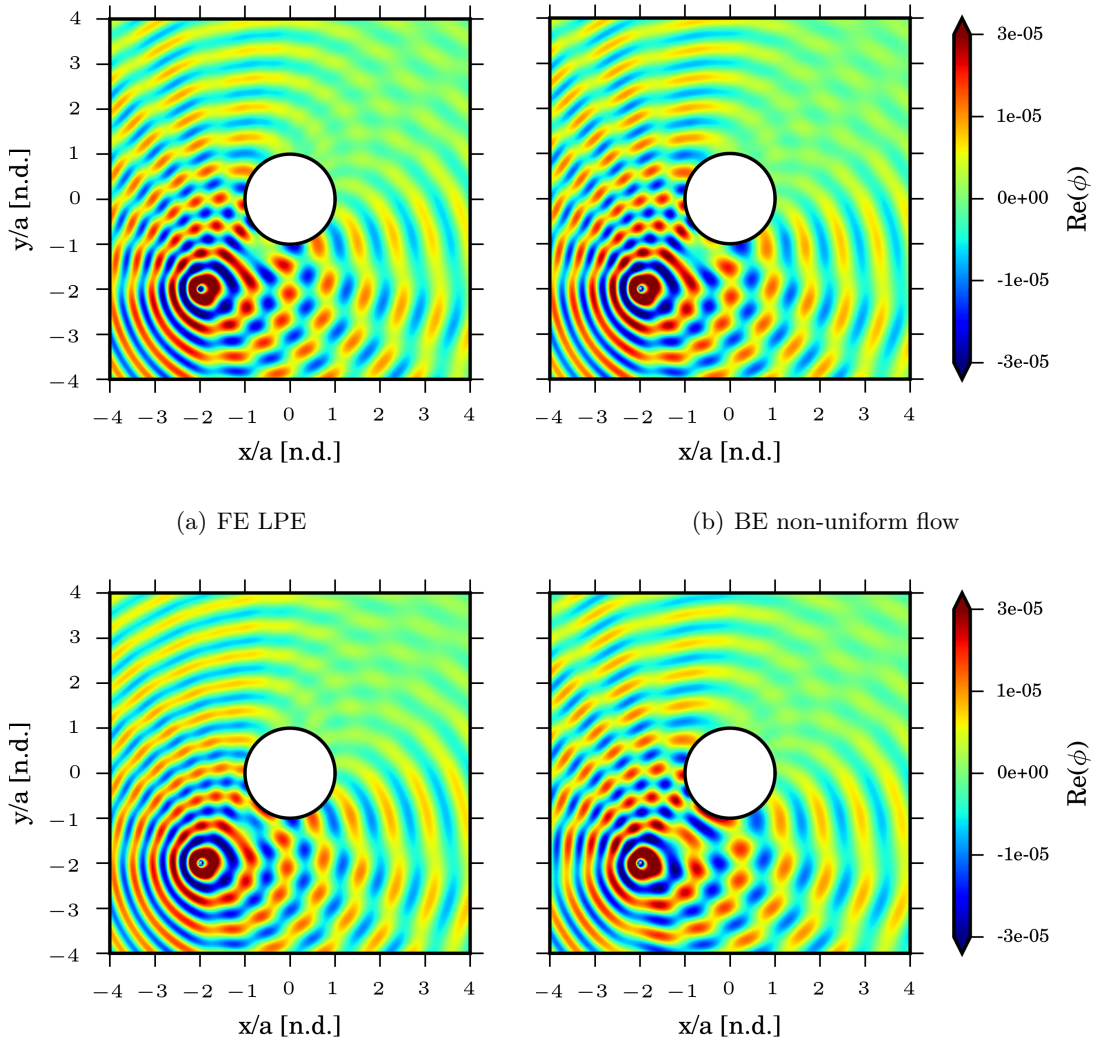

(a) FE LPE

(b) BE non-uniform flow

(c) BE uniform flow

(d) BE Taylor–Helmholtz

Figure 6.28: Real part of the acoustic velocity potential, ϕ, for a non-dimensional frequency $ka = 10$, $M_\infty = 0.3$ and the problem described in Fig. 6.1. The solutions are based on the weakly non-uniform potential flow Helmholtz equation Eq. (5.10), the uniform flow Helmholtz equation [40] and the Taylor-Helmholtz equation Eq. (5.25). A highly refined FE solution of the reference physical model, Eq. (6.2), is provided.

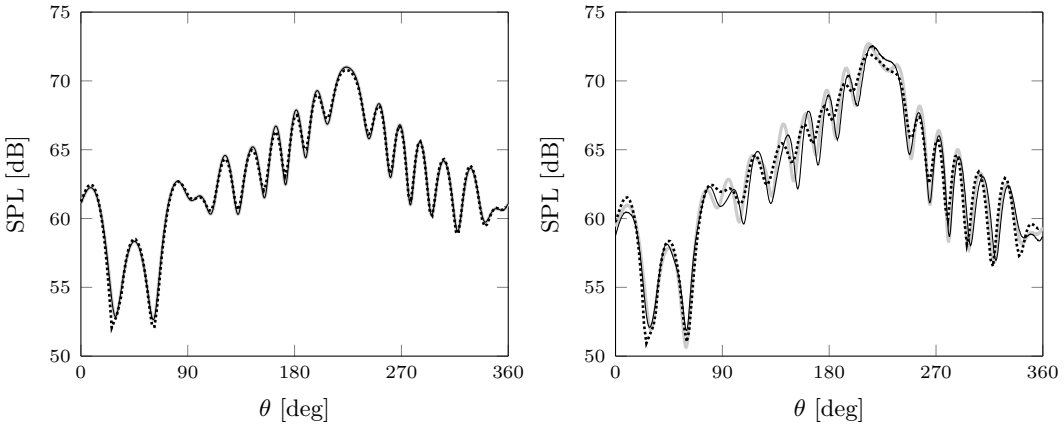

(a) $M_\infty = 0.1$ (b) $M_\infty = 0.3$

Figure 6.29: SPL along a circular arc of field points with radius $r_{fp} = 8a$ for a non-dimensional frequency $ka = 4$ and the problem in Fig. 6.1, with a point source located at $\mathbf{x}_s = (-4a, -4a)$. A BE solution based on the integral formulation in Eq. (5.10) is compared to a FE solution of either the weakly non-uniform flow equation (see Eq. (5.10)) and the linearised potential wave equation (see Eq. (6.2)). Grey, Solid: FE linearised potential. Black, Solid: FE weakly non-uniform flow. Dotted: BE weakly non-uniform flow.

In this section, the previous results have been presented in terms of computed values of the acoustic velocity potential. The acoustic pressure, p', is another quantity of practical interest. The SPL along an arc of field points with radius $r_{fp} = 8a$ is shown in Fig. 6.29 for a non-dimensional frequency $ka = 4$, $M_\infty = 0.1$ and 0.3 with a point source located at $\mathbf{x}_s = (-4a, -4a)$. The boundary element and finite element solutions based on the weakly non-uniform flow formulation are compared to the finite element solution based on the linearised potential wave equation. The solutions at $M_\infty = 0.1$ are overlapped whereas some differences can be seen for $M_\infty = 0.3$. While in the BE solution to the weakly non-uniform flow formulation an approximation has been provided, the corresponding FE solution can account for the exact Green's function to the limit of numerical resolution.

Again, we consider a monopole point source located at $\mathbf{x}_s = (-2a, -2a)$. The SPL along an arc of field points with radius $r_{fp} = 4a$ for $M_\infty = 0.1$ and 0.3 is shown in Fig. 6.30. The FE reference solution is compared to the BE solutions for a number of observer locations (the angle θ is measured from the x-axis and counterclockwise) and a non-dimensional frequency $ka = 10$. For $M_\infty = 0.1$, all the integral formulations are mostly within 1 dB and 5 dB of the reference solution. However, the error for the Taylor–Helmholtz solution reaches 10 dB for $M_\infty = 0.3$. The BE solution based on wave propagation with uniform flows overestimates the reference solution in the shielded area [$\theta = 30 \rightarrow 70$ degrees]. In this region, the incident and the scattered field interfere destructively and the flow is not aligned with the uniform stream. Note that the uniform flow Helmholtz formulation neglects wave refraction effects due to non-uniformities in the mean flow.

In summary, when compared to a highly-refined numerical solution based on the potential linearised wave equation, Eq. (2.30), the L^2-error on the weakly non-uniform potential flow

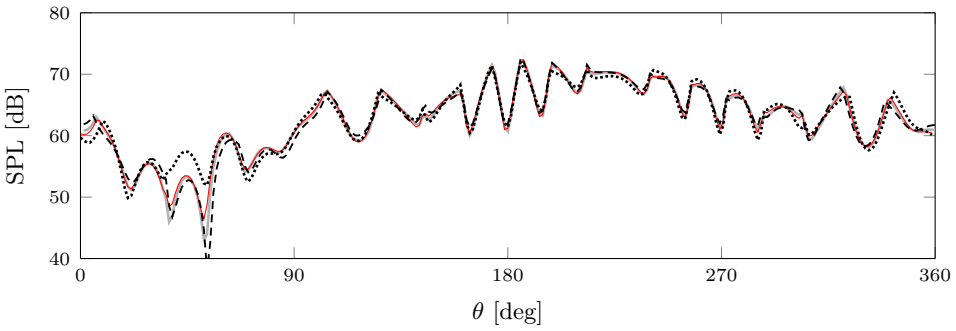

(a) $M_\infty = 0.1$

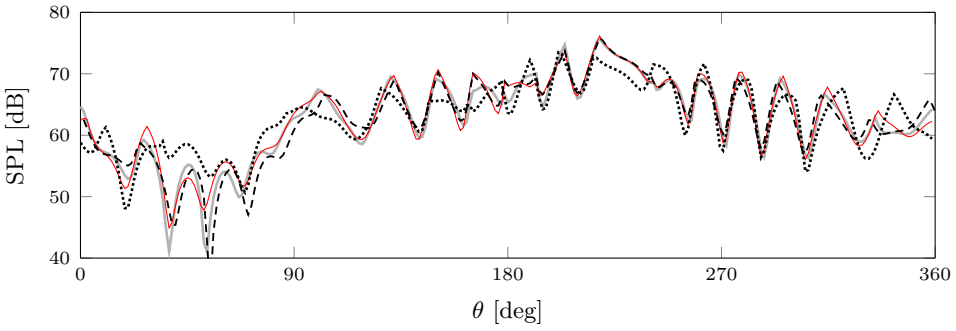

(b) $M_\infty = 0.2$

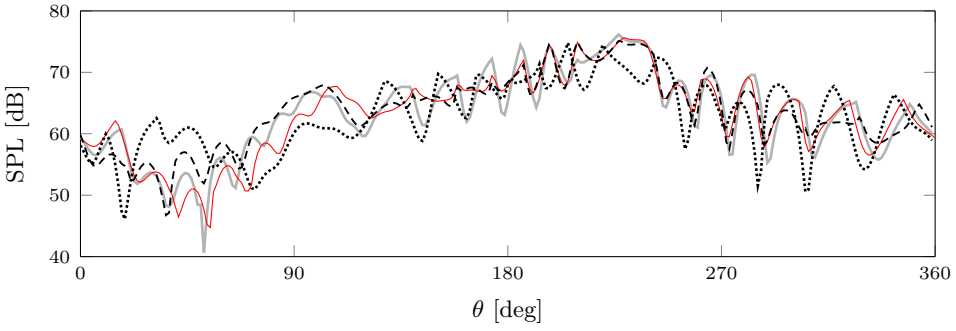

(c) $M_\infty = 0.3$

Figure 6.30: SPL along a circular arc of field points with radius $r_{fp} = 4a$ for a non-dimensional frequency $ka = 10$. The BE solutions of the problem in Fig. 6.1 are based on the integral formulations in Eq. (5.10) (BE weakly non-uniform flow), Wu and Lee [40] (BE uniform flow) and Eq. (5.25) (BE Taylor–Helmholtz). A reference FE solution of the linearised potential wave equation is also reported. Solid, grey: FE LPE. Solid, red: BE non-uniform flow. Dashed: BE uniform flow. Dotted: BE Taylor–Helmholtz.

Helmholtz equation, Eq. (2.35), varies linearly with frequency (see Fig. 6.23) and with M_∞^2 (see Fig. 6.25). The error is independent of the distance to the observer when it is sampled in a region where the flow is almost uniform (see Fig. 6.24). Note that Eq. (2.30) is exact for a uniform flow, namely no additional error is generated when wave propagation occurs in a uniform flow region. These results validate the error analysis in Sec. 4.5. We have also shown that the Green's function proposed for the weakly non-uniform flow formulation favourably agrees with that evaluated using a finite element solution (see Fig. 6.29).

The boundary element results of this section show that the weakly non-uniform flow Helmholtz formulation outperforms both the uniform flow Helmholtz and the Taylor–Helmholtz formulations (see Figs. 6.25). The improvement on the uniform flow Helmholtz solution is larger at low Mach numbers and less significant at higher values (see Figs. 6.25 and 6.26). This can be expected if the error analysis in Sec. 4.5 is considered. It is likely that for increasing M_∞, terms of order $M_\infty M_0'/L_A^2$ in Eq. (4.42) become comparable to those of order M_0'/L_A^2. The latter are the additional error terms generated by the uniform flow formulation compared to the weakly non-uniform flow equation. Since error source terms of order $M_\infty M_0'/L_A^2$ are generated by both these formulations, similar accuracy might be expected at the higher M_∞.

6.5.2.2 Sound source in a non-uniform flow

We consider the same test case as that in Fig. 6.1 but with a point source located at $\mathbf{x}_s = (-1.3a, -0.5a)$ where the non-uniform mean flow component, M_0', is of the same order of magnitude as M_∞. The L^2-error for the acoustic potential, ϕ, and the acoustic pressure, p', along a circular arc of field points with radius $r_{fp} = 4$, are shown in Figs. 6.31 and 6.32 against M_∞, for non-dimensional frequencies $ka = 2$, 5 and 10. Contours of the real part of ϕ are presented in Fig. 6.33 for $M_\infty = 0.3$. We compare the results for the weakly non-uniform flow formulation, the uniform flow [40] and the Taylor–Helmholtz integral equations.

In this case, the Taylor–Helmholtz and the weakly non-uniform flow formulations outperform the uniform flow convected wave equation for $M_\infty \leq 0.2$, (see Figs. 6.31 and 6.32). However, for $M_\infty \geq 0.2$ the uniform flow formulation performs better than that based on the Taylor–Helmholtz equation (see Figs. 6.31 and 6.32). For $M_\infty \geq 0.2$, terms of order M_∞^2 are more significant to the accuracy of the approximation than modelling first order non uniform flow effects in M_0. This result further validates the error analysis in Appendix A, in that the Taylor–Helmhotlz formulation is a reasonable approximation of the reference model, Eq. (2.30), only in the geometric and acoustic near field. However, the approximation deteriorates if the observer moves further away from the scatterer in a uniform flow.

For every Mach number and frequency considered in this example, the weakly non-uniform flow formulation showed, again, the best accuracy compared to the boundary element solutions based on either a uniform mean flow or the Taylor–Helmholtz formulation (see Figs. 6.31 and 6.32). For the weakly non-uniform formulation, the corresponding L^2-error for ϕ was again proportional to M_∞^2 and consistent with the L^2-error on the acoustic pressure (see Figs. 6.31 and 6.32). This is expected as the gradient of the potential was derived by performing an analytical derivation of the kernel in Eq. (4.16). This was also the case for the Taylor–Helmholtz formulations. Therefore an additional error is not provided. The error on the Taylor–Helmholtz formulation also was seen to vary with M_∞^2 while the uniform flow approximation showed a linear dependence on M_∞. However, this dependence is not

representative of the uniform flow formulation; the mean flow is the same for every geometry considered and, therefore, it is likely that the error varies with the shape of the scatterer.

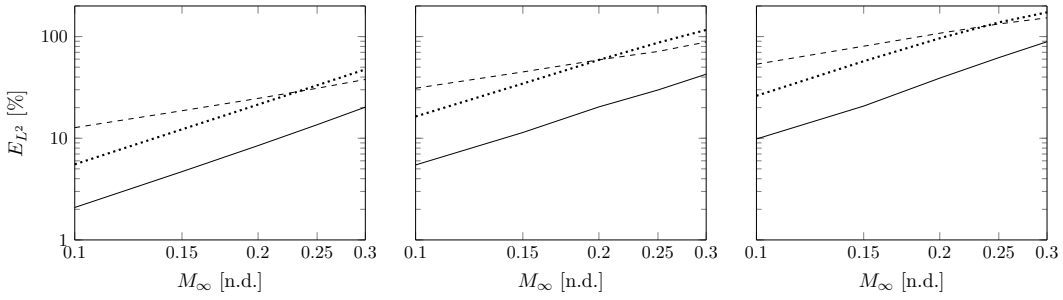

(a) $ka = 2$ (b) $ka = 5$ (c) $ka = 10$

Figure 6.31: L^2-error for ϕ along a circular arc of field points with radius $r_{fp} = 4a$ against M_∞ for the problem in Fig. 6.1 and a point source located at $\mathbf{x}_s = (-1.3a, -0.5a)$. Solid: BE weakly non-uniform potential flow Helmholtz equation, Eq. (5.10). Dashed: BE uniform flow Helmholtz equation [40]. Dotted: Taylor–Helmholtz equation, Eq. (5.25).

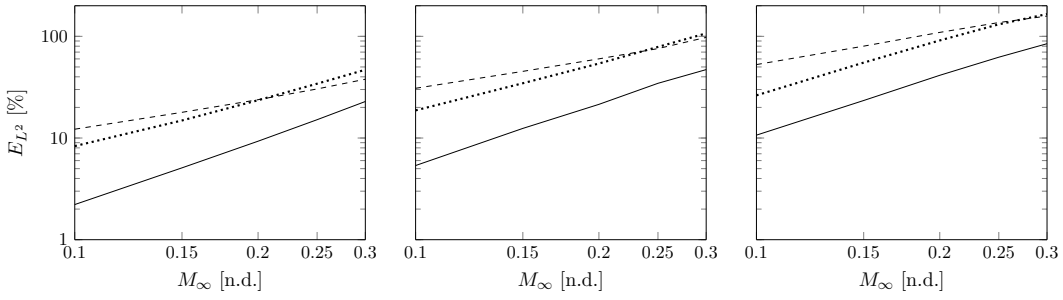

(a) $ka = 2$ (b) $ka = 5$ (c) $ka = 10$

Figure 6.32: L^2-error for p' along a circular arc of field points with radius $r_{fp} = 4a$ against M_∞ for the problem in Fig. 6.1 and a point source located at $\mathbf{x}_s = (-1.3a, -0.5a)$. Solid: BE weakly non-uniform potential flow Helmholtz equation, Eq. (5.10). Dashed: BE uniform flow Helmholtz equation [40]. Dotted: Taylor–Helmholtz equation, Eq. (5.25).

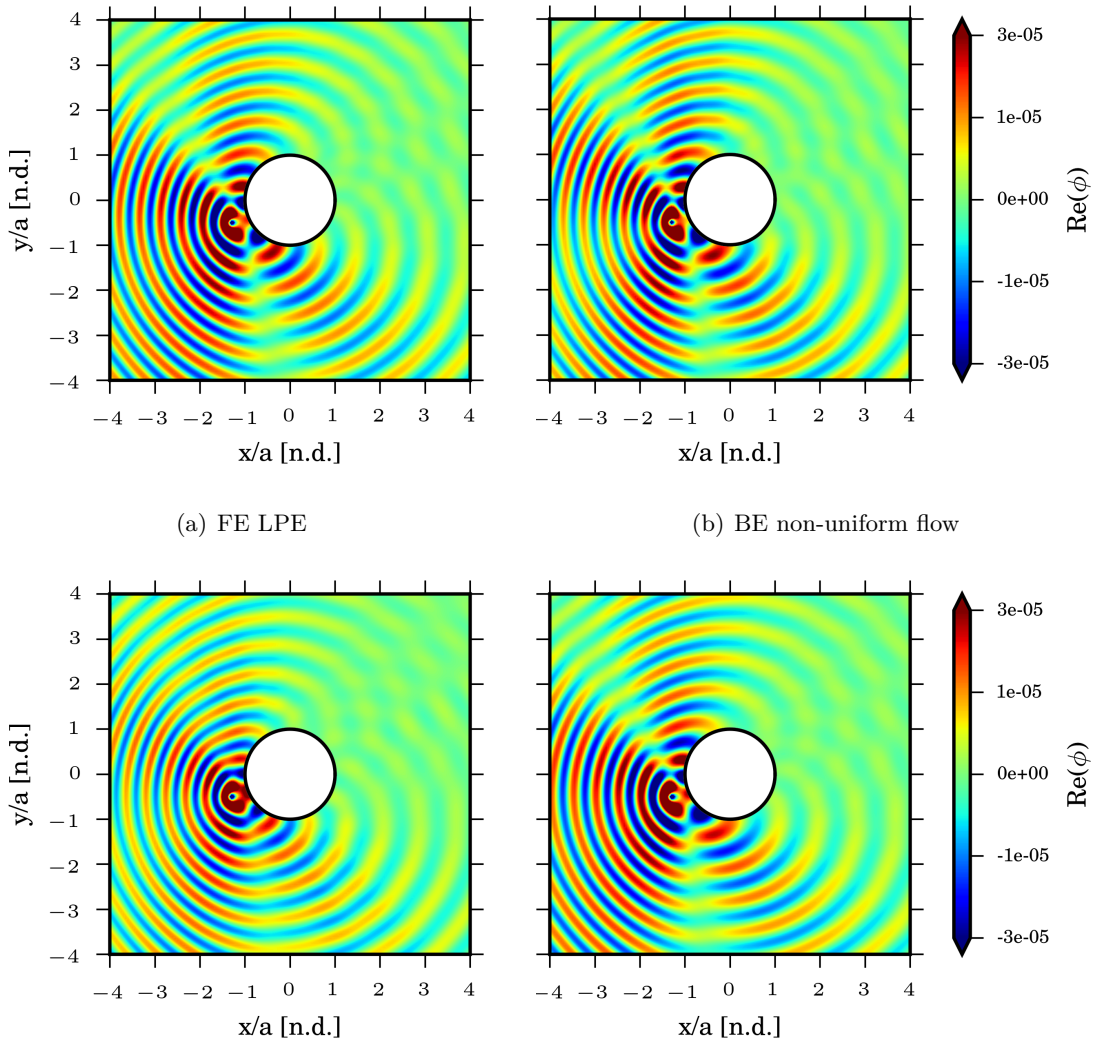

(a) FE LPE

(b) BE non-uniform flow

(c) BE uniform flow

(d) BE Taylor–Helmholtz

Figure 6.33: Real part of the acoustic velocity potential, ϕ, for a non-dimensional frequency $ka = 10$, $M_\infty = 0.3$ and the problem defined in Fig. 6.1 with a point source at $\mathbf{x}_s = (-1.3a, -0.5a)$. The solutions are based on the weakly non-uniform potential flow Helmholtz equation Eq. (5.10), the uniform flow Helmholtz equation [40] and the Taylor–Helmholtz equation, Eq. (5.25). A highly refined FE solution of the reference physical model, Eq. (2.29), is provided.

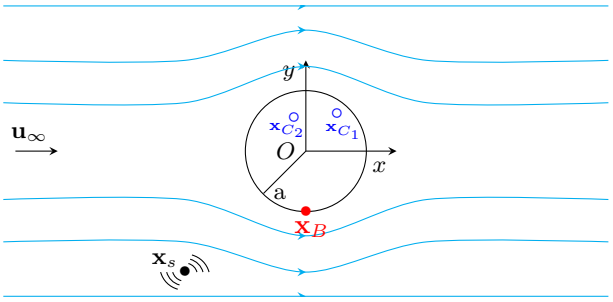

Figure 6.34: Reference domain for the assessment of the combined integral method showing the overdetermination points for the baseline test case. Scattering of a monopole point source by a rigid cylinder in a non-uniform potential subsonic flow.

6.6 Non-uniqueness issue

A generalised combined boundary integral formulation and a Burton–Miller approach with mean flow have been presented in Sec. 5.2.5. First, the problem in Fig. 6.1 is used to give numerical results based on the combined integral formulation. Second, it is used to validate the generalized Burton–Miller formulation.

6.6.1 Overdetermination points and mean flow

Let us consider the problem in Fig. 6.1 and a monopole point source located at $\mathbf{x}_s = (-2a, -2a)$. Following the work of Chen *et al.* [132] for a quiescent medium, two overdetermination points are chosen: $\mathbf{x}_{C_1} = (0.5147a, 0.612a)$ and $\mathbf{x}_{C_2} = (-0.1987a, 0.546a)$ (see Fig. 6.34).

Note that for $M_\infty = 0$ an analytical solution to the present test case is available [203]. For $M_\infty = 0$, a comparison among the analytical solution, the standard BE solution and that based on the combined boundary integral equation formulation is reported in Fig. 6.35 against the non-dimensional frequency ka at $\mathbf{x}_B$ on the boundary surface (see Fig. 6.34). In this case, the non-uniqueness issue can be barely observed. The likely explanation is that the effect of the non-uniqueness issue on the solution with quiescent media depends on the mesh resolution [131]. The current discretisation guarantees a limited bandwidth of this effect so that we are not able to clearly detect the resonant peak with the sampling frequency used in this example, i.e. $\Delta ka = 0.02$.

The same test case is then considered for $M_\infty = 0.1 \to 0.3$, for which the author has not found an analytical solution. In Fig. 6.35, results based on the combined boundary integral solution are presented against the non-dimensional frequency ka for $\mathbf{x}_B$ and then compared to a conventional BE solution. We depicts the solutions based on either Eq. (5.40) "*BE CHIEF-unif. flow*" or the corresponding formulation with a quiescent media "*BE CHIEF-no flow*" at the overdetermination points. For clarity, the notations "*unif. flow*" and "*no flow*" are related to the mean flow at the overdetermination points, while the weakly non-uniform

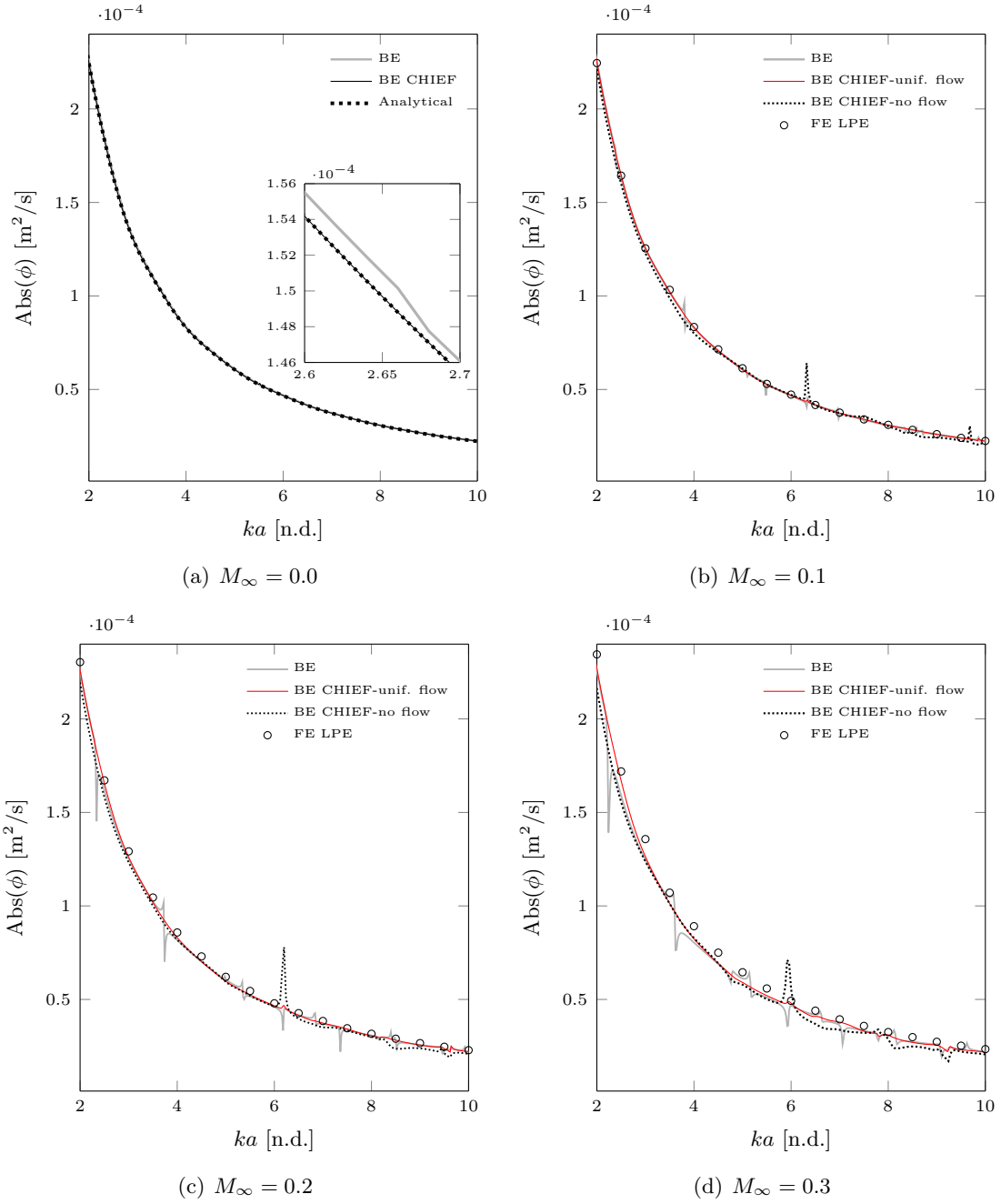

(a) $M_\infty = 0.0$ (b) $M_\infty = 0.1$

(c) $M_\infty = 0.2$ (d) $M_\infty = 0.3$

Figure 6.35: Absolute value of the acoustic velocity potential, ϕ, at a point $\mathbf{x}_B$ against the non-dimensional frequency ka for the problem described in Fig. 6.34. The standard BE solution is based on Eq. (4.21) while the combined integral approach is based on Eq. (5.47). The analytical solution for $M_\infty = 0$ is given in Morris and Brien [203] and the FE solution of the full potential linearised wave equation is shown for reference.

flow formulation is used to solve the problem in both cases. The finite element solution based on the linearised potential wave equation is also illustrated.

The same results as those shown in Figs. 6.35, but based on non-uniform flows at the overdetermination points, were clearly inaccurate and are reported in Appendix C. At the overdetermination points, the potential flow violates the weakly non-uniform ansatz, in that

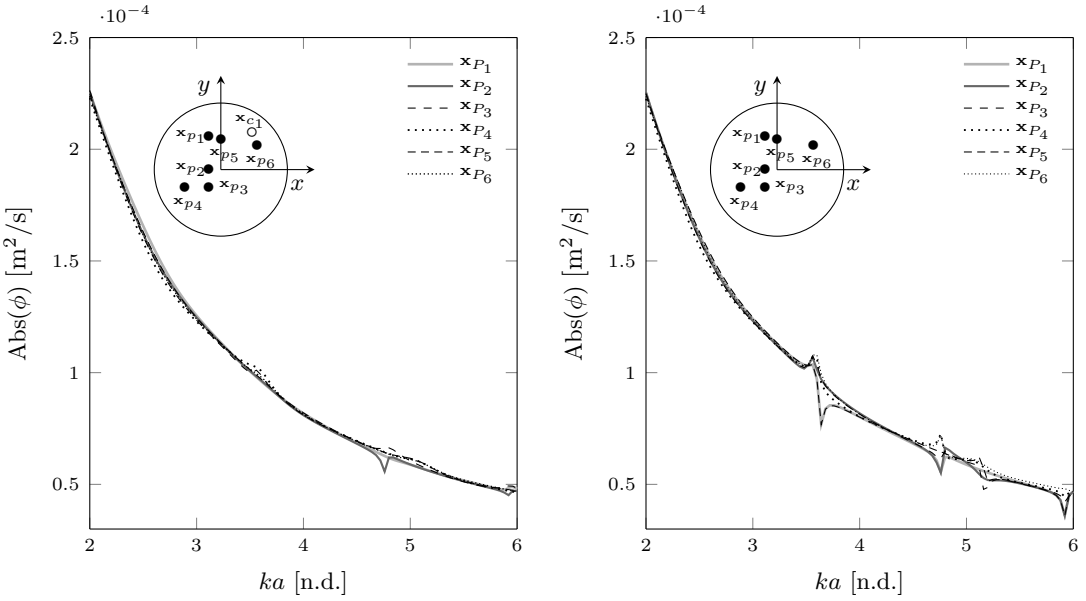

(a) C_1 fixed (b) without C_1

Figure 6.36: Absolute value of the acoustic velocity potential, ϕ, against the non-dimensional frequency ka, at a point $\mathbf{x}_B$, and the problem described in Fig. 6.34 and $M_\infty = 0.3$. Effect of the position of the CHIEF points on the non-uniqueness issue. $\mathbf{x}_{P_1} = (-0.198a, 0.546a)$, $\mathbf{x}_{P_2} = (-0.198a, 0.000)$, $\mathbf{x}_{P_3} = (-0.198a, -0.300a)$, $\mathbf{x}_{P_4} = (-0.600a, -0.300a)$, $\mathbf{x}_{P_5} = (0.500a, 0.000a)$, $\mathbf{x}_{P_6} = (0.600a, 0.400a)$.

$M_0' > M_\infty$, leading to inaccurate results even if only a single overdetermination point is considered.

The sensitivity of the solution, ϕ, to the position of the overdetermination points is assessed in Fig. 6.36 for $M_\infty = 0.3$ against the non-dimensional frequency ka. Again, we show the results for $\mathbf{x}_B$ on the boundary surface (see Fig. 6.34). Initially, $\mathbf{x}_{C_1}$ is fixed and a second overdetermination point, denoted as $\mathbf{x}_{P_1}, \mathbf{x}_{P_2}, ..., \mathbf{x}_{P_6}$, is located in a different position. Then, the same results are obtained omitting $\mathbf{x}_{C_1}$ in the analysis. These results are computed considering a uniform flow at the overdetermination points.

Contours of the real part of the acoustic potential, ϕ, are shown in Fig. 6.37. The results based on the combined integral formulation, Eq. (5.47), are compared to the conventional BE solution for a non-dimensional frequency $ka = 3.62$ and $M_\infty = 0.3$. In this case, the combined integral solution has been obtained including both the overdetermination points $\mathbf{x}_{C_1}$ and $\mathbf{x}_{C_2}$. The non-dimensional frequency has been selected based on the frequency sweep analysis in Fig. 6.35 to trigger an irregular frequency for the current test case. The solution based either on Eq. (5.40) "*BE CHIEF-unif. flow*" or the corresponding no-flow formulation "*BE CHIEF-no flow*" is shown. The FE solution based on the reference physical model is also provided.

In Fig. 6.38, the SPL is depicted against the angle θ along an arc of field points with radius $r_{fp} = 8a$, centred at $\mathbf{x} = (0, 0)$, for non-dimensional frequencies $ka = 5.34$ and $M_\infty = 0.2$. It also illustrates the results for $ka = 3.62$ and $M_\infty = 0.3$. Note that θ is zero along the x-axis

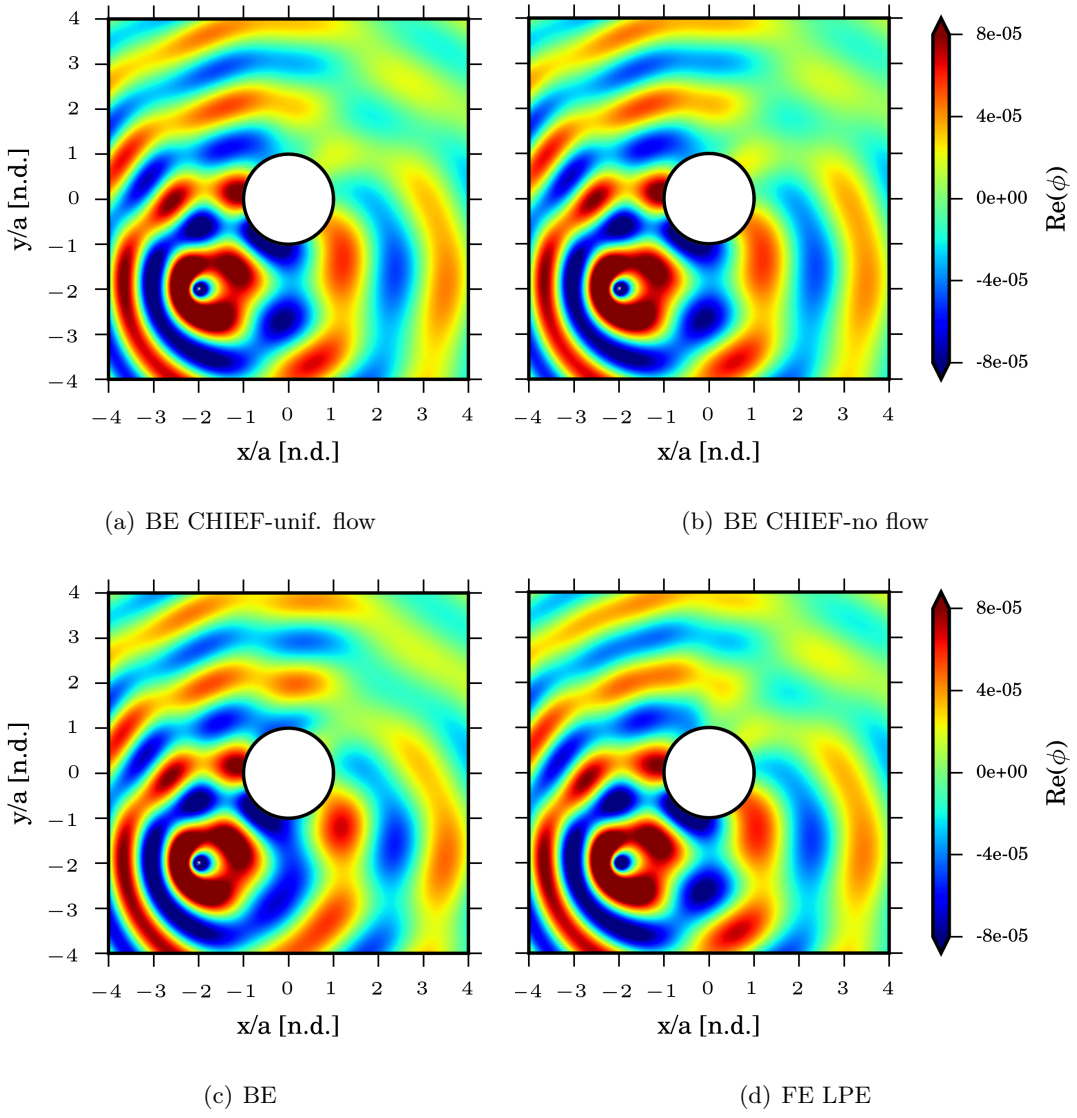

(a) BE CHIEF-unif. flow

(b) BE CHIEF-no flow

(c) BE

(d) FE LPE

Figure 6.37: Real part of the acoustic velocity potential for a non-dimensional frequency $ka = 3.62$, $M_\infty = 0.3$ and the problem described in Fig. 6.34. The BE solution is based on Eq. (4.21), while the combined integral approach in Eq. (5.47) is solved by assuming either a uniform flow or a quiescent medium at the overdetermination points. The finite element (FE) solution is based on Eq. (6.2)

and is measured counterclockwise. The solutions based on the proposed combined integral formulation are compared to the BE solution in Eq. (5.11) and the FE reference solution.

To evaluate possible effects of assuming either a uniform or a quiescent medium at the overdetermination points on the numerical accuracy of the discrete system of equations associated to the BE model, we now report the condition number of the coefficient matrix solving the BE problem in a least-squares sense. It is the matrix obtained by pre-multiplying the boundary element matrix of the coefficients including the constraint equations at the overdetermination points (see Eq. (5.47)) by its transpose. The condition number is relevant to the accuracy of direct solvers and the convergence of those iterative.

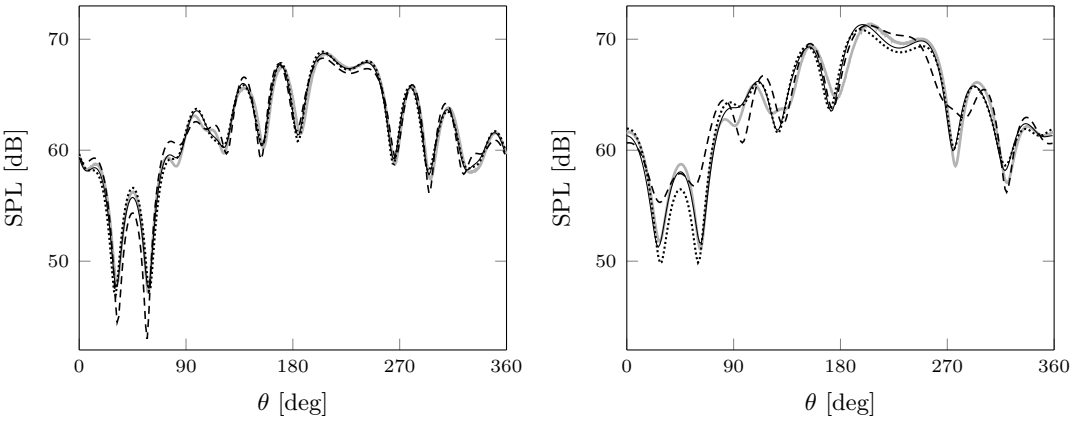

(a) $ka = 5.34$, $M_\infty = 0.2$.

(b) $ka = 3.62$, $M_\infty = 0.3$

Figure 6.38: SPL along an arc of field points centered at $\mathbf{x} = (0, 0)$ with radius $r_{fp} = 8a$ for the problem described in Fig. 6.34. The BE solution is based on Eq. (4.21), the combined integral approach is given in Eq. (5.47) and the finite element (FE) solution is based on Eq. (6.2). Solid, grey: FE LPE. Dashed: BE non-uniform flow. Solid, black: CHIEF with non-unif. flow overdet. points. Dotted: CHIEF with no flow overdet. points.

In this example, the mesh is fixed for every Mach number and accounts for eight degrees of freedom per wavelength based on the largest frequency considered, i.e. $ka = 10$. Figure 6.39 illustrates the condition number against the non-dimensional frequency ka for $M_\infty = 0.1$, 0.2 and 0.3 including either 2 or 4 overdetermination points. It compares the solution for either a uniform or a quiescent medium at the overdetermination points. In Fig. 6.40, we show the condition number against the non-dimensional frequency at $M_\infty = 0.1$ and 0.3 respectively for 2, 4 and 10 overdetermination points. For convenience, we report again the results for 2 and 4 overdetermination points.

It is shown that the condition number clearly increases in the vicinity of the resonant frequencies and is not strongly affected by the assumption of the mean flow at the overdetermination points (see Fig. 6.39). The likely explanation for such a small sensitivity of the condition number to the mean flow assumption at the overdetermination points is that the formulations based on either a uniform flow or a quiescent medium differ only for a small complex constant value, which depends on the Mach number (see Sec. 5.2.5.1). Nonetheless, although an increment in the condition number is expected with an increase in the overdetermination points, an increase in the Mach number seems not to be critical for the conditioning (see Fig. 6.40). However, the results indicate that the condition number is more sensitive to an increase in the number of overdetermination points for higher Mach numbers (see Fig. 6.40).

To sum up, the generalized combined integral formulation worked around the irregular frequency issue in the frequency range considered, i.e. $1 \leq ka \leq 10$. We observed that the mean flow introduced a shift in the irregular frequencies. As indicated by Zhang *et al.* [148] for a uniform flow, the non-uniqueness issue deteriorates with an increase of M_∞. This was also the case for a non-uniform mean flow since the kernel in Eq. (5.11) is dependent on M_0

(see Fig. 6.35). The inaccuracy introduced by the non-uniqueness issue reached 5 dB for $\theta = 25 \rightarrow 75$ degrees (see Fig. 6.38), where the incident and the scattered field interacted destructively. The solutions based on the combined integral formulation were not strongly sensitive to the assumption of a uniform mean flow at the overdetermination points (see Fig. 6.36). Nonetheless, the solution based on this assumption outperformed that based on the no-flow ansatz, while a non-uniform mean flow at the overdetermination points provided inaccurate results (see Sec. C.4).

As expected, the combined integral formulation worked around the non-uniqueness issue for low frequencies but was less effective at higher frequencies. This is expected since the density of the irregular frequencies affecting the rank of the coefficient matrix, related to the resonances of the interior domain, increases with ka. Therefore, an increase in the number of overdetermination points is needed for higher frequencies also in the presence of a mean flow. Therefore, as for conventional formulation with quiescent media [50], the combined integral formulation is not suitable for large-scale short-wave propagation problems since a large number of overdetermination points leads to an ill-conditioned coefficient matrix.

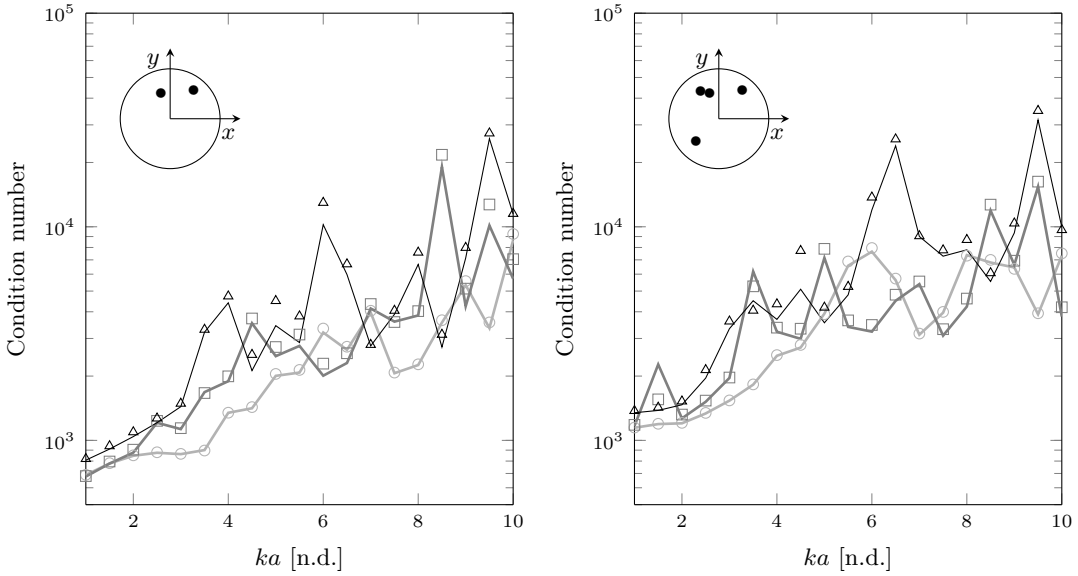

(a) 2 overdetermination points (b) 4 overdetermination points

Figure 6.39: Condition number of the boundary element coefficient matrix against the non-dimensional frequency ka for the problem described in Fig. 6.34. The results are based on the combined integral approach in Eq. (5.47) and a least-squares approximation. Solid line: CHIEF unif. flow. Symbols: CHIEF no flow. Light grey (◯): $M_\infty = 0.1$. Dark grey (□): $M_\infty = 0.2$. Black (△): $M_\infty = 0.3$.

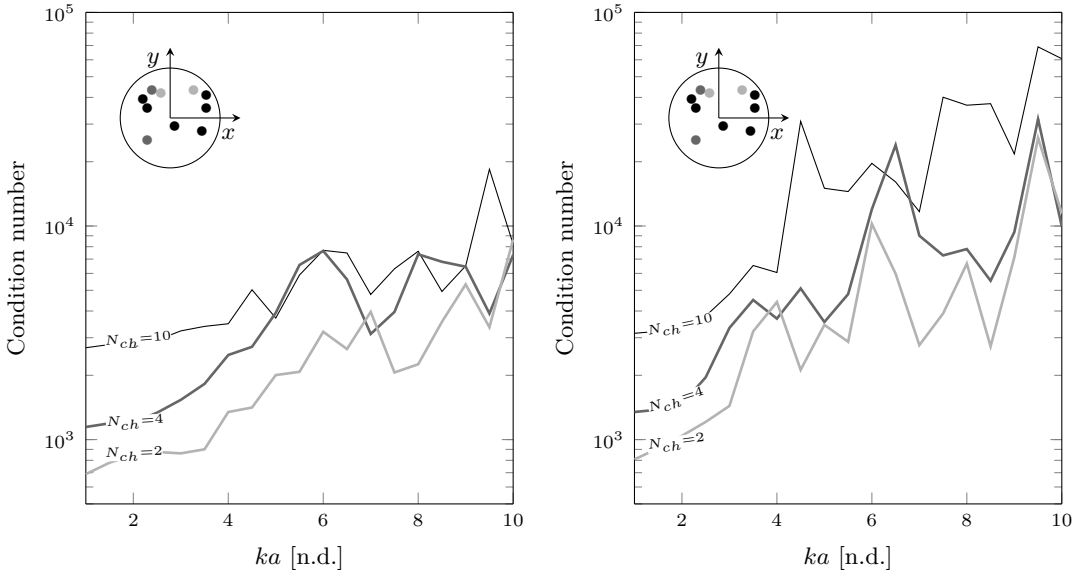

(a) $M_\infty = 0.1$ (b) $M_\infty = 0.3$

Figure 6.40: Condition number of the boundary element coefficient matrix against the non-dimensional frequency ka for the problem described in Fig. 6.34 and a least-squares approximation. The results are based on the combined integral approach in Eq. (5.47) and a uniform flow at the overdetermination points. N_{ch} denotes the number of overdetermination points.

6.6.2 Assessment of the Burton–Miller formulation

The problem in Fig. 6.34 is used in this section as a proof-of-concept for the generalized Burton–Miller formulation developed in Sec. 5.2.5.2. Consider a monopole point source at $\mathbf{x}_s = (-2a, -2a)$. The absolute value of the acoustic potential, ϕ, at $\mathbf{x}_B = (0, -a)$ versus the non-dimensional frequency ka is depicted in Fig. 6.41 for M_∞ in the range $0 \rightarrow 0.3$. It shows the BE solution based on Eq. (5.11) and the Burton–Miller solution given in Eq. (5.59). In the case of $M_\infty = 0$, the analytical solution is, again, provided based on the literature [203]. In the presence of the mean flow, the BE solution based on the combined integral formulation and a uniform flow at the overdetermination points is also depicted. Nonetheless, we illustrate the FE solution based on the linearised potential wave equation and the results of the Burton–Miller formulation solved in the transformed Taylor–Lorentz space. The results based on the Burton–Miller formulation developed in the physical space are in good agreement with the corresponding results based on the Taylor–Lorentz formulation.

Although the results in Fig. 6.41 are based on a non-uniform mean flow, they are consistent with the solutions seen in Zhang and Wu [148] for a uniform mean flow in that for higher frequencies and Mach numbers, i.e. $ka \geq 6$ and $M_\infty \geq 0.2$, the boundary element solution is largely affected by the non-uniqueness issue over the entire frequency range. At these frequencies, the combined boundary integral solution is still slightly affected by this issue while the Burton–Miller formulation clearly improved on it. Note that the decay rate of the acoustic potential field, proportional to $1/\sqrt{ka}$, is recovered in the solutions based on the Burton–Miller formulation for all the frequencies considered in the numerical example. It is not generally seen for the conventional boundary element solution in the vicinity of the irregular frequencies because of the ill-conditioning of the matrix of the coefficient.

Let us consider the point source at $\mathbf{x}_s = (-4a, -4a)$. The SPL for the non-dimensional frequency $ka = 16$ is shown in Fig. 6.42 along an arc of field points with radius $r_{fp} = 8a$ for $M_\infty = 0.1$ and 0.3. The phase of the corresponding pressure field is plotted in Fig. 6.43. Furthermore, the same results as those in Figs. 6.42 and 6.43 are shown for $ka = 30$ in Figs. 6.44 and 6.45. Good agreement is shown between the boundary element solutions whereas a more clear difference is seen between the BE and FE solutions in the case where $M_\infty = 0.3$.

To conclude, note again that the non-uniqueness issue deteriorated with an increase in M_∞ (see Fig. 6.41). The generalized Burton–Miller formulation has worked around the non-uniqueness issue for any frequency and Mach number considered in this numerical example (see Fig. 6.41). As expected, the Burton–Miller solutions based on the weakly non-uniform formulation either in the physical or transformed Taylor–Lorentz space agreed well for all the test cases considered (see Figs. 6.42-6.45).

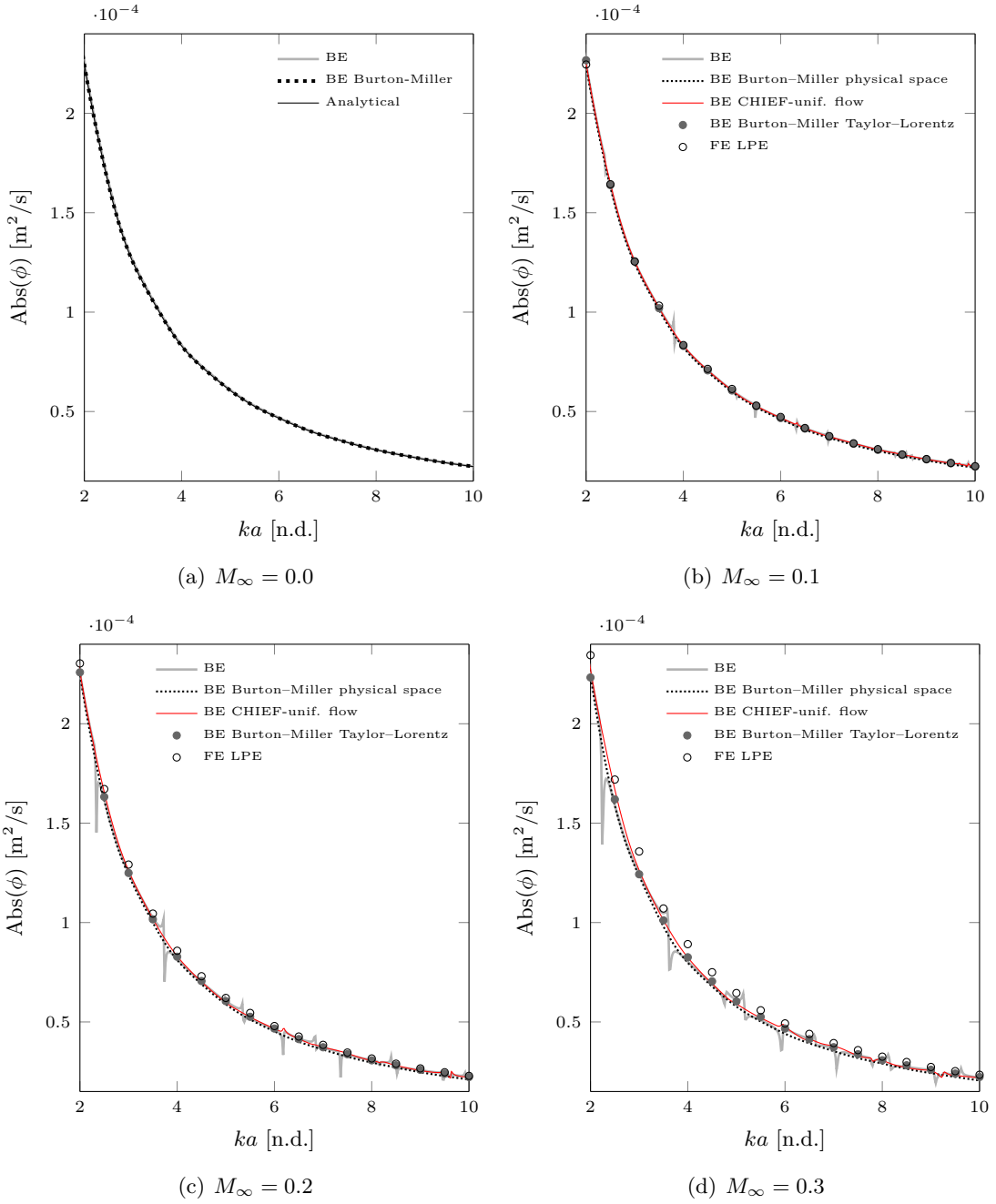

(a) $M_\infty = 0.0$ (b) $M_\infty = 0.1$

(c) $M_\infty = 0.2$ (d) $M_\infty = 0.3$

Figure 6.41: Absolute value of the acoustic velocity potential ϕ against the non-dimensional frequency ka at a point $\mathbf{x}_B$ for the problem described in Fig. 6.34. The solution obtained using Eq. (5.59) (BE Burton–Miller) is compared to the BE solution obtained imposing $\alpha = 0$ in Eq. (5.59) (BE). The solution based on the combined integral formulation, Eq. (5.47) is also shown. The FE solution of the linearised potential wave equation and the BE solution based on the Burton–Miller formulation solved in a Taylor–Lorentz are shown for reference. The analytical solution for $M_\infty = 0$ is given in Morris and Brien [203].

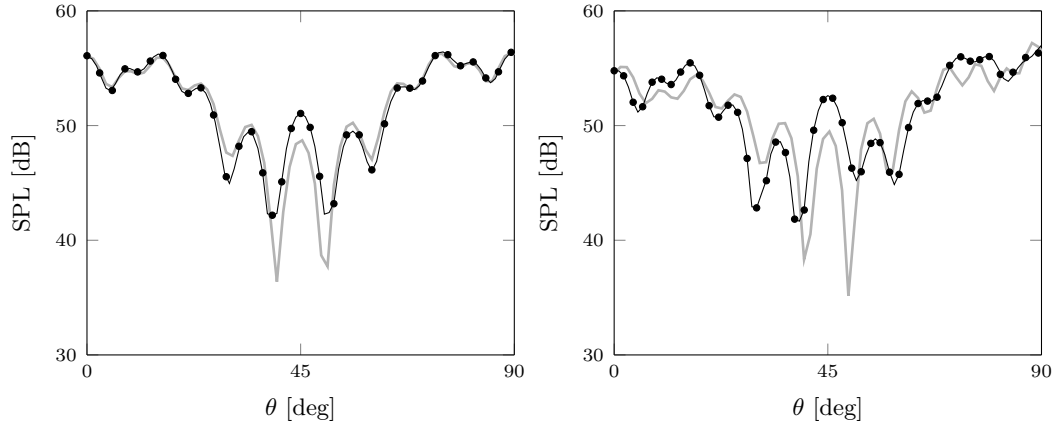

(a) $M_\infty = 0.1$ (b) $M_\infty = 0.3$

Figure 6.42: SPL along an arc of field points with radius $r_{fp} = 8a$ for a non-dimensional frequency $ka = 16$ and the problem in Fig. 6.34. The solutions are based on the Burton–Miller formulation, either in the physical, Eq. (5.59), or in the transformed space, Eq. (5.66). The FE reference solution is also shown. Solid, black: BE Burton–Miller physical space. Symbols: BE Burton–Miller transformed space. Solid, grey: FE LPE.

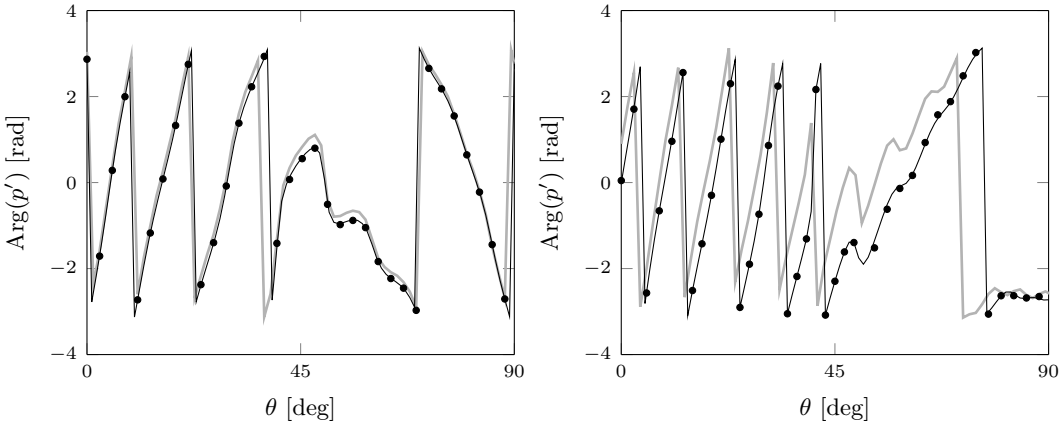

(a) $M_\infty = 0.1$ (b) $M_\infty = 0.3$

Figure 6.43: Phase of the pressure field along an arc of field points with radius $r_{fp} = 8a$ for a non-dimensional frequency $ka = 16$, solution of the problem described in Fig. 6.34. The solutions are based on the Burton–Miller formulation, either in the physical, Eq. (5.59), or in the transformed space, Eq. (5.66). The FE reference solution is also shown. Solid: BE Burton–Miller physical space. Solid, black: BE Burton–Miller physical space. Symbols: BE Burton–Miller transformed space. Solid, grey: FE LPE.

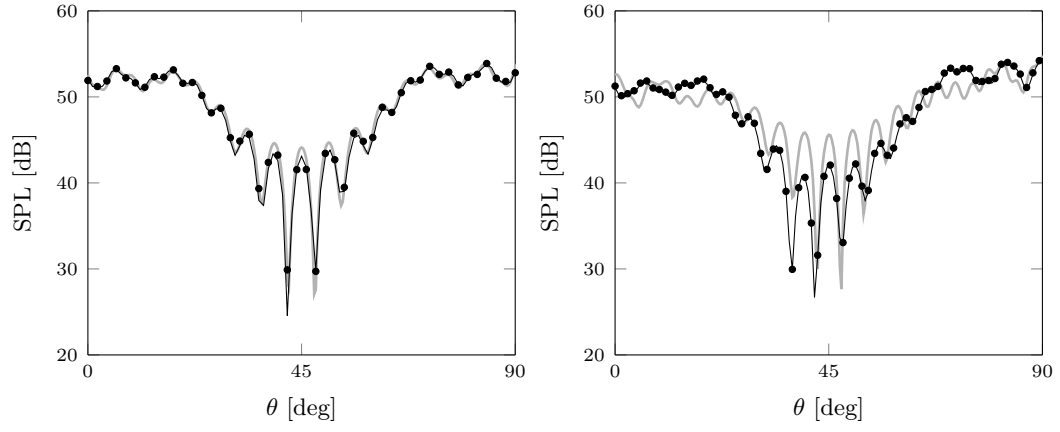

(a) $M_\infty = 0.1$ (b) $M_\infty = 0.3$

Figure 6.44: SPL along an arc of field points with radius $r_{fp} = 8a$ for a non-dimensional frequency $ka = 30$ and the problem in Fig. 6.34. The solutions are based on the Burton–Miller formulation, either in the physical, Eq. (5.59), or in the transformed space, Eq. (5.66). The FE reference solution is also shown. Solid, black: BE Burton–Miller physical space. Symbols: BE Burton–Miller transformed space. Solid, grey: FE LPE.

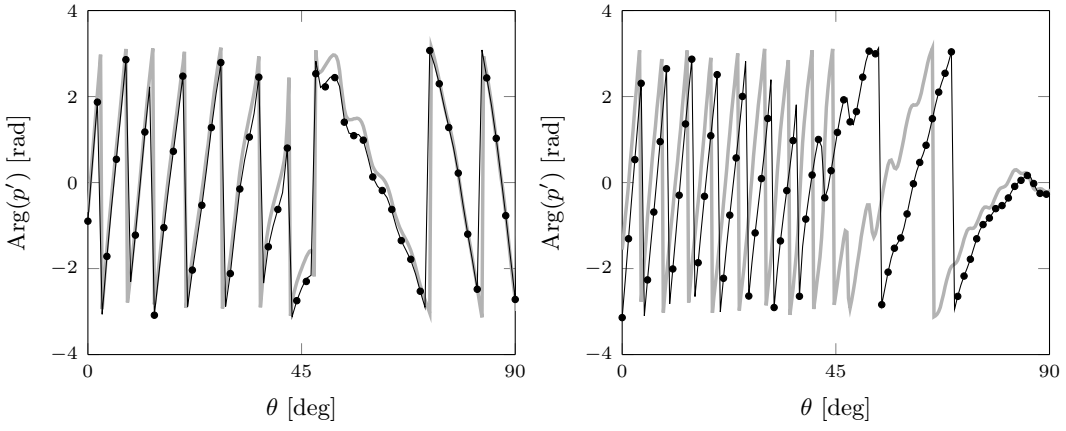

(a) $M_\infty = 0.1$ (b) $M_\infty = 0.3$

Figure 6.45: Phase of the pressure field along an arc of field points with radius $r_{fp} = 8a$ for a non dimensional frequency $ka = 30$, solution of the problem described in Fig. 6.34. The solutions are based on the Burton–Miller formulation, either in the physical, Eq. (5.59), or in the transformed space, Eq. (5.66). The FE reference solution is also shown. Solid, black: BE Burton–Miller physical space. Symbols: BE Burton–Miller transformed space. Solid, grey: FE LPE.

6.7 Concluding remarks

Boundary integral solutions to wave propagation in a non-uniform flow have been verified and benchmarked. The weakly non-uniform flow formulation has been assessed based on numerical examples. First, it has been used as a means of extrapolating a known acoustic field from an inner domain to the far field. In the examples provided, the condition that $M_0' \ll M_\infty$ was satisfied at all points outside the integral surface. Based on the numerical experiments, we showed that the error of the weakly non-uniform potential flow formulation versus a FE reference solution of the linearised potential wave equation scaled as M_∞ for $M_\infty \leq 0.2$ and M_∞^2 for $0.2 < M_\infty \leq 0.3$. Comparisons with alternative formulations have shown that the corresponding error on the Taylor–Helmholtz solution scaled as M_∞^2, while that for the uniform flow formulation with M_∞. In all the test cases, the error increased almost linearly with the frequency, f, consistent with the error analysis in Sec. 4.5. Nevertheless, for every frequency and Mach number, the solutions based on the weakly non-uniform flow formulation outperformed the corresponding solutions based either on a uniform flow or the Taylor–Helmholtz formulation.

Boundary element solutions to wave propagation on a weakly non-uniform flow have also been presented. Noise propagation and scattering has been solved up to a solid surface by using a boundary element method. On the boundary surface itself, the non-uniform flow component M_0' is of the same order of magnitude as M_∞, pushing to the limit the assumption underlying the weakly non-uniform flow wave equation that $M_0' \ll M_\infty$. For $M_\infty \leq 0.3$, the numerical results of this chapter suggest that the solution is consistent with the weakly non-uniform flow ansatz in that the error predicted on the physical model was of the same order of magnitude as that shown for wave extrapolation, where this assumption was more clearly satisfied.

We set $M_\infty = 0.3$ as the threshold in this example since for $M_\infty > 0.3$ the results based on either the physical or the transformed space formulation less favourably agreed. This is due to the approximations performed to obtain either the Green's function for the physical space formulation or the standard Helmholtz equation in a transformed Taylor–Lorentz space. As we have shown in Sec. 4.5, although these approximations are consistent, they deteriorate with an increase of Mach number and frequency. However, it is likely that this limit can be relaxed for 3D problems, where the characteristic length scales of the mean flow non-uniformity compared to the wavelength are larger than for the corresponding 2D problems [204]. This aspect will be further covered by the numerical results of Chapter 8.

Nonetheless, we provided boundary element solutions to the Taylor–Helmholtz formulation. In that case, we solved the same physical model as that used in a number of previous studies for aeroacoustics [26, 32, 33, 36], but without transforming the space-time. Although the Taylor–Helmholtz formulation is a subset of the weakly non-uniform flow formulation, it

was relevant to underline the limitations of this formulation, since it is currently considered in the aeroacoustic research community [105].

First, we benchmarked the Taylor–Helmholtz formulation, Eq. (4.59). An error analysis based on numerical solutions for the scattering of a monopole point source was performed using the linearised potential wave equation as a reference model. The L^2-error on the physical model increased with M_∞^2 consistent with the dimensional error analysis of Astley and Bain [32], while a linear dependence on frequency was shown. However, the error was independent of frequency whenever the distance of the observer was scaled with the wavelength. This conclusion was also supported by a dimensional error analysis, reported in Appendix A. Accurate solutions based on the Taylor–Helmholtz formulation can only be expected in the geometrical and acoustic near field, since the Taylor–Helmholtz equation is not exact when a uniform mean flow region is reached.

Second, boundary element solutions to the weakly non-uniform flow formulation have been benchmarked against finite element solutions of the linearised potential wave equation. The L^2-error against the reference physical model was proportional to M_∞^2 and scaled linearly with frequency. This result was again consistent with the dimensional error analysis performed in Sec. 4.5. An improvement in accuracy was achieved against the integral solutions based on either a uniform mean flow in the whole domain [40] or the Taylor–Helmholtz formulation. A significant advantage of the current weakly non-uniform potential flow Helmholtz solution over the uniform flow Helmholtz solution was clearly seen for $M_\infty \leq 0.2$. The results suggested an incremental improvement in the prediction of the phase of the acoustic field rather than of the absolute value. This improvement was more clearly seen in the regions where the non-uniformity in the mean flow was also significant. This is relevant to applications where an accurate prediction of the phase of the acoustic field is required, such as aircraft cabin noise, although the present formulation does not include the effects of mean flow boundary layer [205].

A boundary element solution based on the generalised combined integral equation formulation in the physical space has been tested to get around the non-uniqueness issue. The numerical examples have shown that the non-uniqueness issue deteriorates with an increase in M_∞. This is due to the dependence of the boundary element kernel on the mean flow and confirms the conclusions of Zhang and Wu [148] based on a uniform mean flow. In the numerical examples, the combined integral formulation effectively mitigated the non-uniqueness issue for $ka \leq 10$ and $M_\infty \leq 0.3$. However, a loss in accuracy was shown for the highest frequencies and Mach number. Therefore, this method is suitable for small-scale large-wavelength problems.

Furthermore, the method based on the assumption of a uniform flow at the overdetermination points outperformed the same approach based on a quiescent medium, while the solutions based on non-uniform flows did not provide reliable results. In the case of a non-uniform flow at the overdetermination points, the problem is that the non-uniform mean

flow component is clearly larger than the uniform flow component, violating the assumptions underlying the weakly non-uniform flow ansatz.

We also verified the implementation of the generalized Burton–Miller formulation developed for sound propagation in a weakly non-uniform potential flow. The solution based on the Burton–Miller formulation developed in the physical space were in good agreement with the corresponding solutions obtained in a Taylor–Lorentz space. In the transformed space, the conventional Burton–Miller formulation with quiescent media was exploited to recover the results in the presence of mean flow. In the numerical example, the solutions were consistent up to $ka = 30$ and $M_\infty = 0.3$. Therefore, we infer that the Burton–Miller formulation written either in the physical or in the transformed space is a good candidate to solve large-scale short-wavelength propagation problems with mean flow.

The proposed Burton–Miller formulation will be used in Chapter 7 to solve a proof-of-concept test case for forward fan noise installation effects, including a full-scale simplified aircraft geometry. For this solution, a Kirchhoff surface integral formulation with non-uniform flow will be used in the context of a weakly-coupled formulation. In other words, the nacelle near field will be solved using a finite element solution of the linearised potential equation. Then, the corresponding acoustic field will be projected onto a fuselage where a boundary element problem with mean flow can be solved.

Chapter 7

Application to Fan Noise Installation Effects

Contents

Fan noise is an important concern for aircraft certification [7], particularly at take-off and approach, and the presence of the airframe affects its noise signature. In the literature, predictions of full-scale whole aircraft acoustic installation effects for forward fan noise are based on fast algorithms applied to boundary element solvers [112, 113]. Mean flows are generally limited to either uniform [45, 123] or non-uniform potential mean flows with low-Mach numbers [26], although there are examples of generic mean flows with small velocity gradients [26, 35]. These solutions are usually based on variable transformations.

In this chapter, the boundary element formulation with non-uniform mean flow developed in Chapter 5 is used to solve a proof-of-concept test case representing aircraft acoustic installation effects. The scattering of forward fan noise by a fuselage is predicted using a simplified geometry. The results are based on the boundary integral solution, in the physical space, to the weakly non-uniform formulation and the generalized Burton–Miller approach presented in Chapters 4 and 5 respectively. The weakly-coupled approach of Chapter 4 is also used to avoid solving the nacelle acoustic near field with BEM, where the weakly non-uniform flow ansatz is more clearly violated. The boundary element solutions

are benchmarked against finite element solutions based on the linearised potential wave equation.

In Sec. 7.1, the numerical model is described. In Sec. 7.2, first, we present numerical results for a wave extrapolation approach based on an open radiating surface. Second, a weakly-coupled approach is benchmarked for forward fan noise scattering by a fuselage. In Sec. 7.3, conclusions are given.

7.1 Numerical model

In this section, the numerical model used to assess the capability of the boundary element approach with non-uniform flow is presented. External sound propagation from a nacelle inlet and scattering from a simplified airframe geometry is assessed for a time harmonic problem. The geometry and the mean flow model are discussed. Then, the boundary element model is presented. A finite element model for the same problem is also devised. Finally, we present a simplified sound source model for forward fan noise radiation.

The finite element and boundary element methods are implemented and solved using the Matlab [202] code validated and benchmarked in Chapter 6. In all that follows, the speed of sound and mean flow density are: $c_\infty = 340$ m·s^{-1} and $\rho_\infty = 1.22$ kg·m^{-3}. The solutions will be provided in the range $M_\infty = 0 \to 0.3$ to be consistent with the weakly non-uniform flow ansatz and the numerical results of Chapter 6. This is also characteristic of modern turbofan aircraft at departure and approach. The reference acoustic pressure for the calculation of the Sound Pressure Level SPL $= 20\log_{10}(p'_{rms}/p'_{ref})$, is $p'_{ref} = 2 \cdot 10^{-5}$ Pa and $p'_{rms} = \|p'\|/\sqrt{2}$.

7.1.1 Geometry

The geometry used in this test case is extracted from the NASA common research model [206]. A fully 2D problem is devised. First, the 3D aircraft model with an angle of attack equal to zero is reduced down to the fuselage and nacelle only. The 2D model is obtained as a slice of the fuselage and the nacelle through their corresponding mid planes, projected onto a common horizontal plane (see Fig. 7.1). The radius of the nacelle $r_n = d_n/2 = 1.5$ m at the fan location, namely $\mathbf{x} = (-11.33r_n, 2.67r_n)$, will be used as a reference length scale for the present analysis.

The objective is to assess the accuracy of the boundary integral formulation with non-uniform flow presented in Chapter 4. The solution is recovered in the fuselage near field and in a region of the far field where the flow is almost uniform (see Fig. 7.1). As shown in Chapter 6, the L^2-error, measured against the linearised potential formulation, is constant when a uniform mean flow region is reached. The near field will assess the applicability to cabin noise while the far field is relevant to airport noise. In the near field, we consider a

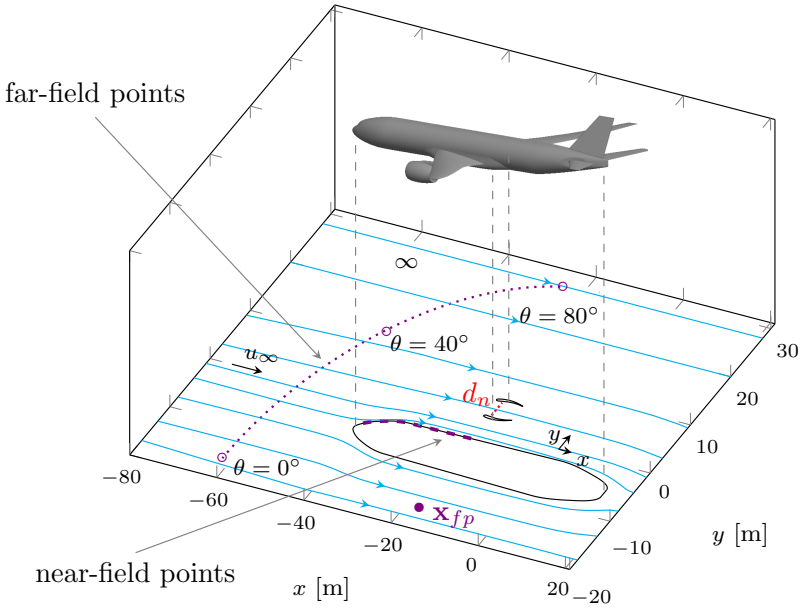

Figure 7.1: Main features of the fan noise installation effect test case, showing the 3D geometry [206], the corresponding simplified 2D geometry with streamlines, and the field points (purple line) for the evaluation of the acoustic field.

number of field points in the forward part of the fuselage, while in the far field an arc of field points centered at $\mathbf{x}_{fp} = (-11.33r_n, -10.83r_n)$ with radius $r_{fp} = 30\ r_n$ is defined (see Fig. 7.1) .

7.1.2 Mean flow

An incompressible potential mean flow without circulation is predicted using a finite element method to solve the Laplace equation for the geometry in Fig. 7.1. The Laplace equation for the mean flow potential, Φ_0, is

$$\boldsymbol{\nabla}^2 \Phi_0 = 0. \tag{7.1}$$

The weak variational formulation solved with finite elements is

$$\int_\Omega \boldsymbol{\nabla}\Phi_0^* \cdot \boldsymbol{\nabla}\Phi_0 dV = \int_{\partial\Omega} \Phi_0^* \mathbf{u}_0 \cdot \mathbf{n} dS, \tag{7.2}$$

where $\mathbf{u}_0 = \boldsymbol{\nabla}\Phi_0$ and "*" denotes the complex conjugate. A quadratic FE solution based on an isoparametric formulation is provided. The mean flow is interpolated on the acoustic mesh based on the k-nearest neighbour algorithm [207] and the method of least squares. In the interpolation, we consider four nodal points on the mean flow mesh per node of the acoustic mesh.

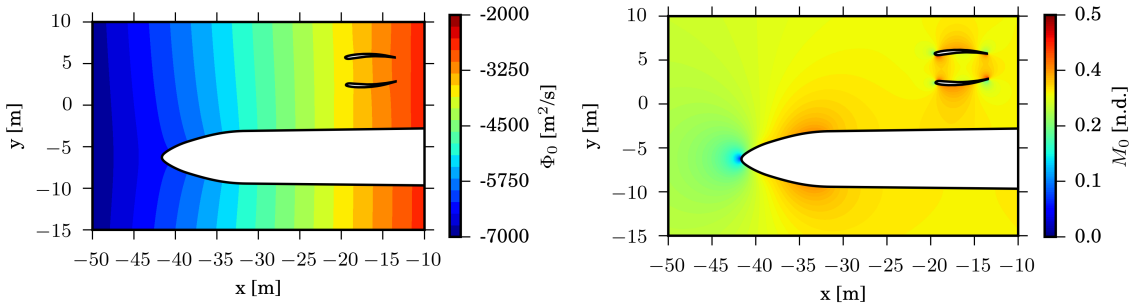

(a) Velocity potential

(b) Mach

Figure 7.2: Incompressible potential mean flow for the problem in Fig. 7.1 based on a finite element solution of the Laplace equation and $M_\infty = 0.3$.

Although the flow is clearly rotational at the nacelle exhaust, considering a potential flow at the inlet and around the fuselage is still a reasonable approximation at low Mach numbers and low angles of attack [208]. It is worth noting that Eq. (7.1) could readily be replaced by a more complex equation for compressible irrotational flows, but this was not done given the low values of the Mach number that are of interest.

Nonetheless, at low Mach numbers ($M_\infty \leq 0.3$), the effects of refraction of sound waves propagating through the mean flow boundary layer developed around the fuselage is less significant than at higher Mach numbers [209]. The effect of the boundary layer is more significant at higher frequencies and smaller fan noise cut-off ratios [205] due to smaller relative wavelength compared to the boundary layer thickness and shallower angles between the main directivity of the sound radiated by the fan and the grazing flow around the fuselage. The magnitude of these effects is sensitive to the thickness of the boundary layer [205]. In this case, we neglect these effects and consider sound propagation in a potential mean flow (see Fig. 7.2).

7.1.3 Wave propagation

In this section, we present 2D models for the problem in Fig. 7.1 relying either on finite or boundary elements. We also present the description of the sound sources. The 2D models describe the scattering of line sources by a fuselage of infinite length in the vertical plane. Although this is not clearly representative of a model for 3D installation effects, it includes the critical features, such as the mean flow and the size of the domain, to test the weakly coupled approach for boundary element solutions (see Sec. 4.8) at the same conditions as for the corresponding three-dimensional problems.

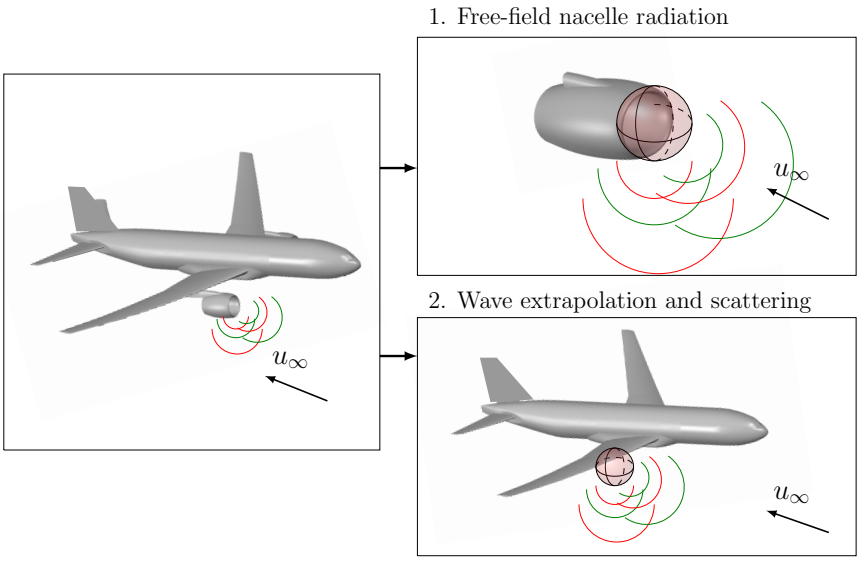

Figure 7.3: Sketch of the procedure used to compute the scattering from the nacelle inlet using a weakly-coupled approach.

7.1.3.1 Boundary element model

The boundary element model is based on Lagrange polynomials and quadratic interpolation with eight degrees of freedom per wavelength (see Table 7.1). Preliminary tests showed that this discretisation is satisfactory for the convergence of the solution. Boundary element problems are then solved based on the weakly non-uniform flow wave equation (see Eq. (2.35)). Results based on the corresponding uniform flow approximation (see Eq. (2.37)) are also provided.

Since the weakly non-uniform flow wave equation is based on the hypothesis of small non-uniform mean flow velocity components, the corresponding boundary element formulation is not suited to solve the nacelle near field. A practical methodology based on a weakly coupled FE-BE approach is devised. The problem is solved in two steps. First, a FE solution including only the nacelle in free field is computed accounting for the mean flow field around the fuselage/nacelle geometry (see Figs. 7.3 and 7.4). The FE solution in the nacelle near field is then sampled along a control surface (see Figs. 7.3 and 7.4). Based on the formulation presented in Sec 4.8, the control surface is devised to project the nacelle acoustic near field along the fuselage (see Fig. 7.4). Hence, scattering is solved using the boundary element method based on Eq. (5.59), namely the generalised Burton–Miller formulation. The nacelle and the fuselage are perfectly rigid and the Sommerfeld radiation condition at infinity is inherently satisfied by the integral formulation.

Table 7.1: Number of degrees of freedom against the non-dimensional frequency kr_n for either the BE or FE models used to solve the problem in Fig. 7.2. The BE solution is based on a weakly-coupled approach exploiting the computation of the nacelle near field performed using a FE model.

	BEM - dofs				FEM - dofs		
	$M_\infty = 0.1$	$M_\infty = 0.2$	$M_\infty = 0.3$		$M_\infty = 0.1$	$M_\infty = 0.2$	$M_\infty = 0.3$
$kr_n = 6$	1744	1890	2060	$kr_n = 6$	1160186	1394313	1687731
$kr_n = 12$	3026	3392	3876	$kr_n = 12$	2212596	2629441	3246386
$kr_n = 24$	4299	4837	5528	$kr_n = 24$	6919673	7784632	8969722

7.1.3.2 Finite element model

Finite element solutions based on the linearised potential wave equation (see Eq. (6.2)) and a quadratic element interpolation are used as a reference. The problem is discretised with eight degrees of freedom per wavelength (see Table 7.1). As mentioned in the previous section, a finite element solution is also used to provide the nacelle near field for the boundary element solution based on weak coupling.

The nacelle and the fuselage are rigid. The radiation condition is satisfied on the outer side of a PML [88] region embedding the physical domain. A PML region is also set inside the nacelle to damp the radiation towards the exhaust (see Fig. 7.4), where a potential formulation cannot be used. The absorbing layer is devised to damp both incoming and outgoing waves in the exhaust region. Note that the potential formulation is not applicable in this region because of the development of rotational mixing layers in the real flow (see Fig. 7.4). In the weakly-coupled solution, a finite model of the isolated nacelle is used for the solution of the acoustic field in the inner domain.

A triangular unstructured mesh is used in the domain except for the PML where we use a structured quadrangular mesh. The PML developed on the outer surface of the physical domain accounts for wavelength thickness ratio per layer of 0.1 and is extruded for three wavelengths. On the other hand, the inner PML is consistent with the discretisation used in the physical domain.

7.1.3.3 Sound source

A distribution of monopole point sources (line sources in the context of this 2D model) along the line representing the fan plane is defined to model fan noise directivity. The magnitude of the volume sound source is prescribed to represent fan noise directivity patterns and scaled to have a unit magnitude independently of the number of sources. The line of sound sources is parallel to the y-axis and centered at $\mathbf{x} = (-11.33r_n, 1.67r_n)$ (see Fig. 7.4). The

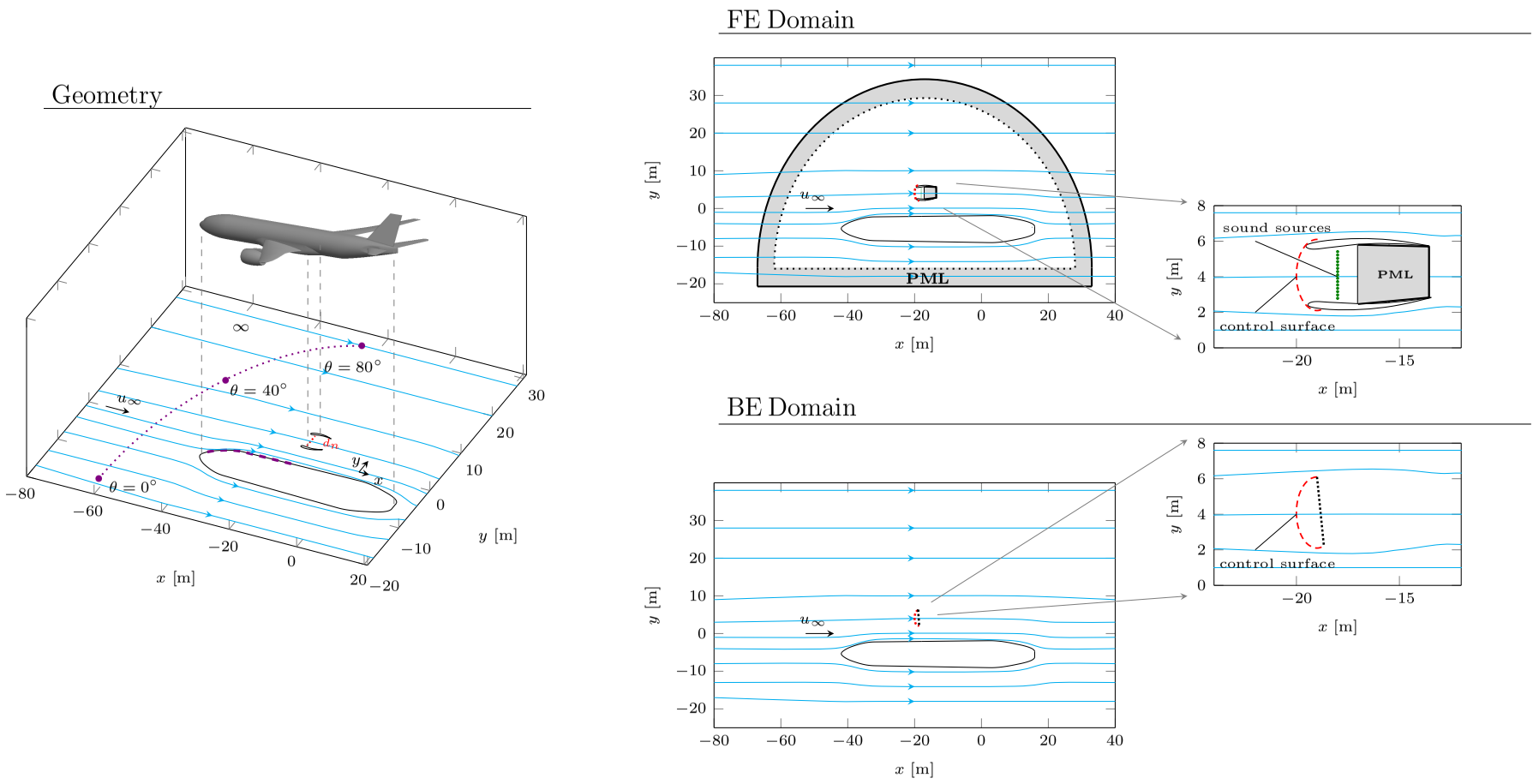

Figure 7.4: Main features of the FE and BE models used to solve the fan noise installation effect test case, showing the 3D geometry [206] and the corresponding simplified 2D finite and boundary element domains with streamlines. Green dots: sound sources. Red dashed line: control surface for weak coupling.

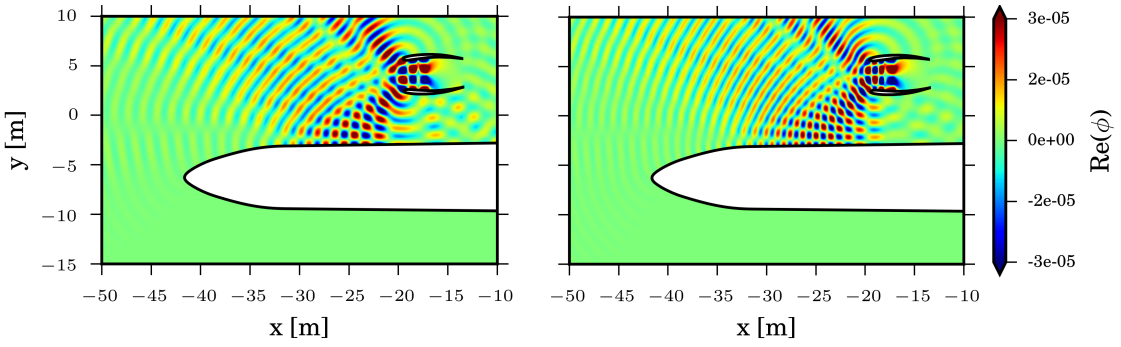

(a) $M_\infty = 0.1$ (b) $M_\infty = 0.3$

Figure 7.5: Real part of the acoustic potential, ϕ, for the problem in Fig. 7.1, $kr_n = 6$ and $n = 3$ in Eq. (7.3). FE solution based on the full potential linearised wave equation.

magnitude and phase of the sources is proportional to a weighting function:

$$w(y_m) = \cos\left(\frac{\pi n y_m}{d_n}\right), \tag{7.3}$$

where y_m ($0 \leq y_m \leq d_n$) denotes the position of the source along the line of the fan measured along a local y-axis with origin at $\mathbf{x} = (-11.33r_n, 1.67r_n)$. The mode number is denoted by n. Note that Eq. (7.3) is an eigenfunction for a two-dimensional square duct with rigid walls. Although the geometry of the nacelle is more complex, we use this approximation to obtain noise radiation from the nacelle inlet.

Time harmonic sound sources are described using Dirac delta functions and scaled by $1/\int_0^{d_n} \|w(y)\| dy$ (see Eq. (7.3)). A discrete distribution of point sources is then considered:

$$g(\mathbf{x}, t) = \frac{\sum_{m=1}^{\mathrm{N}_s} w(y_m)\delta(\mathbf{x} - \mathbf{x}_m)\mathrm{e}^{\mathrm{i}\omega t}}{\sum_{m=1}^{\mathrm{N}_s} w(y_m)}, \tag{7.4}$$

where $\mathbf{x}_m = (x_m, y_m)$ is a generic point of the domain along the line of the fan, N_s denotes the total number of point sources and w is defined in Eq. (7.3).

In the finite element model, a nodal point is defined at every source location and the mesh is refined in its vicinity so that 15 elements with quadratic interpolation contribute to the source nodal point. Figures 7.5 and 7.6 illustrate contours of the real part of the acoustic potential, ϕ, for non dimensional frequencies $kr_n = 6$, 12 with $M_\infty = 0.1$, 0.3, and $n = 3$ and 7 based on the FE solution of the linearised potential wave equation. Although a simplified source model is used, the directivity of the acoustic field radiated from the nacelle resembles that shown by more realistic numerical models [23, 83].

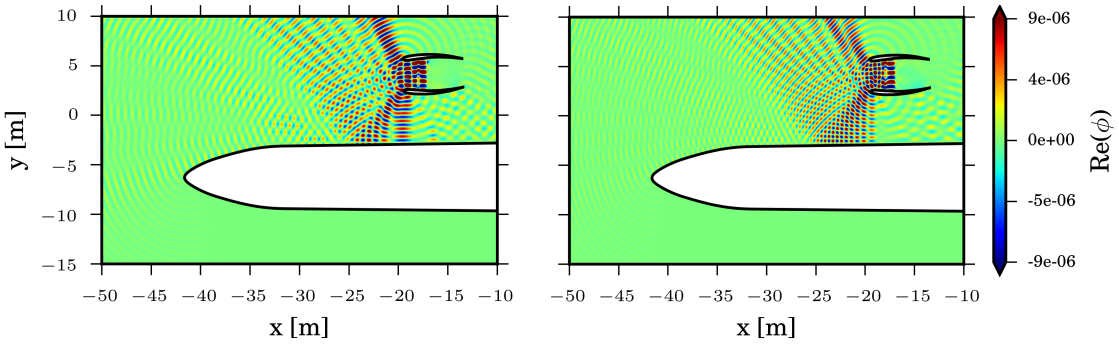

(a) $M_\infty = 0.1$ (b) $M_\infty = 0.3$

Figure 7.6: Real part of the acoustic potential, ϕ, for the problem in Fig. 7.1, $kr_n = 12$ and $n = 7$ in Eq. (7.3). FE solution based on the full potential linearised wave equation.

7.2 Results

In this section, we present numerical results for wave extrapolation from the nacelle inlet by introducing an open Kirchhoff surface with non-uniform mean flow. Then, we present the numerical results for the scattering of forward fan noise by the fuselage based on the weakly-coupled approach, which was presented in Sec. 4.8.

7.2.1 Open Kirchhoff surface

Sound radiation from the nacelle in free field is considered in this case (see Fig. 7.7). The sound source is the same as that defined in Sec. 7.1.3.3. The wave extrapolation approach proposed in the physical space in Sec. 4.8 is assessed. The FE solution based on the linearised potential wave equation (see Eq. (2.30)) is first computed in the nacelle near field and sampled along a control surface. Then, the integral formulation associated with the weakly non-uniform formulation is used to extrapolate the near-field solution from the control surface to the far field. The FE solution is also used as a reference solution in the far field and a PML is imposed outside the computational domain to simulate the Sommerfeld radiation condition at the outer surface.

The objective is to test wave extrapolation based on an "open" Kirchhoff surface with non-uniform flows, where the surface does not contain the entire nacelle but is simply folded around the inlet (see red dashed line in Fig. 7.7). This is achieved using a surface integral formulation, consistent with that proposed in Sec. 4.8, but setting the equivalent sources on the control surface lying inside the nacelle to zero. In other words, we consider Eq. (4.89)

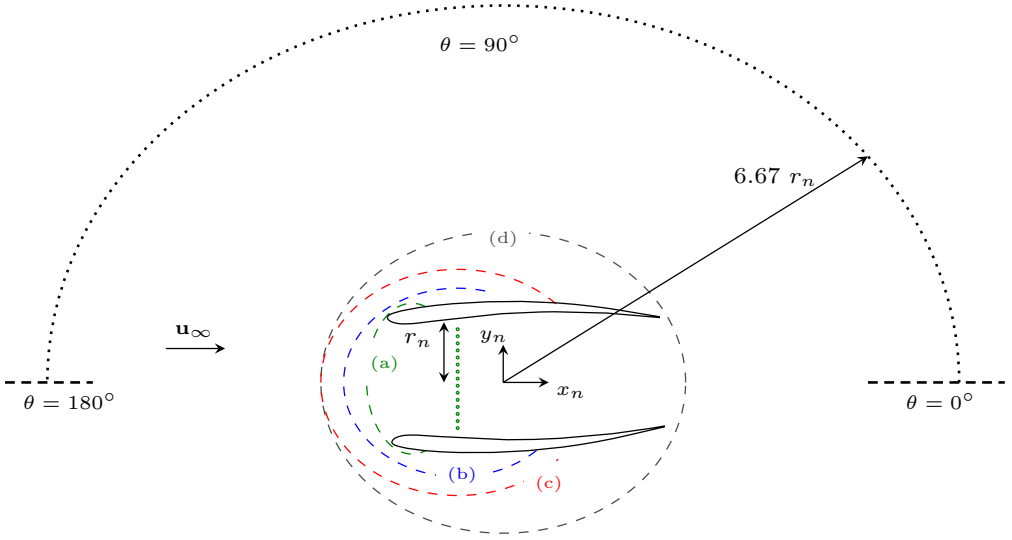

Figure 7.7: Geometry of reference for the problem of radiation from a nacelle with a mean flow. The Kirchhoff surfaces are depicted using dashed lines. The arc of field point where the directivity is measured is depicted with a dotted line.

along the nacelle inlet:

$$\phi_{inc}(\mathbf{x}_p) = \int_{\partial\Omega_{ext}} \left[G\left(\mathbf{u}_s' \cdot \mathbf{n} - u_{s,x}' n_x M_\infty^2\right) - \phi_s \left(\frac{\partial G}{\partial n} - \frac{\partial G}{\partial x} n_x M_\infty^2\right) - 2ik\mathbf{M}_0 \cdot \mathbf{n}\phi_s G \right] dS(\mathbf{x}) + \int_{\partial\Omega_{int}} \left[G\left(\mathbf{u}_s' \cdot \mathbf{n} - u_{s,x}' n_x M_\infty^2\right) - \phi_s \left(\frac{\partial G}{\partial n} - \frac{\partial G}{\partial x} n_x M_\infty^2\right) - 2ik\mathbf{M}_0 \cdot \mathbf{n}\phi_s G \right] dS(\mathbf{x}) \tag{7.5}$$

where Ω_{ext} denotes the part of the control surface external to the nacelle (see Fig. 7.4), Ω_{int} is the part of the surface lying inside the nacelle and ϕ_s and $u_{s,x}'$ are recovered from the FE solution. The equivalent sources on the inner part of the latter surface should represent the acoustic field radiated towards the exhaust, which is damped in this example. Hence, we can impose $\phi_s = 0$ and $\mathbf{u}_s' = \mathbf{0}$ for $\mathbf{x} \in \partial\Omega_{int}$ to give

$$\phi_{inc}(\mathbf{x}_p) = \int_{\partial\Omega_{ext}} \left[G\left(\mathbf{u}_s' \cdot \mathbf{n} - u_{s,x}' n_x M_\infty^2\right) - \phi_s \left(\frac{\partial G}{\partial n} - \frac{\partial G}{\partial x} n_x M_\infty^2\right) - 2ik\mathbf{M}_0 \cdot \mathbf{n}\phi_s G \right] dS(\mathbf{x}). \tag{7.6}$$

An incompressible potential mean flow developed around the nacelle is computed solving the Laplace equation. Although a simplified model is used, the distribution of the mean flow velocity at the control surface is consistent with realistic flows at the intake [23, 83, 210] in that the Mach number is almost constant and equal to M_∞ close to the inlet, and non-uniformity in the mean flows are significant only close to the nacelle lip. However, the acceleration of the flow close to the nacelle lip is small compared to a realistic intake. Moreover, we do not expect a potential mean flow at the exhaust to be representative of a

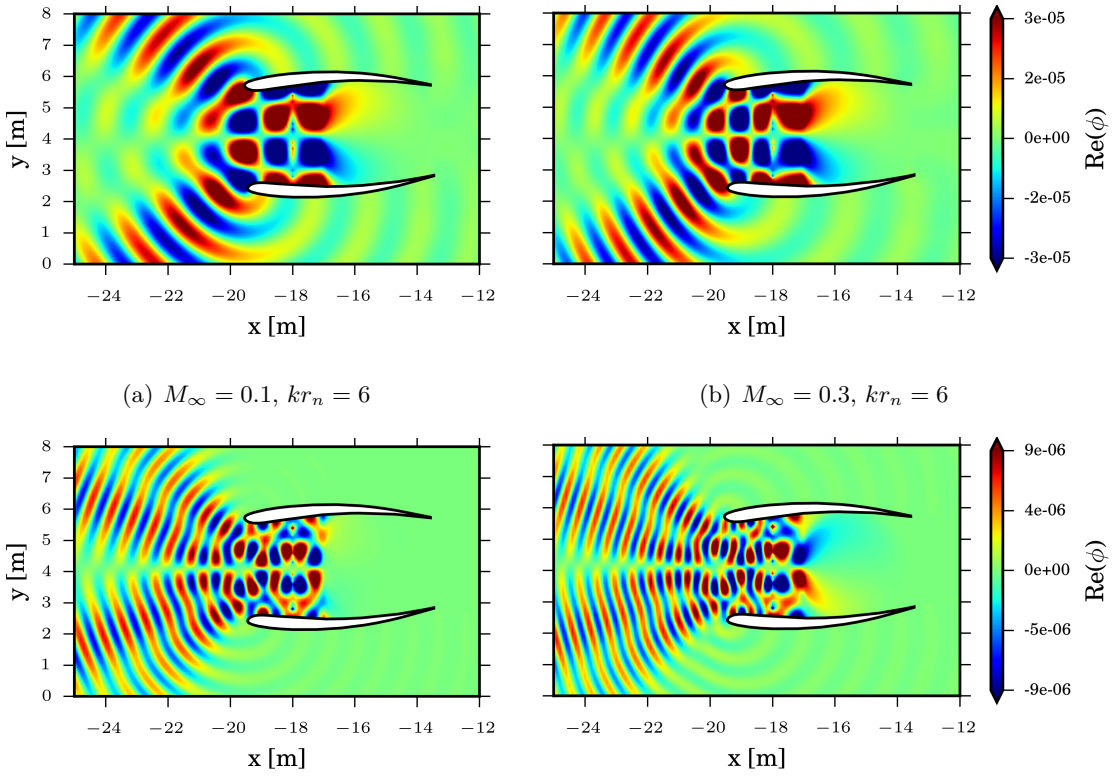

(a) $M_\infty = 0.1$, $kr_n = 6$

(b) $M_\infty = 0.3$, $kr_n = 6$

(c) $M_\infty = 0.1$, $kr_n = 12$

(d) $M_\infty = 0.3$, $kr_n = 12$

Figure 7.8: Contour plot for the real part of the acoustic potential, ϕ, based on the finite element solution of the linearised potential equation (see Eq. (6.2)) for the problem described in Fig. 7.7 and $n = 3$ in Eq. (7.3).

realistic flow. Therefore, wave propagation is only considered in the nacelle forward arc and sound radiation towards the exhaust is damped with PML (see Fig. 7.4).

The solution based on an open radiating surface approach is now compared to the results obtained with a more conventional wave extrapolation based on a closed Kirchhoff surface. The comparison is performed for a number of flow configurations and frequencies. The solutions are developed for discretisations based on eight degrees of freedom per wavelength, which has previously been verified to provide convergence of the solution.

Let us consider $n = 7$ in Eq. (7.3). The SPL along an arc of field points with radius $r_{fp} = 6.67r_n$ is depicted in Figs. 7.9(a) and 7.9(b) against the angle θ for a non-dimensional frequency $kr_n = 6$, with $M_\infty = 0.1$ and 0.3. The FE reference solution is compared to the solutions based on wave extrapolation from either a closed surface with radius $r = 2.67r_n$ centered at $\mathbf{x} = (-11.33r_n, 2.67r_n)$ or open surfaces with radii respectively $r = 1.66r_n$ and $r = 2r_n$ (see Fig. 7.7). The same solutions are depicted in Fig. 7.9(c) and 7.9(d) against the angle θ for a non-dimensional frequency $kr_n = 12$ with $M_\infty = 0.1$ and 0.3.

We consider now $n = 13$ in Eq. (7.3). In Fig. 7.10, the SPL along an arc of field points with radius $r_{fp} = 6.67r_n$, centered at $\mathbf{x} = (-11.53r_n, 2.67r_n)$, is depicted against the angle θ for

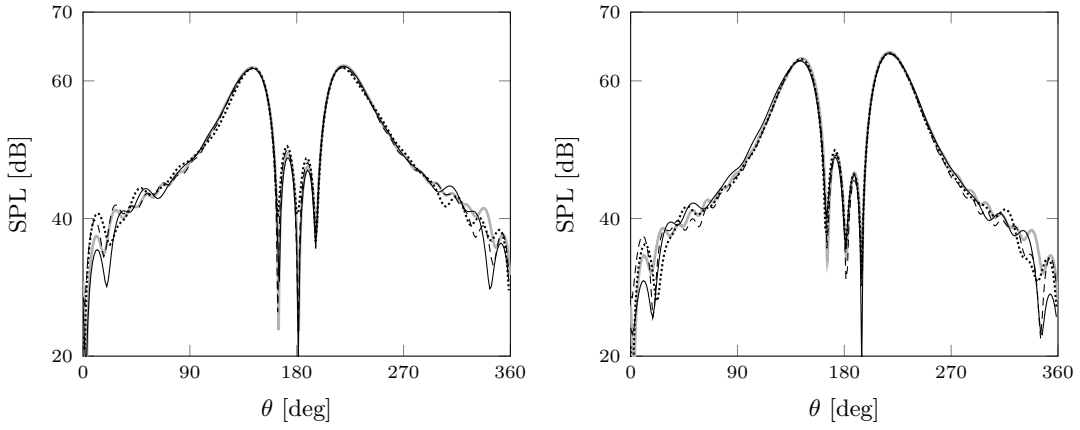

(a) $M_\infty = 0.1$, $kr_n = 6$ (b) $M_\infty = 0.3$, $kr_n = 6$

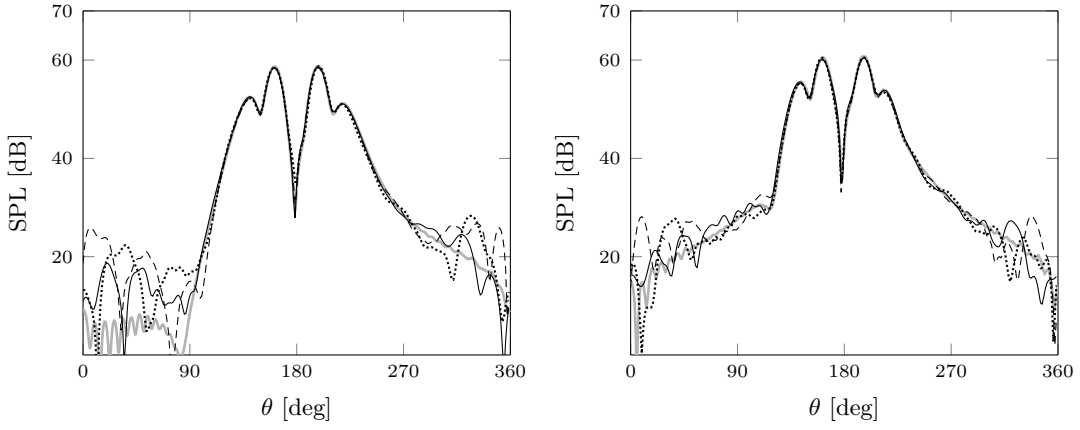

(c) $M_\infty = 0.1$, $kr_n = 12$ (d) $M_\infty = 0.3$, $kr_n = 12$

Figure 7.9: SPL along an arc of field points with radius $r_{fp} = 6.67r_n$ for $n = 7$ in Eq. (7.3) and the problem described in Fig. 7.7. Solid, grey: FE LPE. Dashed: FE LPE + wave extrapolation surface (d), Eq. (4.15). Dotted: FE LPE + wave extrapolation surface (c), Eq. (4.15). FE LPE + wave extrapolation surface (b), Eq. (4.15).

a non-dimensional frequency $kr_n = 24$ with $M_\infty = 0.1$ and 0.3. The FE reference solution is compared to the solutions based on wave extrapolation from either a closed control surface with radius $r = 2.67r_n$ or an open surface centered at $\mathbf{x} = (-11.53r_n, 2.67r_n)$ derived from an ellipse of major and minor axes $a = r_n$ and $b = r_n/2$, respectively.

It is seen that wave extrapolation based on an open radiating surface provides a good estimation of the SPL almost independently of frequency and Mach number (see Figs. 7.9 and 7.10), since the assumption that $M_0' \ll M_\infty$ is clearly satisfied along the control surface. Nonetheless, for the proposed application, wave extrapolation based on an open surface does not generate a significant error compared to a more conventional closed surface. Poor agreement with the reference finite element solution is observed in the shielded area [$\theta = 0 \rightarrow 90$ degrees and $\theta = 270 \rightarrow 360$ degrees] (see Figs. 7.9 and 7.10). This difference is due to the numerical leakage associated with wave extrapolation. In the shielded area, the sound field is so low compared to the corresponding high pressure region that the solution

is strongly affected by the numerical error. In other words, the solution is dominated by numerical noise. However, in this region the SPL is at least 20 dB lower than that around the main lobes (see Figs. 7.9 and 7.10).

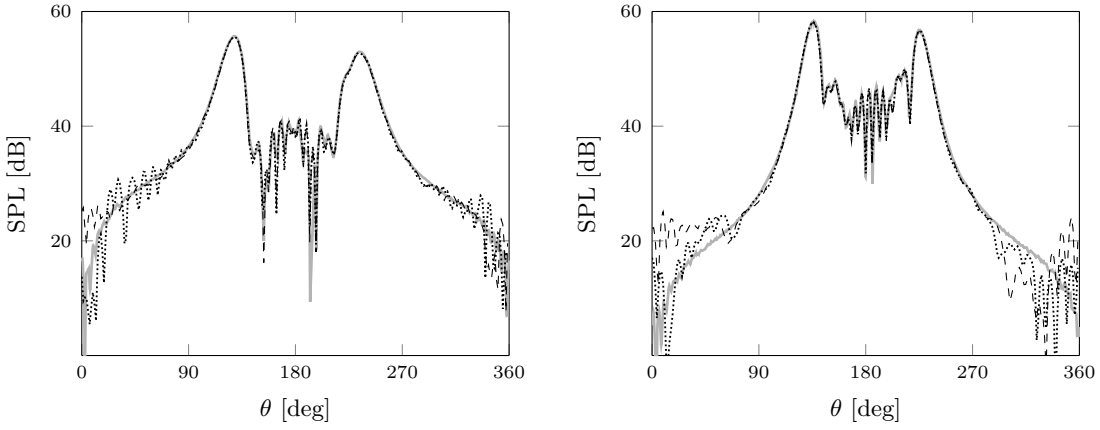

(a) $M_\infty = 0.1$ (b) $M_\infty = 0.3$

Figure 7.10: SPL along an arc of field points with radius $r_{fp} = 6.67 r_n$ for a non-dimensional frequency $kr_n = 24$, $n = 7$ in Eq. (7.3) and the problem described in Fig. 7.7. Solid, grey: FE LPE. Dashed: FE LPE + wave extrapolation surface (d), Eq. (4.15). Dotted: FE LPE + wave extrapolation surface (a), Eq. (4.15).

7.2.2 Radiation and scattering

Sound radiation and scattering for the problem in Fig. 7.1 is predicted in this section. The source model described in Sec. 7.1.3.3 is used. The boundary element solution is based on the integral solution in the physical space proposed in Sec. 5.2. The FE solution of the problem in Fig. 7.1 is provided as a reference. FE and BE solutions are compared in the fuselage near field and along an arc of field points lying in the far field where the mean flow is almost uniform (see Fig. 7.1).

BE solutions based on the weakly non-uniform formulation, Eq. (5.59), are benchmarked. These solutions are based on the weakly-coupled approach proposed in Sec. 7.1.3.1. They are compared to weakly-coupled solutions based on more conventional BE formulations with uniform flow in the entire domain. The uniform flow approximation was used in a number of previous works generally relying on a Lorentz transformation [29, 40, 70]. For both the uniform and non-uniform mean flow formulation, the solution in the nacelle near field is sampled at an interface where the sound field is predicted using a FE solution of the linearised potential wave equation.

FE and BE solutions based on weak coupling are initially compared for $M_\infty = 0$. Consider the case where $n = 1$ in Eq. (2.30) and the non-dimensional frequency is $kr_n = 6$. In Fig. 7.11, the SPL is shown along the fuselage and at the points in the far field (see Fig. 7.1). The phase of the acoustic field is also reported showing good agreement. This result is provided as a baseline for the weakly-coupled formulation with a mean flow in order to justify the applicability of a weakly-coupled approach. It is shown that the error generated by removing the nacelle in the computation of the scattering by the fuselage, namely performing a weak coupling between the nacelle near field and scattering by the fuselage, is within 0.5 dB of the FE reference solution.

We now consider the scattering in the presence of a mean flow. The problem in Fig. 7.1 is solved for non-dimensional frequencies $kr_n = 6$, 12 and 24. Note that $kr_n = 24$ is consistent with the first blade passing frequency of the fan for current civil aircraft [210]. First, let us assume a non-dimensional frequency $kr_n = 6$ and $n = 1$ in Eq. (7.3). Contours of the real part of the acoustic velocity potential, ϕ, based on the FE reference solution and the BE solutions with either uniform or non-uniform mean flow, are presented in Fig. 7.12. In Fig. 7.13, these solutions are compared in terms of SPL either in the near or in the far field for $M_\infty = 0.1 \rightarrow 0.3$. In the far field, the solution is shown against the angle θ, measured along an arc of field points with radius $r = 30\ r_n$. The angle θ is zero at $\mathbf{x} = (-41.33r_n, -10.83r_n)$ and measured clockwise (see Fig. 7.1). In the near field, the SPL along the surface of the fuselage (see Fig. 7.1) is depicted comparing the same solutions as for the far field, while the corresponding phase of the acoustic pressure is depicted in Fig. 7.14 for $M_\infty = 0.1$ and 0.3.

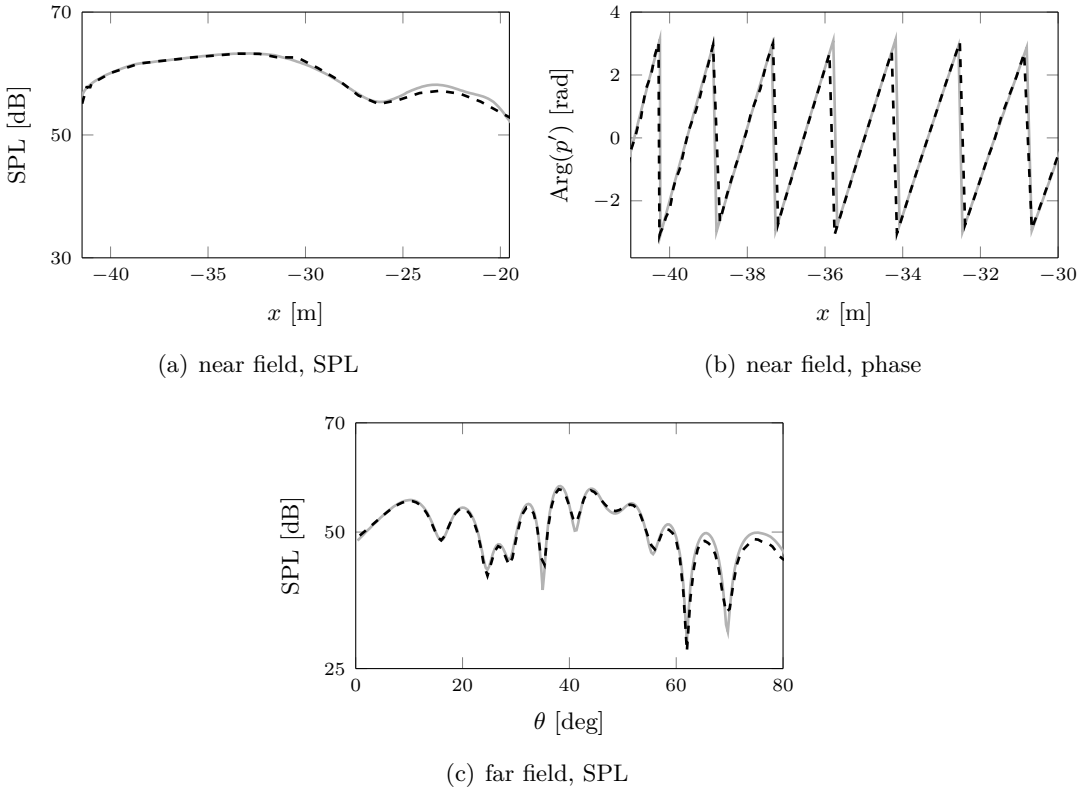

(a) near field, SPL

(b) near field, phase

(c) far field, SPL

Figure 7.11: Solution of the problem described in Fig. 7.1 for a non-dimensional frequency $kr_n = 6$, $M_\infty = 0$ and $n = 1$ in Eq. (7.3). The boundary and finite element solutions of the standard Helmholtz problem are provided. Solid: FE. Dashed: FE/BE weakly-coupled.

The same results as those presented in Figs. 7.13 and 7.14 are shown for $n = 2$ in Figs. 7.15 and 7.16. The mode corresponding to $n = 2$ is more cut-off than that for $n = 1$ and the noise radiated by the nacelle inlet is mostly scattered in the region of the fuselage aligned with the uniform mean flow at infinity $[-35 \leq x \leq -20]$. Modes with higher cut-off ratios [211], namely for higher n and lower M_∞, are scattered towards the region of the fuselage where the non-uniformity in the mean flow velocity is less significant. The results based on the boundary element solutions favourably agree with the FE solution in terms of SPL. Nonetheless, the weakly non-uniform formulation shows a good agreement with the reference solution in terms of phase for $M_\infty = 0.1$, improving on the corresponding uniform flow approximation.

It is also shown that, in the near field for $n = 2$ and $0.2 \leq M_\infty \leq 0.3$, the error on boundary element solution against the FE reference solution reaches 4 dB, for $x \geq -25$ (see Fig. 7.15(f)). On the other hand, this is not seen in the case of $n = 1$ (see Fig. 7.13(f)). Such a difference in the region where the mean flow is aligned with the uniform flow at infinity may arise in the weakly-coupled approach since the nacelle was removed in the BE computation and, therefore, back scattering of the sound field from the nacelle was not represented. This difference is evident in the boundary element results based on either uniform or non-uniform flow and is more clear for $M_\infty = 0.3$. This is seen although the cut-off rate of the mode, n, is less significant than for lower Mach numbers.

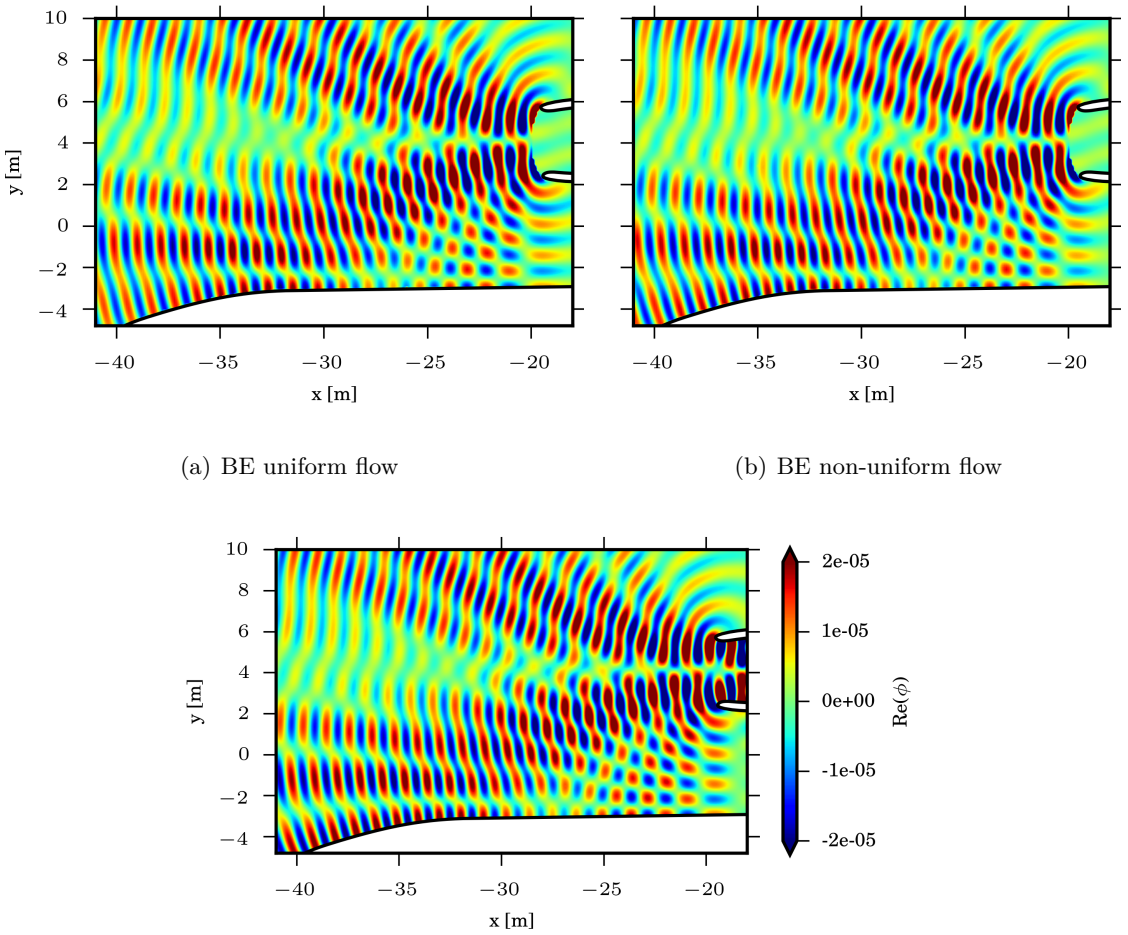

(a) BE uniform flow

(b) BE non-uniform flow

(c) FE LPE

Figure 7.12: Contours of the real part of the acoustic potential, ϕ, for a non-dimensional frequency $kr_n = 6$, $M_\infty = 0.3$ and $n = 1$ in Eq. (7.3) for the problem described in Fig. 7.1. The boundary element solutions to either the weakly non-uniform potential flow wave equation or its uniform flow approximation based on the weakly-coupled approach are compared to the FE solution of the linearised potential wave equation.

However, for $n = 1$ and 2 (see Figs. 7.13 and 7.15), the solutions based on the weakly non-uniform formulation improve on those for the corresponding uniform flow approximations in the near field where the non-uniformity on the mean flow velocity is more significant, namely $x \leq -30$. This is more clearly seen for $0.2 \leq M_\infty \leq 0.3$ where differences up to 3 dB are reported. On the other hand, the solutions are in good agreement in the far field (see Figs. 7.13 and 7.15).

In Fig. 7.17, the SPL at the field points lying in a region of uniform mean flow (see Fig. 7.1) is shown for a non-dimensional frequency $kr_n = 6$ and $M_\infty = 0.3$, for $n = 1$ and $n = 3$ respectively. In this case, the FE solution of the weakly non-uniform flow wave equation is also depicted. While an approximation of the Green's function is provided based on the weakly non-uniform flow ansatz in the BE solution, a FE solution of the weakly non-uniform flow wave equation accounts for the exact Green's function. It is seen that the BE solution

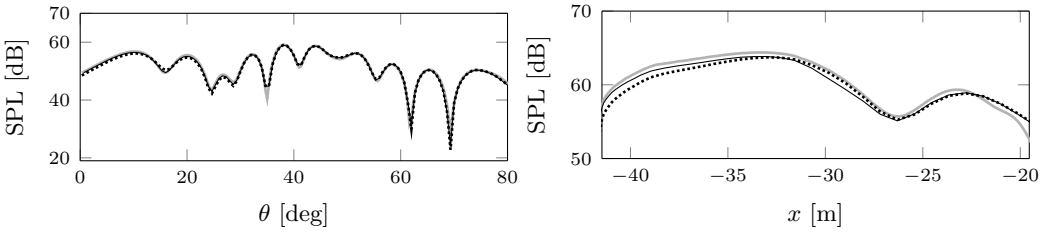

(a) $M_\infty = 0.1$, far field

(b) $M_\infty = 0.1$, near field

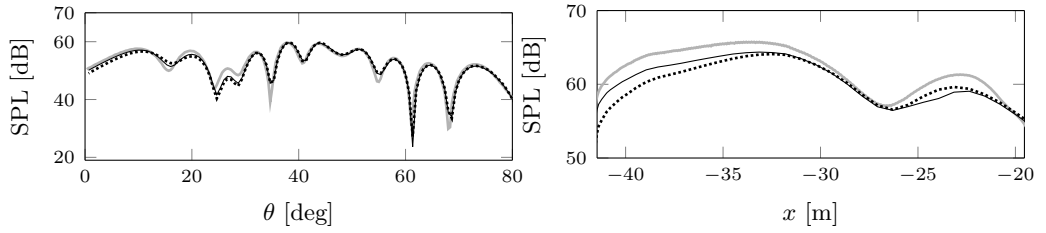

(c) $M_\infty = 0.2$, far field

(d) $M_\infty = 0.2$, near field

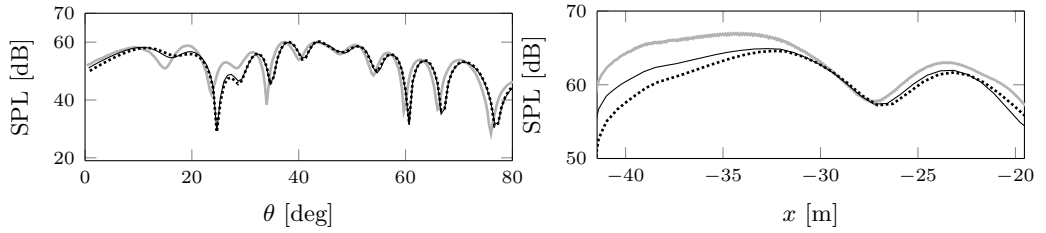

(e) $M_\infty = 0.3$, far field

(f) $M_\infty = 0.3$, near field

Figure 7.13: SPL along an arc of field points with radius $r_{fp} = 30r_n$ (far field) and in the near field (see Fig. 7.1) for a non-dimensional frequency $kr_n = 6$, $n = 1$ in Eq. (7.3) and the problem in Fig. 7.1. Solid, grey: FE LPE. Solid, black: BE weakly non-uniform flow and weak coupling. Dotted: BE uniform flow and weak coupling.

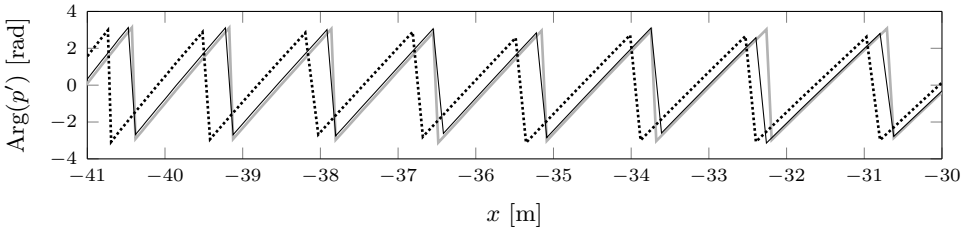

(a) $M_\infty = 0.1$

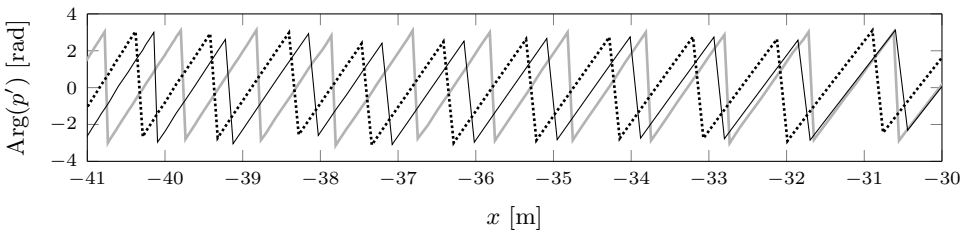

(b) $M_\infty = 0.3$

Figure 7.14: Phase of the acoustic pressure field along the boundary surface of the fuselage (see Fig. 7.1) for a non-dimensional frequency $kr_n = 6$ and the problem described in Fig. 7.1 with $n = 1$ in Eq. (7.3). Solid, grey: FE LPE. Solid, black: BE weakly non-uniform flow and weak coupling. Dotted: BE uniform flow and weak coupling.

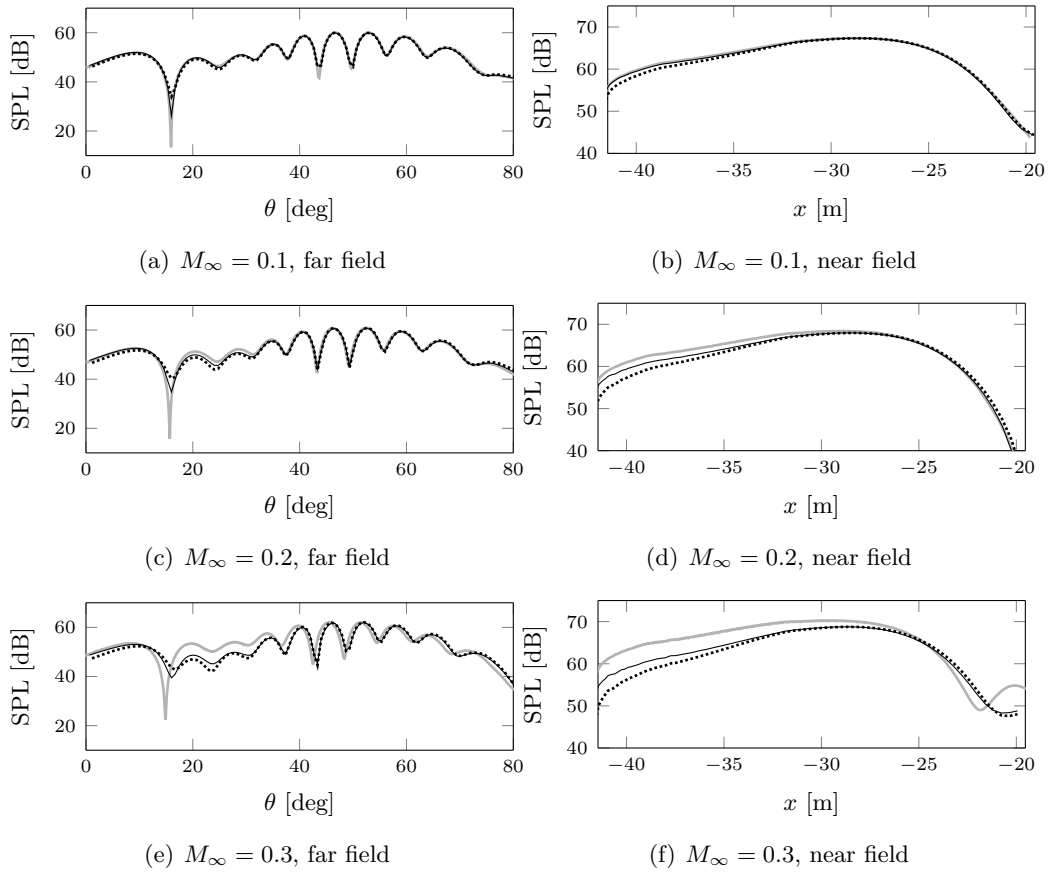

(a) $M_\infty = 0.1$, far field

(b) $M_\infty = 0.1$, near field

(c) $M_\infty = 0.2$, far field

(d) $M_\infty = 0.2$, near field

(e) $M_\infty = 0.3$, far field

(f) $M_\infty = 0.3$, near field

Figure 7.15: SPL along an arc of field points with radius $r_{fp} = 30r_n$ (far field) and in the near field (see Fig. 7.1) for a non-dimensional frequency $kr_n = 6$, $n = 2$ in Eq. (7.3) and the problem in Fig. 7.1. Solid, grey: FE LPE. Solid, black: BE weakly non-uniform flow and weak coupling. Dotted: BE uniform flow and weak coupling.

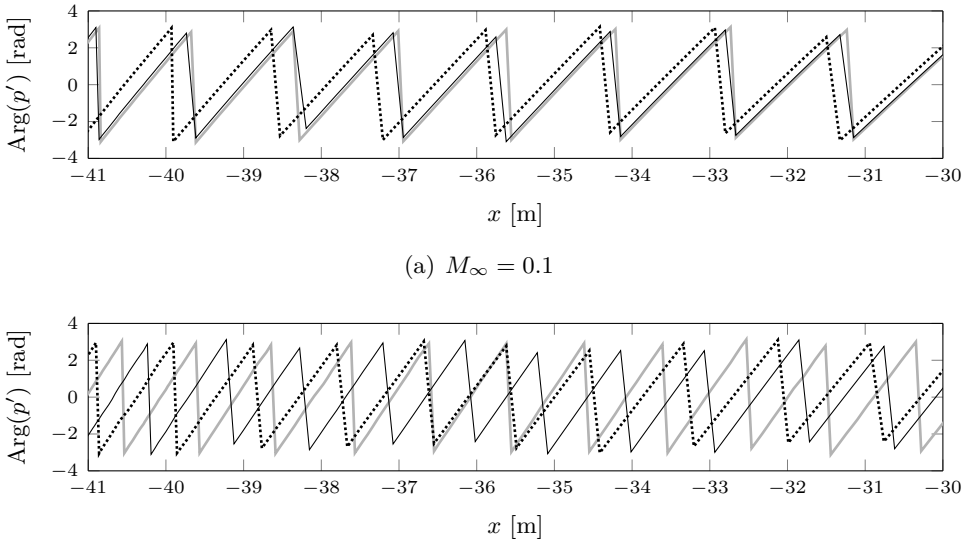

(a) $M_\infty = 0.1$

(b) $M_\infty = 0.3$

Figure 7.16: Phase of the acoustic pressure field along the boundary surface of the fuselage (see Fig. 7.1) for a non-dimensional frequency $kr_n = 6$ and the problem described in Fig. 7.1 with $n = 1$ in Eq. (7.3). Solid, grey: FE LPE. Solid, black: BE weakly non-uniform flow and weak coupling. Dotted: BE uniform flow and weak coupling.

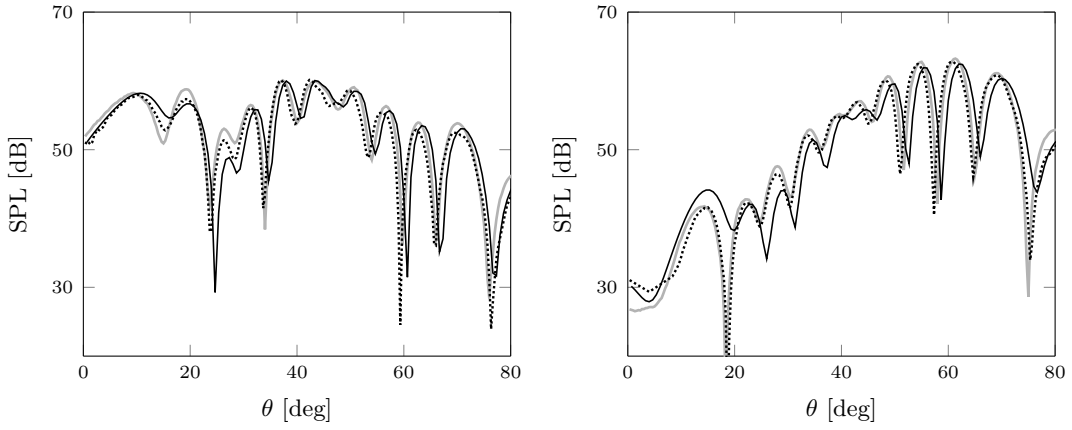

(a) $n = 1$ (b) $n = 3$

Figure 7.17: SPL along an arc of field points with radius $r_{fp} = 30r_n$ for a non dimensional frequency $kr_n = 6$, $M_\infty = 0.3$ and the problem described in Fig. 7.1. Solid, grey: FE LPE. Dotted : FE weakly non-uniform flow. Solid, black: BE weakly non-uniform flow.

is consistent with the corresponding FE solution, meaning that the Green's function well approximates the exact solution of this equation to the limit of numerical accuracy. This was already observed for the numerical solutions in Chapter 6 and current results suggest that this result can be generalised within the weakly non-uniform flow ansatz.

To continue, we consider a non-dimensional frequency $kr_n = 12$ and $n = 3$ in Eq. (7.3). Contours of the real part of the acoustic velocity potential, ϕ, based on the FE reference model and the BE formulations with either non-uniform or uniform mean flow are shown in Fig. 7.18. In Fig. 7.19, the SPL is plotted against the angle θ measured along the arc of field points lying in a uniform flow region (see Fig. 7.1) for $M_\infty = 0.1$, 0.2 and 0.3. The SPL along the fuselage is also plotted and the phase of the acoustic pressure is provided along the fuselage in Fig. 7.20. The corresponding results for $n = 7$ are shown in Figs. 7.21 and 7.22.

Although a difference in the directivities is evident for the cases $n = 3$ and $n = 7$, the boundary element results favourably agree with the FE reference solutions both in the near and far field (see Figs. 7.19 and 7.21). The non-uniform flow formulation again outperforms that for a uniform medium in the region where the non-uniformity in the mean flow velocity is more significant. In this case, an improvement of about 2 dB is shown (see Figs. 7.19 and 7.21). The formulation based on a non-uniform flow predicts the phase accurately for $M_\infty = 0.1$ even though the frequency has been doubled compared to the results shown in Figs. 7.14 and 7.16.

The same results as those of Figs. 7.21 and 7.22 are plotted in Figs. 7.23 and 7.24 for $kr_n = 24$ and $n = 13$. The results indicate that the BE solutions are a robust approximation to the FE reference solution within 3-4 dB in both the near and far field. The weakly-coupled approach provides a good approximation to the reference solution for M_∞ up to 0.3. The phase of the acoustic field is again well captured for $M_\infty = 0.1$.

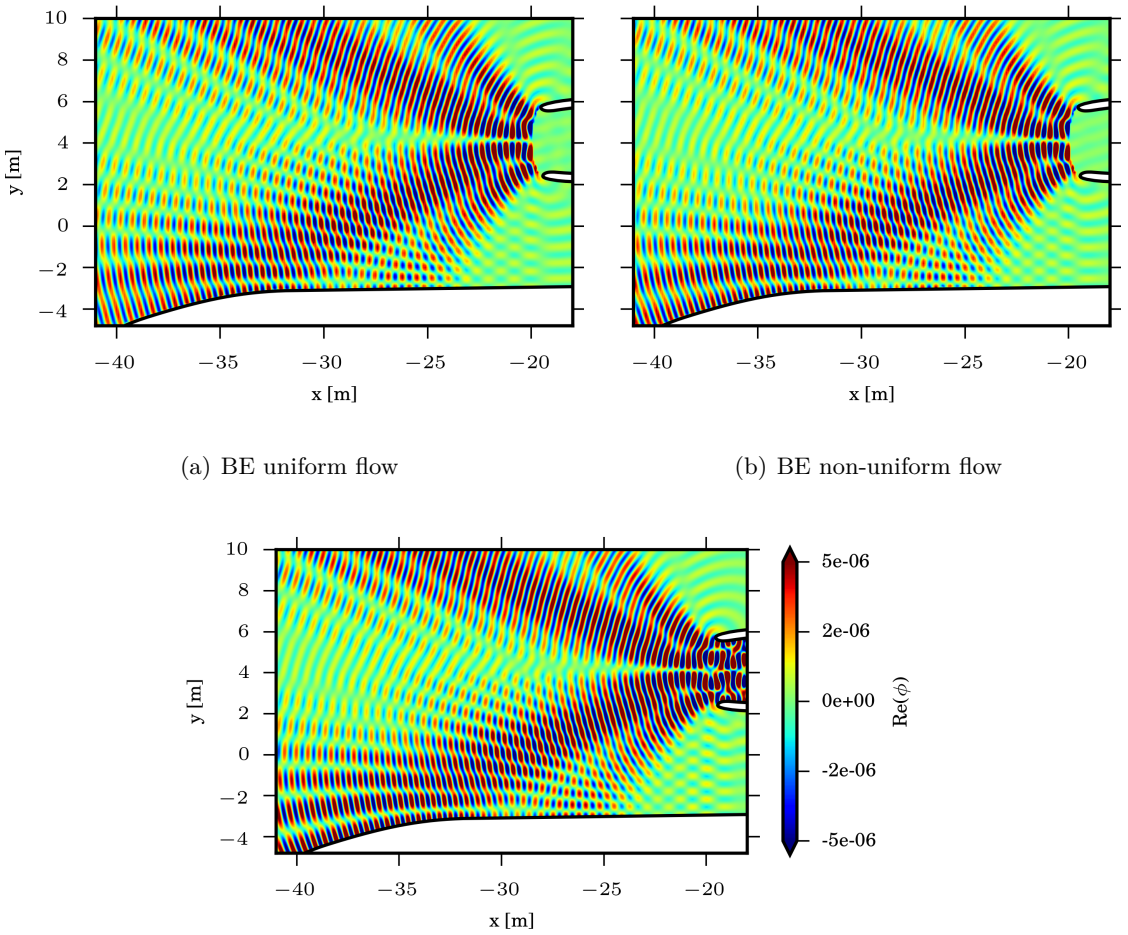

(a) BE uniform flow

(b) BE non-uniform flow

(c) FE LPE

Figure 7.18: Contours of the real part of the acoustic potential ϕ for a non-dimensional frequency $kr_n = 12$, $M_\infty = 0.3$ and $n = 3$ in Eq. (7.3) for the problem described in Fig. 7.1. The boundary element solution to the weakly non-uniform potential flow wave equation based on the weakly-coupled approach is compared to the reference FE solution (LPE) and the BE solution based on a uniform flow.

To sum up, we have solved boundary element problems based on the weakly-coupled approach to solve a simplified two-dimensional test case representing aircraft fan noise installation effects. In a uniform flow region, far away from the airframe, the BE solutions based on either a uniform or a non-uniform mean flow have been consistent in all the test cases. The results based on either the uniform or the weakly non-uniform formulation agreed with the FE reference solution within 3-4 dB for $M_\infty \leq 0.3$ and the error was almost independent of frequency (see Figs. 7.13, 7.15, 7.19, 7.21, 7.23).

As discussed in Sec. 4.5, this is likely to be due to scattering from a slender body, such as the fuselage, where the length scale of the mean flow is larger than for a bluff body, such as for the cylinder considered in the previous chapter. Although it has been shown that the weakly-coupled approach is a robust methodology independent of frequency and Mach number, it generates an additional error of about 1-2 dB in the near field close to the nacelle.

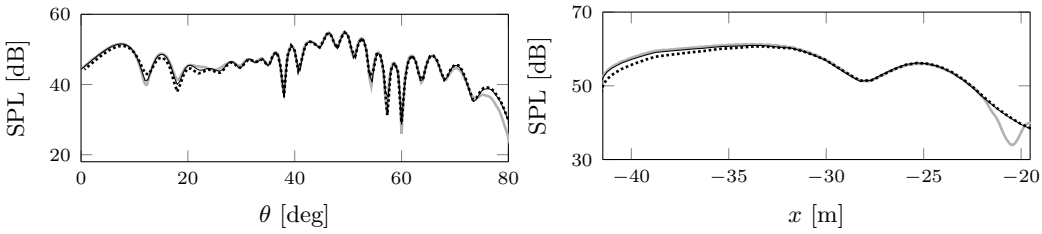

(a) $M_\infty = 0.1$, far field

(b) $M_\infty = 0.1$, near field

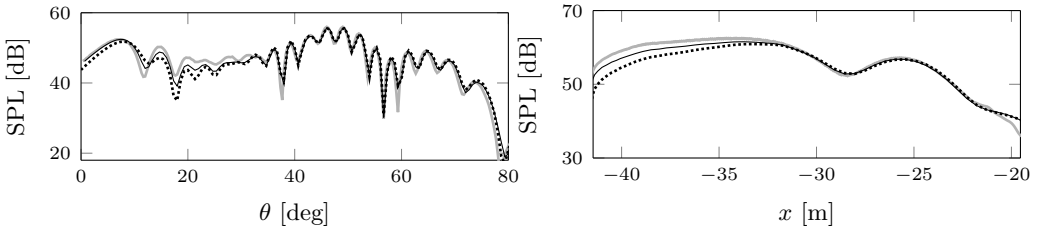

(c) $M_\infty = 0.2$, far field

(d) $M_\infty = 0.2$, near field

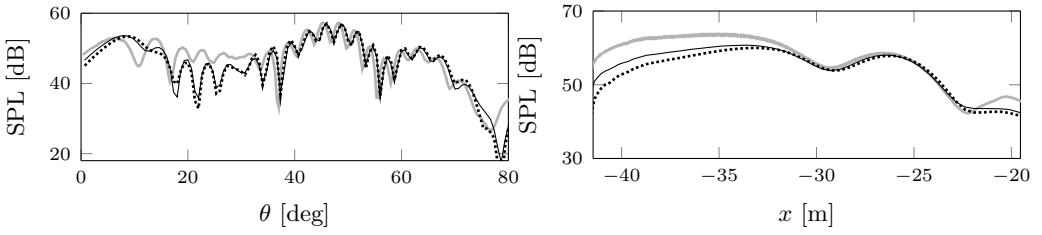

(e) $M_\infty = 0.3$, far field

(f) $M_\infty = 0.3$, near field

Figure 7.19: SPL along an arc of field points with radius $r_{fp} = 30r_n$ (far field) and in the near field (see Fig. 7.1) for a non-dimensional frequency $kr_n = 12$, $n = 3$ in Eq. (7.3) and the problem in Fig. 7.1. Solid, grey: FE LPE. Solid, black: BE weakly non-uniform flow and weak coupling. Dotted: BE uniform flow and weak coupling.

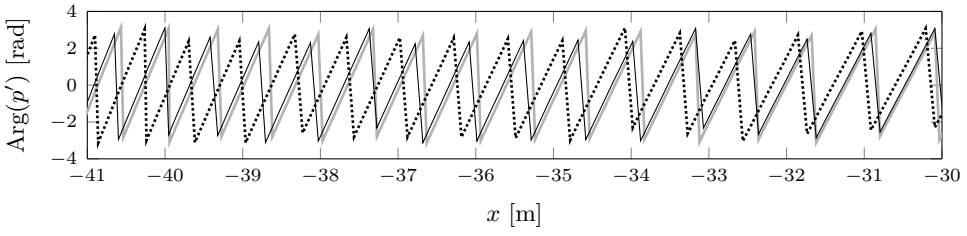

(a) $M_\infty = 0.1$

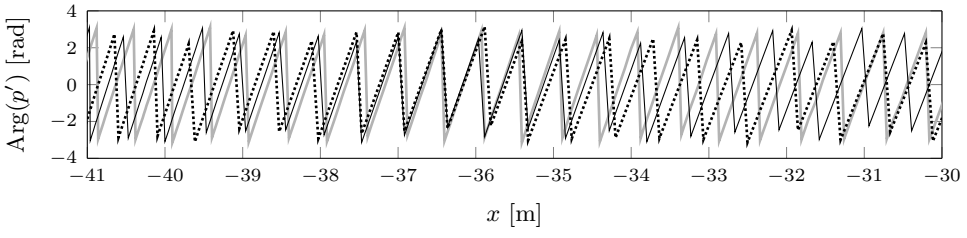

(b) $M_\infty = 0.3$

Figure 7.20: Phase of the acoustic pressure field along the boundary surface of the fuselage (see Fig. 7.1) for a non-dimensional frequency $kr_n = 12$ and the problem described in Fig. 7.1 with $n = 3$ in Eq. (7.3). Solid, grey: FE LPE. Solid, black: BE weakly non-uniform flow and weak coupling. Dotted: BE uniform flow and weak coupling.

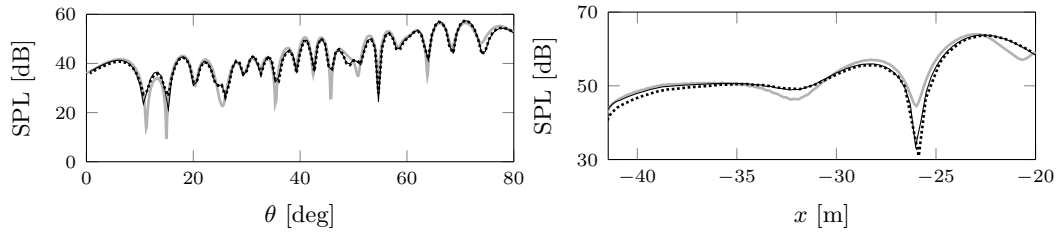

(a) $M_\infty = 0.1$, far field (b) $M_\infty = 0.1$, near field

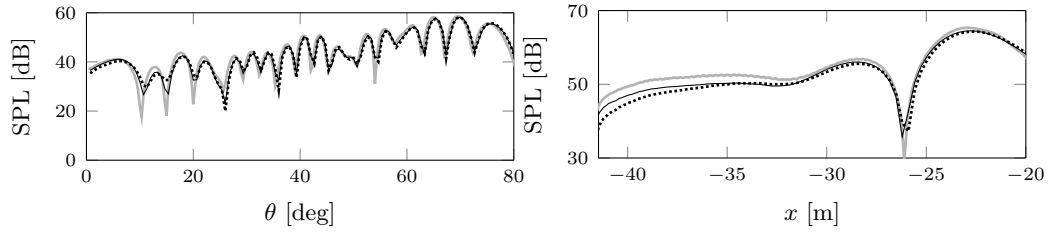

(c) $M_\infty = 0.2$, far field (d) $M_\infty = 0.2$, near field

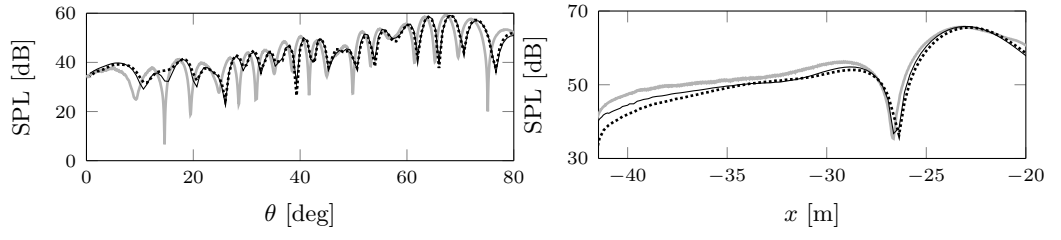

(e) $M_\infty = 0.3$, far field (f) $M_\infty = 0.3$, near field

Figure 7.21: SPL along an arc of field points with radius $r_{fp} = 30r_n$ (far field) and in the near field (see Fig. 7.1) for a non-dimensional frequency $kr_n = 12$, $n = 7$ in Eq. (7.3) and the problem in Fig. 7.1. Solid, grey: FE LPE. Solid, black: BE weakly non-uniform flow and weak coupling. Dotted: BE uniform flow and weak coupling.

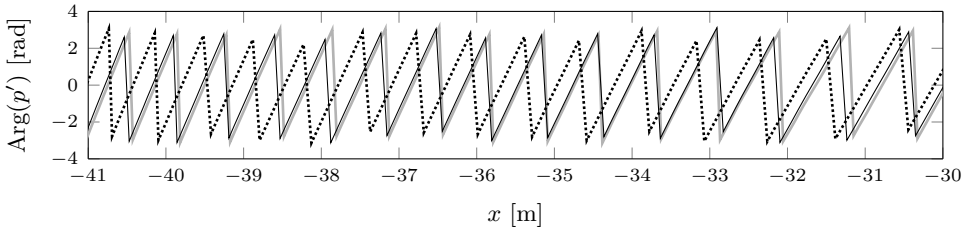

(a) $M_\infty = 0.1$

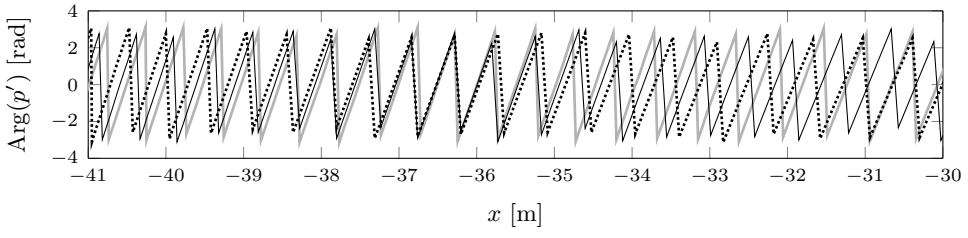

(b) $M_\infty = 0.3$

Figure 7.22: Phase of the acoustic pressure field along the boundary surface of the fuselage (see Fig. 7.1) for a non-dimensional frequency $kr_n = 12$ and the problem described in Fig. 7.1 with $n = 7$ in Eq. (7.3). Solid, grey: FE LPE. Solid, black: BE weakly non-uniform flow and weak coupling. Dotted: BE uniform flow and weak coupling.

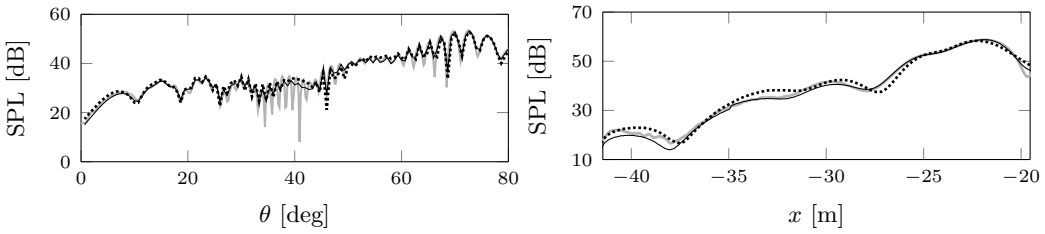

(a) $M_\infty = 0.1$, far field (b) $M_\infty = 0.1$, near field

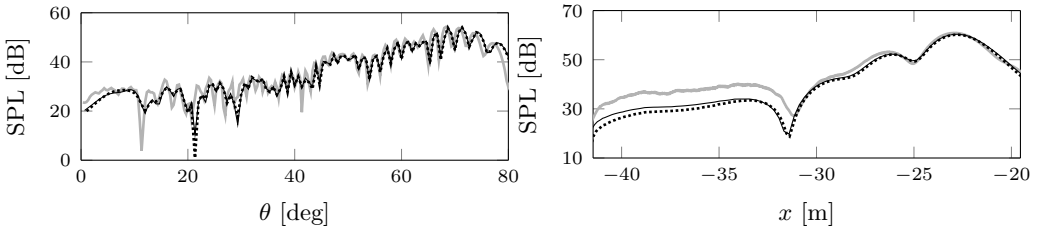

(c) $M_\infty = 0.2$, far field (d) $M_\infty = 0.2$, near-field

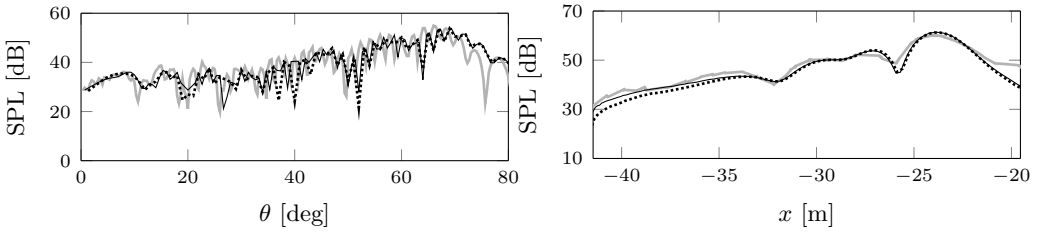

(e) $M_\infty = 0.3$, far field (f) $M_\infty = 0.3$, near field

Figure 7.23: SPL along an arc of field points with radius $r_{fp} = 30r_n$ (far field) and in the near field (see Fig. 7.1) for a non-dimensional frequency $kr_n = 24$, $n = 13$ in Eq. (7.3) and the problem in Fig. 7.1. Solid, grey: FE LPE. Solid, black: BE weakly non-uniform flow and weak coupling. Dotted: BE uniform flow and weak coupling.

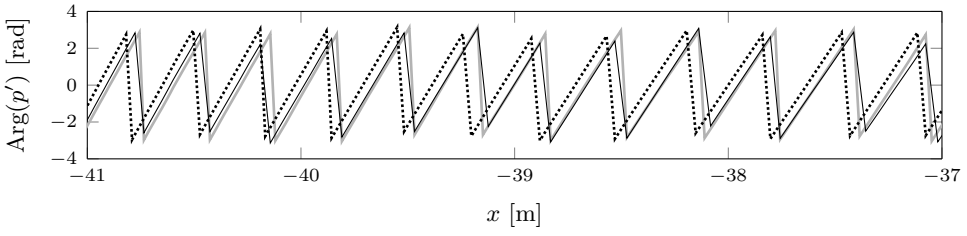

(a) $M_\infty = 0.1$

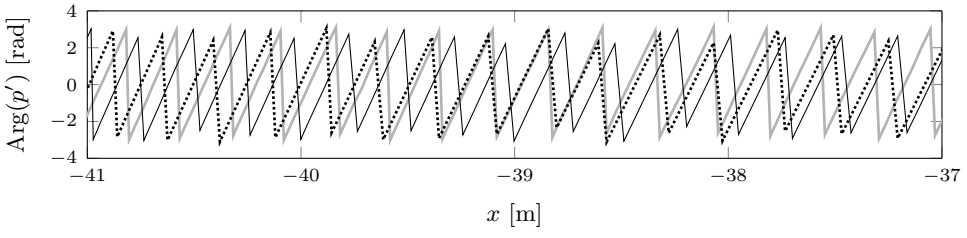

(b) $M_\infty = 0.3$

Figure 7.24: Phase of the acoustic pressure field along the boundary surface of the fuselage (see Fig. 7.1) for a non-dimensional frequency $kr_n = 24$ and the problem described in Fig. 7.1 with $n = 13$ in Eq. (7.3). Solid, grey: FE LPE. Solid, black: BE weakly non-uniform flow and weak coupling. Dotted: BE uniform flow and weak coupling.

While this effect is significant for two-dimensional problems it is expected that it will have a minor impact for three-dimensional domains since acoustic waves are more clearly scattered away from the fuselage rather than trapped in a region within the nacelle and the fuselage.

Nonetheless, in the near field for a low Mach number, $M_\infty = 0.1$, good agreement was obtained in terms of magnitude and phase of the acoustic pressure field among the BE solutions based on the weakly non-uniform flow formulation and the FE reference results. Although BE solutions based on uniform mean flows also agreed favourably in terms of SPL in the near field, they compared poorly to the FE solutions in terms of phase of the acoustic pressure for all Mach numbers in this example (see Figs. 7.14, 7.16, 7.20, 7.22 and 7.24). For $M_\infty = 0.3$, while the weakly non-uniform formulation predicted the SPL within 3-4 dB of the reference solution, the uniform formulation clearly underestimated the reference solution of 5-6 dB (see Figs. 7.13, 7.15, 7.19, 7.21, 7.23).

7.3 Concluding remarks

Boundary element solutions based on the Burton–Miller formulation with non-uniform flow have been benchmarked for a proof-of-concept test case representing forward fan noise installation effects. A weakly-coupled FE-BE method has been benchmarked exploiting an open kirchhoff integral surface and wave propagation in a non-uniform flow. The FE solution has been computed in an inner domain to solve the nacelle near field where non-uniformities in the mean flow are significant and, therefore, where the boundary element method cannot be applied. The integral solution to the weakly non-uniform flow was used to radiate the acoustic near field from an open control surface, where the assumption $M_0' \ll M_\infty$ was satisfied in the numerical examples. The resulting acoustic field was used to compute sound scattering based on the boundary element method and the weakly non-uniform flow formulation. Due to the limitation implicit in the non-uniform flow ansatz, the numerical results have been limited to $M_\infty \leq 0.3$.

The weakly-coupled approach has been assessed by using a simplified full-scale aircraft geometry. BE solutions have been compared to FE solutions to the full potential linearised wave equation, Eq. (2.30), in the nacelle near field and in a uniform flow region. The BE solutions based on the weakly non-uniform flow formulation favourably agreed with the corresponding FE reference solution. The model was assessed up to frequencies representative of the first blade passing frequency for current civil aircraft. The weakly-coupled formulation did not introduce a significant additional error compared to the approximation made by solving the weakly non-uniform formulation, in the outer domain, in lieu of the linearised potential wave equation.

It was shown that the error of the boundary element solution against the finite element reference solution was almost independent of frequency. Nonetheless, it more clearly increased

with M_∞. At $M_\infty = 0.3$, this error was within 3-4 dB for both near and far field predictions. A consistent incremental improvement of about 2 dB was provided by the weakly non-uniform flow formulation on the uniform flow approximation. This improvement was clearly seen in the near field where we have also shown accuracy in the phase of the acoustic pressure field for $M_\infty < 0.3$. This suggests that the non-uniform formulation might be exploited in the prediction of aircraft cabin noise.

In the region where the flow was almost uniform, the boundary element formulations based either on a uniform or non-uniform mean flow provided results which were in good agreement with each other. Although in the near field the weakly non-uniform formulation offers an incremental but consistent improvement of the corresponding uniform flow formulation, this is not seen in the far field. Note that the effect of mean flow can be represented in the transformed Taylor–Lorentz space by an equivalent problem with a quiescent medium. However, this is also the case for a Lorentz transform, which allows only uniform flow effects to be considered. Differences in the solution might arise from the boundary conditions.

For example, for the non-uniform flow formulation, Eq. (4.73) has been considered in the case of velocity boundary conditions. In this equation, dropping the terms depending on the non-uniform mean flow component gives the analogous condition for the problem with uniform flow. These conditions differ in that a term depending on $M_\infty n_x$, which vanishes for surfaces aligned with the uniform flow at infinity, is retained in the uniform flow formulation while in the non-uniform flow formulation we include an exponential term depending on Φ_0', which represents a local effect due to the non-uniform mean flow component. It is reasonable to infer that the effect of these terms is small for slender bodies, such as is the case of the numerical example provided, whenever the non-uniform mean flow velocity component is not significant.

To conclude, it was seen that the boundary element formulation with non-uniform flow provided robust results for a large-scale short-wavelength sound propagation and scattering problem. This suggests that it can be used for the assessment of aircraft noise large-scale installation effects at low Mach numbers. The weakly coupled formulation also provided a practical and flexible methodology to separate the computation of the near and far field for forward fan noise. This has a positive impact on the computational cost compared to a strongly-coupled formulation [42]. However, while these conclusions apply for two-dimensional problems, the weakly non-uniform formulation has yet to be tested and benchmarked for three-dimensional applications. This is performed in Chapter 8.

Chapter 8

3D Simulations

Contents

In this chapter, a practical approach is presented to use conventional boundary element solvers for wave propagation in quiescent media to recover solutions based on the weakly non-uniform flow formulation presented in Chapters 4 and 5. The proposed method is developed for velocity boundary conditions and allows existing boundary element solvers for the Helmholtz problem with quiescent media to solve mean flow effects without modifying the kernels. We use the iterative approach presented in Section 5.3.3.2 to exploit current boundary element solvers for the standard Helmholtz problem with quiescent media. In Sec. 8.1, we review the formulations usually implemented in boundary element solvers. Section 8.2 presents the method used to recover solutions for wave propagation with a mean flow when a boundary element kernel for the standard Helmholtz problem with quiescent media is available. In Sec. 8.3, numerical experiments are performed to test the accuracy of the proposed method. Applications to three-dimensional problems are shown as proof-of-concept test cases. Conclusions are finally given.

8.1 Conventional formulations

In this section, we review how to recover a formulation written in terms of acoustic potential, ϕ, in lieu of acoustic pressure, p', whenever a formulation in the Taylor–Lorentz space is considered. The key point is that the weakly non-uniform flow formulation reduces to the standard Helmholtz equation in a transformed Taylor–Lorentz space (see Sec. 4.7.1). For the standard Helmholtz problem in the transformed space, acoustic pressure and velocity potential are independent of the mean flow.

Conventional boundary element solvers for the Helmholtz problem are written in terms of acoustic pressure, p'. In the transformed Taylor–Lorentz space, the Helmholtz operator (see Sec. 4.7) applied to the acoustic pressure can be written as

$$\boldsymbol{\nabla}^2_{\tilde{X}}\tilde{p}' + \tilde{k}^2\tilde{p}' = \tilde{g}_f, \tag{8.1}$$

where $\tilde{k} = k/\beta_\infty$ and $\tilde{g}_f$ is a generic source term. Again, we denote with "~" the variables written in a Taylor–Lorentz space. In the transformed space, acoustic pressure and velocity can be calculated as

$$\tilde{p}'(\tilde{\mathbf{X}}, \tilde{\omega}) = -\rho_0 \mathrm{i}\tilde{\omega}\tilde{\phi}(\tilde{\mathbf{X}}, \tilde{\omega}), \qquad \tilde{\mathbf{u}}'(\tilde{\mathbf{X}}, \tilde{\omega}) = \boldsymbol{\nabla}_{\tilde{X}}\tilde{\phi}(\tilde{\mathbf{X}}, \tilde{\omega}), \tag{8.2}$$

where $\boldsymbol{\nabla}_{\tilde{X}}$ denotes the gradient in the Taylor–Lorentz space.

On the other hand, the Helmholtz problem written in terms of acoustic potential is

$$\boldsymbol{\nabla}^2_{\tilde{X}}\tilde{\phi} + \tilde{k}^2\tilde{\phi} = \tilde{g}, \tag{8.3}$$

where $\tilde{g} = -\tilde{g}_f/\rho_0 \mathrm{i}\tilde{\omega}$. Note that, although the left-hand side operator in Eqs. (8.1) and (8.3) coincide, the right-hand side terms generally differ. However, for any solution to Eq. (8.1), a solution in terms of acoustic potential can be recovered based on Eq. (8.2).

In the transformed space, it is seen that a scaling factor can be used to recover the acoustic pressure from the acoustic potential. On the other hand, the relation between acoustic pressure, p', and potential, ϕ, becomes more complex with a mean flow. In the physical space, the acoustic pressure can be written as

$$p'(\omega) = -\rho_0(\mathrm{i}\omega\phi + \mathbf{u}_0 \cdot \boldsymbol{\nabla}\phi), \tag{8.4}$$

where the dependence on $\mathbf{x}$ has been implied and $\phi = \phi(\omega)$, while the corresponding formulation in the transformed space has been provided in Eq. (4.71). A standard boundary element solver for the Helmholtz problem can be used to solve Eq. (8.1). The corresponding acoustic potential and its gradient can be calculated from Eq. (8.2). The pressure in the physical space can then be evaluated by using Eq. (4.71).

8.2 Practical implementation

The procedure and the formulation used to include mean flow effects on a standard boundary element solution with quiescent media is discussed in this section. First, we outline the solution process. Second, the kernels that can be used for the solution of the boundary element problem in the transformed space are reported. The modified boundary conditions to account for mean flow effects are then discussed. In particular, a formulation based on velocity boundary conditions is proposed. It was seen that, in the transformed space, the problems based on Dirichlet boundary conditions are compatible with a standard kernel for the Helmholtz problem with quiescent media. On the other hand, boundary conditions based on prescribed pressure and Robin-type boundary conditions require the kernel to be modified (see Sec. 5.3.3).

8.2.1 Solution process

Non-uniform mean flow effects are included in boundary element solutions based on a Taylor–Lorentz transform. In pre-processing, the actual geometry is modified using the Taylor–Lorentz variable transformation in Sec. 2.6.3 and the sound sources are rewritten based on Eq. (4.64). In practice, the domain is stretched in the direction of the uniform mean flow by a factor $\sqrt{1-M_\infty^2}$ whilst a phase shift based on the local mean flow potential is imposed on the acoustic potential. Note that any sound source distribution in a potential flow can be computed in the transformed space using Eq. (8.2).

The transformed boundary element model is then solved by using a conventional BE solver for the Helmholtz problem with quiescent media. The iterative approach developed in Sec. 5.3.3 is then devised with modified boundary conditions to include mean flow effects. The problem is initially solved without the tangential terms (see Sec. 5.3.3.2). Further iterations are performed based on the solution on the boundary at a previous iterative step, including the tangential terms. As a convergence criterium, we use the relative difference between the solutions on the boundary surface at two subsequent steps.

Once the iterative solution has converged, an inverse Taylor–Lorentz transform is applied to recover acoustic potential, ϕ, and acoustic pressure, p', in the physical space (see Eqs. (4.63) and (4.71)). Note that a similar approach can be used to devise a solution based on the Lorentz transform if all the terms depending on the mean flow non-uniformity are neglected.

8.2.2 Available kernels in the transformed space

Conventional boundary integral solutions to the Helmholtz problem are based on Eq. (8.1) [43, 91]. The direct boundary integral solution to Eq. (8.1) for a homogeneous problem is given

by

$$C(\tilde{\mathbf{X}}_p)\tilde{p}'(\tilde{\mathbf{X}}_p,\tilde{\omega})+\int_{\partial\tilde{\Omega}}\tilde{p}'(\tilde{\mathbf{X}},\tilde{\omega})\frac{\partial\tilde{G}(\tilde{\mathbf{X}}_p,\tilde{\mathbf{X}},\tilde{\omega})}{\partial\tilde{n}}d\tilde{S}(\tilde{\mathbf{X}}) = -\mathrm{i}\tilde{\omega}\rho_0\int_{\partial\tilde{\Omega}}G(\tilde{\mathbf{X}}_p,\tilde{\mathbf{X}},\tilde{\omega})\tilde{u}'_{\tilde{n}}(\tilde{\mathbf{X}},\tilde{\omega})d\tilde{S}(\tilde{\mathbf{X}}), \tag{8.5}$$

where $\tilde{u}'_{\tilde{n}}$ is the normal component of the acoustic particle velocity to the boundary surface in the transformed space and $\tilde{G}$ is the free-field Green's function for the Helmholtz problem with quiescent media. The continuous field is then approximated by introducing interpolating functions, $N(\tilde{\mathbf{X}})$, as [91]

$$\tilde{u}'_n(\tilde{\mathbf{X}},\tilde{\omega}) \simeq \sum_{l=1}^{\mathrm{Ndof}} N_l(\tilde{\mathbf{X}})\tilde{V}_{\tilde{n},l}(\tilde{\omega}), \qquad \tilde{p}'(\tilde{\mathbf{X}},\tilde{\omega}) \simeq \sum_{l=1}^{\mathrm{Ndof}} N_l(\tilde{\mathbf{X}})\tilde{p}'_l(\tilde{\omega}), \tag{8.6}$$

where $\tilde{V}_{\tilde{n},l}$ and $\tilde{p}'_l$ represent nodal values. Hence, the discrete linear system, which solves the boundary integral problem in Eq. (8.5) based on a collocation formulation, can be written as

$$\tilde{\mathbf{A}}_c\tilde{\mathbf{p}}' = \mathrm{i}\tilde{\omega}\rho_0\tilde{\mathbf{B}}_c\tilde{\mathbf{V}}_{\tilde{n}}, \tag{8.7}$$

where $\tilde{\mathbf{V}}_{\tilde{n}}$ denotes the nodal vector of the normal particle velocity to the boundary, while $\tilde{\mathbf{A}}_c$ and $\tilde{\mathbf{B}}_c$ are the same matrices as those shown for the solution written in terms of $\tilde{\phi}$, reported in Appendix C. The acoustic pressure on the boundary surface is computed by solving the above system of equations. The solution at any point of the domain can then be recovered based on Eq. (8.5).

Alternatively, an indirect formulation [91] can be used to solve the boundary element problem. In fact, an analogy between the double/single layer potentials, ξ' and σ', and acoustic pressure/velocity on the boundary surface can be stated if either an external or an internal sound propagation problem is solved for closed surfaces [193]. The double and the single layer potentials represent, respectively, the difference in acoustic pressure and acoustic normal velocity through the boundary. On the boundary surface, either σ' or ξ' is zero unless an impedance boundary condition is assigned. For velocity boundary conditions, σ' is equal to 0. That is also the case for the transformed space variable, $\tilde{\sigma}'$, whenever the normal particle velocity in the transformed space, $\tilde{u}'_{\tilde{n}}$, is prescribed (see Appendix C.5). The indirect integral solution [135] in the transformed space for velocity boundary conditions can be written as

$$\int_{\partial\tilde{\Omega}}\tilde{\xi}'(\tilde{\mathbf{X}},\tilde{\omega})\frac{\partial^2\tilde{G}(\tilde{\mathbf{X}}_p,\tilde{\mathbf{X}},\tilde{\omega})}{\partial\tilde{n}\partial\tilde{n}_p}d\tilde{S}(\tilde{\mathbf{X}}) = \mathrm{i}\tilde{\omega}\rho_0\tilde{u}'_{\tilde{n}}(\tilde{\mathbf{X}}_p,\tilde{\omega}). \tag{8.8}$$

The indirect formulation is usually rewritten in a variational formulation to work around the regularisation of the hyper-singular integral [135, 139]. For these conditions, a variational statement associated with the above equation can be discretised as in Eq. (8.6) to give

$$\tilde{\mathbf{H}}\tilde{\boldsymbol{\xi}}' = \mathrm{i}\tilde{\omega}\rho_0\tilde{\mathbf{Q}}\tilde{\mathbf{V}}_{\tilde{n}}, \tag{8.9}$$

where

$$\tilde{H}^{(lm)} = \int_{\partial\tilde{\Omega}} \int_{\partial\tilde{\Omega}} N_l(\tilde{\mathbf{X}}_p) \frac{\partial^2 \tilde{G}(\tilde{\mathbf{X}}_p, \tilde{\mathbf{X}})}{\partial\tilde{n}\partial\tilde{n}_p} N_m(\tilde{\mathbf{X}}) d\tilde{S}(\tilde{\mathbf{X}}) d\tilde{S}(\tilde{\mathbf{X}}_p) \tag{8.10}$$

and

$$\tilde{Q}^{(lm)} = \int_{\partial\tilde{\Omega}} \delta_{lm} N_l(\tilde{\mathbf{X}}_p) N_m(\tilde{\mathbf{X}}_p) d\tilde{S}(\tilde{\mathbf{X}}_p), \tag{8.11}$$

For brevity, in the above equation we omitted the dependence of $\tilde{G}$ on $\tilde{\omega}$. For the hypersingular integral including the double derivative of $\tilde{G}$, Eq. (5.51) can be used again to obtain only weakly singular integrals. Hence, a conventional singularity subtraction approach and Gauss quadrature can be used for the numerical integration and the computation of the coefficient matrix. Once $\tilde{\xi}'$ is solved on the boundary, the pressure field in the domain can be evaluated as [135]

$$\tilde{p}'(\tilde{\mathbf{X}}_p, \tilde{\omega}) = -\int_{\partial\tilde{\Omega}} \tilde{\xi}'(\tilde{\mathbf{X}}, \tilde{\omega}) \frac{\partial \tilde{G}(\tilde{\mathbf{X}}_p, \tilde{\mathbf{X}}, \tilde{\omega})}{\partial\tilde{n}} d\tilde{S}(\tilde{\mathbf{X}}). \tag{8.12}$$

The above equation can also be used on the boundary surface to recover acoustic pressure. In this case, the integral along the boundary surface is solved using the Cauchy principal value. Noentheless, Eqs. (8.8) and (8.12) can alternatively be formulated in terms of the acoustic potential and Eq. (8.4) used to compute acoustic pressure (see Appendix C.5). Note that the right-hand side of Eq. (8.8) is consistent with the right-hand side of Eq. (8.5). This peculiarity will be exploited to devise a standard boundary element kernel to solve the problem with mean flow.

The incident field due to volume distributions of sound sources can be recovered by convolving the source model with the Green's function. This contribution can be added on the right-hand side of Eq. (8.5), provided that the source model is rewritten in the transformed space (see Sec. 4.7). This can be done for Eqs. (8.5) and (8.8). Alternatively, for the indirect formulation, the incident field, p'_{inc}, is usually separated from the scattered field, p'_{sc}, such that $p' = p'_{inc} + p'_{sc}$. The incident field can be defined by convolving the Green's function with the source model, while the scattered field is recovered to satisfy the boundary conditions. This is usually performed for the indirect formulation. Since the incident field satisfies Eq. (8.8), for velocity boundary conditions one has:

$$\int_{\partial\tilde{\Omega}} \tilde{\xi}'_{sc}(\tilde{\mathbf{X}}, \tilde{\omega}) \frac{\partial^2 \tilde{G}(\tilde{\mathbf{X}}_p, \tilde{\mathbf{X}}, \tilde{\omega})}{\partial\tilde{n}\partial\tilde{n}_p} d\tilde{S}(\tilde{\mathbf{X}}) = \mathrm{i}\tilde{\omega}\rho_0 \tilde{u}'_{\tilde{n},sc}(\tilde{\mathbf{X}}_p, \tilde{\omega}), \tag{8.13}$$

where the subscript "$_{sc}$" denotes the scattered field. In the above equation, the right-hand side can be assigned based on the boundary conditions in the physical space,

$$u'_{n,sc}(\mathbf{x}_p, \omega) = -u'_{n,inc}(\mathbf{x}_p, \omega) + h_n(\mathbf{x}_p, \omega), \tag{8.14}$$

where h_n is the same as that given in Sec. 4.7.3. It vanishes for rigid boundary conditions. The above equation must be rewritten in the transformed space to suit the right-hand side

of Eq. (8.13). This can be performed by using the Taylor–Lorentz transform, as will be shown in Sec. 8.2.3.

8.2.3 Recovering standard kernels

In this section, an iterative approach, based on the solution described in Sec. 5.3.3, is proposed to exploit conventional boundary element kernels with quiescent media, such as those reviewed in Sec. 8.2.2, to resolve mean flow effects. Velocity boundary conditions are rewritten in terms of normal and tangential pressure derivatives. Note that the tangential derivatives of the acoustic pressure developed by the Taylor–Lorentz transformation are not conventionally prescribed by the boundary conditions. Therefore, we retain these terms on the right-hand side and treat them as equivalent sources. They can be updated iteratively based on the boundary element solution at a previous iteration (see Sec. 5.3.3.2).

First, we want to specify the normal pressure gradient in a Taylor–Lorentz space in terms of its values in the physical space. The normal particle velocity to the boundary surface in the transformed Taylor–Lorentz space, $\tilde{u}'_{\tilde{n}}$, can be written

$$\tilde{u}'_{\tilde{n}}(\tilde{\omega}) = \frac{\mathrm{i}}{\rho_0 \tilde{\omega}} \frac{\partial \tilde{p}'(\tilde{\omega})}{\partial \tilde{n}}. \tag{8.15}$$

If velocity boundary conditions are prescribed, the value of $\partial p/\partial n$ is assigned in the physical space. However, in the transformed space, the normal pressure gradient can be written (see Sec. 4.7.3.1)

$$\frac{\partial \tilde{p}'(\tilde{\mathbf{X}}, \tilde{\omega})}{\partial \tilde{n}} = \mu(\tilde{\mathbf{X}}) \left[\frac{\partial \tilde{p}'(\tilde{\mathbf{X}}, \tilde{\omega})}{\partial n} - \frac{\partial \tilde{p}'(\tilde{\mathbf{X}}, \tilde{\omega})}{\partial \tilde{\tau}} \frac{\partial \tilde{\tau}}{\partial n} - \frac{\partial \tilde{p}'(\tilde{\mathbf{X}}, \tilde{\omega})}{\partial \tilde{\eta}} \frac{\partial \tilde{\eta}}{\partial n} \right], \tag{8.16}$$

where $\mu(\tilde{\mathbf{X}}) = 1/(\partial \tilde{n}/\partial n)$ is the same geometrical factor as that in Sec. 4.7.3.1. By using Eq. (8.2), the acoustic pressure in the transformed space can be reduced to

$$\tilde{p}'(\tilde{\omega}) = -\mathrm{i}\tilde{\omega}\rho_0 \tilde{\phi} = -\mathrm{i}\tilde{\omega}\rho_0 \phi \mathrm{e}^{-\mathrm{i}k\left(\frac{M_\infty x}{\beta^2} + \frac{\Phi'_0(\mathbf{x})}{c_\infty}\right)}. \tag{8.17}$$

Using the weakly non-uniform ansatz, the normal component of the gradient of the acoustic potential is rewritten as (see Eq. (4.75))

$$\frac{\partial \tilde{\phi}(\tilde{\mathbf{X}})}{\partial n} \simeq \frac{\partial \phi(\mathbf{x})}{\partial n} \mathrm{e}^{-\mathrm{i}k\left(\frac{M_\infty x}{\beta^2_\infty} + \frac{\Phi'_0(\mathbf{x})}{c_\infty}\right)} = u'_n(\mathbf{x}, \omega) \mathrm{e}^{-\mathrm{i}k\left(\frac{M_\infty x}{\beta^2_\infty} + \frac{\Phi'_0(\mathbf{x})}{c_\infty}\right)}, \tag{8.18}$$

where u'_n is the particle velocity normal to the physical-space boundary and $\mathbf{n}$ is the normal vector to this boundary. In the above equation, high-order terms in the Mach number have been neglected, consistent with the weakly non-uniform flow ansatz. Nonetheless, the component of the potential mean flow velocity normal to the boundary surface has been set to zero since we are considering impermeable stationary surfaces. Hence, Eq. (8.16) can be

rewritten based on Eqs. (8.17) and (8.18) to give

$$\frac{\partial \tilde{p}'(\tilde{\mathbf{X}},\tilde{\omega})}{\partial \tilde{n}} = \mu(\tilde{\mathbf{X}})\left[-\mathrm{i}\tilde{\omega}\rho_0\tilde{u}'_n(\tilde{\mathbf{X}},\tilde{\omega}) - \frac{\partial \tilde{p}'(\tilde{\mathbf{X}},\tilde{\omega})}{\partial \tilde{\tau}}\frac{\partial \tilde{\tau}}{\partial n} - \frac{\partial \tilde{p}'(\tilde{\mathbf{X}},\tilde{\omega})}{\partial \tilde{\eta}}\frac{\partial \tilde{\eta}}{\partial n}\right], \tag{8.19}$$

where

$$\tilde{u}'_n(\tilde{\mathbf{X}},\tilde{\omega}) = u'_n(\mathbf{x},\omega)\mathrm{e}^{-\mathrm{i}k\left(\frac{M_\infty x}{\beta_\infty^2}+\frac{\Phi'_0(\mathbf{x})}{c_\infty}\right)}, \tag{8.20}$$

with the acoustic particle velocity to the physical-space boundary, $\tilde{u}'_n$, has been written in terms of the transformed space variables. Note that the terms depending on the tangent vectors are zero for surfaces aligned with the uniform mean flow at infinity. Along these surfaces, the normal vectors to either the physical or the transformed space boundary coincide and, therefore, the component of the tangent vectors in the transformed space along the corresponding normal vector to the physical-space boundary is zero.

We want to derive a discrete system of equations consistent with Eqs. (8.7) and (8.9) including Eq. (8.19). The variable expansion in Eq. (8.6) applied to Eq. (8.19) yields

$$\tilde{u}'_{\tilde{n}}(\tilde{\mathbf{X}},\tilde{\omega}) \simeq \sum_{l=1}^{\mathrm{Ndof}} N_l(\tilde{\mathbf{X}})\left[\mu^{(l)}\tilde{V}_n^{(l)}(\tilde{\omega}) + \frac{\mu^{(l)}}{\mathrm{i}\rho_0\tilde{\omega}}\left(\frac{\partial \tilde{p}'^{(l)}(\tilde{\omega})}{\partial \tilde{\tau}}\frac{\partial \tilde{\tau}^{(l)}}{\partial n} + \frac{\partial \tilde{p}'^{(l)}(\tilde{\omega})}{\partial \tilde{\eta}}\frac{\partial \tilde{\eta}^{(l)}}{\partial n}\right)\right]. \tag{8.21}$$

The vector of the boundary conditions at the nodal points, $\tilde{\mathbf{V}}_{\tilde{n}}$, can then be rewritten in order to include the tangential derivatives,

$$\tilde{V}_{\tilde{n},q}^{(l)} = \mu^{(l)}\tilde{V}_n^{(l)} + \tilde{v}_q^{(l)}, \tag{8.22}$$

where q denotes the q-th iterative step and

$$\tilde{v}_{q+1}^{(l)} = \frac{\mu^{(l)}}{\mathrm{i}\rho_0\tilde{\omega}}\left(\frac{\partial \tilde{p}_q'^{(l)}}{\partial \tilde{\tau}}\frac{\partial \tilde{\tau}^{(l)}}{\partial n} + \frac{\partial \tilde{p}_q'^{(l)}}{\partial \tilde{\eta}}\frac{\partial \tilde{\eta}^{(l)}}{\partial n}\right). \tag{8.23}$$

Hence, the iterative system of equations based on Eq. (8.7) reduces to

$$\tilde{\mathbf{A}}_c\tilde{\mathbf{p}}'_{q+1} = \mathrm{i}\tilde{\omega}\rho_0\tilde{\mathbf{B}}_c\tilde{\mathbf{V}}_{\tilde{n},q}, \tag{8.24}$$

while for the indirect formulation, Eq. (8.9),

$$\tilde{\mathbf{H}}\tilde{\boldsymbol{\xi}}'_{q+1} = \mathrm{i}\tilde{\omega}\rho_0\tilde{\mathbf{Q}}\tilde{\mathbf{V}}_{\tilde{n},q}. \tag{8.25}$$

For the indirect formulation, Eq. (8.12) can be used to recover the solution in terms of acoustic pressure in order to compute the left-hand side at every iteration. Note that, Eqs. (8.24) and (8.25) can be solved whenever the values of u'_n are prescribed on the physical-space boundary.

In the iterative approach, for $q = 0$, we assume that $\tilde{v}_q^{(l)} = 0$. The system of equations in Eqs. (8.24) and (8.25) can be solved by using a conventional boundary element method for the Helmholtz problem with quiescent media and mean flow effects can be resolved based on the methodology proposed in Sec. 8.2.1. Equation (8.25) can also be rewritten using Eq. (8.13) whenever the boundary element problem is solved by separating the incident and the scattered field.

Although the proposed iterative solution has not been considered in previous works, indications on the convergence of this approach can be inferred from other applications. As shown by Perrey-Debain [126] for the Dual Reciprocity BEM, a distribution of equivalent sources on the boundary surface satisfying the integral solution to the wave operator leads to convergence of the boundary element problem. Nonetheless, this is also the case for the Multiple Reciprocity BEM [129] where integrals over the domain are replaced with equivalent sources on the boundary in a recurrent manner. However, convergence of the proposed iterative approach will be assessed with numerical examples.

8.3 Numerical experiments

In this section, numerical examples are performed to benchmark the methodology proposed in Sec. 8.2. In Sec. 8.3.1, a preliminary convergence study is performed to assess the iterative approach based on a two-dimensional problem. In Sec. 8.3.2, a benchmark study is then performed looking at three-dimensional noise radiation and scattering around a sphere. In Sec. 8.3.3, we present sound radiation around a simplified full-scale aircraft geometry. In all the test cases, we assume rigid boundary conditions, namely $u_n' = 0$. A Matlab [202] routine is used to perform the Taylor–Lorentz transformation and recover the solution in the physical space, while the commercial solver Sysnoise [212] is used to solve the boundary element kernel for the Helmholtz problem with quiescent media.

A finite element solution of the linearised potential wave equation is provided as the reference solution (see Eq. (6.2)). The test case of the sphere is a worst-case scenario in that the mean flow length scale relative to the wavelength is short compared to the case of a slender body, such as an aircraft. A full-scale aircraft geometry is a reference application for this work and is used to get an insight into the accuracy of the boundary element solution for slender bodies. In this case, the FE reference solution can be computed only for relatively low frequencies due to the size of the domain and the computational resources required. We assess the solutions both in the near field and in a region where the flow is almost uniform, since the error from the weakly non-uniform flow formulation has been shown to be constant as soon as the latter domain is reached.

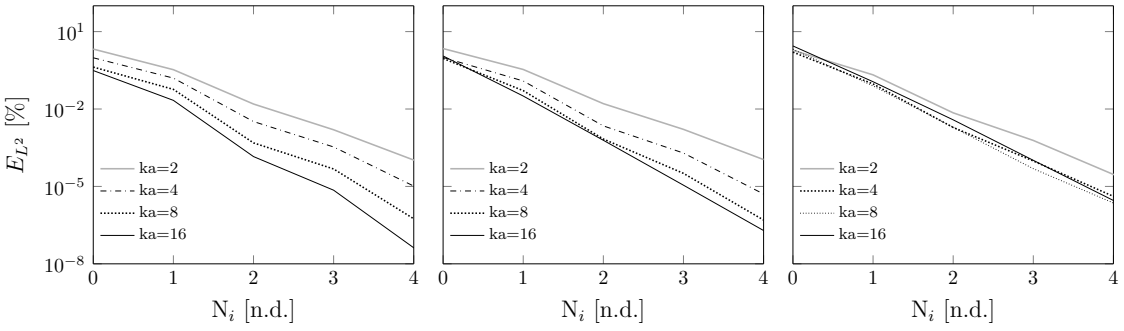

(a) $M_\infty = 0.1$ (b) $M_\infty = 0.2$ (c) $M_\infty = 0.3$

Figure 8.1: L^2-error measured along an arc of field points with radius $R_{fp} = a$ against the number of iterations, N_i, for the iterative scheme in Eq. (5.78) and the problem described in Fig. 6.1. The reference solution for the computation of the error is obtained using Eq. (5.75).

8.3.1 Validation of the iterative approach

The two-dimensional test case presented in Fig. 6.1 is used here to assess the convergence of the iterative scheme proposed in Sec. 5.3.3.2. The reference solution for the computation of the L^2-error is based on Eq. (5.75), i.e. the formulation where all the terms including the tangential derivatives of $\tilde{\phi}$ are retained on the left-hand side. Despite the fact that this chapter is focussed on 3D problems, a two-dimensional problem is used here since the solution including the tangential derivatives on the left-hand side was implemented for a 2D solver. For 3D solutions, we exploit commercial solvers where this formulation is not readily available.

The L^2-error on the velocity potential, ϕ, measured at the scattering surface, is depicted in Fig. 8.1 against the number of iterations, N_i, for $M_\infty = 0.1 \rightarrow 0.3$ with non-dimensional frequencies $ka = 2$, 4, 8 and 16. It is seen that the magnitude of the terms including the tangential derivatives increases with M_∞. For $M_\infty \leq 0.3$ and $N_i = 0$, the error reaches 7-8 % of the reference solution. For $N_i = 3$, it decreases down to 10^{-2} %. Note that this level of error is much lower than that provided by the weakly non-uniform flow formulation compared to the reference physical model, i.e. the linearised potential wave equation (see Figs. 6.25 and 6.32). Therefore, we can rely on the iterative approach to solve the three-dimensional test cases in the following sections.

8.3.2 Sound scattering from a sphere

Three-dimensional sound radiation and scattering around a sphere with a mean flow is now considered (see Fig. 8.2). First, the numerical model is detailed. Second, a validation of the variable transformation approach is performed for a uniform mean flow. Finally, a benchmark study is performed including non-uniform mean flows.

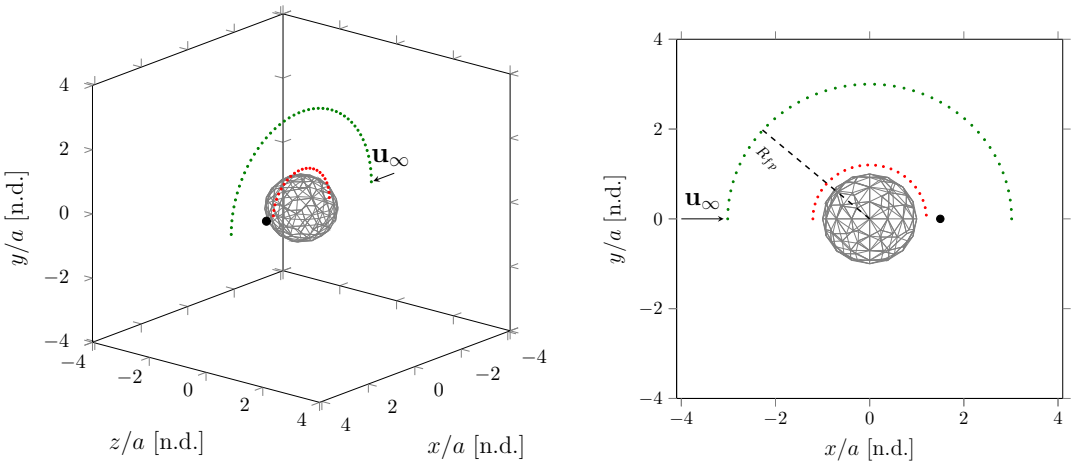

(a) 3D view (b) side view

Figure 8.2: Geometry for the problem of sound scattering of a monopole point source by a sphere in a potential mean flow, showing the field points (dotted line) and the monopole point source (black dot).

8.3.2.1 Numerical model and mesh convergence

Let us consider a rigid sphere of radius a. The incident field is generated by a monopole point source. A uniform mean flow is defined in the direction of the x-axis. The speed of sound is $c_\infty = 340$ m·s^{-1} and the mean flow density is $\rho_0 = 1.22$ kg·m^{-3}. We solve a time harmonic problem written in terms of acoustic velocity potential, ϕ, while acoustic pressure is recovered based on Eq. (8.4). The reference value for the calculation of the SPL $= 20\log_{10}(p'_{rms}/p'_{ref})$ is $p'_{ref} = 2 \cdot 10^{-5}$ Pa and $p'_{rms} = \|p'\|/\sqrt{2}$.

An unstructured triangular grid is used for the boundary element model of the sphere (see Fig. 8.4). A quadratic boundary element solution based on an isoparametric formulation is provided. We consider a boundary element model with 23355 degrees of freedom. This model is used for every test case of this section. The boundary element problem is generally solved by using the indirect boundary element approach (see Sec. 8.2.2). Unless otherwise stated, all the boundary element results are based on $\mathrm{N}_i = 3$ iterative steps, for which the convergence rate has been shown to be of order $10^{-2}\%$ for the example provided in Sec. 8.3.1.

Whenever the Taylor–Lorentz transformation is applied, the boundary element grid is stretched in the direction of the mean flow by a factor $\sqrt{1-M_\infty^2}$. Therefore, grid stretching must be considered to achieve an expected level of convergence if a standard BE kernel is used. This also applies if a more conventional Lorentz transform is used. Nonetheless, the frequency in the transformed space is increased by a factor $\sqrt{1-M_\infty^2}$. Therefore, if for quiescent media we consider $\tilde{k}\tilde{h} \leq 2\pi/n$, where n is the number of degrees of freedom per wavelength and $\tilde{h}$ is the element size in the transformed space with quiescent media, in the presence of mean flow we should discretise the boundary surface using $kh \leq 2\pi(1-M_\infty^2)/n$.

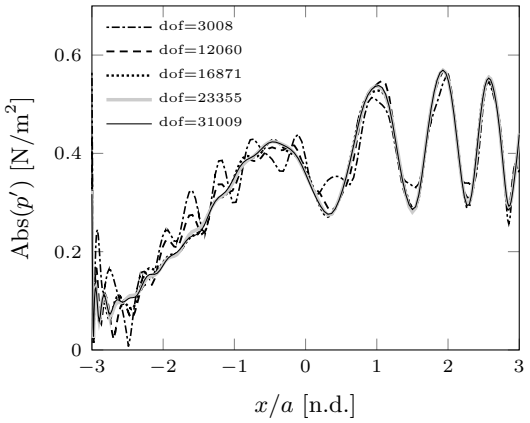

Figure 8.3: Acoustic pressure along an arc of field points with radius $R_{fp} = 3a$ for the problem of the scattering of a monopole point source at $\mathbf{x}_s = (1.5a, 0, 0)$ from a rigid sphere of radius a. Convergence analysis on the BE model based on the Lorentz transform for the problem in Fig. 8.2.

An example of convergence analysis is reported in Fig. 8.3 showing the absolute value of the acoustic pressure along an arc of field points with radius $R_{fp} = 3a$ for a uniform flow, at $M_\infty = 0.4$ and for a non-dimensional frequency $ka = 20$. This is the largest Mach number and frequency considered in this example. These results are obtained for a monopole point source located at $\mathbf{x}_s = (1.5a, 0, 0)$ and the problem shown in Fig. 8.2. All the field points are defined on the plane $z = 0$ and have non-negative y-coordinates (see Fig. 8.2). It is shown that numerical convergence is satisfactory.

An adaptive high-order FE solution [23, 68] for the linearised potential wave equation, Eq. (6.2), with 8 degrees of freedom per wavelength is also solved using Sysnoise. It is "adaptive" in the sense that the order of interpolation is adapted to achieve a prescribed local resolution taking account of the mean flow [68]. The FE solutions are used as references in the rest of this chapter. An unstructured tetrahedral mesh is defined. The domain is truncated with a spherical surface of radius $R = 4a$ (see Fig. 8.4). A PML is used to satisfy the radiation condition at the outer surface. The PML is extruded for four wavelengths and accounts for eight degrees of freedom per wavelength.

A potential incompressible mean flow is provided by solving a finite element model based on the Laplace problem. The flow is mapped onto the acoustic mesh based on the nearest neighbour algorithm [207] and the method of least squares, where we consider three nodes of the aerodynamic mesh per nodal point of the acoustic mesh. The mean flow is limited to $M_\infty \leq 0.4$, where it is still reasonable to assume an incompressible mean flow.

In the boundary element model based on the Taylor–Lorentz transform, the volume point source is written as

$$\tilde{g}(\tilde{\mathbf{X}}, \tilde{T}) = \delta(\tilde{\mathbf{X}} - \tilde{\mathbf{X}}_0) \mathrm{e}^{\mathrm{i}\tilde{\omega}\tilde{T}} \mathrm{e}^{-\mathrm{i}\tilde{k}\beta_\infty \left(\frac{M_\infty \tilde{X}_0}{\beta_\infty} + \frac{\Phi_0'(\mathbf{x}_0(\tilde{\mathbf{X}}_0))}{c_\infty} \right)}, \tag{8.26}$$

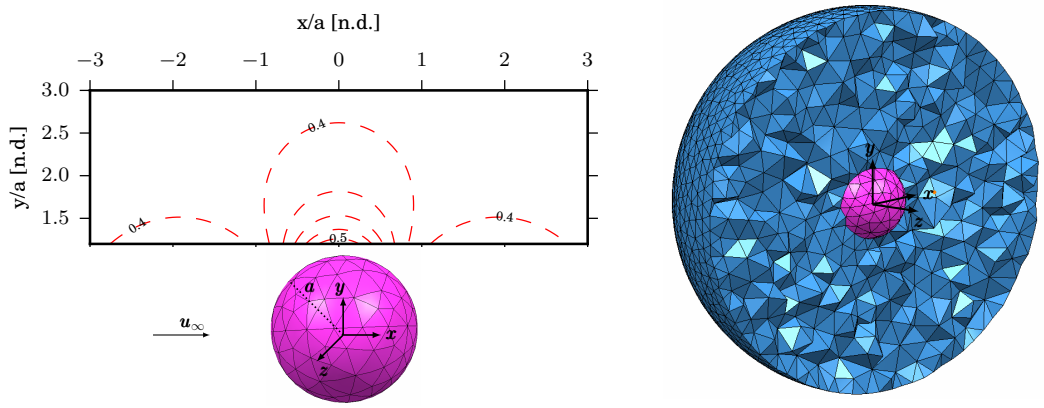

(a) Example of a BE domain, contour of M_0 for $M_\infty = 0.4$

(b) Section of a FE domain

Figure 8.4: Examples of boundary element and finite element domains for the problem of scattering of a monopole point source by a rigid sphere.

where $(\tilde{\mathbf{X}}, \tilde{T})$ can be expressed in terms of $(\mathbf{x}, t)$ based on Eq. (2.56) and δ is the Dirac delta function. In the case of the Lorentz transform, the term Φ_0' in the above equation is dropped. On the other hand, a time harmonic Dirac delta function defined on a nodal point is used to represent the point source in the finite element model (see Eq. (6.3)).

8.3.2.2 Validation of boundary elements with Lorentz transform

The boundary element solution proposed in this chapter is validated first for a uniform mean flow, which is the case of the Lorentz transform. Note that a simulation based on the Lorentz transform can be performed by using the same process as that described in Sec. 8.2.1. It differs from the Taylor–Lorentz formulation in that the terms depending on the mean flow perturbation are neglected. The results obtained using the Lorentz transformation for a canonical BE solution are compared against the solutions obtained by using the commercial solver ActiFMM [45], which is part of the software Virtual.Lab Acoustics R13 [212]. It is a boundary element solver based on a fast multipole scheme that can rely on the Lorentz transform to include mean flow effects. ActiFMM is based on Eq. (8.1) and, therefore, we solve the same equation. However, solutions based on the acoustic potential, ϕ, will be produced in the following sections.

In this instance, a monopole point source lying at $\mathbf{x}_s = (4a, 0, 0)$ is defined. We define an arc of field points in the plane $z = 0$, centered at $\mathbf{x} = (0, 0, 0)$ and with radius $R_{fp} = 8a$, to recover the solution for the problem in Fig. 8.2. In Fig. 8.5, the absolute value of the acoustic pressure is shown along the circular arc of field points for non-dimensional frequencies $ka = 4$ and 8. The BE solution based on the Lorentz transform and $\mathrm{N}_i = 3$ iterations is compared to the solution provided by ActiFMM. Along the same field points, the acoustic pressure for $ka = 8$ and $M_\infty = 0.5$ is shown in Fig. 8.6 comparing the results based on either a direct (see Eq. (8.5)) or indirect BE formulation (see Eq. (8.8)).

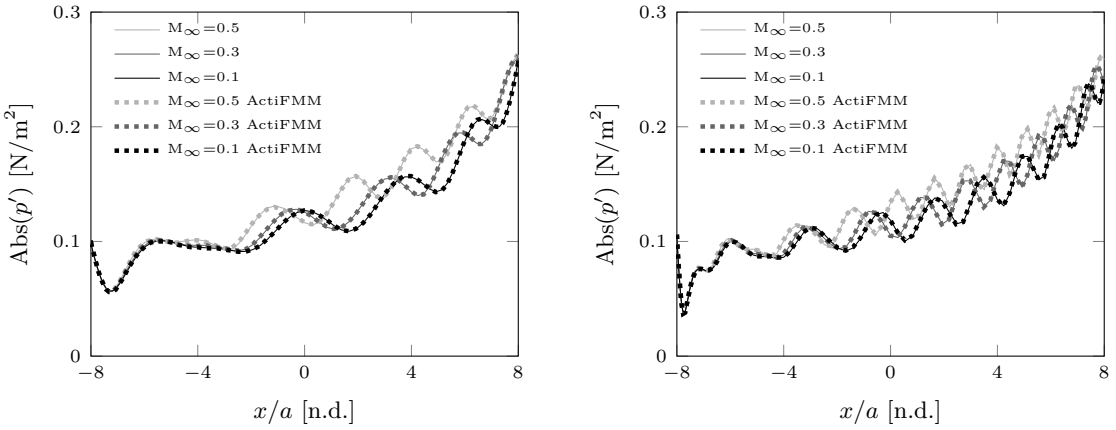

(a) $ka = 4$ (b) $ka = 8$

Figure 8.5: Acoustic pressure along an arc of field points with radius $R_{fp} = 8a$ for the problem described in Fig. 8.2 and a monopole point source at $\mathbf{x}_s = (4a, 0, 0)$. The solutions are based on Lorentz transformation.

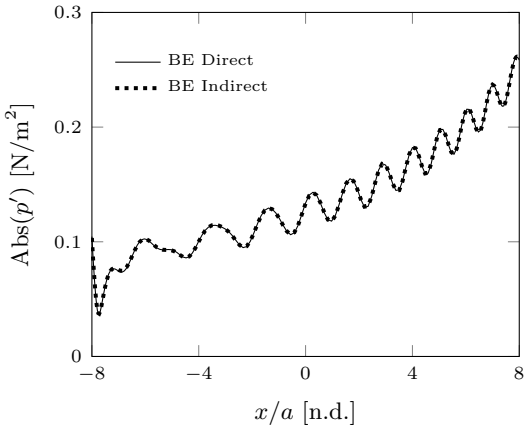

Figure 8.6: Acoustic pressure along an arc of field points with radius $R_{fp} = 8a$ for the problem in Fig. 8.2, a non-dimensional frequency $ka = 8$ and $M_\infty = 0.5$. Comparison of the solutions based on either a direct or indirect BE formulation. Solutions based on Lorentz transformation and the iterative solution to solve mean flow effects.

A good agreement is observed between the results based on the present implementation and those recovered by ActiFMM (see Fig. 8.5) for a uniform mean flow. This allows us to extend the solution to non-uniform flows using the Taylor–Lorentz transform. As expected, the solutions based on either a direct or an indirect boundary element approach coincide (see Fig. 8.6). In all that follows, an indirect formulation is used to recover the results because it can exploit a more efficient solver within Sysnoise.

8.3.2.3 Results

Boundary element solutions based on the Taylor–Lorentz transform and Eq. (8.3) are now benchmarked against finite element solutions of the full potential linearised wave equation. The results are also compared to BE solutions based on the Lorentz transform. A monopole

Table 8.1: Number of elements with order of interpolation P, in percentage, against the overall number of elements for the FE solution of the problem in Fig. 8.2 based on the linearised potential wave equation and $ka = 4$. The total number of degrees of freedom after condensation [163] is also reported.

	ka=4			
	P=1	P=2	P=3	dofs
$M_\infty = 0$	13.90%	86.10%	0%	366739
$M_\infty = 0.1$	9.58%	90.42%	0%	386727
$M_\infty = 0.2$	6.23%	93.41%	0.36%	410483
$M_\infty = 0.3$	3.63%	87.80%	8.57%	474717
$M_\infty = 0.4$	1.73%	59.68%	38.59 %	624796

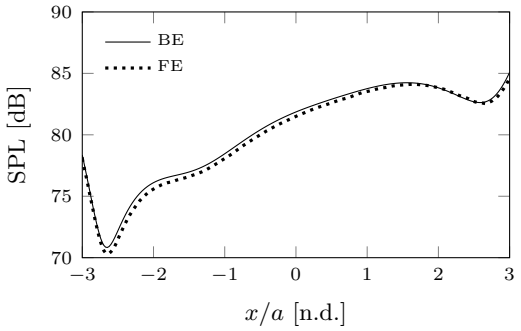

Figure 8.7: SPL along an arc of field points with radius $R_{fp} = 3a$ for the problem described in Fig. 8.2, a non-dimensional frequency ka=4 and $M_\infty = 0$. The FE solution and the BE solution based on the Helmholtz problem are shown.

point source is located at $\mathbf{x}_s = (1.5a, 0, 0)$. The solutions are compared along two arcs of field points lying on the plane $z = 0$, respectively with radius $R_{fp} = 1.2a$ and $3a$ (see Fig. 8.2), for non-dimensional frequencies $ka = 4$ and 20.

Helmholtz number: ka=4

Let us consider the non-dimensional frequency $ka = 4$. The number of degrees of freedom and the order of interpolation used to solve the finite element model are reported in Table 8.1. Figure 8.7 shows the SPL along the arc of field points with radius $R_{fp} = 3a$ comparing the BE and the FE solutions for $M_\infty = 0$ and the problem described in Fig. 8.2. These results are provided as a baseline.

In Fig. 8.8, the SPL is illustrated for a non-dimensional frequency $ka = 4$ and $M_\infty = 0.1 \rightarrow 0.4$ along an arc of field points with radius $R_{fp} = 1.2a$. The FE solution based on the full potential linearised wave equation is compared to the BE solutions based on either Taylor–Lorentz or Lorentz transform. In Fig. 8.9, the same results are presented on an arc of field points with radius $R_{fp} = 3a$. It is shown that the FE and BE solutions agree within 2 dB up to $M_\infty = 0.3$, while a larger difference is reported for $M_\infty = 0.4$.

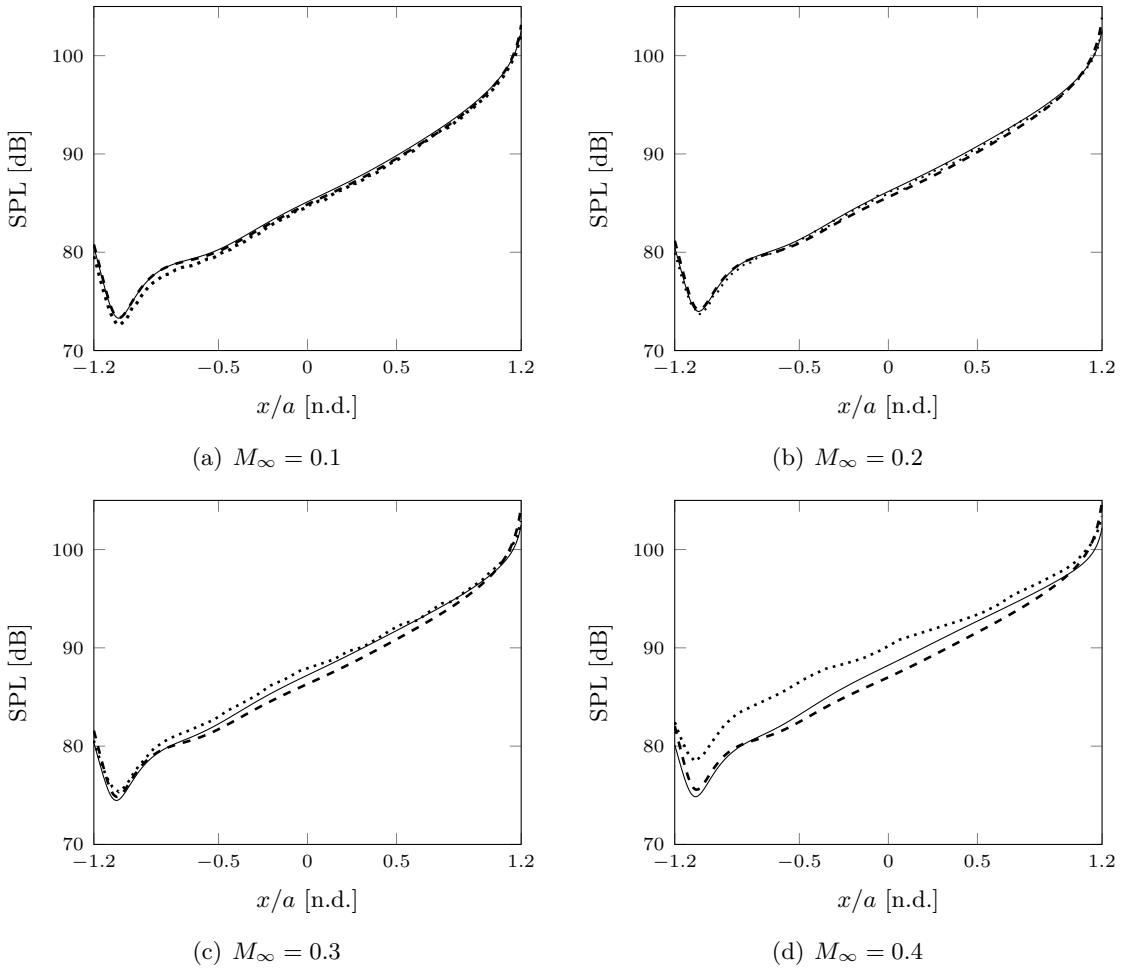

(a) $M_\infty = 0.1$

(b) $M_\infty = 0.2$

(c) $M_\infty = 0.3$

(d) $M_\infty = 0.4$

Figure 8.8: SPL along an arc of field points with radius $R_{fp} = 1.2a$ for the problem described in Fig. 8.2 and a non-dimensional frequency $ka = 4$. Solid: BE Taylor–Lorentz. Dashed: BE Lorentz. Dotted: FE LPE.

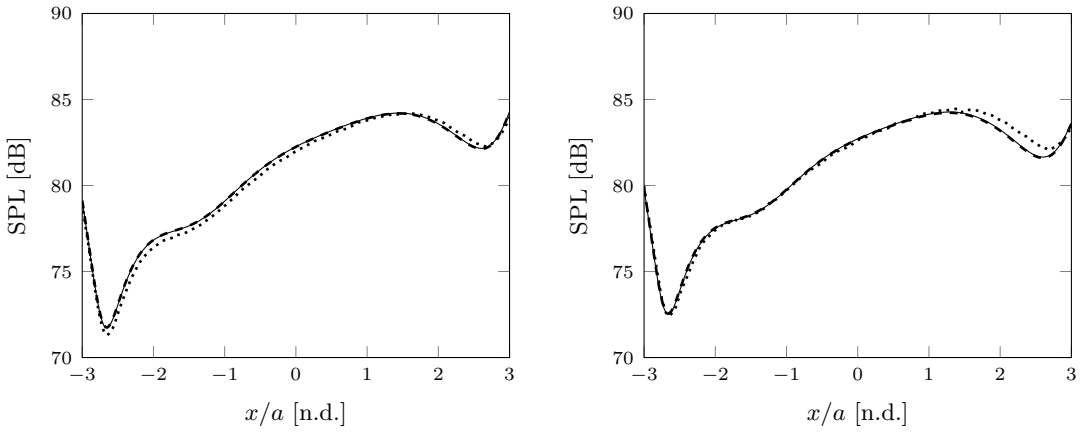

(a) $M_\infty = 0.1$

(b) $M_\infty = 0.2$

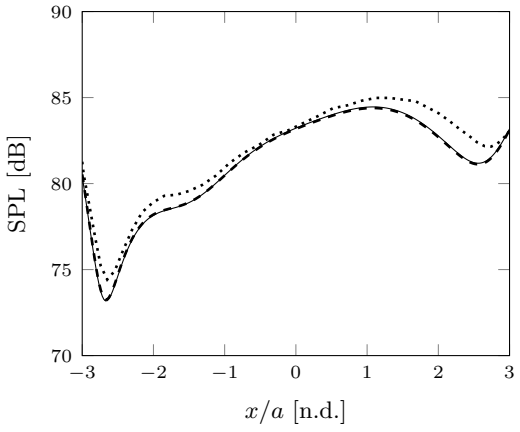

(c) $M_\infty = 0.3$

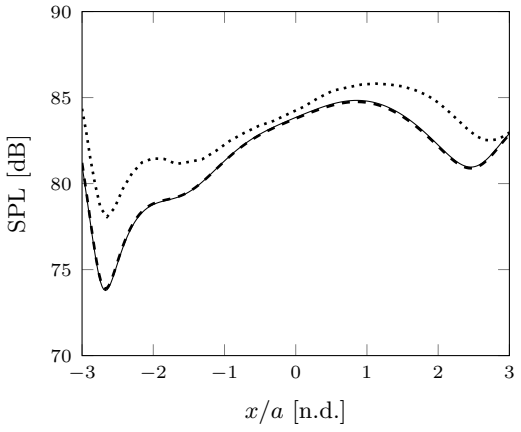

(d) $M_\infty = 0.4$

Figure 8.9: SPL along an arc of field points with radius $R_{fp} = 3a$ for the problem described in Fig. 8.2 and a non-dimensional frequency $ka = 4$. Solid: BE Taylor–Lorentz. Dashed: BE Lorentz. Dotted: FE LPE.

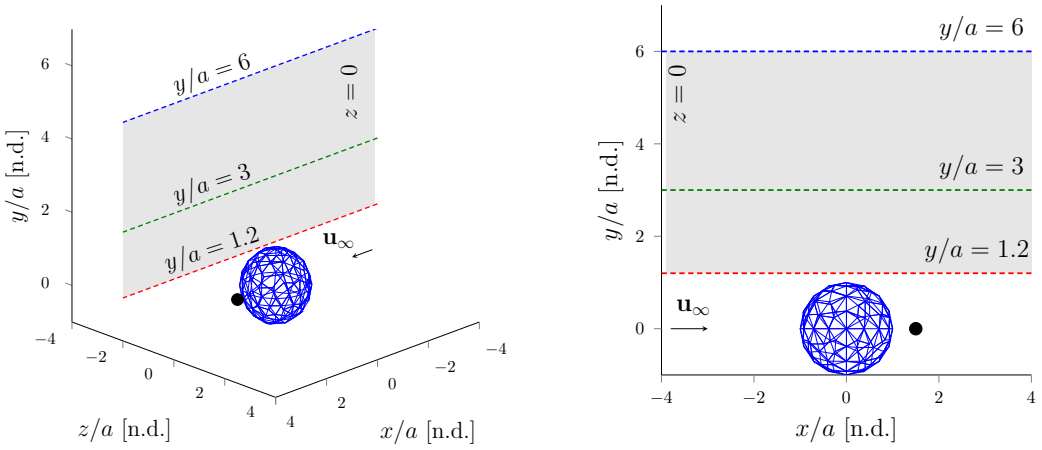

(a) 3D view

(b) Side view

Figure 8.10: Main geometrical features for the problem of scattering of a monopole point source by a sphere with mean flow, showing the plane where contours of the acoustic field are recovered.

Let us consider field points in the plane $z = 0$, as that depicted in Fig. 8.10. In this plane, contours of the real part of the acoustic pressure, p', are depicted in Fig. 8.11, for $M_\infty = 0.3$ and 0.4. The solutions based on the Taylor–Lorentz transform are compared to the solutions based on the Lorentz transform. A comparison with the FE reference solution is also provided. Again, while a good agreement is shown for $M_\infty = 0.3$, a difference between the FE and the BE solutions is clearly seen at $M_\infty = 0.4$.

We now analyse the effect of iterating the boundary conditions. In Fig. 8.12, the SPL based on the Taylor–Lorentz formulation is compared to the difference in acoustic pressure between the iterative solutions for either $\mathrm{N}_i = 3$ or $\mathrm{N}_i = 0$, at $ka = 4$ and $M_\infty = 0.4$. Figure 8.13(a) shows the same quantity as that in Fig. 8.12(b) along arcs of field points with radii $R_{fp} = 1.2a$ and $R_{fp} = 3a$, while Fig. 8.13(b) depicts the corresponding phase difference. The results are shown against the angle θ measured counterclockwise from the x-axis (see Fig. 8.2). Differences between the solutions for $\mathrm{N}_i = 3$ and $\mathrm{N}_i = 0$ are more than 20 dB lower than the SPL predicted in this test case and, therefore, iterating the boundary conditions is not significant to the accuracy of the solution.

These results can be compared to the corresponding differences between the solutions based on either Taylor–Lorentz or Lorentz transform. In Fig. 8.14(a), the phase difference in acoustic pressure between these solutions is shown, on the plane $z = 0$, at $ka = 4$ and $M_\infty = 0.4$. In Fig. 8.14(b), the same quantity is plotted comparing the results based on either the BE or the FE reference solutions. We report a larger difference between the FE and BE solutions than that generated between the BE solutions based on either a uniform or a non-uniform mean flow. This latter difference is larger than that observed between the solutions obtained either iterating or not the boundary conditions.

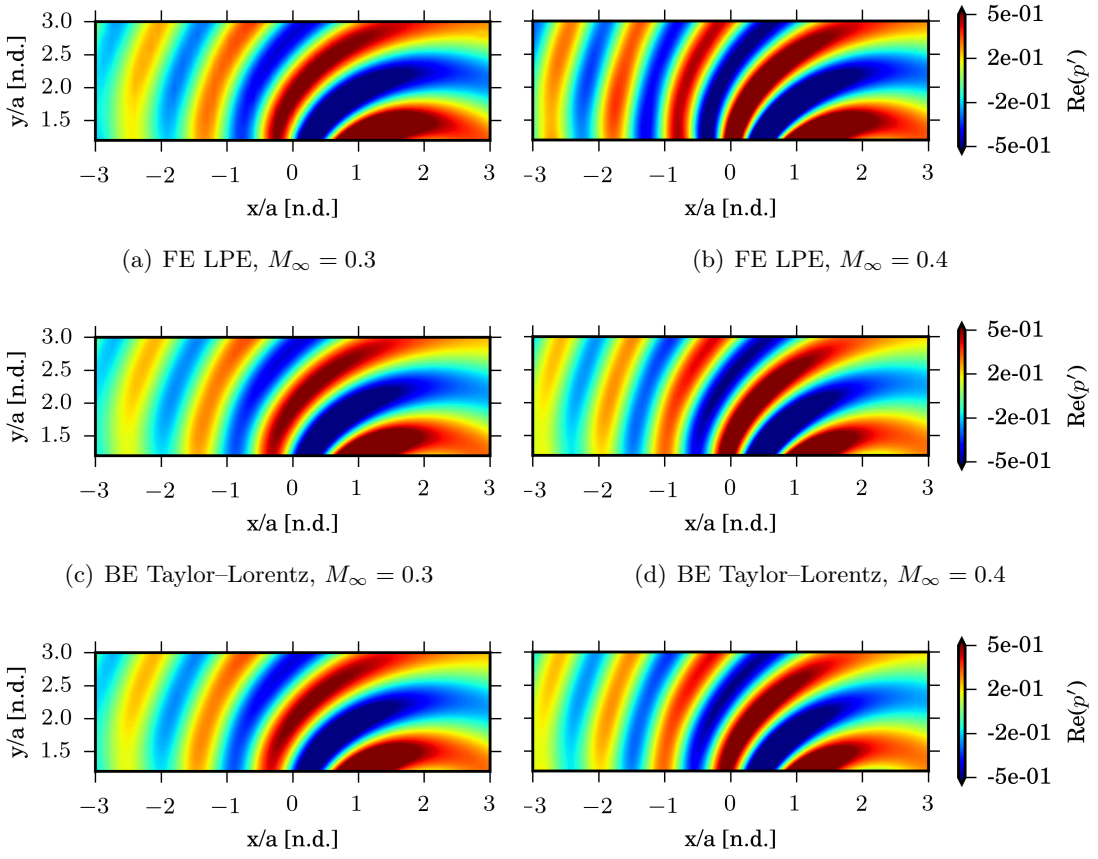

(a) FE LPE, $M_\infty = 0.3$

(b) FE LPE, $M_\infty = 0.4$

(c) BE Taylor–Lorentz, $M_\infty = 0.3$

(d) BE Taylor–Lorentz, $M_\infty = 0.4$

(e) BE Lorentz, $M_\infty = 0.3$

(f) BE Lorentz, $M_\infty = 0.4$

Figure 8.11: Contours of the real part of the acoustic pressure for the problem described in Fig. 8.10, a non-dimensional frequency $ka = 4$, $M_\infty = 0.3$ and 0.4.

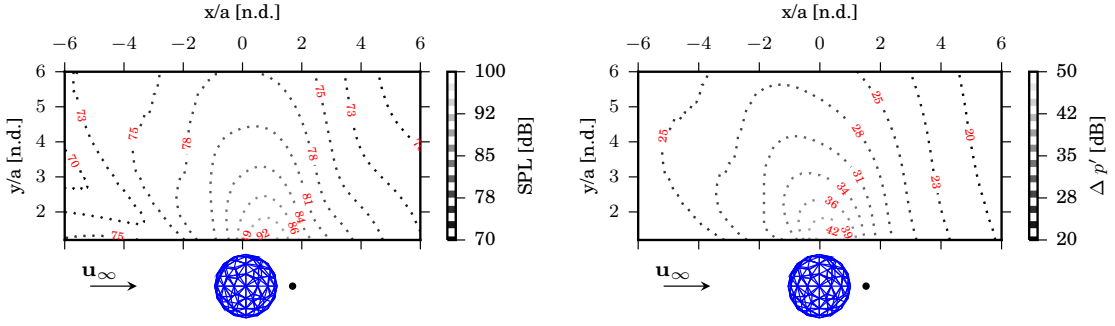

(a) BE solution

(b) BE Taylor–Lorentz: iterative, N_i=3 vs. N_i=0

Figure 8.12: Contour plots for the problem in Fig. 8.10, a non-dimensional frequency $ka = 4$ and $M_\infty = 0.4$. (a) SPL, BE solution based on Taylor–Lorentz transform for N_i=3 iteration. (b) Difference, in dB, between BE solutions based on Taylor–Lorentz transform for either N_i=0 or N_i=3 iterations. ($\Delta p' = 20\log[\|p'_{N_i=3} - p'_{N_i=0}\|/(\sqrt{2}p_{ref})]$)

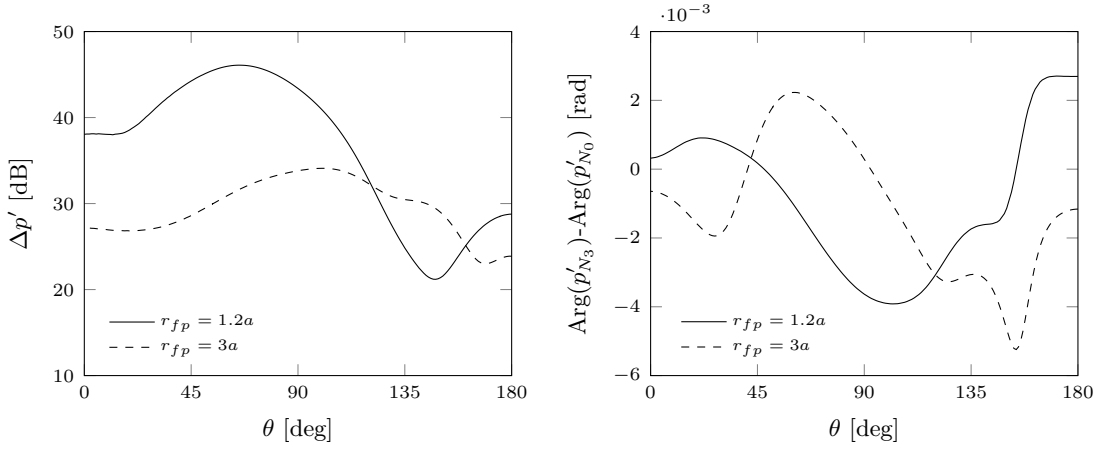

(a) $\Delta p'$ (b) Phase

Figure 8.13: Difference in the acoustic pressure field along arcs of field points with radii $R_{fp} = 1.2a$ and $3a$ for the problem described in Fig. 8.2, a non-dimensional frequency $ka = 4$ and $M_\infty = 0.4$. Difference between the BE results based on the Taylor–Lorentz transform for either N_i=3 or N_i=0 ($\Delta p' = 20\log[\|p'_{N_i=3} - p'_{N_i=0}\|/(\sqrt{2}p_{ref})]$).

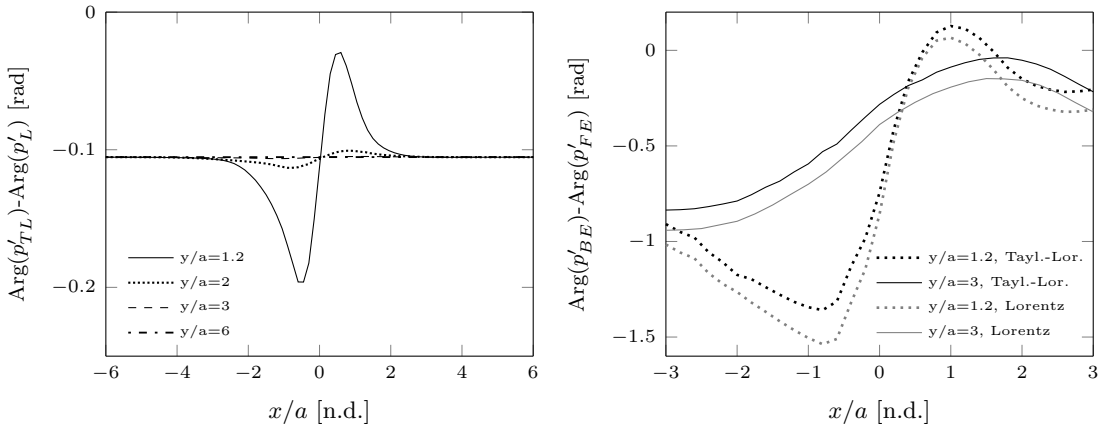

(a) BE Taylor–Lorentz vs. BE Lorentz (b) BE vs. FE LPE

Figure 8.14: Phase difference of the acoustic pressure along lines of field points in the plane $z = 0$ for the problem described in Fig. 8.10, a non-dimensional frequency $ka = 4$ and $M_\infty = 0.4$. (a) Comparison of the BE solutions based on either the Taylor–Lorentz or the Lorentz transform. (b) Comparison of the BE solutions with the FE reference solution based on the linearised potential wave equation (see Eq. (6.2)).

Helmholtz number: ka=20

The results are here provided for a non-dimensional frequency $ka = 20$. The number of degrees of freedom and the order of interpolation used to solve the finite element reference model are reported in Table 8.2.

In Fig. 8.15, a comparison in terms of SPL between the boundary element and the finite element solution, is provided for $M_\infty = 0$. These results are again provided as a baseline. Good agreement is shown except for the points in the shielded area, i.e. $x/a \leq -1$. This is due to numerical "leakage" in the BE solution. The BE problem is solved splitting the incident and the scattered field. In the shielded area, the scattered field is so low in magnitude compared to the high-pressure side that the numerical error can pollute the solution. However, in this region, the SPL is 30 dB lower than in the high-pressure region.

In Fig. 8.16, the SPL is plotted along arcs of field points with radii of $R_{fp} = 1.2a$ and $3a$, respectively. The results are shown for $ka = 20$ and $M_\infty = 0.3$ and 0.4. For $M_\infty = 0.3$, differences up to 3 dB are shown between the FE and BE solutions and larger differences are reported for $M_\infty = 0.4$. Contours of the real part of the acoustic pressure, p', comparing the BE solutions based on either the Taylor–Lorentz or the Lorentz transform are shown in Fig. 8.17 for $ka = 20$ and $M_\infty = 0.3$ and 0.4. A comparison with the FE reference solution

Table 8.2: Number of elements with order of interpolation P, in percentage, against the overall number of elements for the FE solution of the problem in Fig. 8.2 based on the linearised potential wave equation and $ka = 20$. The total number of degrees of freedom after condensation [100] is reported.

	ka=20					
	P=1	P=2	P=3	P=4	P=5	dofs
$M_\infty = 0$	0.0%	0.16%	99.37%	0.47 %	0%	2196592
$M_\infty = 0.3$	0.0%	0.0%	8.19%	90.36 %	1.45%	2196592
$M_\infty = 0.4$	0.0%	0.0%	1.11 %	74.55 %	24.34 %	5448404

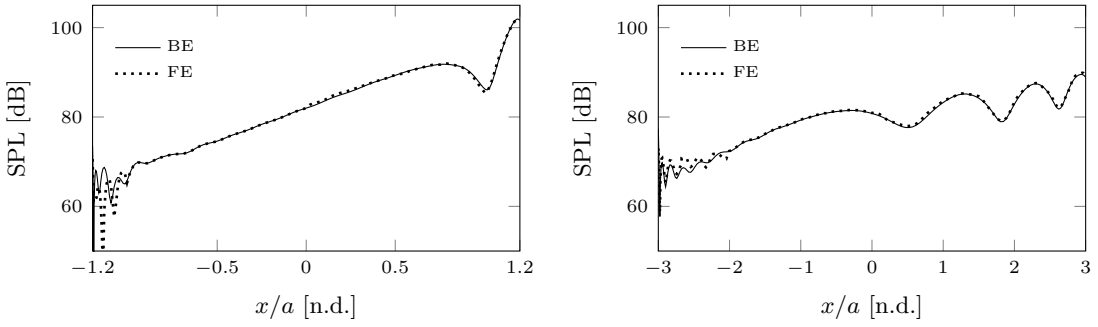

(a) $R = 1.2a$ (b) $R = 3a$

Figure 8.15: SPL along arcs of field points with radius $R_{fp} = 1.2a$ and $3a$ for the problem described in Fig. 8.2 and a non-dimensional frequency $ka = 20$ with $M_\infty = 0$.

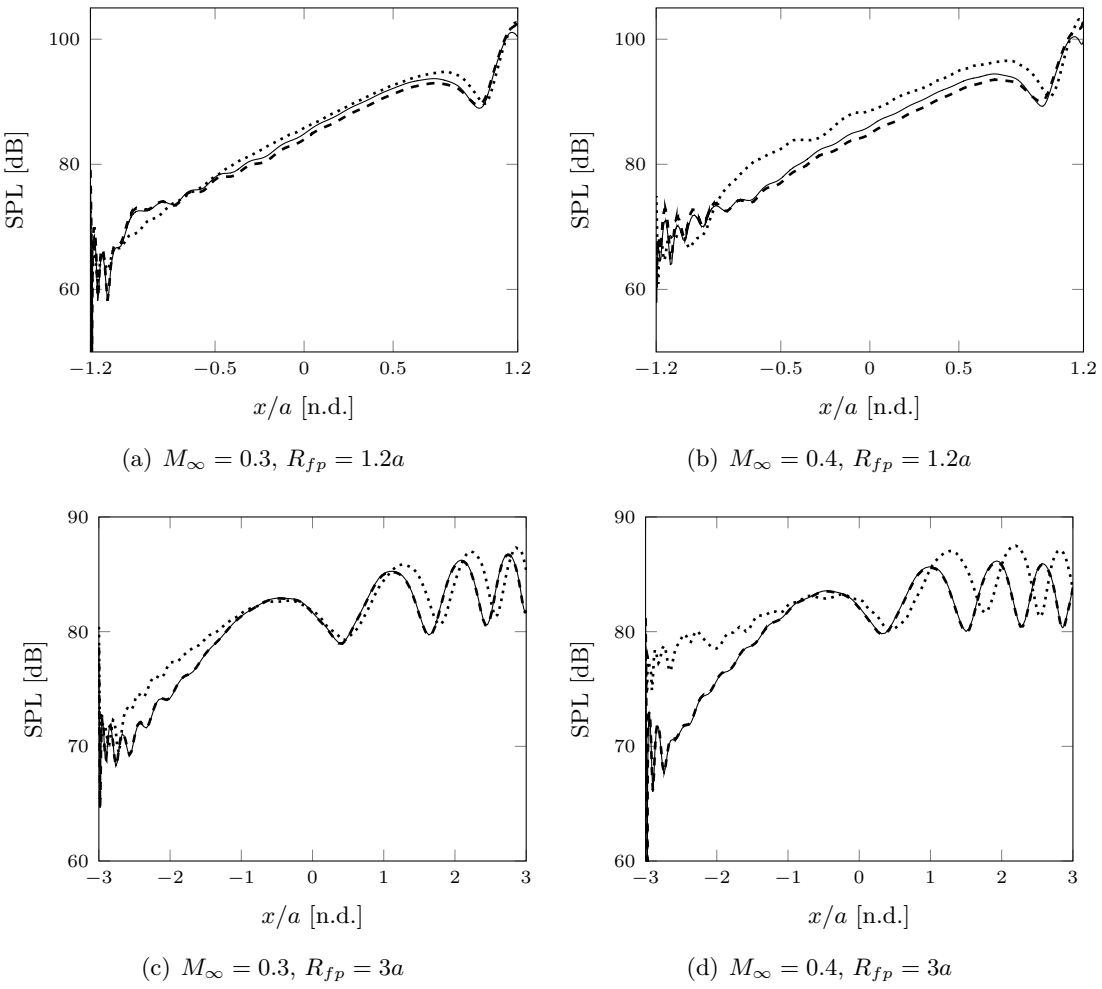

(a) $M_\infty = 0.3$, $R_{fp} = 1.2a$

(b) $M_\infty = 0.4$, $R_{fp} = 1.2a$

(c) $M_\infty = 0.3$, $R_{fp} = 3a$

(d) $M_\infty = 0.4$, $R_{fp} = 3a$

Figure 8.16: SPL along an arc of field points with radius R_{fp} for the problem described in Fig. 8.2 and a non-dimensional frequency $ka = 20$. Solid: BE Taylor–Lorentz. Dashed: BE Lorentz. Dotted: FE LPE.

is also provided. The results are shown on field points in the plane $z = 0$ for the problem in Fig. 8.10.

The acoustic pressure phase difference between the boundary element solutions based either on the Taylor–Lorentz or the Lorentz transform is depicted in Fig. 8.18 at different distances for an observer lying on the plane $z = 0$. The results are shown for $M_\infty = 0.4$ and a non-dimensional frequency $ka = 20$. We also provide the same results but with a monopole point source at $\mathbf{x}_s = (8a, 0, 0)$. In this case, the sound source lies in an almost uniform flow. It is seen that the phase difference tends to constant values both upstream and downstream the source location.

Figure 8.19 compares the results based on the iterative approach for $\mathrm{N}_i = 3$ and $\mathrm{N}_i = 0$. It illustrates the difference in terms of either absolute value, expressed in dB, or phase of the acoustic pressure, against the angle θ, along arcs of field points with radii $R_{fp} = 1.2a$ and $3a$, at $M_\infty = 0.4$. Again, the results indicate that the difference between the solutions for $\mathrm{N}_i = 3$ and $\mathrm{N}_i = 0$, are about 20-30 dB lower than the SPL predicted in this test case.

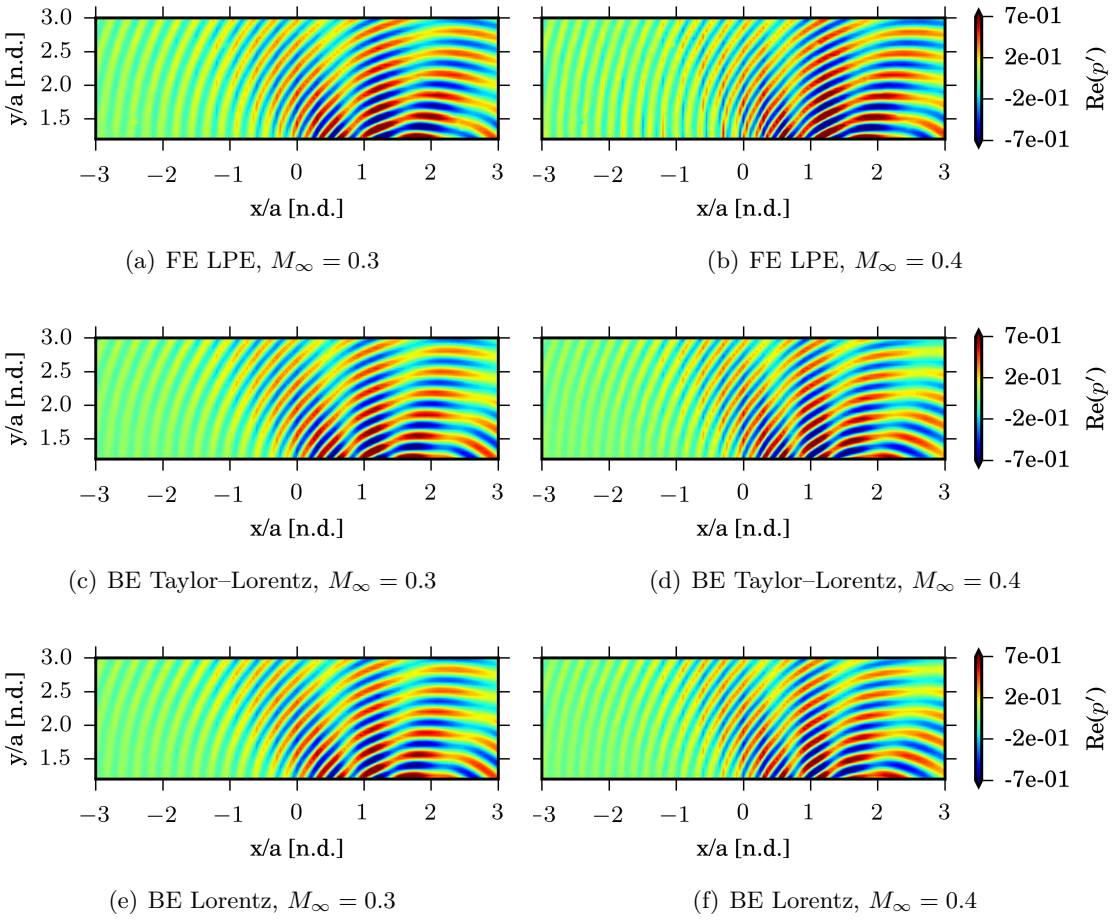

(a) FE LPE, $M_\infty = 0.3$

(b) FE LPE, $M_\infty = 0.4$

(c) BE Taylor–Lorentz, $M_\infty = 0.3$

(d) BE Taylor–Lorentz, $M_\infty = 0.4$

(e) BE Lorentz, $M_\infty = 0.3$

(f) BE Lorentz, $M_\infty = 0.4$

Figure 8.17: Contours of the real part of the acoustic pressure for the problem described in Fig. 8.10, a non-dimensional frequency $ka = 20$, $M_\infty = 0.3$ and 0.4.

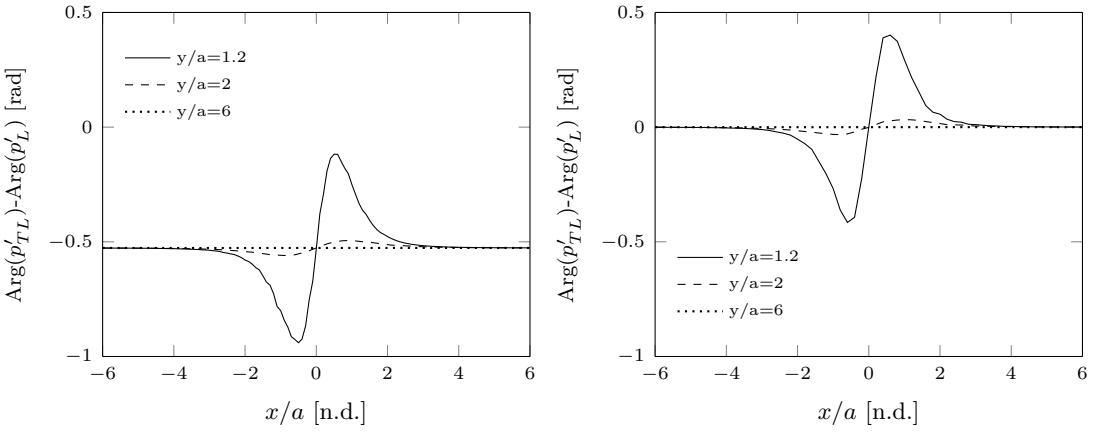

(a) $\mathbf{x}_s = (1.5a, 0, 0)$ (b) $\mathbf{x}_s = (8a, 0, 0)$

Figure 8.18: Phase difference in acoustic pressure between the BE solutions based on either the Taylor–Lorentz or the Lorentz transform for the problem described in Fig. 8.10, a non-dimensional frequency $ka = 20$ and $M_\infty = 0.4$. Two different source positions are considered: $\mathbf{x}_s = (1.5a, 0, 0)$ and $\mathbf{x}_s = (8a, 0, 0)$.

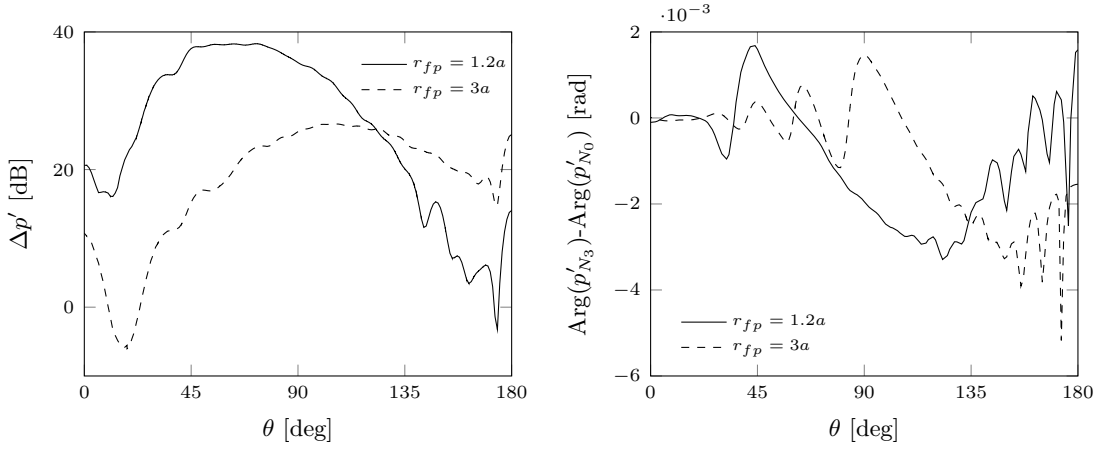

(a) SPL (b) Phase

Figure 8.19: Difference in the acoustic pressure field along arcs of field points with radii $R_{fp} = 1.2a$ and $R_{fp} = 3a$ for the problem described in Fig. 8.2, a non-dimensional frequency $ka = 20$ and $M_\infty = 0.4$. Difference between the BE results based on the Taylor–Lorentz transform for either N_i=3 or N_i=0 ($\Delta p' = 20\log(\|p'_{N_i=3} - p'_{N_i=0}\|/(\sqrt{2}p_{ref}))$).

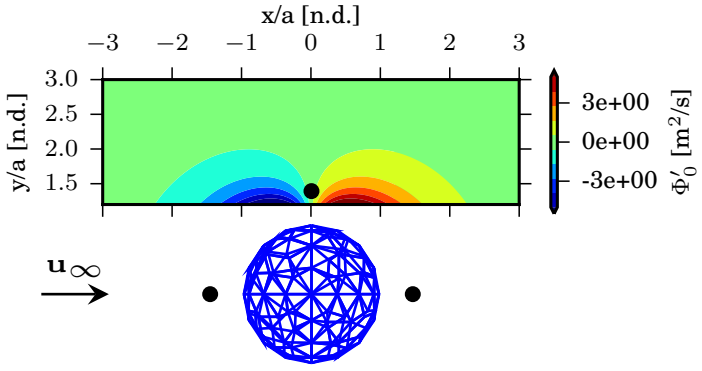

Figure 8.20: Sketch of the scattering problem for the sound generated by a distribution of monopole point sources around a sphere in a potential mean flow, showing the field points and the non-uniform part of the mean flow potential for $M_\infty = 0.3$.

Source interference

Let us consider a more complex source scenario to assess the accuracy of the boundary element solutions including the effect of source interference. Convection and refraction of the sound radiated from a source depends on the local mean flow at the source location. Therefore, the interference between the sound radiated and scattered from the sources lying in different regions of a non-uniform mean flow is influenced by the local non-uniform velocity of the medium. We want to assess the accuracy of the boundary element solutions for the following scenario: a distribution of monopole point sources, as defined in Sec. 8.3.2.1, is used in this instance. We consider three monopole point sources distributed around the sphere, respectively lying at $\mathbf{x}_s = (1.5a, 0, 0)$, $\mathbf{x}_s = (-1.5a, 0, 0)$, $\mathbf{x}_s = (0, 1.5a, 0)$ (see Fig. 8.20).

We assume $M_\infty = 0.4$. The SPL along the arcs of field points with radii $R_{fp} = 1.2a$ and $3a$, respectively, is shown in Fig. 8.21 for $ka = 4$ and 20. The phase of the acoustic pressure field is depicted in Fig. 8.22. We compare the boundary element solutions against the finite element solutions of the linearised potential wave equation. For $kL = 20$, although it is difficult to draw conclusions, note that the solid and the dashed lines, representing the boundary element solutions, are almost superimposed, while a more clear difference is shown by the dotted line, which represents the FE reference solution.

8.3.2.4 Discussion

It was shown that the BE solutions based on either the Taylor–Lorentz or Lorentz transform are in good agreement. Nonetheless, they compare favourably with finite element solutions of the full potential linearised wave equation for $M_\infty \leq 0.3$, while differences are more clear for larger M_∞. In the region where the flow is almost uniform, the BE results agree with the FE solution up to 2-3 dB for $M_\infty \leq 0.3$. The error increases to 4-5 dB for $M_\infty = 0.4$. In the near field, the solutions based on the Taylor–Lorentz transform are an improvement

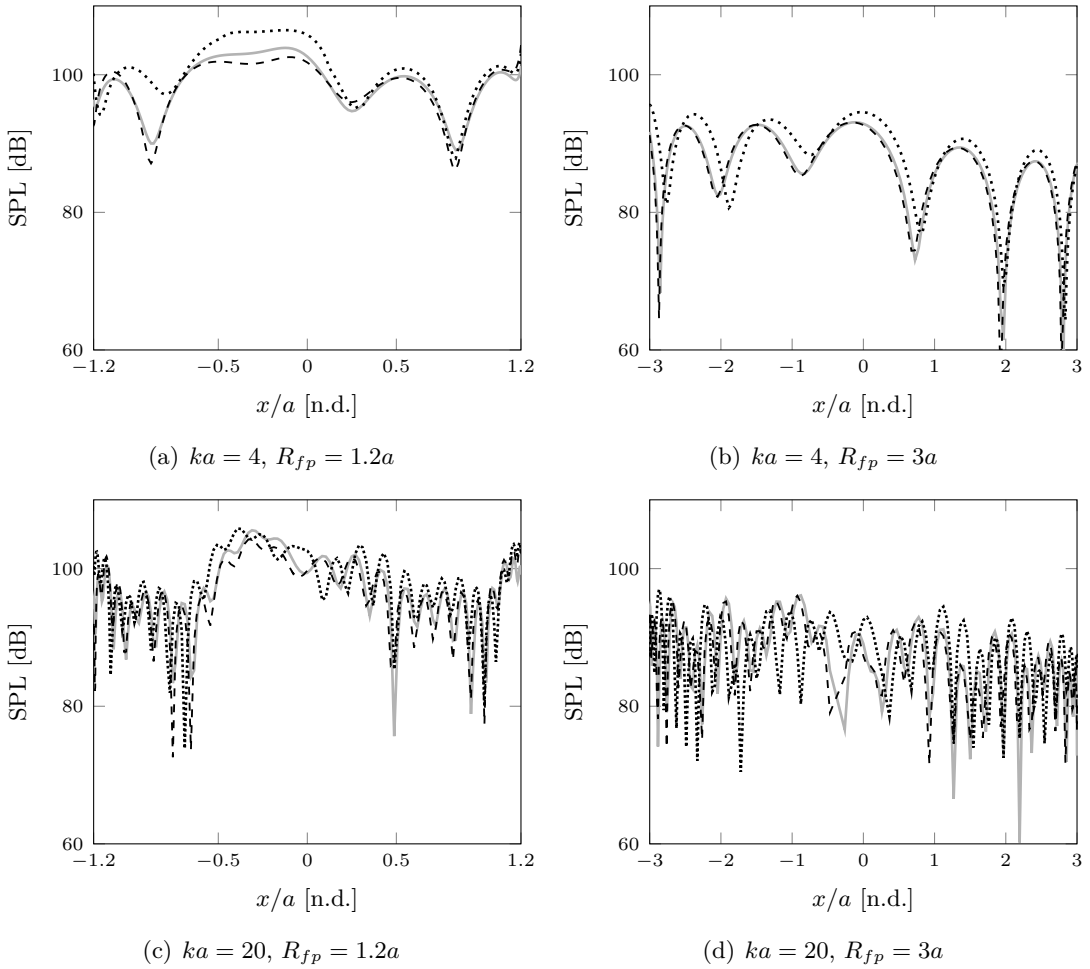

(a) $ka = 4$, $R_{fp} = 1.2a$

(b) $ka = 4$, $R_{fp} = 3a$

(c) $ka = 20$, $R_{fp} = 1.2a$

(d) $ka = 20$, $R_{fp} = 3a$

Figure 8.21: SPL along an arc of field points with radius R_{fp} for the problem described in Fig. 8.20, non-dimensional frequencies $ka = 4$ and 20, $M_\infty = 0.4$. Solid: BE Taylor–Lorentz. Dashed: BE Lorentz. Dotted: FE LPE.

on the solutions based on the Lorentz transform by as much as 0.5 dB, while in the uniform mean flow region they both provide similar solutions (see Figs. 8.8, 8.9 and 8.16).

In this test case, the error shown for $M_\infty = 0.4$ is of the same order as that recovered in two-dimensions for $M_\infty = 0.3$ (see Chapter 6). This may result from the different behaviour of the mean flow and the acoustic field compared to a 2D problem. For example, a three-dimensional problem differs from that in two-dimensions in that the non-uniformity in the velocity potential, for an incompressible mean flow due to a volume point source, decays as $1/R$, while in 2D it decays as $-\log(R)$, where R is the distance to the observer. Nonetheless, the acoustic far field decays as $1/R$ for three-dimensional problems, while in 2D it decays as $1/\sqrt{R}$. Therefore, considering a fixed wavelength, we infer that the non-uniformity in the mean flow is more significant for 2D than 3D problems [204].

Nonetheless, it was seen that phase difference in the acoustic pressure field between the solutions based on either the Taylor–Lorentz or Lorentz transform increased with frequency and was constant as soon as a uniform flow was reached (see Figs. 8.14 and 8.18). This

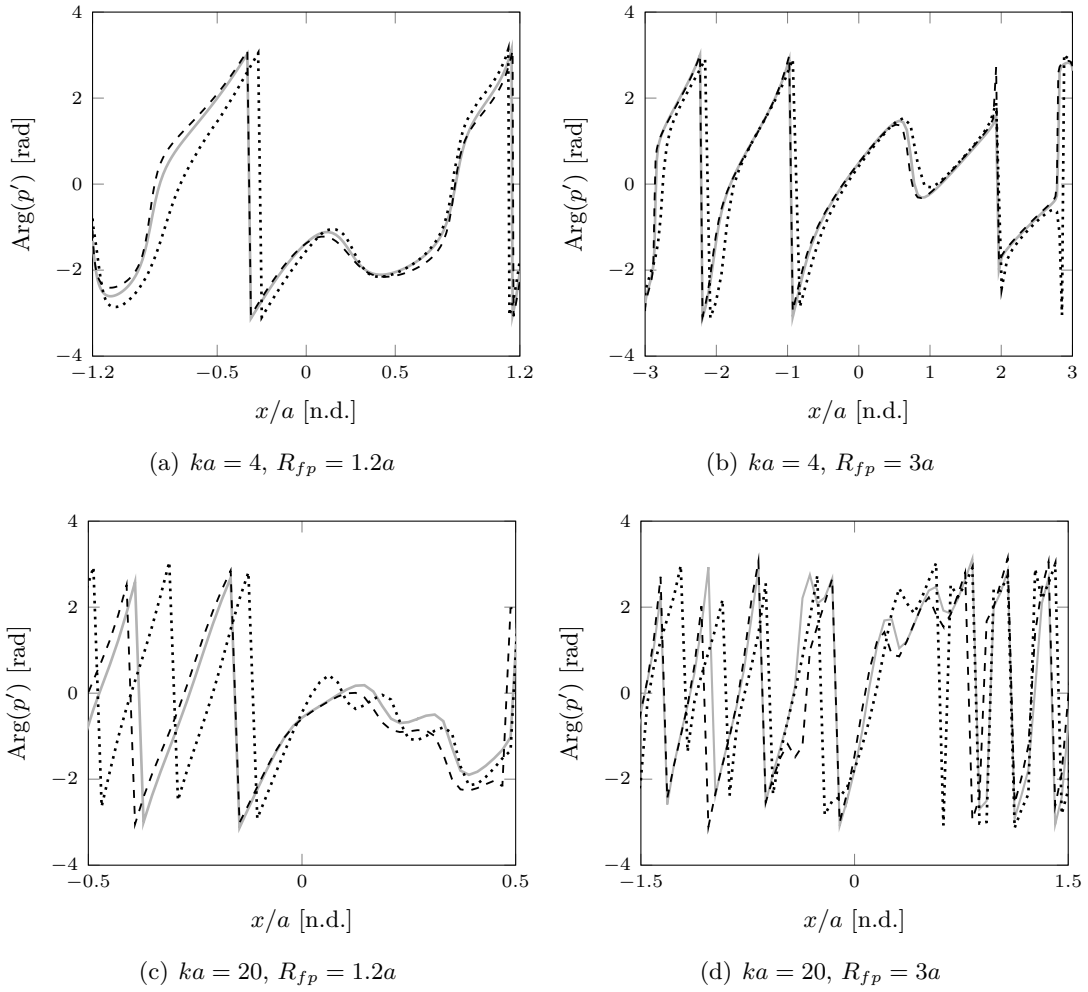

(a) $ka = 4$, $R_{fp} = 1.2a$

(b) $ka = 4$, $R_{fp} = 3a$

(c) $ka = 20$, $R_{fp} = 1.2a$

(d) $ka = 20$, $R_{fp} = 3a$

Figure 8.22: Phase of the acoustic pressure field along an arc of field points with radius R_{fp} for the problem described in Fig. 8.20, non-dimensional frequencies $ka = 4$ and 20, $M_\infty = 0.4$. Solid: BE Taylor–Lorentz. Dashed: BE Lorentz. Dotted: FE LPE.

difference is due to the local mean flow potential at the source location (see Fig. 8.18). For a monopole point source lying on a uniform flow, we showed that this difference vanishes in the far field and generally tends to the same value upstream and downstream. The term driving this difference is the exponential introduced in the acoustic potential to account for mean flow effects (see Eq. (4.63)).

On the other hand, the phase difference between the boundary element solutions and finite element reference solutions showed different values upstream and downstream of the scattering body (see Figs. 8.14). A better agreement was shown downstream. This is expected since the wavelength is larger downstream than upstream and the non-uniformity in the mean flow has the same length-scale in these regions. However, note that the difference between the BE solutions based either on the Taylor–Lorentz or the Lorentz transform was smaller than the corresponding difference between the boundary element results and the finite element reference solutions.

The approximation of the boundary conditions, based on neglecting the tangential terms, has favourably agreed with the solutions based on the iterative approach (see Fig. 8.12). The difference between these solutions was 20-30 dB lower than the predicted SPL (see Figs. 8.13 and 8.19) and was almost independent of frequency. Nonetheless, the phase difference in acoustic pressure between either the iterative or the non-iterative solutions was two orders of magnitude lower than the corresponding difference between boundary and finite element solutions (see Figs. 8.13 and 8.19). A practical outcome of this result is that the boundary element problem can be solved without iterating the boundary conditions, reducing the computational cost.

Considering a more complex source distribution has not caused the accuracy of the predictions to deteriorate further compared to the case of a single monopole point source. For $ka = 20$ and $M_\infty = 0.4$, we have seen an error up to 4-5 dB (see Fig. 8.21). In the near field, a better agreement was shown compared to the region where the mean flow was almost uniform (see Figs. 8.21 and 8.22). Consistent with the results of Chapters 6 and 7, the accuracy of the boundary element solution deteriorated whenever the characteristic wavelength was decreased. Therefore, we infer that the accuracy of the solution is not strongly dependent of the sound source distribution.

8.3.3 Aircraft installation effects

In this section, we model sound generated by a monopole point source and scattered by a simplified airframe. Boundary element solutions including either a uniform or a non-uniform flow are compared to finite element solutions based on the potential linearised wave equation.

8.3.3.1 Numerical model

In this test case, the aircraft geometry is taken from the NASA Common Research Model [206] and is simplified to the wing and fuselage, considering the configuration without incidence (see Fig. 8.23). The boundary surface is rigid and impervious. The speed of sound is $c_\infty = 340$ m·s^{-1} and $\rho_0 = 1.22$ kg·m^{-3}. The reference pressure for the calculation of the SPL is again $p'_{ref} = 2 \cdot 10^{-5}$ Pa.

A monopole point source is located at $\mathbf{x}_s = (27, -9, 3)$ (see Fig. 8.23). The source is the same as that described in Sec. 8.3.2.1. An incompressible potential mean flow without circulation is computed by solving the Laplace equation with a finite element method and is limited

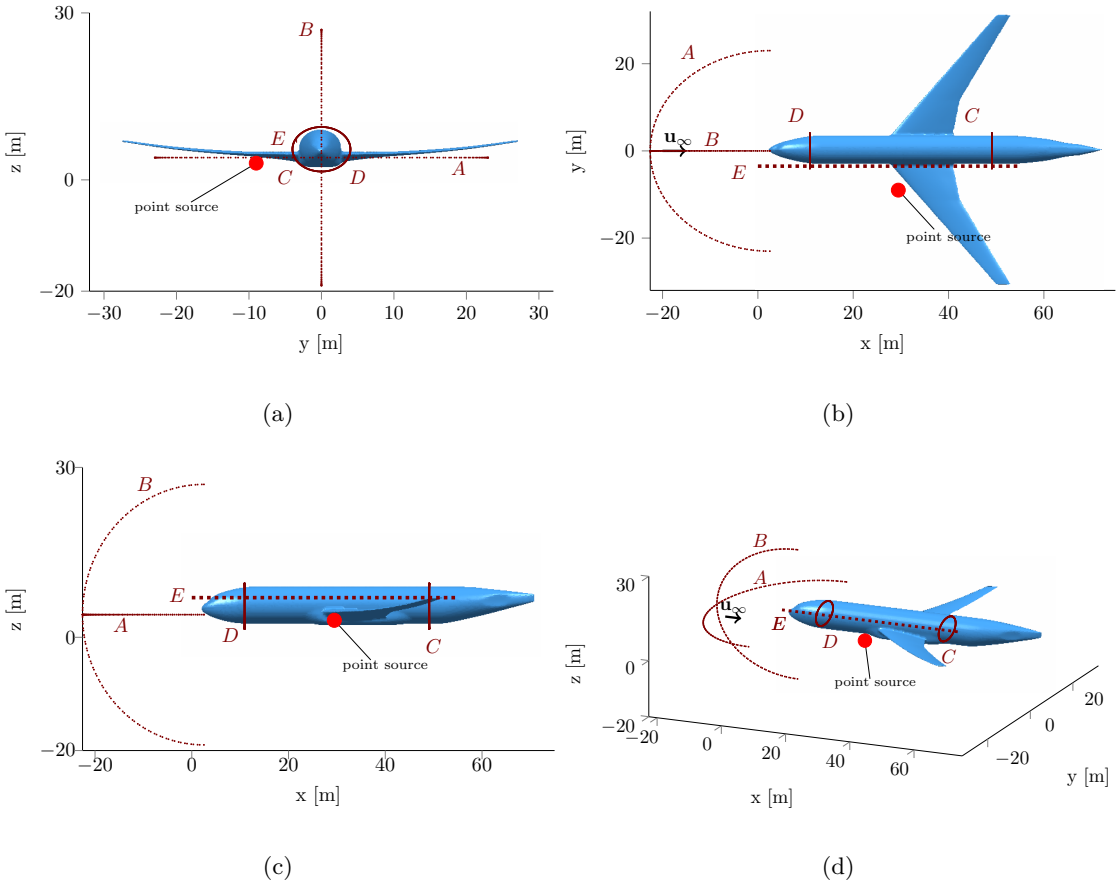

Figure 8.23: Sketch of the main feature for the test case of aircraft acoustic installation effects. The geometry, the field points, and the sound source are shown. Dots: field points.

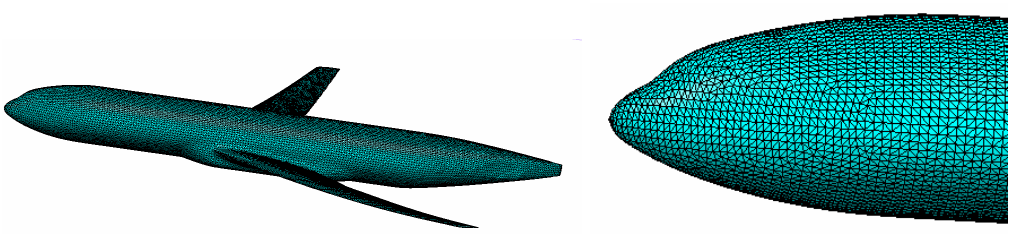

(a) Full mesh (b) Detail of the fuselage

Figure 8.24: BE mesh defined to discretise the geometry [206].

to $M_\infty = 0.4$. The flow is mapped onto an acoustic mesh based on the nearest neighbour algorithm and four influence points per node of the acoustic mesh.

Field points are defined to recover the sound field as indicated in Fig. 8.23. An arc of field points located in the plane $x = 10$ with radius $R_{fp} = 4$ m is centered at $\mathbf{x} = (10, 0, 5.5)$. A second arc in the plane $x = 45$ with radius $R_{fp} = 4$ is centered at $\mathbf{x} = (45, 0, 5.5)$. These field points are considered to assess the near field either upstream or downstream of the source location. Then, two arcs of field points are defined on the planes $y = 0$ and $z = 0$, respectively. They are centered at $\mathbf{x} = (2.3, 0, 4)$ with radius $R_{fp} = 23$ m. These points are used to evaluate the directivity in a region where the flow is almost uniform. A set of field points is also located on the plane $z = 10$ and a line of field points is defined between $\mathbf{x}_1 = (0, -3.5, 7)$ and $\mathbf{x}_2 = (55, -3.5, 7)$.

We consider two test cases corresponding to non-dimensional frequencies $kL = 20$ and $kL = 100$, where $L = 60$ m is the wing span. A boundary element model with 28252 degrees of freedom (see Fig. 8.24) is defined and an indirect BE solution based on Eq. (8.3) is used to solve the boundary element kernel. Mesh convergence is demonstrated for the current mesh for up to $kL = 100$ and $M_\infty = 0.4$ (see Fig. 8.25). The results of Sec. 8.3.2 and a preliminary assessment performed on this test case allow us to solve the problem without iterating the boundary conditions.

An adaptive high-order FE solution [68] based on the full potential linearised wave equation is also provided as a reference. The FE domain is truncated by a spherical surface with radius $R = 55$ m (see Fig. 8.25). A PML is extruded from the envelope of the FE domain to satisfy the Sommerfeld radiation condition at the outer surface. The PML is extruded for three wavelengths and account for eight degrees of freedom per wavelength. The polynomial order of interpolation for the FE solution has been chosen to be comparable to a conventional finite element solution with eight degrees of freedom per wavelength (see Tables 8.3 and 8.4).

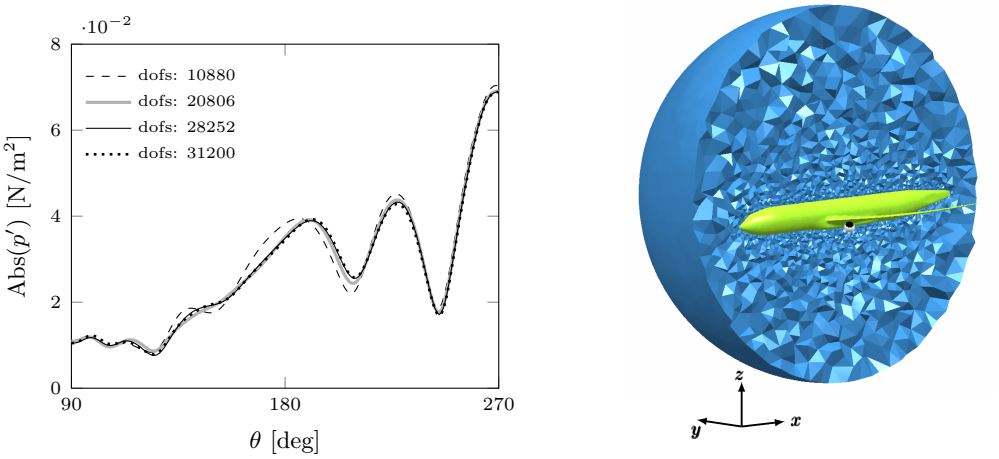

(a) BE, convergence study

(b) Example of FE domain

Figure 8.25: (a) Acoustic pressure along the arc of field points (B) based on the boundary element solution of the problem in Fig. 8.23. Convergence analysis for $kL = 100$ and $M_\infty = 0.4$ including a uniform flow. (b) FE domain for the problem in Fig. 8.23.

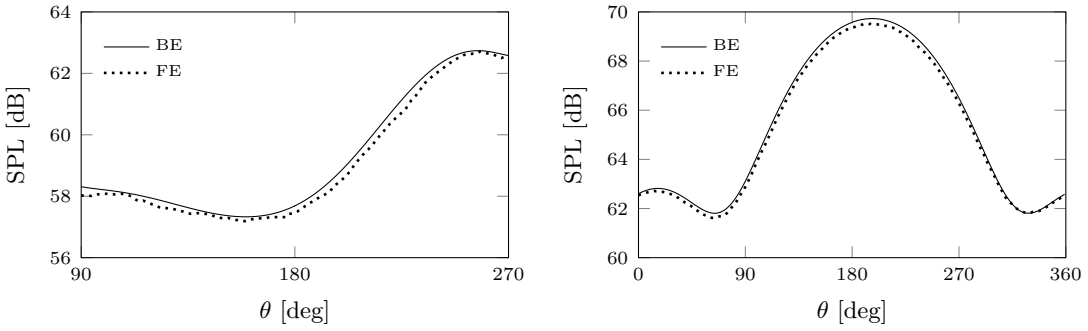

(a) Field points (B)

(b) Field points (D)

Figure 8.26: SPL along an arc of field points for a non-dimensional frequency $kL = 20$ and $M_\infty = 0$ for the problem described in Fig. 8.23. BE and FE solutions of the Helmholtz problem with quiescent media are compared.

8.3.3.2 Results

Helmholtz number: kL=20

We consider the non-dimensional frequency $kL = 20$. Figure 8.26 illustrates the finite element and the boundary element solution along the arc of field points denoted by (B) and (D) in Fig. 8.26 for $M_\infty = 0$. This solution is provided for reference. The FE solution is computed for M_∞ in the range $0 \rightarrow 0.4$. Table 8.3 shows the order of interpolation used for each Mach number as a percentage of the total number of elements, and the total number of degrees of freedom for each mesh after condensation [163].

Table 8.3: Number of elements with order of interpolation P, in percentage, against the overall number of elements for the FE solution of the problem in Fig. 8.23 based on the linearised potential wave equation and $kL = 20$. The total number of degrees of freedom is reported after condensation [163].

	kL=20				
	P=1	P=2	P=3	P=4	dofs
$M_\infty = 0$	9.60%	86.82%	3.58%	0%	360689
$M_\infty = 0.2$	5.29%	54.01%	40.70%	0%	498260
$M_\infty = 0.3$	4.42%	34.22%	61.36%	0%	627543
$M_\infty = 0.4$	3.13%	21.85%	73.39%	1.63%	725107

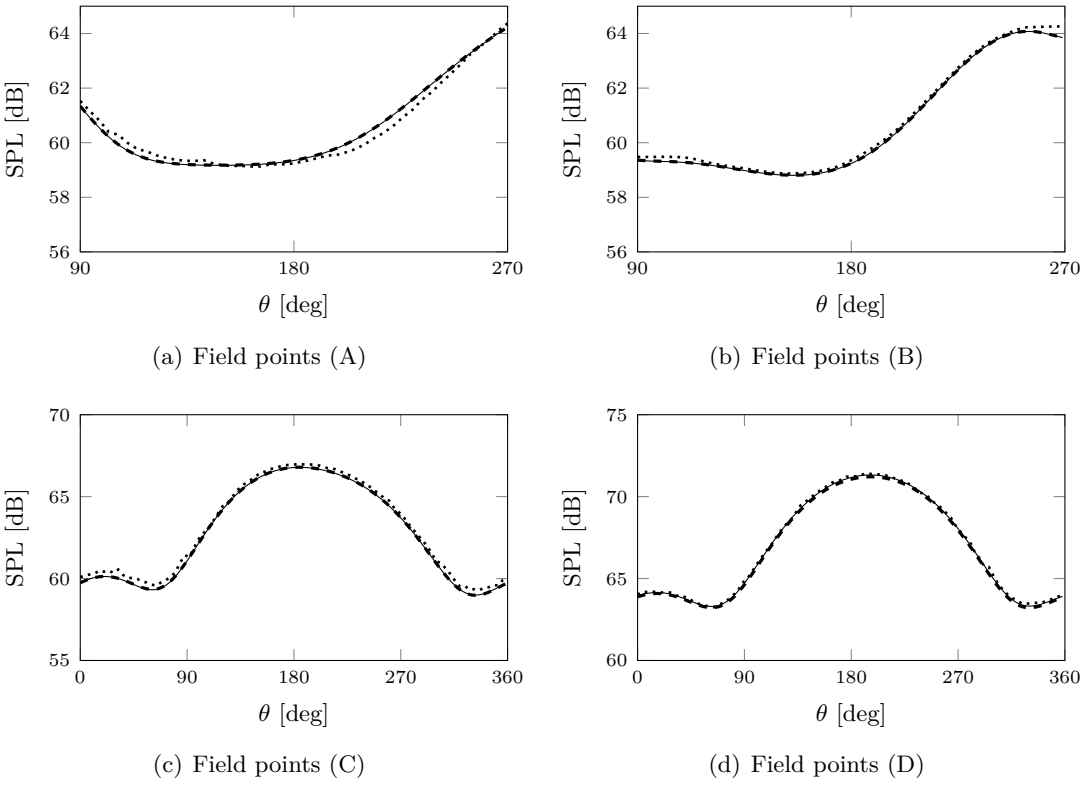

(a) Field points (A)

(b) Field points (B)

(c) Field points (C)

(d) Field points (D)

Figure 8.27: SPL along an arc of field points for a non-dimensional frequency $kL = 20$, $M_\infty = 0.2$ and the problem described in Fig. 8.23. Solid: BE Taylor–Lorentz. Dashed: BE Lorentz. Dotted: FE LPE.

In Figs. 8.27 and 8.28, the SPL is plotted against the angle θ along the arc of field points denoted in Fig. 8.23 by (A), (B), (C) and (D) for a non-dimensional frequency $kL = 20$ and M_∞ in the range $0.2 \rightarrow 0.4$. The angle θ is defined respectively in the plane of each set of field points and is measured counterclockwise from either the x-axis or y-axis. For $kL = 20$ and $M_\infty = 0.4$, Fig. 8.29 illustrates contours of the SPL on field points lying in the plane $z = 10$, above the aircraft. For $M_\infty \leq 0.4$, the results in this example show that the boundary element solutions agree with the finite element reference solutions within 2 dB.

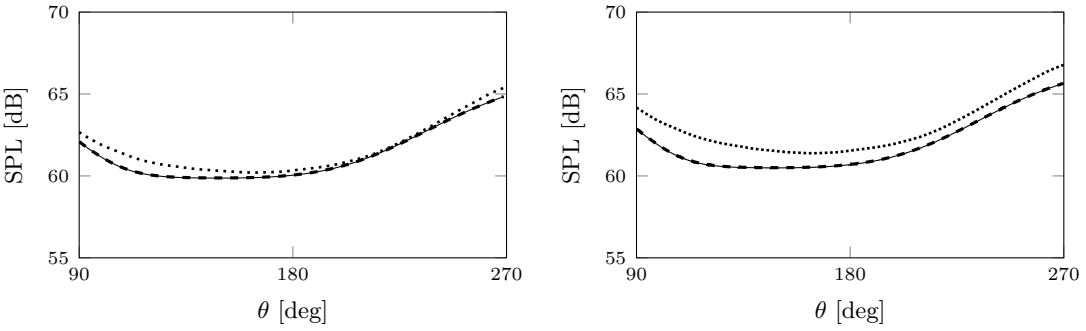

(a) $M_\infty = 0.3$, field points (A)

(b) $M_\infty = 0.4$, field points (A)

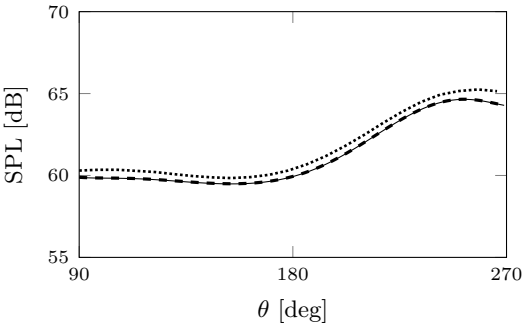

(c) $M_\infty = 0.3$, field points (B)

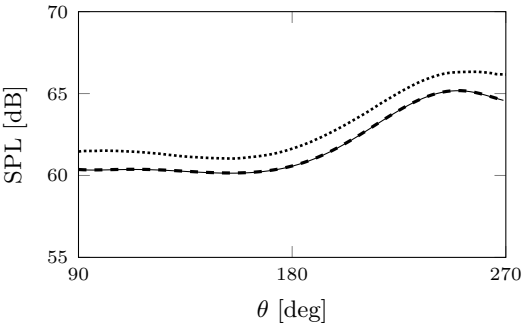

(d) $M_\infty = 0.4$, field points (B)

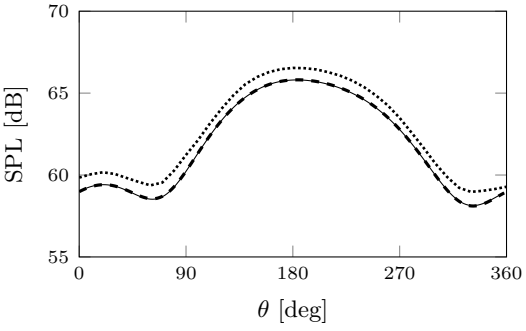

(e) $M_\infty = 0.3$, field points (C)

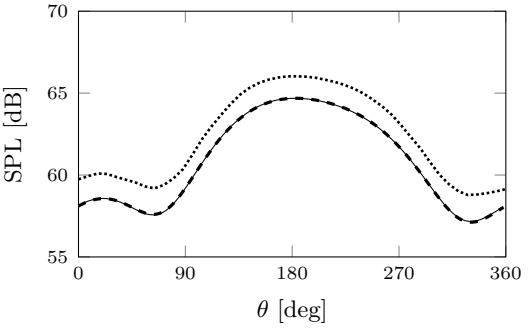

(f) $M_\infty = 0.4$, field points (C)

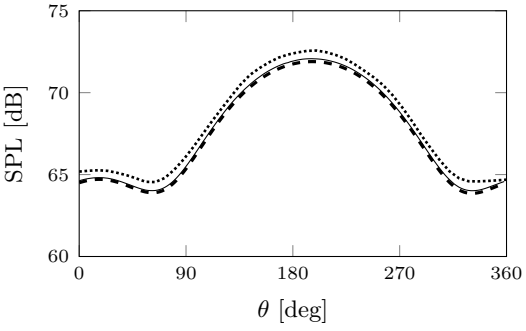

(g) $M_\infty = 0.3$, field points (D)

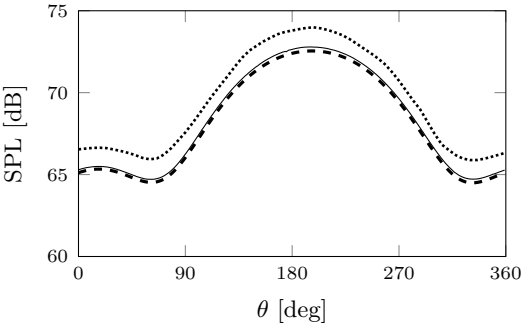

(h) $M_\infty = 0.4$, field points (D)

Figure 8.28: SPL along an arc of field points for a non-dimensional frequency $kL = 20$ and the problem described in Fig. 8.23. Solid: BE Taylor–Lorentz. Dashed: BE Lorentz. Dotted: FE LPE.

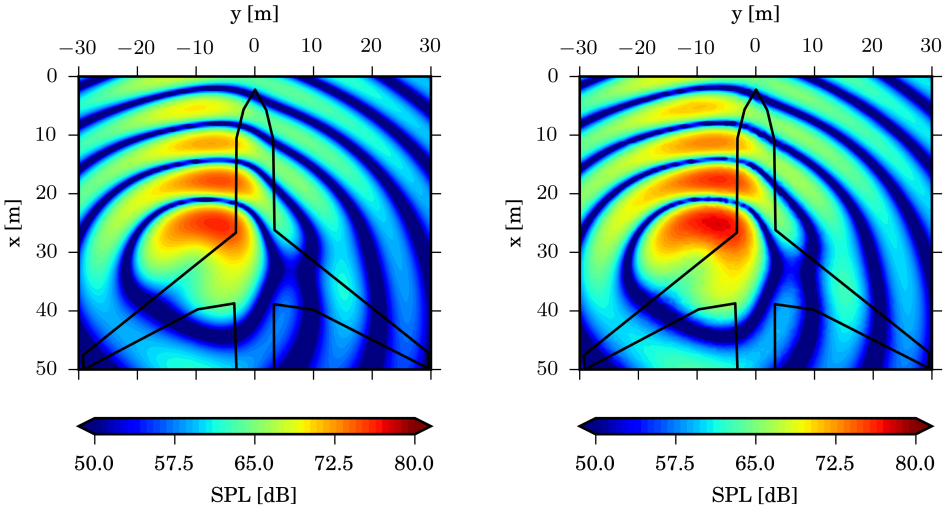

(a) BE Taylor–Lorentz (b) FE LPE

Figure 8.29: SPL along the plane $z = 10$ for a non-dimensional frequency $kL = 20$, $M_\infty = 0.4$ and the problem described in Fig. 8.23.

Helmholtz number: kL=100

Let us consider the case where $kL = 100$. We limit the analysis to $M_\infty \geq 0.3$ – below this values the BE and FE solutions are almost overlapped. The number of degrees of freedom and the order of interpolation for the finite element reference solution is shown in Table 8.4. In Fig. 8.30, the SPL is depicted along the arc of field points denoted by (A), (B), (C) and (D) for $M_\infty = 0.3$ and 0.4 comparing the boundary element to the finite element reference solutions. For the same problem at $M_\infty = 0.4$, the phase of the acoustic pressure along the arc of field points denoted by (C) and (D) are reported in Fig. 8.31. For $M_\infty = 0.3$ and 0.4, the SPL and the phase of the acoustic field along the line of field points denoted by (E) are shown in Fig. 8.32. The BE and FE solutions agree within 2.5 dB. Nonetheless, it is shown that the phase of the acoustic field is clearly well represented.

Table 8.4: Number of elements with order of interpolation P, in percentage, against the overall number of elements for the FE solution of the problem in Fig. 8.23 based on the linearised potential wave equation, at $kL = 100$. Total number of degrees of freedom after condensation [163].

	kL=100						
	P=1	P=2	P=3	P=4	P=5	P=6	dofs
$M_\infty = 0.3$	0.0%	0.0%	8.76%	90.36%	0.88%	0%	4335492
$M_\infty = 0.4$	0.0%	0.0%	0.7%	74.55%	24.34%	0.41%	5448404

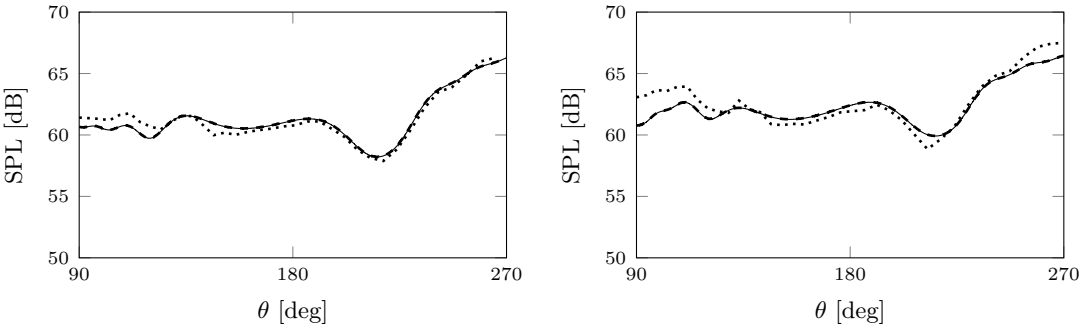

(a) $M_\infty = 0.3$, field points (A)

(b) $M_\infty = 0.4$, field points (A)

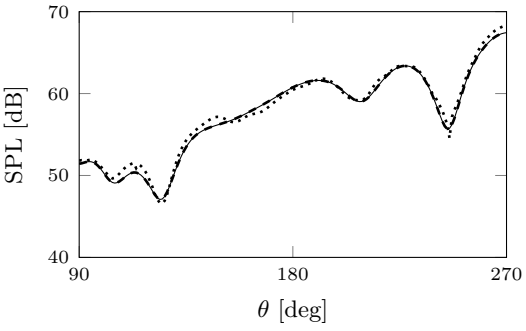

(c) $M_\infty = 0.3$, field points (B)

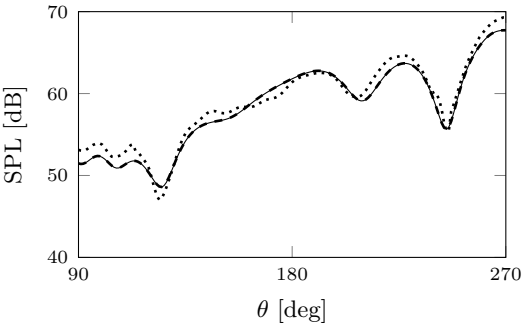

(d) $M_\infty = 0.4$, field points (B)

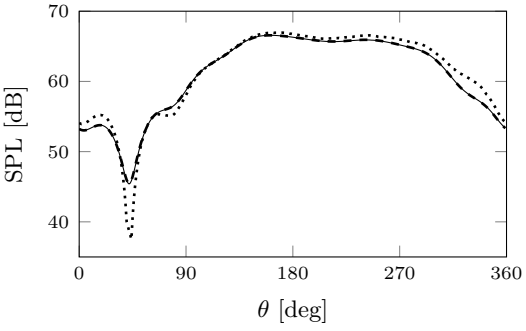

(e) $M_\infty = 0.3$, field points (C)

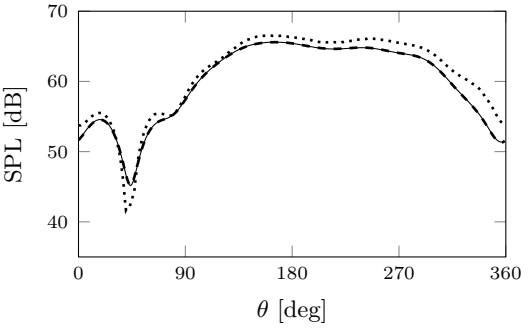

(f) $M_\infty = 0.4$, field points (C)

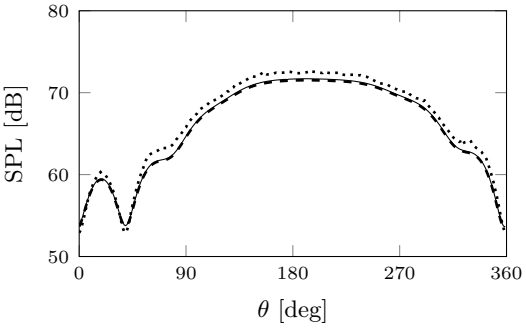

(g) $M_\infty = 0.3$, field points (D)

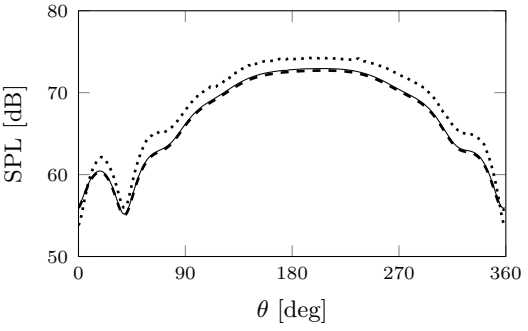

(h) $M_\infty = 0.4$, field points (D)

Figure 8.30: SPL along an arc of field points for a non-dimensional frequency $kL = 100$ and the problem described in Fig. 8.23. Solid: BE Taylor–Lorentz. Dashed: BE Lorentz. Dotted: FE LPE.

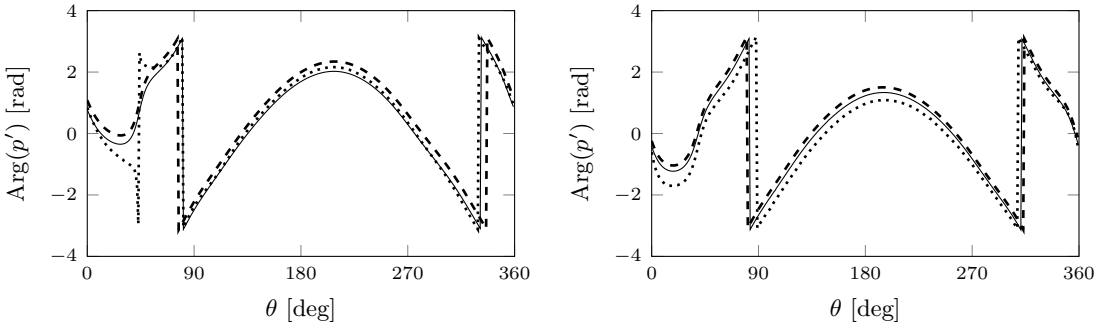

(a) Field points (C)

(b) Field points (D)

Figure 8.31: Phase of the acoustic pressure field along an arc of field points for a non-dimensional frequency $kL = 100$, $M_\infty = 0.4$ and the problem described in Fig. 8.23. Solid: BE Taylor–Lorentz. Dashed: BE Lorentz. Dotted: FE LPE.

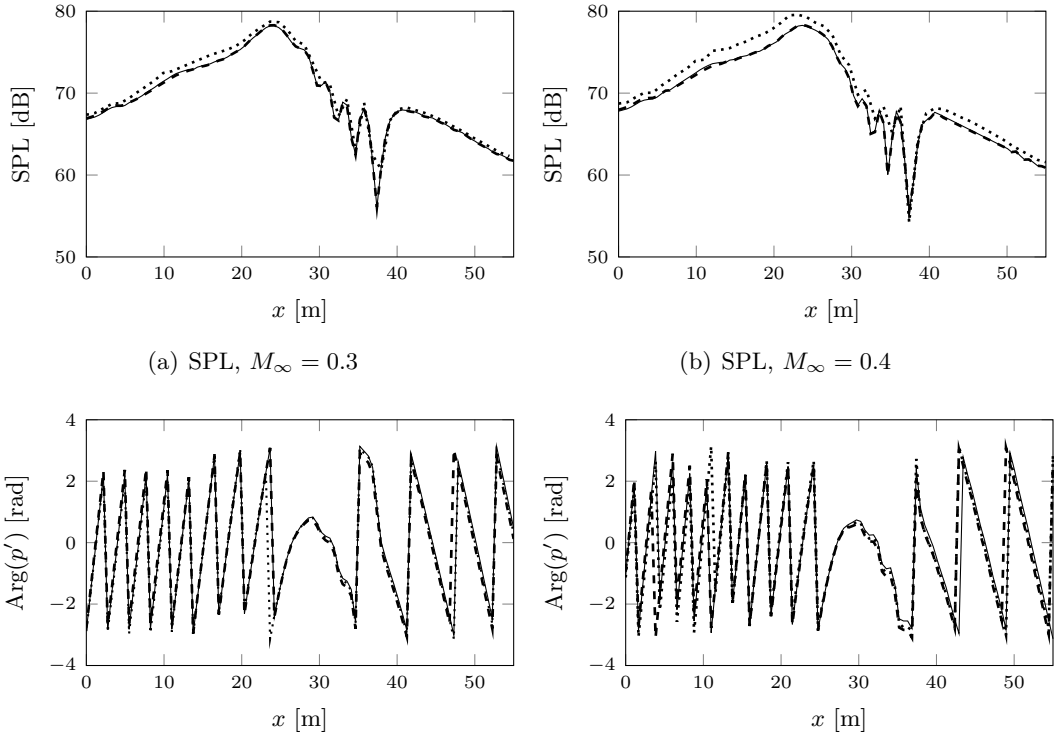

(a) SPL, $M_\infty = 0.3$

(b) SPL, $M_\infty = 0.4$

(c) Phase, $M_\infty = 0.3$

(d) Phase, $M_\infty = 0.4$

Figure 8.32: SPL and phase of the acoustic pressure field along a line of field points denoted by (E) in the problem described in Fig. 8.23 and a non-dimensional frequency $kL = 100$. Solid: BE Taylor–Lorentz. Dashed: BE Lorentz. Dotted: FE LPE.

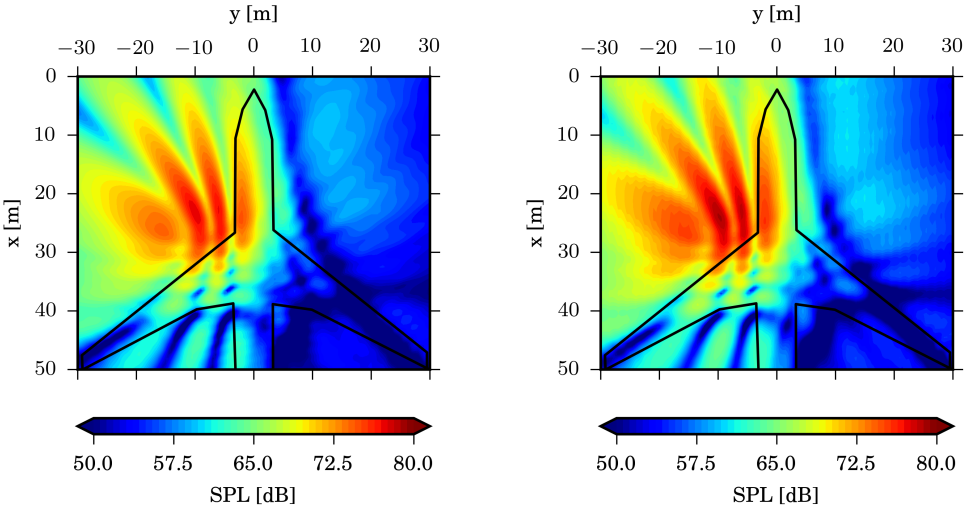

(a) BE Taylor–Lorentz

(b) FE LPE

Figure 8.33: SPL on the plane $z = 10$ for a non-dimensional frequency $kL = 20$, $M_\infty = 0.4$ and the problem described in Fig. 8.23.

We now analyse the difference between the results based either on the Taylor–Lorentz or Lorentz transform. In Fig. 8.33, contours of the SPL are shown on the plane $z = 10$ and compared to the FE solution and the BE solution based on the Taylor–Lorentz transform, for $M_\infty = 0.4$. Contours of the difference in the acoustic pressure, expressed in dB, between the boundary element solutions based on either the Taylor–Lorentz or the Lorentz transform are shown in Fig. 8.34 for non-dimensional frequencies $kL = 20$, 100 and $M_\infty = 0.4$. Consistent with the previous results, it is shown that these differences are 20-30 dB lower than the SPL predicted in this example and increase with frequency.

8.3.3.3 Discussion

The present test case showed that boundary element solutions including mean flows are a robust approximation of the finite element solutions based on the linearised potential equation for non-dimensional frequency $kL \leq 100$. An error up to 2.5 dB was reported for $M_\infty = 0.4$ while for $M_\infty \leq 0.3$ the error did not exceed 1.5 dB (see Figs. 8.27 and 8.28 and 8.30). The phase of the acoustic pressure field also agreed well close to the fuselage surface (see Figs. 8.31 and 8.32). This is an important indication for applications to cabin noise predictions.

The solutions based on the Lorentz transform were again a consistent approximation of the FE solutions based on the linearised potential equation. The use of the Taylor–Lorentz transform slightly improved the results compared to the Lorentz transform alone where non-uniformities in the mean flow were significant (see Figs. 8.31-8.33). Nevertheless, this improvement was more limited than for the test case of the sphere. The likely explanation

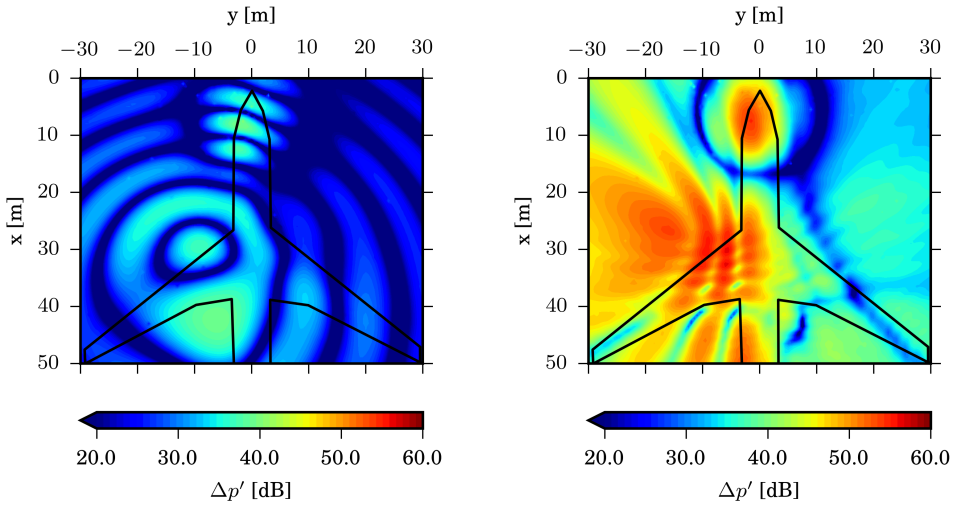

(a) $kL = 20$ (b) $kL = 100$

Figure 8.34: Difference in acoustic pressure (dB) along the plane $z = 10$ m between the boundary element solutions based either on the Taylor–Lorentz or the Lorentz transform for $M_\infty = 0.4$ and the problem described in Fig. 8.23 ($\Delta p' = 20\log[\|p'_{TL} - p'_L\|)/(\sqrt{2}p'_{ref})]$).

for this is that the wavelength considered in this example is still large compared to the characteristic length scale of the mean flow and, therefore, the non-uniform flow effects modelled by the Taylor–Lorentz formulation are more limited compared to the previous test case. The difference in the acoustic pressure field recovered by using either transform increased with frequency. However, the largest difference in the results, between the Taylor–Lorentz and the Lorentz-based solutions, was 20-30 dB lower than the SPL predicted for this example (see Figs. 8.29, 8.33 and 8.34).

8.4 Concluding remarks

A method to include mean flow effects on wave propagation based on standard boundary element solvers of the Helmholtz problem with quiescent media has been presented and benchmarked. An iterative approach to include velocity boundary conditions with a mean flow has also been demonstrated. While convergence was shown in all the numerical examples, three-dimensional applications indicate that the terms pertaining to the iterative approach can be neglected for $M_\infty \leq 0.4$. This is an important indication for practical applications because the computational cost is not increased compared to a standard boundary element solution with quiescent media.

For $M_\infty \leq 0.4$, boundary element solutions including mean flow effects were in agreement with finite element solutions based on the linearised potential equation. Despite the assumption of uniform mean flow, even the results based on the Lorentz transform positively agreed with the results based on the linearised potential equation. This was shown for

noise radiation and scattering around bluff bodies, such as a sphere. Nonetheless, solving sound radiation and scattering around slender bodies, such as an aircraft, showed even better agreement. This was expected, since the characteristic length scale of the mean flow compared to the wavelength is larger for slender than for bluff bodies.

The approach based on the Taylor–Lorentz transform was found to be slightly more accurate than the method based on the Lorentz transform in the regions where the flow non-uniformity were more significant. This confirms the conclusions given in Chapter 7 although this improvement was less clear than that observed for 2D problems. The BE solutions performed well also in the near field. Note that an accurate prediction of the phase in the near field is important for cabin noise predictions.

Differences between the solutions based on either the Taylor–Lorentz or the Lorentz transform increased with frequency. It was shown that their difference does not generally vanish in a uniform flow. However, this difference was more than 20 dB lower than the SPL in all the numerical test cases provided in this chapter. It is likely that more clear differences between the solutions based on both transforms can be observed at larger frequencies than those considered in the numerical examples of this chapter.

In summary, the weakly non-uniform ansatz has shown to be a reasonable assumption for three-dimensional applications and $M_\infty \ll 1$. The results indicated that the boundary element method with mean flow can be used for the predictions of aircraft acoustic installation effects in the limit of considering potential flows and $M_\infty < 0.4$, such as would be the case for forward fan noise at approach and take-off. However, assuming a uniform mean flow in the whole computational domain also provided a consistent approximation of the linearised potential formulation within these limits. Nonetheless, since there is not an additional computational cost associated with the Taylor–Lorentz compared to the Lorentz transform, except for computing the mean flow, boundary element formulations based on the Taylor–Lorentz physical model offer a slight but consistent improvement on the solutions based on a uniform mean flow in the near field where the non-uniformities in the mean flow velocity are significant. These conclusions also agree with the results of Chapters 6 and 7.

Chapter 9

Conclusions

9.1 Summary of contributions

The work reported in this thesis was focussed on developing numerical solutions to include non-uniform mean flow effects on wave propagation based on boundary element approaches. The main gaps identified in the literature reviewed in Chapter 3 were:

- Boundary integral solutions in the physical space, i.e. without transformations, including non-uniform mean flow effects on wave propagation.
- Boundary element kernels combining Taylor and Lorentz transformations.
- Coupled formulations exploiting boundary integral solutions with non-uniform flow.
- Benchmark studies of boundary element solutions based on approximate formulations with non-uniform mean flow, against solutions based on uniform mean flows.

The intention for this work was the need to improve current methods used to predict large-scale aircraft acoustic installation effects. The main challenges in modelling these problems are the size of the domain compared to the wavelength and modelling non-uniform mean flow effects on wave propagation. While the boundary element method in combination with either the fast multiple method or the H-matrix approach can deal with wave propagation and scattering for this kind of problems when a uniform mean flow is assumed, a gap exists when non-uniform mean flow effects are included. We focussed on this latter aspect.

In Chapter 4, a time harmonic boundary integral solution was developed for wave propagation with low Mach number potential mean flows in the physical space. The proposed integral formulation was used to solve an approximation of the linearised potential wave equation based on low Mach numbers and small non-uniform mean flow velocity components. This formulation was shown to be consistent with a combination of the physical

models associated with the Taylor and Lorentz transforms. It is termed the weakly non-uniform mean flow integral equation since it is a solution to the corresponding physical model presented in Chapter 2. In comparison to existing approaches based on variable transformations, boundary conditions and sound sources do not need to be modified. This is the key advantage of the proposed method compared to more conventional formulations based on variable transformations and solved in a transformed space. A physical space formulation makes modelling practices, such as meshing and coupling with other numerical methods, more straightforward.

In Chapter 4, a free-field Green's function has been proposed to solve the kernel of the weakly non-uniform flow integral formulation. The Green's function is an approximation of that for the weakly non-uniform flow fundamental operator which satisfies the weakly non-uniform flow ansatz. For mean flows at low Mach number, it has shown to be a robust approximation to the corresponding exact Green's function in that the predictions based on either the approximate boundary formulation or the exact domain-based formulation (to the limit of the numerical resolution) were in agreement in all the numerical examples provided.

The proposed integral formulation was used to solve both wave extrapolation and boundary element problems in a non-uniform flow. In Chapter 5, two strategies were developed to work around the non-uniqueness issue inherent in boundary element solutions to external noise propagation and scattering problems with non-uniform mean flow. A generalised combined integral equation formulation was devised to deal with the non-uniqueness issue for small-scale large-wavelength problems. A generalised Burton–Miller formulation with mean flow has also been demonstrated to solve large-scale short-wavelength problems, with higher interior modal densities. An approach to regularise hyper-singular integrals generated by this formulation was presented.

It has been shown that the integral solution in the physical space to the weakly non-uniform formulation was consistent with integral solutions to the Helmholtz problem with quiescent media written in the Taylor–Lorentz space. The clear advantage of using the formulation in the transformed space is that boundary element solutions developed for the standard Helmholtz equation with quiescent media can be used to simulate mean flow effects. However, in order to exploit existing kernels for the standard Helmholtz problem an iterative algorithm was devised for velocity boundary conditions (see Chapter 5). Dirichlet problems in the transformed space can directly exploit standard Helmholtz kernels, while for Robin-type boundary conditions, such as prescribed pressure or impedance, this was not the case due to the local mean flow effects in the transformed formulation.

The proposed formulations were benchmarked against solutions for the linearised potential equation by using numerical examples, and compared to more conventional boundary element solutions obtained by assuming a uniform flow in the whole domain. In Chapter 6, the integral solution with non-uniform mean flow was used to solve wave extrapolation and boundary element problems.

A weakly-coupled approach either in the physical or in the transformed space was developed to include more complex sound sources in the proposed boundary integral formulations and to extend the capability of the integral formulation to solve scattering problems in a non-uniform flow. An inner domain solution is recovered on an interface, where a high-fidelity source model and a surface integral formulation are coupled in order to solve noise radiation and scattering problem in a larger domain. In Chapter 7, this approach was applied to a proof-of-concept test case representing forward fan noise installation effects. A Kirchhoff integral based on an open surface in a non-uniform flow was proposed to extrapolate the nacelle near field in order to compute scattering from the airframe.

In Chapter 8, applications to three-dimensional problems were presented. The iterative approach proposed in Chapter 5 was benchmarked to exploit conventional boundary element solvers for the standard Helmholtz problem with quiescent media to resolve mean flow effects. It was shown that the formulation in the Taylor–Lorentz transformed space can be solved by existing boundary element kernels for quiescent media, where velocity boundary conditions are prescribed.

9.2 Main findings

A Taylor–Helmholtz equation was developed in the physical space based on the Taylor wave equation as a subset of the weakly non-uniform mean flow formulation. This solution generally performed less well than boundary element solutions based on a uniform mean flow in the entire domain. In numerical studies, the L^2-error on the Taylor–Helmholtz physical model compared to full solutions of the linearised potential equation scaled linearly with frequency and the distance of the observer. In other words, the error was constant if the distance to the observer was scaled with the wavelength. The Taylor–Helmholtz equation performed accurately only for near-field sound propagation and for $M_\infty < 0.2$. This formulation is not exact for a uniform mean flow leading to large errors in the far field for cases where the flow is almost uniform.

When compared to solutions of the linearised full potential equation, the integral solutions based on the weakly non-uniform flow formulation performed somewhat better than those based on either the Taylor or Lorentz physical model applied separately. The weakly non-uniform flow formulation gave better results than the corresponding uniform flow approximation. A more accurate prediction of the acoustic pressure was shown in the near field where the non-uniformity in the mean flow velocity were more significant, while similar results were produced in the far field. The numerical results indicated that the L^2-error in the physical model based on the weakly non-uniform flow formulation increased almost linearly with frequency and quadratically with Mach number. This was observed both for the case of wave extrapolation, where the weakly non-uniform flow ansatz was more clearly satisfied, and for the boundary element solutions.

Nonetheless, it was shown that the proposed integral formulation generally performed better for downstream than for upstream wave propagation. For a fixed length-scale of variation of the mean flow, the wavelength is shorter when propagation occurs upstream of the sound source and, therefore, the effects of the flow gradient are likely to be more severe than for waves travelling downstream.

Numerical results showed that the non-uniqueness issue pertaining to the boundary element solution in the physical space becomes more acute with an increase in Mach number since the corresponding kernel explicitly depends on M_∞. The combined integral equation based on a uniform flow at the overdetermination points outperformed solutions based on an assumption of a quiescent media or a non-uniform potential flow at these points. However, the generalized Burton–Miller formulation was seen to be more robust in treating this issue for all the frequencies considered in the numerical examples.

In the case of the transformed space formulation, the iterative solution devised to include velocity boundary conditions showed convergence for every numerical experiment performed. The error introduced by neglecting the iterative terms, however, was one order of magnitude lower than the actual solution. This result suggests that the iterative terms can generally be dropped for low Mach number mean flows, limiting the computational cost to a standard boundary element kernel for the Helmholtz problem.

Although simplified by the assumption of a weak coupling, the solution proposed to solve installation effects for forward fan noise performed well independently of frequency and Mach number. The open radiating surface approach was robust enough to extrapolate forward fan noise and the integral formulations with non-uniform flow to solve scattering by the fuselage. This approach has been shown to be reliable in all the numerical experiments conducted in this thesis up to the first blade passing frequency and $M_\infty \leq 0.3$. However, higher frequencies were not considered and three-dimensional computations have yet to be performed.

9.3 Limitations to the present work

The solutions proposed in this work are limited to potential flows and exclude the effects of lift generation on wave propagation. The interaction of acoustic waves with vorticity and entropy waves was also not modelled. However, for isentropic media these effects have been shown to be of second order compared to those due to potential mean flows whenever low Mach numbers are considered [36, 70]. This is a reasonable assumption for the applications targeted by this work, i.e. aircraft noise large-scale installation effects [26, 41, 45].

The proposed integral solutions were limited to low Mach numbers, meaning that compressibility of the mean flow was also neglected. Nonetheless, the assumption of small non-uniform mean flow components was pushed to the limit for boundary element problems

in that $M_0' \sim M_\infty$ on the boundary surface. However, numerical results showed that the condition $M_0' \ll M_\infty$ is rapidly recovered away from the boundary, particularly for slender bodies. Any real application of the proposed model to bluff bodies with higher aspect ratios is not expected although an extensive use of non-slender geometries has been performed in this work. Bluff bodies represented a worst-case scenario in terms of mean flow non-uniformity and therefore they were meaningful to benchmark the proposed models.

Accuracy of the integral solution to the weakly non-uniform flow formulation reduced with an increase in frequency compared to the solutions based on the linearised potential equations. For slender bodies, the reduction in accuracy with increasing frequency was small compared to the error introduced by increasing the Mach number. For three-dimensional applications, $M_\infty = 0.4$ was set as a threshold Mach number but compressibility effects on the mean flow were not considered.

An incremental but discernible improvement was shown by the integral formulation based on the weakly non-uniform flow equation compared to traditional integral solutions based on a uniform mean flow. This improvement was shown in the near field where the non-uniformity in the mean flow velocity is significant. However, the uniform flow approximation was still consistent with the reference results based on the linearised potential equation, particularly in the far field.

Although a weakly-coupled approach between the boundary element solution to the weakly non-uniform flow formulation and the finite element solution to the linearised potential equation provided a practical solution to estimate aircraft installation effects, potential improvements based on a strong coupling were not assessed.

Finally, three-dimensional solutions were not performed for realistic frequencies and full-scale whole aircraft acoustic installation effects although three-dimensional examples were devised to evaluate worst-case scenarios based on simplified geometries, such as a sphere. The main reason for this gap in the analysis is that the finite element reference models could not be solved at high frequencies with the computational resources and FE solvers available. Solutions based on non-rigid boundary conditions were also not performed. However, the same approach can be applied to these conditions.

9.4 Future work and recommendations

While a number of objectives have been accomplished, improvements and further development can be proposed based on the limitations shown, the gaps remaining and the additional questions created by this work. Possible developments are outlined below based on the outcome of the work performed.

9.4.1 Numerical applications

The wave extrapolation based on the proposed integral formulation can be applied to real nacelle intakes to assess the potential improvement in computational cost and accuracy. In fact, the radiating surface can be positioned closer to the inlet, namely in a non-uniform flow, compared to current practices [23]. Note that conventional wave extrapolation methods rely on control surfaces lying within an almost uniform mean flow, while the proposed formulations relax this constraint.

Moreover, the weakly coupled formulation for sound scattering, devised to assess forward fan noise installation effects, should be applied to real aircraft geometries and fan noise sources and include both non-rigid boundary conditions and compressible mean flows. This would further validate the proposed method and its application to aircraft design for noise certification.

9.4.2 Reduction of the computational cost

A reduction in the computational cost for the proposed boundary element solutions in the physical space are needed for industrial application. To date, the application of the method is viable for small-scale long-wavelength problems.

Boundary element solutions in the physical space have been obtained in the current study by using a conventional boundary element method. Fast algorithms applied to the proposed integral solutions would extend the applicability of the physical space formulation to higher frequencies. This can be achieved by a suitable expansion of the kernel developed in this work based on a fast multipole method [24, 45]. Alternatively, the H-matrix approach [25] is also directly applicable to the proposed formulation.

A reduction of the computational cost can also be achieved by using high-order interpolation, as proposed for finite element methods [68, 83] and by exploiting the adaptivity of the order of interpolation.

9.4.3 Extension to quasi-potential flows

An extension to quasi-potential flows, including the effects of infinitely thin shear layers, can be performed on the basis of the proposed physical space formulation and the work of Morino [46, 199]. This would allow lift generation effects on wave propagation to be modelled using the proposed integral formulation without variable transformations [36]. This enhancement would allow more general configurations for aircraft noise installation effects to be considered compared to the actual formulation, even though the influence of lift generation on these effects is generally negligible for low Mach number mean flows and small angles of attack [36, 70].

9.4.4 Coupled formulation

One can also aim to extend the work of Casanave *et al.* [42] where a strong coupled formulation in the transformed space was proposed based on a finite element model for the linearised potential equation and a boundary integral formulation with a uniform mean flow. In this case, the use of the weakly non-uniform formulation would allow the coupling of the finite element with the boundary integral formulation to be performed within a non-uniform flow. Nonetheless, the use of the physical space formulation from Chapter 4 would greatly simplify the coupling conditions and, therefore, the formulation.

For large-scale aircraft acoustic installation effects, a strong coupled formulation would extend the approach proposed in this work to more complex geometries and mean flows. Finite element solutions based on the linearised potential equation could be used where the non-uniform component of the mean flow velocity is more significant while the boundary element method based on the weakly non-uniform flow formulation could be applied where this component is small.

Appendix A

Taylor–Helmholtz Formulation

Astley and Bain [32] provided an approximate formulation for wave propagation on low Mach number mean flows based on Taylor transformation [31, 33]. In the same work, Astley and Bain [32] reported an error analysis for the corresponding wave equation which shows that the accuracy of the physical model depends only on mean flow Mach number and characteristic acoustic and mean flow length scales. This approach was used by a number of researchers in aeroacoustics [26, 33, 34]. We solve, here, the same physical model as that used by Astley and Bain [32] using an integral formulation in the physical space, i.e. without transformation.

First, the governing equation is reviewed. Second, a boundary integral solution is derived. A free field Green's function is also presented. Finally, an error analysis on the physical model is performed.

A.1 Physical model

The reference problem is external radiation and scattering of a sound source in a domain, Ω, by a body, $\partial\Omega$, in a non-uniform potential mean flow (see Fig. 4.1). As shown in Sec. 2, for $M_\infty \ll 1$ and $L_A \ll L_M$, Eq. (2.28) can be reduced to the Taylor–Helmholtz formulation, Eq. (2.38). Including a source term, q, it can be rewritten as

$$\frac{1}{c_\infty^2}\frac{\partial^2\hat{\phi}}{\partial t^2} + 2\frac{\mathbf{u}_0}{c_\infty^2}\cdot\boldsymbol{\nabla}\frac{\partial\hat{\phi}}{\partial t} - \boldsymbol{\nabla}^2\hat{\phi} = \hat{q}(\mathbf{x},t). \tag{A.1}$$

Since the problem is solved in an unbounded domain, for $\|\mathbf{x}\| \to \infty$, the Sommerfeld radiation condition with mean flow (see Eq. 2.40) must be satisfied at infinity while on any other boundary, $\partial\Omega$, the condition depends on the specific problem (see Sec. 2.5.5).

A harmonic solution to Eq. (A.1) is sought. Considering the angular frequency, ω, and the convention $\mathrm{e}^{\mathrm{i}\omega t}$, the above equations yields

$$k^2\phi - 2\mathrm{i}k(\mathbf{M}_0 \cdot \boldsymbol{\nabla}\phi) + \boldsymbol{\nabla}^2\phi = g(\mathbf{x}), \tag{A.2}$$

where $k = \omega/c_\infty$ is the wavenumber and $g = -q$ is a complex number, with q the amplitude of $\hat{q}$. Since Eq. (A.2) is a subset of the weakly non-uniform flow operator (see Sec. 4.2), the corresponding adjoint operator is obtained by reversing the mean flow. The above equation is referred to as the Taylor–Helmholtz equation, because it is consistent with the formulation associated with the Taylor transformation [31].

A.2 Boundary integral formulation

A boundary integral solution to the Taylor–Helmholtz equation is derived in this section. First, a Taylor transformation [31] is applied to Eq. (A.1). The aim is to obtain the standard wave equation in the Taylor space. The independent variables are transformed as

$$X = x, \qquad Y = y, \qquad Z = z, \qquad T = t + \frac{\Phi_0(\mathbf{x})}{c_\infty^2}, \tag{A.3}$$

where Φ_0 is the mean flow velocity potential, $(x, y, z; t)$ and $\mathbf{X} = (X, Y, Z; T)$ are the space-time coordinates in the physical and Taylor domain respectively. The corresponding derivative operators are

$$\frac{\partial}{\partial t} = \frac{\partial}{\partial T}, \qquad \boldsymbol{\nabla} = \boldsymbol{\nabla}_X + \frac{\mathbf{M}_0}{c_\infty}\frac{\partial}{\partial T}. \tag{A.4}$$

Let us apply the Taylor transform to Eq. (A.1) to give [32]

$$\frac{1}{c_\infty^2}\frac{\partial^2\bar{\phi}}{\partial T^2} - \nabla_X^2\bar{\phi} = \bar{g}(\mathbf{X}, T), \tag{A.5}$$

where terms of order M_∞^2 or higher have been dropped. In the frequency domain, a solution of the form $\bar{\phi} = \bar{\bar{\phi}}\mathrm{e}^{\mathrm{i}\omega T}$, for $\bar{g}(\mathbf{X}, T) = \bar{\bar{g}}(\mathbf{X})\mathrm{e}^{\mathrm{i}\omega T}$ is sought so that the above equation can be reduced to

$$k^2\bar{\bar{\phi}} + \nabla_X^2\bar{\bar{\phi}} = \bar{\bar{g}}(\mathbf{X}). \tag{A.6}$$

The integral solution to Eq. (A.6) is well-known [90], i.e.

$$C(\mathbf{X}_p)\bar{\bar{\phi}}(\mathbf{X}_p) = \int_{\partial\Omega}\left[\frac{\partial\bar{\bar{G}}_T(\mathbf{X}_p, \mathbf{X})}{\partial\bar{n}}\bar{\bar{\phi}} - \frac{\partial\bar{\bar{\phi}}}{\partial\bar{n}}\bar{\bar{G}}_T(\mathbf{X}_p, \mathbf{X})\right] dS(\mathbf{X}) + \int_\Omega \bar{\bar{G}}_T(\mathbf{X}_p, \mathbf{X})\bar{\bar{g}}(\mathbf{X})dV(\mathbf{X}), \tag{A.7}$$

where $\bar{\bar{G}}_T = \bar{\bar{G}}_T(\mathbf{X}_p, \mathbf{X})$ is the Green's function for the Helmholtz problem with quiescent media [43] in the Taylor space and $\bar{\mathbf{n}}$ is outgoing normal vector to the boundary surface.

The normal derivative to the transformed boundary, $\partial/\partial\bar{n}$, is defined in Eq. (2.55). On the other hand, $C(\mathbf{X}_p)$ is derived by solving the integral equation on the boundary surface using the Cauchy principal value [43]:

$$C(\mathbf{X}_p) = \begin{cases} 1 & \mathbf{X}_p \in \Omega \\ 0 & \mathbf{X}_p \notin \Omega \cup \partial\Omega \\ 1 - \int_{\partial\Omega} \frac{\partial G_0(\mathbf{X}_p,\mathbf{X})}{\partial n} dS(\mathbf{X}) & \mathbf{X}_p \in \partial\Omega, \end{cases} \tag{A.8}$$

where G_0 is the Green function associated to the Laplace operator, i.e. $\nabla^2 G_0 = -\delta(\mathbf{X}-\mathbf{X}_p)$. Hence, G_0 is equal to $1/(4\pi R)$, where R is the distance between the observer and the sound source.

The solution in the physical space can then be recovered using an inverse Taylor–Lorentz transform. We consider a harmonic solution in the physical space, $\hat{\phi}(\mathbf{x},t) = \phi(\mathbf{x})\mathrm{e}^{\mathrm{i}\omega t}$. In the Taylor space, the acoustic velocity potential can then be rewritten as $\bar{\phi}(\mathbf{X},T) = \bar{\bar{\phi}}\mathrm{e}^{\mathrm{i}\omega T}$. Applying an inverse Taylor transform to the above equation gives,

$$\bar{\bar{\phi}}(\mathbf{X}) = \phi(\mathbf{x})\mathrm{e}^{-\mathrm{i}k\frac{\Phi_0(\mathbf{x})}{c_\infty}}. \tag{A.9}$$

Similarly, the source term, g, is transformed as

$$\bar{\bar{g}}(\mathbf{X}) = g(\mathbf{x})\mathrm{e}^{-\mathrm{i}k\frac{\Phi_0(\mathbf{x})}{c_\infty}}. \tag{A.10}$$

Let us use Eq. (A.4) to recover the normal derivative of ϕ to the boundary surface

$$\frac{\partial\bar{\bar{\phi}}(\mathbf{X})}{\partial\bar{n}} = \frac{\partial\phi(\mathbf{x})}{\partial n}\mathrm{e}^{-\mathrm{i}k\frac{\Phi_0(\mathbf{x})}{c_\infty}} - \mathrm{i}k\mathbf{M}_0\cdot\mathbf{n}\phi(\mathbf{x})\mathrm{e}^{-\mathrm{i}k\frac{\Phi_0(\mathbf{x})}{c_\infty}}. \tag{A.11}$$

We now include Eqs. (A.9), (A.10) and (A.11) in Eq. (A.7) to give

$$\begin{aligned} C(\mathbf{x}_p)\phi(\mathbf{x}_p) = &\int_{\partial\Omega}\left[\frac{\partial\phi}{\partial n}\bar{\bar{G}}_T - \left(\frac{\partial\bar{\bar{G}}_T}{\partial n} + \mathrm{i}k\bar{\bar{G}}_T\mathbf{M}_0\cdot\mathbf{n}\right)\phi\right]\mathrm{e}^{\mathrm{i}k\frac{\Phi_0(\mathbf{x}_p)-\Phi_0(\mathbf{x})}{c_\infty}}dS(\mathbf{x}) \\ &+ \int_\Omega \bar{\bar{G}}_T(\mathbf{x}_p,\mathbf{x})g(\mathbf{x})\mathrm{e}^{\mathrm{i}k\frac{\Phi_0(\mathbf{x}_p)-\Phi_0(\mathbf{x})}{c_\infty}}dV(\mathbf{x}), \end{aligned} \tag{A.12}$$

where $\bar{\bar{G}}_T = \bar{\bar{G}}_T(\mathbf{x}_p,\mathbf{x})$ and $\phi = \phi(\mathbf{x})$.

Based on the above equation we define the Green's function

$$G_T(\mathbf{x}_p,\mathbf{x}) = \bar{\bar{G}}_T(\mathbf{x}_p,\mathbf{x})\mathrm{e}^{\mathrm{i}k\frac{\Phi_0(\mathbf{x}_p)-\Phi_0(\mathbf{x})}{c_\infty}}. \tag{A.13}$$

Hence, Eq. (A.12) can be rewritten as

$$C(\mathbf{x}_p)\phi(\mathbf{x}_p) = \int_{\partial\Omega}\left[G_T\left(\frac{\partial\phi}{\partial n} - 2\mathrm{i}k\mathbf{M}_0\cdot\mathbf{n}\phi\right) - \frac{\partial G_T}{\partial n}\phi\right]dS(\mathbf{x}) + \int_\Omega G_T(\mathbf{x}_p,\mathbf{x})g(\mathbf{x})dV(\mathbf{x}), \tag{A.14}$$

where

$$C(\mathbf{x}_p) = \begin{cases} 1 & \mathbf{x}_p \in \Omega \\ 0 & \mathbf{x}_p \in \Omega \cup \partial\Omega \\ 1 - \int_{\partial\Omega} \frac{\partial G_0(\mathbf{x}_p,\mathbf{x})}{\partial n} dS(\mathbf{x}) & \mathbf{x}_p \in \partial\Omega. \end{cases} \tag{A.15}$$

The above equation represents an extension of the Kirchhoff integral to low Mach numbers subsonic flows.

Equation (A.14) vanishes for $\|\mathbf{x}\| \to \infty$ if ϕ and G_T satisfy the Sommerfeld radiation condition with a mean flow. In particular, the first term on the right-hand side of Eq. (A.14), integrated over the boundary surface $\partial\Omega$, varies with $1/R$, with R the distance of the observer. The second and third terms also vary with $1/R$, satisfying the Sommerfeld radiation condition with a mean flow. Note that, these terms can be written as a combination of the potential and its normal derivative to the boundary in the transformed domain as for the standard Helmholtz problem where this condition is satisfied [43].

A.3 Green's function

The free-field Green's function associated with the Taylor–Helmholtz equation, Eq. (A.2), has been derived in the previous section. An alternative derivation is provided below. The Green's function for the Taylor operator and a reverse mean flow, namely considering $-\mathbf{M}_0$ in lieu of $\mathbf{M}_0$ satisfies

$$k^2 G_T + 2\mathrm{i}k\mathbf{M}_0 \cdot \boldsymbol{\nabla} G_T + \boldsymbol{\nabla}^2 G_T = -\delta(\mathbf{x}_p - \mathbf{x}). \tag{A.16}$$

A Taylor transformation is used to reduce the reverse flow operator to the standard wave equation for which the free-field Green's function is well-known. The inverse transformation is then applied to recover the Green's function in the physical space.

First, we consider the fundamental Taylor wave operator Eq. (A.2) and apply a Taylor transformation [31] to it (see Eq. (A.3)). As shown in Sec. A.2, the above equation can be reduced to

$$\frac{1}{c_\infty^2} \frac{\partial^2 \bar{G}_T}{\partial T^2} - \nabla_X^2 \bar{G}_T = \delta(\mathbf{X}, T). \tag{A.17}$$

In the frequency domain, it yields

$$k^2 \bar{\bar{G}}_T + \nabla_X^2 \bar{\bar{G}}_T = -\delta(\mathbf{X}), \tag{A.18}$$

where $\bar{G}_T(\mathbf{X}, \mathbf{T}) = \bar{\bar{G}}_T(\mathbf{X})\mathrm{e}^{\mathrm{i}\omega T}$ is the Green's function in the Taylor space.

Note that, the left hand side of the above equation is simply the standard Helmholtz operator in the Taylor space. The fundamental solution to this operator is well-known [43]:

$$\bar{\bar{G}}_T(\mathbf{X}, \mathbf{X}_s) = \frac{\mathrm{e}^{-\mathrm{i}kR}}{4\pi R}, \tag{A.19}$$

where $R = \sqrt{(X - X_s)^2 + (Y - Y_s)^2 + (Z - Z_s)^2} = \sqrt{(x - x_s)^2 + (y - y_s)^2 + (z - z_s)^2}$ is the amplitude radius [190].

An equivalent solution of the form $G_T(\mathbf{x}) = G_T(\mathbf{x})\mathrm{e}^{\mathrm{i}\omega t}$ is sought in the physical space. Applying the inverse Taylor transformation to $\bar{G}_T$ gives

$$\bar{\bar{G}}_T(\mathbf{X})\mathrm{e}^{\mathrm{i}\omega T} = \bar{\bar{G}}_T(\mathbf{x})\mathrm{e}^{\mathrm{i}\omega\left(t - \Phi_0(\mathbf{x})/c_\infty^2\right)} = G_T(\mathbf{x})\mathrm{e}^{\mathrm{i}\omega t}, \tag{A.20}$$

where

$$G_T(\mathbf{x}) = \bar{\bar{G}}_T(\mathbf{x})\mathrm{e}^{-\mathrm{i}\omega\Phi_0(\mathbf{x})/c_\infty^2}. \tag{A.21}$$

Equation (A.19) can be used in the above equation to give

$$G_T = \frac{\mathrm{e}^{-\mathrm{i}k(R + \Phi_0(\mathbf{x})/c_\infty)}}{4\pi R}, \tag{A.22}$$

and for a generic point source $\mathbf{x}_s = (x_s, y_s, z_s)$ one has

$$G_T = \frac{\exp\left(-\mathrm{i}k\left\{R + \left[\Phi_0(\mathbf{x}) - \Phi_0(\mathbf{x}_s)\right]/c_\infty\right\}\right)}{4\pi R}. \tag{A.23}$$

We define the phase radius [190] as $\sigma_T = R + \left[\Phi_0(\mathbf{x}) - \Phi_0(\mathbf{x}_s)\right]/c_\infty$ and rewrite the Green's function as

$$G_T = \frac{\mathrm{e}^{-\mathrm{i}k\sigma_T}}{4\pi R}. \tag{A.24}$$

The functions G_T reduces to the Green's function for the standard Helmholtz problem for $M_0 \to 0$. On the contrary, G_T does not reduce to the Green's function for the uniform flow convected wave equation [190] when $M_0 \to M_\infty$.

A.4 Error estimate

In this section, a dimensional analysis of the accuracy of Eq. (A.1) against the full potential linearised wave equation, Eq. (2.28), is presented. The analysis follows the same logic as that presented in Sec. 4.5. Equation (A.1) is derived from Eq. (2.28) by using an approximation to the first order with respect to the mean flow component $\mathbf{u}_0$. The present dimensional error analysis extends the works of Astley and Bain [32] and Mayoral and Papamoschou [34]. Following Astley and Bain [32], the terms in Eqs. (2.28) and (A.1) can be rewritten in terms of mean flow Mach number, M_∞, the characteristic acoustic length scale, L_A, and the mean flow length scale, L_M.

The operator associated with Eq. (A.1) written in the Fourier domain is

$$\omega^2\phi - 2\mathrm{i}\omega\mathbf{u}_0 \cdot \boldsymbol{\nabla}\phi + c_\infty^2\boldsymbol{\nabla}^2\phi = \Xi, \tag{A.25}$$

where

$$\Xi = \mathbf{u}_0\cdot\boldsymbol{\nabla}(\mathbf{u}_0\cdot\boldsymbol{\nabla}\phi)+\frac{1}{2}\boldsymbol{\nabla}\phi\cdot(\mathbf{u}_0\cdot\mathbf{u}_0)+(\gamma-1)\boldsymbol{\nabla}\cdot\mathbf{u}_0(\mathrm{i}\omega\phi+\mathbf{u}_0\cdot\boldsymbol{\nabla}\phi)+\frac{\gamma-1}{2}(u_0^2-u_\infty^2)\boldsymbol{\nabla}^2\phi \quad \text{(A.26)}$$

Equation (A.26) is divided by c_∞^2 and the right-hand side is rewritten in terms of M_∞, L_A and L_M to give

$$\begin{aligned}
&\frac{1}{c_\infty^2}\mathbf{u}_0\cdot\boldsymbol{\nabla}(\mathbf{u}_0\cdot\boldsymbol{\nabla}\phi)\sim M_\infty^2\frac{[\phi]}{L_AL_M},\\
&\frac{1}{c_\infty^2}\frac{1}{2}\boldsymbol{\nabla}\phi\cdot(\mathbf{u}_0\cdot\mathbf{u}_0)\sim M_\infty^2\frac{[\phi]}{L_AL_M},\\
&\frac{1}{c_\infty^2}(\gamma-1)\boldsymbol{\nabla}\cdot\mathbf{u}_0\mathrm{i}\omega\phi\sim M_0'^3\frac{[\phi]}{L_AL_M},\\
&\frac{1}{c_\infty^2}(\gamma-1)\boldsymbol{\nabla}\cdot\mathbf{u}_0(\mathbf{u}_0\cdot\boldsymbol{\nabla}\phi)\sim M_0'^3M_\infty\frac{[\phi]}{L_AL_M},\\
&\frac{1}{c_\infty^2}\frac{\gamma-1}{2}(u_0^2-u_\infty^2)\boldsymbol{\nabla}^2\phi\sim M_0'M_\infty\frac{[\phi]}{L_A^2},
\end{aligned} \quad \text{(A.27)}$$

where $\boldsymbol{\nabla}\cdot\mathbf{M}_0$ is written considering Eq. (4.9). The left-hand side of Eq. (A.26) can also be rewritten as,

$$\begin{aligned}
&\frac{1}{c_\infty^2}\omega^2\phi\sim\frac{[\phi]}{L_A^2},\\
&\frac{1}{c_\infty^2}2\mathrm{i}\omega\mathbf{u}_0\cdot\boldsymbol{\nabla}\phi\sim M_\infty\frac{[\phi]}{L_A^2},\\
&\frac{1}{c_\infty^2}c_\infty^2\boldsymbol{\nabla}^2\phi\sim\frac{[\phi]}{L_A^2}.
\end{aligned} \quad \text{(A.28)}$$

Moreover, when Eq. (A.25) is written in the Taylor space, further terms of order M_∞^2 and M_∞^3 are neglected. In the Taylor space, Eq. (A.25) is reduced to

$$\omega^2\bar{\bar{\phi}}+c_\infty^2\boldsymbol{\nabla}_X^2\bar{\bar{\phi}}=\Xi_X, \quad \text{(A.29)}$$

where

$$\bar{\Xi}_X=\Xi_X-\mathbf{u}_0\cdot\mathbf{u}_0\frac{\omega^2}{c_\infty^2}\bar{\bar{\phi}}+2\mathrm{i}\omega(\boldsymbol{\nabla}_X\cdot\mathbf{u}_0)\bar{\bar{\phi}} \quad \text{(A.30)}$$

and

$$\begin{aligned}
&\frac{1}{c_\infty^4}\mathbf{u}_0\cdot\mathbf{u}_0\omega^2\bar{\bar{\phi}}\sim M_\infty^2\frac{[\phi]}{L_A^2},\\
&\frac{1}{c_\infty^2}2\mathrm{i}\omega(\boldsymbol{\nabla}_X\cdot\mathbf{u}_0)\bar{\bar{\phi}}\sim M_0'^3\frac{[\phi]}{L_AL_M}.
\end{aligned} \quad \text{(A.31)}$$

Considering the right-hand side of Eq. (A.29), the source of error associated with the Taylor formulation reduces to

$$\bar{\bar{\Xi}} \sim C_1 \frac{M_\infty^2[\phi]}{L_A L_M} + C_2 \frac{M_\infty^2[\phi]}{L_A^2} + C_3 \frac{M_0' M_\infty[\phi]}{L_A^2} + C_4 \frac{M_0'^3[\phi]}{L_A L_M} + C_5 \frac{M_0'^3 M_\infty[\phi]}{L_A L_M}, \tag{A.32}$$

where $C_1, C_2, ...C_5$ are constants of order 1. Note that the first two terms on the right-hand side do not vanish on a uniform flow.

The term $\bar{\bar{\Xi}}$ scales with $1/L_A = f/c_\infty$. In other words, it increases linearly with frequency. Moreover, the error varies with $1/L_M$ and it decreases for smooth mean flows. For $L_M \to \infty$, namely in a uniform flow, $\bar{\bar{\Xi}}$ increases with $1/L_A^2$. The error on ϕ in every point of the domain is propagated by using the integral formulation, Eq. (A.14). Thereby, the error on ϕ is determined by convolving $\bar{\bar{\Xi}}$ with the Green's function in the Taylor space, $\bar{\bar{G}}$, as

$$\varepsilon_T(\mathbf{X}_p) = \int_\Omega \bar{\bar{G}}_T(\mathbf{X}_p, \mathbf{X}) \bar{\bar{\Xi}}(\mathbf{X}) \, dV(\mathbf{X}). \tag{A.33}$$

$\bar{\bar{G}}_T$ scales with $1/R$ where R is the amplitude radius. Introducing the geometrical length scale of the problem, D, the first term in Eq. (A.27) gives

$$\varepsilon_{T,1} \sim [\phi] M_\infty^2 \frac{D}{L_M} \frac{D^2}{L_A R}. \tag{A.34}$$

Therefore, the error on ϕ increases linearly with frequency. Note that if $L_A R$ is constant, namely the distance of the observer is scaled with the wavelength, the error depends only on L_M. This analysis applies to all the terms in $\bar{\bar{\Xi}}$ except for the terms of order $1/L_A^2$ - the last term in Eq. (A.27) gives

$$\varepsilon_{T,2} \sim [\phi] M_\infty^2 D \frac{D^2}{R L_A^2}. \tag{A.35}$$

It is seen that the error terms $\varepsilon_{T,1}$ and $\varepsilon_{T,2}$ can be rewritten based on the acoustic and geometric distances of the observer, i.e. R/D and R/L_A, as

$$\varepsilon_{T,1} \sim [\phi] M_\infty^2 \frac{D}{L_M} \frac{D^2}{R^2} \frac{R}{L_A}, \qquad \varepsilon_{T,2} \sim [\phi] M_\infty^2 \frac{D^3}{R^3} \frac{R^2}{L_A^2}. \tag{A.36}$$

The error in the Taylor–Helmholtz formulation decreases in the geometric far field but increases in the acoustic far field. This behaviour applies to both wave propagation either on a non-uniform and uniform flow since some error terms do not vanish on a uniform flow. The present analysis can be extended to 2D cases where the Green's function scales as $1/\sqrt{kR}$, achieving analogous conclusions (see Sec. 4.5).

Appendix B

Green's Function for Weakly Non-Uniform Flows

B.1 2D Green's function

B.1.1 General formulation

This section presents the 2D Green's function for wave propagation on a weakly non-uniform potential mean flow. The formulation is suitable for low Mach number potential flows. The solution is based on the proof given in Sec. 4.4. The Green's function for the Taylor–Helmholtz formulation is also derived.

The Green's function for the Helmholtz operator in the Taylor–Lorentz space, Eq. (4.33), is given by

$$\tilde{G}(\tilde{\mathbf{X}}) = -\frac{\mathrm{i}}{4} H_0^{(2)}\left(\tilde{k}\tilde{R}_{2D}\right), \tag{B.1}$$

where $\tilde{R}_{2D} = \sqrt{\tilde{X}^2 + \tilde{Y}^2}$, $H_0^{(2)}$ is the Hankel function of the second type of order zero and $\tilde{k} = k/\beta_\infty$. A time harmonic solution is sought for $\hat{\tilde{G}}$, namely $\hat{\tilde{G}}(\tilde{\mathbf{X}}, \tilde{T}) = \tilde{G}(\tilde{\mathbf{X}})\mathrm{e}^{\mathrm{i}\tilde{\omega}\tilde{T}}$. An inverse Taylor–Lorentz transformation is applied to the above equation in order to recover the Green's function in the physical space (see Sec. 4.4)

$$G(\mathbf{x}) = -\frac{\mathrm{i}}{4\beta_\infty} H_0^{(2)}\left(\frac{k\sqrt{x^2 + \beta_\infty^2 y^2}}{\beta_\infty^2}\right) \mathrm{e}^{-\mathrm{i}k\left(\frac{M_\infty x}{\beta_\infty^2} + \frac{\Phi_0'(\mathbf{x})}{c_\infty}\right)}. \tag{B.2}$$

Extending the Green's function to a generic source position $\mathbf{x}_s = (x_s, y_s)$ yields

$$G(\mathbf{x}, \mathbf{x}_s) = -\frac{\mathrm{i}}{4\beta_\infty} H_0^{(2)}\left(\frac{kR_{M,2D}}{\beta_\infty^2}\right) \mathrm{e}^{-\mathrm{i}k\left(\frac{M_\infty(x-x_s)}{\beta_\infty^2} + \frac{\Phi_0'(\mathbf{x}) - \Phi_0'(\mathbf{x}_s)}{c_\infty}\right)} \tag{B.3}$$

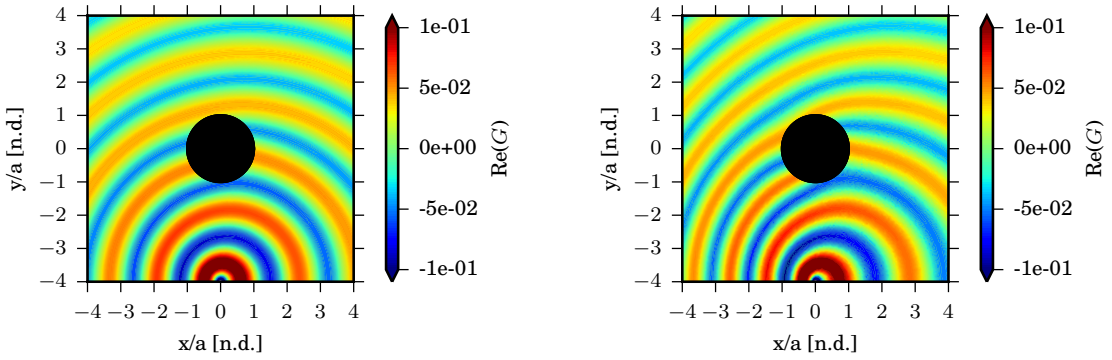

(a) $M_\infty = 0.1$, $ka = 4$

(b) $M_\infty = 0.3$, $ka = 4$

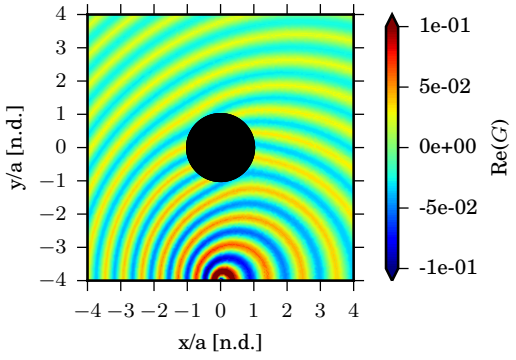

(c) $M_\infty = 0.3$, $ka = 8$

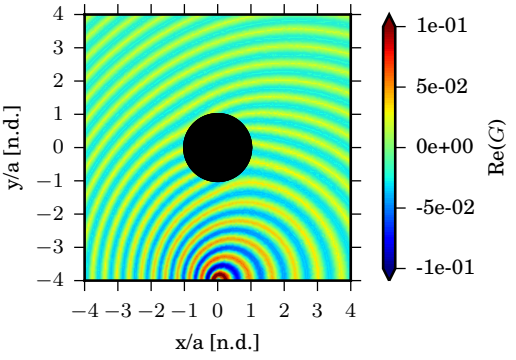

(d) $M_\infty = 0.3$, $ka = 12$

Figure B.1: Real part of the Green function in Eq. (B.5) for the problem in Fig 6.1 and a point source at $\mathbf{x}_s = (0, -4a)$.

where $R_{M,2D} = \sqrt{(x - x_s)^2 + \beta_\infty^2 (y - y_s)^2}$. Contours of the real part of the Green's function in the above equation, for the problem in Fig 6.1, are shown in Fig. B.1 for a point source at $\mathbf{x}_s = (0, -4a)$. For completeness, the corresponding Green's function associated with the static operator Eq. (4.18) is

$$G_0(\mathbf{x}, \mathbf{x}_s) = -\frac{\log(R_{M,2D})}{2\pi}. \tag{B.4}$$

For a uniform flow, Eq. (B.3) reduces to the expression provided by Bailly and Juvé [62]. On the other hand, the 2D Green's function for the Taylor–Helmholtz formulation is written dropping the dependence on M_∞^2 in Eq. (B.3),

$$G_T(\mathbf{x}, \mathbf{x}_s) = -\frac{\mathrm{i}}{4\beta_\infty} H_0^{(2)}(kR_{2D}) \mathrm{e}^{-\mathrm{i}k\frac{\Phi_0(\mathbf{x}) - \Phi_0(\mathbf{x}_s)}{c_\infty}}, \tag{B.5}$$

where $R_{2D} = \sqrt{(x - x_s)^2 + (y - y_s)^2}$.

B.1.2 Green's function at the overdetermination points

Based on Eq. (B.3), the 2D Green's function corresponding to Eq. (5.40) can be written as

$$G_{ch}(\mathbf{x}_{ch},\mathbf{x}) = -\frac{\mathrm{i}}{4\beta_\infty} H_0^{(2)}\Big(\frac{kR_{M,2D}}{1-M_\infty^2}\Big)\exp\Big\{-\mathrm{i}k\Big([M_\infty(x_{ch}-x)]/\beta_\infty^2 - \Phi_0'(\mathbf{x})/c_\infty\Big)\Big\}. \quad \text{(B.6)}$$

Equation (B.6) is analogous to that recovered in Sec. 5.2.5.2 for a three-dimensional problems. Alternatively, a quiescent media at the overdetermination points can be assumed by dropping the term $M_\infty x_{ch}$ in the above equation.

B.2 Alternative derivation

An alternative derivation for the Green's function of the weakly non-uniform flow formulation (see Sec. 4.4) is presented in this section. We look for the Green's function in the physical space $G(\mathbf{x},t)$ to Eq. (4.25). In the frequency domain one has

$$G(\mathbf{x},\omega) = \int_{-\infty}^{+\infty} G(\mathbf{x},t)\mathrm{e}^{-\mathrm{i}\omega t}dt. \quad \text{(B.7)}$$

We replace the independent variables $(\mathbf{x},t)$ with the Taylor–Lorentz space-time variables $(\tilde{\mathbf{X}},\tilde{T})$ (see Sec. 2.6.3) to give

$$\begin{aligned} G(\mathbf{x},\omega) &= \int_{-\infty}^{+\infty} G(\mathbf{x}(\tilde{\mathbf{X}},\tilde{T}),t(\tilde{\mathbf{X}},\tilde{T}))\mathrm{e}^{-\mathrm{i}\omega\left(\frac{\tilde{T}}{\beta_\infty}+M_\infty\frac{\tilde{X}}{\beta_\infty^2 c_\infty}+\frac{\Phi_0'(\mathbf{X})}{\beta_\infty c_\infty^2}\right)}\frac{d\tilde{T}}{\beta_\infty} = \\ &= \frac{\mathrm{e}^{-\mathrm{i}\omega\left(\frac{M_\infty\tilde{X}}{\beta_\infty c_\infty}+\frac{\Phi_0'(\mathbf{X})}{\beta_\infty c_\infty^2}\right)}}{\beta_\infty}\int_{-\infty}^{+\infty} G(\tilde{\mathbf{X}},\tilde{T})\mathrm{e}^{-\mathrm{i}\tilde{\omega}\tilde{T}}d\tilde{T}. \end{aligned} \quad \text{(B.8)}$$

In the Taylor–Lorentz space where we solve the standard Helmholtz problem, a harmonic solution $G(\tilde{\mathbf{X}},\tilde{T}) = G(\tilde{\mathbf{X}},\tilde{\omega})\mathrm{e}^{\mathrm{i}\tilde{\omega}\tilde{T}}$ is considered. A harmonic solution is also sought in the physical space, $G(\mathbf{x},t) = G(\mathbf{x},\omega)\mathrm{e}^{\mathrm{i}\omega t}$. Hence, the above equation can be rewritten as

$$G(\mathbf{x},\omega) = \frac{\mathrm{e}^{-\mathrm{i}\omega\left(\frac{M_\infty x}{\beta_\infty^2 c_\infty}+\frac{\Phi_0'(\mathbf{x})}{c_\infty^2}\right)}}{\beta_\infty}\tilde{G}(\tilde{\mathbf{X}},\tilde{\omega}). \quad \text{(B.9)}$$

$\tilde{G}(\tilde{\mathbf{X}},\tilde{\omega})$ is simply the Green's function for the standard Helmholtz problem with quiescent media, i.e.

$$\tilde{G}(\tilde{\mathbf{X}},\tilde{\omega}) = \frac{\mathrm{e}^{-\mathrm{i}\tilde{k}\tilde{R}}}{4\pi\tilde{R}}, \quad \text{(B.10)}$$

where $\tilde{R} = \sqrt{\tilde{X}^2+\tilde{Y}^2+\tilde{Z}^2}$. Transforming the independent variables in $G(\tilde{\mathbf{X}},\tilde{\omega})$ to the physical space and including a generic sound source position, $\mathbf{x}_s$, allow Eq. (B.9) to be written as

$$G(\mathbf{x},\mathbf{x}_s) = \frac{\mathrm{e}^{-\mathrm{i}k\sigma_M}}{4\pi R_M}, \quad \text{(B.11)}$$

where $\sigma_M = [R_M + M_\infty(x - x_s)]/\beta_\infty^2 + [\Phi_0'(\mathbf{x}) - \Phi_0'(\mathbf{x}_s)]/c_\infty$ and the amplitude radius is $R_M = \sqrt{(x-x_s)^2 + \beta_\infty^2[(y-y_s)^2 + (z-z_s)^2]}$. It seen that the time contraction, β_∞, in the Taylor–Lorentz transform simply represents a scaling factor, weighting the distance of the observer with M_∞ (see Eq. (B.9)).

B.3 Generalized normal derivatives

In this section, we present the derivatives of the Green's function based on the generalized normal derivative operator of Sec. 2.6.3. We consider the relationship between the Green's function in the physical and in the transformed space (see Sec. 4.4),

$$\tilde{G}(\tilde{\mathbf{X}}_p, \tilde{\mathbf{X}})\mathrm{e}^{\mathrm{i}\tilde{\omega}\tilde{T}} = \frac{\bar{G}(\mathbf{x}_p, \mathbf{x})}{\beta_\infty}\mathrm{e}^{-\mathrm{i}\omega\left[\frac{M_\infty(x_p - x)}{c_\infty\beta_\infty^2} + \frac{\Phi_0'(\mathbf{x}_p) - \Phi_0'(\mathbf{x})}{c_\infty^2}\right]}\mathrm{e}^{\mathrm{i}\omega t} = G(\mathbf{x}_p, \mathbf{x})\mathrm{e}^{\mathrm{i}\omega t}. \tag{B.12}$$

The generalized normal derivatives based on the weakly non-uniform flow formulation (see Sec. 2.6.3) is

$$\frac{\partial}{\partial\tilde{n}} = \frac{1}{\sqrt{1 - M_\infty^2 n_x^2}}\left[\frac{\partial}{\partial n} - n_x M_\infty^2\frac{\partial}{\partial x} - (\mathbf{M}_0\cdot\mathbf{n} - M_{0,x}' M_\infty^2)\frac{\partial}{\partial t}\right]. \tag{B.13}$$

Consistent with the approximations used to derive Eq. (2.35), the terms of order $M_\infty^2 M_{0,x}'$ in the above equation can be neglected, to give

$$\frac{\partial}{\partial\tilde{n}} = \frac{1}{\sqrt{1 - M_\infty^2 n_x^2}}\left[\frac{\partial}{\partial n} - n_x M_\infty^2\frac{\partial}{\partial x} - \mathbf{M}_0\cdot\mathbf{n}\frac{\partial}{\partial t}\right]. \tag{B.14}$$

First, deriving Eq. (5.52) along the normal direction, $\tilde{\mathbf{n}}$, yields

$$\frac{\partial\tilde{G}(\tilde{\mathbf{X}}_p, \tilde{\mathbf{X}})}{\partial\tilde{n}}\mathrm{e}^{\mathrm{i}\tilde{\omega}\tilde{T}} = \frac{\mathrm{e}^{\mathrm{i}\omega t}}{\sqrt{1 - M_\infty^2 n_x^2}}\left[\frac{\partial G(\mathbf{x}_p, \mathbf{x})}{\partial n} - n_x M_\infty^2\frac{\partial G(\mathbf{x}_p, \mathbf{x})}{\partial x} - \mathbf{M}_0\cdot\mathbf{n}\mathrm{i}\omega G(\mathbf{x}_p, \mathbf{x})\right]. \tag{B.15}$$

If both the right and left-hand side terms in the above equations are multiplied by $e^{-\mathrm{i}\tilde{\omega}\tilde{T}}$, where T depends on the relative position of the observer $\mathbf{x}_p$ and the sound source $\mathbf{x}$, namely $T = \beta_\infty(t + [\Phi_0'(\mathbf{x}) - \Phi_0'(\mathbf{x}_p)]/c_\infty^2) + M_\infty(x - x_p)/c_\infty\beta_\infty$, one has

$$\begin{aligned}\frac{\partial\tilde{G}(\tilde{\mathbf{X}}_p, \tilde{\mathbf{X}})}{\partial\tilde{n}} = \\ \frac{\mathrm{e}^{-\mathrm{i}\omega\left[\frac{M_\infty(x_p - x)}{c_\infty\beta_\infty^2} + \frac{\Phi_0'(\mathbf{x}_p) - \Phi_0'(\mathbf{x})}{c_\infty^2}\right]}}{\sqrt{1 - M_\infty^2 n_x^2}}\left[\frac{\partial G(\mathbf{x}_p, \mathbf{x})}{\partial n} - n_x M_\infty^2\frac{\partial G(\mathbf{x}_p, \mathbf{x})}{\partial x} - \mathbf{M}_0\cdot\mathbf{n}\mathrm{i}\omega G(\mathbf{x}_p, \mathbf{x})\right].\end{aligned} \tag{B.16}$$

The above equation is the generalised normal derivative of the first order.

Second, deriving Eq. (B.15) in the generalized normal direction $\tilde{\mathbf{n}}_p$ gives

$$\begin{aligned}\frac{\partial^2\tilde{G}(\tilde{\mathbf{X}}_p,\tilde{\mathbf{X}})}{\partial\tilde{n}_p\partial\tilde{n}}\mathrm{e}^{\mathrm{i}\tilde{\omega}\tilde{T}} &= \frac{\mathrm{e}^{\mathrm{i}\omega t}}{\sqrt{1-M_\infty^2n_x^2}\sqrt{1-M_\infty^2n_{x,p}^2}}\left[\frac{\partial^2G(\mathbf{x}_p,\mathbf{x})}{\partial n\partial n_p}-n_xM_\infty^2\frac{\partial^2G(\mathbf{x}_p,\mathbf{x})}{\partial x\partial n_p}-\mathbf{M}_0\cdot\mathbf{n}\mathrm{i}k\frac{\partial G(\mathbf{x}_p,\mathbf{x})}{\partial n_p}\right]\\ &+\frac{n_{x,p}M_\infty^2\mathrm{e}^{\mathrm{i}\omega t}}{\sqrt{1-M_\infty^2n_x^2}\sqrt{1-M_\infty^2n_{x,p}^2}}\left[\frac{\partial^2G(\mathbf{x}_p,\mathbf{x})}{\partial n\partial x_p}-n_xM_\infty^2\frac{\partial^2G(\mathbf{x}_p,\mathbf{x})}{\partial x\partial x_p}-\mathbf{M}_0\cdot\mathbf{n}\mathrm{i}k\frac{\partial G(\mathbf{x}_p,\mathbf{x})}{\partial x_p}\right]\\ &+\frac{\mathbf{M}_0\cdot\mathbf{n}\mathrm{i}\omega\mathrm{e}^{\mathrm{i}\omega t}}{\sqrt{1-M_\infty^2n_x^2}\sqrt{1-M_\infty^2n_{x,p}^2}}\left[\frac{\partial G(\mathbf{x}_p,\mathbf{x})}{\partial n}-n_xM_\infty^2\frac{\partial G(\mathbf{x}_p,\mathbf{x})}{\partial x}-\mathbf{M}_0\cdot\mathbf{n}\mathrm{i}kG(\mathbf{x}_p,\mathbf{x})\right].\end{aligned} \tag{B.17}$$

For an impermeable steady surface, i.e. $\mathbf{M}_0\cdot\mathbf{n}=0$, Eq. (B.15) can be rewritten as

$$\frac{\partial\tilde{G}(\tilde{\mathbf{X}}_p,\tilde{\mathbf{X}})}{\partial\tilde{n}}=\frac{\mathrm{e}^{-\mathrm{i}\omega\left[\frac{M_\infty(x_p-x)}{c_\infty\beta_\infty^2}+\frac{\Phi_0'(\mathbf{x}_p)-\Phi_0'(\mathbf{x})}{c_\infty^2}\right]}}{\sqrt{1-M_\infty^2n_x^2}}\left[\frac{\partial G(\mathbf{x}_p,\mathbf{x})}{\partial n}-n_xM_\infty^2\frac{\partial G(\mathbf{x}_p,\mathbf{x})}{\partial x}\right], \tag{B.18}$$

and Eq. (B.17) gives

$$\frac{\partial^2\tilde{G}}{\partial\tilde{n}\partial\tilde{n}_p}=\frac{\mathrm{e}^{-\mathrm{i}\omega\left[\frac{M_\infty(x_p-x)}{c_\infty\beta_\infty^2}+\frac{\Phi_0'(\mathbf{x}_p)-\Phi_0'(\mathbf{x})}{c_\infty^2}\right]}}{\sqrt{1-M_\infty^2n_x^2}\sqrt{1-M_\infty^2n_{x,p}^2}}\left[\frac{\partial^2G}{\partial n\partial n_p}-n_{x_p}M_\infty^2\frac{\partial^2G}{\partial n\partial x_p}-n_xM_\infty^2\frac{\partial^2G}{\partial x\partial n_p}+n_xn_{x_p}M_\infty^4\frac{\partial^2G}{\partial x\partial x_p}\right]. \tag{B.19}$$

The above equation has been used in Sec. 5.2.5.2.

Appendix C

Complements to Boundary Element Solutions

C.1 Direct collocation method

Equation (5.4) can be solved numerically based on a collocation approach [40]. A boundary value expansion of Eq. (4.21) is proposed. This expansion is used to evaluate the integral equation at the nodal points of the discrete boundary surface. The discrete system is presented for both the weakly non-uniform formulation and the Taylor–Helmholtz equation.

C.1.1 Weakly non-uniform flow formulation

First, a collocation formulation is presented in the physical space. Second, the solution in a Taylor–Lorentz space is discussed.

C.1.1.1 Physical space-time

A direct collocation method is presented to solve Eq. (5.4). This equation can be approximated using the variable expansion in Eqs. (5.6)-(5.9) to give

$$\boldsymbol{A}_c\boldsymbol{\phi} + \boldsymbol{B}_c\frac{\partial\boldsymbol{\phi}}{\partial n} = \boldsymbol{F}_c, \tag{C.1}$$

where the subscript "$_c$" denotes the collocation method and

$$\begin{aligned} A_c^{(lm)} = \delta_{lm}\hat{C}(\mathbf{x}_l) + \int_{\partial\Omega} N_m(\mathbf{x}) \left(\frac{\partial G(\mathbf{x}_l,\mathbf{x})}{\partial n} + 2\mathrm{i}k\mathbf{M}_0\cdot\mathbf{n}G(\mathbf{x}_l,\mathbf{x}) - M_\infty^2\frac{\partial G(\mathbf{x}_l,\mathbf{x})}{\partial x}n_x \right) dS(\mathbf{x}) \\ + \int_{\partial\Omega}\left[M_\infty^2 G(\mathbf{x}_l,\mathbf{x}) \left(\frac{\partial N_m(\mathbf{x})}{\partial\tau}\tau_x + \frac{\partial N_m(\mathbf{x})}{\partial\eta}\eta_x \right) n_x \right] dS(\mathbf{x}) \end{aligned} \tag{C.2}$$

$$B_c^{(lm)} = -\int_{\partial\Omega} G(\mathbf{x}_l, \mathbf{x}) N_m(\mathbf{x}) \left[1 - M_\infty^2 n_x^2\right] dS(\mathbf{x}) \tag{C.3}$$

and

$$F_c^{(l)} = \int_{\Omega} G(\mathbf{x}_l, \mathbf{x}) g(\mathbf{x}) dV(\mathbf{x}), \tag{C.4}$$

where l= 1,2,...,N_{dof} and m=1,2,...,N_{dof} with N_{dof} the number of degrees of freedom. The collocation points are denoted by $\mathbf{x}_l$, while $\mathbf{x}$ is a point on the boundary, $\partial\Omega$. In Eq. (C.1), either ϕ or $\partial\phi/\partial n$ is assigned on the boundary surface. A relationship between ϕ and $\partial\phi/\partial n$ can also be assigned. Once the boundary problem in Eq. (C.1) is solved, the solution at any point of the domain can be calculated using Eq. (5.15).

C.1.1.2 Transformed space-time

A direct collocation method is here provided to solve Eq. (4.65) in a transformed Taylor-Lorentz space. Applying the variable expansion in Eqs. (5.6) and (5.7), in the transformed space, to Eq. (4.65) gives

$$\tilde{\boldsymbol{A}}_c \tilde{\boldsymbol{\phi}} + \tilde{\boldsymbol{B}}_c \frac{\partial \tilde{\boldsymbol{\phi}}}{\partial \tilde{n}} = \tilde{\boldsymbol{F}}_c, \tag{C.5}$$

where

$$\tilde{A}_c^{(lm)} = \delta_{lm} C(\tilde{\mathbf{X}}_l) + \int_{\partial\tilde{\Omega}} N_m(\tilde{\mathbf{X}}) \frac{\partial \tilde{G}(\tilde{\mathbf{X}}_l, \tilde{\mathbf{X}})}{\partial \tilde{n}} d\tilde{S}(\tilde{\mathbf{X}}), \tag{C.6}$$

$$\tilde{B}_c^{(lm)} = -\int_{\partial\tilde{\Omega}} N_m(\tilde{\mathbf{X}}) \tilde{G}(\tilde{\mathbf{X}}_l, \tilde{\mathbf{X}}) d\tilde{S}(\tilde{\mathbf{X}}), \tag{C.7}$$

and

$$\tilde{F}^{(l)} = \int_{\tilde{\Omega}} \tilde{G}(\tilde{\mathbf{X}}_l, \tilde{\mathbf{X}}) \tilde{g}(\tilde{\mathbf{X}}) d\tilde{V}(\tilde{\mathbf{X}}), \tag{C.8}$$

where l= 1, 2,...,N_{dof}, m= 1, 2,...,N_{dof} and N_{dof} is the total number of degrees of freedom. $\tilde{\mathbf{X}}_l$ is a collocation point and $\tilde{\mathbf{X}}$ denotes a point on the transformed boundary surface. The solution in the physical domain can be calculated using the solution on the boundary and Eq. (5.72), and applying an inverse Taylor–Lorentz transform (see Sec. 2.6.3).

C.1.2 Taylor–Helmholtz formulation

A collocation formulation is here presented for Eq. (5.23). A discrete formulation of Eq. (5.23) is derived using the polynomial expansion in Eqs. (5.6) and (5.7) to yield

$$\boldsymbol{A}_{c,T} \boldsymbol{\phi} + \boldsymbol{B}_{c,T} \frac{\partial \boldsymbol{\phi}}{\partial n} = \boldsymbol{F}_{c,T} \tag{C.9}$$

where the subscript "$_c$" denotes the collocation matrix, "$_T$" is the Taylor–Helmholtz formulation and

$$A_{c,T}^{(lm)} = \delta_{lm} C(\mathbf{x}_l) + \int_{\partial\Omega} \left[N_m(\mathbf{x}) \left(\frac{\partial G_T(\mathbf{x}_l, \mathbf{x})}{\partial n} + 2ik\mathbf{M}_0 \cdot \mathbf{n} G_T(\mathbf{x}_l, \mathbf{x}) \right) \right] dS(\mathbf{x}), \tag{C.10}$$

$$B_{c,T}^{(lm)} = -\int_{\partial\Omega} N_m(\mathbf{x}) G_T(\mathbf{x}_l, \mathbf{x}) dS(\mathbf{x}), \tag{C.11}$$

$$F_{c,T}^{(l)} = \int_{\Omega} G_T(\mathbf{x}_l, \mathbf{x}) g(\mathbf{x}) dV(\mathbf{x}), \tag{C.12}$$

where l= 1, 2,...,N$_{dof}$, m=1, 2,...,N$_{dof}$ with N$_{dof}$ the total number of degrees of freedom. The collocation point is denoted as $\mathbf{x}_l$ and $\mathbf{x}$ denotes a point on the boundary surface. To solve Eq. (C.9), either ϕ or $\partial\phi/\partial n$ is assigned. Alternatively, a relationship between ϕ and $\partial\phi/\partial n$ can be prescribed. After solving the problem on the boundary based on Eq. (C.9), the solution at any point of the domain can be computed using Eq. (5.28).

C.2 Derivatives of the integral equation in the physical space

In this section, the integral formulation in Eq. (5.2) is derived to obtain the corresponding gradient, $\boldsymbol{\nabla}\phi$. The derivatives of Eq. (5.2) at $\mathbf{x}_p$ in the domain, Ω, can be written as

$$\begin{aligned}\hat{C}(\mathbf{x}_p)\frac{\partial\phi(\mathbf{x}_p)}{\partial x_{p_i}} + \phi(\mathbf{x}_p)\frac{\partial\hat{C}(\mathbf{x}_p)}{\partial x_{p_i}} = &\int_{\partial\Omega}\left[\frac{\partial G}{\partial x_{p_i}}\left(\frac{\partial\phi}{\partial n} - 2ik\mathbf{M}_0\cdot\mathbf{n}\phi\right) - \frac{\partial^2 G}{\partial n\partial x_{p_i}}\phi\right] dS(\mathbf{x}) \\ &- \int_{\partial\Omega}\left[M_\infty^2\left(\frac{\partial G}{\partial x_{p_i}}\frac{\partial\phi}{\partial x} - \phi\frac{\partial^2 G}{\partial x\partial x_{p_i}}\right)n_x\right] dS(\mathbf{x}) + \int_{\Omega_s}\frac{\partial G}{\partial x_{p_i}} g dV(\mathbf{x}),\end{aligned} \tag{C.13}$$

where x_{p_i} denotes the derivative along the i-th axis computed at $\mathbf{x} = \mathbf{x}_p$, with $G = G(\mathbf{x}_p, \mathbf{x})$.

The above equation can be rewritten projecting $\boldsymbol{\nabla}\phi$ in the normal direction, $\mathbf{n}$, to the boundary surface, $\partial\Omega$,

$$\begin{aligned}\hat{C}(\mathbf{x}_p)\frac{\partial\phi(\mathbf{x}_p)}{\partial n_p} + \phi(\mathbf{x}_p)\frac{\partial\hat{C}(\mathbf{x}_p)}{\partial n_p} = &\int_{\partial\Omega}\left[\frac{\partial G}{\partial n_p}\frac{\partial\phi}{\partial n} - \frac{\partial^2 G}{\partial x\partial n_p}\phi\right] dS(\mathbf{x}) \\ &- \int_{\partial\Omega}\left[M_\infty^2\left(\frac{\partial G}{\partial n_p}\frac{\partial\phi}{\partial x} - \phi\frac{\partial^2 G}{\partial x\partial n_p}\right)n_x\right] dS(\mathbf{x}) + \int_{\Omega_s}\frac{\partial G}{\partial n_p} g dV(\mathbf{x}),\end{aligned} \tag{C.14}$$

where $\mathbf{M}_0 \cdot \mathbf{n} = 0$ on an impermeable stationary surface and $\mathbf{n}_p$ is the normal vector to the boundary, $\partial\Omega$, at $\mathbf{x}_p$. The derivative in the above equation differs from the generalised normal derivative (see Eq. (2.59)) in that the terms depending on the mean flow are neglected. In this case, we are not interested in recovering the equation in terms of acoustic velocity consistent with Eq. (5.2) but we want to estimate the acoustic particle velocity normal to a generic surface. Hence, the above equation is not an integral solution to the weakly non-uniform flow equation. This is a subtle point related to the formulation with mean flow.

C.3 Regularisation of 2D hyper-singular integrals

The regularisation approach proposed for the hyper-singular integral in Sec. 5.2.5.2 is extended to 2D problems. For a 2D problem in the transformed space, it can be shown that [89]

$$\int_{\partial\tilde{\Omega}}\int_{\partial\tilde{\Omega}}\tilde{\phi}_p^*\frac{\partial^2\tilde{G}}{\partial\tilde{n}\partial\tilde{n}_p}\tilde{\phi}d\tilde{S}(\tilde{\mathbf{X}})d\tilde{S}(\tilde{\mathbf{X}}_p)=\int_{\partial\tilde{\Omega}}\int_{\partial\tilde{\Omega}}\tilde{G}\left[\tilde{k}^2\tilde{\mathbf{n}}\cdot\tilde{\mathbf{n}}_p\tilde{\phi}\tilde{\phi}_p^*-\frac{\partial\tilde{\phi}}{\partial\tilde{\tau}}\frac{\partial\tilde{\phi}_p}{\partial\tilde{\tau}_p}\right]d\tilde{S}(\tilde{\mathbf{X}})d\tilde{S}(\tilde{\mathbf{X}}_p), \tag{C.15}$$

where $\tilde{\boldsymbol{\tau}}$ and $\tilde{\boldsymbol{\tau}}_p$ are the tangent vectors to the boundary surface, $\partial\tilde{\Omega}$, respectively at $\tilde{\mathbf{X}}$ and $\tilde{\mathbf{X}}_p$. According to Taylor-Lorentz transform (see Sec. 2.6.3), the tangent vector in the transformed space can be written as

$$\tilde{\boldsymbol{\tau}}=\frac{1}{\sqrt{1-M_\infty^2\tau_y^2}}(\tau_x\mathbf{i}+\beta_\infty\tau_y\mathbf{j}). \tag{C.16}$$

Considering Eq. (5.54), the tangential derivative of $\tilde{\phi}$ can be rewritten as

$$\frac{\partial}{\partial\tilde{\tau}}=\frac{1}{\sqrt{1-M_\infty^2\tau_y^2}}\left[\beta_\infty\frac{\partial}{\partial\tau}-\frac{1}{c_\infty}\left(\frac{M_\infty}{\beta_\infty}\tau_x+\beta_\infty\mathbf{M}_0'\cdot\boldsymbol{\tau}\right)\frac{\partial}{\partial t}\right]. \tag{C.17}$$

For a harmonic problem, Eqs. (5.52), (5.53), (5.56) and (C.15) can be used to yield

$$\begin{aligned}\int_{\partial\Omega}\int_{\partial\Omega}\phi_p^*\mathcal{L}_n(G)\phi dS(\mathbf{x})dS(\mathbf{x}_p)&=\int_{\partial\Omega}\int_{\partial\Omega}G\left\{\frac{k^2}{\beta_\infty^2}\hat{\mathbf{n}}\cdot\hat{\mathbf{n}}_p\phi\phi_p^*\right\}dS(\mathbf{x})dS(\mathbf{x}_p)\\-\int_{\partial\Omega}\int_{\partial\Omega}\beta_\infty G\left[\frac{\partial\phi}{\partial\tau}-\mathrm{i}k\left(\frac{M_\infty\tau_x}{\beta_\infty^2}+\mathbf{M}_0'\cdot\boldsymbol{\tau}\right)\phi\right]&\left[\frac{\partial\phi_p^*}{\partial\tau}-\mathrm{i}k\left(\frac{M_\infty\tau_{x,p}}{\beta_\infty^2}+\mathbf{M}_0'\cdot\boldsymbol{\tau}_p\right)\phi_p^*\right]dS(\mathbf{x})dS(\mathbf{x}_p),\end{aligned} \tag{C.18}$$

where $\hat{\mathbf{n}}(\mathbf{x})=(\beta_\infty n_x,n_y)$, $(n_x,n_y)=(-\tau_y,\tau_x)$ and $\mathcal{L}_n(G)$ denotes the generalised second order normal derivative (see Eq. (5.50)). In the above equation, the norm of the Jacobian associated with the geometrical transformation of lines operated by the Taylor–Lorentz transform has been applied (see Eq. (2.52)). In the above equation, terms of order $M_\infty^2M_0'$ can be neglected based on the weakly non-uniform flow ansatz.

C.4 Non-uniform flow at the overdetermination points

In this section, we show the results for the test case presented in Sec. 6.6.1 (see Fig. 6.34) based on the combined integral formulation developed in Sec. 5.2.5.2 and a non-uniform flow at the overdetermination points.

In Fig. C.1, we show the absolute value of the acoustic velocity potential against the non-dimensional frequency, ka, for $M_\infty=0.1$ and 0.3 at $\mathbf{x}_B$ (see Fig. 6.34). The results based on a non-uniform flow at the overdetermination points are compared with the results based on a uniform flow. In Figure C.2, the SPL is depicted against the angle θ along an arc of

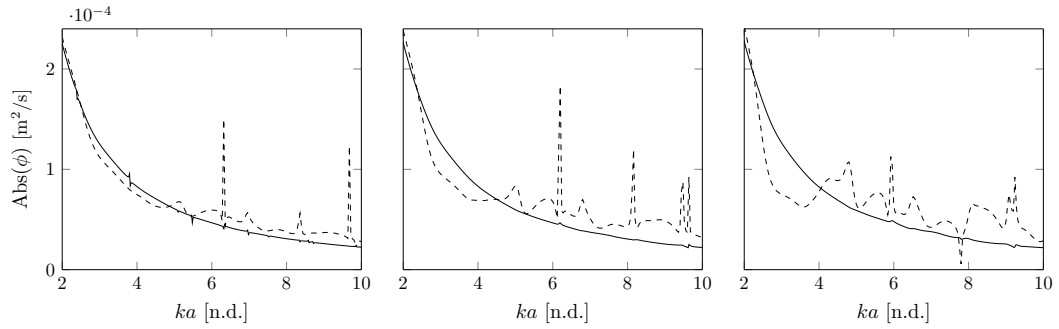

(a) $M_\infty = 0.1$ (b) $M_\infty = 0.2$ (c) $M_\infty = 0.3$

Figure C.1: Absolute value of the acoustic velocity potential ϕ at a point $\mathbf{x}_B$ against the non-dimensional frequency ka for the problem described in Fig. 6.34, based on Eq. (5.40). Solid: uniform flow overdet. points. Dashed: non-uniform flow overdet. points.

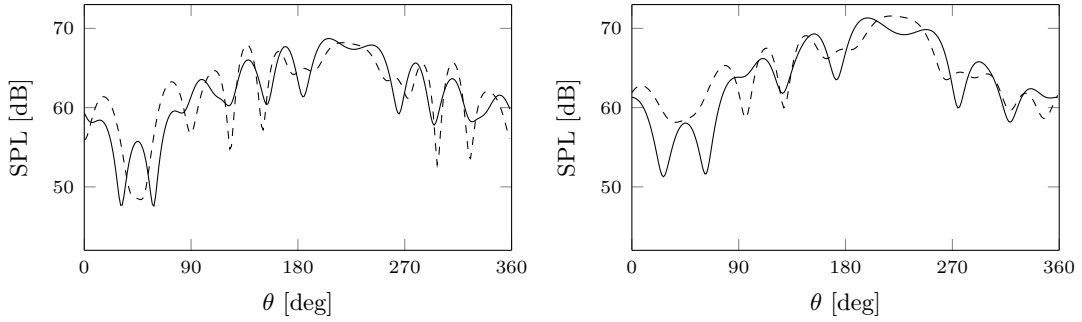

(a) $ka = 5.34$, $M_\infty = 0.2$. (b) $ka = 3.62$, $M_\infty = 0.3$

Figure C.2: SPL along an arc of field points centered at $\mathbf{x} = (0, 0)$ with radius $r_{fp} = 8a$ for the problem described in Fig. 6.34. The combined integral approach is given in Eq. (5.47), based on Eq. (5.40). Solid: uniform flow overdet. points. Dashed: non-uniform flow overdet. points.

field points with radius $r_{fp} = 8a$, centered at $\mathbf{x} = (0, 0)$, for a non-dimensional frequency $ka = 5.34$ and $M_\infty = 0.2$. It also illustrates the results for $ka = 3.62$ and $M_\infty = 0.3$. Again, we compare the results based on a non-uniform flow to the results based on a uniform flow at the overdetermination points.

It is shown that the solution based on a non-uniform flow at the overdetermination points is inaccurate compared to the corresponding solution with uniform flow that provided reliable results (see Sec. 6.6.1). The non-uniform mean flow component is large compared to the corresponding uniform flow component, clearly violating the weakly non-uniform flow ansatz. This leads to inconsistent results along all the frequencies considered in this example.

C.5 Indirect boundary integral formulation in a Taylor–Lorentz space

We derive the integral solution to the weakly non-uniform flow formulation in a transformed Taylor–Lorentz space based on velocity boundary conditions and an indirect formulation. First, we formulate an indirect statement of the integral solution provided in Sec. 4.3. Second, we apply a Taylor–Lorentz transformation. Finally, we simplify the formulation for velocity boundary conditions. In this section, the problem is formulated in terms of velocity potential provided that it can be accommodated for acoustic pressure without effort.

The integral solution to the weakly non-uniform flow formulation is

$$\hat{C}(\mathbf{x}_p)\phi(\mathbf{x}_p) = \int_{\partial\Omega} \left[G\frac{\partial\phi}{\partial n} - \phi\frac{\partial G}{\partial n} - 2ik\mathbf{M}_0\cdot\mathbf{n}G\phi - M_\infty^2\left(G\frac{\partial\phi}{\partial x} - \phi\frac{\partial G}{\partial x}\right)n_x \right] dS(\mathbf{x}). \quad \text{(C.19)}$$

We assume an impermeable stationary open surface where $\mathbf{M}_0\cdot\mathbf{n} = 0$. The, we consider the above equation written along an infinitely thin boundary surface, where we denote with "$\pm$" two opposite sides (see Fig. C.3):

$$\begin{aligned}\phi(\mathbf{x}_p) = &\int_{\partial\Omega^+} \left[G^+\frac{\partial\phi^+}{\partial n^+} - \phi^+\frac{\partial G^+}{\partial n^+} - M_\infty^2\left(G^+\frac{\partial\phi^+}{\partial x} - \phi^+\frac{\partial G^+}{\partial x}\right)n_x^+ \right] dS(\mathbf{x}^+) \\ &+ \int_{\partial\Omega^-} \left[G^-\frac{\partial\phi^-}{\partial n^-} - \phi^-\frac{\partial G^-}{\partial n^-} - M_\infty^2\left(G^-\frac{\partial\phi^-}{\partial x} - \phi^-\frac{\partial G^-}{\partial x}\right)n_x^- \right] dS(\mathbf{x}^-),\end{aligned} \quad \text{(C.20)}$$

where $\phi^\pm = \phi(\mathbf{x}^\pm)$, $G^\pm = G(\mathbf{x}_p, \mathbf{x}^\pm)$. Let us reduce the thickness of the surface to zero, giving $\mathbf{n}^+ = -\mathbf{n}^- = \mathbf{n}$. The convention on the normal vector, $\mathbf{n}$, has already been applied to the coefficient, $\hat{C}(\mathbf{x}_p)$, which yields a unit value (see Sec. 4.3). The above equation can then be rewritten as

$$\phi(\mathbf{x}_p) = \int_{\partial\Omega} \left[G\sigma' - \frac{\partial G}{\partial n}\xi' - M_\infty^2\left(G\sigma'_x - \xi'\frac{\partial G}{\partial x}\right)n_x \right] dS(\mathbf{x}), \quad \text{(C.21)}$$

where $\xi' = \phi(\mathbf{x}^+) - \phi(\mathbf{x}^-)$, $\sigma' = \partial\phi(\mathbf{x}^+)/\partial n - \partial\phi(\mathbf{x}^-)/\partial n$, $\sigma'_x = \partial\phi(\mathbf{x}^+)/\partial x - \partial\phi(\mathbf{x}^-)/\partial x$ and $dS(\mathbf{x}^-) = dS(\mathbf{x}^+) = dS(\mathbf{x})$. For convenience, we have denoted the single and double layer potentials, σ' and ξ', using the same notation as that reported in Sec. 8.2.2 although in this case we refer to acoustic velocity potential rather than acoustic pressure.

Using the approach proposed in Sec. 5.2.5.1, i.e. applying a Taylor–Lorentz transform, the above equation can be rewritten in the transformed space as

$$\tilde{\phi}(\tilde{\mathbf{X}}_p) = \int_{\partial\tilde{\Omega}} \left[\tilde{\sigma}\tilde{G} - \frac{\partial\tilde{G}}{\partial\tilde{n}}\tilde{\xi}' \right] d\tilde{S}(\tilde{\mathbf{X}}), \quad \text{(C.22)}$$

where $\tilde{\xi}' = \tilde{\phi}(\tilde{\mathbf{X}}^+) - \tilde{\phi}(\tilde{\mathbf{X}}^-)$ and $\tilde{\sigma}' = \partial\tilde{\phi}(\tilde{\mathbf{X}}^+)/\partial\tilde{n} - \partial\tilde{\phi}(\tilde{\mathbf{X}}^-)/\partial\tilde{n}$ denote the variables in the Taylor–Lorentz space. Equation (C.22) can also be obtained by reducing the weakly

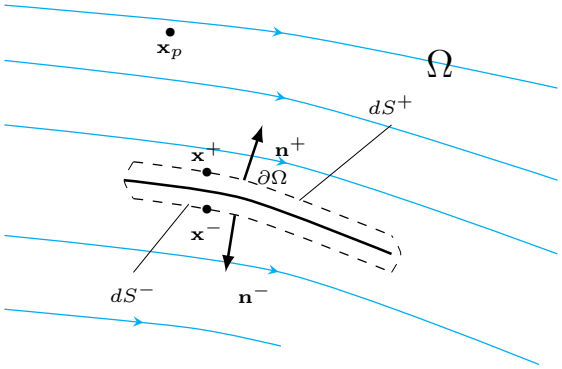

Figure C.3: Sketch of an open radiating surface in a mean flow. An open surface is simply seen as the limit of a closed control surface for the thickness that goes to zero.

non-uniform formulation to the standard Helmholtz problem in the transformed space for which an indirect boundary integral solution is well-known [135].

Equation (C.22) is independent of the mean flow and can be used to solve a boundary element problem for either an open or a coupled internal/external noise propagation problem. Nonetheless, it can be derived in the normal direction $\tilde{\mathbf{n}}$ to the transformed boundary surface and rewritten in terms of the particle velocity, $\tilde{u}'_{\tilde{n}} = \partial\tilde{\phi}(\tilde{\mathbf{X}})/\partial\tilde{n}$. If the particle velocity, $u'_{\tilde{n}}$, is assigned on the boundary surface, $\tilde{\sigma}'$ is equal to 0 and

$$\tilde{u}'_{\tilde{n}}(\tilde{\mathbf{X}}_p) = -\int_{\partial\tilde{\Omega}} \frac{\partial\tilde{G}}{\partial\tilde{n}}\tilde{\xi}' d\tilde{S}(\tilde{\mathbf{X}}). \tag{C.23}$$

Equation (C.23) has been used in Sec. 8.2.2 where the problem was conveniently rewritten in terms of acoustic pressure, $\tilde{p}$, rather than velocity potential.

C.6 Potential mean flow in a Taylor–Lorentz space-time

In this section, we rewrite the derivatives of the mean flow potential in a transformed Taylor–Lorentz space in terms of those for the physical space. Note that, the mean flow is time independent and, therefore, the Taylor–Lorentz transform simply reduces to the Prandtl-Glauert transform, i.e.

$$\tilde{X} = \frac{x}{\beta_\infty}, \quad \tilde{Y} = y, \quad \tilde{Z} = z, \tag{C.24}$$

where we assume that the uniform mean flow is aligned with the x-axis. The corresponding derivative operator can then be written as

$$\left(\frac{\partial}{\partial\tilde{X}}, \frac{\partial}{\partial\tilde{Y}}, \frac{\partial}{\partial\tilde{Z}}\right) = \left(\beta_\infty\frac{\partial}{\partial x}, \frac{\partial}{\partial y}, \frac{\partial}{\partial z}\right). \tag{C.25}$$

For convenience, in the above equation, we retained the notation used for the variables in a transformed Taylor–Lorentz space but we dropped the dependence on the time variable. If we apply the above equation to the non-uniform component of the mean flow potential, $\Phi'_0(\mathbf{x})$, one has

$$\left(\frac{\partial\Phi'_0(\mathbf{x})}{\partial\tilde{X}}, \frac{\partial\Phi'_0(\mathbf{x})}{\partial\tilde{Y}}, \frac{\partial\Phi'_0(\mathbf{x})}{\partial\tilde{Z}}\right) = \left(\beta_\infty M'_{0,x}, M'_{0,y}, M'_{0,z}\right), \tag{C.26}$$

where $\left(M'_{0,x}, M'_{0,y}, M'_{0,z}\right) = (\partial\Phi'_0/\partial x, \partial\Phi'_0/\partial y, \partial\Phi'_0/\partial z)$. Equation (C.26) has been used in Sec. 2.6.3 for the definition of the derivative operators in a transformed Taylor–Lorentz space.

References

[1] S. Mancini, R.J. Astley, G. Gabard, S. Sinayoko, and M. Tournour. A quasi-potential flow formulation for the prediction of the effect of the circulation on the acoustic shielding from a lifting body by means of a finite element method. 10th European Conference on Noise Control Engineering, Maastricht, Netherlands, 2015.

[2] S. Mancini, R.J. Astley, G. Gabard, S. Sinayoko, and M. Tournour. On the numerical accuracy of a combined FEM/radiating-surface approach for noise propagation in unbounded domains. 22nd International Congress on Sound and Vibration, Florence, Italy, 2015.

[3] S. Mancini, R.J. Astley, S. Sinayoko, G. Gabard, and M. Tournour. An integral formulation for wave propagation on weakly non-uniform potential flows. *Journal of Sound and Vibration*, 385:184–201, 2016.

[4] S. Mancini, S. Sinayoko, R.J. Astley, G. Gabard, and M. Tournour. Boundary element formulation for wave propagation in weakly non-uniform potential flows. Number AIAA 2016-2713 in AIAA/CEAS Aeroacoustics conference, Lyon, France, 2016.

[5] S. Mancini, R.J. Astley, S. Sinayoko, G. Gabard, and M. Tournour. A combined boundary integral formulation for wave propagation in weakly non-uniform flows. The 23rd International Congress on Sound and Vibration, Athens, Greece, 2016.

[6] S. Mancini, R.J. Astley, S. Sinayoko, G. Gabard, and M. Tournour. A variable transformation approach for boundary element solutions of wave propagation in non-uniform potential flows. 45th International Congress and Exposition of Noise Control Engineering, Hamburg, Germany, 2016.

[7] R.J. Astley. Can technology deliver acceptable levels of aircraft noise? 43rd International Congress on Noise Control Engineering, Melbourne, Australia, 2014.

[8] U.S. Department of Transportation (DOT). Federal Aviation Regulations (FAR) - part 36; noise standards: Aircaft type and airworthiness certification. Technical report, Federal Aviation Administration (FAA), 1969.

[9] N. Dickinson. ICAO noise standards. Technical report, ICAO, 2013.

[10] X. Zhang. Aircraft noise and its nearfield propagation computations. *Acta Mechanica Sinica*, 28(4):960–970, 2012.

[11] High Level Group on Aviation Research. Flightpath 2050. Europe's Vision for Aviation. Technical report, European Commission, 2011.

[12] Annual report 2015. Technical report, ICAO, 2015.

[13] W.M. Dobrzynski. Almost 40 years of airframe noise research: what did we achieve. *Journal of Aircraft*, 47:353–367, 2010.

[14] W.M. Dobrzynski. *Airframe noise: landing gear noise*, volume 6 of *Encyclopedia of Aerospace Engineering*, pages 3529–3539. 2008.

[15] R.W. Stoker, Y.P. Guo, C. Street, and N. Burnside. Airframe noise source locations of a 777 aircraft in flight and comparisons with past model scale tests. Number AIAA 2003-3232 in 9th AIAA/CEAS Aeroacoustics Conference, pages 1–12, Hilton Head, South Carolina, 2003.

[16] D.G. Crighton. Basic principles of aerodynamic noise generation. *Progress in Aerospace Sciences*, 16(1):31–96, 1975.

[17] Airport Commission. Discussion paper 05: Aviation noise. Technical report, UK Government, 2013.

[18] M. J. T. Smith. *Aircaft Noise*. Cambridge University Press, New York, 1989.

[19] R. J. Astley. Numerical methods for noise propagation in moving flows, with application to turbofan engines. *Acoustical Science and Technology*, 30(4):227–239, 2009.

[20] R.J. Astley and W. Eversman. Acoustic transmission in lined ducts with flow, part 2: the finite element method. *Journal of Sound and Vibration*, 74:103–121, 1981.

[21] S. Petersen, C. Farhat, and R. Tezanur. A space-time discontinuous Galerkin method for the solution of the wave equation in the time-domain. *International Journal of Numerical Methods in Engineering*, 78(3):275–295, 2008.

[22] C.K.W. Tam and J.C. Webb. Dispersion-relation-preserving finite difference schemes for computational acoustics. *Journal of Computational Physics*, 107:262–281, 1993.

[23] G. Gabard, H. Bériot, A.G. Prinn, and K. Kucukcoskun. An Adaptive, High-Order Finite-Element Method for Aeroengine Acoustics. Number AIAA 2016-2970 in 22nd AIAA/CEAS Aeroacoustics Conference, Lyon, France, 2016.

[24] A.N. Gumerov and R. Duraiswami. *Fast Multipole Methods for Helmholtz Equation in Three Dimensions*. Elsevier, London, 2004.

[25] W. Hackbusch. A sparse matrix arithmetic based on H-matrices. Part I: Introduction to H-matrices. *Computing*, 62(2):89–108, 1999.

[26] W. R. Wolf and S. K. Lele. Fast acoustic scattering predictions with non-uniform potential flow effects. *Journal of the Brazilian Society of Mechanical Sciences and Engineering*, 35(4):407–418, 2013.

[27] N. Balin, F. Casenave, F. Dubois, E. Duceau, S. Duprey, and I. Terrasse. Boundary element and finite element coupling for aeroacoustics simulations. *Journal of Computational Physics*, 294:274–296, 2015.

[28] A. Agarwal, A.P. Dowling, H. Shin, W. Graham, and S. Sefi. Ray-tracing approach to calculate acoustic shielding by a flying wing airframe. *AIAA Journal*, 45(5):1080–1090, 2007.

[29] D. Papamoschou and S. Mayoral. Modeling of jet noise sources and their diffraction with uniform flow. Number AIAA 2013-0326 in 51st Aerospace Science Meeting, Grapevine, Texas, 2013.

[30] E. Perrey-Debain, Y. Gervais, and M. Guilbaud. Development and application of the Dual Reciprocity Boundary Element Method for acoustic propagation in inhomogeneous axisymmetric domains. *Acustica*, 86(1):83–92, 2000.

[31] K. Taylor. A transformation of the acoustic equation with implications for wind-tunnel and low-speed flight tests. *The Royal Society*, 65(1):125–136, 1979.

[32] R.J. Astley and J.G. Bain. A 3D boundary element scheme for acoustic radiation in low Mach number. *Journal of Sound and Vibration*, 109(1):445–465, 1986.

[33] A. Agarwal and A. P. Dowling. Low-frequency acoustic shielding by the silent aircraft airframe. *AIAA Journal*, 45(2):358–365, 2007.

[34] S. Mayoral and D. Papamoschou. Prediction of jet noise shielding with forward flight effects. Number AIAA 2013-0010 in 51st Aerospace Science Meeting, Grapevine, Texas, 2013.

[35] A. Tinetti and M. Dunn. Aeroacoustic noise prediction using the fast scattering code. Number AIAA 2005-3061 in 11th AIAA/CEAS Aeroacoustics Conference, Monterey, California, 2005.

[36] C. Clancy. *Boundary Element methods for the prediction of aircraft noise shielding in flight*. Ph.D. thesis, University of Dublin, Dep. of Mechanical and Manufacturing Eng., 2010.

[37] J.E. Ffowcs Williams and D.L. Hawkings. Sound generation by turbulence and surfaces in arbitrary motion. *Philosophical Transactions of the Royal Society*, 264A:321–342, 1969.

[38] F. Farassat and M.K. Myers. Extension of the Kirchhoff formula to radiation from moving surfaces. *Journal Sound and Vibration*, (123):451–460, 1988.

[39] A. Najafi-Yazdi, G.A. Bres, and L. Mongeau. An acoustic analogy formulation for moving sources in uniformly moving media. *Proceedings of the Royal Society of London A*, 467:144–165, 2011.

[40] T.W. Wu and L. Lee. A direct boundary integral formulation for acoustic radiation in a subsonic uniform flow. *Journal of Sound and Vibration*, 175(1):51–63, 1994.

[41] F. Q. Hu. An efficient solution of time domain boundary integral equations for acoustic scattering and its acceleration by Graphics Processing Units. Number AIAA 2013-2018 in 19th AIAA/CEAS Aeroacoustics Conference, Berlin, Germany, 2013.

[42] F. Casenave, A. Ern, and G. Sylvand. Coupled BEM-FEM for the convected Helmholtz equation with non-uniform flow in a bounded domain. *Journal of Computational Physics*, (257):627–644, 2014.

[43] T.W. Wu (ed.). *Boundary Element acoustics: Fundamental and computer codes*. WIT Press, Southampton, 2000.

[44] A. Gregory, S. Sinayoko, A. Agarwal, and J. Lasenby. An acoustic spacetime and the Lorentz transformation in aeroacoustics. *International Journal of Aeroacoustics*, 14(7):977–1003, 2015.

[45] N. Balin, G. Sylvand, and J. Robert. Fast methods applied to BEM solvers for acoustic propagation problems. Number AIAA 2016-2712 in 22nd AIAA/CEAS Aeroacoustics Conference, Lyon, France, 2016.

[46] L. Morino. Is there a difference between Aeroacoustics and Aerodynamics? an aeroelastician's viewpoint. *AIAA Journal*, 41(7):1209–1223, 2003.

[47] A. Gregory, A. Agarwal, J. Lasenby, and S. Sinayoko. Geometric algebra and an acoustic space time for propagation in non-uniform flow. 22nd International Congress on Sound and Vibration, Florence, Italy, 2015.

[48] A. D. Pierce. Wave equation for sound in fluids with unsteady inhomogeneous flow. *Journal of the Acoustical Society of America*, 87(6):2292–2299, 1990.

[49] R.J. Astley. A finite element, wave envelope formulation for acoustical radiation in moving flows. *Journal of Sound and Vibrations*, 3:471–485, 1985.

[50] H.A. Schenck. Improved integral formulation for acoustic radiation problems. *Journal Acoustical Society of America*, 44:41–58, 1968.

[51] A.J. Burton and G.F. Miller. The application of integral equation methods to the numerical solution of some exterior boundary-value problems. *Proceedings of the Royal Society of London A*, 323:201–210, 1971.

[52] S. Marburg and S. Amini. A cat's eye radiation with boundary elements: comparative study on treatment of irregular frequencies. *Journal of Computational Acoustics*, 13:21–45, 2005.

[53] G.K. Batchelor. *An Introduction to Fluid Dynamics*. Cambridge University Press, Cambridge, United-Kingdom, 1967.

[54] M. Sukop and D.T. Thorne. *Lattice Boltzmann Modeling: an introduction for geoscientists and engineers*. Springer Verlag, 2006.

[55] Z.S. Guo and N. Wang. Lattice BGK model for incompressible Navier-Stokes equation. *Journal of Computational Physics*, 165:288–306, 2000.

[56] A. Michalke. On spatially growing disturbances in an inviscid shear layer. *Journal of Fluid Mechanics*, 23(3):521–544, 1965.

[57] P.G Drazin and W.H. Reid. *Hydrodynamic Stability*. Cambridge University Press, New York, 1989.

[58] A. Hirschberg and S.W. Rienstra. *An introduction to Acoustics*. Eindhoven University of Technology, 2004.

[59] T. Toulorge. *Efficient Runge-Kutta Discontinuous Galerkin Methods Applied to Aeroacoustics*. Ph.D. thesis, Katholieke Universiteit Leuven, 2012.

[60] J. Tournadre, P. Martinez-Lera, and W. Desmet. Numerical study of the acosutic response of a single orifice with turbulent mean flow. 22nd International Congress on Sound and Vibration, Florence, Italy, 2015.

[61] J. Delfs. *Basics of Aeroacoustics*. Lecture notes at Technische Universit at Braunschweig, 2012.

[62] C. Bailly and D. Juvé. Numerical solution of acoustic propagation problems using linearized euler equations. *AIAA Journal*, 38:22–28, 2000.

[63] R. Ewert and W. Schröder. Acoustic Perturbations equations based on flow decomposition via source filtering. *Journal of Computational Physics*, 4(188):365–398, 2003.

[64] D.C. Pridmore-Brown. Sound propagation in a fluid flowing through an attenuating duct. *Journal of Fluid Mechanics*, (4):393–406, 1958.

[65] W. Möring. A well posed acoustic analogy based on moving medium. Number 2008-6919 in Aeroacoustic workshop SWING, pages 142–178, Dresden, Germany, 1999.

[66] L.M.B.C. Campos. On 36 forms of the acosutic wave equation in potential flows and inhomogenous media. *Applied Mechanics Review, Transactions of the ASME*, (60):149–171, 2007.

[67] S. W. Rienstra. Sound diffraction at a trailing edge. *Journal of Fluid Mechanics*, 108(1):443, 2006.

[68] A.G. Prinn. *Efficient Finite Element Methods for Aircraft Engine Noise Prediction*. Ph.D. thesis, University of Southampton, 2014.

[69] C. Clancy and H.J. Rice. Acoustic shielding at low Mach number potential flow incorporating a wake model using BEM. Number AIAA 2009-3174 in 15th AIAA/CEAS Aeroacoustics conference, Miami, Florida, 2009.

[70] T. Heffernon, D. Angland, X. Zhang, and M. Smith. The effect of flow circulation on the scattering of landing gear noise. Number AIAA 2015-3257 in 21st AIAA/CEAS Aeroacoustics Conference, Dallas, Texas, 2015.

[71] M.K. Myers. On the acoustic boundary condition in the presence of flow. *Journal of Sound and Vibration*, 71(3):429–434, 1980.

[72] K.U. Ingard. Influence of fluid motion past a plane boundary on sound reflection, absorption and transmission. *Journal of the Acoustical Society of America*, 31(7):1035, 1959.

[73] G. Gabard. A comparison of impedance boundary conditions for flow acoustics. *Journal of Sound and Vibration*, 332:714–724, 2013.

[74] W. Eversman. The boundary condition at an impedance wall in a non-uniform duct with potential mean flow. *Journal of Sound and Vibration*, 246(1):63–69, 2001.

[75] C.J. Chapman. Similarity variables for sound radiation in a uniform flow. *Journal of Sound and Vibration*, 233(1):157–164, 2000.

[76] C.K.W. Tam and L. Auriault. Jet mixing noise from fine scale-turbulence. *AIAA Journal*, 37(2):145–153, 1999.

[77] R.D. Sandberg and N.D. Sandham. Direct numerical simulation of turbulent flow past a trailing edge and the associated noise generation. *Journal of Fluid Mechanics*, 596:353–385, 2008.

[78] R.D. Sandberg and L.E. Jones. Direct numerical simulations of low Reynolds number flow over airfoils with trailing-edge serration. *Journal of Sound and Vibration*, 330(9):3818–3831, 2011.

[79] D. Casalino, A. Hazir, and A. Mann. Turbofan broadband noise prediction using the Lattice Boltzmann Method. Number AIAA 2016-2945 in 22nd AIAA/CEAS Aeroacoustics Conference, Lyon,France, 2016.

[80] E.J. Brambley. Well-posed boundary condition for acoustic liners in straight ducts with flow. *AIAA Journal*, 49(6):1272–1282, 2011.

[81] G. Gabard and E.J. Brambley. A full discrete dispersion analysis of time-domain simulations of acoustic liners with flow. *Journal of Computational Physics*, 273(15):310–326, 2014.

[82] C. Bogey, Bailly. C., and D. Juvé. Computation of flow noise using source terms in linearized Euler's equations. *AIAA Journal*, 40(2):235–242, 2002.

[83] K. Hamiche. *A High-Order Finite Element Model for Acoustic Propagation.* Ph.D. thesis, University of Southampton, 2016.

[84] R.J. Astley, R. Sugimoto, and P. Mustafi. Computational Aero-acoustics for fan duct propagation and radiation. current status and application to turbofan liner optimisation. *Journal of Sound and Vibration*, 330:3832–3845, 2011.

[85] B. Engquist and A. Majda. Absorbing boundary conditions for the numerical simulation of waves. *Mathematics of Computation*, 31(139):629–651, 1977.

[86] W. Eversman. Mapped infinite wave envelope elements for acoustic radiation in a uniformly moving media. *Journal Sound and Vibration*, (224):665–687, 1999.

[87] Astley R.J. Infinite elements for wave problems: A review of current formulations and an assessment of accuracy. *International Journal for Numerical Methods in Engineering*, 49(7):951–976, 2000.

[88] A. Bermudez, L. Hervella-Nieto, A. Prieto, and R. Rodriguez. An optimal perfectly matched layer with unbounded absorbing function for time-harmonic acoustic scattering problems. *Journal of Computational Physics*, 223(2):469–488, 2007.

[89] H. Beriot and M. Tournour. On the locally-conformal perfectly matched. Number 086 in NOVEM Conference, Oxford, UK, 2009.

[90] J.C.F. C.A. Brebbia, Telles and L.C. Wrobel. *Boundary element techniques. Theory and application in engineering.* Springer-Verlag, Berlin, 1984.

[91] S. Marburg and B. Nolte. *Computational Acoustics of Noise Propagation in Fluids - Finite and Boundary Element Methods.* Springer, 2008.

[92] S.M. Kirkup. *The boundary element method in acoustics.* Integrated sound software, 2007.

[93] K. Ho-Le. Finite element mesh generation methods: a review and classification. *Computer-Aided Design*, 20(1):27–38, 1988.

[94] R. Dautray and J.L. Lions. *Mathematical Analysis and Numerical Methods for Science and Technology*, volume 4. Springer-Verlag, Berlin, 1993.

[95] D.J. Chappell, P.J. Harris, D Henwood, and R. Chakrabarti. A stable boundary element method for modelling transient acoustic radiation. *Journal of Acoustical Society of America*, 120(1):74–80, 2006.

[96] E. Van't Wout, P. Gelat, T. Betcke, and S. Arridge. A fast boundary element method for the scattering analysis of high-intensity focused ultrasound. *Journal of Acoustical Society of America*, 138:2726, 2015.

[97] M.R. Hestenes and E. Stiefel. Methods of conjugate gradients for solving linear systems. *Journal of Research of the National Bureau of Standards*, 49(6):409–436, 1952.

[98] Y. Saad and M.H. Schultz. GMRES: A generalized minimal residual algorithm for solving nonsymmetrical linear systems. *SIAM Journal on Scientific and Statistical Computing*, 7(3):856–869, 1986.

[99] S. Marburg and S. Schneider. Performance of iterative solvers for acoustic problems. Part I. Solvers and effect of diagonal preconditioning. *Engineering Analysis with Boundary Elements*, 7(27):727–750, 2003.

[100] H. Bériot, E. Perrey-Debain, M. Ben Tahar, and C. Vayssade. Plane wave basis in Galerkin BEM for bidimensional wave scattering. *Engineering Analysis with Boundary Elements*, 34(2):130–143, 2010.

[101] E. Perrey-Debain, J. Trevelyan, and Bettes P. Plane wave interpolation in direct collocation boundary element method for radiation and wave scattering: numerical aspects and applications. *Journal of Sound and Vibration*, 261:839–858, 2003.

[102] E. Perrey-Debain, J. Trevelyan, and P. Bettess. Wave boundary elements: a theoretical overview presenting applications in scattering of short waves. *Engineering Analysis with Boundary Elements*, 28:131–141, 2004.

[103] E. Perrey-Debain, Laghrouche, P. O. Bettess, and J. Trevelyan. Plane wave basis finite elements and boundary elements for three-dimensional wave scattering. *Philosophical Transactions of the Royal Society A*, 362:561–577, 2004.

[104] S. Redonnet, G. Desquesnes, E. Manoha, and C. Parzani. Numerical Study of Acoustic Installation Effects with a Computational Aeroacoustics Method. *AIAA Journal*, 48(5):929–937, 2010.

[105] M. Karimi, P. Croacker, N. Kessissoglou, and N. Peake. Aeroacoustic analysis of a cylinder in low Mach number flow using a periodic CFD-BEM technique. Number AIAA 2016-2842 in 22nd AIAA/CEAS Aeroacoustics Conference, 2016.

[106] P. Croaker, N. Kessisoglou, R. Kinns, and S. Marburg. Fast low-storage method for evaluating Lighthill's volume quadrupoles. *AIAA Journal*, 51(4):867–884, 2013.

[107] P. Croaker, N. Kessisoglou, and S. Marburg. Strongly singular and hypersingular integrals for aeroacoustic incident fields. *International Journal of Numerical Methods in Fluids*, 77:274–318, 2015.

[108] N. Papaxanthos and E. Perrey-Debain. Integral formulations for the predictions of low Mach number flow noise with non-compact solid surfaces. Number AIAA 2016-2716 in 22nd AIAA/CEAS Aeroacoustics Conference, Lyon, France, 2016.

[109] K. Mimani, P. Croaker, M. Karimi, C.J. Doolan, and N. Kessisoglou. Hybrid CFD-BEM and time-reversal techniques applied to localise flow-induced noise sources generated by a flat-plate. ACOUSTICS Conference, Brisbane, Australia, 2016.

[110] P. Croaker, Karimi M. Moreau, D., and N. Kessisoglou. Low Mach number flow induced noise prediction of a wall–mounted airfoil using a hybrid RANS-BEM technique. 45th International Congress and Exposition of Noise Control Engineering, Hamburg, Germany, 2016.

[111] S. Chandler-Wilde and S. Langdon. *Boundary element methods for Acoustics*. Department of Mathematics, University of Reading, 2007. Lecture Notes.

[112] M. Bebendorf. *Hierarchichal Matrices: A Means to Efficiently Solve Elliptic Boundary Values Problems*. Springer-Verlag, Berlin, 2008.

[113] A. Delnevo, S. Le Saint, G. Sylvand, and I. Terrasse. Numerical methods: fast multipole method for shielding effects. Number AIAA 2005-3061 in 11th AIAA/CEAS Aeroacoustics Conference, Monterey, California, 2005.

[114] L. Greengard and V. Rokhlin. A fast algorithm for particle simulations. *Journal of Computational Physics*, 73(2):325–348, 1987.

[115] M. Messner, M. Schanz, and E. Darvé. Fast directional multilevel summation for oscillatory kernels based on chebyshev interpolation. *Journal of Computational Physics*, 231(4):1175–1196, 2012.

[116] C.C. Lu and W.C. Chew. Fast far field approximation for calculating the RCS of large objects. *Microwave and Optical Technology Letters*, 8(5):238–241, 1995.

[117] M. Messner. *Fast Boundary Element Methods in Acoustics*. Monographic Series TU Graz, 2012.

[118] S. Börm, L. Grasedyck, and W. Hackbusch. *Hierarchical Matrices*. Lecture notes, Max Plank Institut. 2006.

[119] M. Gennaretti and C. Testa. A boundary integral formulation for sound scattered by moving bodies. *Journal of Sound and Vibration*, 314(3-5):712–737, 2008.

[120] M. Gennaretti, G. Bernardini, C. Poggi, and C. Testa. A boundary-field integral formulation for sound scattering of moving bodies. Number AIAA 2016-2715 in 22nd AIAA/CEAS Aeroacoustics conference, Lyon, France, 2016.

[121] G. Gatica, N Heuer, and F.J. Sayas. A direct coupling of local discontinuous Galerkin method and boundary element method. *Journal of Mathematics of Computation*, 79:1369–1394, 2010.

[122] R. Bustinza, G. N. Gatica, and F.J. Sayas. On the coupling of local discontinuous Galerkin and boundary element methods for non-linear exterior transmission problems. *IMA Journal of Numerical Analysis*, 28(2):225–244, 2007.

[123] F. Q. Hu. Further Development of a Time Domain Boundary Integral Equation Method for Aeroacosutic Scattering Computations. Number AIAA 2014-3194 in 20th AIAA/CEAS Aeroacoustics Conference, Atlanta, GA, 2014.

[124] M. Barbarino and D. Bianco. BEM-FMM simulation of uniform mean flows with a new internal-point algorithm for the CHIEF spurious solutions removals. 23rd International Congress on Sound and Vibration, Athens, Greece, 2016.

[125] W.R. Wolf and S.K. Lele. Wideband fast multipole boundary element method: application to acoustic scattering from aerodynamic bodies. *International Journal for Numerical Methods in Fluids*, 67(12):2108–2129, 2011.

[126] E. Perrey-Debain. Analysis of convergence and accuracy of the DRBEM for axisymmetric Helmholtz-type equation. *Engineering Analysis with Boundary Elements*, 23:703–711, 1999.

[127] L. Lee, T.W. Wu, and P. Zhang. A dual-reciprocity method for acoustic radiation in a subsonic non-uniform flow. *Engineering Analysis with Boundary Elements*, 13:365–370, 1994.

[128] P.W. Partridge and C.A. Brebbia. Computer implementation of the BEM dual reciprocity method for the solution of general field equations. *Communications in applied numerical methods*, 6:83–92, 1990.

[129] A. J. Nowak and P. W. Partridge. Comparison of the dual reciprocity and the multiple reciprocity methods. *Engineering Analysis with Boundary Elements*, 10(2):155–160, 1992.

[130] J. Zhenlin and W. Xueren. Application of dual reciprocity boundary element method to predict acoustic attenuation characteristics of silencers with mean flow. 14th International Congress on Sound and Vibration, Cairn, Australia, 2007.

[131] P. Juhl. A numerical study of the coefficient matrix of the boundary element method near the characteristic frequencies. *Journal of Sound and Vibration*, 175(1):39–50, 1994.

[132] I.L. Chen, J.T. Chen, and M.T. Liang. Analytical study and numerical experiments for radiation and scattering problems using the CHIEF method. *Journal of Sound and Vibration*, 248(5):809–828, 2001.

[133] L. Lee and T.W. Wu. An enhanced CHIEF method for steady-state elastodynamics. *Engineering Analysis with Boundary Elements*, 12(2):75–83, 1993.

[134] G. Bartolozzi, R. D'Amico, A. Pratellesi, and M. Pierini. An efficient method for selecting CHIEF points. 8th International Conference on Structural Dynamics, EURODYN, pages 3091–3098, Leuven, Belgium, 2011.

[135] R. D'Amico, A. Pratellesi, M. Pierini, and M. Tournour. Efficient method to avoid fictitious eigenvalues for indirect BEM. ISMA Conference, Leuven, Belgium, 2010.

[136] T.W. Wu and A.F. Syebert. A weighted residual formulation for the CHIEF method in acoustics. *Journal of the Acoustical Society of America*, 90:1608–1614, 1991.

[137] G.W. Benthien and H.A. Schenck. Nonexistence and Nonuniqueness Problems Associated with Integral Equation Methods in Acoustics. *Computers and Structures*, 65(3):295–305, 1997.

[138] K.A. Cunefare and G. Koopmann. A boundary element method for acoustic radiation valid for all wavenumbers. *Journal of the Acoustical Society of America*, 85(1):39–48, 1989.

[139] S.G. Mikhlin. *Variational Methods in Mathematical physics*. MacMillan, 1964.

[140] C.-J. Zheng, H.-B. Chen, H.-F. Gao, and L. Du. Is the Burton-Miller formulation really free of fictitious eigenfrequencies? *Engineering Analysis with Boundary Elements*, 59:43–51, 2015.

[141] S. Marburg. The Burton and Miller method: unlocking another mystery of its coupling parameter. *Journal of Computational Acoustics*, 24(1), 2015.

[142] S. Amini. On the choice of the coupling parameter in boundary integral formulations of the exterior acoustic problem. *Applicable Analysis*, 35:75–92, 1990.

[143] T. Terai. On the calculation of sound fields around three dimensional objects by integral equations methods. *Journal of Sound and Vibration*, 69(1):71–100, 180.

[144] S. Marburg. A review of the coupling parameter of the Burton and Miller boundary element method. 43rd International Congress and Exposition on Noise Control Engineering, Melbourne, 2014, 2014.

[145] M.A. Hamdi. An integral variational formulation for the resolution of the Helmholtz equation including mixed boundary conditions. *Comptes Rendus de l'Académie des Sciences*, 292:17–20, 1981.

[146] A.G. Polimeridis and V.T. Yioultsis. On the Direct Evaluation of Weakly Singular Integrals in Galerkin Mixed Potential Integral Equation Formulations. *IEEE Transaction on antennas and propagation*, 56(9):3011–3019, 2008.

[147] A. Agarwal, P.J. Morris, and M. Ramani. Calculation of sound propagation in non-uniform flows: suppression of instability waves. *AIAA Journal*, 42(1):80–88, 2004.

[148] P. Zhang and T.W. Wu. A hypersingular integral formulation for acoustic radiation in moving flows. *Journal of Sound and Vibration*, 206(3):309–326, 1997.

[149] D. Stanescu, M.Y. Hussaini, and F. Farassat. Aircraft engine noise scattering by fuselage and wings: a computational approach. *Journal of Sound and Vibration*, 263(2):319–333, 2003.

[150] G. Gabard. Discontinuous Galerkin methods with plane waves for time-harmonic problems. *Journal of Computational Physics*, 225(2):1961–1984, 2007.

[151] K. Hamiche, G. Gabard, and H. Bériot. A higher-order finite element method for the linearised Euler equations. ISMA Conference, pages 1311–1326, 2014.

[152] I. Babuška and S. Sauter. Is the pollution effect of the FEM avoidable for the Helmholtz equation considering high wave numbers? *SIAM Journal of Numerical analysis*, (34):2392–2423, 1997.

[153] H. Bériot, G. Gabard, and E. Perrey-Debain. Analysis of high-order finite elements for convected wave propagation. *International Journal for Numerical Methods in Engineering*, 96(11):665–688, 2013.

[154] M. Williamschen, G. Gabard, and H. Bériot. Performance of the dgm for the linearized Euler equations with non-uniform mean-flow. Number AIAA 2015-3277 in 21st AIAA/CEAS Aeroacoustics Conference, Dallas, Texas, 2015.

[155] S. Wang and F.L. Teixeira. Dispersion-relation-preserving FDTD algorithms for large-scale three-dimensional problems. *IEEE Transactions on Antennas and Propagation*, 51(8):1818–1828, 2003.

[156] G. Ashcroft and X. Zhang. Optimized prefactored compact schemes. *Journal of Computational Physics*, 190(2):459–477, 2003.

[157] A.A. Iob, R. Arina, and C. Schipani. Frequency-domain linearized Euler model for turbomachinery noise radiation through engine exhaust. *AIAA Journal*, 48(4):848–858, 2010.

[158] N. Chevaugeon, J.-F. Remacle, X. Gallez, P. Ploumans, and S. Caro. Efficient discontinuous Galerkin methods for solving acoustic problems. Number AIAA 2005-2823 in 11th AIAA/CEAS Aeroacoustics Conference, Monterey, California, 2005.

[159] Y. Zhao and P. Morris. The prediction of fan exhaust noise propagation. Number 2005-2815 in 11th AIAA/CEAS Aeroacoustics Conference, Monterey, California, 2005.

[160] G. Bériot H. Lieu, A. Gabard. A comparison of high-order polynomial and wave based methods for the Helmholtz problem. *Journal of Computational Physics*, 321:105–125, 2016.

[161] Z. Rarata. *Application and Assessment of Time-Domain DGM for Intake Acoustics Using 3D Linearized Euler Equations*. Ph.D. thesis, University of Southampton, 2014.

[162] S. Solin, P. Karel and I. Dolezel. *Higher-Order Finite Element Menthods*. Chapman & Hall/CRC, Boca Raton, 2004.

[163] H. Bériot, G. Gabard, and E. Perrey-Debain. Analysis of high-order finite elements for convected wave propagation. *International Journal for Numerical Methods in Engineering*, 96(11):665–688, 2013.

[164] H. Bériot, A. Prinn, and G. Gabard. Efficient implementation of high-order finite elements for Helmholtz problems. *International Journal for Numerical Methods in Engineering*, 106:213–240, 2016.

[165] I.M. Babuška and B.Q. Guo. The h, p and h-p version of the finite element method; basis theory and applications. *Advances in Engineering Software*, 15(3-4):159–174, 1992.

[166] J.M. Melenk and I. Babuška. The partition of unity finite element method: basic theory and applications. *Computer Methods in Applied Mechanics and Engineering*, 139:289–314, 1996.

[167] J.D. Chazot, B. Nennig, and E. Perrey-Debain. Performances of the partition of unity finite element method for the analysis of two-dimensional interior sound fields with absorbing materials. *Journal of Sound and Vibration*, 332:1918–1929, 2013.

[168] P. Gamallo and R. J. Astley. The partition of unity finite element method for short wave acoustic propagation on nonuniform potential flows. *International Journal of Numerical Methods in Engineering*, 65:425–444, 2006.

[169] O. Cessenat and B. Després. Application of an ultra-weak variational formulation of elliptic PDEs to the two-dimensional helmholtz problem. *SIAM Journal on Numerical Analysis*, 35(1):225–299, 1998.

[170] C. Farhat, I. Harari, and L.P. Franca. The discontinuous enrichment method. Computer methods in applied mechanics and engineering. *SIAM Journal on Numerical Analysis*, 190(48):6455–6479, 2001.

[171] M.J. Lighthill. On Sound Generated Aerodynamically. I. General Theory. *Proceedings of the Royal Society of London*, 211(1107):564–587, 1952.

[172] G.M. Lilley. On the noise from jets. Number 131 on Noise Mechanisms in AGARD Conference Proceedings, Brussels, Belgium, 1974.

[173] M.E. Goldstein. *Aeroacoustics*. McGraw-Hill International Book Company, 1976.

[174] E. Manoha, B. Troff, and P. Sagaut. Trailing edge noise prediction using large eddy simulation and acoustic analogy. *AIAA Journal*, 38(4):575–583, 2000.

[175] K. S. Brentner and F. Farassat. Modeling aerodynamically generated sound of helicopter rotors. *Progress in Aerospace Sciences*, 39:83–120, 2003.

[176] D. J. Bodony and S. K. Lele. Current status of jet noise predictions using large-eddy simulation. *AIAA Journal*, 46(2):364–380, 2008.

[177] S. Sinayoko, A. Agarwal, and Z. Hu. Flow decomposition and aerodynamic sound generation. *Journal of Fluid Mechanics*, 668:335–350, 2011.

[178] M.T. Kube-McDowell, G.A. Blaisdell, and A.S. Lyrintzis. Empirical source strength correlations for RANS-based acoustic analogy methods. 53rd AIAA Aerospace Science Meeting, Kissimmee, Florida, 2015.

[179] V. Rosa, R. Self, C. Ilario, I. Naqavi, and P. Tucker. Modelling velocity correlations with LES and RANS for prediction of noise from isothermal or hot jets. Number AIAA 2016-2810 in 22nd AIAA/CEAS Aeroacoustics Conference, Lyon, France, 2016.

[180] A.D. Pierce. *Acoustics: an introduction to its physical principles and applications*. Acoustical Society of America, 1989.

[181] J.B. Keller and R.M. Lewis. Asymptotic methods for partial differential equations: The reduced wave equation and Maxwell's equation. D. McLaughlin, J.B. Keller, G. Papanicolau (Editors), Survey in applied Mathematics, 1995.

[182] J.B. Freund and T. G. Fleischman. Ray traces through unsteady jet turbulence. *International Journal of Aeroacoustics*, 1(1):83–96, 2002.

[183] M.E. Goldstein. High frequency sound emission from moving point multipole sources embedded in arbitrary transversely sheared mean flows. *Journal of Sound and Vibration*, 80(14):448–522, 1982.

[184] I.D. Abrahams, G.A. Kriegsmann, and E.L. Reiss. Sound radiation and caustic formation from a point source in a wall shear layer. *AIAA journal*, 32(6):1135–1144, 1994.

[185] S. Redonnet, C. Parzani, E. Manoha, and D. Lizarazu. Numerical study of 3D acoustic installation effects through a hybrid Euler/BEM method. Number AIAA 2007-3500 in 13th AIAA/CEAS Aeroacoustics Conference, Rome, Italy, 2007.

[186] D. Papamoschou. Prediction of Jet Noise Shielding. Number AIAA 2010-653 in 48th AIAA Aerospace Sciences Meeting, Orlando, Florida, 2010.

[187] A. Mosson, D. Binet, and J. Caprile. Simulation of Installation Effects of Aircraft Engine Rear Fan Noise with ACTRAN/DGM. Number AIAA 2014-3188 in 20th AIAA/CEAS Aeroacoustics Conference, Atlanta, GA, 2014.

[188] F.G. Hu, M.E. Pizzo, and M.N. Douglass. On the assessment of acoustic scattering and shielding by time domain boundary integral equation solutions. Number AIAA 2016-2779 in 22nd AIAA/CEAS Aeroacoustics Conference, Lyon, France, 2016.

[189] D. Casalino and A. Hazir. Lattice Boltzmann based aeroacoustic simulation of turbofan noise installation effects. 23rd International Congress on sound and Vibration, Athens, Greece, 2016.

[190] I.E. Garrick and C.E. Watkins. A theoretical study of the effect of forward speed on the free-space sound-pressure field around propellers. Technical report, NACA Technical Note 3018, 1953.

[191] A.G. Polimeridis, S. Järvenpää, P. Ylä-Oijala, L.J. Gray, S.P. Kiminki, and J.R. Mosing. On the evaluation of hyper-singular double normal derivative kernels in surface integral equation methods. *Engineering Analysis with Boundary Elements*, 37:205–210, 2003.

[192] K.M. Mitzner. Acoustic scattering from an interface between media of greately different density. *Journal of Mathematical Physics*, 18:2053–2060, 1966.

[193] C.A. Brebbia and R. Butterfield. Formal equivalence of direct and indirect boundary element methods. *Applied Mathematical Modelling*, 2:132–134, 1978.

[194] W. Hackbusch. *Integral Equations: Theory and Numerical Treatment.* Birkhaäuser-Verlag, Basel-Boston-Berlin, 1995.

[195] S. Caorsi, D. Moreno, and F. Sidoti. Theoretical and numerical treatment of surface integrals involving the free-space Green's function. *IEEE Transactions on Antennas and Propagation*, 41(9):1448–1457, 1993.

[196] M.A. Khayat and D.R. Wilton. Numerical evaluation of singular and near-singular integrals. *IEEE Transactions on Antennas and Propagation*, 53:3180–3190, 2005.

[197] M. Bonnet and M. Guiggiani. Galerkin BEM with direct evaluation of hypersingular integrals. *Electronic Journal of Boundary elements*, 1(2):95–111, 2003.

[198] S. Sauter and C. Schwab. *Boundary Element Methods.* Springer-Verlag Berlin, Heidelberg, 2011.

[199] L. Morino. A general theory of unsteady compressible potential aerodynamics. Technical report, *NASA* CR 2464, 1974.

[200] A.-W. Maue. Zur formulierung eines allegemeinen begungsprobelms durch eine integralgleichung. *Z. Phys.*, (126):601–618, 1943.

[201] A. Prinn, G. Gabard, and H. Bériot. Finite element simulation of noise radiation through shear layers. Acoustics, pages 1329–1334, 2012.

[202] The Mathworks Inc., Natick, MA, USA. *MATLAB documentation for Matlab R2014b*, 2014.

[203] J. Morris and O. Brien. The scattering of sound from a spatially distributed axisymmetric cylindrical source by a circular cylinder. *Journal of Acousical Society of America*, 97(5):2651–2656, 1994.

[204] R.H. Kirchhoff. *Potential flows: computer graphic solutions.* Marcel Dekker, Inc., 1985.

[205] J. Gaffney, A. McAlpine, and M. Kingan. Sound radiation of fan tones from an installed turbofan aero-engine: fuselage boundary-layer refraction effects. Number AIAA 2016-2878 in 22nd AIAA/CEAS Aeroacoustics Conference, Lyon, France, 2016.

[206] J. Vassberg, M. DeHaan, S. Rivers, and R. Wahls. Development of a common research model for applied CFD validation studies. Number 2008-6919 in AIAA Applied Aerodynamics Conference, pages 10–13, Honolulu, Hawaii, 2008.

[207] N. S. Altman. An introduction to kernel and nearest-neighbor nonparametric regression. *The American Statistician*, 46(3):175–185, 1992.

[208] G. Gabard. Discontinuous Galerkin methods with plane waves for the displacement-based acoustic equation. *International Journal for Numerical Methods in Engineering*, 66(3):549–569, 2006.

[209] M. Siefert, J. Delfs, and B. Caruelle. Refraction and Scattering in High Mach Number Boundary Layer. Number AIAA 2011-2847 in 17th AIAA/CEAS Aeroacoustics Conference, Portland, Oregon, 2011.

[210] A. Adetifa. *Prediction of supersonic fan noise generated by turbofan aircraft engines.* Ph.D. thesis, University of Southampton, 2015.

[211] E.J. Rice, M. F. Heidmann, and T.G. Sofrin. Modal propagation angles in a cylindrical duct with flow and their relation to sound radiation. Technical report, *NASA* TM 79030, 1979.

[212] LMS International, Leuven, Belgium. *Virtual.Lab Acoustics R13, user's manual*, 2014.